

Molecular rubies: novel spin-flip NIR-emitter

Synthesis, understanding and first applications

Dissertation

Zur Erlangung des Grades
“Doktor der Naturwissenschaften”
Im Promotionsfach Chemie

am Fachbereich Chemie, Pharmazie und Geowissenschaften
der Johannes Gutenberg-Universität Mainz

Sven Fabian Otto

geboren in Gießen

20. Juni 2018

Colophon

This thesis was typeset with $\text{\LaTeX} 2_{\epsilon}$. It uses the *Clean Thesis* style developed by Ricardo Langner. The design of the *Clean Thesis* style is inspired by user guide documents from Apple Inc.

Download the *Clean Thesis* style at <http://cleanthesis.der-ric.de/>.

Die vorliegende Arbeit wurde in der Zeit von März 2015 bis Juni 2018 am Institut für Anorganische Chemie und Analytische Chemie der Johannes Gutenberg-Universität Mainz unter Anleitung von Prof. Dr. Katja Heinze angefertigt.

Mainz, 20. Juni 2018

Dekan [REDACTED]

1. Berichterstatter [REDACTED]

2. Berichterstatter [REDACTED]

Tag der mündlichen Prüfung 25. Juli 2018

Kurzzusammenfassung

Verbindungen, welche Emission im nahen Infrarot (NIR) zeigen, sind interessant für eine Vielzahl von Anwendungen. Diese reichen vom Einsatz in (O)LEDs und Lichtleitern, als Lasermedium über fälschungssichere Tinte bis Sensoren. Insbesondere für die Anwendung in Sensoren sind lösliche, molekulare Emitter nötig, wofür zur Zeit meist Komplexe von Seltenerdmetallen oder Edelmetallen eingesetzt werden. Obwohl es sehr schwierig ist, Emission von Metallkomplexen der ersten Übergangsmetallreihe zu erreichen, ist es, aufgrund des hohen Preises und der Seltenheit der aktuell eingesetzten Materialien, ein schnell wachsendes Forschungsfeld.

Diese Arbeit beschreibt die Entwicklung einer neuen Klasse von hoch emissiven NIR-Emittern, basierend auf Chrom(III). Die präsentierten Chrom(III)-Komplexe weisen Lumineszenzquantenausbeuten von bis zu 11 % in Wasser und bis zu 30 %, mit deuterierten Liganden auf. Die Emissionslebensdauern erreichen dabei Werte von fast einer Millisekunde (mehr als zwei Millisekunden mit deuterierten Liganden) und aufgrund des Spin-Flip-Charakters der Phosphoreszenz sind die Emissionsbanden außerordentlich scharf.

Erste Anwendungen wurden ebenfalls untersucht. Die duale NIR-Emission von $[\text{Cr}(\text{ddpd})_2]^{3+}$ erlaubt Temperaturmessungen in Lösung und in Nanopartikeln ohne Referenzfarbstoff, da sich die emittierenden Zustände in einem thermisch populiertem Gleichgewicht befinden und die entsprechenden Emissionsbanden gut aufgelöst sind.

Weitere vielversprechende Anwendungsmöglichkeiten für Sensoren sind der Nachweis von molekularem Sauerstoff mittels Phosphoreszenzlöschung und die Messung von Druck durch die starke Rotverschiebung der Emissionsbanden beim Anlegen von hydrostatischem Druck.

Das Löschen der Phosphoreszenz durch molekularen Sauerstoff wurde weiterhin verwendet, um Singulett-Sauerstoff photokatalytisch zu produzieren. Dieser wurde dann *in situ* zur Oxidation von tertiären, aliphatischen Aminen genutzt, welche anschließend mit Cyaniden α -Aminonitrile in guten Ausbeuten ergaben.

Die Emission des ebenfalls hochemissiven Komplex $[\text{Cr}(\text{H}_2\text{tpda})_2]^{3+}$ kann durch Deprotonieren gelöscht und in wasserfreien Lösungsmitteln durch Reprotonieren wiederhergestellt werden.

Zum vollständigen Verständnis der beteiligten angeregten Zustände und um die erhaltenen experimentellen Daten zu ergänzen, wurden theoretische Methoden, wie Dichtefunktionaltheorie als auch *ab initio*-Berechnungen, eingesetzt.

Weiterhin wurde der Zink(II)-Komplex $[\text{Zn}(\text{ddpd})_2]^{2+}$ untersucht. Aufgrund der geringen Präferenz des d^{10} Ions Zink(II) für eine bestimmte Koordinationsgeometrie und der Flexibilität des Liganden, befindet sich der Komplex in der Gegenwart von Chloridionen befindet in einem Gleichgewicht mit $[\text{ZnCl}_4]^{2-}$ und $[\text{ZnCl}_2(\text{ddpd})]$.

Ebenfalls strukturell interessant ist der, von Sebastian Preiß hergestellte und charakterisierte, erste mononukleare Gold(II)-Komplex $[\text{Au}(\text{tpp})]$. DFT-Berechnungen konnten die Jahn-Teller-Verzerrung zweiter Ordnung reproduzieren, diese wird durch die relativistische Kontraktion der 6s-Orbitale des Metalls hervorgerufen.

Abstract

Near infrared (NIR) emissive compounds are of great interest for many applications ranging from (O)LEDs and laser media over fiber optics and security inks to optical chemical sensors. The latter in particular requires molecular and soluble emitters, a role filled at most times by complexes of rare earth or precious metals.

Even though it is very challenging to achieve emission from earth abundant metal complexes, it recently is, due the high price and scarcity of the currently employed materials, a rapidly growing field of research.

This work describes the development of a new class of strong NIR emitter, based on chromium(III). The presented chromium(III) complexes feature luminescence quantum yields up to 11 % in water and up to 30 % if the ligand is deuterated, with lifetimes of close to a millisecond (more than two milliseconds in the deuterated cases). Due to the spin-flip nature of the emission, the emission bands are exceptionally sharp.

First applications of these new emitters have also been explored. The dual emission of $[\text{Cr}(\text{ddpd})_2]^{3+}$ allows the measurement of temperature in solution and nanoparticles without a reference, since the emissive states are in a thermal equilibrium and the emission bands are well resolved.

Further promising sensing applications include the detection of molecular oxygen by the quenching of the phosphorescence and the measurement of pressure, due to a strong red shift of the emission bands upon applied pressure.

The luminescence quenching by molecular oxygen, has further been exploited for the photocatalytic production of singlet oxygen. This has been used *in situ* for the oxidation of tertiary, aliphatic amines and their subsequent reaction with cyanide gave α -amino-nitriles in good yields.

The strong emission of $[\text{Cr}(\text{H}_2\text{tpda})_2]^{3+}$ is quenched by deprotonation and can, in the absence of water, be recovered by re-protonation.

To fully understand the involved excited states and supplement the experimental data, theoretical methods have been employed. These include density functional theory as well as ab initio calculations.

Furthermore, the zinc(II) complex $[\text{Zn}(\text{ddpd})_2]^{2+}$ has been investigated. It enters an equilibrium with $[\text{ZnCl}_4]^{2-}$ and $[\text{ZnCl}_2(\text{ddpd})]$ in the presence of chloride ions, as a result of the d^{10} ions coordination diversity and the ligands flexibility.

Also structurally interesting is the first mononuclear gold(II) complex [Au(tp₂)], synthesized and characterized by Sebastian Preiß. High level DFT calculations could verify the second order Jahn-Teller distortion arising from the relativistic contraction of the metals 6s orbital.

Contents

1	Introduction	3
1.1	Near infrared emission	5
1.1.1	Excited state decay mechanisms	5
1.1.2	Applications	13
1.2	Luminescent sensor materials	14
1.2.1	pH sensing	15
1.2.2	Oxygen sensing	16
1.2.3	Temperature sensing	18
1.2.4	Responsive nanoprobes	19
1.2.5	Sensing multiple analytes	20
1.3	Chromium(III) complexes	22
1.3.1	Photophysical properties: the d^3 electron configuration	23
1.3.2	Strategies towards strong emission	25
1.3.3	Applications	27
2	Aim of the work	31
3	Results and discussion	35
3.1	$[\text{Cr}(\text{ddpd})_2]^{3+}$: a Molecular, Water-Soluble, Highly NIR-Emissive Ruby Analogue	39
3.2	Thermo-Chromium: A Contactless Optical Molecular Thermometer	45
3.3	Photo-Chromium: Sensitizer for Visible-Light-Induced Oxidative C–H Bond Functionalization – Electron or Energy Transfer?	51
3.4	Deuterated Molecular Ruby with Record Luminescence Quantum Yield	59
3.5	Molecular Ruby under pressure	65
3.6	A strongly luminescent chromium(III) complex acid	71
3.7	Three-in-One Crystal: The Coordination Diversity of Zinc Polypyridine Complexes	79
3.8	Structure and reactivity of a mononuclear gold(II) complex	89
4	Summary and Outlook	99
4.1	Understanding and exploiting long-lived near-infrared emission of a molecular ruby	101
4.2	Outlook	112

5	References	115
6	Appendix	123
6.1	Supporting Information: $[\text{Cr}(\text{ddpd})_2]^{3+}$: a Molecular, Water-Soluble, Highly NIR-Emissive Ruby Analogue	124
6.2	Supporting Information: Thermo-Chromium: A Contactless Optical Molecular Thermometer	159
6.3	Supporting Information: Photo-Chromium: Sensitizer for Visible-Light-Induced Oxidative C–H Bond Functionalization – Electron or Energy Transfer?	165
6.4	Supporting Information: Deuterated Molecular Ruby with Record Luminescence Quantum Yield	177
6.5	Supporting Information: Molecular ruby under pressure	205
6.6	Supporting Information: A strongly luminescent chromium(III) complex acid	225
6.7	Supporting Information: Three-in-One Crystal: The Coordination Diversity of Zinc Polypyridine Complexes	249
6.8	Supporting Information: Structure and reactivity of a mononuclear gold(II) complex	273
6.9	Conductivity measurements of $[\text{Cr}(\text{ddpd})_2](\text{X})_3$	305
7	Acknowledgments	313

List of Abbreviations

Å	Ångström
Abs.	absorption
acac	acetylacetonato
bpmp	2,6-bis((pyridin-2-yl)methyl)pyridine
bpy	2,2'-bipyridine
CP	coproporphyrin
dcpp	2,6-bis(2-pyridylketone)pyridine
ddpd	<i>N,N'</i> -dimethyl- <i>N,N'</i> -dipyridine-2-ylpyridine-2,6-diamine
DFT	density functional theory
dGMP	deoxy-guanosine monophosphate
DNA	deoxyribonucleic acid
dpp	4,7-diphenyl-1,10-phenantrolin
DSSC	dye sensitized solar cell
E_A	activation energy
EnT	energy transfer
ES	excited state
¹ES	singlet excited state
³ES	triplet excited state
ET	electron transfer
Fl.	Fluorescence
FRET	Förster resonance energy transfer
GS	ground state
¹GS	singlet ground state
H₂tpda	2,6-bis(2-pyridylamino)pyridine
HOMO	highest occupied molecular orbital
ISC	intersystem crossing

k_B	Boltzman constant
λ	wavelength
λ_{em}	emission wavelength
λ_{exc}	excitation wavelength
LED	light emitting device
LMCT	ligand-to-metal charge transfer
LUMO	lowest unoccupied molecular orbital
MB	molecular beacon
MLCT	metal-to-ligand charge transfer
NIR	near infrared
NR	non-radiative
OLED	organic light emitting device
Φ	luminescence quantum yield
PES	potential energy surface
Ph.	phosphorescence
phen	1,10-phenanthroline
ppa	2-phenylpyridine
PSP	pressure sensitive paint
RNA	ribonucleic acid
r.t.	room temperature
τ	luminescence lifetime
TADF	thermally activated delayed fluorescence
tpy	2,2';6',2"-terpyridine
VR	vibrational relaxation

Introduction

Polypyridine complexes of transition metal ions have a long and successful history. The first known complex $[\text{Fe}(\text{bpy})_3]\text{Cl}_2$ (bpy = 2,2'-bipyridine) was synthesized in 1888 by Fritz Blau even before bipyridine itself was isolated, which he did one year later.^[1,2] Thirty-five years later the first terpyridine complex $[\text{Fe}(\text{tpy})_2]\text{Cl}_2$ (tpy = 2,2';6',2''-terpyridine) and five years later terpyridine was isolated.^[3,4] From there on it took nearly 60 years until polypyridine complexes started to draw attention beyond mere structural curiosity, first as building blocks in supramolecular chemistry.^[5] Today, polypyridine complexes of transition metal ions are omnipresent in coordination chemistry and they are extensively studied resulting in a plethora of different applications, arising from the favorable photophysical and redox properties.

An important group of complexes used in photochemical applications are ruthenium complexes, which are for example employed as light-harvesting sensitizer in dye sensitized solar cells (DSSC),^[6] a wide range of applications exploiting luminescence, be it in NIR light emitting electrochemical cells,^[7,8] optical switches^[9] or sensors^[10] and photocatalysis.^[11] To this end ruthenium complexes of terpyridine and derivatives thereof have been studied extensively by experimental and theoretical means and today there exists a deep understanding of the complexes' photophysical capabilities and limits.^[12]

Due to the scarcity of ruthenium and other successfully employed metals (e.g. rhenium, iridium, osmium, palladium or platinum), a lot of the research, while resulting in a deep knowledge of the involved systems and , mostly satisfied scientific curiosity with only minimal applications, often limited to academic use.

Thus the focus recently shifted towards the utilization of earth-abundant and hence more sustainable metal ions, mainly first row transition metal ions for applications. In the last decade quite a number of catalytical active complexes, especially nickel(0) and nickel(II) complexes, which are able to replace palladium and platinum complexes for cross coupling reactions, emerged.^[13] The crucial steps in the catalytic cycle of the Negishi coupling, the oxidative addition and the reductive elimination, involve the transfer of two electrons, a reaction which nickel is in principle not capable of. Utilizing a polypyridine ligand enables this reaction by storing the second electron/hole on the ligand, exploiting the often observed redox non-innocent nature of polypyridines.^[14,15]

A very striking example for the redox non-innocent behavior of polypyridine ligands are the terpyridine complexes of chromium and manganese. These exist in five (four in case of manganese) different formal oxidation states, but closer investigation reveals, that in all cases the metal ion stays in its most stable oxidation state (Cr^{III} and Mn^{II}), while all reductions are ligand centered:^[16–18]

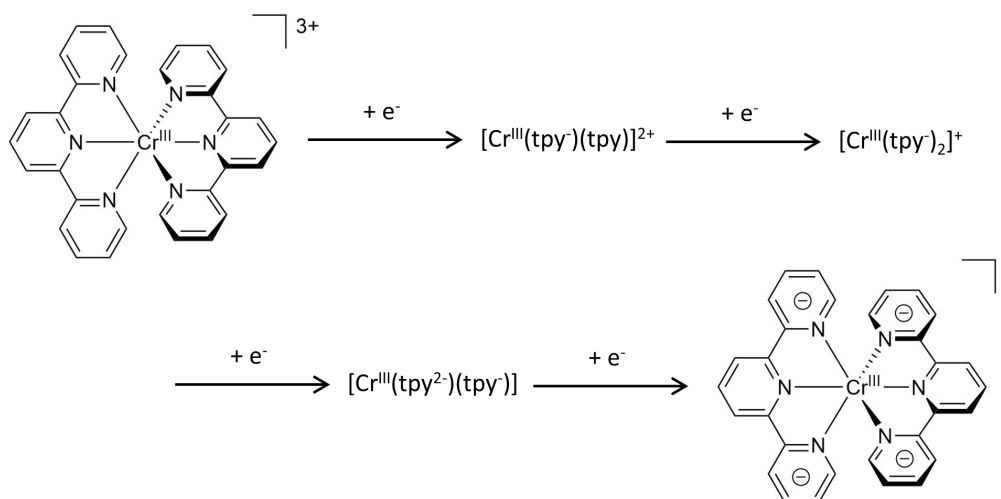


Fig. 1.1: Reduction of $[\text{Cr}(\text{terpy})_2]^{3+}$.

Due to the lower inherent ligand field strength of 3d metal complexes, which give rise to low-energy ligand field excited (MC) states, enabling efficient non-radiative decay to the ground state,^[19] photophysical applications, are more challenging. One possibility to circumvent this obstacle is the use of metal ions like copper(I) with a closed shell d^{10} electron configuration, which lack any MC excited states.^[20,21] But apart from copper(I) complexes, only a very limited number of highly luminescent complexes of earth-abundant metal ions exists, which all emerged only in the last few years.

Notable examples being an emissive d^0 zirconium(IV) complex presented by Milsman and coworkers ($\lambda_{\text{em}} = 594 \text{ nm}$, $\Phi = 0.08$)^[22] and a low-spin d^5 iron(III) complex by the group of Wärnmark ($\lambda_{\text{em}} = 600 \text{ nm}$, $\Phi = 3 \times 10^{-4}$, $\tau = 0.1 \text{ ns}$)^[23] both emitting from excited ligand-to-metal charge transfer (LMCT) states. Wenger and Blüdt introduced a new class of isocyanide complexes of chromium(0) ($\lambda_{\text{em}} = 630 \text{ nm}$, $\Phi = 1 \times 10^{-5}$, $\tau = 2.2 \text{ ns}$)^[23] and molybdenum(0) ($\lambda_{\text{em}} = 597 \text{ nm}$, $\Phi = 0.045$, $\tau = 225 \text{ ns}$)^[23] with emissive MLCT states. Two, at room temperature emissive, cobalt(III) complexes with strong σ -donating guanidine ligands have very recently been presented by Hanan and coworkers.^[24] Their blue emission ($\lambda_{\text{em}} = 440$ and 412 nm) arises from $^3\text{LMCT}$ states with quantum yields of $\Phi = 0.70 \%$ and 0.40% . It is more of a challenge to achieve emission in the near infrared (NIR) spectral region, which is even difficult using noble metal ions.^[25] Often lanthanides like ytterbium^[26–31] or extended organic

molecules, that require elaborate and time consuming synthesis,^[32] are employed to this purpose.

1.1 Near infrared emission

The near infrared (NIR) spectral region is generally considered to spread from the low energy edge of the for the human eye visible region (approximately 700 nm) up to 3000 nm, where the highest energy molecular vibrations occur.

1.1.1 Excited state decay mechanisms

Due to the low energy of near infrared light, emission generally involves phosphorescence, which means, that after excitation of an emitter from its ground to its excited state, intersystem crossing (ISC) has to occur and an excited state of different multiplicity is populated (Figure 1.2 depicts the situation with singlet ground (1GS) and singlet (1ES) and triplet excited states (3ES), which shall be used as a generalized example from here on). Since the transition from the 3ES to the 1GS is spin-forbidden, the excited state is typically long-lived (from nanoseconds up to several seconds) and has several decay pathways to recover the ground state, like phosphorescence, non-radiative decay or bimolecular quenching and will be discussed in the following.

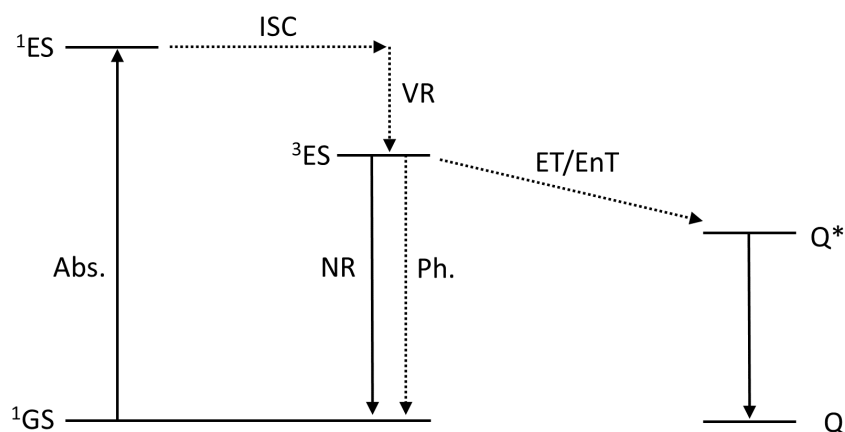


Fig. 1.2: Simplified Jablonski diagram of phosphorescent molecules.

Phosphorescence

To compare the different excited state decay pathways, it is necessary to know their respective decay rate constants. The radiative rate constant for phosphorescence k_r is described, the same as for fluorescence, by the Einstein coefficients for spontaneous emission. In conjunction with the Franck-Condon approximation, the decay rate constant for the transition from an triplet excited state (^3ES) to the singlet ground state (^1GS) is given by:^[33,34]

$$k_r (^3\text{ES} \rightarrow ^1\text{GS}) = \frac{8\pi^2\eta^3}{3\epsilon_0\hbar} |M_{\text{T}}(Q_0)|^2 \sum_{\tilde{\nu}} \tilde{\nu}^3 \int |\chi_{^1\text{GS},\nu'}^* \chi_{^3\text{ES},\nu''}|^2 dQ \quad (1.1)$$

where η is the solvent refractive index, $M_{\text{T}}(Q_0)$ the transition dipole moment of the $^3\text{ES} \rightarrow ^1\text{GS}$ transition at the ^3ES geometry Q_0 and $\tilde{\nu}$ the emission energy. The nuclear wavefunctions of the ground and excited state with the quantum numbers ν' and ν'' are given by $\chi_{^1\text{GS},\nu'}^*$ and $\chi_{^3\text{ES},\nu''}$. The overlap integrals of these vibrational wavefunction $\int |\chi_{^1\text{GS},\nu'}^* \chi_{^3\text{ES},\nu''}|^2 dQ$ is the Franck-Condon factor. Equation 1.1 reveals that k_r is directly proportional to the third power of the emission energy $\tilde{\nu}$, meaning, that at lower emission energies, like emission in the NIR, the radiative decay rate constant is lower.

Further, k_r is proportional to the second power of $M_{\text{T}}(Q_0)$. The main contribution to the transition dipole moment $M_{\text{T}}(Q_0)$ for a spin-forbidden transition in first order perturbation theory is the strength of the spin-orbit coupling and the singlet excited state (S_m) \rightarrow ^1GS transition dipole moments $M_{S_m,j}(Q_0)$ of energetically close lying singlet states (equation 1.2).^[34] The strength of the spin-orbit coupling is dependent on the mass of the surrounding atoms, complexes of first row transition metals have lower radiative decay constants than noble or rare earth metal complexes.

$$M_{\text{T}}(Q_0) = \sum_{j \in x,y,z} \left| \frac{\langle ^3\text{ES} | \hat{H}_{\text{SOC}} | S_m \rangle}{E(S_m) - E(^3\text{ES})} M_{S_m,j}(Q_0) \right|^2 \quad (1.2)$$

The Franck-Condon factors do not effect the overall emission rate, but determine the shape of the emission spectrum. They take the distortion of the excited state with respect to the ^1GS into account and weigh the vibrational wavefunctions of the ground state. A large distortion of the excited state yields a spectrum with a pronounced vibronic progression (figure 1.3 a) while an undistorted excited state results a spectrum without vibronic progression (figure 1.3 b).

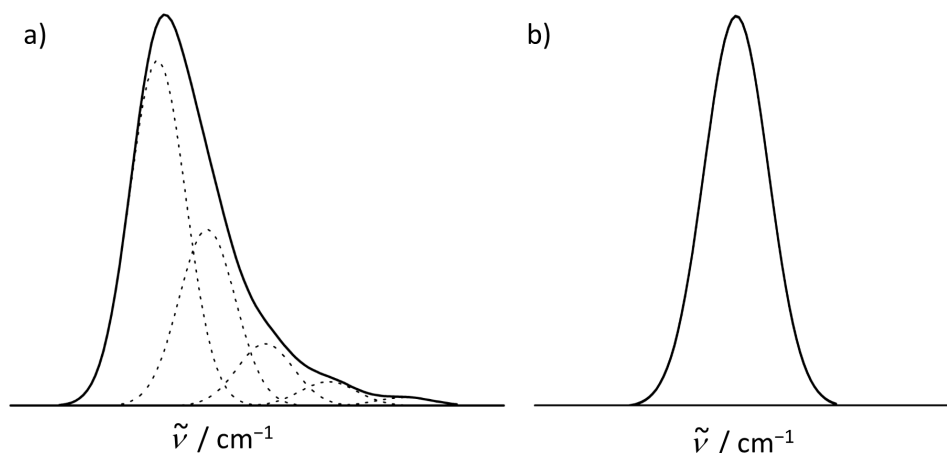


Fig. 1.3: Emission spectra a) with vibronic progression (the dotted lines represent the individual vibronic transitions) and b) without vibronic progression.

Non-radiative decay

An excited state can also depopulate spontaneously into the ground state without emission of a photon. This non-radiative decay is generally ascribed to two different processes, depending on the displacement of the potential energy surface (PES) of the excited state relative to the ground state potential energy surface. The case where there is a large displacement of these surfaces is referred to as strong coupling limit and because of the large displacement the excited and ground state PES cross at low energies relative to the minimum of the excited state PES and thus depopulation via this crossing point becomes the main non-radiative deactivation pathway. The weak coupling limit describes the case where there is only a minimal displacement of the respective surfaces and depopulation occurs via multi-phonon relaxation.^[35]

Strong coupling limit

In the strong coupling limit the non-radiative decay constant k_{nr} is described as:^[35]

$$k_{\text{nr}} = \left(\frac{k_{\text{B}}T}{\hbar} \right) H_{ab}^2 \sqrt{\frac{2\pi}{E_{\text{M}}(k_{\text{B}}T)^3}} \exp\left(-\frac{\Delta E_{\text{A}}}{k_{\text{B}}T}\right) \quad (1.3)$$

H_{ab}^2 is the electronic coupling matrix element for the ES to GS transition, E_{M} the Stokes shift between excitation and emission energy and ΔE_{A} the energy difference

between the lowest excited vibronic state and the crossing point of the excited and ground state PES (figure 1.4).

Basically, k_{nr} is temperature dependent and follows an Arrhenius-like behavior with ΔE_A as the energy barrier for non-radiative deactivation. Decreasing temperature hence slows the non-radiative decay, as often observed in luminescence spectroscopy at low temperatures.

Since the activation barrier depends on the excited state distortion it can, under the right circumstances, reach values close to zero, at which point the non-radiative decay becomes barrier-free and thus very fast.

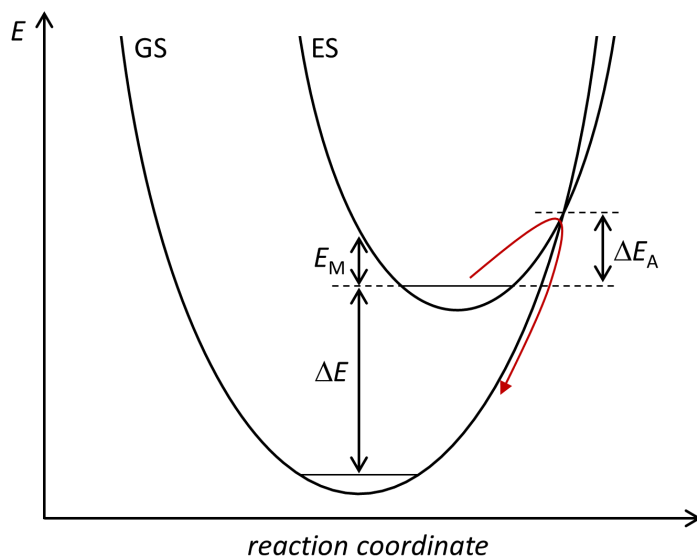


Fig. 1.4: Potential energy surfaces of the ground (GS) and excited state (ES) at the strong coupling limit, the red arrow indicates the non-radiative decay path.

Weak coupling limit

In the weak coupling limit the non-radiative decay constant k_{nr} is described as:^[34–36]

$$k_{nr} = \frac{2\pi}{\hbar} \frac{H_{ab}^2}{(4\pi\lambda_s k_B T)^{-1/2}} \sum_{n_M} \left[\frac{S_M^{n_M}}{n_M!} \exp(-S_M) \exp\left(-\frac{(\Delta E - n_M \hbar \omega_M - \lambda_s)^2}{4\lambda_s k_B T}\right) \right] \quad (1.4)$$

Again, k_{nr} is dependent on H_{ab}^2 , further on λ_s , the solvents' reorganisational energy and S_M , the Huang-Rhys factor. The later describes the geometrical distortion between the equilibrium geometries of ground and excited state in dimensionless fractional displacements along the complex's normal modes. ΔE is the energy difference between ground and excited state, ω_M and n_M are the frequency and quantum number of intramolecular high-frequency vibrational modes of the ground

state.

Deactivation in the weak coupling limit occurs in two steps. The first is a horizontal transition, namely tunneling from the electronically excited state (ES) to a vibrationally excited ground state (i in figure 1.5). This is followed by vibrational relaxation to the vibrational and electronic ground state under emission of infrared radiation (vertical transition, ii in figure 1.5).

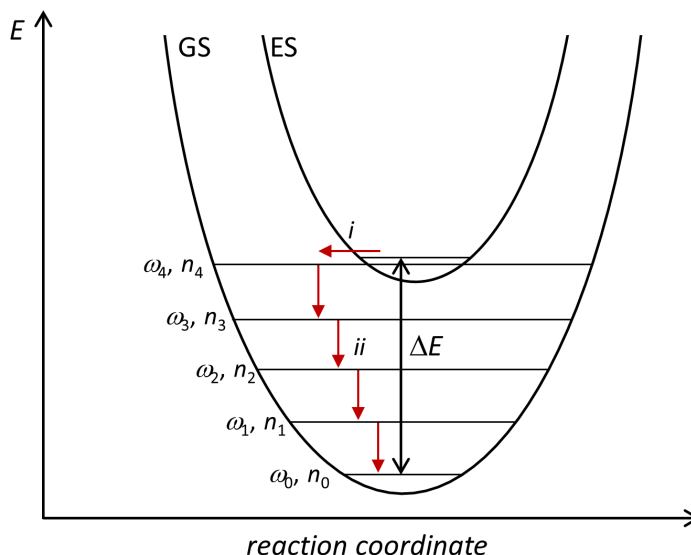


Fig. 1.5: Potential energy surfaces of the ground (GS) and excited state (ES) at the weak coupling limit, the red arrows indicate the non-radiative decay path (harmonic approximation with equidistant vibrational levels).

Equation 1.4 reveals, that the largest contribution to k_{nr} originates from the vibrationally excited states with the lowest quantum numbers n_M . This means that vibrational modes of high energy like C-H, O-H or N-H stretching vibrations ($\omega_M(\text{X-H}) = 3000 - 3600 \text{ cm}^{-1}$) are the main contributors, since they require overtones of significantly lower quantum numbers than for example C=C vibrations ($\omega_M(\text{C-C}) = 1200 - 1600 \text{ cm}^{-1}$) to be in resonance with with the excited state ($\Delta E = 8000 - 14500 \text{ cm}^{-1}$). In the case of polypyridine transition metal complexes, these are predominantly the aromatic C-H stretching frequencies, but other high energy oscillators, like N-H or O-H stretchings can also contribute significantly if present. Non-radiative decay via this pathway can also happen by transferring the energy to a different molecule which is very close to the complex, in most case these are solvent molecules, due to the distance dependence of the transfer rate ($k_{\text{nr}} \propto r^{-6}$).^[37]

Since the energy of X-H oscillators can be reduced by exchanging hydrogen with heavier atoms or groups (the energy of the corresponding X-D vibration is a factor 0.73 lower in the harmonic approximation), deuteration, fluorination or methylation of the responsible positions in the ligand and solvent can significantly decrease

the non-radiative decay.^[38–40] While deuteration does not influence the electronic structure of the ligand, fluorination and methylation can change the electronic and geometric structure a lot, making predictions of the resulting photophysical properties difficult. ^[38–40]

Additionally there are two more factors playing a role in promoting non-radiative decay, one is the displacement of the excited state with respect to the ground state, reducing it will reduce k_{nr} . Secondly, the rate decay depends of the energy gap ΔE between excited and ground state, posing an inherent problem for NIR emission, since k_{nr} rises with decreasing ΔE . This is often referred to as “energy gap law”.^[35,41,42]

Bimolecular processes

Alongside the unimolecular deactivation channels luminescence and non-radiative decay, the excited state can evolve into the ground state via bimolecular quenching when it's lifetime is long enough ($\tau > 1$ ns). The involved processes are either energy transfer to a molecule with a suitable excited state or electron transfer from or to the excited molecule by an oxidant or reductant with matching potential.

Energy transfer

For energy transfer to occur, the excited states of the donor and an acceptor have to be in resonance, meaning that the energy emitted by the donor needs to be sufficient to excite the acceptor. Quantum mechanically there exist two mechanisms that contribute to the energy transfer between donor and acceptor molecule, namely interaction through-space or through-bond. The transfer is generally called either Förster- (through-space) or Dexter-type (through-bond), depending which mechanism dominates (figure 1.6).^[43,44]

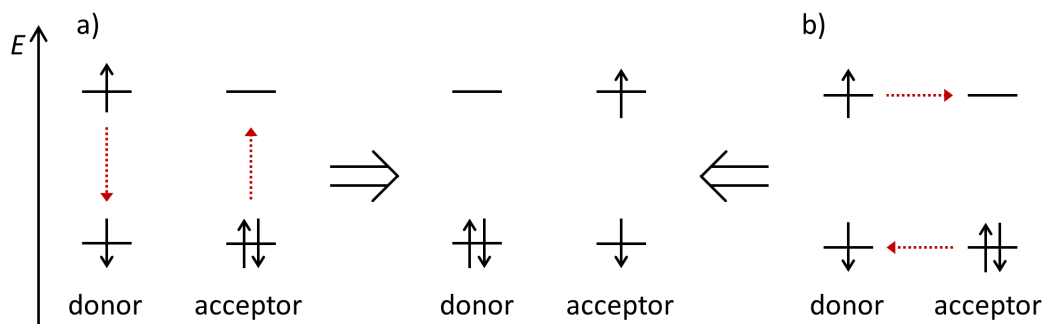


Fig. 1.6: Schematic representation of excited state decay via energy transfer via the a) Förster and b) Dexter mechanism.

The energy transfer rate k_{EnT} for the Förster resonance energy transfer (FRET) amounts to:^[43,45]

$$k_{\text{EnT}} = 8.8 \cdot 10^{-25} \frac{\kappa^2 \Phi}{\eta^4 \tau r^6} J_{\text{F}} \quad J_{\text{F}} = \frac{\int f_{\text{D}}(\lambda) \epsilon_{\text{A}}(\lambda) \lambda^4 d\lambda}{\int f_{\text{D}}(\lambda) d\lambda} \quad (1.5)$$

where η is the solvent refractive index, Φ and τ are the luminescence quantum yield and lifetime of the donor in absence of an acceptor, κ is an orientation factor, to account for the directional nature of dipole-dipole interaction ($\kappa^2 = 2/3$ for random orientation) and r is the distance between donor and acceptor. J_{F} is the spectral overlap between the normalized emission spectrum of the donor f_{D} and the absorption spectrum of the acceptor ϵ_{A} , which is basically the resonance condition.

The Förster-type energy transfer has a distance dependence of r^{-6} , enabling transfer far beyond the dimensions of single molecules. FRET has to follow spin selection rules, thus it only occurs, when all involved states exhibit the same multiplicity.

Since FRET is very efficient and long ranged, Dexter-type energy transfer only becomes relevant when the involved states differ in multiplicity and no Förster-type transfer is possible. The Dexter-type transfer requires orbital overlap between donor and acceptor, either directly or via a bridge (through-bond) and therefore its rate constant decreases exponentially with the distance:^[44,45]

$$k_{\text{EnT}} = \frac{2\pi}{\hbar} H_{\text{AD}}^2 \left[-\frac{\beta^{\text{en}}}{2} (r - r_0) \right] J_{\text{D}} \quad (1.6)$$

For the Dexter energy transfer the electronic coupling matrix element H_{AD} is the most crucial variable, since the Dexter type mechanism is formally a double electron transfer, one electron “moving” from the LUMO of the excited donor to the LUMO of the acceptor, while simultaneously another “moves” from the HOMO of the acceptor to the HOMO of the donor. In contrast to FRET, the spectral overlap J_{D} is less important but instead the attenuation factor β^{en} has to be taken into account. It describes the tunneling probability for both transfer processes.

The spin selection rules for the Dexter transfer apply for the reaction pair as whole, and thus the multiplicity at the donor and acceptor can change in this process, when the overall multiplicity stays the same.

An important example of the Dexter-type energy transfer is the phosphorescence quenching by triplet oxygen, producing singlet oxygen.

Electron transfer

Encountering a reductant or an oxidant with suitable potential, meaning either a HOMO higher in energy than the one of the excited molecule or a LUMO lower in energy than the one of the excited molecule, quenching of a long lived excited state can occur. In this case the ground state is not recovered, since the molecule is reduced or oxidized by the quencher.

The Rehm-Weller equations (equation 1.7 and 1.8)^[46] allow to estimate the redox potentials $E_{\text{red}}^*/E_{\text{ox}}^*$ of a molecule in its excited state, from the ground state redox potentials $E_{\text{red}}/E_{\text{ox}}$ and the energy gap E_{00} between excited and ground state in their respective vibronic ground states:

$$E_{\text{red}}^* = E_{\text{red}} - E_{00} \quad (1.7)$$

$$E_{\text{ox}}^* = E_{\text{ox}} + E_{00} \quad (1.8)$$

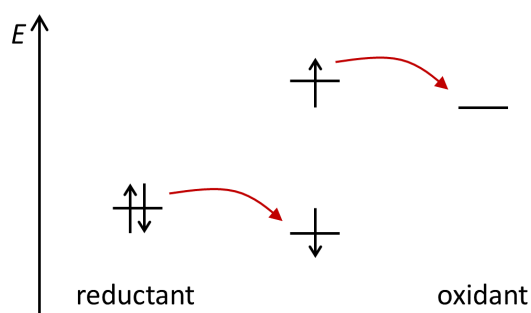


Fig. 1.7: Schematic representation of excited state decay via electron transfer.

Quantification

Bimolecular quenching processes can be quantified spectroscopically by utilizing the Stern-Volmer equation, which relates the dependence of the luminescence intensity and lifetime on the concentration of an external quencher to a quenching constant:^[47]

$$\frac{\Phi_0}{\Phi([Q])} = \frac{\tau_0}{\tau([Q])} = 1 + K_{\text{SV}} [Q] = 1 + k_q \tau_0 [Q] \quad (1.9)$$

Φ_0 and $\Phi([Q])$ are the luminescence quantum yields without and in presence of a quencher in concentration $[Q]$ and τ_0 the lifetime without a quencher. K_{SV} is the Stern-Volmer constant and k_q the bimolecular quenching constant including both, the rate of electron or energy transfer and the diffusion rate.

Luminescence lifetime and quantum yield

The lifetime τ of an excited state is the reciprocal of the sum over the deactivation rate constants, radiative and non-radiative (generally several):^[45]

$$\tau = \frac{1}{k_r + \sum_i k_{nr,i}} \quad (1.10)$$

The luminescence quantum yield Φ is the ratio between the radiative decay constant k_r and the sum over all decay constants:

$$\Phi = \frac{k_r}{k_r + \sum_i k_{nr,i}} = k_r \tau \quad (1.11)$$

From these equations it is quite obvious, that to achieve strong luminescence from transition metal complexes, the number of non-radiative decay pathways has to be minimized. In some cases this is possible, either by the choice of solvent and conditions or ligand design, but in other cases intrinsic physical properties like the behavior of the energy gap law at low excited state energies, a property necessary for NIR emission, can not be changed.

1.1.2 Applications

NIR emissive dyes are employed in a wide variety of applications, like in materials for fiber-optic telecommunication, light emitting devices (LED), security inks or as laser media.^[26,48,49] A lot of these applications used purely inorganic substances, like oxides or doped semiconductors, but in the last 25 years, originally stimulated by the development of electroluminescence in conjugated polymers, which lead to the development of OLEDs, complexes with organic ligands came into focus for the same applications.^[26,50,51]

One of the main application of NIR emitters is their utilization as luminescent sensor materials, where they are used in numerous imaging and sensor applications and shall be discussed in the following section in detail.

1.2 Luminescent sensor materials

The capability to emit light in the near infrared region is of particular interest for imaging and sensing applications due to the fact that only very few materials absorb light of this energy, and thus allowing for deep penetration of the sample.^[52] Furthermore, there is generally very little or no background emission from the sample, resulting in a very good signal to noise ratio, since it is very challenging to achieve NIR emission and only carefully designed chromophores are capable of efficient NIR emission, because of several intrinsic problems related to the low energy of the radiated light, as discussed in section 1.1.1.^[52]

Since NIR emission often involves phosphorescence, the observed background emission can be further reduced in this case by using time resolved techniques, allowing the short lived background fluorescence to decay after an excitation pulse, before the actual measurement is taken.^[53] But the usage of near infrared light also introduces some technical challenges. The efficiency of many commercially available optics degrades above 700 nm and detection of light above 1100 nm is considered particularly challenging. While challenging, these are not insurmountable obstacles and can be overcome with reasonable effort.^[54]

Luminescent molecules are very commonly used in biological and medical research for either imaging or sensing purposes and have advanced the field of life sciences tremendously.^[55,56] The development of advanced imaging techniques like confocal microscopy allows the observation of cellular processes with great spatial and time resolution.^[57]

For the imaging of specific cellular processes, the luminophor has to be localized in the cell at the place of interest. To this end simple and efficient organic reactions (e.g. click chemistry)^[58,59] have been developed to attach the luminophor covalently to the biomolecule of interest (e.g. proteins, DNA or RNA, membranes, etc.) *in vitro* or even *in vivo*. Alternatively the luminophor can be attached to groups that allow the label to interact with receptors, intercalate into DNA or be incorporated in membranes. Further, the simultaneous use of multiple labeling molecules with different excitation and emission wavelengths allows the observation of multiple processes at once.

There exist a plethora of different luminescent molecules to label virtually every imaginable biomolecule (there are more than 3000 different luminescent probes in “The molecular probes handbook” listed alone)^[60]

Beyond the spatial information that can be retrieved by labeling, further information can be accessed by probes, whose luminescence properties depend on the properties of their environment, such as pH value, the presence of oxygen or metal ions, temperature, pressure. Their advantage lies in the contactless measurement

of these properties directly in the sample. In particular, this enables measurement on molecular scales (\sim nm), while the dimensions of the probes of “classical” measurement techniques (e.g. pH electrode, thermometer, barometer etc.) are several orders of magnitude larger (\sim mm).

The sensing mechanism of a luminescent probe can be diverse, as such there exist i) quenching probes, ii) fluorogenic probes, iii) dual-wavelength probes, iv) Förster resonance energy transfer (FRET) and v) photoinduced electron transfer (PET) based systems.

The probe does not only have to respond to its analyte, there also has to be a reliable referencing method. Referencing in many cases uses ratiometric methods, either by addition of a reference dye which is not influenced by the analyte or by using a 2- λ probe. Two principle approaches for dual-wavelength probes are possible, either the collecting of the emission intensity at two different excitation wavelengths or the collection of emission intensity at two different emission wavelengths at a fixed excitation wavelength. Also internally referenced is imaging of the luminescence lifetime (fluorescence lifetime imaging - FLIM), which is, in contrast to the emission intensity, independent of the probes concentration and absorption from the sample. Internally referenced methods are independent of the probes concentration and do not suffer from errors that might occur by different behavior of probe and reference in the sample, which is especially important in biological samples, where probe and reference might exhibit different uptake rates into the cell/cell compartment or other interactions.

In the following, probes for some of the most targeted parameters pH, pO_2 , pressure and temperature shall be discussed in more detail.

1.2.1 pH sensing

Dyes like bromothymol blue or phenolphthalein, which change their absorption spectrum (and thus their color) upon protonating or deprotonating, are used as pH indicators. This behavior can be exploited for an 2- λ pH probe, if both forms of the molecule are also emissive. This is the case for the highly emissive, water soluble 8-hydroxypyrene-1,3,6-trisulfonate (HPTS), the most commonly used fluorescent pH indicator.^[61] The deprotonated form emits at 520 nm with a quantum yield close to 100 %, when excited at 450 nm. At pH 7.5, it gets protonated and the absorption maximum of lowest energy shifts to 405 nm, while the emission wavelength does not change. The absorption spectra of both forms cross at 427 nm, resulting in an isoemissive point, which can be used for internal referencing. HPTS can also be immobilized on polymers or cellulose, allowing its use in flow cells.^[62]

The absorption spectra of some fluorescein derivatives also behave in this way, and optimization lead to 2',7'-bis(2-carboxyethyl)-5-carboxyfluorescein (BCEFC, figure 1.8 b). Since it is water soluble, reacts sensitive to small pH changes around pH

7 and possesses the right polarity to permeate membranes, it is very successfully used for intracellular pH measurements.^[63]

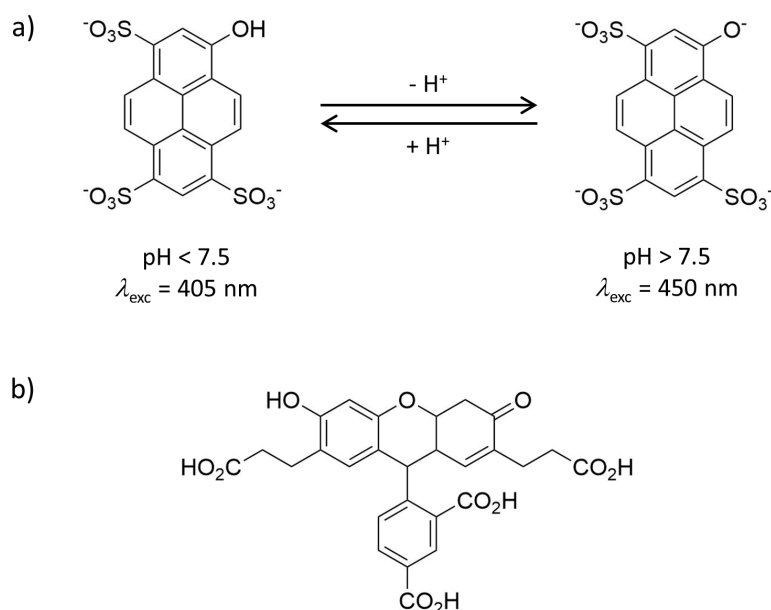


Fig. 1.8: a) Protonated and deprotonated form of HPTS and b) the cell membrane penetrating indicator BCEFC.

pH sensitive probes can also be used to detect ammonia^[64] or CO₂^[65], if embedded in a polymer matrix together with water. The polymer matrix has to be impermeable to protons and ionic compounds to use the equilibria formed between ammonia, water and ammonium hydroxide or CO₂, water and carbonic acid and the resulting pH change for detection.

1.2.2 Oxygen sensing

Since molecular oxygen quenches phosphorescence, measurement of O₂ is conducted with phosphorescent dyes.^[56,66] The efficiency of the bimolecular quenching process determines the sensitivity of the measurement and is described by the Stern-Volmer constant K_{SV} (equation 1.9). That means, the emission of dyes with long lifetimes τ_0 gets efficiently quenched and thus are good candidates for oxygen sensing applications. A sufficiently long lifetime also simplifies the quantification by the internally referenced method of fluorescence lifetime imaging.

Their brightness makes metalloporphyrins and derivatives very interesting for oxygen sensing, and in particular palladium(II) and platinum(II) complexes are frequently used, because of their high photostabilities and Stern-Volmer constants. Benzoporphyrins like [Pd(TPTBP)] (TPTBP = tetraphenyltetrabenzoporphyrin)^[67,68] and coproporphyrins like [Pt(CP)] (CP = coporphyrin) emit in the red and near infrared

spectral region and while [Pd(TPTBP)], like most porphyrine and benzoporphyrine derivatives are insoluble in water, the coporphyrins are well soluble in water.^[69] The latter are commonly used to measure the oxygen concentration in cells.^[70]

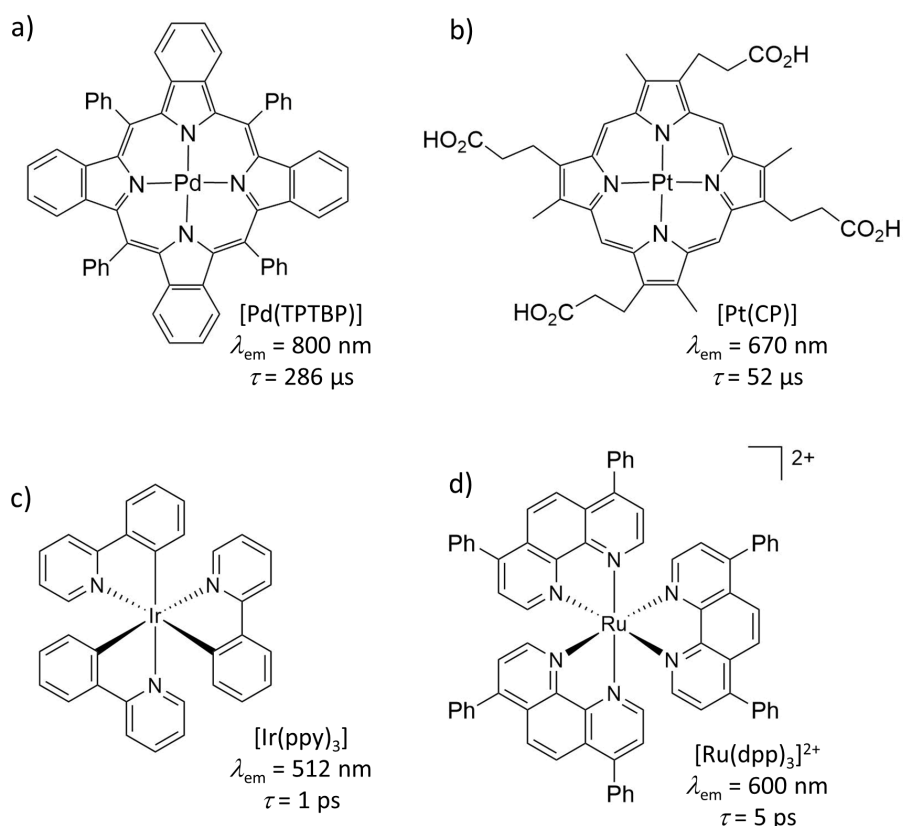


Fig. 1.9: Oxygen sensitive probes: a) [Pd(TPTBP)], b) [Pt(CP)], c) [Ir(ppy)₃] and d) [Ru(dpp)₃]²⁺.

Alternatives to porphyrin based systems are cyclometalated iridium(III) complexes like [Ir(ppy)₃](ppy = deprotonated 2-phenylpyridine)^[71] and [Ru(dpp)₃]²⁺ (dpp = 4,7-diphenyl-1,10-phenanthroline).^[72] These are often employed in solid materials, like polymer films or fiber optical devices.^[73–75]

The fluorescence of fullerene C₇₀ is exceptionally efficiently quenched by oxygen, hence it is used to detect trace amounts of oxygen (< 1 μg L⁻¹).^[76]

Pressure sensing

Oxygen sensitive probes are capable of determining the partial pressure of oxygen and are thus used to measure the atmospheric pressure. This only works if the ratio of oxygen in the measured atmosphere is known (~21 % in air) and is obviously limited to atmospheres that actually contain a reasonable amount of oxygen.

So far, there are no molecular, soluble systems reported, that are able to detect pressure in oxygen free gases or liquids.

1.2.3 Temperature sensing

Raising temperature increases the non-radiative decay constant and thus reduces luminescence intensity and lifetime (equation 1.3 and 1.4). This is exploited for temperature sensing and materials with high thermal quenching rates are referred to as thermographic phosphors. There exists a plethora of inorganic ceramic compounds that are used for broad temperature ranges ($> 1000\text{ }^{\circ}\text{C}$).^[77] They offer great thermal stability but are insoluble.

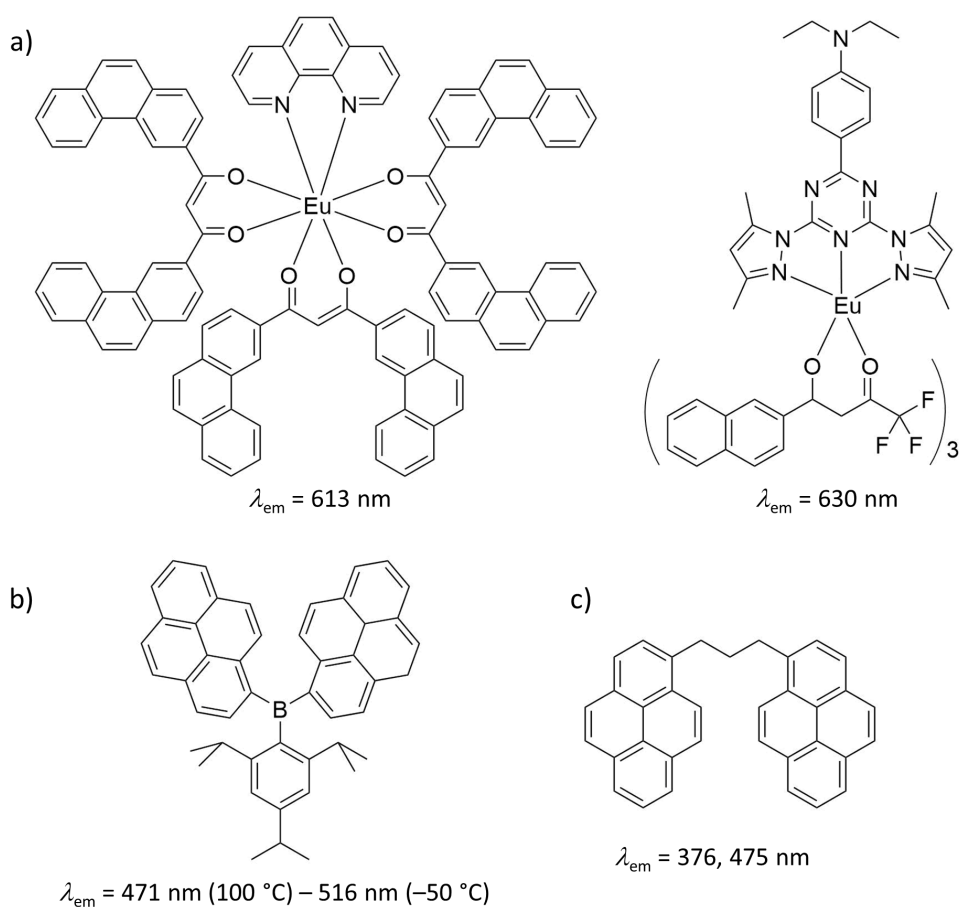


Fig. 1.10: Temperature sensitive probes: a) based on europium(II) β -diketonates, and the dual emissive probes [dipyren-1-yl(2,4,6-triisopropylphenyl)-borane] (b) and 1,3-bis(1-pyrenyl)propane (c).

Molecular compounds used in applications, are mainly europium(III) complexes with β -diketonato ligands, whose emission intensity is very temperature sensitive (figure 1.10 a).^[78,79]

The emission of ruthenium(II) and iridium(III) complexes also reacts sensitive to temperature and are also employed in applications.^[71,80] But since the same complexes are also used as oxygen sensors (e.g. $[\text{Ir}(\text{ppy})_3]$ and $[\text{Ru}(\text{dpp})_3]^{2+}$, figure 1.9 c) and d), the O_2 concentration has to be known for reliable measurements. This shows a major problem with probes that rely on luminescence quenching, since the decrease in luminescence intensity and lifetime is often dependent of more than one property (see section 1.1.1). Thus, these indicators are mostly used in dual sensors, with a second indicator to determine temperature or oxygen concentration independently.^[78]

A more elegant way to record the temperature is the use of a dye exhibiting dual emission. If the emissive states are thermally equilibrated and thus behave according to the Maxwell-Boltzmann distribution, the temperature can be calculated from the intensity ratio of both emission bands. Therefore, the energy difference between the emissive states has to be in the range of $k_{\text{B}}T$ ($\approx 400 - 800 \text{ cm}^{-1}$ at r.t.) and the emission bands have to be very sharp to be resolved.

A rare example for a luminophor behaving this way is [dipyren-1-yl(2,4,6-triisopropylphenyl)-borane] (figure 1.10 b).^[81] It shows emission from a local excited state and from a twisted intramolecular charge transfer excited state. But, the individual emission bands are not resolved, due to the structural changes between ground and excited states, and thus a overall shift in emission wavelength is observed with temperature changes.

A similar example is the behavior of 1,3-bis(1-pyrenyl)propane (figure 1.10 c) in ionic liquids.^[82] It possesses similar dynamics but the emission bands are better resolved in this case.

Another class of luminescent T sensors exploits the distance dependence of the Förster resonance energy transfer ($\sim r^{-6}$, equation 1.5). These so called molecular beacons (MB) consist of flexible, single-stranded oligonucleotides, that are dually labeled at the 3'- and 5'-end.^[83-86] The labels are either an emitter and a non-emissive quencher (non-ratiometric MB) or two spectrally distinguishable emitters (ratiometric MB).

For measurement, only one of the two labels gets excited. Energy transfer from the excited label to the second label either results in quenching of the emission or appearance of a second emission band. Since the conformation of the oligonucleotide and thus the distance r of the two different label is temperature dependent, the energy transfer rate is also temperature dependent.

1.2.4 Responsive nanoprob es

Responsive dyes can be encapsulated into polymeric nanoparticles or micelles, which are mainly used for sensing in biological matrices. The surface of these nanoprob es can be functionalized to control solubility, interactions with the environ-

ment and localization in the cell. To this purpose, a great number of biocompatible polymers have already been developed.^[87] This allows the use of hydrophobic non-polar probes in polar environments.

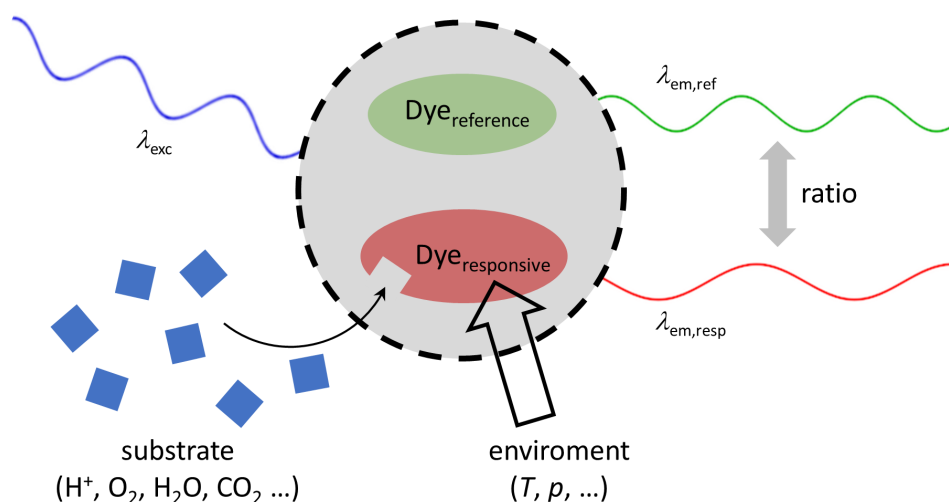


Fig. 1.11: Ratiometric sensing with two dyes incorporated in a nanoparticle or micelle.

Most used materials for the preparation of polymeric nanoparticles are silica, polystyrene or derivatives of polyacrylic acid and their properties can greatly influence the behavior of the nanoprobe. The polymer matrix can protect the dye from quenching by oxygen, chemical interaction with the environment or changes of pH value and ion concentration and thus increase the photostability of the system. It can also provide great selectivity if the polymer matrix is solely permeable for specific molecules (i.e. the analyte).

Encapsulation of a responsive dye together with a reference dye further is a very successful and commonly used method to internally reference measurements ratiometrically (figure 1.11).^[88–92]

1.2.5 Sensing multiple analytes

Systems capable of sensing multiple properties at once are of high interest in several fields, just as medical chemistry, chemical industry or aerodynamics research, where there are already commercially available applications for blood analysis (sensing pH, CO₂, O₂, Na⁺, K⁺ and Ca²⁺)^[93] and pressure sensitive paints (PSP, sensing O₂/pressure and temperature on surfaces)^[94] to mention typical examples.

There are many incentives to develop multiple sensors: gathering complementary information about a sample simultaneously, the decrease in time necessary if measured in parallel can be crucial in clinical chemistry or simply to increase the

accuracy of a single analytes determination. The latter arises from the fact, that all luminescence is temperature dependent and phosphorescence is quenched by molecular oxygen. Thus knowing the temperature and oxygen concentration in the sample is important for an accurate measurement. As a matter of fact, most sensor systems that determine oxygen or temperature also measure the other quantity, since both quench the emission. In addition, many sensor systems employed in a biological context contain an oxygen sensor, since O_2 is produced and consumed by biological processes, the O_2 can vary substantially at different locations in the sample.

The obvious approach to assemble a multisensor would be to simply mix the respective sensor molecules. But, this does not work, for two main reasons: i) the emission bands of many indicators are rather broad and overlapping signals make clear assignment difficult or even impossible, ii) Förster resonance energy transfer (FRET) can occur between two luminescent probes that are in close proximity (< 10 nm) to each other, which would affect the measurements.

Thus the probes have to be chosen carefully to prevent overlapping emission bands. Preventing FRET usually is done by encapsulating the respective dyes in nanoparticles, so there is a minimal distance between the different probes. These are then embedded into a polymer matrix, which has to be permeable for the respective analytes.^[93]

1.3 Chromium(III) complexes

Complexes of chromium(III) are capable of NIR luminescence. If emissive, they exhibit very sharp emission bands at wavelengths between 670 and 820 nm. Although the quantum yields of literature known complexes are generally considered too low for any practical applications ($\Phi < 0.1\%$), their emission lifetimes are, due to the spin- and Laporte-forbidden nature of the emission, very long, up to several hundred microseconds (figure 1.12).^[49] While molecular, highly luminescent Cr^{III} compounds are missing to date, efficient emission of solid materials, mainly doped solids with chromium(III) ions in octahedral coordination environments, such as ruby (chromium-doped sapphire), are well known.^[95–98] The latter is historically particularly important, since it led to the development of the ruby laser in 1960.^[99,100] It further is widely used as pressure calibrator in diamond anvil cells, since its very sharp phosphorescence lines shift pressure induced by $-0.7\text{ cm}^{-1}/\text{kbar}$.^[101–103] The success of solid, chromium(III) based emitters, as well as the long lifetimes of Cr^{III} complexes suggest a potential of molecular, highly emissive chromium(III) complexes. To achieve this, one has to understand the underlying photophysical and photochemical properties arising from the d^3 electron configuration of the Cr^{III} ion in an octahedral coordination environment and, which be discussed in detail in the following section.

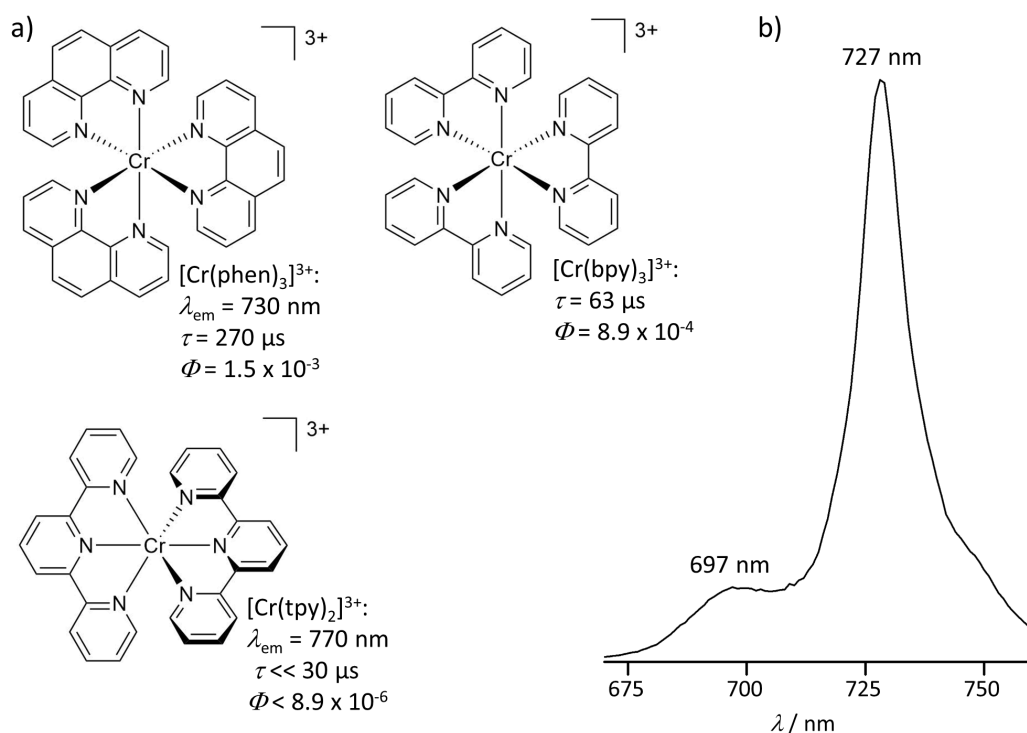


Fig. 1.12: a) Emissive polypyridine chromium(III) complexes and b) emission spectrum of [Cr(bpy)₃](PF₆)₃ at r.t. in CH₃CN ($\lambda_{exc} = 430\text{ nm}$).

physically senseless to ascribe a specific part of the electron-electron interactions to the individual parameters.^[115]

While there is a large number of states that arise from these calculations, only the excited states of lowest energy are relevant for the photochemical properties of a complex, as stated by Kasha's rule, since vibrational relaxation and internal conversion are generally several orders of magnitude faster than other processes.^[116] Thus, the most relevant states for the photochemical behavior of chromium(III) complexes apart from the 4A_2 ground state are the quartet excited 4T_2 state and the doublet states 2E and 2T_1 (for simplicity the O_h point-group classification will be used, even though most actual complexes do not possess an exact octahedral coordination geometry).

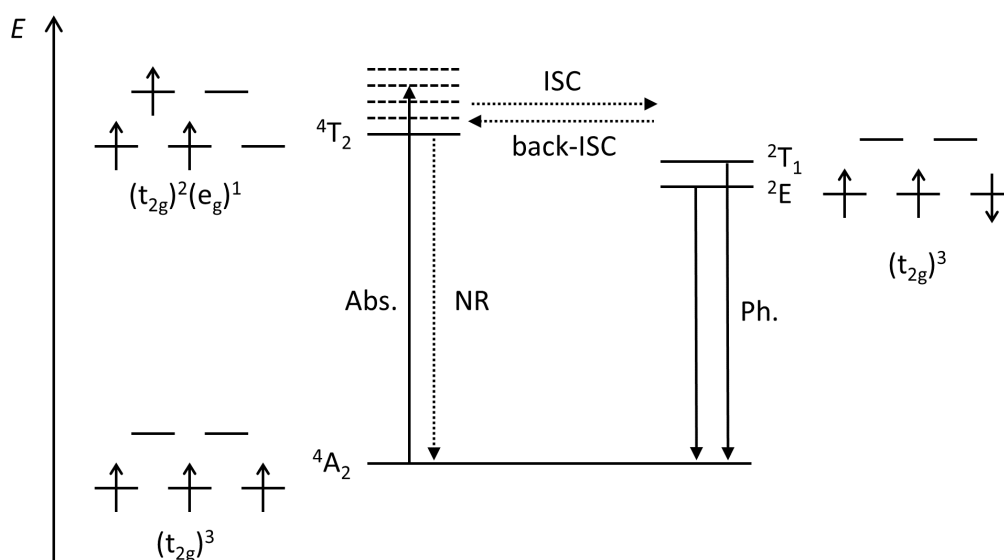


Fig. 1.14: Jablonski diagram, depicting the excited state environment of chromium(III) compounds.

Absorption of visible light initially leads to population of vibrationally excited 4T_2 states, from which extremely fast intersystem (ISC) crossing onto the doublet hypersurface occurs. As a matter of fact, McCusker could show that in $[\text{Cr}(\text{acac})_3]$ (acac = acetylacetonato) the intersystem crossing happens on the same timescale as vibrational relaxation to the vibronic ground state and thus can even occur in vibrationally excited ("hot") states.^[117,118]

The, by ISC populated doublet states, are the 2E and 2T_1 , which only differ by a few hundred cm^{-1} in energy and are thermally equilibrated.

These states are phosphorescent and give rise to exceptionally sharp dual emission in the NIR, as usually observed for emissive chromium(III) complexes. Examination of the doublet state's electronic structure reveals the reason for the emission's

sharpness. The microstates that describe the 2E state are identical in occupation to those of the 4A_2 ($(t_{2g})^3$, figure 1.14) and thus the quartet and doublet ground state are structurally very similar, which results in emission bands without vibrational progression (see section 1.1.1, figure 1.3).

The fact, that only the spin of one electron has to change in the emission process also lead to the naming as “spin-flip emitter” of these type of luminophors.

Since the phosphorescence from the 2E and 2T_1 states is Laporte- and spin-forbidden, the lifetimes of these states is in the micro- to millisecond range, hence giving enough time for radiationless processes to occur. In octahedral or close to octahedral complexes, these mainly are non-radiative decay via energy transfer to high energy oscillators of the ligand or solvent and quenching by molecular oxygen (as discussed in section 1.1.1). Even though their lifetimes are sufficiently long, the 2E and 2T_1 states do not participate in any redox reactions, that the ground state would not also undergo, again because of the similar electron configuration.

Another, very important pathway to depopulate the doublet states, is the back intersystem crossing (back-ISC) to the 4T_2 state. This state posses a $(t_{2g})^2(e_g)^1$ electron configuration, with the t_{2g} and e_g orbitals partially occupied, giving rise to a strong Jahn-Teller distortion and because of the latter, it is also prone to ligand substitution, which is a typical decomposition reaction of polypyridine chromium(III) complexes under irradiation.^[104] Due to its strong distortion the 4T_2 state also shows a fast non-radiative decay via direct surface crossing.

Further, the $(t_{2g})^2(e_g)^1$ electron configuration is, with an electron of high energy (e_g) and an electron hole of low energy (t_{2g}), a strong reductant and oxidant and thus very redox active.

1.3.2 Strategies towards strong emission

Since the 4T_2 state does not only decay non-radiatively into the ground state but can also lead to decomposition of the complex, avoiding the back intersystem crossing from the 2E and 2T_1 and thus the population of the quartet state is a necessity to achieve strong emission. Therefore, the energy difference between the 4T_2 and the ${}^2E/{}^2T_1$ states has to be too high for thermally activated back-ISC to occur. The Tanabe-Sugano diagram for the d^3 configuration (figure 1.13) reveals that, while the energy of the 4T_2 increases linearly with the ligand field splitting Δ , the energy of the 2E and 2T_1 is basically constant with increasing Δ . This is not surprising, comparing the electron configurations of theses states. The energy difference between the ground state and the doublet states, on the one hand, is solely governed by the difference in multiplicity and thus the ground state experiences a stronger stabilization by the exchange interaction than the doublet states, which is independent of Δ . Since one electron occupies the e_g orbitals in the 4T_2 state, the difference in energy

to the 4A_2 state on the other hand is directly influenced by Δ , as it describes the energetic separation of the t_{2g} and e_g orbitals.

But, even though bipyridine and phenanthroline are generally considered strong-field ligands, the corresponding chromium(III) complexes are very weakly emissive, showing that the ligand field is not the only factor to consider.

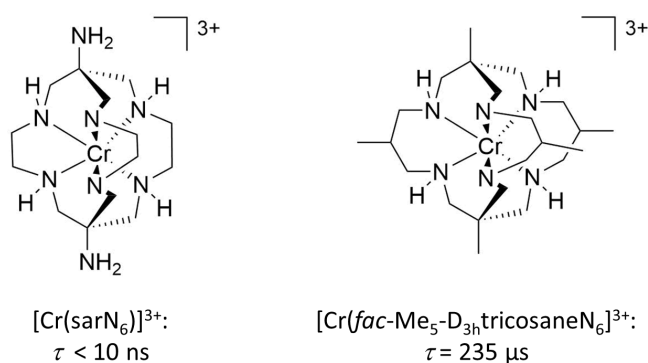


Fig. 1.15: Cage complexes of Cr^{III} .

Another important factor is the coordination actual geometry of the complex. Sargeson and coworkers could show that especially trigonal distortions reduce the excited state lifetime significantly. By hindering the twisting that is occurring in the cage complex $[Cr(sarN_6)]^{3+}$, the lifetimes have been increased from under 10 ns to 235 μs for $[fac\text{-}Me_5\text{-}D_{3h}\text{tricosane}N_6]^{3+}$ (figure 1.15).^[119]

The chromium(III) complex of terpyridine, another strong field ligand, is not prone to trigonal distortions, but spectral overlap with C-H overtones allows very efficient non-radiative decay to the ground state, resulting in a very low quantum yield (figure 1.12).^[120] To suppress non-radiative decay via multi-phonon relaxation, oscillators of high energy (e.g. C-H, O-H or N-H) should be avoided in the ligands or at least in close proximity to the metal ion.

To summarize, a chromium(III) complex with a strong ligand field splitting, an ideal or close to octahedral coordination geometry and no high energy oscillators should be highly emissive.

Such a compound actually already exists, the highly emissive ruby. Therein the Cr^{3+} cation replaces Al^{3+} in corundum (Al_2O_3). No X-H oscillators are present, the coordination sphere is very close to octahedral and the ligand field splitting is, due to the short Cr-O (1.97 Å)^[121] distance very high.

Since the ligand-metal bond lengths in a molecular system cannot be shortened in a straightforward manner, the more obvious way to increase the ligand field is the use of strong σ -donating ligands instead. This ligand should also promote an octahedral

coordination, which would also increase the ligand field due to the increased orbital overlap.

1.3.3 Applications

Even though the luminescence quantum yields of known molecular chromium(III) compounds are considered too low for applications, there are some applications exploiting the excited state reactivity of chromium(III) complexes.

Many of these use the excited state redox properties, presumably of the 4T_2 state.

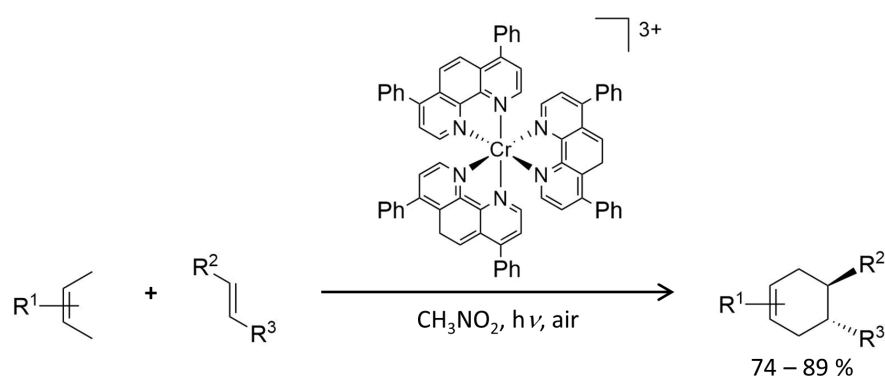


Fig. 1.16: Chromium(III) complexes as photoredox catalysts.

[Cr(bpy)₃]³⁺, [Cr(phen)₃]³⁺ and derivatives thereof have recently been employed as photoredox catalysts for radical cation based Diels-Alder cycloaddition reactions.^[122,123]

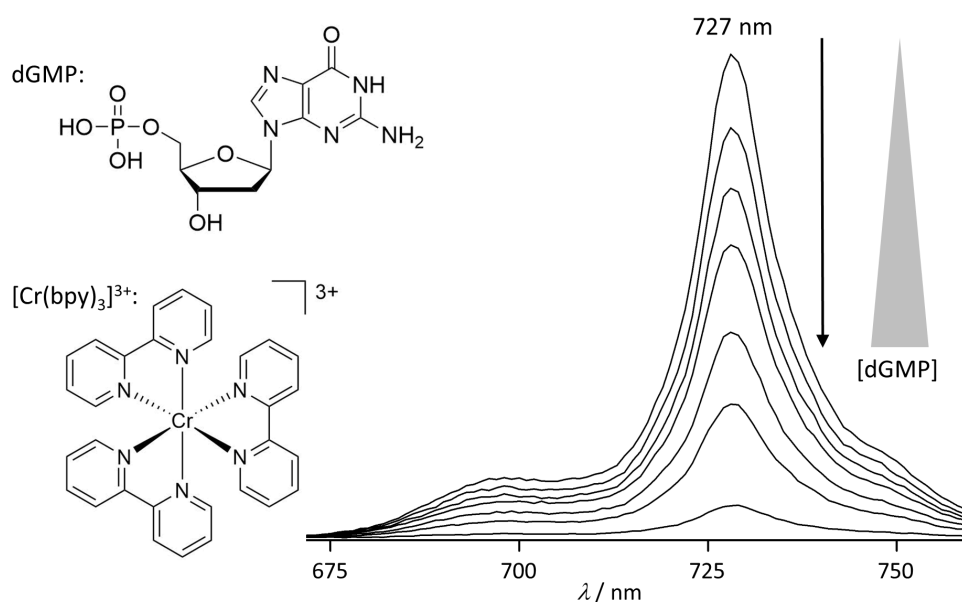


Fig. 1.17: Phosphorescence quenching of [Cr(bpy)₃]³⁺ by addition of deoxy-guanosine monophosphate (dGMP).

$[\text{Cr}(\text{phen})_3]^{3+}$ and $[\text{Cr}(\text{bpy})_3]^{3+}$ are also capable of oxidizing the guanine base of DNA under irradiation.^[107,124,125] Oxidation of guanine is known to serve as starting point for DNA strand scission, chromium(III) complexes can be used for the photocleavage of DNA. If the complex is bearing an extended ligand, that is capable to intercalate into the DNA, this photooxidation can be accelerated and is only limited by diffusion.^[126]

At first glance a bit peculiar, is the incorporation of Cr^{III} in bi- or trimetallic complexes together with lanthanide(III) ions (Nd^{III} , Eu^{III} , Gd^{III} , Tb^{III} , Er^{III} , Yb^{III} or Lu^{III}).^[127–129] The chromium complex serves as sensitizer for the lanthanide ions and therefore gets directly excited from the $^4\text{A}_2$ ground state to the ^2E state. Since this transition is Laporte- and spin-forbidden, the absorption is very low ($\approx 1 \text{ M}^{-1}\text{cm}^{-1}$)^[125] and irradiation by high powered lamps or lasers is necessary. Energy transfer excites the lanthanide, which then emits in the NIR with quite long lifetimes (e.g. $\tau = 1.3 \text{ ms}$ for an ytterbium compound).^[129] This rather complicated way of exciting lanthanide ions is still more efficient than the direct excitation, since transition between states derived from the f-orbitals are even weaker.

An application, that does not rely on the photochemical properties, is the capability of half sandwich complexes of chromium(III) to catalyze the polymerization of ethylene and α -olefin derivatives at atmospheric pressure.^[130] In addition, a very recent publication reports very efficient, homogeneous polymerization of β -olefines by chromium(III) complexes bearing polypyridine ligands together with labile inorganic ligands.^[131]

Aim of the work

Solid, highly emissive materials like ruby, prove, that it is possible to achieve bright luminescence from chromium(III). Thus the aim of this work is to synthesize strongly emissive chromium(III) complexes.

In order to achieve the same favorable excited state behavior as in ruby a ligand that induces a strong ligand field splitting is essential. But as highlighted in section 1.3.2, this alone is not sufficient. Otherwise, $[\text{Cr}(\text{tpy})_2]^{3+}$ should exhibit stronger emission than it actually does.^[49] Additionally, a close to octahedral coordination geometry is necessary.

To this end, flexible, expanded terpyridine ligands, like the literature known ligands ddpd (*N,N'*-dimethyl-*N,N'*-dipyridine-2-ylpyridine-2,6-diamine),^[132] H_2tpda (2,6-bis(2-pyridylamino)pyridine),^[133] dcpp (2,6-bis(2-pyridylketone)pyridine)^[134] or bpmp (2,6-bis((pyridin-2-yl)methyl)pyridine),^[135] that are more flexible than terpyridine and form 6-membered chelate rings, seem very promising (figure 2.1).

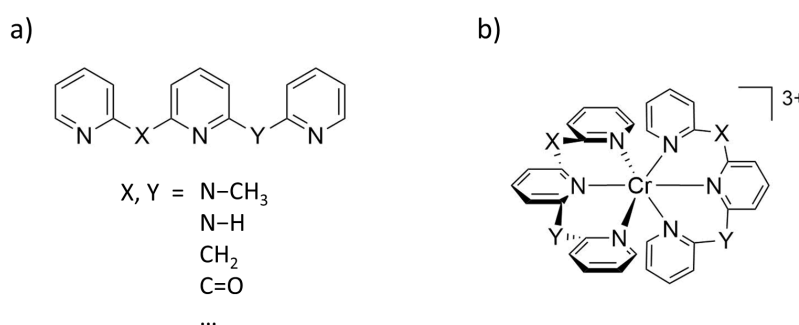


Fig. 2.1: a) Expanded terpyridine ligands and b) envisioned chromium(III) complexes.

The ligands featuring an amine bridge (i.e. ddpd and H_2tpda) are, in addition to their flexibility very electron rich and should be very strong σ -donors. Because of these properties, in conjunction with the fact, that they have already been employed successfully in a number of occasions, resulting in transition metal complexes of nearly ideal octahedral coordination geometry in the Heinze group, special focus shall be given to them.^[132,136–145]

The resulting complexes' structure will be investigated by experimental (single crystal x-ray diffraction) and theoretical (DFT) means to verify the octahedral coordination

geometry. Their photophysical and photochemical properties will be studied extensively employing spectroscopic (steady state and time resolved UV-VIS and emission spectroscopy, IR, raman and EPR spectroscopy) and theoretical (TD-DFT, CAS-SCF and ligand field calculations) methods, to fully map the excited state landscape and thus understand their excited state dynamics.

If the complexes exhibit emission of reasonable quantum yields, first applications in the fields of molecular sensing and photocatalysis shall be explored.

Results and discussion

All findings of this dissertation have been published/submitted as scientific articles in/to peer-reviewed chemistry journals. These articles will be reprinted in the following with permission of the respective publishers.

The synthesis and characterization of a strongly emissive chromium(III) complex bearing the expanded terpyridine ligand ddpd is presented in section 3.1 “[Cr(ddpd)₂]³⁺: a Molecular, Water-Soluble, Highly NIR-Emissive Ruby Analogue”. The title complex features two sharp, very intense emission bands in the near infrared region with exceptional high quantum yield and lifetimes close to a millisecond and the similarities of this new class of spin-flip emitters lead to their naming as “molecular rubies”. The manuscript describes the investigation of the complex’ extraordinary properties by experimental and theoretical means and was prepared in collaboration with the group of Dr. Ute Resch-Genger at the *Bundesanstalt für Materialforschung und -prüfung* (BAM) in Berlin, Germany, who measured absolute luminescence quantum yields and lifetimes.

In Section 3.2, “*Thermo-Chromium: A Contactless Optical Molecular Thermometer*” the emissions temperature dependence of [Cr(ddpd)₂]³⁺ is investigated. The presented results reveal the existence of a thermally accessible equilibrium between the two emissive doublet states (²E and ²T₁) of the complex. This results in a very promising opportunity for ratiometric temperature determination in solution and nanoparticles (prepared by collaboration partners at the BAM) using a single dye, as presented in the manuscript.

The manuscript “*Photo-Chromium: Sensitizer for Visible-Light-Induced Oxidative C–H Bond Functionalization – Electron or Energy Transfer?*” in section 3.3 demonstrates the application of [Cr(ddpd)₂]³⁺ in photocatalytical conversion of tertiary amines into α-amino-nitriles, which it does more efficiently than the previous used organic sensitizer rose bengal (4,5,6,7-tetrachloro-2',4',5',7'-tetraiodofluorescein). Close investigation of the reaction, by UV-VIS and emission spectroscopical means, show that singlet oxygen, produced by quenching of the chromium complex’ the excited state is the oxidant and the complex does not undergo photo-redox reactions. This publication was developed in a joint effort of Sven Otto, who provided the chromium complex, performed DFT calculations and conducted the electrochemical,

UV-VIS and emission spectroscopic investigations and Alexander Nauth from the group of Prof. Dr. Till Opatz, who carried out the photocatalysis experiments.

Eliminating high energy oscillators by deuteration can reduce radiation-less deactivation of the excited state, as discussed in section 1.1.1, thus the article "*Deuterated Molecular Ruby with Record Luminescence Quantum Yield*" presented in section 3.4, describes the syntheses of deuterated derivatives of ddpd. These boost the quantum yields of the resulting chromium(III) complexes up to 30 % and lifetimes exceed 2 milliseconds. The photophysical data in combination with IR spectroscopic measurements and vibrational overtone analysis gave a deeper insight into the excited state dynamics of $[\text{Cr}(\text{ddpd})_2]^{3+}$. This study was the result of a collaboration with the group of Prof. Dr. Micheal Seitz from the University of Tübingen, Germany, who synthesized some of the deuterated ligands and performed the overtone analysis.

A study on the pressure dependence of the phosphorescence bands of $[\text{Cr}(\text{ddpd})_2]^{3+}$ is presented in section 3.5 "*Molecular Ruby under pressure*", which was conducted in close collaboration with Joe Harris and Christian Reber at the Université de Montréal, Canada. It reveals a very strong red shift of the emission upon the application of pressure, more than twenty times stronger than exhibited by the pressure calibrant ruby and detailed theoretical investigations in the form of ligand field and complete active space calculations on high levels of theory are presented in this publication. Further, this presents the first time hydrostatic pressure could be measured by a molecular compound dissolved in solution.

The synthesis and characterization of a chromium(III) complex bearing the, closely to ddpd related, ligand H_2tpda is presented in section 3.6 "*A strongly luminescent chromium(III) complex acid*". To investigate the influence of the NH protons on the emission quantum yield and lifetime of the highly emissive complex, deuteration experiments were carried out.

The article "*Three-in-One Crystal: The Coordination Diversity of Zinc Polypyridine Complexes*" in section 3.7 describes the complexation of zinc(II) with ddpd. The resulting homoleptic complex $[\text{Zn}(\text{ddpd})_2]^{2+}$ enters an equilibrium in the presence of chloride giving three different complexes that co-crystallize. This is not only a testament to the coordination diversity of the d^{10} ion Zn^{2+} , but also to the flexibility of ddpd.

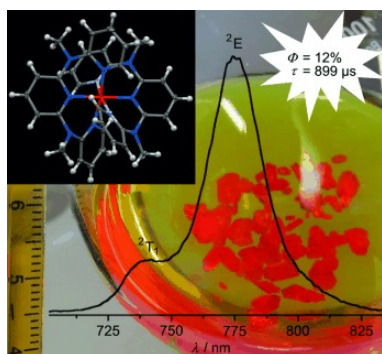
Section 3.8, "*Structure and reactivity of a mononuclear gold(II) complex*" highlights the synthesis and characterization of the first stable mononuclear gold(II) complex. The manuscript gives important insight into many before unknown properties of mononuclear gold(II) species and is an important addition in this field.

The synthetic and spectroscopic work presented in this manuscript have been conducted by Sebastian Preiß. Sven Otto performed and evaluated the DFT calculations on a high level of theory, with special focus on the relativistic effects arising from the heavy gold atom and the arising structural characteristics.

3.1 [Cr(ddpd)₂]³⁺: a Molecular, Water-Soluble, Highly NIR-Emissive Ruby Analogue

Sven Otto, Markus Grabolle, Christoph Förster, Christoph Kreitner, Ute Resch-Genger and Katja Heinze

Angew. Chem. **2015**, *127*, 11735–11739. *Angew. Chem. int. Ed.* **2015**, *54*, 11572–11576.



Strong, long-lived and sharp NIR phosphorescence (775 nm, $\Phi = 12\%$, $\tau = 899 \mu\text{s}$) is achieved in the soluble chromium(III) complex [Cr(ddpd)₂]³⁺ (ddpd=N,N'-dimethyl-N,N'-dipyridin-2-ylpyridine-2,6-diamine) by ligand-field tuning through optimization of the ligand's bite angle and σ -donor strength. ³O₂ quenches the emission, allowing for optical oxygen sensing. The highly stable complex is easy to prepare in high yields from inexpensive starting materials.

Author Contributions

Sven Otto synthesized and characterized the chromium complexes presented in this manuscript and conducted the electrochemical, UV-VIS and emission spectroscopic experiments. Markus Grabolle and Ute Resch-Genger determined the emission quantum yields and excited state lifetimes at the *Bundesanstalt für Materialforschung und -prüfung* in Berlin, Germany. The crystal structures were solved and refined by Christoph Förster. Christoph Kreitner and Sven Otto performed the DFT calculations of the relevant states. The english version of the manuscript was written by Katja Heinze (90%) and Sven Otto (10%), the german translation was prepared by Christoph Kreitner and Sven Otto.

Supporting Information

for this article is found at pp. 125.

“Otto, S.; Grabolle, M.; Förster, C.; Kreitner, C.; Resch-Genger, U.; Heinze, K. *Angew. Chem. Int. Ed.* **2015**, *54*, 11572–11575. Copyright Wiley-VCH Verlag GmbH & Co. KGaA. Reproduced with permission.”



[Cr(ddpd)₂]³⁺: A Molecular, Water-Soluble, Highly NIR-Emissive Ruby Analogue

Sven Otto, Markus Grabolle, Christoph Förster, Christoph Kreitner, Ute Resch-Genger,* and Katja Heinze*

Abstract: Bright, long-lived emission from first-row transition-metal complexes is very challenging to achieve. Herein, we present a new strategy relying on the rational tuning of energy levels. With the aid of the large N-Cr-N bite angle of the tridentate ligand ddpd (*N,N'*-dimethyl-*N,N'*-dipyridine-2-ylpyridine-2,6-diamine) and its strong σ -donating capabilities, a very large ligand-field splitting could be introduced in the chromium(III) complex [Cr(ddpd)₂]³⁺, that shifts the deactivating and photoreactive ⁴T₂ state well above the emitting ²E state. Prevention of back-intersystem crossing from the ²E to the ⁴T₂ state enables exceptionally high near-infrared phosphorescence quantum yields and lifetimes for this 3d metal complex. The complex [Cr(ddpd)₂](BF₄)₃ is highly water-soluble and very stable towards thermal and photo-induced substitution reactions and can be used for fluorescence intensity- and lifetime-based oxygen sensing in the NIR.

Dyes with room-temperature emission in the near infrared (NIR) spectral region (> 650 nm) have emerged as promising candidates for NIR organic light emitting diodes (OLEDs), fiber-optic telecommunication applications, night-vision readable displays, security inks for identification systems, oxygen sensing, and in vivo imaging.^[1–7] Essentially, all currently employed (water-)soluble, NIR emissive dyes are based on lanthanide complexes,^[4–7] complexes of the second- and third-row metal ions,^[8–10] complex organic scaffolds,^[11] or a combination of them.^[12] All of them feature specific advantages, such as long-lived emissive states and large energy differences between absorption and emission maxima (lanthanides, 4d/5d metal complexes), medium to high quantum yields, and rational tuning of the emission energy (organic dyes). Typical drawbacks are, however, multi-step syntheses and poor water solubility and dye aggregation for the more extended π -systems required for NIR emission (organic dyes),^[11b] short

lifetimes in the range of 1–10 ns (organic dyes, many transition-metal complexes), or high costs (e.g. Eu, Rh, Ir, Ru, Os, Pd, Pt, Au). Furthermore, NIR emitters typically suffer from radiationless relaxation to the ground state (energy gap law).^[13] An emerging class of luminophores comprises first-row transition-metal complexes. They are, however, limited to complexes of d¹⁰ ions (Zn^{II}, Cu^I), such as [Zn(tpp)] or [Cu(PPh₃)₂(phen)]⁺ (tpp = *meso*-tetraphenylporphyrinato, phen = 1,10-phenanthroline) derivatives with quantum yields around 2–3%, lifetimes in the nanosecond range,^[1] and in most cases emission in the visible. Although considerable progress has been made in the field of Cu^I complexes,^[14] octahedral Cr^{III} complexes^[15] have been also suggested as NIR emitters partly because the Cr^{III} emission in solid materials, such as chromium-doped sapphire (ruby), has led to the historically important development of the ruby laser in 1960.^[16] The phosphorescence quantum efficiencies for most of these complexes were, however, too low ($\Phi < 0.1\%$) for practical applications^[1] despite the fascinating photophysical aspects observed in [Cr(ox)₃]³⁻ (ox = oxalato) polymeric networks^[17a,b] and the use of Cr^{III} complexes as energy donors for lanthanide emission in heterometallic complexes.^[17c–e] [Cr(bpy)₃]³⁺ and [Cr(phen)₃]³⁺ (byp = 2,2'-bipyridine) complexes have recently found renewed interest as photo-redox catalysts.^[18]

The reasons for the poor quantum yields of Cr^{III} complexes can be understood from ligand field theory.^[15] The desired luminescence of octahedral d³ Cr^{III} complexes with a (t_{2g})³(e_g)⁰ electron configuration occurs from a transition from doublet states (²E and ²T₁) to the quartet ground state (⁴A₂), in the red to near-infrared spectral region (for simplicity, we use the O_h point-group classification). The ²E and ²T₁ spectroscopic terms as well as the ⁴A₂ ground term arise from the (t_{2g})³ electron configuration and hence, the geometric reorganization is very minor, yielding sharp emission bands like the ruby emission.^[16] At low ligand-field strength, the doublet states lie above the ⁴T₂ state of electron configuration (t_{2g})²(e_g)¹ yielding weak, broad fluorescence from ⁴T₂ instead.^[19] Even for classical strong-field ligands, such as bpy, phen, or 2,2':6',2''-terpyridine (tpy), the energy difference between ⁴T₂ and the emitting ²E/²T₁ states is so small that back-intersystem crossing occurs, strongly reducing phosphorescence quantum yields and lifetimes.^[1,15] Furthermore, the ⁴T₂ state is prone to photosubstitution and hence, its back-population should be avoided.^[15,20] To increase the phosphorescence quantum yield, the energy difference between the ⁴T₂ and ²E states should be large to prevent back-intersystem crossing to the detrimental ⁴T₂ state. This should be achievable by using a strong ligand-field to shift

[*] S. Otto, Dr. C. Förster, C. Kreitner, Prof. K. Heinze
Institute of Inorganic and Analytical Chemistry
Johannes Gutenberg-University of Mainz
Duesbergweg 10–14, 55128 Mainz (Germany)
E-mail: katja.heinze@uni-mainz.de

Dr. M. Grabolle, Dr. U. Resch-Genger
Division 1.10
Federal Institute for Materials Research and Testing (BAM)
Richard-Willstätter-Strasse 11, 12489 Berlin (Germany)
E-mail: ute.resch@bam.de

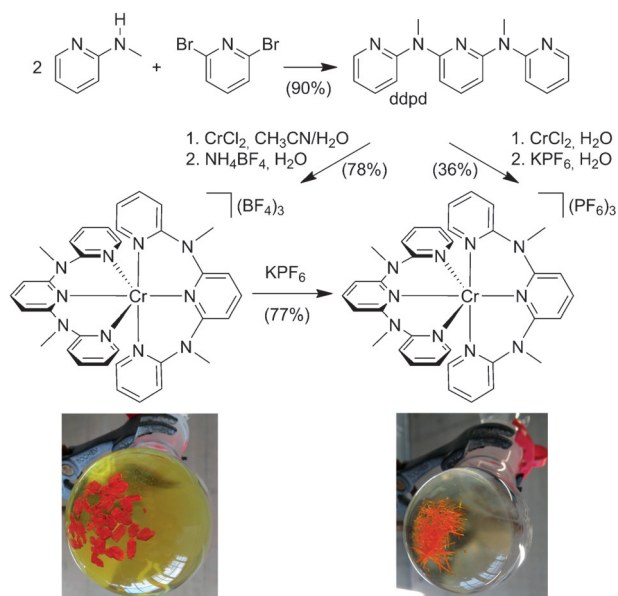
C. Kreitner
Graduate School Materials Science in Mainz
Staudingerweg 9, 55128 Mainz (Germany)



Supporting information for this article is available on the WWW under <http://dx.doi.org/10.1002/anie.201504894>.

the 4T_2 state to higher energy in conjunction with a strong nephelauxetic effect lowering the energy of the doublet states 2E and 2T_1 and hence should be made possible by proper ligand design.

Recently, we introduced the tridentate ddpd ligand (*N,N'*-dimethyl-*N,N'*-dipyridin-2-ylpyridine-2,6-diamine) with a large bite angle N-M-N of around 90° in six-coordinate metal complexes to optimize metal–ligand orbital overlap and to induce a stronger ligand field compared to bpy or tpy (Scheme 1).^[21] Also, ddpd is a poor π -acceptor ligand, that is,



Scheme 1. High-yield syntheses of $\mathbf{1}(X)_3$ and photographs of crystals of $\mathbf{1}(X)_3$ grown from CH_3CN solutions.

rather electron rich and difficult to reduce, but a quite strong σ -donor ligand.^[21] With these properties of ddpd in mind, we envisaged that ddpd could increase the energy of the 4T_2 state in a $[\text{Cr}(\text{ddpd})_3]^{3+}$ complex $\mathbf{1}^{3+}$ (Scheme 1) and simultaneously decrease the energy of the 2E state, resulting in an enlarged ${}^4T_2/{}^2E$ energy gap, which impedes back-intersystem crossing.

$[\text{Cr}(\text{bpy})_3]^{3+}$ and $[\text{Cr}(\text{tpy})_2]^{3+}$ are substitutionally labile under alkaline conditions giving the hydroxido complexes $[\text{Cr}(\text{bpy})_2(\text{OH})_2]^+$ and $[\text{Cr}(\text{tpy})(\text{OH})_x]_n^{(3-x)n}$.^[22] Possibly, the π -accepting ligands bpy and tpy reduce the electron density between the ligand axes by back-donation from t_{2g} orbitals, facilitating a nucleophilic attack of hydroxide. The π -accepting nature of bpy/tpy also accounts for the special redox properties, as reduction of $[\text{Cr}^{\text{III}}(\text{bpy})_3]^{3+}$ or $[\text{Cr}^{\text{III}}(\text{tpy})_2]^{3+}$ does not yield Cr^{II} , Cr^{I} , Cr^0 , Cr^{-1} oxidation states but is ligand centered.^[23] The envisaged ddpd complex $\mathbf{1}^{3+}$ should resist ligand-centered reductions and nucleophilic attack at the metal center due to the strong electron donating power of ddpd.

The synthesis of $\mathbf{1}^{3+}$ is straightforward from CrCl_2 and ddpd^[21a] in water. Ion exchange with $(\text{BF}_4)^-$ or $(\text{PF}_6)^-$ gives the bright orange salts $\mathbf{1}(\text{BF}_4)_3$ and $\mathbf{1}(\text{PF}_6)_3$ (Scheme 1, Supporting Information). Both were obtained as single

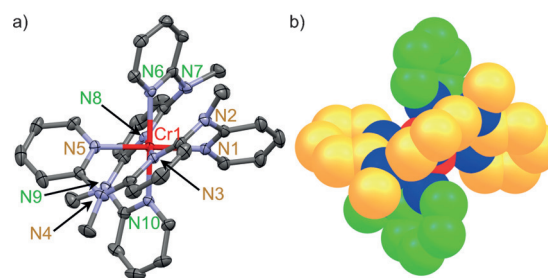


Figure 1. a) Molecular structure of the cation of $\mathbf{1}(\text{BF}_4)_3$ in the solid state (thermal ellipsoids set at 50% probability); b) space-filling representation of $\mathbf{1}^{3+}$ with the two ligands are shown in yellow and green, respectively (hydrogen atom omitted for clarity).

crystals suitable for X-ray diffraction analysis (Figure 1, Supporting Information, Figure S1). The complex cations feature an essentially octahedral CrN_6 coordination geometry with Cr-N distances of 2.028–2.054 Å and N-Cr-N angles close to 90° and 180° as required for a large ligand-field splitting. Similar to structurally comparable $[\text{M}(\text{ddpd})_2]^{2+}$ complexes, the ligands are wrapped around the metal center (Figure 1) and the counter ions fill the pockets between the ligands with $\text{Cr}\cdots\text{B/P}$ distances between 5.3 and 7.0 Å (Supporting Information, Figure S1).^[21]

Magnetic susceptibility and EPR data are consistent with a quartet ground state ($\chi T = 1.833 \text{ cm}^3 \text{ K mol}^{-1}$ at 300 K; $g_{\text{av}} = 1.990$ at 77 K, Figure S14, Supporting Information) similar to $[\text{Cr}(\text{tpy})_3]^{3+}$.^[24] A reversible $\text{Cr}^{\text{III/II}}$ reduction is observed at -1.11 V versus ferrocene (Supporting Information, Figure S13). Compared to $[\text{Cr}(\text{bpy})_3]^{3+}$ ($E_{1/2} = -0.63 \text{ V}$) and $[\text{Cr}(\text{tpy})_2]^{3+}$ ($E_{1/2} = -0.53 \text{ V}$), this reduction occurs at much more negative potential.^[23] DFT calculations (B3LYP, RIJ-COSX, Def2-SVP/J, Def2-SVP, ZORA) confirm the metal-centered reduction to Cr^{II} (Supporting Information, Figure S25,S26). The next reduction at $E_p = -1.94 \text{ V}$ is irreversible as coordinated ddpd cannot be reduced to its radical anion. Interestingly, $\mathbf{1}(\text{BF}_4)_3$ is highly soluble in water ($0.0479 \text{ mol L}^{-1}$) while $\mathbf{1}(\text{PF}_6)_3$ is more soluble in CH_3CN (0.208 mol L^{-1}), enabling different applications of the two salts. The absorption spectra of $\mathbf{1}^{3+}$ in H_2O or CH_3CN show maxima at 220(sh), 302, 315(sh), 350(sh), and 435 nm (Figure 2, Supporting Information, Figure S5) which can be assigned to $\pi\pi^*$, ligand-to-metal charge transfer (LMCT) and mixed metal-centered (MC)/LMCT excitations according to time-dependent DFT calculations (Supporting Information, Figure S20). No metal-to-ligand charge transfer (MLCT) transitions were identified in this energy region because of the weak electron-accepting properties of ddpd and the inaccessible $\text{Cr}^{\text{III/IV}}$ oxidation. The low-energy absorption maximum is ascribed to the ${}^4A_2 \rightarrow {}^4T_2$ transition (TD-DFT: 427.7, 436.9, and 439.0 nm) and an LMCT (Supporting Information, Figure S20). Three Laporte- and spin-forbidden transitions are found at 697, 736, and 776 nm in the single-crystal absorption spectrum of $\mathbf{1}(\text{BF}_4)_3$. These are assigned to ${}^4A_2 \rightarrow {}^2T_2$ (tentative), 2T_1 , and 2E excitations (Supporting Information, Figure S10). Excitation of a solution of $\mathbf{1}(\text{BF}_4)_3$ in water or CH_3CN (Supporting Information, Figure S8) at 435 nm leads to emission spectra that can be superimposed, as

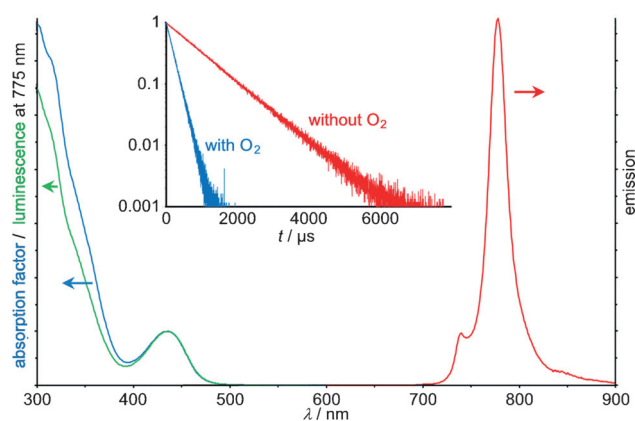


Figure 2. Absorption factor (blue), excitation ($\lambda_{\text{obs}} = 775$ nm, green) and emission spectrum ($\lambda_{\text{exc}} = 435$ nm, red) of $\mathbf{1}(\text{BF}_4)_3$ in deaerated H_2O at room temperature; the inset shows the emission decay curves of $\mathbf{1}(\text{BF}_4)_3$ in H_2O with and without O_2 .

depicted in Figure 2 for CH_3CN . The strong, sharp emission band at 775 nm (full width at half maximum height (FWHM) = 420 cm^{-1}) is ascribed to the ${}^2\text{E}$ emission and the weaker band at 738 nm to the ${}^2\text{T}_1$ emission.^[15,25] A single crystal of $\mathbf{1}(\text{BF}_4)_3$ emits at 740 and 778 nm (Supporting Information, Figure S11). Clearly, these two intraconfigurational doublet states equilibrate at room temperature both in solution and in the solid state. At 100 K in a frozen butyronitrile glass, only the ${}^2\text{E}$ emission at 779 nm is observed (Supporting Information, Figure S9). The emission of $\mathbf{1}^{3+}$ is considerably red shifted relative to $[\text{Cr}(\text{bpy})_3]^{3+}$ (727 nm) and $[\text{Cr}(\text{phen})_3]^{3+}$ (730 nm), but similar to that of $[\text{Cr}(\text{tpy})_2]^{3+}$ (770 nm).^[1,15] The solid material ruby emits at 694 nm.^[16]

The luminescence quantum yields (Φ) of $\mathbf{1}^{3+}$ in deaerated CH_3CN and H_2O were determined absolutely with an integrating-sphere setup to $\Phi = 12.1\%$ and 11.0% , respectively. In D_2O , Φ increases to 14.2% . To our knowledge, these Φ values are by far the highest values reported for Cr^{III} complexes in solution at room temperature to date.^[1,15] For instance, $[\text{Cr}(\text{bpy})_3]^{3+}$, $[\text{Cr}(\text{phen})_3]^{3+}$, and $[\text{Cr}(\text{tpy})_2]^{3+}$ have $\Phi = 0.089\%$, 0.15% , and $< 0.00089\%$ in water.^[1] The lifetimes (τ) of the emitting doublet states of $\mathbf{1}^{3+}$ were determined to $\tau = 899$, 898 , and $1164\ \mu\text{s}$ in deaerated CH_3CN , in H_2O , and in D_2O , respectively. Again, these are the highest values reported to date for a molecular Cr^{III} complex in solution at room temperature. The lifetimes of $[\text{Cr}(\text{bpy})_3]^{3+}$, $[\text{Cr}(\text{phen})_3]^{3+}$, and $[\text{Cr}(\text{tpy})_2]^{3+}$ are $\tau = 63\ \mu\text{s}$, $270\ \mu\text{s}$, and $\ll 30\ \mu\text{s}$, respectively.^[1] The solid laser material ruby has $\tau = 4270\ \mu\text{s}$ ^[16] while a single crystal of $\mathbf{1}(\text{BF}_4)_3$ reveals $\tau = 443\ \mu\text{s}$.

Excitation spectra recorded at 775 nm in CH_3CN and H_2O perfectly match with the absorption spectrum around the 435 nm maximum (Figure 2, Supporting Information, Figure S8) suggesting efficient population of the ${}^2\text{E}/{}^2\text{T}_1$ states from these ${}^4\text{T}_2$ ligand-field and LMCT states. At higher energies, the excitation spectra deviate from the absorption factor suggesting that not all high-energy states of $\mathbf{1}^{3+}$ populate the ${}^2\text{E}/{}^2\text{T}_1$ states. Excitation at 435 nm also yields a very weak broad emission band around 500 nm with τ of 3 ns, independent of the presence of O_2 (Supporting Information, Figure S7). As ddpd emits at 398 nm in CH_3CN ($\Phi =$

8.0% , $\tau = 3.0\text{ ns}$; Supporting Information, Figure S12), the weak 500 nm emission cannot be assigned to ddpd fluorescence but is ascribed to the spontaneous ${}^4\text{T}_2 \rightarrow {}^4\text{A}_2$ fluorescence of $\mathbf{1}^{3+}$. Delayed ${}^4\text{T}_2 \rightarrow {}^4\text{A}_2$ fluorescence^[15,19] fed by back-intersystem crossing from ${}^2\text{E}/{}^2\text{T}_1$ states is ruled out on the basis of the short lifetime. Hence, back-intersystem crossing is efficiently prevented in $\mathbf{1}^{3+}$ which accounts for its exceptionally high quantum yield and lifetime. The minimal energy difference between the relaxed ${}^2\text{E}$ and ${}^4\text{T}_2$ states is estimated at around 7100 cm^{-1} (0.88 eV ; 85 kJ mol^{-1}) from the emission spectra. Although the geometry of the ${}^2\text{E}$ state is close to that of the ${}^4\text{A}_2$ ground state, a large reorganization energy barrier is expected as the relaxed ${}^4\text{T}_2$ state features a Jahn–Teller distorted octahedron with $\text{Cr}-\text{N}_{\text{ax}}$ bonds elongated by approximately $0.3\ \text{\AA}$ according to DFT calculations (Supporting Information, Figure S24–S26).^[26] For back-intersystem crossing (${}^2\text{E} \rightarrow {}^4\text{T}_2$), the large energy gap and the reorganizational barrier must be overcome which is clearly impossible at room temperature (Figure 3).^[15] Direct intersystem crossing from ${}^4\text{T}_2$ to the vibrationally excited ${}^2\text{T}_1/{}^2\text{E}$ states or to the ${}^2\text{T}_2$

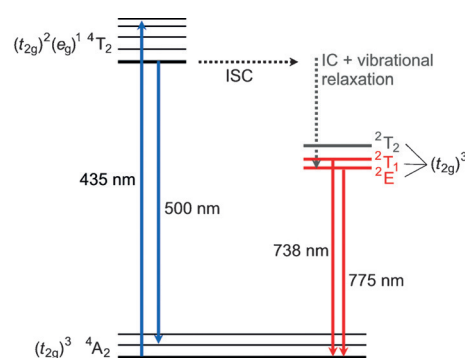


Figure 3. Jablonski diagram of $\mathbf{1}^{3+}$ constructed from experimental solution data (${}^2\text{T}_2$ state tentatively from single-crystal absorption). ISC = intersystem crossing, IC = internal conversion.

state and subsequent internal conversion is conceivable (Figure 3). For $\text{Cr}(\text{acac})_3$ (acac = acetylacetonato), McCusker et al. have shown that intersystem crossing to ${}^2\text{E}$ is faster than vibrational cooling within the ${}^4\text{T}_2$ state along the Jahn–Teller modes.^[27] Intersystem crossing might also occur from vibrationally hot states in $\mathbf{1}^{3+}$ before the Jahn–Teller distortion. Independent of the details of the intersystem crossing processes, the use of the strong-field ddpd ligand is very efficient in inducing high phosphorescence quantum yields and lifetimes as a result of the large barrier for back-intersystem crossing.^[15]

As expected, the phosphorescence quantum yield is sensitive to the presence of O_2 .^[28,29] In air, Φ is reduced by factors of 5.2 (H_2O) and 17 (CH_3CN) and the lifetimes are correspondingly shortened from $898\ \mu\text{s}$ to $177\ \mu\text{s}$ (H_2O) and $51\ \mu\text{s}$ (CH_3CN) (Figure 2). The bimolecular O_2 quenching constant has been estimated from a Stern–Volmer plot of $\mathbf{1}(\text{BF}_4)_3$ in H_2O as $k_q = 1.77 \times 10^7\text{ M}^{-1}\text{s}^{-1}$ and the Stern–Volmer constant as $K_{\text{SV}} = k_q \times \tau = 1.59 \times 10^4\text{ M}^{-1}$ (Supporting Information, Figure S15). These quenching efficiencies^[29] suggest possible applications of $\mathbf{1}^{3+}$ in optical oxygen sensors.^[2,30]

with the large difference between excitation and emission easing the combination with a spectrally distinguishable O₂-inert reference dye. The quenching efficiency is explained on the basis of the very long ²E lifetime and on the basis of spin statistics, although k_q is not particularly large.^[29c] The k_q value might be associated with an effective shielding of Cr^{III} by the ligands and the counterions (Figure 1, Figure S1). Commonly employed optical oxygen sensors are based on the quenching of their dye's excited triplet states, for example, ³MLCT or ³ππ*, by ³O₂ yielding the dye's singlet ground state and ¹O₂.^[2,30] For these triplet states, spin statistics predict that 1/9 (11%) of the possible encounters (quintet, triplet, singlet: 9 possibilities), namely the singlets, are productive. For the ²E state of **1**³⁺ and ³O₂, a quartet and a doublet encounter complex is conceivable giving six microstate possibilities. The quartet encounter is productive giving the ⁴A₂ state of **1**³⁺ and ¹O₂. Hence, 4/6 (67%) of the encounters should yield ¹O₂ which explains the O₂ sensitivity of Cr^{III} complexes in general.

The substitutional stability of **1**(BF₄)₃ was probed in aqueous solution (pH 7) as well as in the presence of HCl (pH 2.1) and NaOH (pH 11.9). The cation **1**³⁺ is stable for at least 2.5 months according to UV/Vis spectroscopy (Figure S16,S17). This stability is in stark contrast to the lability of [Cr(bpy)₃]³⁺ and [Cr(tpy)₂]³⁺.^[22] Also, **1**³⁺ is perfectly stable in 0.1 M [nBu₄N]Cl and in [nBu₄N](OH) (pH 11.4) H₂O/CH₃CN (1:1) solution under illumination with LEDs at 430 nm in air according to absorption and emission spectra while an isoabsorptive solution of [Cr(bpy)₃]³⁺ undergoes complete photosubstitution within a few hours (Figure S18).^[15] These experiments demonstrate the superior stability of **1**³⁺ compared to [Cr(bpy)₃]³⁺ in aqueous solution.

Thanks to the difficult Cr^{III}/Cr^{II} reduction and the low ²E energy, the oxidative power of the ²E state of **1**³⁺ is rather small [$E(\text{Cr}^{\text{III/II}}) = E(\text{Cr}^{\text{III/II}}) + E_{00}(\text{^2E}) = -1.11 \text{ V} + 1.60 \text{ V} = 0.49 \text{ V}$ versus ferrocene (+1.12 V vs. normal hydrogen electrode (NHE))]. Hence, no photooxidative damage to organic material is expected. In contrast [Cr(bpy)₃]³⁺ or [Cr(tpy)₂]³⁺ photooxidize dGMP and hence, cleave DNA in their excited states (ttpy = *p*-tolylterpyridine, dGMP = deoxyguanosine monophosphate).^[31] Indeed, dGMP ($E = 1.29 \text{ V}$ vs. NHE) quenches the emission of [Cr(bpy)₃]³⁺ under our conditions but not that of **1**³⁺ (Figure S19).

Based upon rational ligand design, we could obtain the first molecular, water- or CH₃CN-soluble ruby analogues **1**(BF₄)₃ and **1**(PF₆)₃ with excellent phosphorescence quantum yields. Together with their high stability, their simple high-yield synthesis, their large excitation/emission energy gap and long lifetime these properties will allow a plethora of applications, such as time-gated imaging, the design of optical probes, and integration into multiplexed sensing schemes. We aim to explore their full potential in the near future.

Acknowledgements

We thank Luca Carrella and Eva Rentschler for collecting the SQUID data of **1**(PF₆)₃. Parts of this research were conducted using the supercomputer Mogon and advisory services offered by Johannes Gutenberg University Mainz

(www.hpc.uni-mainz.de), which is a member of the AHRP and the Gauss Alliance e.V. This work was financially supported by the Deutsche Forschungsgemeinschaft (GSC 266, Materials Science in Mainz, scholarship for C.K.).

Keywords: chromium complexes · intersystem crossing · ligand-field splitting · NIR luminescence · photophysics

How to cite: *Angew. Chem. Int. Ed.* **2015**, *54*, 11572–11576
Angew. Chem. **2015**, *127*, 11735–11739

- [1] H. Xiang, J. Cheng, X. Ma, X. Zhou, J. Chruma, *Chem. Soc. Rev.* **2013**, *42*, 6128–6185.
- [2] M. Quaranta, S. M. Borisov, I. Klimant, *Bioanal. Rev.* **2012**, *4*, 115–157.
- [3] a) “Luminescent lanthanide complex, and articles and inks containing the luminescent complex”: F. Thomas, C. Laporte, PCT Int. Appl. WO 2014048702A1, **2014**; b) “Secure document comprising luminescent chelates”: V. Aboutanos, T. Tiller, C. Reinhard, S. Rascagnères, PCT Int. Appl. WO 2010130681A1, **2010**.
- [4] A. J. Amoroso, S. J. A. Pope, *Chem. Soc. Rev.* **2015**, *44*, 4723–4742.
- [5] E. Pershagen, K. E. Borbas, *Coord. Chem. Rev.* **2014**, *273–274*, 30–46.
- [6] E. J. New, D. Parker, D. G. Smith, J. W. Walton, *Curr. Opin. Chem. Biol.* **2010**, *14*, 238–246.
- [7] S. V. Eliseeva, J.-C. G. Bünzli, *Chem. Soc. Rev.* **2010**, *39*, 189–227.
- [8] a) Q. Zhao, C. Huanga, F. Li, *Chem. Soc. Rev.* **2011**, *40*, 2508–2524; b) O. S. Wenger, *Chem. Rev.* **2013**, *113*, 3686–3733.
- [9] V. W.-W. Yam, K. M.-C. Wong, *Chem. Commun.* **2011**, *47*, 11579–11592.
- [10] P.-T. Chou, Y. Chi, *Chem. Eur. J.* **2007**, *13*, 380–395.
- [11] Selection of examples: a) S. Wiktorowski, C. Rosazza, M. J. Winterhalder, E. Daltrozzo, A. Zumbusch, *Chem. Commun.* **2014**, *50*, 4755–4758; b) T. Marks, E. Daltrozzo, A. Zumbusch, *Chem. Eur. J.* **2014**, *20*, 6494–6504; c) D. Frath, J. Massue, G. Ulrich, R. Ziessel, *Angew. Chem. Int. Ed.* **2014**, *53*, 2290–2310; *Angew. Chem.* **2014**, *126*, 2322–2342; d) J. C. Er, C. Leong, C. L. Teoh, Q. Yuan, P. Merchant, M. Dunn, D. Sulzer, D. Sames, A. Bhinge, D. Kim, S.-M. Kim, M.-H. Yoon, L. W. Stanton, S. H. Je, S.-W. Yun, Y.-T. Chang, *Angew. Chem. Int. Ed.* **2015**, *54*, 2442–2446; *Angew. Chem.* **2015**, *127*, 2472–2476; e) S. Wiktorowski, E. Daltrozzo, A. Zumbusch, *RSC Adv.* **2015**, *5*, 29420–29423; f) D. Jansch, C. Li, L. Chen, M. Wagner, K. Müllen, *Angew. Chem. Int. Ed.* **2015**, *54*, 2285–2289; *Angew. Chem.* **2015**, *127*, 2314–2319; g) E. Heyer, P. Lory, J. Leprince, M. Moreau, A. Romieu, M. Guardigli, A. Roda, R. Ziessel, *Angew. Chem. Int. Ed.* **2015**, *54*, 2995–2999; *Angew. Chem.* **2015**, *127*, 3038–3042; h) U. Resch-Genger, M. Grabolle, S. Cavaliere-Jaricot, R. Nitschke, T. Nann, *Nat. Methods* **2008**, *5*, 763–775.
- [12] M. Schulze, A. Steffen, F. Würthner, *Angew. Chem. Int. Ed.* **2015**, *54*, 1570–1573; *Angew. Chem.* **2015**, *127*, 1590–1593.
- [13] a) J. V. Caspar, E. M. Kober, B. P. Sullivan, T. J. Meyer, *J. Am. Chem. Soc.* **1982**, *104*, 630–632; b) J. V. Caspar, T. J. Meyer, *J. Am. Chem. Soc.* **1983**, *105*, 5583–5590; c) J. V. Caspar, T. J. Meyer, *J. Phys. Chem.* **1983**, *87*, 952–957; d) T. J. Meyer, *Pure Appl. Chem.* **1986**, *58*, 1193–1206.
- [14] a) N. Armaroli, G. Accorsi, F. Cardinalli, A. Listorti, *Top. Curr. Chem.* **2007**, *280*, 69–115; b) C. E. McCusker, F. N. Castellano, *Inorg. Chem.* **2013**, *52*, 8114–8120; c) M. S. Lazorski, F. N. Castellano, *Polyhedron* **2014**, *33*, 57–70.
- [15] a) A. D. Kirk, *Chem. Rev.* **1999**, *99*, 1607–1640; b) L. S. Forster, *Coord. Chem. Rev.* **2002**, *227*, 59–92; c) N. A. P. Kane-Maguire, *Top. Curr. Chem.* **2007**, *280*, 37–67; d) V. Balzani, P. Ceroni, A.

- Juris, *Photochemistry and Photophysics*, Wiley-VCH, Weinheim, **2014**, pp. 216–219; e) M. A. Jamieson, N. Serpone, M. Z. Hoffman, *Coord. Chem. Rev.* **1981**, *39*, 121–179; f) C. K. Ryu, J. F. Endicott, *Inorg. Chem.* **1988**, *27*, 2203–2214.
- [16] a) T. H. Maiman, *Nature* **1960**, *187*, 493–494; b) C. Degli Esposti, L. Bizzocchi, *J. Chem. Educ.* **2007**, *84*, 1316–1318.
- [17] a) A. Hauser, M. E. Von Arx, R. Pellaux, S. Decurtins, *Mol. Cryst. Liq. Cryst.* **1996**, *286*, 225–230; b) M. Milos, S. Kairouani, S. Rabaste, A. Hauser, *Coord. Chem. Rev.* **2008**, *252*, 2540–2551; c) L. Aboshyan-Sorgho, H. Nozary, A. Aebischer, J.-C. G. Bünzli, P.-Y. Morgantini, K. R. Kittilstved, A. Hauser, S. V. Eliseeva, S. Petoud, C. Piguët, *J. Am. Chem. Soc.* **2012**, *134*, 12675–12684; d) M. Cantuel, F. Gumy, J.-C. G. Bünzli, C. Piguët, *Dalton Trans.* **2006**, 2647–2660; e) S. Torelli, D. Imbert, M. Cantuel, G. Bernardinelli, S. Delahaye, A. Hauser, J.-C. G. Bünzli, C. Piguët, *Chem. Eur. J.* **2005**, *11*, 3228–3242.
- [18] S. M. Stevenson, M. P. Shores, E. M. Ferreira, *Angew. Chem. Int. Ed.* **2015**, *54*, 6506–6510; *Angew. Chem.* **2015**, *127*, 6606–6610.
- [19] a) H. Yersin, P. Huber, G. Gietl, D. Trümbach, *Chem. Phys. Lett.* **1992**, *199*, 1–9; b) F. Castelli, L.-S. Forster, *J. Am. Chem. Soc.* **1975**, *97*, 6306–6309.
- [20] a) N. Sabbatini, V. Balzani, *J. Am. Chem. Soc.* **1972**, *94*, 7587–7589; b) H. F. Wasgestian, *J. Phys. Chem.* **1972**, *76*, 1947–1951.
- [21] a) A. Breivogel, C. Förster, K. Heinze, *Inorg. Chem.* **2010**, *49*, 7052–7056; b) K. Mack, A. Wünsche von Leupoldt, C. Förster, M. Ezhevskaya, D. Hinderberger, K. W. Klinkhammer, K. Heinze, *Inorg. Chem.* **2012**, *51*, 7851–7858; c) A. Breivogel, M. Meister, C. Förster, F. Laquai, K. Heinze, *Chem. Eur. J.* **2013**, *19*, 13745–13760; d) C. Förster, K. Mack, L. M. Carrella, V. Ksenofontov, E. Rentschler, K. Heinze, *Polyhedron* **2013**, *52*, 576–581; e) A. Breivogel, M. Park, D. Lee, S. Klassen, A. Kühnle, C. Lee, K. Char, K. Heinze, *Eur. J. Inorg. Chem.* **2014**, 288–295; f) A. Breivogel, C. Kreitner, K. Heinze, *Eur. J. Inorg. Chem.* **2014**, 5468–5490; g) A. K. C. Mengel, C. Förster, A. Breivogel, K. Mack, J. R. Ochsmann, F. Laquai, V. Ksenofontov, K. Heinze, *Chem. Eur. J.* **2015**, *21*, 704–714.
- [22] a) M. Maestri, F. Bolletta, N. Serpone, L. Moggi, V. Balzani, *Inorg. Chem.* **1976**, *15*, 2048–2051; b) E. C. Constable, C. E. Housecroft, M. Neuburger, J. Schönle, J. A. Zampese, *Dalton Trans.* **2014**, *43*, 7227–7235.
- [23] a) C. C. Scarborough, K. M. Lancaster, S. DeBeer, T. Weyhermüller, S. Sproules, K. Wieghardt, *Inorg. Chem.* **2012**, *51*, 3718–3732; b) C. C. Scarborough, S. Sproules, T. Weyhermüller, S. Serena DeBeer, K. Wieghardt, *Inorg. Chem.* **2011**, *50*, 12446–12462.
- [24] U. Casellato, R. Graziani, R. P. Bonomo, A. J. Di Bilio, *J. Chem. Soc. Dalton Trans.* **1991**, 23–31.
- [25] N. A. P. Kane-Maguire, J. Conway, C. H. Langford, *J. Chem. Soc. Chem. Commun.* **1974**, 801–802.
- [26] a) F. Gilardoni, J. Weber, K. Bellafrouh, C. Daul, H. U. Güdel, *J. Chem. Phys.* **1996**, *104*, 7624–7632; b) O. S. Wenger, H. U. Güdel, *J. Chem. Phys.* **2001**, *114*, 5832–5841.
- [27] a) E. A. Juban, J. K. McCusker, *J. Am. Chem. Soc.* **2005**, *127*, 6857–6865; b) E. A. Juban, A. L. Smeigh, J. E. Monat, J. K. McCusker, *Coord. Chem. Rev.* **2006**, *250*, 1783–1791.
- [28] a) N. Serpone, M. A. Jamieson, M. S. Henry, M. Z. Hoffman, F. Bolletta, M. Maestri, *J. Am. Chem. Soc.* **1979**, *101*, 2907–2916; b) B. Brunshwig, N. Sutin, *J. Am. Chem. Soc.* **1978**, *100*, 7568–7577.
- [29] a) M. Isaacs, A. G. Sykes, S. Ronco, *Inorg. Chim. Acta* **2006**, *359*, 3847–3854; b) K. D. Barker, K. A. Barnett, S. M. Connell, J. W. Glaeser, A. J. Wallace, J. Wildsmith, B. J. Herbert, J. F. Wheeler, N. A. P. Kane-Maguire, *Inorg. Chim. Acta* **2001**, *316*, 41–49; c) M. Z. Hoffman, F. Bolletta, L. Moggi, G. L. Hug, *J. Phys. Chem. Ref. Data* **1989**, *18*, 219–543.
- [30] J. Napp, T. Behnke, L. Fischer, C. Würth, M. Wottawa, D. M. Katschinski, F. Alves, U. Resch-Genger, M. Schäferling, *Anal. Chem.* **2011**, *83*, 9039–9046.
- [31] a) R. T. Watson, N. Desai, J. Wildsmith, J. F. Wheeler, N. A. P. Kane-Maguire, *Inorg. Chem.* **1999**, *38*, 2683–2687; b) V. G. Vaidyanathan, B. U. Nair, *Eur. J. Inorg. Chem.* **2004**, 1840–1846.

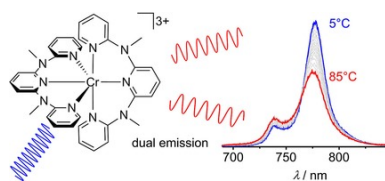
Received: May 29, 2015

Published online: August 12, 2015

3.2 Thermo-Chromium: A Contactless Optical Molecular Thermometer

Sven Otto, Norman Scholz, Thomas Behnke, Ute Resch-Genger and Katja Heinze

Chem. Eur. J. **2017**, *23*, 12131–12135.



The unparalleled excited-state potential-energy landscape of the chromium(III)-based dye [Cr(ddpd)₂]³⁺ (ddpd = N,N'-dimethyl-N,N'-dipyridin-2-ylpyridine-2,6-diamine) enables a strong dual emission in the near infrared region. The temperature dependence of this dual emission allows its use as an unprecedented molecular ratiometric thermometer in the 210–373 K temperature range in organic and in aqueous media.

Author Contributions

Sven Otto carried out the temperature dependent emission spectroscopic experiments in solution. Norman Scholz, Thomas Behnke and Ute Resch-Genger carried out the temperature dependent emission spectroscopic experiments of [Cr(ddpd)₂]³⁺ embedded in nanoparticles and micelles at the *Bundesanstalt für Materialforschung und -prüfung* in Berlin, Germany. The manuscript was written by Katja Heinze (90 %) and Sven Otto (10 %).

Supporting Information

for this article is found at pp.160.

“Otto, S.; Scholz, N.; Behnke, T.; Resch-Genger, U.; Heinze, K. *Chem. Eur. J.* **2017**, *23*, 12131–12135. Copyright Wiley-VCH Verlag GmbH & Co. KGaA. Reproduced with permission.”

Photochemistry



Thermo-Chromium: A Contactless Optical Molecular Thermometer

Sven Otto,^[a, b] Norman Scholz,^[c] Thomas Behnke,^[c] Ute Resch-Genger,^{*[c]} and Katja Heinze^{*[a]}

Abstract: The unparalleled excited-state potential-energy landscape of the chromium(III)-based dye $[1]^{3+}$ ($[\text{Cr}(\text{ddpd})_2]^{3+}$; $\text{ddpd} = N,N'$ -dimethyl- N,N' -dipyridin-2-yl-pyridin-2,6-diamine) enables a strong dual emission in the near infrared region. The temperature dependence of this dual emission allows the use of $[1]^{3+}$ as an unprecedented molecular ratiometric thermometer in the 210–373 K temperature range in organic and in aqueous media. Incorporation of $[1]^{3+}$ in biocompatible nanocarriers, such as 100 nm-sized polystyrene nanoparticles and solutol micelles, provides nanodimensional thermometers operating under physiological conditions.

Optical sensing of physicochemical quantities, such as temperature (T), pressure, oxygen concentration, or pH, is of tremendous importance in many fields.^[1] Applications requiring T sensing range from biology (e.g., intracellular thermometry)^[2] and medical diagnostics (e.g., point-of-care diagnostics^[3] using amplifying enzymatic reactions^[4] to chemical synthesis (e.g., microfluidics^[5]), and materials sciences (e.g., T -sensitive paints^[6] for spatial sensing in wind tunnels).

Optical T measurements utilizing T -dependent fluorometric parameters, such as luminescence intensity (or intensity ratios) and lifetime, have been achieved with different classes of molecular and nanoscale emitters.^[1c, d] Examples are polymer-based nanoparticles,^[7] lanthanide-based nanocrystals,^[8] and DNA-based systems, such as molecular beacons (MBs).^[9]

Fluorometric T sensing can be done nonratiometrically, exploiting the T sensitivity of the fluorescence intensity of

a single-emission band (e.g., rhodamine B),^[10] which is prone to artefacts due to fluctuations in, for example, excitation light intensity, or ratiometrically requiring two emission bands, one being T sensitive and one not responding to changes in T for signal referencing. Ratiometric T sensing can be achieved with three design concepts: a) a combination of two emissive dyes (T -responsive probe and T -inert reference); b) a combination of two dyes which interact by a distance-dependent process, such as fluorescence resonance energy transfer (EnT) in systems, in which dye distance is modified by T ; and c) a single dye displaying dual emission (Figure 1).^[1]

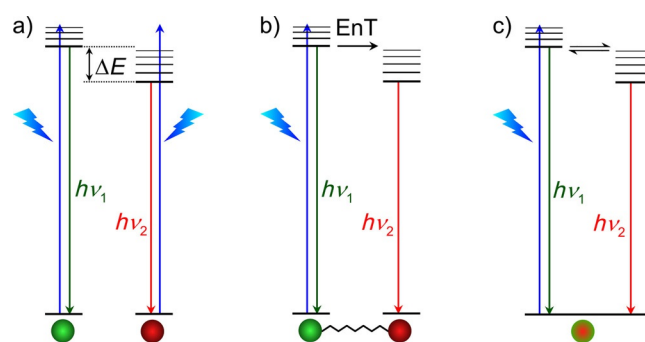


Figure 1. Principles of dual-emission optical thermometers: a) two distinct dyes; b) two fluorophores interacting through energy transfer EnT; and c) single dye with two equilibrating excited states.

Scenario a) is commonly achieved by combining two organic fluorophores in a fixed ratio, for example, within nanoparticles (Figure 1a). Both dyes must be excitable at the same wavelength and show spectrally distinguishable emission bands to allow separating and integrating the luminescence signals for the calculation of the excitation light intensity-independent T -sensitive quotient $I_{\text{probe}}/I_{\text{ref}}$.

Fluorescent T sensors, which exploit T -dependent structural features communicated as changes in fluorescence intensity of the reporter dyes are fluorophore-labeled MBs (Figure 1b).^[9] These flexible single-stranded oligonucleotides are either dually labeled at their 5'- and 3'-ends with a fluorophore and a nonemissive quencher (nonratiometric MBs) or with two spectrally distinguishable emitters (ratiometric MBs). The fluorescence properties of these MBs are determined by the T -dependent conformation of the stem region, which defines the label distance. Because large molecular motions are involved, thermometers based on MBs are only operative in solution.

Scenario c), internal referencing of the T -sensitive optical signal of a single dual emissive fluorophore, is principally the more straightforward approach than the use of two separate

[a] S. Otto, Prof. K. Heinze
Institute of Inorganic Chemistry and Analytical Chemistry
Johannes Gutenberg-University of Mainz
Duesbergweg 10–14, 55128 Mainz (Germany)
E-mail: katja.heinze@uni-mainz.de

[b] S. Otto
Graduate School Materials Science in Mainz
Staudingerweg 9, 55128 Mainz (Germany)

[c] N. Scholz, Dr. T. Behnke, Dr. U. Resch-Genger
Division 1.10, Federal Institute for Materials Research and
Testing (BAM), Richard-Willstätter-Strasse 11, 12489 Berlin (Germany)
E-mail: ute.resch@bam.de

Supporting information and the ORCID identification number for the author of this article can be found under <https://doi.org/10.1002/chem.201701726>.

Part of a Special Issue to celebrate the 150th anniversary of the German Chemical Society (GDCh). To view the complete issue, visit <https://doi.org/chem.v23.50>.

emitters (Figure 1 c). Herein, nonspecific environmental factors affecting the dye luminescence differently, concentration variations, and a different photostability are eliminated.^[1b] This design concept is seldom realized, particularly for small molecular sensors, because most emitters display only a single-luminescence band. To date, this has been achieved with a few nanoscale systems, such as $\text{Er}^{3+}:\text{Yb}^{3+}:\text{NaYF}_4$ nanocrystals, exploiting the dual f-f emission of erbium(III) ions from ${}^2\text{H}_{11/2}$ and ${}^4\text{S}_{3/2}$ states.^[11] Another examples are Mn^{2+} -doped ZnSe quantum dots, in which the ${}^4\text{T}_1$ excited state of the Mn^{2+} ions is brought into equilibrium with excitonic states of the semiconductor nanocrystal.^[12] One of the very few small molecular *T* sensors based on a single chromophore with dual emission^[1,13] is [dipyren-1-yl(2,4,6-triisopropylphenyl)-borane], which features a locally excited state and a twisted intramolecular charge-transfer state. The latter state is preferred at lower *T*, changing the emission color from blue to green. Yet, the two emission bands are poorly resolved, and a *T*-dependent overall wavelength shift was observed.^[1b,13a] Because geometrical reorganization accompanies the equilibration between both states, molecular thermometers reported to date operate only in solution.^[1b,13]

Also, the *T*-sensitivity of thermally activated delayed luminescence from a triplet to a singlet excited state can be exploited for optical *T* measurements. For instance, the fluorescence/phosphorescence intensity ratio of acridine yellow in a rigid saccharide glass is sensitive to *T*.^[14] Similarly, copper(I) clusters and silver(I), gold(I), and platinum(II) complexes can display thermochromic behavior, yet this has not been utilized for *T* sensing, most likely because of stability issues.^[15] Furthermore, the emission is typically restricted to the solid state.

For biological applications, luminescence in the red or near infrared (NIR) spectral region is commonly desired to avoid interferences from the auto-fluorescence of the biological matrix. This renders molecular emitters with sharp, non-overlapping red-NIR emission bands above 650 nm particularly attractive.^[16] Except for some nanocrystalline lanthanide-based emitters, such as upconversion nanoparticles, which suffer from a low brightness, a different excitation power density dependence of the red and green emission, and luminescence quenching by water molecules, these requirements are very challenging to achieve.^[8] Up to date, molecular thermometers with *T*-dependent dual NIR emission have not yet been reported.^[2-17]

An ideal molecular system for ratiometric optical *T*-sensing requires two long-term stable, spectrally well-distinguishable emission bands^[17] with the two emitting excited states being in thermal equilibrium. For *T* sensing by thermal population of these states, their energy difference ΔE should be in the range of the thermal energy. To achieve a population ratio and hence an emission intensity ratio of 1:15, an energy difference of $RT \ln(1/15) \approx 7 \text{ kJ mol}^{-1}$ ($\approx 555 \text{ cm}^{-1}$) is required at room temperature. For spectral discrimination, the width of the emission bands (full width at half maximum, FWHM) should be below ΔE without interference from vibrational progressions. This is a particularly challenging criterion due to the required small energy difference ΔE (ca. $400\text{--}800 \text{ cm}^{-1}$) and can be solely met by emissive states that are only weakly distorted relative to the

ground state. This is extremely difficult to realize with organic dyes and seldom fulfilled in metal-to-ligand-charge transfer emitters, such as ruthenium(II) or iridium(III) molecular complexes.^[17] Furthermore, the two emissive states should feature large energy differences with respect to the excitation energy to enable the combination with other spectrally discriminable stimuli-responsive molecules, such as pH probes in multiparametric sensor systems, which can be excited at the same wavelength. Moreover, a large energy difference is beneficial to avoid interferences from scattered excitation light.

These properties are all combined in Cr^{III} complexes $[\text{Cr}(\text{ddpd})_2][\text{X}]_3$ $[\mathbf{1}][\text{X}]_3$ ^[19] based on the tridentate N[^]N[^]N[^] ligand ddpd (ddpd = *N,N'*-dimethyl-*N,N'*-dipyridin-2-yl-pyridin-2,6-diamine,^[20] X = BF_4 , PF_6 ; Figure 2) recently reported by us. These

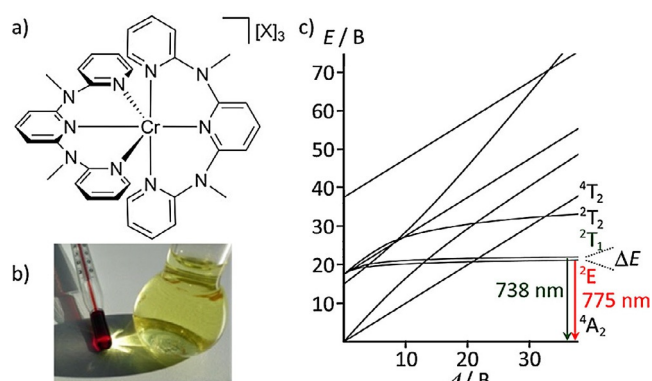


Figure 2. a) Molecular structure of the dual NIR emitters $[\mathbf{1}][\text{X}]_3$; b) photograph of an aqueous solution of $[\mathbf{1}][\text{BF}_4]_3$; and c) Tanabe–Sugano diagram of the d^3 electron configuration including term energies and energy difference ΔE relevant for $[\mathbf{1}]^{3+}$.^[18]

chromium(III) dyes are soluble and stable in water even at high pH and under illumination with 430 nm light (Figure 2 b). Both complexes displayed NIR emission with a high quantum yield (Φ) of 11% and a lifetime of 899 μs in water.^[19] The unique excited-state potential-energy landscape of Cr^{III} ions with a ground state $(t_{2g})^3$ electron configuration provides two closely lying ${}^2\text{E}$ and ${}^2\text{T}_1$ states^[18] (Figure 2 c) with emission at 775 nm (${}^2\text{E}$) and 738 nm (${}^2\text{T}_1$).^[19] The energy difference between these doublet states of $\Delta E = 7.7 \text{ kJ mol}^{-1}$ (650 cm^{-1}) is in the range of the thermal energy. Because the ${}^2\text{E}$ and ${}^2\text{T}_2$ states originate from the same $(t_{2g})^3$ electron configuration as the ${}^4\text{A}_2$ ground state, they are essentially undistorted yielding sharp emission bands with FWHM around 400 cm^{-1} .^[19] Hence, we anticipated that the unique strong dual NIR emission of $[\mathbf{1}]^{3+}$ will enable ratiometric *T* sensing in the NIR. To the best of our knowledge, this unique feature of the d^3 electron configuration has not yet been explored for *T* sensing due to the poor Φ and photolability of conventional chromium(III) complexes.^[16]

As shown in Figure 3 a, cooling a solution of $[\mathbf{1}][\text{BF}_4]_3$ in MeCN/PrCN from 300 to 210 K increased the intensity of the low-energy ${}^2\text{E}$ emission band at 775 nm and concomitantly decreases the ${}^2\text{T}_1$ emission band at 738 nm. The absorption spectrum remains basically unchanged proving the absence of major structural changes. The emission intensity remains con-

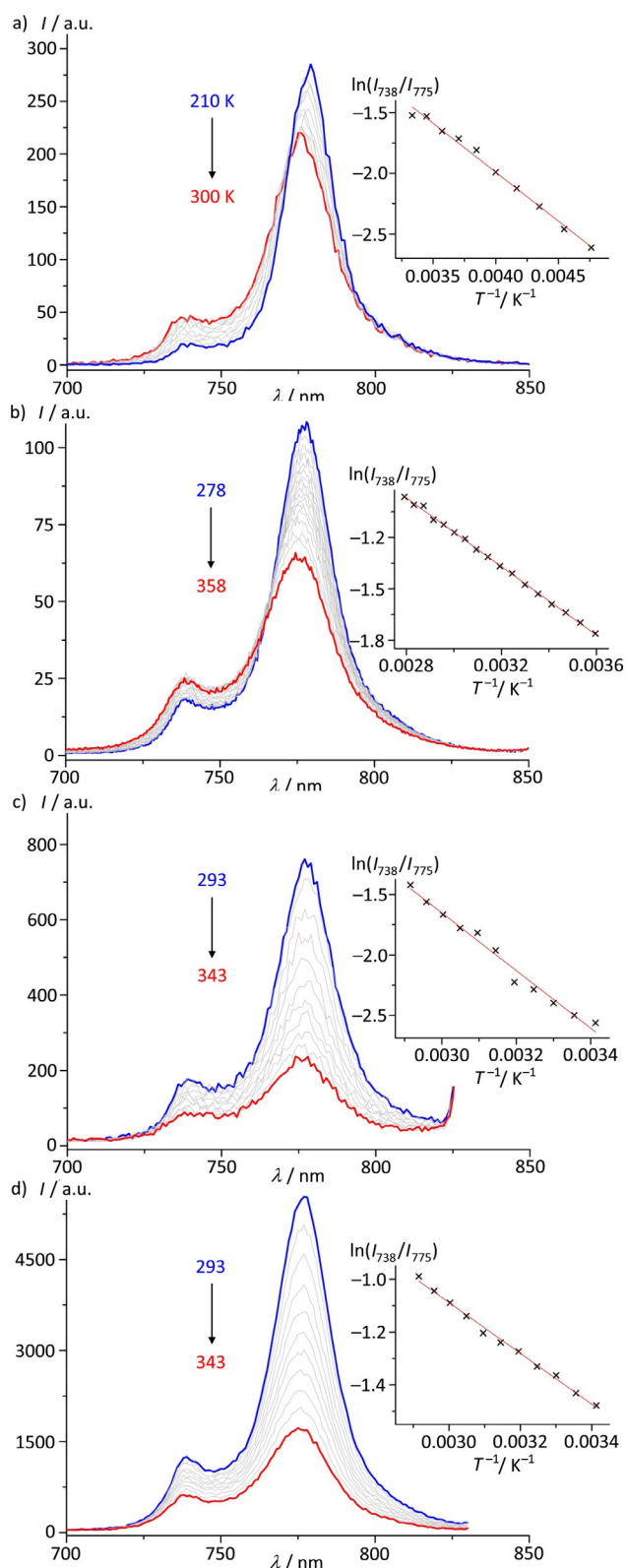


Figure 3. Variable-temperature (VT) emission spectra of: a) $[1][\text{BF}_4]_3$ in MeCN/PrCN (1:6) from 210 to 300 K (Ar saturated); b) $[1][\text{BF}_4]_3$ in H_2O from 278 to 358 K (air saturated); c) $[1][\text{PF}_6]_3$ in PSP-COOH in H_2O from 293–343 K (Ar saturated); and d) $[1][\text{PF}_6]_3$ in solutol micelles in H_2O from 293–343 K (Ar saturated); the insets show the respective Boltzmann plots $\ln(I_{738}/I_{775})$ vs. T^{-1} . The T -induced changes in emission are fully reversible.

stant excluding a thermally activated decay pathway, for example, through the ligand-field $^4\text{T}_2$ state (Figures 2c and S1 in the Supporting Information). Hence, no thermally activated delayed fluorescence through back-intersystem crossing is operative up to 358 K.^[15b] This is expected from the huge energy difference between the ^2E and $^4\text{T}_2$ states in $[\text{1}]^{3+}$ of more than 85 kJ mol^{-1} (Figure 2c).^[19] Plotting the logarithm of the ratio of the emission band intensities $\ln(I_{738}/I_{775})$ versus the inverse temperature T^{-1} gave a straight line with a slope corresponding to the energy difference ΔE between the states (Figure 3a, inset). Hence, Boltzmann-type behavior was clearly observed. Using the areas under the emission bands a_{738}/a_{775} instead of the intensities gave basically the same results (Figure S2 in the Supporting Information).^[21]

Thermochromic behavior of $[\text{1}]^{3+}$ was also observed upon heating a solution of $[\text{1}]^{3+}$ in H_2O from 278 to 358 K (Figure 3b). The ^2E emission diminished, while the $^2\text{T}_1$ emission increased. The combined Φ remained constant, and thermal deactivation through high-energy states or thermal decomposition is negligible. The Boltzmann plot $\ln(I_{738}/I_{775})$ versus T^{-1} is linear, and the slope corresponds to ΔE between the ^2E and $^2\text{T}_1$ states (Figure 3b). Hence, the molecular thermometer $[\text{1}]^{3+}$ operates in the physiological temperature range in water.

In a water/diethylene glycol (1:2) mixture, the operating T of the molecular Cr^{III} thermometer was further expanded to 223–373 K, covering a wide range of 150 K in fluid solution (Figure S3 in the Supporting Information). This range might even be expandable in both directions employing adequate solvents or solvent mixtures. Moreover, because of the extremely large energy gap between excitation ($^4\text{A}_2 \rightarrow ^4\text{T}_2$) and emission ($^2\text{E}/^2\text{T}_1 \rightarrow ^4\text{A}_2$) of $[\text{1}]^{3+}$ (Figure 2c), the T -sensing dye $[\text{1}]^{3+}$ can be easily combined with other stimuli-responsive dyes for the simultaneous sensing of physiologically and biologically relevant analytes, such as pH, operating in the visible spectral region without spectral crosstalk. These features, together with the long luminescence lifetime of the Cr^{III} complex, overcompensate for excitation at a relatively short wavelength, which can favor autofluorescence in biological systems, which can be, however, easily separated from the NIR emission of the Cr^{III} complex, either spectrally or by time-gated emission.

Subsequently, to further examine and broaden the application potential of our Cr^{III} complexes, the less water-soluble complex $[\text{1}][\text{PF}_6]_3$ was encapsulated in different biocompatible nanocarriers, herein, exemplarily polymer nanoparticles and micelles. Both nanoobjects are easy to prepare; they allow subsequent (bio)functionalization and offer a high versatility regarding choice of payload and payload combinations without the need for chromophore functionalization with reactive groups for covalent dye coupling.^[22] Hence, this presents a first step to the design of multiparametric sensor systems with readout in the spectral domain. Although polymer nanoparticles with sizes around 100 nm are often used as stable and inert model systems, the main advantages of micelles, which are dynamic nanostructures with typical sizes of about 10–20 nm and can only incorporate a smaller number of payload molecules, is their ease of preparation. Both nanocarriers are successful strategies for signal amplification to increase the

sensitivity and for the design of targeted optical probes, because their large surface area can be equipped with different functionalities including target-specific ligands.

For the design of nanoscale T sensors, $[1][PF_6]_3$ was incorporated into 100 nm-sized polystyrene nanoparticles (PSP-COOH) employing an established staining procedure.^[22] Heating of aqueous suspensions of these PSP-loaded $[1][PF_6]_3$ from 293 to 343 K (Figures 3c and S4 in the Supporting Information) showed a similar thermochromic behavior, as was observed for $[1][BF_4]_3$ in MeCN/PrCN and H₂O.^[23] The slope of the Boltzmann plot is linear, and this nanoscale T sensor is fully functional in the physiological T range. Although heating reduces the overall emission intensity of the chromium(III) dye-loaded nanocarriers, it does not compromise the I_{738}/I_{775} ratio of the emission bands.^[24] The T response of $[1][PF_6]_3$ in solutol micelles revealed a similar thermochromic behavior in the T range of 293–343 K (Figure 3d). Similar to $[1][PF_6]_3$ in PSP-COOH, the total emission intensity of $[1][PF_6]_3$ in this dynamic system of surfactants decreases with increasing T , yet the I_{738}/I_{775} ratio still reflects the relative excited state population (Figure 3d).^[24] Upon cooling, the full intensity of both emission bands is completely restored demonstrating the system's reversibility (Figure S5 in the Supporting Information).

In summary, the unique features of the molecular Cr^{III}-based thermometer $[1]^{3+}$ are 1) sharp, dual NIR emission above 700 nm realized with earth-abundant elements; 2) high thermal and photochemical stability; 3) large temperature range covered in different environments; 4) possible use in liquid (including water), rigid, and dynamic media; 5) high reversibility and fast response times in different matrices; and 6) spectral and temporal discrimination of scattered excitation light and possible background fluorescence due to long-lived NIR emission, respectively. Moreover, 7) its long luminescence lifetimes can be utilized also for sensing. In addition, 8) due to its extremely large energy difference between excitation and emission and the excitation in the visible range, $[1]^{3+}$ can be combined with many other fluorescent probes with absorption and emission in the visible spectral region in multiparametric sensor systems,^[19] utilizing, for example, easily prepared nanocarriers, such as polymer particles or micelles, which can be equipped with surface ligands, such as proteins targeting, for example, disease-related biomarkers. This will enable a plethora of applications of $[1]^{3+}$ in biology, medicine, and material sciences in the future.

Acknowledgements

This work was financially supported by the Deutsche Forschungsgemeinschaft (GSC 266, Materials Science in Mainz, scholarship for S.O., HE 2778/10-1 and RE 1203/23-1). Funding from the internal university research funds of the Johannes Gutenberg University, Mainz is gratefully acknowledged.

Conflict of interest

The authors declare no conflict of interest.

Keywords: chromium · dual emission · NIR emission · temperature sensing · thermometry

- [1] a) H. Zhou, M. Sharma, O. Berezin, D. Zuckerman, M. Y. Berezin, *Chem-PhysChem* **2016**, *17*, 27–36; b) X. Wang, O. S. Wolfbeis, R. J. Meier, *Chem. Soc. Rev.* **2013**, *42*, 7834–7869; c) D. Jaque, F. Vetrone, *Nanoscale* **2012**, *4*, 4301–4326; d) M. Schäferling, *Angew. Chem. Int. Ed.* **2012**, *51*, 3532–3554; *Angew. Chem.* **2012**, *124*, 3590–3614.
- [2] a) S. Uchiyama, T. Tsuji, K. Ikado, A. Yoshida, K. Kawamoto, T. Hayashi, N. Inada, *Analyst* **2015**, *140*, 4498–4506; b) J. Liu, X. Guo, R. Hu, J. Xu, S. Wang, S. Li, Y. Li, G. Yang, *Anal. Chem.* **2015**, *87*, 3694–3698; c) X. Hu, Y. Li, T. Liu, G. Zhang, S. Liu, *ACS Appl. Mater. Interfaces* **2015**, *7*, 15551–15560; d) C. Gota, K. Okabe, T. Funatsu, Y. Harada, S. Uchiyama, *J. Am. Chem. Soc.* **2009**, *131*, 2766–2767.
- [3] C. D. Chin, V. Linder, S. K. Sia, *Lab. Chip* **2012**, *12*, 2118–2134.
- [4] a) J. B. Mahony, A. Petrich, M. Smieja, *Crit. Rev. Clin. Lab. Sci.* **2011**, *48*, 217–249; b) O. Scheler, B. Glynn, A. Kurg, *Expert Rev. Mol. Diagn.* **2014**, *14*, 489–500; c) Y.-J. Jeong, K. Park, D. Kim, *Cell. Mol. Life Sci.* **2009**, *66*, 3325–3336.
- [5] D. Ross, L. E. Locascio, *Fluorescence Thermometry in Microfluidics, CP684, Temperature: Its Measurement and Control in Science and Industry*, American Institute of Physics, **2003**.
- [6] a) O. S. Wolfbeis, *Adv. Mater.* **2008**, *20*, 3759–3763; b) T. Liu, *Pressure- and Temperature-Sensitive Paints*, Springer, Berlin, **2005**; c) M. Gouterman, J. Callis, L. Dalton, G. Khalil, Y. Mebarki, K. R. Cooper, M. Grenier, *Meas. Sci. Technol.* **2004**, *15*, 1986–1994.
- [7] Q. Xiao, Y. Li, F. Li, M. Zhang, Z. Zhang, H. Lin, *Nanoscale* **2014**, *6*, 10179–10186.
- [8] a) C. Wurth, M. Kaiser, S. Wilhelm, B. Grauel, T. Hirsch, U. Resch-Genger, *Nanoscale* **2017**, *9*, 4283–4294; b) L. Marciniak, K. Waszniewska, A. Bednarkiewicz, D. Hreniak, W. Strek, *J. Phys. Chem. C* **2016**, *120*, 8877–8882; c) E.-K. Lim, T. Kim, S. Paik, S. Haam, Y.-M. Huh, K. Lee, *Chem. Rev.* **2015**, *115*, 327–394; d) A. Sayoud, J. P. Jouart, N. Trannoy, M. Diaf, T. Duvaut, *J. Lumin.* **2012**, *132*, 566–569; e) L. H. Fischer, G. S. Harms, O. S. Wolfbeis, *Angew. Chem. Int. Ed.* **2011**, *50*, 4546–4551; *Angew. Chem.* **2011**, *123*, 4640–4645.
- [9] a) Z. Fidan, A. Wende, U. Resch-Genger, *Anal. Bioanal. Chem.* **2017**, *409*, 1519–1529; b) S. Ebrahimi, Y. Akhlaghi, M. Kompany-Zareh, A. Rinnan, *ACS Nano* **2014**, *8*, 10372–10382; c) G. L. Ke, C. M. Wang, Y. Ge, N. F. Zheng, Z. Zhu, C. J. Yang, *J. Am. Chem. Soc.* **2012**, *134*, 18908–18911; d) C. Nellaker, U. Wallgren, H. Karlsson, *Clin. Chem.* **2007**, *53*, 98–103.
- [10] D. Ross, M. Gaitan, L. E. Locascio, *Anal. Chem.* **2001**, *73*, 4117–4123.
- [11] F. Vetrone, R. Naccache, A. Zamarrón, A. Juarraz de la Fuente, F. Sanz-Rodríguez, L. Martínez Maestro, E. Martín Rodríguez, D. Jaque, J. García Solé, J. A. Capobianco, *ACS Nano* **2010**, *4*, 3254–3258.
- [12] E. J. McLaurin, V. A. Vlaskin, D. R. Gamelin, *J. Am. Chem. Soc.* **2011**, *133*, 14978–14980.
- [13] a) J. Feng, K. J. Tian, D. Hu, S. Wang, S. Li, A. Zeng, Y. Li, G. Yang, *Angew. Chem. Int. Ed.* **2011**, *50*, 8072–8076; *Angew. Chem.* **2011**, *123*, 8222–8226; b) G. A. Baker, S. N. Baker, T. M. McCleskey, *Chem. Commun.* **2003**, 2932–2933.
- [14] J. C. Fister, D. Rank, J. M. Harris, *Anal. Chem.* **1995**, *67*, 4269–4275.
- [15] a) T. Hofbeck, Y. C. Lam, M. Kalbáč, S. Zális, A. Vlček, Jr., H. Yersin, *Inorg. Chem.* **2016**, *55*, 2441–2449; b) R. Czerwieniec, M. J. Leidl, H. H. H. Homeier, H. Yersin, *Coord. Chem. Rev.* **2016**, *325*, 2–28; c) D. Cauzzi, R. Pattacini, M. Delferro, F. Dini, C. Di Natale, R. Paolesse, S. Bonacchi, M. Montalti, N. Zaccheroni, M. Calvaresi, F. Zerbetto, L. Prodi, *Angew. Chem. Int. Ed.* **2012**, *51*, 9662–9665; *Angew. Chem.* **2012**, *124*, 9800–9803; d) S. Perruchas, C. Tard, X. F. Le Goff, A. Fargues, A. Garcia, S. Kahlal, J.-Y. Saillard, T. Gacoin, J.-P. Boilot, *Inorg. Chem.* **2011**, *50*, 10682–10692; e) S. Perruchas, X. F. Le Goff, S. Maron, I. Maurin, F. Guillen, A. Garcia, T. Gacoin, J. P. Boilot, *J. Am. Chem. Soc.* **2010**, *132*, 10967–10969; f) A. A. Rachford, F. N. Castellano, *Inorg. Chem.* **2009**, *48*, 10865–10867; g) M. A. Omary, M. A. Rawashdeh-Omary, M. A. Gonser, O. Elbjairami, T. Grimes, T. R. Cundari, H. V. Diyabalanage, C. S. P. Gamage, H. R. Dias, *Inorg. Chem.* **2005**, *44*, 8200–8210; h) P. C. Ford, E. Cariati, J. Bourassa, *Chem. Rev.* **1999**, *99*, 3625–3648; i) V. W.-W. Yam, K. K.-W. Lo, *Chem. Soc. Rev.* **1999**, *28*, 323–334.

- [16] H. Xiang, J. Cheng, X. Ma, X. Zhou, J. Chroma, *Chem. Soc. Rev.* **2013**, *42*, 6128–6185.
- [17] a) J. Romanova, Y. Sadik, M. R. Ranga Prabhat, J. D. Carey, P. D. Jarowski, *J. Phys. Chem. C* **2017**, *121*, 2333–2343; b) D. Magde, M. D. Magde, Jr., E. Z. Glazer, *Coord. Chem. Rev.* **2016**, *306*, 447–467; c) C. Kreitner, K. Heinze, *Dalton Trans.* **2016**, *45*, 5640–5658; d) C. Kreitner, M. Grabolle, U. Resch-Genger, K. Heinze, *Inorg. Chem.* **2014**, *53*, 12947–12961; e) S. Ladouceur, L. Donato, M. Romain, B. P. Mudraboyina, M. B. Johansen, J. A. Wisner, E. Zysman-Colman, *Dalton Trans.* **2013**, *42*, 8838–8847; f) R. Siebert, A. Winter, U. S. Schubert, B. Dietzek, J. Popp, *Phys. Chem. Chem. Phys.* **2011**, *13*, 1606–1617; g) K. K. W. Lo, K. Y. Zhang, S.-K. Leung, M.-C. Tang, *Angew. Chem. Int. Ed.* **2008**, *47*, 2213–2216; *Angew. Chem.* **2008**, *120*, 2245–2248.
- [18] a) Y. Tanabe, S. Sugano, *J. Phys. Soc. Jpn.* **1954**, *9*, 753–766; b) Y. Tanabe, S. Sugano, *J. Phys. Soc. Jpn.* **1954**, *9*, 766–779; c) A. Hauser, C. Reber, in *Structure and Bonding*, Springer, Berlin, Heidelberg, **2016**, p.291.
- [19] S. Otto, M. Grabolle, C. Förster, U. Resch-Genger, K. Heinze, *Angew. Chem. Int. Ed.* **2015**, *54*, 11572–11576; *Angew. Chem.* **2015**, *127*, 11735–11739.
- [20] a) A. K. C. Mengel, C. Förster, A. Breivogel, K. Mack, J. R. Ochsmann, F. Laquai, V. Ksenofontov, K. Heinze, *Chem. Eur. J.* **2015**, *21*, 704–714; b) A. K. C. Mengel, W. Cho, A. Breivogel, K. Char, Y. S. Kang, K. Heinze, *Eur. J. Inorg. Chem.* **2015**, 3299–3306; c) A. Breivogel, S. Wooh, J. Dietrich, T. Y. Kim, A. S. Kang, K. Char, K. Heinze, *Eur. J. Inorg. Chem.* **2014**, 2720–2734; d) A. Breivogel, M. Park, D. Lee, S. Klassen, A. Kühnle, C. Lee, K. Char, K. Heinze, *Eur. J. Inorg. Chem.* **2014**, 288–295; e) A. Breivogel, M. Meister, C. Förster, F. Laquai, K. Heinze, *Chem. Eur. J.* **2013**, *19*, 13745–13760; f) K. Mack, A. Wünsche von Leupoldt, C. Förster, M. Ezhvskaya, D. Hinderberger, K. W. Klinkhammer, K. Heinze, *Inorg. Chem.* **2012**, *51*, 7851–7858; g) A. Breivogel, C. Förster, K. Heinze, *Inorg. Chem.* **2010**, *49*, 7052–7056.
- [21] I_{738}/I_{775} ratios were obtained by averaging the intensities between 736–742 nm and 772–778 nm, respectively. The areas a_{738} and a_{775} under the emission bands were obtained by fitting two Gaussian functions on an energy scale [cm^{-1}] by using OriginPro 8, OriginLab Corporations, Northhampton.
- [22] J. Napp, T. Behnke, L. Fischer, C. Würth, M. Wottawa, D. M. Katschinski, F. Alves, U. Resch-Genger, M. Schäferling, *Anal. Chem.* **2011**, *83*, 9039–9046.
- [23] Counterion $[\text{BF}_4]^-$ or $[\text{PF}_6]^-$ did not influence the photophysical properties of $[1]^{3+}$, only the solubility in different solvents; see Reference [19].
- [24] Similarly, the emission intensity of europium(III) chelates depends on the environment (solution/polymer) due to differently efficient non-radiative processes, such as coupling of the electronic energy level to the environment through molecular vibration energy levels: G. E. Khalil, K. Lau, G. D. Phelan, B. Carlson, M. Gouterman, J. B. Callis, L. R. Dalton, *Rev. Sci. Instrum.* **2004**, *75*, 192–206.

Manuscript received: April 19, 2017

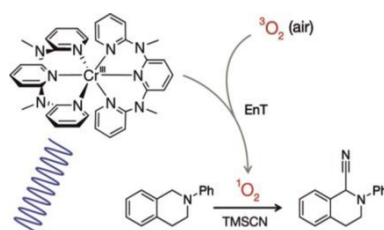
Accepted manuscript online: April 21, 2017

Version of record online: May 15, 2017

3.3 Photo-Chromium: Sensitizer for Visible-Light-Induced Oxidative C–H Bond Functionalization – Electron or Energy Transfer?

Sven Otto, Alexander M. Nauth, Eugenyi Ermilov, Norman Scholz, Aleksej Friedrich, Ute Resch-Genger, Stefan Lochbrunner, Till Opatz and Katja Heinze

ChemPhotoChem **2017**, *1*, 344–349.



In two minds: The unique excited-state potential-energy landscape of the Cr^{III} sensitizer [Cr(ddpd)₂]³⁺ enables a selective sensitization of ³O₂ to give ¹O₂. Ultrafast intersystem crossing precludes electron-transfer pathways from the ultrashort-lived redox-active excited state and enables a selective visible-light-induced C–H bond activation of tertiary amines with ¹O₂ and subsequent trapping with cyanide to yield α -amino-nitriles.

Author Contributions

Sven Otto carried out the electrochemical, UV-VIS and emission spectroscopic experiments and performed the DFT calculations on the photosensitizer. Alexander M. Nauth and Till Opatz conducted the photocatalysis experiments. Aleksej Friedrich and Stefan Lochbrunner performed the transient absorption spectroscopic experiments at the University of Rostock, Germany. Eugenyi Ermilov, Norman Scholz and Ute Resch-Genger determined the quantum yield of ¹O₂ production at the *Bundesanstalt für Materialforschung und -prüfung* in Berlin, Germany. Katja Heinze performed the DFT calculations on the amine/O₂ system and the manuscript was written by Katja Heinze (90 %) and Sven Otto (10 %).

Supporting Information

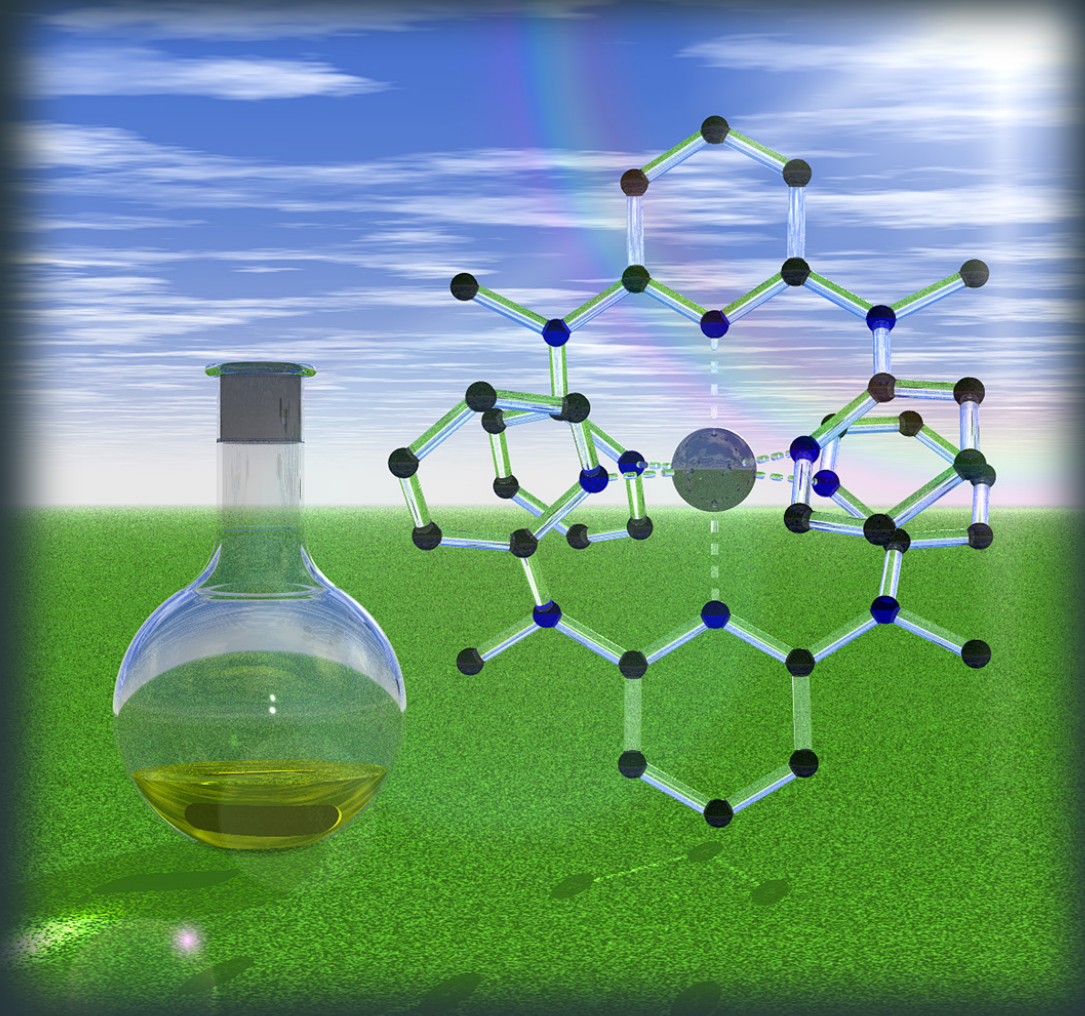
for this article is found at pp. 166.

“Otto, S.; Nauth, A. M.; Ermilov, E.; Scholz, N.; Friedrich, A.; Resch-Genger, U.; Lochbrunner, S.; Opatz, T.; Heinze, K. *ChemPhotoChem* **2017**, *1*, 344–349. Copyright Wiley-VCH Verlag GmbH & Co. KGaA. Reproduced with permission.”

CHEMISTRY OF LIGHT INTERACTION

CHEMPHOTOCHEM

ACROSS THE WHOLE SPECTRUM



8/2017

Front Cover:

S. Lochbrunner, T. Opatz, K. Heinze and co-workers
Photo-Chromium: Sensitizer for Visible-Light-Induced Oxidative
C–H Bond Functionalization – Electron or Energy Transfer?

WILEY-VCH

www.chemphotochem.org

A Journal of





Photo-Chromium: Sensitizer for Visible-Light-Induced Oxidative C–H Bond Functionalization—Electron or Energy Transfer?

Sven Otto^{+, [a, b]} Alexander M. Nauth^{+, [c]} Eugenyi Ermilov,^[d] Norman Scholz,^[d] Aleksej Friedrich,^[e] Ute Resch-Genger,^[d] Stefan Lochbrunner,^{*, [e]} Till Opatz,^{*, [c]} and Katja Heinze^{*, [a]}

The chromium(III) sensitizer $[\text{Cr}(\text{ddpd})_2]^{3+}$ (ddpd = *N,N'*-dimethyl-*N,N'*-dipyridine-2-ylpyridine-2,6-diamine), based on an earth-abundant metal centre, possesses a unique excited-state potential-energy landscape. The very large energy gap between the redox-active and substitutionally labile $^4\text{T}_2$ state and the long-lived low-energy ^2E spin-flip state enables a selective, efficient sensitization of triplet dioxygen to give singlet dioxygen. Ultrafast intersystem crossing after the Franck Condon point from the $^4\text{T}_2$ to the ^2E excited state within 3.5 ps precludes intermolecular electron-transfer pathways from the ultrashort-lived excited $^4\text{T}_2$ state. This specific excited-state reactivity enables a selective visible-light-induced C–H bond activation of tertiary amines with $^1\text{O}_2$ and subsequent trapping with cyanide to yield α -aminonitriles in good to excellent yields.

Photocatalysis is an enormously emerging field in synthetic organic chemistry.^[1] Typically, iridium(III), ruthenium(II), platinum-

m(II) or gold(III) photoredox catalysts^[2,3] are employed (Scheme 1a). The challenging search for catalysts based on earth-abundant metal centres has recently succeeded in some copper(I),^[4] iron(II),^[5] chromium(0)/molybdenum(0)^[6] and the first chromium(III)-based^[7] photocatalytic reactions (Scheme 1 b, c). All mentioned metal-based photoredox catalysts operate through charge-transfer (mostly triplet metal-to-ligand

[a] S. Otto,⁺ Prof. K. Heinze
Institute of Inorganic and Analytical Chemistry
Johannes Gutenberg University of Mainz
Duesbergweg 10–14
55128 Mainz (Germany)
E-mail: katja.heinze@uni-mainz.de

[b] S. Otto,⁺
Graduate School Materials Science in Mainz
Staudingerweg 9
55128 Mainz (Germany)

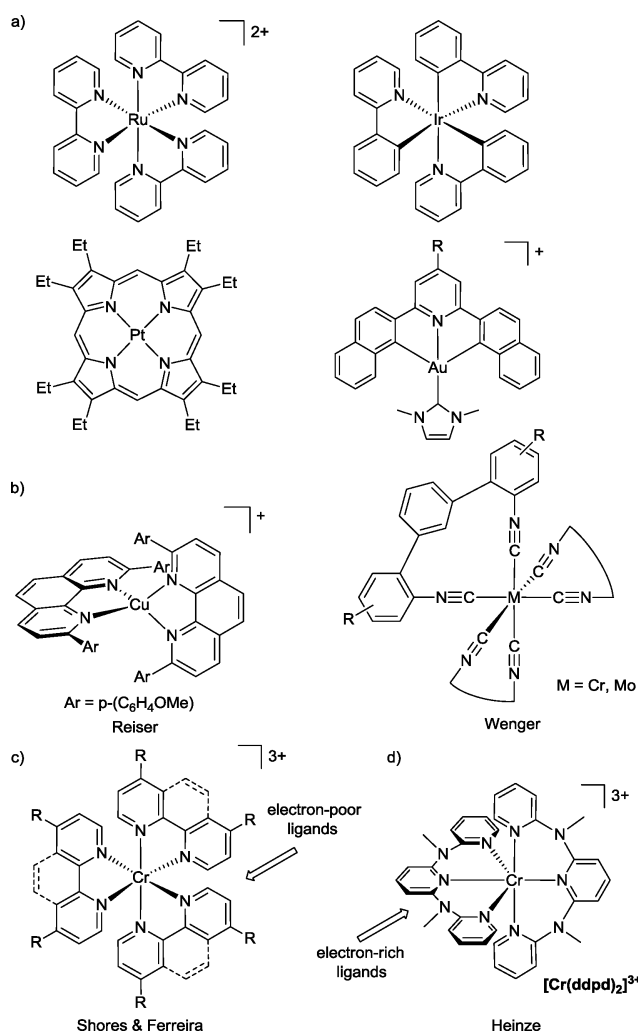
[c] A. M. Nauth⁺ Prof. T. Opatz
Institute of Organic Chemistry
Johannes Gutenberg University of Mainz
Duesbergweg 10–14
55128 Mainz (Germany)
E-mail: opatz@uni-mainz.de

[d] E. Ermilov, N. Scholz, Dr. U. Resch-Genger
Division 1.10
Federal Institute for Materials Research and Testing (BAM)
Richard-Willstätter-Str. 11
12489 Berlin (Germany)

[e] A. Friedrich, Prof. S. Lochbrunner
Institute of Physics, University of Rostock
Albert-Einstein-Str. 23
18059 Rostock (Germany)
E-mail: stefan.lochbrunner@uni-rostock.de

[*] These authors contributed equally to this work.

Supporting Information and the ORCID identification number(s) for the author(s) of this article can be found under:
<https://doi.org/10.1002/cptc.201700077>.



Scheme 1. a) Common precious-metal-containing charge-transfer photosensitizers,^[2,3] b) MLCT sensitizers with earth-abundant metal centres,^[4,6] c) chromium(III)-based sensitizers $[\text{Cr}(\text{bpyR}_2)_3]^{3+}$ and $[\text{Cr}(\text{phenR}_2)_3]^{3+}$ ^[7] and d) the $[\text{Cr}(\text{ddpd})_2]^{3+}$ sensitizer.^[9]

charge transfer, $^3\text{MLCT}$) states, except for chromium(III). For most chromium(III) complexes in reasonably strong ligand fields, the lowest electronically excited state is the interconfigurational ^2E state ($t_{2g}: \uparrow\downarrow\uparrow$).^[8] This state derives from the same (t_{2g})³ electron configuration as its $^4\text{A}_2$ ground state ($t_{2g}: \uparrow\uparrow\uparrow$) but features a spin flip.^[8] The initially populated $^4\text{T}_2$ ligand field state with a (t_{2g})²(e_g)¹ electron configuration would be a strong photooxidant featuring a hole in the t_{2g} orbital set. However, the lower-energy ^2E state is not particularly redox-active. In most Cr^{III} sensitizers these two states are sufficiently close in energy to allow for fast forward and reverse intersystem crossing (ISC) between these two states.^[8] Thus, there is considerable diversity in potential mechanisms with respect to the initial photoactivation step as demonstrated by Shores et al. and Ferreira and co-workers, and some of them (namely electron and energy transfer) have recently been considered to be operative simultaneously.^[7]

All reported chromium(III) sensitizers based on $[\text{Cr}(\text{bpy})_3]^{3+}$ or $[\text{Cr}(\text{phen})_3]^{3+}$ derivatives incorporate non-innocent electron-poor oligopyridine ligands (bpy = 2,2'-bipyridine, phen = 1,10-phenanthroline; Scheme 1 c).^[7] Wieghardt et al. convincingly demonstrated that all redox chemistry in such Cr^{III} complexes with electron-poor pyridine ligands is ligand centred.^[10] The one-electron reduced species $[\text{Cr}(\text{bpy})_3]^{2+}$ features a Cr^{III} central ion coordinated to a $[\text{bpy}]^{\cdot-}$ radical anion^[10] instead of the previously assumed Cr^{II} metal centre. This ligand non-innocence of bpy and phen has considerable impact onto the stability and reactivity of the sensitizers in different formal oxidation states, for example, chromium(II) complexes are susceptible to Jahn–Teller distortion^[9a] and ligand substitution while chromium(III) complexes with coordinated bpy radical anions are less labile.

In addition to Ferreira's work on chromium(III) based sensitizers (Scheme 1 c),^[7] we had designed a chromium(III) complex $[\text{Cr}(\text{ddpd})_2]^{3+}$ with electron-rich ddpd ligands confining the redox chemistry to the metal centre instead of the pyridine ligand (Scheme 1 d; ddpd = *N,N'*-dimethyl-*N,N'*-dipyridine-2-ylpyridine-2,6-diamine^[11]).^[9] Due to the electron-rich nature of the ligands, reduction of $[\text{Cr}(\text{ddpd})_2]^{3+}$ gives the labile, Jahn–Teller distorted chromium(II) complex $[\text{Cr}^{\text{II}}(\text{ddpd})_2]^{2+}$ instead of a ddpd radical anion coordinated to Cr^{III}.^[9a] Importantly, the energy difference between the $^4\text{T}_2$ and ^2E states in this complex is extremely large. This large gap precludes any back intersystem crossing from the low-energy ^2E state to the $^4\text{T}_2$ state and inhibits equilibration of these two excited states.^[9a] This excited state level ordering enables a strong NIR luminescence (quantum yield $\Phi > 10\%$) with a high ^2E lifetime of 899 μs .^[9a]

We hypothesized that $[\text{Cr}(\text{ddpd})_2]^{3+}$ in its electronically excited states would be a less efficient photooxidant, but a selective sensitizer for the formation of singlet oxygen from triplet oxygen (Figure 1).^[9a, 12] Using this sensitizer would then allow differentiation between different mechanistic pathways in chromium(III)-sensitized photocatalytic reactions (Figure 1), namely photoinduced electron transfer (PET) versus energy transfer (EnT). As an example, we employed $[\text{Cr}(\text{ddpd})_2]^{3+}$ in the photocatalytic formation of α -aminonitriles from tertiary

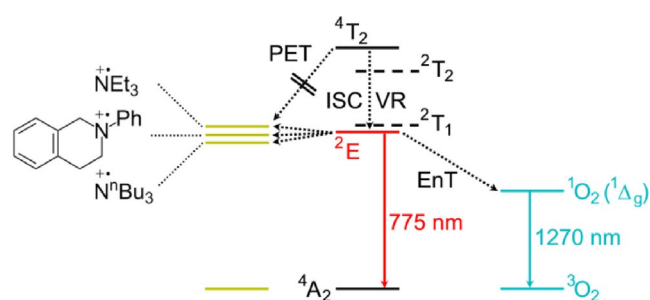


Figure 1. Energy state diagram of $[\text{Cr}(\text{ddpd})_2]^{3+}$ including reactions with amines (PET) and dioxygen (EnT). PET = photoinduced electron transfer, EnT = energy transfer, ISC = intersystem crossing, VR = vibrational relaxation.

amines, a cyanide source and dioxygen as terminal oxidant.^[13] Based on this model reaction, we investigated whether PET or EnT is the dominant mechanism in this Cr^{III}-catalysed reaction by a combined in-depth experimental and theoretical mechanistic study, including electrochemistry, quenching experiments, ultrafast transient absorption spectroscopy and density functional theory (DFT) calculations.

We selected three amine substrates, tri-*n*-butylamine (NnBu_3), *N*-phenyl-1,2,3,4-tetrahydroisoquinoline (Ph-isoq) and triethylamine (NEt_3), for the photocyanation reaction sensitized by $[\text{Cr}(\text{ddpd})_2]^{3+}$. Their (irreversible) oxidation (peak) potentials have been determined by cyclic voltammetry as $E_p = 0.38, 0.46$ and 0.55 V vs. ferrocene/ferrocenium, respectively (Figure 2 a). The ground state reduction process of $[\text{Cr}(\text{ddpd})_2]^{3+/2+}$, giving the labile chromium(II) species, had been reported at -1.11 V (vs. ferrocene).^[9a] With the excited-state energy of the sensitizer's ^2E state of 1.6 eV ($\lambda_{\text{em}} = 775$ nm), the excited-state redox potential amounts to $E^*(\text{Cr}^{\text{III}}/\text{Cr}^{\text{II}}) = 0.49$ V (Figure 1).^[9a] Consequently, the driving force for PET from the amine to the excited sensitizer varies from weakly exergonic ($\Delta G_{\text{PET}} = -0.11$ V), via essentially thermoneutral ($\Delta G_{\text{PET}} = -0.03$ V) to slightly endergonic ($\Delta G_{\text{PET}} = +0.06$ V), as calculated by the Rehm–Weller equation (Table 1).^[14, 15]

These three substrates were subjected to photocyanation conditions in acetonitrile using trimethylsilylcyanide (TMSCN) as the cyanide source, dioxygen from air as the terminal oxidant under continuous air flow (slow bubbling of air via a cannula into the solution), $[\text{Cr}(\text{ddpd})_2]^{3+}$ as the sensitizer (1.0 mol%) and a compact fluorescent lamp (CFL Dynasun,

Table 1. Electrochemical data for sensitizers and substrates.

	E vs. FcH (vs. SCE) [V]	$\Delta G_{\text{PET}}^{\text{[a]}}$ [eV]	Ref.
$[\text{Cr}(\text{ddpd})_2]^{3+/2+}$	-1.11 (-0.73)	-	9 a
$*[\text{Cr}(\text{ddpd})_2]^{3+/2+}$	$+0.49$ ($+0.87$)	-	9 a
$*[\text{Cr}(\text{Ph}_2\text{phen})_3]^{3+/2+}$	$+1.02$ ($+1.40$)	-	7 a
$*[\text{Au}(\text{C}^{\wedge}\text{N}^{\wedge}\text{C})\text{L}]^{+/0}$	$+0.75$ ($+1.13$)	-	3
$*[\text{rose bengal}]^{0/-}$	$+0.61$ ($+0.99$)	-	13 d
$[\text{NEt}_3]^{+/0}$	$+0.55$ ($+0.93$)	$+0.06$	this work
$[\text{N}^n\text{Bu}_3]^{+/0}$	$+0.38$ ($+0.76$)	-0.11	this work
$[\text{Ph-isoq}]^{+/0}$	$+0.46$ ($+0.84$)	-0.03	this work

[a] ΔG_{PET} value for $[\text{Cr}(\text{ddpd})_2]^{3+}$.

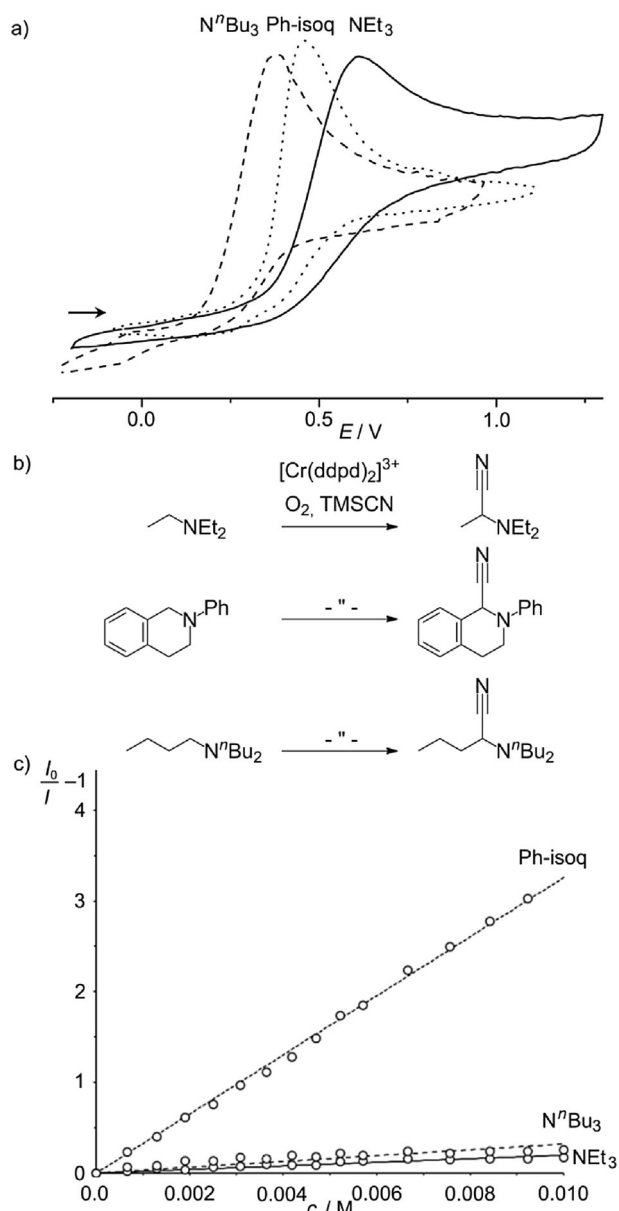


Figure 2. a) Cyclic voltammograms of the amine substrates in CH₃CN/[nBu₄N][PF₆]; potential is given vs. ferrocene/ferrocenium. b) α-Aminonitrile formation using [Cr(ddpd)₂]³⁺, light, TMSCN under an air flow in CH₃CN. c) Stern–Volmer plots of [Cr(ddpd)₂]³⁺ and the amine substrates in deaerated CH₃CN (λ_{exc} = 435 nm).^[16]

105 W) as the light source (Figures S1–S6 in the Supporting Information; Table 2). Interestingly, the respective α-aminonitriles form in all cases, irrespective of the amine's redox potential (Figure 2b; Table 2, entries 1–3). Full conversion is achieved for Ph-isoq and NⁿBu₃ within a few hours (Table 2, entries 4, 5). The aromatic Ph-isoq performs even better than NⁿBu₃ in spite of its lower driving force for PET. Due to the high volatility of NEt₃ and hence loss of the starting material through the air flow, full conversion is not achieved in this particular case under the employed conditions (Table 2, entry 1).

Quenching of the long-lived ²E state of [Cr(ddpd)₂]³⁺ by the amine substrates was probed by Stern–Volmer plots (Fig-

Table 2. Screening of reaction conditions.

Entry	Substrate	TMSCN (equiv)	Cr [mol%]	Reaction time [min]	Yield [%] (conversion)
1	NEt ₃	10	1.0	60	20 ^[a]
2	Ph-isoq	10	1.0	60	87
3	N ⁿ Bu ₃	10	1.0	60	63
4	Ph-isoq	10	1.0	120	100
5	N ⁿ Bu ₃	10	1.0	360	99
6	Ph-isoq	3	1.0	30	44
7	Ph-isoq ^[b]	3	1.0	30	34
8	Ph-isoq	10	1.0	20	89
9	Ph-isoq	10	0.5	20	81
10	Ph-isoq	10	0.1	20	48
11	Ph-isoq	10	0.05	20	36
12	Ph-isoq	10	0.01	20	23
13	Ph-isoq	3	1.0 (1st)	60	84
14	Ph-isoq	3	1.0 (2nd)	60	78
15	Ph-isoq	3	1.0 (3rd)	60	39
16	Ph-isoq	3	1.0 (4th)	60	7
17	Ph-isoq	3	1.0	30	73 ^[c]
18	Ph-isoq	3	1.0	30	79 ^[d]
19	Ph-isoq	3	1.0	30	43 ^[e]
20	Ph-isoq	3	1.0	30	41 ^[f]
21	Ph-isoq	3	1.0	30	63 ^[g]
22	atropine	3	1.0	960	63

[a] NEt₃ is volatile and hence, some starting material is lost via the airflow. [b] CH₃CN/H₂O 9:1 v/v. [c] CFL (100 W). [d] Blue LED (100 W, 462 nm). [e] CFL (25 W). [f] Medical blue light PL-S (9 W). [g] UV-A; 440 W; 380–315 nm.

ure 2c). The aliphatic amines NEt₃ and NⁿBu₃ do not significantly quench the phosphorescence (K_{SV} = 19.7 and 32.1, respectively), whereas Ph-isoq quenches the excited complex to a somewhat greater extent (K_{SV} = 326). The nature of the quenching process (PET giving [Ph-isoq]⁺⁺ or Dexter energy transfer^[17] giving ³[Ph-isoq]) is yet to be elucidated. However, we disfavor the PET mechanism involving the excited ²E state for the following three reasons:

- 1) The formation of [Ph-isoq]⁺⁺ has a low driving force (Table 1);
- 2) From the long-lived ²E state, the chromium(II) complex would be initially formed in an electronically excited state (t_{2g} : ↑↓↑; e_g : ↑) instead of the electronically relaxed configuration of a high-spin Cr^{II} ion (t_{2g} : ↑↑↑; e_g : ↑);
- 3) [Cr(ddpd)₂]²⁺ is unstable, would rapidly decompose under these conditions and consequently its efficient formation would shut down the catalysis (which is not observed).

In principle, PET could also occur from the ⁴T₂ excited state (ca. 2.45 eV)^[9a] initially formed after excitation with 435 nm light. This state would deliver a much larger driving force for PET by 0.85 eV (Figure 1). For this bimolecular quenching to occur, the lifetime of this initially populated excited state must be long enough. Cr(acac)₃ (acac[−] = acetylacetonato) had been investigated in detail by femtosecond transient absorption spectroscopy by McCusker and co-workers.^[18] After excitation into the ⁴T₂ state, *[Cr(acac)₃] evolves into the vibrationally relaxed ²E state within picoseconds (τ = 1.1 ps). This time con-

stant had been attributed to vibrational relaxation (VR) in the 2E state. Thus, ISC and departure from the 4T_2 state occurs in the sub-100 fs timescale.^[18]

Transient absorption spectra of $[\text{Cr}(\text{ddpd})_2]^{3+}$ in acetonitrile, recorded after excitation at its $^4A_2 \rightarrow ^4T_2$ ligand-field absorption by femtosecond laser pulses at 440 nm, exhibit a monoexponential decay with a time constant of 3.5 ps and reflect relaxation into the long-lived 2E state (Figure 3). The residual absorption is dominated by a characteristic band around 530 nm

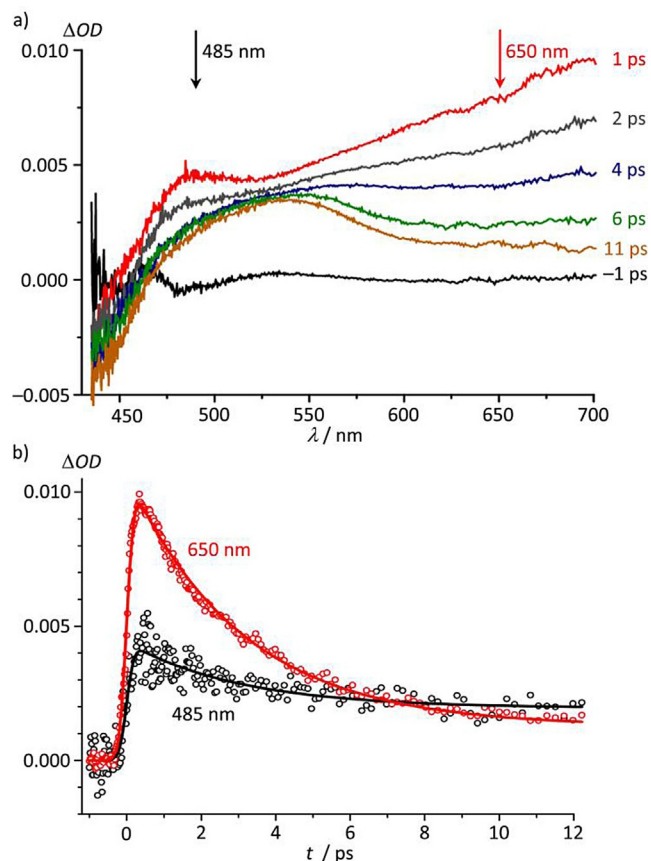


Figure 3. a) Transient absorption spectra of $[\text{Cr}(\text{ddpd})_2][\text{BF}_4]_3$ in CH_3CN excited with 440 nm laser pulses and b) transient signals as a function of the pump-probe delay time observed at 485 nm (black) and 650 nm (red). Both fits to the experimental data correspond to monoexponential decays with $\tau = 3.5$ ps.

which is attributed to the relaxed 2E state and can be assigned to spin-allowed transitions within the t_{2g} set ($\uparrow\downarrow\uparrow$) and ligand-to-metal charge-transfer transitions according to time-dependent DFT calculations (RI-B3LYP-D3/def2-TZVPP/ZORA//RI-B3LYP-D3/def2-TZVPP/J; Figure S7).

While transient spectra of $\text{Cr}(\text{acac})_3$ show on the picosecond timescale mostly a narrowing and slight red-shift of the band at 530 nm,^[18] the measurements on $[\text{Cr}(\text{ddpd})_2]^{3+}$ yield an initially strong absorption in the red spectral region which decays within 3.5 ps. It indicates that contrary to $\text{Cr}(\text{acac})_3$ not only vibrational relaxation and cooling is observed but also ISC from the 4T_2 state to the doublet states (2T_2 , 2T_1 , 2E ; Figure 1) or internal conversion within the doublet manifold. The detailed

relaxation cascade of electronically excited $[\text{Cr}(\text{ddpd})_2]^{3+}$ will be scrutinized by further ultrafast spectroscopic techniques in the future. In any case, the lifetime of the 4T_2 state below 3.5 ps is too short to allow for collisional reaction with a substrate. To conclude, PET from the amine substrates to the 4T_2 and 2E states of the sensitizer is disfavoured both kinetically and thermodynamically.

The major pathway consequently involves energy-transfer processes from the long-lived 2E state to triplet oxygen reforming the 4A_2 ground state of $[\text{Cr}(\text{ddpd})_2]^{3+}$ and yielding $^1\text{O}_2$ ($^1\Delta_g$). The driving force for this spin-allowed energy transfer amounts to 0.62 eV (Figure 1). In fact, $^3\text{O}_2$ quenches the dye's phosphorescence with $K_{\text{SV}} = 2.82 \times 10^4 \text{ M}^{-1}$ and $k_q = 1.20 \times 10^8 \text{ M}^{-1} \text{ s}^{-1}$ in CH_3CN (Figure S8). In water, these values are reduced to $K_{\text{SV}} = 1.59 \times 10^4 \text{ M}^{-1}$ and $k_q = 0.18 \times 10^8 \text{ M}^{-1} \text{ s}^{-1}$.^[9a] Together with the poorer solubility of dioxygen in water (H_2O : 0.26 mM; CH_3CN : 2.42 mM) and the lower lifetime of $^1\text{O}_2$ in H_2O (CH_3CN : $(3-9) \times 10^{-5} \text{ s}$; H_2O : $(0.3-0.4) \times 10^{-5} \text{ s}$),^[19,20] the lower quenching rate in water should compromise photocatalysis in water. Indeed, addition of water to the reaction mixture (CH_3CN : H_2O 9:1 v/v) reduced the yield of the α -aminonitrile from 44% to 34% (Table 2, entries 6,7). Hydrolysis of TMSCN to HCN might also occur in water, but HCN should be similarly competent to attack iminium ions.

The formation of $^1\text{O}_2$ by irradiation of $[\text{Cr}(\text{ddpd})_2]^{3+}$ in the presence of $^3\text{O}_2$ has been independently confirmed by the observation of the characteristic $^1\text{O}_2$ emission at $\lambda = 1270 \text{ nm}$ in DMF. The singlet oxygen quantum yield has been determined as 61% in DMF and in CH_3CN (see the Supporting Information for details).

For completeness, we also confirmed that the cyanide source TMSCN (up to 1000 equiv) does not significantly quench the luminescence of $[\text{Cr}(\text{ddpd})_2]^{3+}$ and hence plays no role in the initial light-driven step of the photoactivation (Figure S9). In addition, no evidence was found for complex decomposition in the presence of TMSCN which is remarkable considering the excellent ligating properties of cyanide.

From the combined experimental data (redox potentials, excited-state lifetimes and ISC rate, Stern-Volmer analyses, solvent dependence and product analysis), we conclude that Dexter energy transfer from the long-lived 2E state of $[\text{Cr}(\text{ddpd})_2]^{3+}$ to $^3\text{O}_2$ outperforms any PET pathway from excited states of this Cr^{III} sensitizer to amines.

The reaction of $^1\text{O}_2$ with amines has been discussed before.^[21,22] A charge-transfer complex between $^1\text{O}_2$ and the amine has been suggested.^[21,22] Indeed, DFT (b3lyp/Def2-TZVP; PCM CH_3CN) calculations suggest that the amine polarizes the O_2 molecule in the charge-transfer complex with a short N...O distance of 1.882 Å and a hydrogen bond from the α -CH group to the oxygen atom with a H...O distance of 2.258 Å (Figure 4). Hydrogen-atom transfer (or consecutive electron/proton transfer) from the α -CH of the amine to $^1\text{O}_2$ gives the carbon-centered $[\text{Me}_2\text{NCHMe}]^\cdot$ radical and the hydroperoxyl radical $[\text{HO}_2]^\cdot$ which is slightly uphill by 8 kJ mol⁻¹ and hence not particularly favoured (radical pathway, Figure 4).

However, a low-energy transition state ($\Delta G^\ddagger = 8 \text{ kJ mol}^{-1}$; imaginary frequency -761 cm^{-1}) of a hydride transfer giving

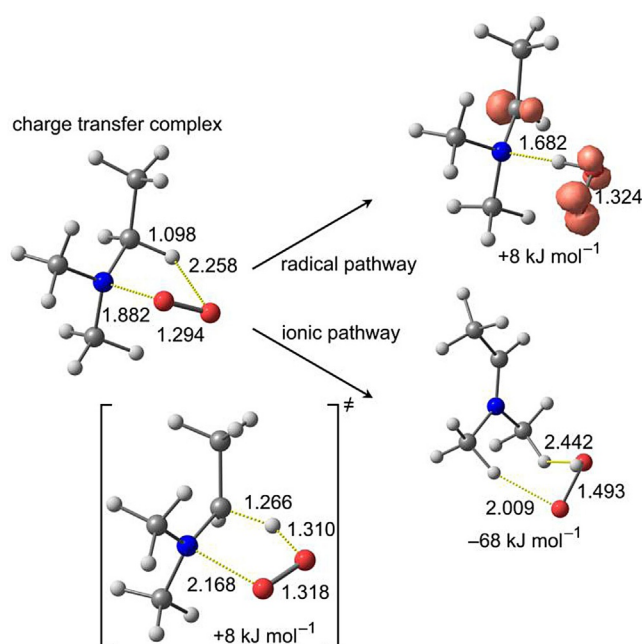
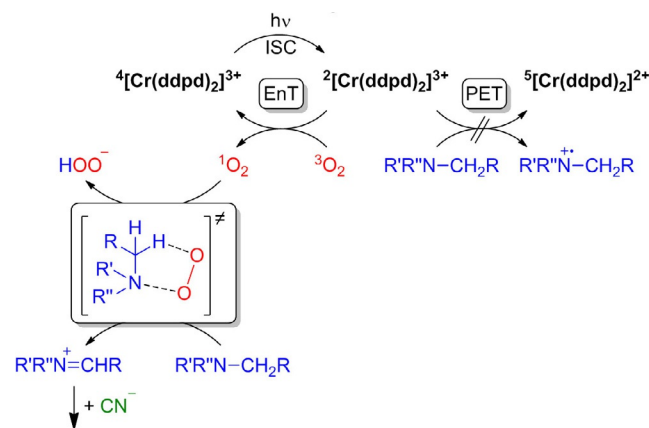


Figure 4. DFT-calculated geometries of the charge-transfer complex of $^1\text{O}_2$ and the model amine NEtMe_2 , the hydrogen-atom transfer products (radical pathway, spin density given at 0.05 a.u.) and the hydride-transfer products (ionic pathway including the corresponding low-energy transition state). Distances given in Å. N = blue; O = oxygen; C = gray; H = white.

the thermodynamically favourable iminium ion and hydroperoxide ($\Delta G = -68 \text{ kJ mol}^{-1}$) in one step has been identified by the DFT calculations (ionic pathway; Figure 4). This pathway enables a rather rapid and selective reaction towards the iminium ion without reactive intermediates. The iminium ion is subsequently trapped by the cyanide. In fact, we note a cleaner reaction with the $^1\text{O}_2$ -selective $[\text{Cr}(\text{ddpd})_2]^{3+}$ sensitizer than with rose bengal (4,5,6,7-tetrachloro-2',4',5',7'-tetraiodofluorescein) under identical reaction conditions (Figure S10). The excited-state redox potential of rose bengal is significantly higher than that of $[\text{Cr}(\text{ddpd})_2]^{3+}$ (Table 1; $E(^*S/S^-) = 0.61 \text{ V}$ vs. ferrocene). This enables a parallel but less selective PET pathway for rose bengal^[22] as sensitizer via amine radical cations^[23] and superoxide. These radicals could be responsible for the formation of side products. The proposed mechanism for the photocyanation of amines using $[\text{Cr}(\text{ddpd})_2]^{3+}$ and oxygen as terminal oxidant is summarized in Scheme 2.

Finally, the performance of the $[\text{Cr}(\text{ddpd})_2]^{3+}$ sensitizer was evaluated under different conditions. Decreasing the catalyst loading from 1 mol% to 0.01 mol% demonstrates that appreciable reaction rates are still achieved down to 0.05 mol% (Table 2, entries 8–12). In contrast to the organic sensitizer rose bengal, $[\text{Cr}(\text{ddpd})_2]^{3+}$ can be re-used after the photocyanation several times, demonstrating its high (photo)stability (Table 2, entries 13–16).^[13d] The best yields with the $[\text{Cr}(\text{ddpd})_2]^{3+}$ sensitizer were obtained using a CFL (100 W) or a blue LED (100 W, 462 nm), while a lower power [CFL (25 W), medical blue light PL-S (9 W)] or an unsuitable wavelength (UV-A; 440 W; 380–315 nm) resulted in poorer conversion (Table 2, entries 17–21). This further demonstrates that photoactivation via the excited



Scheme 2. Proposed mechanism for the photocyanation of amines using $[\text{Cr}(\text{ddpd})_2]^{3+}$ as sensitizer.

sensitizer is the rate-determining step. The $[\text{Cr}(\text{ddpd})_2]^{3+}$ sensitizer is also compatible with complicated substrates such as atropine giving the photocyanated product (in TMS-protected form) in higher yields and improved purity than using rose bengal as photosensitizer (Table 2, entry 22).

In summary, we have demonstrated that the $[\text{Cr}(\text{ddpd})_2]^{3+}$ sensitizer with an earth-abundant metal centre selectively generates $^1\text{O}_2$ from $^3\text{O}_2$ by visible-light irradiation without providing alternative PET pathways. This enables a selective α -CH activation of amines by $^1\text{O}_2$. Subsequent trapping with cyanide yields synthetically valuable α -aminonitriles. Based on its unique excited state energy landscape, the reactivity of $[\text{Cr}(\text{ddpd})_2]^{3+}$ contrasts with that of other reported Cr^{III} sensitizers featuring a higher redox potential and redox-active ligands^[7] and with that of the commonly employed $^3\text{MLCT}$ sensitizers with strong oxidation power.^[2–4] Thus, $[\text{Cr}(\text{ddpd})_2]^{3+}$ perfectly complements the existing portfolio of metal-based sensitizers providing a selective $^1\text{O}_2$ pathway. The application of $[\text{Cr}(\text{ddpd})_2]^{3+}$ in further selective energy-transfer-mediated^[12,17] transformations is currently underway.

Acknowledgements

This work was financially supported by the Deutsche Forschungsgemeinschaft (GSC 266, Materials Science in Mainz, scholarship for S.O., HE 2778/10-1 and RE 1203/23-1). Funding from the internal university research funds of the Johannes Gutenberg University, Mainz is gratefully acknowledged. Parts of this research were conducted using the supercomputer Mogon and advisory services offered by Johannes Gutenberg University Mainz (www.hpc.uni-mainz.de), which is a member of the AHRP and the Gauss Alliance e.V.

Conflict of interest

The authors declare no conflict of interest.

Keywords: aminonitriles · chromium · photocatalysis · photophysics · singlet oxygen

- [1] a) N. A. Romero, D. A. Nicewicz, *Chem. Rev.* **2016**, *116*, 10075–10166; b) C. K. Prier, D. A. Rankic, D. W. C. MacMillan, *Chem. Rev.* **2013**, *113*, 5322–5363; c) J. Hu, J. Wang, T. H. Nguyen, N. Zheng, *Beilstein J. Org. Chem.* **2013**, *9*, 1977–2001; d) L. Shi, W. Xia, *Chem. Soc. Rev.* **2012**, *41*, 7687–7697; e) M. N. Hopkinson, B. Sahoo, J.-L. Li, F. Glorius, *Chem. Eur. J.* **2014**, *20*, 3874–3886.
- [2] a) T. P. Nicholls, D. Leonori, A. C. Bissember, *Nat. Prod. Rep.* **2016**, *33*, 1248–1254; b) M. H. Shaw, J. Twilton, D. W. C. MacMillan, *J. Org. Chem.* **2016**, *81*, 6898–6926; c) M. N. Hopkinson, A. Tlahuext-Aca, F. Glorius, *Acc. Chem. Res.* **2016**, *49*, 2261–2272; d) A. Arora, J. D. Weaver, *Acc. Chem. Res.* **2016**, *49*, 2273–2283; e) T. Chatterjee, N. Iqbal, Y. You, E. J. Cho, *Acc. Chem. Res.* **2016**, *49*, 2284–2294; f) D. Staveness, I. Bosque, C. R. J. Stephenson, *Acc. Chem. Res.* **2016**, *49*, 2295–2306; g) D. C. Fabry, M. Rueping, *Acc. Chem. Res.* **2016**, *49*, 1969–1979; h) T. Koike, M. Akita, *Acc. Chem. Res.* **2016**, *49*, 1937–1945; i) J.-P. Goddard, C. Ollivier, L. Fensterbank, *Acc. Chem. Res.* **2016**, *49*, 1924–1936; j) K. Nakajima, Y. Miyake, Y. Nishibayashi, *Acc. Chem. Res.* **2016**, *49*, 1946–1956; k) J.-R. Chen, X.-Q. Hu, L.-Qiu Lu, W.-J. Xiao, *Acc. Chem. Res.* **2016**, *49*, 1911–1923; l) S. A. Morris, J. Wang, N. Zheng, *Acc. Chem. Res.* **2016**, *49*, 1957–1968; m) C. R. Jamison, L. E. Overman, *Acc. Chem. Res.* **2016**, *49*, 1578–1586; n) I. Ghosh, L. Marzo, A. Das, R. Shaikh, B. König, *Acc. Chem. Res.* **2016**, *49*, 1566–1577.
- [3] W.-P. To, G. S.-M. Tong, W. Lu, C. Ma, J. Liu, A. L.-F. Chow, C.-M. Che, *Angew. Chem. Int. Ed.* **2012**, *51*, 2654–2657; *Angew. Chem.* **2012**, *124*, 2708–2711.
- [4] a) O. Reiser, *Acc. Chem. Res.* **2016**, *49*, 1990–1996; b) A. C. Hernandez-Perez, S. K. Collins, *Acc. Chem. Res.* **2016**, *49*, 1557–1565; c) D. B. Bagal, G. Kachkovskiy, M. Knorn, T. Rawner, B. M. Bhanage, O. Reiser, *Angew. Chem. Int. Ed.* **2015**, *54*, 6999–7002; *Angew. Chem.* **2015**, *127*, 7105–7108; d) M. Knorn, T. Rawner, R. Czerwieńiec, O. Reiser, *ACS Catal.* **2015**, *5*, 5186–5193.
- [5] a) P. Zimmer, P. Müller, L. Burkhardt, R. Schepper, A. Neuba, J. Steube, F. Dietrich, U. Flörke, S. Mangold, M. Gerhards, M. Bauer, *Eur. J. Inorg. Chem.* **2017**, 1504–1509; b) S. Parisien-Collette, A. C. Hernandez-Perez, S. K. Collins, *Org. Lett.* **2016**, *18*, 4994–4997; c) A. Gualandì, M. Marchini, L. Mengozzi, M. Natali, M. Lucarini, P. Ceroni, P. G. Cozzi, *ACS Catal.* **2015**, *5*, 5927–5931.
- [6] a) L. A. Büldt, O. S. Wenger, *Angew. Chem. Int. Ed.* **2017**, *56*, 5676–5682; *Angew. Chem.* **2017**, *129*, 5770–5776; b) L. A. Büldt, X. Guo, R. Vogel, A. Prescimone, O. S. Wenger, *J. Am. Chem. Soc.* **2017**, *139*, 985–992; c) L. A. Büldt, X. Guo, A. Prescimone, O. S. Wenger, *Angew. Chem. Int. Ed.* **2016**, *55*, 11247–11251; *Angew. Chem.* **2016**, *128*, 11413–11417.
- [7] a) S. M. Stevenson, M. P. Shores, E. M. Ferreira, *Angew. Chem. Int. Ed.* **2015**, *54*, 6506–6510; *Angew. Chem.* **2015**, *127*, 6606–6610; b) R. F. Higgins, S. M. Fatur, S. G. Shepard, S. M. Stevenson, D. J. Boston, E. M. Ferreira, N. H. Damrauer, A. K. Rappé, M. P. Shores, *J. Am. Chem. Soc.* **2016**, *138*, 5451–5464; c) S. M. Stevenson, R. F. Higgins, M. P. Shores, E. M. Ferreira, *Chem. Sci.* **2017**, *8*, 654–660.
- [8] a) A. D. Kirk, *Chem. Rev.* **1999**, *99*, 1607–1640; b) L. S. Forster, *Coord. Chem. Rev.* **2002**, *227*, 59–92; c) N. A. P. Kane-Maguire, *Top. Curr. Chem.* **2007**, *280*, 37–67; d) V. Balzani, P. Ceroni, A. Juris, *Photochemistry and Photophysics*, Wiley-VCH, Weinheim, **2014**, pp. 216–219; e) M. A. Jamieson, N. Serpone, M. Z. Hoffman, *Coord. Chem. Rev.* **1981**, *39*, 121–179; f) C. K. Ryu, J. F. Endicott, *Inorg. Chem.* **1988**, *27*, 2203–2214; g) M. Asano, J. A. Koningstein, in *Picosecond Phenomena II*, (Eds. R. Hochstrasser, W. Kaiser, C. V. Shank), Springer Series in Chemical Physics, Springer, Berlin, Heidelberg, Vol. 14, **1980**, pp. 351–356.
- [9] a) S. Otto, M. Grabolle, C. Förster, C. Kreitner, U. Resch-Genger, K. Heinze, *Angew. Chem. Int. Ed.* **2015**, *54*, 11572–11576; *Angew. Chem.* **2015**, *127*, 11735–11739; b) S. Otto, N. Scholz, T. Behnke, U. Resch-Genger, K. Heinze, *Chem. Eur. J.* **2017**, in press <https://doi.org/10.1002/chem.201701726>.
- [10] a) C. C. Scarborough, K. M. Lancaster, S. DeBeer, T. Weyhermüller, S. Sproules, K. Wieghardt, *Inorg. Chem.* **2012**, *51*, 3718–3732; b) C. C. Scarborough, S. Sproules, T. Weyhermüller, S. Serena DeBeer, K. Wieghardt, *Inorg. Chem.* **2011**, *50*, 12446–12462.
- [11] a) A. Breivogel, C. Förster, K. Heinze, *Inorg. Chem.* **2010**, *49*, 7052–7056; b) K. Mack, A. Wünsche von Leupoldt, C. Förster, M. Ezhevskaya, D. Hinderberger, K. W. Klinkhammer, K. Heinze, *Inorg. Chem.* **2012**, *51*, 7851–7858; c) A. Breivogel, M. Meister, C. Förster, F. Laquai, K. Heinze, *Chem. Eur. J.* **2013**, *19*, 13745–13760; d) C. Förster, K. Mack, L. M. Carrella, V. Ksenofontov, E. Rentschler, K. Heinze, *Polyhedron* **2013**, *52*, 576–581; e) A. Breivogel, M. Park, D. Lee, S. Klassen, A. Kühnle, C. Lee, K. Char, K. Heinze, *Eur. J. Inorg. Chem.* **2014**, 288–295; f) A. Breivogel, C. Kreitner, K. Heinze, *Eur. J. Inorg. Chem.* **2014**, 5468–5490; g) A. K. C. Mengel, C. Förster, A. Breivogel, K. Mack, J. R. Ochsmann, F. Laquai, V. Ksenofontov, K. Heinze, *Chem. Eur. J.* **2015**, *21*, 704–714.
- [12] a) M. C. DeRosa, R. J. Crutchley, *Coord. Chem. Rev.* **2002**, *233–234*, 351–371; b) C. Schweitzer, R. Schmidt, *Chem. Rev.* **2003**, *103*, 1685–1757; c) P. R. Ogilby, *Chem. Soc. Rev.* **2010**, *39*, 3181–3209; d) A. O. Terent'ev, D. A. Borisov, V. A. Vi, V. M. Dembitsky, *Beilstein J. Org. Chem.* **2014**, *10*, 34–114; e) K. Gilmore, D. Kopetzki, J. W. Lee, Z. Horváth, D. T. McQuade, A. Seidel-Morgenstern, P. H. Seeberger, *Chem. Commun.* **2014**, *50*, 12652–12655; f) W. Fan, P. Li, *Angew. Chem. Int. Ed.* **2014**, *53*, 12201–12204; *Angew. Chem.* **2014**, *126*, 12397–12400; g) S. Vukelić, D. B. Ushakov, K. Gilmore, B. Kokschi, P. H. Seeberger, *Eur. J. Org. Chem.* **2015**, 3036–3039; h) A. A. Ghogare, A. Greer, *Chem. Rev.* **2016**, *116*, 9994–10034; i) P. Irmiler, R. F. Winter, *Dalton Trans.* **2016**, *45*, 10420–10433.
- [13] a) D. Enders, J. P. Shillock, *Chem. Soc. Rev.* **2000**, *29*, 359–373; b) J.-M. Mattalia, C. Marchi-Delapierre, H. Azimeh, M. Chanon, *ARKIVOC* **2006**, *4*, 90–118; c) T. Opatz, *Synthesis* **2009**, 1941–1959; d) J. C. O. Pacheco, A. Lipp, A. M. Nauth, F. Acke, J.-P. Dietz, T. Opatz, *Chem. Eur. J.* **2016**, *22*, 5409–5415; e) D. Kopetzki, F. Lévesque, P. H. Seeberger, *Chem. Eur. J.* **2013**, *19*, 5450–5456; f) N. Otto, T. Opatz, *Chem. Eur. J.* **2014**, *20*, 13064–13077.
- [14] a) A. Weller, *Z. Phys. Chem.* **1982**, *133*, 93–98; b) D. Rehm, A. Weller, *Isr. J. Chem.* **1970**, *8*, 259–271.
- [15] $\Delta G_{ET} = E_{1/2}(^2E) - E_{1/2}(\text{amine}) - e_0^2/(4\pi\epsilon_0\epsilon(CH_3CN)r_{AD}) - E(^2E)$ with $\epsilon_0 = 8.8519 \times 10^{-12} \text{ Fm}^{-1}$; $\epsilon(CH_3CN) = 37.5$; r = distance between reactants; $E(^2E) = 1.6 \text{ eV}$. As the distance r is unknown, we neglect the (typically small) Coulomb term.
- [16] J. R. Lakowicz, *Principles of Fluorescence Spectroscopy*, 3rd ed, Springer, New York, **2006**.
- [17] a) E. R. Welin, C. Le, D. M. Arias-Rotondo, J. K. McCusker, D. W. C. MacMillan, *Science* **2017**, *355*, 380–385; b) S. O. Scholz, E. P. Farney, S. Kim, D. M. Bates, T. P. Yoon, *Angew. Chem. Int. Ed.* **2016**, *55*, 2239–2242; *Angew. Chem.* **2016**, *128*, 2279–2282; c) M. N. Hopkinson, A. Gómez-Suárez, M. Teders, B. Sahoo, F. Glorius, *Angew. Chem. Int. Ed.* **2016**, *55*, 4361–4366; *Angew. Chem.* **2016**, *128*, 4434–4439; d) E. Brachet, T. Ghosh, I. Ghosh, B. König, *Chem. Sci.* **2015**, *6*, 987–992; e) X.-D. Xia, J. Xuan, Q. Wang, L.-Q. Lu, J.-R. Chen, W.-J. Xiao, *Adv. Synth. Catal.* **2014**, *356*, 2807–2812.
- [18] a) J. N. Schrauben, K. L. Dillman, W. F. Beck, J. K. McCusker, *Chem. Sci.* **2010**, *1*, 405–410; b) E. A. Juban, A. L. Smeigh, J. E. Monat, J. K. McCusker, *Coord. Chem. Rev.* **2006**, *250*, 1783–1791; c) E. A. Juban, J. K. McCusker, *J. Am. Chem. Soc.* **2005**, *127*, 6857–6865.
- [19] M. Quaranta, M. Murkovic, I. Klimant, *Analyst* **2013**, *138*, 6243–6245.
- [20] F. Wilkinson, W. P. Helman, A. B. Ross, *J. Phys. Chem. Ref. Data* **1995**, *24*, 663–1021.
- [21] a) R. S. Davidson, K. R. Trethewey, *J. Chem. Soc. Perkin Trans. 2* **1977**, 169–173; b) R. S. Davidson, K. R. Trethewey, *J. Chem. Soc. Perkin Trans. 2* **1977**, 173–178; c) R. S. Davidson, K. R. Trethewey, *J. Chem. Soc. Perkin Trans. 2* **1977**, 178–182; d) P. J. DeLaive, T. K. Foreman, C. Giannotti, D. G. Whitten, *J. Am. Chem. Soc.* **1980**, *102*, 5627–5631; e) C. Ferroud, P. Rool, J. Santamaria, *Tetrahedron Lett.* **1998**, *39*, 9423–9426; f) E. Baciocchi, T. Del Giacco, A. Lapi, *Helv. Chim. Acta* **2006**, *89*, 2273–2280.
- [22] R. H. Young, D. Brewer, R. Kayser, R. Martin, D. Feriozi, R. A. Keller, *Can. J. Chem.* **1974**, *52*, 2889–2893.
- [23] H. Bartling, A. Eisenhofer, B. König, R. M. Gschwind, *J. Am. Chem. Soc.* **2016**, *138*, 11860–11871.

Manuscript received: May 11, 2017

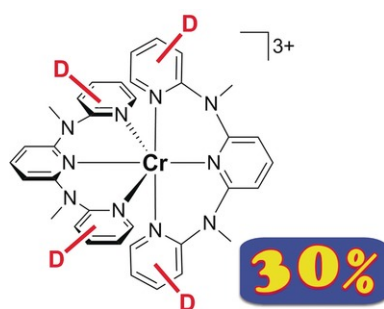
Accepted manuscript online: May 12, 2017

Version of record online: June 1, 2017

3.4 Deuterated Molecular Ruby with Record Luminescence Quantum Yield

Cui Wang, Sven Otto, Matthias Dorn, Elisabeth Kreidt, Jakob Lebon, Laura Sršan, Patrick Di Martino-Fumo, Markus Gerhards, Ute Resch-Genger, Michael Seitz and Katja Heinze

Angew. Chem. **2018**, *130*, 1125–1130. *Angew. Chem. int. Ed.* **2018**, *57*, 1112–1116.



Record ruby: Deuteration of the solvent and especially the ligand boosts the photoluminescence quantum yield of the chromium(III) complex with strong-field ddpd ligands (molecular ruby) from 12 % to a record value of 30 % in solution at room temperature. At the same time, the luminescence lifetime more than doubles to over two milliseconds. The α -CH group of the ddpd ligand provides the most decisive oscillator.

Author Contributions

Elisabeth Kreidt, Jakob Lebon, Laura Sršan, Michael Seitz at the University of Tübingen, Germany and Sven Otto synthesized and characterized the deuterated ligands, Matthias Dorn and Sven Otto synthesized the complexes presented in this manuscript. Cui Wang and Ute Resch-Genger determined the emission quantum yields and excited state lifetimes at the *Bundesanstalt für Materialforschung und -prüfung* in Berlin, Germany. Elisabeth Kreidt, Jakob Lebon, Laura Sršan and Michael Seitz at the University of Tübingen performed NIR absorption spectroscopy and vibrational overtone analysis of the ligands. Patrick Di Martino-Fumo and Markus Gerhards conducted VT-FTIR spectroscopy of the complexes. The english version of the manuscript was written by Katja Heinze (90 %) and Sven Otto (10 %), the german translation was prepared by Matthias Dorn and Sven Otto.

Supporting Information

for this article is found at pp. 178.

“Wang, C.; Otto, S.; Dorn, M.; Kreidt, E.; Lebon, J.; Sršan, L.; Di Marino-Fumo, P.; Gerhards, M.; Resch-Genger, U.; Seitz, M.; Heinze, K. *Angew. Chem. Int. Ed.* **2018**, *57*, 1112–1116. Copyright Wiley-VCH Verlag GmbH & Co. KGaA. Reproduced with permission.”

Luminescent Complexes

International Edition: DOI: 10.1002/anie.201711350
German Edition: DOI: 10.1002/ange.201711350

Deuterated Molecular Ruby with Record Luminescence Quantum Yield

Cui Wang, Sven Otto, Matthias Dorn, Elisabeth Kreidt, Jakob Lebon, Laura Sršan, Patrick Di Martino-Fumo, Markus Gerhards, Ute Resch-Genger,* Michael Seitz,* and Katja Heinze*

Abstract: The recently reported luminescent chromium(III) complex $\mathbf{1}^{3+}$ ($[\text{Cr}(\text{ddpd})_2]^{3+}$; $\text{ddpd} = N,N'$ -dimethyl- N,N' -dipyridine-2-yl-pyridine-2,6-diamine) shows exceptionally strong near-IR emission at 775 nm in water under ambient conditions ($\Phi = 11\%$) with a microsecond lifetime as the ligand design in $\mathbf{1}^{3+}$ effectively eliminates non-radiative decay pathways, such as photosubstitution, back-intersystem crossing, and trigonal twists. In the absence of energy acceptors, such as dioxygen, the remaining decay pathways are energy transfer to high energy solvent and ligand oscillators, namely OH and CH stretching vibrations. Selective deuteration of the solvents and the ddpd ligands probes the efficiency of these oscillators in the excited state deactivation. Addressing these energy-transfer pathways in the first and second coordination sphere furnishes a record 30% quantum yield and a 2.3 millisecond lifetime for a metal complex with an earth-abundant metal ion in solution at room temperature.

The development of photoactive complexes with earth-abundant metal ions is challenging and rapidly growing research field. It is motivated by the desire to replace expensive noble-metal ions and rare-earth-metal ions by

earth-abundant metal ions in the fields of photosensitizing, photoluminescence, and photoredox reactions.^[1,2] Except for copper(I) complexes,^[2] strongly luminescent molecular complexes of earth-abundant-metal ions were essentially unknown until very recently. Near-IR (NIR) emission with mononuclear copper(I) complexes is still very rare.^[2b] Even with noble metal complexes, strong NIR emission is challenging.^[3]

A handful of examples of luminescent complexes based on earth-abundant-metal ions with d^n electron configuration ($n < 10$) only became available in the last three years (Scheme 1). They include ligand-to-metal charge transfer (LMCT), metal-to-ligand (MLCT), and spin-flip emitters.^[4–8] Milsman and co-workers reported a luminescent zirconium(IV) complex bearing 2,6-bis(pyrrylo)pyridine ligands.^[4] A unique low-spin hexacarbene iron(III) complex with LMCT emission has been reported by Wärnmark.^[5] Wenger's d^6 metal(0) isocyanide chelate complexes display MLCT luminescence in solution (Scheme 1).^[6,7]

The chromium(III) complex $[\text{Cr}(\text{ddpd})_2]^{3+}$ ($\mathbf{1}^{3+}$)^[8] with a d^3 electron configuration is based on the tridentate strong-field ligand N,N' -dimethyl- N,N' -dipyridine-2-yl-pyridine-2,6-diamine (ddpd) introduced into coordination chemistry by the Heinze group (Scheme 1).^[9] The “molecular ruby” $\mathbf{1}^{3+}$

[*] C. Wang, Dr. U. Resch-Genger

Division Biophotonics, Federal Institute for Materials Research and Testing (BAM)

Richard-Willstätter-Strasse 11, 12489 Berlin (Germany)

E-mail: ute.resch@bam.de

C. Wang

Institut für Chemie und Biochemie, Freie Universität Berlin
14195 Berlin (Germany)

S. Otto, M. Dorn, Prof. K. Heinze

Institute of Inorganic Chemistry and Analytical Chemistry
Johannes Gutenberg University of Mainz

Duesbergweg 10–14, 55128 Mainz (Germany)

E-mail: katja.heinze@uni-mainz.de

S. Otto

Graduate School Materials Science in Mainz
Staudingerweg 9, 55128 Mainz (Germany)

E. Kreidt, J. Lebon, L. Sršan, Prof. M. Seitz

Institute of Inorganic Chemistry, University of Tübingen
Auf der Morgenstelle 18, 72076 Tübingen (Germany)

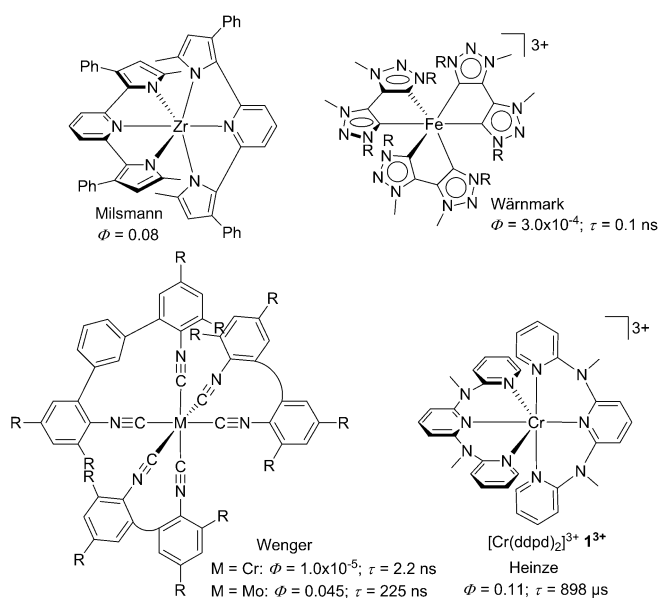
E-mail: michael.seitz@uni-tuebingen.de

P. Di Martino-Fumo, Prof. M. Gerhards

Department of Chemistry and Research Center Optimas
University Kaiserslautern

Erwin-Schrödinger-Strasse, 67663 Kaiserslautern (Germany)

Supporting information and the ORCID identification number(s) for the author(s) of this article can be found under:

<https://doi.org/10.1002/anie.201711350>

Scheme 1. Luminescent complexes with earth-abundant-metal centers (d^n electron configuration; $n < 10$); at room temperature, in solution.^[4–8]

displays a sharp, unprecedentedly intense spin-flip emission in the NIR with a photoluminescence quantum yield of $\Phi = 0.11$ and a luminescence lifetime of $\tau = 898 \mu\text{s}$ in H_2O at room temperature.^[8]

Emerging novel applications of these extraordinary emitters such as triplet–triplet annihilation upconversion,^[6a] demanding photoredox reactions,^[6] optical temperature sensing with a single dye^[10] and selective energy transfer/singlet oxygen formation^[11] have already been realized in this short time and a plethora of others are expected in the future. Clearly, some applications even reach beyond the obvious replacing of standard noble-metal complexes, such as $[\text{Ru}(\text{bpy})_3]^{2+}$, $\text{Ir}(\text{ppy})_3$, and their derivatives (bpy = 2,2'-bipyridine; ppy = deprotonated 2-phenylpyridine).^[12,13] Especially, chromium(III) complexes enjoy a growing interest in these areas.^[8,10,11,14–16]

In many of the above-mentioned complexes (Scheme 1), detrimental ligand-field excited states,^[17,18] which lead to non-radiative deactivation, are either absent (d^0 and d^{10} electron configuration) or have been successfully shifted to high-enough energy, so that these states do not provide an efficient deactivation pathway. As these typically dissociative ligand-field states are not populated for a sufficiently long time, photosubstitution is virtually impossible. This photostability is especially pronounced for $\mathbf{1}^{3+}$ with a high-energy ${}^4\text{T}_2$ ligand-field state preventing substitution reactions (k_{chem} ; Figure 1, center) as back-intersystem crossing (BISC) from the doublet states to the ${}^4\text{T}_2$ state is thermodynamically impeded (k_{BISC} ; Figure 1, center).^[8,19] In the absence of an electronic quencher, such as ${}^3\text{O}_2$, electronic energy transfer (k_{EnT} ; Figure 1, center) does not contribute to the excited state decay of $\mathbf{1}^{3+}$.^[11]

Excited state distortion followed by surface crossing to the ground state is a commonly observed non-radiative decay path for many copper(I)^[2a] and some gold(III) and ruthenium(II) complexes.^[20,21] In octahedral ligand fields the emissive ${}^2\text{E}$ state of $\mathbf{1}^{3+}$ is essentially undistorted relative to the ${}^4\text{A}_2$ ground state resulting in nested states (Figure 1). Direct surface crossing of the excited doublet states with the ground state does not contribute to the non-radiative excited state decay of $\mathbf{1}^{3+}$. However, in trigonally distorted $[\text{CrN}_6]$ complexes, such as $[\text{Cr}(\text{sen})]^{3+}$ (sen = 4,4',4''-ethylidynetris(3-

azabutan-1-amine), the trigonal distortion mixes the d orbitals, reduces the excited quartet–doublet energy gap and leads to different relaxed geometries for the doublet excited state and the quartet ground state. This results in efficient excited state relaxation (k_{trig} ; Figure 1, right).^[22] Thermally enabled twisting distortions in the cage complex $[\text{Cr}(\text{sar})]^{3+}$ also account for its low excited-state lifetime ($< 10 \text{ ns}$) as compared to $[\text{Cr}(\text{fac-Me}_5\text{-D}_{3\text{h}}\text{tricosaneN}_6)]^{3+}$ (235 μs).^[23] Such twisting is absent in the molecular ruby $\mathbf{1}^{3+}$.

With the ${}^4\text{T}_2$ states of Cr^{III} (k_{BISC} , k_{chem}), surface crossing with the ground state (k_{trig}) and electronic energy transfer (k_{EnT}) being excluded as non-radiative deactivation pathways for $\mathbf{1}^{3+}$, k_{nr} should remain as sole substantive contributor to the non-radiative decay of $\mathbf{1}^{3+}$.

Non-radiative decay k_{nr} of the nested ${}^2\text{E}$ state of Cr^{III} depends on vibrational coupling with the environment (Figure 1, left).^[18b,24] Such a situation is typically observed for the luminescence of lanthanoid complexes displaying electronic-to-vibrational energy transfer to overtones of high energy oscillators, such as OH, NH, or CH.^[25] For lanthanoid complexes and Yb/Er upconversion nanoparticles, a significant decrease of k_{nr} can be achieved by removing high-energy XH oscillators from the photoactive site by deuteration.^[26] The ${}^2\text{E}$ lifetimes of $[\text{Cr}(\text{bpy})_3]^{3+}$ (Table 1) and $[\text{Cr}(\text{CN})_6]^{3-}$ show only weak (and inverse) isotope effects upon $\text{H}_2\text{O}/\text{D}_2\text{O}$ exchange.^[27] Probably other pathways (such as, k_{trig} , k_{BISC} , k_{chem}) dominate the ${}^2\text{E}$ lifetime in these classical chromium(III) complexes.

Molecular ruby $\mathbf{1}^{3+}$ shows, however, a quite pronounced $\text{D}_2\text{O}:\text{H}_2\text{O}$ excited state lifetime effect of 1164 $\mu\text{s}:$ 898 μs (D:H factor 1.3).^[8] Clearly, in the absence of other quenching effects, for example, k_{EnT} or k_{trig} , reduction of k_{nr} via deuteration of XH moieties becomes relevant. This can be accomplished by first replacing the solvents with deuterated analogues. Second and most importantly, this excited state deactivation pathway can be controlled by ligand C–H/D exchange. To this end, a statistically deuterated ligand $[\text{D}_9]\text{-ddpd}$ (with ca. 53% average deuterium incorporation at different positions; Scheme 2), as well as $[\text{D}_6]\text{-ddpd}$ with the methyl groups selectively deuterated and $[\text{D}_{14}]\text{-ddpd}$ with the methyl groups and the terminal pyridines deuterated (with deuteration grades above 99.5%) were synthesized (Scheme 2; Supporting Information). The corresponding chromium(III) complexes $[\text{Cr}([\text{D}_9]\text{-ddpd})_2]^{3+}$ ($\mathbf{2}^{3+}$), $[\text{Cr}([\text{D}_6]\text{-ddpd})_2]^{3+}$ ($\mathbf{3}^{3+}$), and $[\text{Cr}([\text{D}_{14}]\text{-ddpd})_2]^{3+}$ ($\mathbf{4}^{3+}$) were prepared as tetrafluoroborate salts according to established procedures.^[8] IR spectra of $\mathbf{1}^{3+}$ and $\mathbf{3}^{3+}$ measured in KBr disks at different temperatures show the typical vibrational signatures in the region of the C–(H/D) stretching modes ($\mathbf{1}^{3+}$: aromatic and methyl CH $\tilde{\nu}_{\text{CH}} = 3150\text{--}2850 \text{ cm}^{-1}$ vs. $\mathbf{3}^{3+}$: aromatic CH $\tilde{\nu}_{\text{CH}} = 3150\text{--}3050 \text{ cm}^{-1}$ and methyl CD $\tilde{\nu}_{\text{CD}} = 2300\text{--}2050 \text{ cm}^{-1}$; Figures S34–S35; Tables S5–S6, Supporting Information).

Table 1 summarizes the luminescence lifetimes τ of $\mathbf{1}^{3+}$ – $\mathbf{4}^{3+}$ in deuterated and non-deuterated solvents with O_2 saturation^[28] and under O_2 exclusion. Corresponding Φ values and radiative lifetimes $\tau_{\text{rad}} = \tau/\Phi$ are collected in the Supporting Information (Tables S1–S3). Dioxygen (${}^3\text{O}_2$) strongly quenches the emission by energy transfer yielding ${}^1\text{O}_2$.^[11] Different oxygen solubility in the different solvents leads to

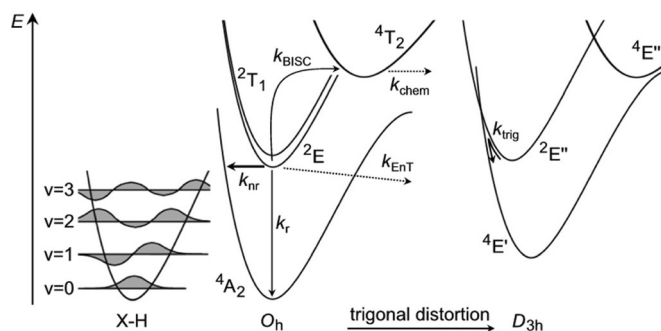
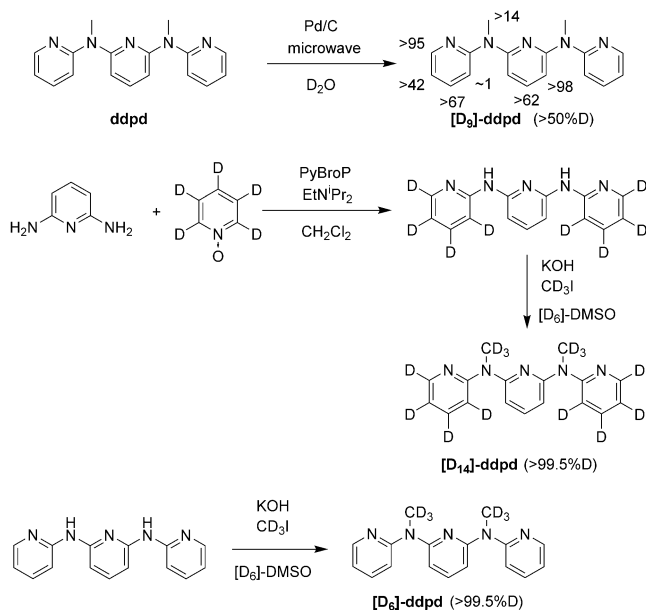


Figure 1. Center: Decay pathways of electronically excited chromium(III) complexes (radiative decay k_r ; back-ISC k_{BISC} ; chemical reaction k_{chem} ; electronic energy transfer k_{EnT}). Left: Non-radiative decay via electronic-to-vibrational energy transfer to high-energy XH oscillators (k_{nr}). Right: Surface crossing in trigonally distorted complexes (k_{trig}).^[22]

Table 1. 2E lifetime $\tau/\mu\text{s}$ of [1][BF₄]₃, [2][BF₄]₃, [3][BF₄]₃, and [4][BF₄]₃ under different conditions at 295 K ($\lambda_{\text{exc}} = 434/435$ nm; $\lambda_{\text{em}} = 778/780$ nm for **1**³⁺, **2**³⁺, **3**³⁺ and **4**³⁺).

Conditions	1 ³⁺ [a,c]	2 ³⁺ [b,c]	3 ³⁺ [b,c]	4 ³⁺ [b,c]	[Cr(bpy) ₃] ³⁺ [d]
H ₂ O/Ar	898	1300 (1.4)	870 (1.0)	1200 (1.3)	60 ^[d] /66 ^[e]
H ₂ O/O ₂	177	190 (1.1)	180 (1.0)	190 (1.1)	41 ^[d]
ratio Ar:O ₂	5.1	6.8	4.8	6.3	1.5
D ₂ O/Ar	1164	1700 (1.5)	1200 (1.0)	2100 (1.8)	61 ^[e]
D ₂ O/O ₂	150	190 (1.3)	160 (1.1)	170 (1.1)	37 ^[d]
ratio Ar:O ₂	7.8	8.9	7.5	12.4	1.7
D ₂ O/H ₂ O (Ar)	1.3	1.3	1.4	1.7	0.9 (O ₂) ^[d] 0.9 (Ar) ^[e]
CH ₃ CN/Ar	899	1800 (2.0)	910 (1.0)	–	51
CH ₃ CN/O ₂	44	28 (0.6)	28 (0.6)	–	28
ratio Ar:O ₂	17.6	64.3	32.5	–	1.8
CD ₃ CN/Ar	810	2300 (2.8)	1000 (1.2)	–	–
CD ₃ CN/O ₂	24	48 (2.0)	34 (1.4)	–	–
ratio Ar:O ₂	33.8	47.9	29.4	–	–
CD ₃ CN:CH ₃ CN (Ar)	0.9	1.3	1.1	–	–

[a] Ref. [8]. [b] The lifetime ratio with respect to **1**³⁺ is given in parenthesis (D:H factor). [c] D₂O and CD₃CN deuteration levels over 99.8%. [d] Ref. [27b]. [e] Ref. [27c].



different quenching efficiencies and hence changes in Φ and τ in H₂O and CH₃CN.^[11] The very strong luminescence quenching of **1**³⁺ by ³O₂ in CH₃CN had already been exploited in the photosensitized formation of ¹O₂ for selective C–H activation of tertiary amines.^[11] In the presence of O₂, luminescence lifetimes (Table 1) and quantum yields (1–3%) are low and weakly affected by solvent or ligand

deuteration. Under O₂ saturation, electronic energy transfer to O₂ (k_{ENT}) dominates over k_{nr} .

In the absence of ³O₂, energy transfer to CH vibrations of the ligand plays a major role. However, not all CH oscillators contribute equally to k_{nr} . Isotopologue **3**³⁺ with the methyl groups of ddpd selectively deuterated ([D₆]-ddpd) behaves similar as **1**³⁺ with respect to τ . Consequently, these oscillators contribute negligibly to the excited state decay which is primarily a function of the rather large Cr...H distance of 4.8–5.3 Å according to DFT models (Figure 2).^[8] Furthermore, this is likely also related to the lower vibrational energies ($\tilde{\nu}_{\text{CH}} < 3050$ cm⁻¹) and the decreased oscillator strengths of the associated overtones.^[29,30]

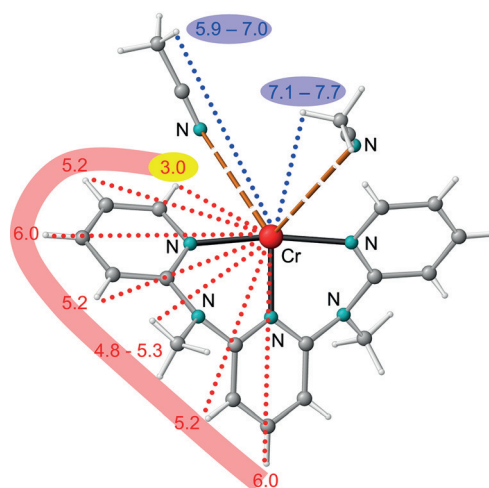


Figure 2. Cr...H distances to the ddpd ligand of **1**³⁺ as determined by a DFT calculation and to CH₃CN as estimated by single-crystal X-ray diffraction,^[8] illustrating the first coordination sphere in red and the second coordination sphere in blue (one ddpd ligand omitted for clarity). Distances given in Å.

Compounds **2**³⁺ and **4**³⁺ achieve the maximum effect on τ by ligand deuteration with the highest D:H factors observed in H₂O (1.4), D₂O (1.5), CH₃CN (2.0), and CD₃CN (2.8) for **2**³⁺ (Table 1). Clearly, the aromatic CH bonds ($\tilde{\nu}_{\text{CH}} > 3050$ cm⁻¹) of the pyridines contribute most to the decay of the ²E state. Unprecedentedly high quantum yields were obtained for **2**³⁺ with $\Phi = 22.4\%$ and 30.1% in D₂O and CD₃CN, respectively, and for **4**³⁺ ($\Phi = 21.6\%$ in D₂O). The corresponding lifetimes reach the two milliseconds range (Table 1, $\tau = 2.3$ ms for **2**³⁺ in CD₃CN under Ar).

While the luminescence efficiencies of the deuterated complexes **2**³⁺ and **4**³⁺ are unprecedentedly high, the improve-

ment factors observed for ligand deuteration are modest compared with other examples in the literature, reaching more than an order of magnitude in some cases.^[26] A careful qualitative analysis of the relative positions of the 2E emission and the energetically close vibrational overtones of aromatic CH oscillators using a simplified model system reveals a very fortunate spectral overlap mismatch between the emission and CH absorption bands (Figure 3a). This in turn leads to

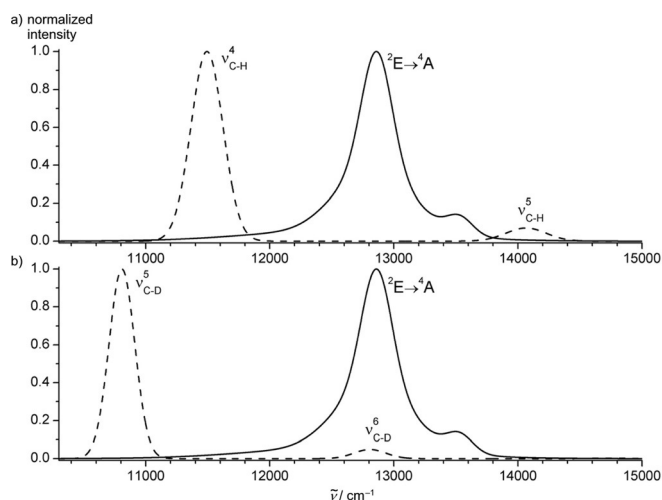


Figure 3. a) Normalized 2E emission spectrum of 1^{3+} (solid line) and the relevant vibrational aromatic CH overtone absorption bands (dashed line) showing the lack of substantial spectral overlap which is responsible for the only limited vibrational energy transfer (k_{nr}) to the CH oscillators ($\nu=4,5$) in 1^{3+} . b) Normalized 2E emission spectrum of 1^{3+} (solid line) and the relevant vibrational aromatic CD overtone absorption bands ($\nu=5,6$; dashed line) (see the Supporting Information for details).

only limited non-radiative energy transfer (k_{nr}) in the non-deuterated complex 1^{3+} , while the emission of $[\text{Cr}(\text{bpy})_3]^{3+}$ (13737 cm^{-1}) overlaps considerably with the fourth CH overtone accounting for efficient quantum yield reduction (Figure S33, Supporting Information). The CD oscillators (the fifth CD vibrational overtones; $\nu=6$) have considerable spectral overlap with the emission of 1^{3+} and contribute significantly to the deactivation of the doublet states (Figure 3b). This, among other important factors (see above), accounts for the already very high NIR luminescence efficiency without deuteration and consequently leaves less room for improvement upon deuteration.

In the highly emissive isotopologues 2^{3+} and 4^{3+} the α -CH group closest to the chromium center with a $\text{Cr}\cdots\text{H}$ distance of 3.0 \AA (Figure 2) is nearly quantitatively deuterated. This result suggests that this CH oscillator contributes significantly to k_{nr} fitting to the expected distance dependence ($k_{nr} \propto r_{\text{CrH}}^{-6}$)^[31] of the quenching efficiency. Hence, in future efforts towards highly luminescent spin-flip complexes it might be sufficient to just deuterate the ligands at this privileged position to achieve significant luminescence enhancement—provided that all other decay pathways are already inhibited.

The least important deactivation pathway is energy transfer to higher XH vibrational levels of the solvent (OH

stretching vibrations D:H factor 1.3–1.7; CH stretching vibrations D:H factor 0.9–1.3). OH oscillators appear slightly more effective as energy acceptors than CH oscillators for the complexes under study. Again, this is a combined effect of the higher vibrational energy ($\tilde{\nu}_{\text{OH}} \approx 3400\text{ cm}^{-1}$ vs. $\tilde{\nu}_{\text{CH}} \approx 2900\text{ cm}^{-1}$) and anharmonicity ($x_{\text{OH}} \approx 90\text{ cm}^{-1}$ vs. $x_{\text{CH}} \approx 60\text{ cm}^{-1}$)^[30,32] of the OH oscillators.

In summary, complex 2^{3+} shows a record luminescence lifetime of 2.3 ms and a record luminescence quantum yield of 30% for $3d^n$ metal complexes ($n < 10$) in CD_3CN solution at room temperature. This fundamental photophysical and deuteration study on molecular rubies paves the way for future spin-flip emitters with even higher photoluminescence quantum yield based on earth-abundant-metal ions, with strong-field multidentate ligands providing a rigid idealized octahedral geometry with a minimum of deuterium incorporation at decisive positions. A plethora of applications employing strongly luminescent complexes with earth-abundant-metal ions is certainly within reach.

Acknowledgements

This work was supported by the Deutsche Forschungsgemeinschaft (GSC 266, Materials Science in Mainz, scholarship for S.O., HE 2778/10-1, RE 1203/23-1, SE 1448/6-1, SFB-TR88_TP C2). Funding from the internal university research funds of the Johannes Gutenberg University of Mainz and from the Studienstiftung des deutschen Volkes (predoctoral fellowship for E.K.) is gratefully acknowledged. Parts of this research were conducted using the supercomputer MOGON and advisory services offered by Johannes Gutenberg University of Mainz (www.hpc.uni-mainz.de), which is a member of the AHRP and the Gauss Alliance e.V.

Conflict of interest

The authors declare no conflict of interest.

Keywords: chromium · deuteration · excited states · luminescence · spin-flip

How to cite: *Angew. Chem. Int. Ed.* **2018**, *57*, 1112–1116
Angew. Chem. **2018**, *130*, 1125–1130

- [1] C. B. Larsen, O. S. Wenger, *Chem. Eur. J.* **2017**, <https://doi.org/10.1002/chem.201703602>.
- [2] a) M. Iwamura, S. Takeuchi, T. Tahara, *Acc. Chem. Res.* **2015**, *48*, 782–791; b) B. Hupp, C. Schiller, C. Lenczyk, M. Stanoppi, K. Edkins, A. Lorbach, A. Steffen, *Inorg. Chem.* **2017**, *56*, 8996–9008.
- [3] M. Schulze, A. Steffen, F. Würthner, *Angew. Chem. Int. Ed.* **2015**, *54*, 1570–1573; *Angew. Chem.* **2015**, *127*, 1590–1593.
- [4] Y. Zhang, J. L. Peterson, C. Milsman, *J. Am. Chem. Soc.* **2016**, *138*, 13115–13118.
- [5] a) P. Chábera, Y. Liu, O. Prakash, E. Thyraug, A. El Nahhas, A. Honarfar, S. Essén, L. A. Fredin, T. C. B. Harlang, K. S. Kjaer, K. Handrup, F. Ericsson, Y. Tatsuno, K. Morgan, J. Schnadt, L. Hågström, T. Ericsson, A. Sobkowiak, S. Lidin, P. Huang, S. Styring, J. Uhlíř, J. Bendix, R. Lomoth, V. Sundström, P. Persson,

- K. Wärnmark, *Nature* **2017**, *543*, 695–699; b) B. Sarkar, L. Suntrup, *Angew. Chem. Int. Ed.* **2017**, *56*, 8938–8940; *Angew. Chem.* **2017**, *129*, 9064–9066.
- [6] a) L. A. Büldt, X. Guo, R. Vogel, A. Prescimone, O. S. Wenger, *J. Am. Chem. Soc.* **2017**, *139*, 985–992; b) L. A. Büldt, X. Guo, A. Prescimone, O. S. Wenger, *Angew. Chem. Int. Ed.* **2016**, *55*, 11247–11250; *Angew. Chem.* **2016**, *128*, 11413–11417.
- [7] L. A. Büldt, O. S. Wenger, *Angew. Chem. Int. Ed.* **2017**, *56*, 5676–5682; *Angew. Chem.* **2017**, *129*, 5770–5776.
- [8] S. Otto, M. Grabolle, C. Förster, C. Kreitner, U. Resch-Genger, K. Heinze, *Angew. Chem. Int. Ed.* **2015**, *54*, 11572–11576; *Angew. Chem.* **2015**, *127*, 11735–11739.
- [9] a) A. Breivogel, C. Förster, K. Heinze, *Inorg. Chem.* **2010**, *49*, 7052–7056; b) K. Mack, A. Wünsche von Leupoldt, C. Förster, M. Ezhevskaya, D. Hinderberger, K. W. Klinkhammer, K. Heinze, *Inorg. Chem.* **2012**, *51*, 7851–7858; c) A. Breivogel, M. Meister, C. Förster, F. Laquai, K. Heinze, *Chem. Eur. J.* **2013**, *19*, 13745–13760; d) C. Förster, K. Mack, L. M. Carrella, V. Ksenofontov, E. Rentschler, K. Heinze, *Polyhedron* **2013**, *52*, 576–581; e) A. Breivogel, M. Park, D. Lee, S. Klassen, A. Kühnle, C. Lee, K. Char, K. Heinze, *Eur. J. Inorg. Chem.* **2014**, 288–295; f) A. Breivogel, C. Kreitner, K. Heinze, *Eur. J. Inorg. Chem.* **2014**, 5468–5490; g) A. K. C. Mengel, C. Förster, A. Breivogel, K. Mack, J. R. Ochsmann, F. Laquai, V. Ksenofontov, K. Heinze, *Chem. Eur. J.* **2015**, *21*, 704–714; h) A. K. C. Mengel, C. Bissinger, M. Dorn, O. Back, C. Förster, K. Heinze, *Chem. Eur. J.* **2017**, *23*, 7920–7931; i) S. Otto, J. Moll, C. Förster, D. Geißler, C. Wang, U. Resch-Genger, K. Heinze, *Eur. J. Inorg. Chem.* **2017**, *43*, 5033–5040.
- [10] S. Otto, N. Scholz, T. Behnke, U. Resch-Genger, K. Heinze, *Chem. Eur. J.* **2017**, *23*, 12131–12135.
- [11] S. Otto, A. M. Nauth, E. Ermilov, N. Scholz, A. Friedrich, U. Resch-Genger, S. Lochbrunner, T. Opatz, K. Heinze, *ChemPhotoChem* **2017**, *1*, 344–349.
- [12] a) Q. Zhao, C. Huang, F. Li, *Chem. Soc. Rev.* **2011**, *40*, 2508–2524; b) O. S. Wenger, *Chem. Rev.* **2013**, *113*, 3686–3733; c) V. W.-W. Yam, K. M.-C. Wong, *Chem. Commun.* **2011**, 47, 11579–11592; d) P.-T. Chou, Y. Chi, *Chem. Eur. J.* **2007**, *13*, 380–395.
- [13] H. Xiang, J. Cheng, X. Ma, X. Zhou, J. Chruma, *Chem. Soc. Rev.* **2013**, *42*, 6128–6185.
- [14] L. A. Büldt, O. S. Wenger, *Chem. Sci.* **2017**, *8*, 7359–7367.
- [15] a) S. M. Stevenson, M. P. Shores, E. M. Ferreira, *Angew. Chem. Int. Ed.* **2015**, *54*, 6506–6510; *Angew. Chem.* **2015**, *127*, 6606–6610; b) R. F. Higgins, S. M. Fatur, S. G. Shepard, S. M. Stevenson, D. J. Boston, E. M. Ferreira, N. H. Damrauer, A. K. Rappé, M. P. Shores, *J. Am. Chem. Soc.* **2016**, *138*, 5451–5464; c) S. M. Stevenson, R. F. Higgins, M. P. Shores, E. M. Ferreira, *Chem. Sci.* **2017**, *8*, 654–660.
- [16] D. Zare, B. Doistau, H. Nozary, C. Besnard, L. Guénée, Y. Suffren, A.-L. Pelé, A. Hauser, C. Pigué, *Dalton Trans.* **2017**, 46, 8992–9009.
- [17] a) Y. Tanabe, S. Sugano, *J. Phys. Soc. Jpn.* **1954**, *9*, 753–766; b) Y. Tanabe, S. Sugano, *J. Phys. Soc. Jpn.* **1954**, *9*, 766–779; c) A. Hauser, C. Reber, in *Structure and Bonding*, Vol. 172, Springer, Berlin, **2016**, pp. 291.
- [18] a) A. D. Kirk, *Chem. Rev.* **1999**, *99*, 1607–1640; b) L. S. Forster, *Coord. Chem. Rev.* **2002**, *227*, 59–92; c) N. A. P. Kane-Maguire, *Top. Curr. Chem.* **2007**, *280*, 37–67; d) V. Balzani, P. Ceroni, A. Juris, *Photochemistry and Photophysics*, Wiley-VCH, Weinheim, **2014**, pp. 216–219; e) M. A. Jamieson, N. Serpone, M. Z. Hoffman, *Coord. Chem. Rev.* **1981**, *39*, 121–179; f) C. K. Ryu, J. F. Endicott, *Inorg. Chem.* **1988**, *27*, 2203–2214; g) “Picosecond Phenomena II”: M. Asano, J. A. Koningstein, in *Springer Series in Chemical Physics*, Vol. 14 (Eds.: R. Hochstrasser, W. Kaiser, C. V. Shank), Springer, Berlin, **1980**, pp. 351–356.
- [19] N. Serpone, M. Z. Hoffman, *J. Chem. Educ.* **1983**, *60*, 853–860.
- [20] a) W. H. Lam, E. S.-H. Lam, V. W.-W. Yam, *J. Am. Chem. Soc.* **2013**, *135*, 15135–15143; b) E. S.-H. Lam, W. H. Lam, V. W.-W. Yam, *Inorg. Chem.* **2015**, *54*, 3624–3630.
- [21] C. Kreitner, K. Heinze, *Dalton Trans.* **2016**, *45*, 13631–13647.
- [22] M. W. Perkovic, M. Jane Heeg, J. F. Endicott, *Inorg. Chem.* **1991**, *30*, 3140–3147.
- [23] K. N. Brown, R. J. Geue, G. Moran, S. F. Ralph, H. Riesen, A. M. Sargeson, *Chem. Commun.* **1998**, 2291–2292.
- [24] P. S. Wagenknecht, P. C. Ford, *Coord. Chem. Rev.* **2011**, *255*, 591–616.
- [25] a) R. M. Supkowski, W. D. Horrocks, Jr., *Inorg. Chim. Acta* **2002**, *340*, 44; b) A. Beeby, I. M. Clarkson, R. S. Dickins, S. Faulkner, D. Parker, L. Royle, A. S. de Sousa, J. A. G. Williams, M. Woods, *J. Chem. Soc. Perkin Trans. 2* **1999**, 493.
- [26] Selected examples: a) W. R. Browne, J. G. Vos, *Coord. Chem. Rev.* **2001**, *219–221*, 761–787; b) S. Yanagida, Y. Hasegawa, K. Murakoshi, Y. Wada, N. Nakashima, T. Yamanaka, *Coord. Chem. Rev.* **1998**, *171*, 461–480; c) C. Doffek, M. Seitz, *Angew. Chem. Int. Ed.* **2015**, *54*, 9719–9721; *Angew. Chem.* **2015**, *127*, 9856–9858; d) J.-Y. Hu, Y. Ning, Y.-S. Meng, J. Zhang, Z.-Y. Wu, S. Gao, J.-L. Zhang, *Chem. Sci.* **2017**, *8*, 2702–2709; e) C. Doffek, J. Wahsner, E. Kreidt, M. Seitz, *Inorg. Chem.* **2014**, *53*, 3263–3265; f) C. Würth, M. Kaiser, S. Wilhelm, B. Grauel, T. Hirsch, U. Resch-Genger, *Nanoscale* **2017**, *9*, 4283–4294.
- [27] a) M. S. Henry, *J. Am. Chem. Soc.* **1977**, *99*, 6138–6139; b) N. A. P. Kane-Maguire, R. C. Kerr, J. R. Walters, *Inorg. Chim. Acta* **1979**, *33*, L163–L165; c) R. Sriram, M. Z. Hoffman, N. Serpone, *J. Am. Chem. Soc.* **1981**, *103*, 997–998; d) R. Dannöhl-Fickler, H. Kelm, F. Wasgestian, *J. Lumin.* **1975**, *10*, 103–112.
- [28] M. Quaranta, M. Murkovic, I. Klimant, *Analyst* **2013**, *138*, 6243–6245.
- [29] R. J. Proos, B. R. Henry, *J. Phys. Chem. A* **1999**, *103*, 8762–8771.
- [30] C. Doffek, N. Alzakhem, C. Bischof, J. Wahsner, T. Guden-Silber, J. Lügger, C. Platas-Iglesias, M. Seitz, *J. Am. Chem. Soc.* **2012**, *134*, 16413–16423.
- [31] V. L. Ermolaev, E. B. Sveshnikova, *Russ. Chem. Rev.* **1994**, *63*, 905–922.
- [32] R. L. Swofford, M. E. Long, M. S. Burberry, A. C. Albrecht, *J. Chem. Phys.* **1977**, *66*, 664–668.

Manuscript received: November 7, 2017

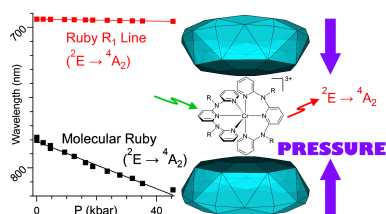
Accepted manuscript online: December 7, 2017

Version of record online: January 2, 2018

3.5 Molecular Ruby under pressure

Sven Otto, Joe Harris, Katja Heinze and Christian Reber

Submitted to *Angewandte Chemie International Edition* **2018**.



Luminescence under pressure: The spin-flip emission band of the highly luminescent molecular ruby $[\text{Cr}(\text{ddpd})_2]^{3+}$ shifts by $-15 \text{ cm}^{-1} \text{ kbar}^{-1}$ under hydrostatic pressure, surpassing that of the standard pressure calibrant ruby $\text{Al}_2\text{O}_3:\text{Cr}^{3+}$ by a factor of 20 (ddpd = *N,N'*-dimethyl-*N,N'*-dipyridine-2-yl-pyridine-2,6-diamine). Unique to the molecular ruby is its applicability also in solution (aqueous and methanolic), enabling unprecedented pressure sensing in solution with a single dye.

Author Contributions

Sven Otto and Joe Harris recorded the pressure dependent emission and Raman spectra. Sven Otto performed the CAS-SCF calculations on $[\text{Cr}(\text{ddpd})_2]^{3+}$, Joe Harris and Christian Reber carried out the ligand field calculations. The manuscript was written by Christian Reber (50 %), Katja Heinze (40 %), Joe Harris (10 %) and Sven Otto (10 %).

Supporting Information

for this article is found at pp. 206.

Molecular ruby under pressure

Sven Otto^[a,b], Joe P. Harris^[c], Katja Heinze^{*[a]}, and Christian Reber^{*[c]}

The intensely luminescent chromium(III) complexes $[\text{Cr}(\text{ddpd})_2]^{3+}$ and $[\text{Cr}(\text{H}_2\text{tpda})_2]^{3+}$ show unprecedentedly large pressure-induced red shifts of up to $-15 \text{ cm}^{-1} \text{ kbar}^{-1}$ for their sharp spin-flip emission bands (ddpd = *N,N*-dimethyl-*N,N*-dipyridine-2-yl-pyridine-2,6-diamine; H_2tpda = 2,6-bis(2-pyridylamino)pyridine). This shift surpasses that of the gold standard ruby $\text{Al}_2\text{O}_3:\text{Cr}^{3+}$ by a factor of 20. Beyond the common application in the crystalline state, the very high quantum yield of $[\text{Cr}(\text{ddpd})_2]^{3+}$ enables optical pressure sensing in aqueous and methanolic solution. These unique features of the molecular rubies $[\text{Cr}(\text{ddpd})_2]^{3+}$ and $[\text{Cr}(\text{H}_2\text{tpda})_2]^{3+}$ pave the way for highly sensitive optical pressure determination and so far unprecedented molecule-based pressure sensing with a single type of emitter.

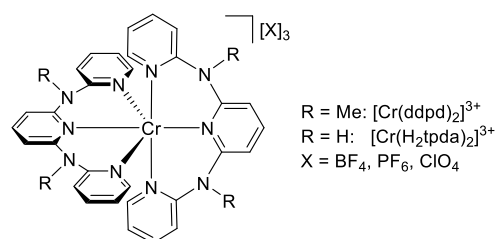
Chromium(III) complexes and solids doped with Cr^{3+} ions (d^3 electron configuration) show rich luminescence phenomena, providing insight on many spectroscopic and photochemical processes.^[1,2] Solid luminophores based on chromium(III) centers have found applications as laser active media, phosphor materials and luminescent sensors.^[3-7] The most outstanding example is probably ruby ($\text{Al}_2\text{O}_3:\text{Cr}^{3+}$) and its decisive role in the development of the first laser.^[7]

Luminescence intensities from chromium(III) complexes in solution are typically very low.^[6] Despite this deficiency, applications of molecular chromium(III) complexes, such as $[\text{Cr}(\text{phen})_3]^{3+}$ derivatives, in oxidative photoredox catalysis have been recently developed capitalizing on the high excited state redox potential (phen = 1,10-phenanthroline).^[8-11] In contrast to previously reported molecular Cr^{3+} complexes is the recently reported intense solution luminescence of $[\text{Cr}(\text{ddpd})_2]^{3+}$ (Chart 1, ddpd = *N,N*-dimethyl-*N,N*-dipyridine-2-yl-pyridine-2,6-diamine). This complex is denoted a molecular ruby analogue due to its exceptionally high quantum yields of 10 – 14 % in solution at room temperature and up to 30 % for deuterated derivatives.^[12,13] These molecular rubies have emerging applications in photocatalysis^[14] and sensing.^[15,16] The two sharp spin-flip transitions ${}^2\text{E} \rightarrow {}^4\text{A}_2$ and ${}^2\text{T}_1 \rightarrow {}^4\text{A}_2$ (O_h symmetry group labels) of $[\text{Cr}(\text{ddpd})_2]^{3+}$ are close in energy and enable optical

radiometric temperature sensing in solution, in micelles and in nanoparticles containing the molecular ruby $[\text{Cr}(\text{ddpd})_2]^{3+}$ as a single dye.^[15]

Pressure-sensing using molecular luminescent complexes typically relies on the quenching of the luminescence by O_2 .^[17] In combination with an oxygen-independent fluorophore, ratiometric optical pressure sensing with molecular systems has been achieved capitalizing on *intensity differences* of the emission bands.^[17]

In contrast, pressure-dependent luminescence *energy differences* have been recorded for many solid chromium(III) materials.^[18-38] The best known example is ruby itself, with a pressure-induced red shift of the R_1 line luminescence (${}^2\text{E} \rightarrow {}^4\text{A}_2$) of $-0.7 \text{ cm}^{-1} \text{ kbar}^{-1}$. This material is widely used to calibrate pressures of samples in diamond anvil cells.^[18-20,39] Shifts of similar magnitude have been observed for other Cr^{3+} doped lattices (Supporting Information, Table S1). However, reports on pressure-induced shifts of molecular chromium(III) species are very rare even in the solid state due to the typically low phosphorescence quantum yields (Supporting Information, Table S1). An illustrative example is $[\text{Cr}(\text{urea})_6][\text{ClO}_4]_3$ with a shift of $-5.4 \text{ cm}^{-1} \text{ kbar}^{-1}$ for the ${}^2\text{E} \rightarrow {}^4\text{A}_2$ spin-flip luminescence (solid state, $T < 120 \text{ K}$).^[40] In spite of the larger shift compared to oxidic lattices such as ruby, any applications of this molecular material are hampered by the weak phosphorescence which is only observed at low temperature.



Scheme 1. Schematic structure of the intensely luminescent chromium(III) complexes employed in this study.

In this study, we combine the unique favorable luminescence properties of the molecular rubies with pressure-dependent studies in order to exploit the potentially larger shifts and hence sensitivities of “softer” molecular materials as compared to oxidic lattices. This should enable pressure sensing using a single type of luminescent molecules in contrast to the commonly employed combination of two emissive dyes for ratiometric sensing.^[17] Furthermore, we will explore for the first time whether the two spin-flip emission bands of Cr^{3+} (${}^2\text{E} \rightarrow {}^4\text{A}_2$ and ${}^2\text{T}_1 \rightarrow {}^4\text{A}_2$) experience the same or distinct pressure-induced shifts. The current study marks the first recording of such pressure-induced shifts for both spin-flip bands in chromium(III) complexes in the solid state and in solution.

[a] S. Otto, Prof. K. Heinze
Institute of Inorganic Chemistry and Analytical Chemistry
Johannes Gutenberg University of Mainz
Duesbergweg 10-14, 55128 Mainz, Germany
E-mail: katja.heinze@uni-mainz.de

[b] S. Otto
Graduate School Materials Science in Mainz
Staudingerweg 9, 55128 Mainz, Germany

[c] Dr. J. Harris, Prof. C. Reber
Département de chimie
Université de Montréal
Montréal, Québec, H3C 3J7, Canada
E-mail: christian.reber@umontreal.ca

Supporting information for this article is given via a link at the end of the document.

We present variable-pressure luminescence spectra of $[\text{Cr}(\text{ddpd})_2][\text{BF}_4]_3$, $[\text{Cr}(\text{ddpd})_2][\text{PF}_6]_3$, and $[\text{Cr}(\text{H}_2\text{tpda})_2][\text{ClO}_4]_3$ ($\text{H}_2\text{tpda} = 2,6\text{-bis}(2\text{-pyridylamino})\text{pyridine}$)^[41] in the solid state (Scheme 1), up to 49 kbar. $[\text{Cr}(\text{ddpd})_2][\text{BF}_4]_3$ is furthermore studied in aqueous and in methanolic solution. The pressures were achieved with a diamond anvil cell and spectra were measured with a commercial Renishaw microscope spectrometer with an excitation wavelength of 488 nm.^[42]

At ambient pressure, $[\text{Cr}(\text{ddpd})_2]^{3+}$ shows ${}^2\text{E} \rightarrow {}^4\text{A}_2$ emission at 775 nm, which is strongly redshifted relative to the corresponding transition in Cr^{3+} doped solids.^[12–16] Variable-pressure luminescence spectra of $[\text{Cr}(\text{ddpd})_2][\text{BF}_4]_3$ are depicted in Figures 1 and S1 – S2 (Supporting Information), for both the crystalline sample and molecularly dissolved in water.

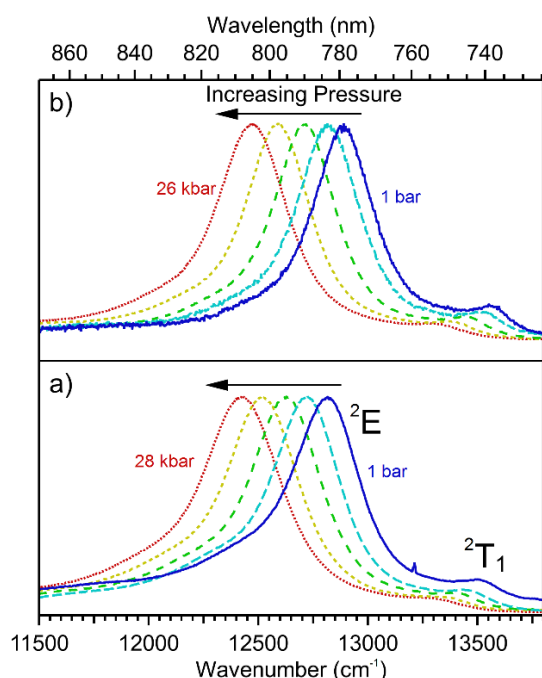


Figure 1. Variable pressure luminescence spectra of $[\text{Cr}(\text{ddpd})_2][\text{BF}_4]_3$ for the solid sample (a) and in aqueous solution (b). Excitation wavelength was 488 nm.

Both series show a pronounced linear red shift of the ${}^2\text{E}$ emission upon application of pressure, with large slopes of $-14.1 \text{ cm}^{-1} \text{ kbar}^{-1}$ and $-14.8 \text{ cm}^{-1} \text{ kbar}^{-1}$ for the solid and for the (frozen) solution, respectively, up to 21 kbar. The crystalline sample exhibits a constant slope up to 35 kbar. The aqueous solution is expected to freeze at a pressure of around 10 kbar,^[43] although a corresponding change in wavelength due to the phase transition is not evident from these spectra (Figure 1; Supporting Information, Figure S4). However, at 21 kbar, the frozen aqueous solution undergoes a phase change from ice VI to ice VII,^[43] and the subsequent slope is smaller ($-4.7 \text{ cm}^{-1} \text{ kbar}^{-1}$) to 49 kbar. This observation suggests that $[\text{Cr}(\text{ddpd})_2][\text{BF}_4]_3$ molecularly dissolved in water could enable sensing of phase transitions which would naturally be impossible

using solid materials as optical sensor materials. Experiments were also successfully carried out with a solution of $[\text{Cr}(\text{ddpd})_2][\text{BF}_4]_3$ in methanol (Supporting Information, Figure S3). The slope of $-14.5 \text{ cm}^{-1} \text{ kbar}^{-1}$ is similar to the solid and unchanging upon increasing pressure to 18 kbar as methanol remains liquid under these conditions.^[44] Crystals of $[\text{Cr}(\text{ddpd})_2][\text{PF}_6]_3$ and $[\text{Cr}(\text{H}_2\text{tpda})_2][\text{ClO}_4]_3$ display a comparable, slightly smaller shift of $-13.0 \text{ cm}^{-1} \text{ kbar}^{-1}$ for both, up to 39 kbar and 31 kbar respectively (Supporting Information, Figures S4 and S5).

The observed shifts for the chromium(III) complexes $[\text{Cr}(\text{ddpd})_2][\text{BF}_4]_3$, $[\text{Cr}(\text{ddpd})_2][\text{PF}_6]_3$, and $[\text{Cr}(\text{H}_2\text{tpda})_2][\text{ClO}_4]_3$ are higher by more than a factor of ten than those of the typical doped solids, and higher by around a factor of three than shifts for the molecular chromium(III) complexes reported so far (Table S1). With respect to the standard pressure calibrant ruby, these molecular materials show enhanced sensitivity by up to a factor of 20, opening the door to pressure-sensing applications requiring a higher sensitivity. The shifts are also stronger by at least a factor of six than many Sm^{2+} doped solids, which have been proposed as improvements over ruby as pressure standards.^[45–48] Further, these unexpectedly strong red shifts of intraconfigurational bands are comparable in absolute value but different in sign than the typical shifts reported for interconfigurational d-d transitions with broad emission bands, both in doped solids such as $\text{YAG}:\text{Cr}^{3+}$ ($+9 \text{ cm}^{-1} \text{ kbar}^{-1}$)^[27,38] and molecular complexes such as $[(\text{NH}_3)_5\text{Cr}(\mu\text{-OH})\text{Cr}(\text{NH}_3)_5]\text{Cl}_5 \cdot \text{H}_2\text{O}$ ($+21 \text{ cm}^{-1} \text{ kbar}^{-1}$).^[38,49]

To the best of our knowledge, the pressure-dependence of the ${}^2\text{T}_1$ spin-flip transition has not been previously reported for any Cr^{3+} system. The favorable luminescence properties of $[\text{Cr}(\text{ddpd})_2]^{3+}$ with a reasonably intense ${}^2\text{T}_1$ band allow determination of its pressure-dependence for the first time. The slope of this transition for $[\text{Cr}(\text{ddpd})_2][\text{BF}_4]_3$ is $-7.7 \text{ cm}^{-1} \text{ kbar}^{-1}$ in the solid state (Figures 1 and 2). Since the ${}^2\text{T}_1$ emission is at higher energy and shifts less, the separation between the two luminescence transitions increases with increasing pressure. Table 1 summarizes all pressure-induced ${}^2\text{E}$ and ${}^2\text{T}_1$ shifts of $[\text{Cr}(\text{ddpd})_2][\text{BF}_4]_3$, $[\text{Cr}(\text{ddpd})_2][\text{PF}_6]_3$, and $[\text{Cr}(\text{H}_2\text{tpda})_2][\text{ClO}_4]_3$ in the crystalline state and in solution. The ratio between the two shifts varies from 1.5 to 2.8, depending on the ligand (ddpd/ H_2tpda), the counter ion ($\text{BF}_4^-/\text{PF}_6^-$), and the environment (solid/solution).

The effect of pressure on the molecular structure and geometry and hence the excited state energies (especially ${}^2\text{E}$ and ${}^2\text{T}_1$) is difficult to estimate. In order to gain more insight, pressure-dependent Raman spectra were recorded for the solid materials $[\text{Cr}(\text{ddpd})_2][\text{BF}_4]_3$ and $[\text{Cr}(\text{H}_2\text{tpda})_2][\text{ClO}_4]_3$ (Supporting Information, Figures S8 – S10). Shifts of Raman peaks are expected to be rather slight, and any large changes or discontinuous variations usually indicate a phase transition of the material. As the Raman spectra at high pressure are nearly identical to the ambient pressure spectra, phase transitions of $[\text{Cr}(\text{ddpd})_2][\text{BF}_4]_3$ and $[\text{Cr}(\text{H}_2\text{tpda})_2][\text{ClO}_4]_3$ are absent in this pressure range at room temperature. Of the three prominent Raman peaks selected, the lowest energy peak at around 300 cm^{-1} , in the range expected for Cr-N vibrations, shows a slightly

more pronounced pressure-induced response than the other two (Supporting Information, Figures S8 – S10). This possibly reflects some influence of pressure on the Cr-N bond lengths and/or N-Cr-N angles, although none of the observed shifts are particularly remarkable.^[50] Consequently, geometry changes of $[\text{Cr}(\text{ddpd})_2][\text{BF}_4]_3$ and $[\text{Cr}(\text{H}_2\text{tpda})_2][\text{ClO}_4]_3$ under pressure are likely not very pronounced, yet even small geometric changes might influence the doublet excited state energies differently.

Table 1. Ambient pressure luminescence energies of the ${}^2\text{E}$, ${}^2\text{T}_1 \rightarrow {}^4\text{A}_2$ transitions, and their pressure induced shifts.

	emissive state	$E_{\text{max}} / \text{cm}^{-1}$ (ambient pressure)	$\Delta E_{\text{max}} \Delta p^{-1} / \text{cm}^{-1} \text{ kbar}^{-1}$
$[\text{Cr}(\text{ddpd})_2][\text{BF}_4]_3$	${}^2\text{E}$	12811	-14.1 ± 0.5
(crystalline state)	${}^2\text{T}_1$	13492	-7.7 ± 0.4
$[\text{Cr}(\text{ddpd})_2][\text{BF}_4]_3$	${}^2\text{E}$	12876	-14.8 ± 0.5
(H_2O solution)	${}^2\text{T}_1$	13556	-9.5 ± 0.4
$[\text{Cr}(\text{ddpd})_2][\text{BF}_4]_3$	${}^2\text{E}$	12872	-14.5 ± 0.5
(MeOH solution)	${}^2\text{T}_1$	13554	-9.8 ± 0.4
$[\text{Cr}(\text{ddpd})_2][\text{PF}_6]_3$	${}^2\text{E}$	12827	-13.0 ± 0.4
(crystalline state)	${}^2\text{T}_1$	13511	-4.7 ± 0.5
$[\text{Cr}(\text{H}_2\text{tpda})_2][\text{ClO}_4]_3$	${}^2\text{E}$	12743	-13.0 ± 0.6
(crystalline state)	${}^2\text{T}_1$	13503	-8.4 ± 0.6

Ligand field calculations were employed to better understand the different effects of pressure on the ${}^2\text{E}$ and ${}^2\text{T}_1$ energy levels. The Tanabe-Sugano diagram of the d^3 electron configuration shows a nearly constant energy gap between the ${}^2\text{E}$ and ${}^2\text{T}_1$ states as the ligand field splitting Δ_o increases, suggesting that Δ_o is not responsible for the observed shifts. Ligand field calculations using standard Δ_o and Racah B and C parameters reproduce the energies of the ${}^2\text{E}$ and ${}^2\text{T}_1$ transitions at ambient pressure. However, neither variation of B or C (nor of Δ_o of course) reproduces the experimentally observed shift difference (Figure 2; Supporting Information, Figure S11). Further calculations were carried out using the Angular Overlap Model parameterization where Δ_o is replaced by e_σ and e_π (Supporting Information, Figure S11).^[51,52] Again, no reasonable parameter variation reproduces the increasing energy difference between the spin-flip bands.

As the crystal structure analysis of $[\text{Cr}(\text{ddpd})_2][\text{BF}_4]_3$ shows that the coordination site of the chromium ion is slightly distorted with *cis*-N-Cr-N angles deviating from the ideal octahedral angle (90°) by up to six degrees,^[12] additional ligand field calculations were carried out at the experimental geometry of the cation of $[\text{Cr}(\text{ddpd})_2][\text{BF}_4]_3$. Again, each parameter was varied individually (Supporting Information, Figure S12), yet the results are very similar to the results at perfect octahedral geometry.

Finally, calculations with structures varying from perfect octahedral to the exact experimental structure (at ambient pressure) but with constant ligand field parameters were conducted (Supporting Information, Figure S13). Importantly, this last set of calculations shows that the ${}^2\text{E}$ and ${}^2\text{T}_1$ energies strongly depend on the variation of N-Cr-N angles. Indeed, the difference of the doublet state energies increases as the geometry distorts (Supporting Information, Figure S13, Table S2). Consequently, the effects of structure perturbation induced by pressure likely dominate over any effects arising from ligand field parameter variations with pressure in the molecular rubies.

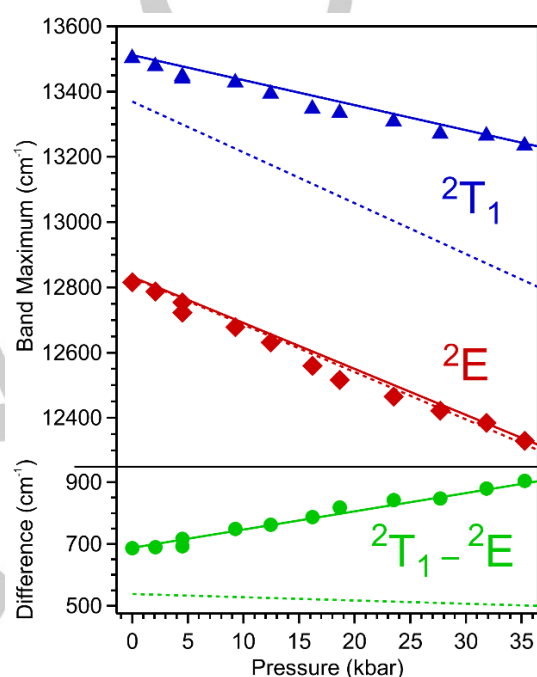


Figure 2. Luminescence maxima of solid $[\text{Cr}(\text{ddpd})_2][\text{BF}_4]_3$ versus pressure. The experimental points are symbols (diamonds for ${}^2\text{E}$, triangles for ${}^2\text{T}_1$), fits to determine slopes given in Table 1 are shown as solid lines, and results of ligand field calculations are depicted as dashed lines. The ligand field calculations were fit to the ${}^2\text{E}$ energies, with the resulting ${}^2\text{T}_1$ energies from the same parameters also shown. Differences between the ${}^2\text{E}$ and ${}^2\text{T}_1$ states are shown in the bottom panel (green), with symbols for the experimental differences, fit with a solid line, and a dashed line to show the ligand field calculated differences.

CASSCF(7,12) calculations combined with N-electron valence state perturbation theory (NEVPT2) to account for dynamic electron correlation on the CPCM(MeOH)-RI-B3LYP-D3BJ-ZORA/def2-TZVPP^[53] optimized geometry of $[\text{Cr}(\text{ddpd})_2]^{3+}$ correctly place the relevant doublet states below the lowest-lying quartet state (Supporting Information, Figure S14). In the optimized geometry, the degeneracies of the ${}^2\text{E}$ and ${}^2\text{T}_1$ states are lifted, as expected from the non-perfect octahedral geometry. The spread of these states is 1143 cm^{-1} , which compares well with the spread of the same doublet states calculated by ligand field theory (1280 cm^{-1}). The energy difference between the two lowest calculated excited states is 584 cm^{-1} , close to the

difference between the experimentally observed bands of 681 cm^{-1} (at ambient pressure). Orbital occupancies and hence the interelectronic repulsion differ for the different doublet states and unequal effects along the molecular axes could contribute to the individual pressure-dependences of the observed doublet state energies.

In summary, the high quantum yield of the spin-flip luminescence from $[\text{Cr}(\text{ddpd})_2]^{3+}$ and $[\text{Cr}(\text{H}_2\text{tpda})_2]^{3+}$ ions in various environments and the strong pressure-induced linear shifts of up to $-14.8\text{ cm}^{-1}\text{ kbar}^{-1}$ enable pressure-sensing with unprecedented sensitivity in the crystalline state and as a unique asset in solution as well. The simple preparation, the cheap starting materials, the high shelf stability^[12] and the good availability of chromium (compared to for instance critical raw materials such as iridium or europium) combined with the high quantum yield and strong pressure dependence should enable a widespread application of these materials in pressure sensing, possibly substituting the standard calibrant ruby itself.

The two spin-flip emission bands of $[\text{Cr}(\text{ddpd})_2]^{3+}$ and $[\text{Cr}(\text{H}_2\text{tpda})_2]^{3+}$ shift to lower energy with increasing pressure, but with different slopes. According to ligand field analyses of the slopes, (angular) structural distortions likely play a more decisive role than variations of interelectronic repulsion parameters. These so far unique examples of strong pressure-induced redshifts of spin-flip luminescence bands illustrate the high potential of first row transition metal complexes for a plethora of applications, which are not straightforwardly achieved by conventional luminescent complexes with charge transfer excited states, such as $[\text{Ru}(\text{bpy})_3]^{2+}$ or $\text{Ir}(\text{ppy})_3$ (bpy = 2,2'-bipyridine, ppy = anion of 2-phenylpyridine).

Acknowledgements

This work was supported by the Deutsche Forschungsgemeinschaft (GSC 266, Materials Science in Mainz and HE 2778/10-1), the internal university research funds of the Johannes Gutenberg University, Mainz (Germany) and the Natural Sciences and Engineering Research Council (Canada). Parts of this research were conducted using the supercomputer Mogon and advisory services offered by the Johannes Gutenberg University Mainz (www.hpc.uni-mainz.de), which is a member of the AHRP and the Gauss Alliance e.V. The authors thank Pierre-Olivier Roy for help with the ligand field calculations.

Conflict of interest

The authors declare no conflict of interest. S. O. and J. H. contributed equally to the work.

Keywords: chromium • excited states • luminescence • pressure • spin-flip

[1] N. A. P. Kane-Maguire, in *Photochemistry and Photophysics of Coordination Compounds I*, Balzani, V.; Campagna, S., Eds. Springer Berlin Heidelberg: Berlin, Heidelberg, 2007, pp. 37–67.

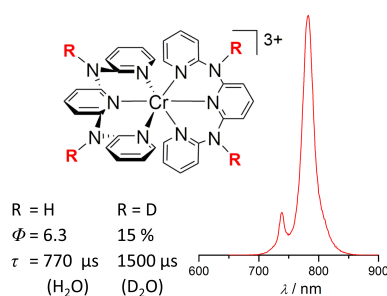
- [2] D. A. Friesen, S. H. Lee, J. Lilie, W. L. Waltz, L. Vincze, *Inorg. Chem.* **1991**, *30*, 1975–1980.
- [3] P. Pichon, A. Barbet, J.-P. Blanchot, F. Druon, F. Balembos, P. Georges, *Opt. Lett.* **2017**, *42*, 4191–4194.
- [4] Z. Fang, D. Sun, J. Luo, H. Zhang, X. Zhao, C. Quan, M. Cheng, Q. Zhang, S. Yin, *SPIE* **2017**; p. 6.
- [5] G. Boulon, *Optical Materials* **2012**, *34*, 499–512.
- [6] H. Xiang, J. Cheng, X. Ma, X. Zhou, J. J. Chruma, *Chem. Soc. Rev.* **2013**, *42*, 6128–6185.
- [7] T. H. Maiman, *Nature* **1960**, *187*, 493–494.
- [8] S. M. Stevenson, M. P. Shores, E. M. Ferreira, *Angew. Chem.* **2015**, *127*, 6606–6610; *Angew. Chem. Int. Ed.* **2015**, *54*, 6506–6510.
- [9] R. F. Higgins, S. M. Fatur, S. G. Shepard, S. M. Stevenson, D. J. Boston, E. M. Ferreira, N. H. Damrauer, A. K. Rappé, M. P. Shores, *J. Am. Chem. Soc.* **2016**, *138*, 5451–5464.
- [10] S. M. Stevenson, R. F. Higgins, M. P. Shores, E. M. Ferreira, *Chem. Sci.* **2017**, *8*, 654–660.
- [11] F. J. Sarabia, E. M. Ferreira, *Org. Lett.* **2017**, *19*, 2865–2868.
- [12] S. Otto, M. Grabolle, C. Förster, C. Kreitner, U. Resch-Genger, K. Heinze, *Angew. Chem.* **2015**, *127*, 11735–11739; *Angew. Chem. Int. Ed.* **2015**, *54*, 11572–11576.
- [13] C. Wang, S. Otto, M. Dorn, E. Kreidt, J. Lebon, L. Sršan, P. Di Martino-Fumo, M. Gerhards, U. Resch-Genger, M. Seitz, K. Heinze, *Angew. Chem.* **2018**, *130*, 1125–1130; *Angew. Chem. Int. Ed.* **2017**, *57*, 1112–1116.
- [14] S. Otto, A. M. Nauth Alexander, E. Ermilov, N. Scholz, A. Friedrich, U. Resch-Genger, S. Lochbrunner, T. Opatz, K. Heinze, *ChemPhotoChem* **2017**, *1*, 344–349.
- [15] S. Otto, N. Scholz, T. Behnke, U. Resch-Genger, K. Heinze, *Chem. Eur. J.* **2017**, *23*, 12131–12135.
- [16] S. Otto, M. Dorn, C. Förster, M. Bauer, M. Seitz, K. Heinze, *Coord. Chem. Rev.* **2018**, *359*, 102–111.
- [17] a) I. J. Stich Matthias, S. Nagl, S. O. Wolfbeis, U. Henne, M. Schäferling, *Adv. Funct. Mater.* **2008**, *18*, 1399–1406; b) M. Schäferling, *Angew. Chem.* **2012**, *124*, 3590–3614; *Angew. Chem. Int. Ed.* **2012**, *51*, 3532–3554.
- [18] G. J. Piermarini, S. Block, J. D. Barnett, R. A. Forman, *J. Appl. Phys.* **1975**, *46*, 2774–2780.
- [19] H. K. Mao, P. M. Bell, J. W. Shaner, D. J. Steinberg, *J. Appl. Phys.* **1978**, *49*, 3276–3283.
- [20] R. G. Munro, G. J. Piermarini, S. Block, W. B. Holzapfel, *J. Appl. Phys.* **1985**, *57*, 165–169.
- [21] A. Chopelas, N. Malcolm, *J. Geophys. Res.* **1982**, *87*, 8591–8597.
- [22] T. Kottke, F. Williams, *Phys. Rev. B* **1983**, *28*, 1923–1927.
- [23] J. Liu, R. Tang, Y. Wang, W. Jia, Y. Shang, S. He, *J. Lumin.* **1988**, *40–41*, 419–420.
- [24] A. H. Jahren, M. B. Kruger, R. Jeanloz, *J. Appl. Phys.* **1992**, *71*, 1579–1582.
- [25] A. G. Rinzler, J. F. Dolan, L. A. Kappers, D. S. Hamilton, R. H. Bartram, *J. Phys. Chem. Solids* **1993**, *54*, 89–100.
- [26] D. Galanciak, P. Perlin, M. Grinberg, A. Suchocki, *J. Lumin.* **1994**, *60–61*, 223–226.
- [27] P. R. Wamsley, K. L. Bray, *J. Lumin.* **1994**, *59*, 11–17.
- [28] Y. R. Shen, K. L. Bray, *Phys. Rev. B* **1997**, *56*, 10882–10891.
- [29] U. Hömmerich, K. L. Bray, *Phys. Rev. B* **1995**, *51*, 12133–12141.
- [30] G. Quérel, B. Reynard, *Chem. Geol.* **1996**, *128*, 65–75.
- [31] M. Grinberg, J. Barzowska, Y. R. Shen, K. L. Bray, B. V. Padlyak, P. P. Buchynskii, *Phys. Rev. B* **2002**, *65*, 064203.
- [32] M. Grinberg, J. Barzowska, Y. R. Shen, K. L. Bray, P. Dereñ, J. Hanuza, *J. Lumin.* **2003**, *102–103*, 699–704.
- [33] M. A. Sánchez-Alejo, F. Rodríguez, J. A. Barreda-Argüeso, I. Camarillo, J. C. Flores, S. H. Murrieta, A. J. M. Hernández, F. Jaque, E. Camarillo, *Opt. Mater.* **2016**, *60*, 94–100.
- [34] E. O'Bannon III, Q. Williams, *Am. Min.* **2016**, *101*, 1406–1413.

- [35] J. W. Kenney III, J. W. Clymire, S. F. Agnew, *J. Am. Chem. Soc.* **1995**, *117*, 1645–1646.
- [36] O. S. Wenger, R. Valiente, H. U. Güdel, *J. Chem. Phys.* **2001**, *115*, 3819–3826.
- [37] M. Milos, P. Pal, A. Hauser, *ChemPhysChem* **2010**, *11*, 3161–3166.
- [38] K. L. Bray, in *Transition Metal and Rare Earth Compounds: Excited States, Transitions, Interactions I*, Yersin, H., Ed. Springer Berlin Heidelberg: Berlin, Heidelberg, **2001**, pp. 1–94.
- [39] R. A. Forman, G. J. Piermarini, J. D. Barnett, S. Block, *Science* **1972**, *176*, 284.
- [40] H. Yersin, P. Huber, G. Gietl, D. Trümbach, *Chem. Phys. Lett.* **1992**, *199*, 1–9.
- [41] S. Otto, C. Förster, C. Wang, U. Resch-Genger, K. Heinze, submitted.
- [42] A. Rodrigue-Witchel, D. L. Rochester, S.-B. Zhao, K. B. Lavelle, J. A. G. Williams, S. Wang, W. B. Connick, C. Reber, *Polyhedron* **2016**, *108*, 151–155.
- [43] A. N. Dunaeva, D. V. Antsyshkin, O. L. Kuskov, *Sol. Sys. Res.* **2010**, *44*, 202–222.
- [44] M. V. Kondrin, A. A. Pronin, Y. B. Lebed, V. V. Brazhkin, *J. Chem. Phys.* **2013**, *139*, 084510.
- [45] Y. R. Shen, T. Gregorian, W. B. Holzapfel, *High Press. Res.* **1991**, *7*, 73–75.
- [46] F. Datchi, A. Dewaele, P. Loubeyre, R. Letoullec, Y. Le Godec, B. Canny, *High Press. Res.* **2007**, *27*, 447–463.
- [47] Q. Jing, Q. Wu, L. Liu, J.-a. Xu, Y. Bi, Y. Liu, H. Chen, S. Liu, Y. Zhang, L. Xiong, Y. Li, J. Liu, *J. Appl. Phys.* **2013**, *113*, 023507.
- [48] C. Zhao, H. Li, Y. Wang, J. Jiang, Y. He, *High Press. Res.* **2017**, *37*, 18–27.
- [49] H. Riesen, H.-U. Güdel, *J. Chem. Phys.* **1987**, *87*, 3166–3172.
- [50] J. R. Ferraro, *Vibrational Spectroscopy at High External Pressures*, Academic Press: **1984**, pp. 120–162.
- [51] C. E. Schäffer, C. K. Jørgensen, *Mol. Phys.* **1965**, *9*, 401–412.
- [52] R. G. Woolley, *Mol. Phys.* **1981**, *42*, 703–720.
- [53] F. Neese, *WIREs Comput. Mol. Sci.* **2012**, *2*, 73–78.
- [54] A. Breivogel, C. Förster, K. Heinze, *Inorg. Chem.* **2010**, *49*, 7052–7056.
- [55] K.-Y. Ho, W.-Y. Yu, K.-K. Cheung, C.-M. Che, *J. Chem. Soc., Dalton Trans.* **1999**, 1581–1586.

3.6 A strongly luminescent chromium(III) complex acid

Sven Otto, Cristoph Förster, Cui Wang, Ute Resch-Genger and Katja Heinze

Submitted to *Chemistry a European Journal*, 2018.



The amine protons of the tridentate strong-field ligand H₂tpda (2,6-bis(2-pyridylamino)pyridine) acidify considerably upon complexation to Cr^{III} ions, resulting in acidochromic behaviour and in an easy route to ligand NH-deuteration, which more than doubles the already strong NIR luminescence quantum yield of the chromium(III) complex to 15 % and doubles the luminescence lifetime to 1500 μs in water at room temperature.

Author Contributions

Sven Otto synthesized and characterized the chromium complexes presented in this manuscript, carried out the electrochemical, UV-VIS and emission spectroscopic experiments and performed the DFT calculations as well. Cui Wang and Ute Resch-Genger determined the emission quantum yields and excited state lifetimes at the *Bundesanstalt für Materialforschung und -prüfung* in Berlin, Germany. The crystal structure was solved and refined by Christoph Förster. The manuscript was written by Sven Otto (90%) and Katja Heinze (10%).

Supporting Information

for this article is found at pp. 226.

A strongly luminescent chromium(III) complex acid

Sven Otto,^[a,b] Christoph Förster,^[a] Cui Wang,^[c,d] Ute Resch-Genger^{*[c]} and Katja Heinze^{*[a]}

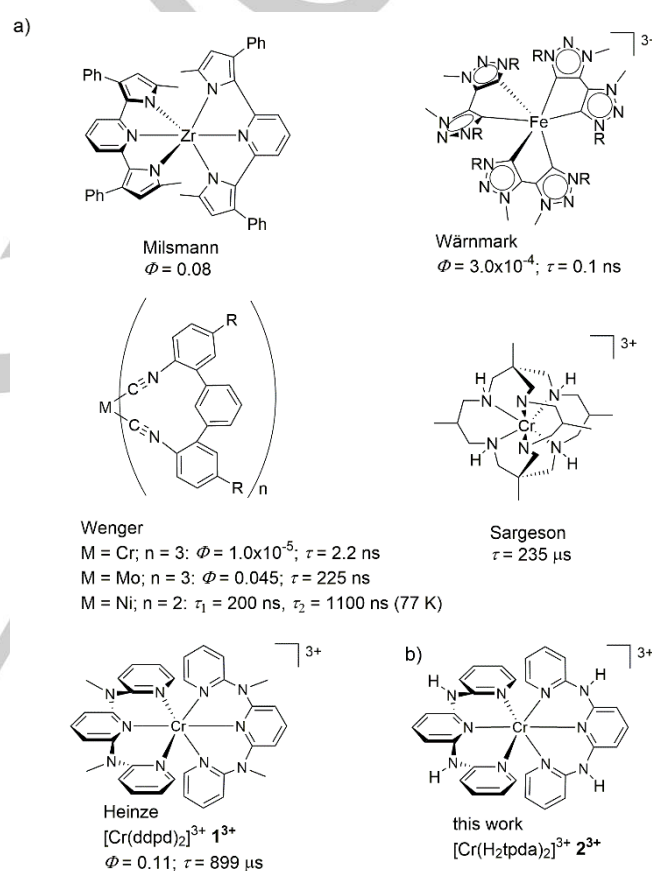
Dedicated to Prof. Dietmar Stalke on the occasion of his 60th birthday.

Abstract: The synthesis, structural and photophysical properties of a novel chromium(III) complex bearing the tridentate H₂tpda (2,6-bis(2-pyridylamino)pyridine) ligand is presented. Structural investigations have been carried out by single crystal X-ray diffractometry, IR spectroscopy and Density Functional Theory calculations. Complexation with Cr³⁺ resulted in acidification of the ligands NH protons (pK_a = 8.8). Acidochromic behavior of the highly NIR emissive complex was observed by UV-VIS and emission spectroscopy in the pH = 4.9 – 9.9 range. This also allowed for a straightforward access of a complex with partially deuterated ligands exhibiting luminescence quantum yields up to 15 % at room temperature in D₂O.

Introduction

Although it is very challenging to design photoactive complexes with earth abundant metal ions, it is currently a very active and rapidly growing field of research. This is rooted in the ultimate aim to replace expensive noble and rare earth metal ions with earth abundant metals for applications such as photosensitizing, photoluminescence or photoredox reactions.^[1,2] Apart from copper(I) complexes,^[2] only a small number of highly luminescent complexes of earth abundant metal ions exists. Most of them have only been introduced into the field very recently. Even more difficult to achieve is emission in the near infra-red (NIR), which, for most applications, is done by using lanthanide ions,^[3] since strong NIR emission of noble metal ions is very difficult to achieve.^[4] There are also some rare cases of mononuclear copper(I) complexes showing NIR emission.^[2a] Emissive 3d metal complexes with dⁿ electron configuration (n < 10) only emerged in the last years, comprising ligand-to-metal charge transfer (LMCT), metal-to-ligand charge transfer (MLCT) and spin-flip emitters.^[4-9]

An emissive zirconium(IV) complex with 2,6-bis(pyrrrolyl)pyridine ligands has been reported by Milsmann and coworkers.^[5] Wärnmark introduced the first example of a luminescent iron(III) complex showing LMCT emission.^[6] The d⁶ isocyanide chelate complexes of Wenger also show luminescence in solution (Scheme 1).^[7]



Scheme 1. a) Luminescent complexes with earth abundant metal ions (dⁿ electron configuration; n < 10, at room temperature, in solution if not indicated otherwise) b) target complex 2³⁺.

Chromium(III) complexes have been known to show NIR phosphorescence for quite some time, but the quantum yields of previously known complexes are generally very low and thus considered unsuitable for applications.^[8] A reason for the low emission quantum yield is a small ligand field splitting allowing back inter system crossing (back ISC) to the ⁴T₂ state and subsequent non-radiative deactivation to the ground state. But even though the strong field ligand 2,2';6',2''-terpyridine (tpy) induces a strong enough ligand field, [Cr(tpy)₂]³⁺ is only very weakly emissive ($\phi < 0.00089\%$ in H₂O)^[9], which is probably

[a] S. Otto, C. Förster, K. Heinze
Institute of Inorganic Chemistry and Analytical Chemistry
Johannes Gutenberg University of Mainz
Duesbergweg 10-14, 55128 Mainz, Germany
E-mail: katja.heinze@uni-mainz.de
www.ak-heinze.chemie.uni-mainz.de

[b] S. Otto
Graduate School Materials Science in Mainz
Staudingerweg 9, 55128 Mainz, Germany

[c] C. Wang, U. Resch-Genger
Division 1.10 Biophotonics
Federal Institute for Materials Research and Testing (BAM)
Richard Willstätter-Strasse 11, 12489 Berlin, Germany
E-mail: ute.resch@bam.de
www.bam.de/

[d] C. Wang
Institut für Chemie und Biochemie, Freie Universität Berlin
14195 Berlin (Germany)

Supporting information for this article is given via a link at the end of the document.

FULL PAPER

caused by surface crossing due to distortions. While substituted tpy ligands can improve the emissions' brightness, it is mainly due to increasing of the absorption by ILCT transitions than an increase of the quantum yield.^[10] Sargeson showed that hindering this distortion in the cage complex $[\text{Cr}(\text{fac-Me}_5\text{-D}_3\text{tricosaneN}_6)]^{3+}$ (Scheme 1) improved the excited state lifetime considerably as compared to other Cr^{III} cage complexes.^[11]

We recently introduced the chromium(III) complex $[\text{Cr}(\text{ddpd})_2]^{3+}$ (**1³⁺**)^[12] based on the tridentate strong field ligand *N,N'*-dimethyl-*N,N'*-dipyridine-2-ylpyridine-2,6-diamine (ddpd) (scheme 1).^[13] The "molecular ruby" **1³⁺** features two very sharp emission bands arising from metal centered spin-flip transitions. **1³⁺** shows an unprecedented quantum yield of $\Phi = 11\%$ and a luminescence lifetime of $\tau = 898\ \mu\text{s}$ in H_2O at room temperature.

First applications of the "molecular ruby", such as optical temperature sensing with a single dye^[14] and selective energy transfer/singlet oxygen formation,^[15] have already been realized and further applications are envisioned.^[16]

Very recently a deuteration study on the "molecular ruby" revealed that deuteration of the ligand at different positions shifted the energy of the associated high energy C-H oscillators, and thus inhibited the energy transfer to these overtones. This resulted in increased quantum yields up to a record value of $\Phi = 30\%$ and luminescence lifetimes of $\tau = 2300\ \mu\text{s}$ in D_2O , when the C-H oscillator closest to the metal ion (Cr-H/D distance 3.0 Å) was exchanged.^[17]

A straightforward variation of the ddpd ligand is the removal of the amines' methyl groups, resulting in the literature known 2,6-bis(2-pyridylamino)pyridine (H_2tpda) ligand,^[18] known to form polynuclear linear chain complexes with chromium(II) and other transition metal ions (e.g.: Ni^{2+} , Co^{2+} , Cu^{2+} , Ru^{2+} and Rh^{2+}) in its deprotonated state (tpda^{2-}).^[19]

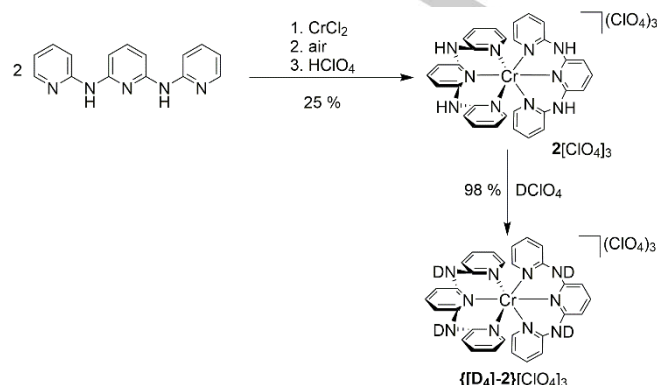
The mononuclear chromium(III) complex $[\text{Cr}(\text{H}_2\text{tpda})_2]^{3+}$ (**2³⁺**) envisioned with this ligand should possess the same favorable coordination geometry as **1³⁺** and thus also be highly NIR-emissive.

The ligand's amine protons should become acidic upon complexation with the charged Cr^{3+} ion, as is the case in the corresponding iron complexes.^[13f] The potential acidochromic behavior could be exploited for utilization as an optical pH probe. This complex also provides a convenient route to a N-deuterated complex (**[D₄]-2³⁺**) to study the impact of the NH oscillator on the luminescence quantum yield and lifetime.

Results and Discussion

Synthesis and geometrical structure. In this study, we describe the synthesis and properties of a new Cr^{3+} complex with the tridentate H_2tpda ligand (Scheme 2) and the deuteration of the ligand's NH positions. The complex was prepared by treating a deaerated solution of H_2tpda in methanol with CrCl_2 , adding perchloric acid after exposing the solution to air and precipitating the product complex $2[\text{Cr}(\text{O}_4)_3]$ by adding diethyl ether. Complex formation was confirmed by ESI⁺ mass spectrometry (Supporting Information, Figure S1) and elemental analysis.

The deuterated complex was obtained by treating $2[\text{Cr}(\text{O}_4)_3]$ with DClO_4 in CH_3OD .



Scheme 2. Synthesis of $2[\text{Cr}(\text{O}_4)_3]$ and $\{[\text{D}_4]\text{-}2\}[\text{Cr}(\text{O}_4)_3]$.

While ESI⁺ mass spectrometry showed signals of fully and partially deuterated complexes, as expected, due to the high presence of protons in the ESI mass spectrometer (Supporting Information, Figure S2), successful deuteration was confirmed by IR spectroscopy, which revealed the absence of NH stretching vibrations at 3568 and 3424 cm^{-1} in the deuterated compound **[D₄]-2³⁺**. The corresponding ND vibrations are shifted to lower energy as expected (2389 and 2323 cm^{-1} ; Figure 1, Supporting Information Figures S3 and S4). The ratio of ND/NH oscillator energies amount to 0.67 and 0.68 respectively, harmonic approximation predicts a ratio of $1/\sqrt{2} = 0.73$. Numerical frequency calculations on the DFT optimized structures of **2³⁺** and **3³⁺** (CPCM(CH_3OH)-RIJCOSX-B3LYP-D3BJ-ZORA/def2-TZVPP, vibrational energies scaled with 0.9614^[20]) place the NH and ND vibrations at 3454 and 2538 cm^{-1} respectively (ratio = 0.73, Supporting Information, Figures S4, S5, S6 and S7, Table S6). The fact, that the energies obtained from DFT calculations are more than 100 cm^{-1} lower than the experimental values can be ascribed to the fact, that the calculations didn't take explicit counter ions into account, while the protons have short contacts to the perchlorate anions in the solid state (vide infra).

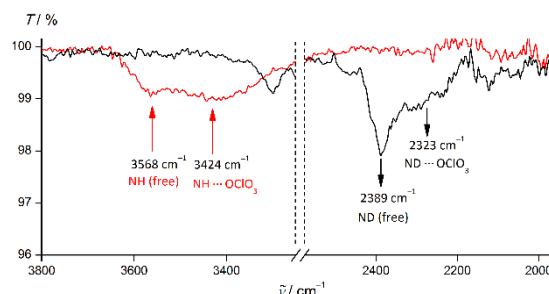


Figure 1. ATR infrared spectra of solid $2[\text{Cr}(\text{O}_4)_3]$ (red line) and $3[\text{Cr}(\text{O}_4)_3]$ (black line) (see Supporting Information, Figure S3 for full spectra).

Diffusion of diethyl ether into a concentrated solution of $2[\text{Cr}(\text{H}_2\text{tpda})_2](\text{ClO}_4)_3$ in acetonitrile yielded orange colored single crystals suitable for crystal structure determination by X-ray diffraction (Figure 2a). $2[\text{Cr}(\text{H}_2\text{tpda})_2](\text{ClO}_4)_3$ crystallizes with one (disordered) acetonitrile molecule as $[\text{Cr}(\text{H}_2\text{tpda})_2](\text{ClO}_4)_3 \times \text{CH}_3\text{CN}$ in the monoclinic space group $P2_1/c$.

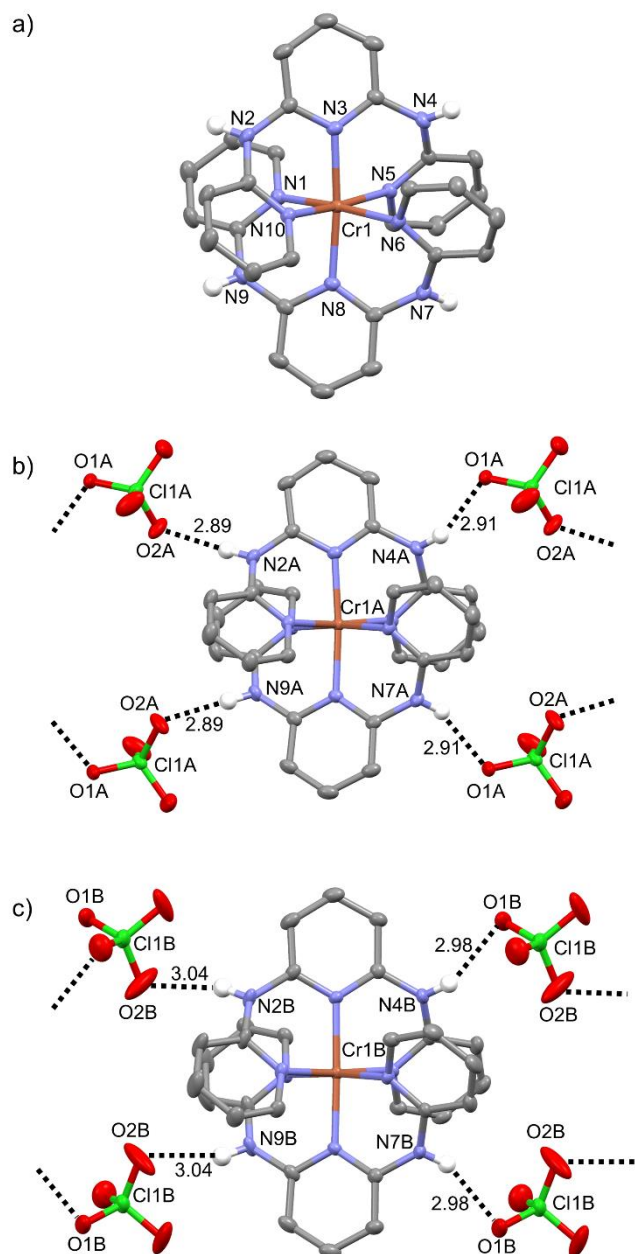


Figure 2. a) Molecular structure of the cation of $[\text{Cr}(\text{H}_2\text{tpda})_2](\text{ClO}_4)_3 \times \text{CH}_3\text{CN}$ in the crystal, b) hydrogen bonding of four perchlorate counter ions to the NH protons of $2\mathbf{A}^{3+}$ and c) hydrogen bonding of four perchlorate counter ions to the NH protons of $2\mathbf{B}^{3+}$ (thermal ellipsoids set at 50 % probability, N-O distances in Å, H atoms except NH protons omitted for clarity, atom numbering differs from deposited data for clarity).

The unit cell contains two independent complex cations ($2\mathbf{A}^{3+}$ and $2\mathbf{B}^{3+}$) with basically identical coordination geometry. The meridional CrN_6 coordination geometry of $2\mathbf{A}^{3+}$ corresponds to a slightly compressed octahedron with four longer Cr-N distances to the terminal pyridine rings (Cr1A-N1A 2.044(2) Å, Cr1A-N5A 2.040(2) Å) and two shorter ones to the central pyridine rings (Cr1A-N3A 2.037(2) Å) of the H_2tpda ligand (Figure 2a, Table 1). The intraligand N1A-Cr1A-N2A and N1A-Cr1A-N3A angles amount to 86.94(9)° and 173.52(9)°, respectively. Comparison with low spin d^6 $[\text{Fe}(\text{H}_2\text{tpda})_2]\text{Cl}_2 \times 2\text{CH}_3\text{OH}$,^[13f,21] reveals a similar situation concerning the relative Fe-N bond length but the local FeN_6 geometry is closer to an octahedron with an intraligand bite angle of 178.54°.^[21]

Similar to the corresponding iron(II) complex $[\text{Fe}(\text{H}_2\text{tpda})_2]\text{Cl}_2 \times 2\text{CH}_3\text{OH}$,^[13f,21] the crystal packing in $[\text{Cr}(\text{H}_2\text{tpda})_2](\text{ClO}_4)_3 \times \text{CH}_3\text{CN}$ is dominated by hydrogen bonding of the counter ions to the amine protons of the complex (Figure 2b and 2c). $2\mathbf{A}^{3+}$ possess four hydrogen bonds (N-O distances 2.892(3) and 2.908(3) Å), one to each N-H proton. In this way connected counterions are pairwise identical and possess a second short contact to a neighboring complex cation $2\mathbf{A}^{3+}$ resulting in a linear linked structure (Figure 2b). The situation regarding $2\mathbf{B}^{3+}$ is similar, with slightly longer N-O contacts (2.982(3) and 3.036(4) Å) (Figure 2c) resulting in alternating parallel linear chains of the different cations (Supporting Information, Figure S8).

Table 1. Selected bond distances (Å) and angles (°) of $2\mathbf{A}^{3+}$, $2\mathbf{B}^{3+}$ (as BF_4^- salt)^[12] and $[\mathbf{2-H}]^{2+}$ in the different crystalline environments and obtained from DFT calculations.

	$2\mathbf{A}^{3+}$	$2\mathbf{B}^{3+}$	$2\mathbf{A}^{3+}$ (DFT)	$1\mathbf{A}^{3+}$ [12]	$[\mathbf{2-H}]^{2+}$ (DFT)
Cr1-N1	2.044(2)	2.038(2)	2.059	2.049(2)	2.070
Cr1-N3	2.037(2)	2.037(2)	2.054	2.039(2)	2.073
Cr1-N5	2.040(2)	2.040(2)	2.059	2.039(2)	2.062
Cr1-N6	2.044(2)	2.038(2)	2.059	2.047(2)	2.080
Cr1-N8	2.037(2)	2.037(2)	2.054	2.044(2)	2.028
Cr1-N10	2.040(2)	2.040(2)	2.059	2.049(2)	2.022
N1-Cr1-N3	86.94(9)	88.20(10)	88.07	85.13(8)	87.87
N1-Cr1-N5	173.52(9)	176.07(10)	176.20	171.86(8)	175.83
N6-Cr1-N8	86.94(9)	88.20(10)	88.07	85.89(8)	88.63
N6-Cr1-N10	173.52(9)	176.07(10)	176.20	170.88(7)	177.26
N2-O2	2.892(3)	2.982(3)	-	-	-
N4-O1	2.908(3)	3.036(4)	-	-	-
N7-O1	2.908(3)	3.036(4)	-	-	-
N9-O2	2.892(3)	2.982(3)	-	-	-

FULL PAPER

Comparison with the solid-state structure of $1[\text{BF}_4]_3$ shows, that the local CrN_6 geometry in 2^{3+} is closer to an ideal octahedron and thus 2^{3+} should benefit from the same large ligand field stabilisation as 1^{3+} does.

Density Functional Theory (CPCM(CH_3OH)-RIJCOSX-B3LYP-D3BJ-ZORA/def2-TZVPP) calculations of 2^{3+} reproduce the bond distances and angles and reasonably well (Table 1, Supporting Information, Figure S5).

Optical properties. The absorption spectra of $2[\text{ClO}_4]_3$ in H_2O or CH_3CN (both containing 0.1 M HClO_4 (10.9 μl aqueous HClO_4 (60 %) per ml solvent) to prevent deprotonation) show maxima at 307, 358 (sh), and 442 nm (Figure 4, Supporting Information, Figure S11), which can be assigned to $\pi\pi^*$, ligand-to-metal charge transfer (LMCT) and mixed metal-centered (MC)/LMCT excitations according to time-dependent DFT calculations (Supporting Information, Table S8). The low energy absorption is ascribed to the metal centered $^4\text{A}_2 \rightarrow ^4\text{T}_2$ transition and LMCT transitions, which is slightly lower in energy than in 1^{3+} (Supporting Information, Table S8).^[12]

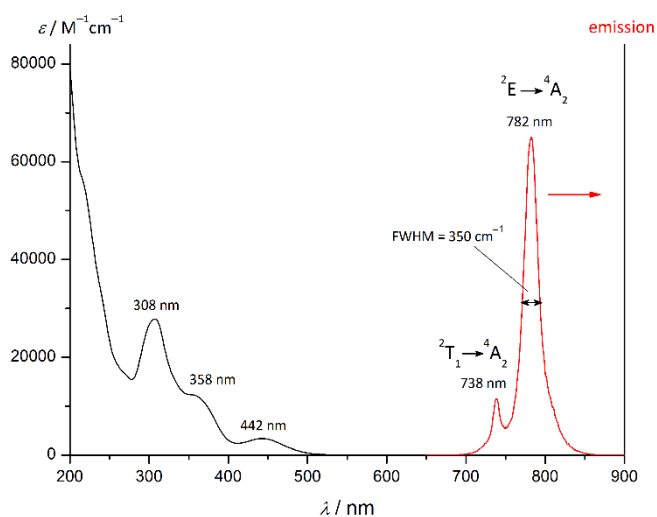
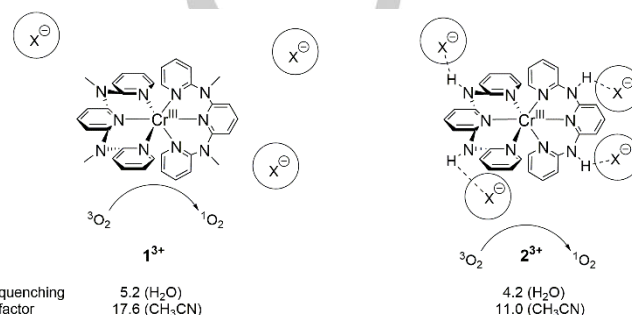


Figure 3. Absorption (black) and emission spectrum (red, $\lambda_{\text{exc}} = 442$ nm) of $2[\text{Cr}(\text{Htpda})_2(\text{OH})_3]^{3+}$ in 0.1 M aqueous perchloric acid under inert conditions.

Upon irradiation with 442 nm light, the complex, similar to 1^{3+} , exhibits two sharp phosphorescence bands in the near infrared region at 738 and 782 nm originating from the spin forbidden $^2\text{E} \rightarrow ^4\text{A}_2$ and $^2\text{T}_1 \rightarrow ^4\text{A}_2$ transitions, with the ^2E emission being slightly lower in energy than that of 1^{3+} (Figure 4, Supporting Information, Figure S9). Both bands are very sharp with a full width at half maximum height (FWHM) of 350 cm^{-1} of the main band (782 nm), which is even narrower than the corresponding emission band of the molecular ruby 1^{3+} (FWHM = 420 cm^{-1}).^[12] The absolute emission quantum yields in deaerated H_2O and CH_3CN amount to $\Phi = 6.3\%$ and 8.8% with luminescence lifetimes of $\tau = 670\ \mu\text{s}$ and $770\ \mu\text{s}$, respectively. This is slightly lower than the emission quantum yields and lifetimes of 1^{3+} , showing the quenching effect of the NH oscillators in 2^{3+} .

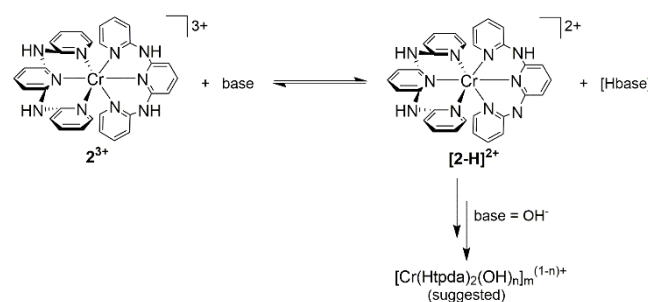
Expectedly, the phosphorescence quantum yields and lifetimes are strongly reduced by the presence of molecular oxygen similar to 1^{3+} , producing singlet oxygen.^[15] The emission quantum yield Φ of 2^{3+} is reduced by factors of 4.2 (H_2O) and 11 (CH_3CN) (factors for 1^{3+} : 5.1 (H_2O); 17.6 (CH_3CN)).^[12] Supporting Information, Tables S2 and S4).

Since 2^{3+} forms hydrogen bonds to its counter ions in the solid state (Figure 2, Supporting Information, Figure S8), it should form contact ion pairs in solution, which would block some collision pathways for $^3\text{O}_2$ and thus reduce the quenching efficiency (Scheme 3).



Scheme 4. Hydrogen bonding and suggested shielding from O_2 .

Acid-base chemistry. 1^{3+} is stable up to $\text{pH} = 11.4$ over long times, even under irradiation.^[12] Titration of an aqueous solution of $2[\text{Cr}(\text{Htpda})_2(\text{OH})_3]^{3+}$ with aqueous NaOH gradually decreases the emission band. Complete quenching is achieved at a pH above 9.5. This allowed to estimate a $\text{p}K_{\text{a}} = 8.8 \pm 0.2$ for the first deprotonation of 2^{3+} ($\text{p}K_{\text{a}} = 8.9 \pm 0.2$ according to UV-VIS spectroscopy, Figure 4), which means 2^{3+} is a stronger acid than NH_4^+ ($\text{p}K_{\text{a}} = 9.3$)^[22] in water. The absorption spectrum of the deprotonated complex $[\text{Cr}(\text{Htpda})_2(\text{OH})_n]^{(1-n)+}$ shows maxima at 309, 424 and 488 nm. During the deprotonation of 2^{3+} to $[\text{Cr}(\text{Htpda})_2(\text{OH})_n]^{(1-n)+}$ isosbestic points at 211, 242, 287, 318 and 461 nm are present (Figure 4a, Supporting Information, Figure S10).



Scheme 4. Acid-base chemistry of $2[\text{Cr}(\text{Htpda})_2(\text{OH})_3]^{3+}$.

The acidochromic behavior of 2^{3+} clearly originates from the ligands' amine protons, which acidify significantly due to the coordination to the Cr^{3+} cation and thus deprotonation leads to

$[\text{Cr}(\text{Htpda})(\text{H}_2\text{tpda})]^{2+}$ $[\mathbf{2}\text{-H}]^{2+}$. According to DFT calculations, the CrN_6 geometry in $[\mathbf{2}\text{-H}]^{2+}$ is stronger distorted from an idealized octahedron in comparison to $\mathbf{2}^{3+}$, with Cr-N bond lengths varying from 2.02 Å (to the pyridine nitrogen in direct vicinity of the deprotonated amine) to 2.08 Å (trans to the deprotonated amine; Supporting Information, Table S7). Time-dependent DFT calculations show that the low energy excitations consist of either asymmetric LMCT (charge transfer from the deprotonated ligand to the metal) or mixed asymmetric LMCT/MC transitions (Supporting Information, Table S9). This should lead to an even stronger distorted excited state (the ${}^4\text{T}_2$ state by itself is strongly Jahn-Teller distorted due to the $(t_{2g})^2(e_g)^1$ electron configuration) allowing for fast non-radiative recovery of the ground state. Further, an absorption is observed above 600 nm (Supporting Information, Figure S10), indicating a significantly lower ligand field splitting in $[\mathbf{2}\text{-H}]^{2+}$ than in $\mathbf{2}^{3+}$. This could be explained by a partial amide character of the pyridine nitrogen, conferring π -donor character to the coordinating pyridine and thus lowering the ligand field splitting. This could enable back ISC to the ${}^4\text{T}_2$ state, giving a possible explanation for the non-emissive behavior of $[\mathbf{2}\text{-H}]^{2+}$.

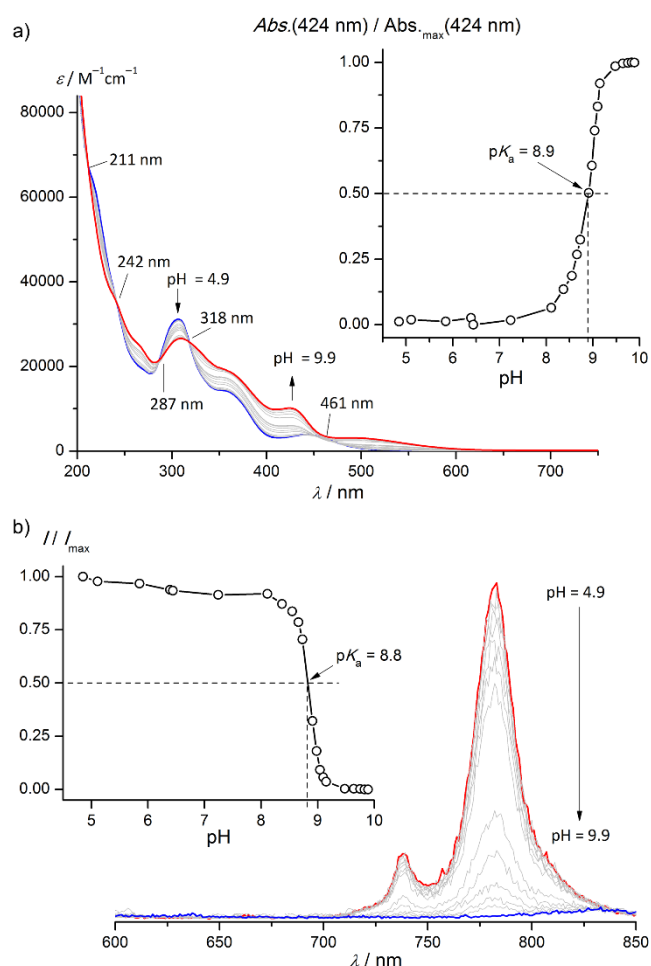


Figure 4. pH dependent a) absorption and b) emission ($\lambda_{\text{exc}} = 442$ nm) of $[\mathbf{2}][\text{CrO}_4]_3^-$ in aqueous solution.

The existence of isosbestic points in the UV/VIS during the titration with aqueous NaOH together with the fact that no emission of free ligand is observed (H_2tpda shows emission at 357 nm, $[\text{Htpda}]^-$ at 550 nm and $[\text{tpda}]^{2-}$ at 539 nm, $[\text{H}_3\text{tpda}]^+$ is non emissive, Supporting Information, Figures S11, S12, S13 and S14) suggest that the complex initially stays intact during deprotonations. However, the original emission intensity could not be fully recovered when adding perchloric acid after 30 min and after 12 h under basic conditions. Addition of acid did not recover the NIR emission as well. Also, the absorption spectrum completely changed after 12 h under basic conditions (Supporting Information, Figure S15).

Deprotonation in dry acetonitrile with $\text{P}_1\text{-}^t\text{Bu}$ (*tert*-Butylimino-tris(dimethylamino)phosphorene) also quenches the emission, but under this conditions the full emission intensity is recovered after 14 h by adding perchloric acid (Supporting Information, Figure S16). This observation suggests, that the deprotonated complex $[\mathbf{2}\text{-H}]^{2+}$ undergoes substitution reactions with hydroxide in the $\text{NaOH}_{(\text{aq})}$ experiments. However, no distinct hydroxide containing reaction product could be identified by ESI^+ mass spectroscopy. Thus, all further spectroscopic measurements were carried out in 0.1 M HClO_4 or DClO_4 solution to prevent deprotonation of the complexes.

The fact, that the ligands' amine protons acidify significantly when coordinated to the Cr^{3+} cation, allowed for a straightforward exchange of these protons with deuterium by treating the complex with deuterated perchloric acid to obtain the fully deuterated species $[\mathbf{D}_4]\text{-}\mathbf{2}^{3+}$ (Scheme 2).

Since the amine protons exchange rapidly, the emission quantum yield and lifetime of $[\mathbf{D}_4]\text{-}\mathbf{2}^{3+}$ dissolved in H_2O are identical to the ones of $\mathbf{2}^{3+}$ (Supporting Information, Tables S1 and S3) and thus the effects of ligand and solvent deuteration cannot be investigated separately. The quantum yield of $[\mathbf{D}_4]\text{-}\mathbf{2}^{3+}$ in D_2O increases by a factor of 2.5 to $\Phi = 15.0\%$ and the lifetime to $\tau = 1500$ μs , again $\mathbf{2}^{3+}$ gives basically identical values in this solvent (Supporting Information, Table S1 and S3).

In contrary to in water, in acetonitrile the deuteration of $[\mathbf{D}_4]\text{-}\mathbf{2}^{3+}$ is preserved, which gives a 1.4-fold increase in quantum yield to $\Phi = 12.0\%$ with an increase in lifetime from 770 to 1200 μs . Using CD_3CN as solvent in contrast has only minimal effect on the emission quantum yields and lifetimes of $\mathbf{2}^{3+}$ and $[\mathbf{D}_4]\text{-}\mathbf{2}^{3+}$ (Supporting Information, Tables S1 and S3). While the solvent molecules' hydrogen atoms are relatively far away from the Cr^{III} ion (approximately 6.5 Å in the solid state, according to the crystal structure of $[\mathbf{2}][\text{ClO}_4]_3 \times \text{CH}_3\text{CN}$), the Cr-H/D distances to the amines amount to 4.1 Å according to DFT calculations. This is most certainly one reason for the strong increase by exchanging the amine protons. Interestingly, the quantum yields and lifetimes of $[\mathbf{D}_4]\text{-}\mathbf{2}^{3+}$ are quite similar to the ones of $\mathbf{1}^{3+}$ ($\Phi = 14.2\%$, $\tau = 1200$ μs in D_2O ; $\Phi = 11.7\%$, $\tau = 810$ μs in CD_3CN),^[12] where this oscillator is eliminated by methylation of the amine.

Electrochemical properties. Since $\mathbf{2}^{3+}$ is acidic, cyclic and square wave voltammetry have been carried out with perchloric acid as conducting electrolyte with a glassy carbon electrode as working electrode. The solvent window extends only to approximately -0.6 V in the cathodic region before proton

reduction sets in. Consequently, the Cr^{III/II} reduction of **2**³⁺ cannot be observed (the **1**^{3+/2+} reduction occurs at -1.11 V^[12]). While no oxidation of **1**³⁺ can be observed,^[12] **2**³⁺ exhibits two overlapping irreversible oxidation waves at peak potentials of 1.020 and 1.260 V vs. ferrocene, most probably from oxidation of the ligands' amine functions with concomitant proton loss (Supporting Information, Figures S17 and S18).

Conclusions

A novel highly emissive chromium(III) complex **2**³⁺ containing the electron-rich H₂tpda ligand was prepared. The ligands' amine protons in **2**³⁺ are acidic ($pK_a = 8.8$) and the resulting acidochromic behavior of was investigated. But **2**[CrO₄]₃ is not a suitable candidate as an optical pH probe due to the reactivity towards hydroxide of the deprotonated species, as deprotonation is only reversible with non-coordinating bases (P₁-t-Bu). As such a chromophore is needed, which is stable in both protonation states and ideally changes the emission wavelength instead of experiencing quenching, a feat probably achievable by a complex with an acidic site farther away from the metal center.

The acidification of the amine protons was further exploited to obtain the quadruply deuterated complex **[D₄]-2**[CrO₄]₃, which improved the luminescence quantum yield and lifetime considerably, contrary to deuteration of the solvent. This highlights the importance of controlling high energy oscillators in the first coordination sphere for designing strongly NIR emissive complexes.

Experimental Section

General Procedures. All reagents were used as received from commercial suppliers (ABCR, Acros, Sigma Aldrich and Euriso-Top). NMR spectra were recorded on a Bruker Avance DRX 400 spectrometer at 400.31 MHz (¹H). All resonances are reported in ppm versus the solvent signal as an internal standard [dmsO-d₆ (¹H, $\delta = 2.50$ ppm)]. The ligand UV/Vis/near-IR spectra were recorded on a Varian Cary 5000 spectrometer using 1.0 cm cells (Hellma, Suprasil). Emission spectra were recorded on a Varian Cary Eclipse spectrometer. Fluorescence decays were recorded using an Edinburgh Instruments lifetime spectrometer (FLS 920) equipped with a MCP-PMT (R3809U-50, Hamamatsu) with a 330 nm ps-laserdiode (EPLD, Edinburgh Instruments) for excitation. All measurements were performed at magic angle condition (polarization 0° in the excitation and 54.7° in the emission channel). The luminescence quantum yield was determined using an Ulbricht integrating sphere (Quantaurus-QY C11347-11, Hamamatsu).^[23] Relative uncertainty is estimated to be $\pm 5\%$. ESI MS spectra were recorded on a Micromass Q-TOF-Ultima spectrometer. IR spectra were recorded on a Bruker Alpha FT-IR spectrometer with ATR unit containing a diamond crystal. Electrochemical measurements were carried out on a BioLogic SP-50 voltammetric analyzer using platinum wires as counter and working electrode and 0.01 M Ag/AgNO₃ as reference electrode. The measurements were carried out at a scan rate of 50 mV s⁻¹ for cyclic voltammetry experiments and at 10 mV s⁻¹ for square-wave voltammetry experiments using 0.1 M HClO₄ (10.9 μ l ml⁻¹ aqueous HClO₄ (60%)) as the supporting electrolyte in CH₃CN. Potentials are referenced to the ferrocene/ferrocenium couple (0.40 V vs. SCE,^[24] $E_{1/2} = 90 \pm 5$ mV under experimental conditions). Elemental analyses were performed by the microanalytical laboratory of the chemical institutes of the University of Mainz.

Crystal Structure Determinations. Diffusion of diethyl ether into a concentrated solution of **2**[CrO₄]₃ in CH₃CN (0.1 M HClO₄) yielded

diffraction quality crystals. Intensity data were collected with STOE IPDS-2T diffractometer an Oxford cooling system and corrected for absorption and other effects using Mo K α radiation ($\lambda = 0.71073$ Å) at 173(2) K. The diffraction frames were integrated using the SAINT package, and most were corrected for absorption with MULABS.^[25] The structures were solved by direct methods and refined by the full-matrix method based on F^2 using the SHELXTL software package.^[26] All non-hydrogen atoms were refined anisotropically, while the positions of all hydrogen atoms were generated with appropriate geometric constraints and allowed to ride on their respective parent carbon atoms with fixed isotropic thermal parameters. See Table S2 for crystal and structure refinement data.

CCDC 1832900 **2**[CrO₄]₃·xCH₃CN contains the supplementary crystallographic data for this paper. These data can be obtained free of charge from The Cambridge Crystallographic Data Center via a www.ccdc.cam.ac.uk/data_request/cif.

Density functional theoretical calculations on the chromium complex cations **2**³⁺, **[2-H]**²⁺ and **[D₄]-2**³⁺ were carried out using the ORCA program package (version 4.0.1).^[27] Tight convergence criteria were chosen for all calculations (Keywords TightSCF and TightOpt, convergence criteria for the SCF part: energy change 1.0×10^{-8} Eh, 1-EI. energy change 1.0×10^{-5} Eh, orbital gradient 1.0×10^{-5} , orbital rotation angle 1.0×10^{-5} , DIIS Error 5.0×10^{-7} ; for geometry optimizations: energy change: 1.0×10^{-6} Eh, max. gradient 1.0×10^{-4} Eh bohr⁻¹, RMS gradient 3.0×10^{-5} Eh bohr⁻¹, max. displacement 21.0×10^{-3} bohr, RMS displacement 6.0×10^{-4} bohr). All calculations make use of the resolution of identity (Split-RJ-J) approach for the coulomb term in combination with the chain-of-spheres approximation for the exchange term (COSX).^[28] Geometry optimization was performed using the B3LYP functional^[29] in combination with Ahlrichs' split-valence triple- ζ basis set def2-TZVPP for all atoms.^[30] The optimized geometry was confirmed to be local minima on the respective potential energy surface by subsequent numerical frequency analysis ($N_{\text{imag}} = 0$) and the resulting vibrational energies were corrected using Scott and Radoms scaling factor.^[20] TD-DFT calculations were performed at the same level of theory. The ZORA relativistic approximation was used to describe relativistic effects in all calculations.^[31] Grimme's empirical dispersion correction D3(BJ) was employed.^[32] To account for solvent effects, a conductor-like screening model (CPCM) modeling acetonitrile was used in all calculations.^[33] Explicit counterions and/or solvent molecules were neglected. Fifty vertical transitions were calculated in TD-DFT calculations.

Synthesis of H₂tpda. H₂tpda was synthesized according to a modified literature procedure.^[18] 2,6-Diaminopyridine (2.44 g, 22.3 mmol) was dried in vacuum at 40°C overnight. After adding 1,4-dioxane (100 ml) and NaOtBu (8.9 g, 92.3 mmol) the mixture was heated to reflux for 1 h. The solution was allowed to cool to r.t. and after addition of 2-bromopyridine (9.0 ml, 94.4 mmol) it was refluxed for 4.5 days. Addition of 100 ml water to the mixture at room temperature resulted in a grey precipitate, which was collected by filtration, washed with dichloromethane (3 x 25 ml) and diethyl ether (3x 25 ml) and dried under reduced pressure. Yield: 2.2 g (8.35 mmol, 37%). ¹H NMR (dmsO-d₆, 400 MHz) δ /ppm = 9.40 (2H), 8.21 (d, ³J_{HH} = 3.6 Hz, 2H), 7.84 (d, ³J_{HH} = 8.4 Hz, 2H), 7.64 (t, ³J_{HH} = 6.9 Hz, 2H), 7.51 (t, ³J_{HH} = 8.0 Hz, 1H), 7.14 (d, ³J_{HH} = 8.0 Hz), 6.85 (m, 2H).

Synthesis of [Cr(H₂tpda)₂](ClO₄)₃·2[CrO₄]₃. H₂tpda (444 mg, 1.67 mmol) was added to methanol (150 mL) and the resulting suspension was deaerated by purging it with Ar. After 40 minutes, CrCl₂ (167 mg, 1.36 mmol) was added. The deeply green colored solution was stirred at room temperature for 3 days under argon. After stirring the solution for 60 min under air, the solution was filtered over celite to give an orange colored solution. Perchloric acid (90 μ l, 60%, aq, 2.29 mmol) was added and the solution concentrated under reduced pressure until first crystals formed. The precipitation was completed by slowly adding diethyl ether. Yield: 182 mg (0.208 mmol, 25%). MS (ESI⁺): m/z (int%) = 264.13 (100) [H₂tpda+H]⁺, 576.16 (20) [Cr(H₂tpda)₂]⁺, 608.19 (15) [Cr(H₂tpda)₂+CH₃OH]⁺. Elem. Anal. Calcd for C₃₀H₂₆Cl₃CrN₁₀O₁₂: C, 40.09; H, 2.99; N, 15.97. Found: C, 40.58; H, 3.41; N, 15.86. UV-VIS: $\lambda_{\text{abs}}/\text{nm}$ ($\epsilon/\text{M}^{-1}\text{cm}^{-1}$) = 442 (3390), 358 (12200) 308 (31100), 219 (54500). IR (ATR): $\tilde{\nu}$ = 3480 (w, br, NH), 3060 (w, CH_{ar}) 2835 (br), 1627 (m), 1577 (m), 1491 (m), 1478 (m), 1439 (s), 1420 (s), 1362 (w), 1220 (m), 1159 (m), 1089 (m, br, ClO), 1014 (m), 874 (w), 806 (w), 773 (s), 656 (w), 621 (m), 524 (w), 441 (w) cm⁻¹.

Synthesis of [Cr(D₂tpda)₂](ClO₄)₃·[D₄]-2[CrO₄]₃. [Cr(H₂tpda)₂](ClO₄)₃ (46.5 mg, 0.0530 mmol) were dissolved in CH₃OD (15 mL) containing 13.3 μ l DClO₄ (68% in D₂O). The resulting orange colored solution was stirred for 12 h. Slowly adding diethyl ether resulted in precipitation of the product. Yield: 44.3 mg (0.0503 mmol, 98%). MS (ESI⁺): m/z (int%) = 322.5 (20)

[Cr(H₂tppda)₂(CH₃OH)(H₂O)(OH)]²⁺, 323.5 (14) [Cr(HDtppda)₂(CH₃OH)(H₂O)(OH)]²⁺, 339.5 (5) [Cr(HDtppda)₂(ClO₄)₂]²⁺, 340.5 (5) [Cr(D₂tppda)₂(ClO₄)₂]²⁺, 644.1 (100) [Cr(H₂tppda)₂(CH₃OH)(OH)]²⁺, 646.1 (69) [Cr(HDtppda)₂(CH₃OH)(OH)]²⁺, 678.0 (20) [Cr(H₂tppda)(Dtppda)(ClO₄)₂]⁺, 680.0 (22) [Cr(D₂tppda)(Dtppda)(ClO₄)₂]⁺. IR (ATR): $\tilde{\nu}$ = 3084 (w, CH_{ar}), 2390 (w, ND), 1639 (w), 1612 (m), 1585 (m), 1494 (m), 1433 (s), 1233 (w), 1167 (w) 1055 (s, br, ClO), 1014 (w), 856 (w), 800 (w), 775 (m), 744 (w), 621 (s), 513 (w), 437 (w) cm⁻¹.

Acknowledgements

This work was financially supported by the Deutsche Forschungsgemeinschaft (GSC 266, Materials Science in Mainz, scholarship for S.O., HE 2778/10-1 and RE 1203/23-1). Funding from the internal university research funds of the Johannes Gutenberg University, Mainz is gratefully acknowledged. Parts of this research were conducted using the supercomputer Mogon and advisory services offered by Johannes Gutenberg University Mainz (www.hpc.uni-mainz.de), which is a member of the AHRP and the Gauss Alliance e.V. We thank Dr. Dieter Schollmeyer for collection of the diffraction data.

Keywords: luminescence • pH sensing • polypyridine • tridentate ligands • chromium

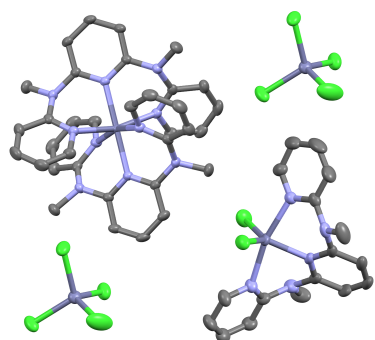
- [1] C. B. Larsen, O. S. Wenger, *Chem. Eur. J.* **2018**, *24*, 2039–2058.
 [2] a) B. Hupp, C. Schiller, C. Lenczyk, M. Stanoppi, K. Edkins, A. Lorbach, A. Steffen, *Inorg. Chem.* **2017**, *56*, 8996–9008; b) M. Iwamura, S. Takeuchi, T. Tahara, *Acc Chem Res* **2015**, *48*, 782–791.
 [3] a) S. V. Eliseeva, J.-C. G. Bünzli, *Chem Soc Rev* **2010**, *39*, 189–227; b) E. J. New, D. Parker, D. G. Smith, J. W. Walton, *Curr Opin Chem Biol* **2010**, *14*, 238–246; c) E. Pershagen, K. E. Borbas, *Coord. Chem. Rev.* **2014**, *273–274*, 30–46; d) C. Doffek, J. Wahnsner, E. Kreidt, M. Seitz, *Inorg. Chem.* **2014**, *53*, 3263–3265; e) A. J. Amoroso, S. J. A. Pope, *Chem Soc Rev* **2015**, *44*, 4723–4742; f) C. Doffek, M. Seitz, *Angew. Chem.* **2015**, *127*, 9856–9858; *Angew. Chem. Int. Ed.* **2015**, *54*, 9719–9721.
 [4] M. Schulze, A. Steffen, F. Würthner, *Angew. Chem.* **2015**, *127*, 1590–1593; *Angew. Chem. Int. Ed.* **2015**, *54*, 1570–1573.
 [5] Y. Zhang, J. L. Petersen, C. Milsman, *J. Am. Chem. Soc.* **2016**, *138*, 13115–13118.
 [6] a) P. Chábera, Y. Liu, O. Prakash, E. Thyraug, A. E. Nahhas, A. Honarfar, S. Essén, L. A. Fredin, T. C. B. Harlang, K. S. Kjær *et al.*, *Nature* **2017**, *543*, 695–699; b) B. Sarkar, L. Suntrup, *Angew. Chem.* **2017**, *129*, 9064–9066; *Angew. Chem. Int. Ed.* **2017**, *56*, 8938–8940.
 [7] a) L. A. Büldt, X. Guo, A. Prescimone, O. S. Wenger, *Angew. Chem.* **2016**, *128*, 11413–11417; *Angew. Chem. Int. Ed.* **2016**, *55*, 11247–11250; b) L. A. Büldt, O. S. Wenger, *Angew. Chem.* **2017**, *129*, 5770–5776; *Angew. Chem. Int. Ed.* **2017**, *56*, 5676–5682; c) L. A. Büldt, X. Guo, R. Vogel, A. Prescimone, O. S. Wenger, *J. Am. Chem. Soc.* **2017**, *139*, 985–992.
 [8] H. Xiang, J. Cheng, X. Ma, X. Zhou, J. J. Chruma, *Chem Soc Rev* **2013**, *42*, 6128–6185.
 [9] a) A. D. Kirk, G. B. Porter, *J. Phys. Chem.* **1980**, *84*, 887–891; b) N. Serpone, M. A. Jamieson, M. S. Henry, M. Z. Hoffman, F. Bolletta, M. Maestri, *J. Am. Chem. Soc.* **1979**, *101*, 2907–2916.
 [10] J. C. Barbour, A. J. I. Kim, E. deVries, S. E. Shaner, B. M. Lovaasen, *Inorg. Chem.* **2017**, *56*, 8212–8222.
 [11] a) K. N. Brown, R. J. Geue, A. M. Sargeson, G. Moran, S. F. Ralph, H. Riesen, *Chem. Commun.* **1998**, 2291–2292; b) A. M. McDaniel, H.-W. Tseng, E. A. Hill, N. H. Damrauer, A. K. Rappé, M. P. Shores, *Inorg. Chem.* **2013**, *52*, 1368–1378.
 [12] S. Otto, M. Grabolle, C. Förster, C. Kreitner, U. Resch-Genger, K. Heinze, *Angew. Chem.* **2015**, *127*, 11735–11739; *Angew. Chem. Int. Ed.* **2015**, *54*, 11572–11576.

- [13] a) A. Breivogel, C. Förster, K. Heinze, *Inorg. Chem.* **2010**, *49*, 7052–7056; b) C. Förster, T. E. Gorelik, U. Kolb, V. Ksenofontov, K. Heinze, *Eur. J. Inorg. Chem.* **2015**, *2015*, 920–924; c) C. Förster, K. Mack, L. M. Carrella, V. Ksenofontov, E. Rentschler, K. Heinze, *Polyhedron* **2013**, *52*, 576–581; d) A. K. C. Mengel, W. Cho, A. Breivogel, K. Char, Y. Soo Kang, K. Heinze, *Eur. J. Inorg. Chem.* **2015**, *2015*, 3299–3306; e) K. Mack, A. Wunsche von Leupoldt, C. Förster, M. Ezhevskaya, D. Hinderberger, K. W. Klinkhammer, K. Heinze, *Inorg. Chem.* **2012**, *51*, 7851–7858; f) A. K. C. Mengel, C. Bissinger, M. Dorn, O. Back, C. Förster, K. Heinze, *Chem. Eur. J.* **2017**, *23*, 7920–7931; g) A. K. C. Mengel, C. Förster, A. Breivogel, K. Mack, J. R. Ochsmann, F. Laquai, V. Ksenofontov, K. Heinze, *Chem. Eur. J.* **2015**, *21*, 704–714; h) A. Breivogel, C. Kreitner, K. Heinze, *Eur. J. Inorg. Chem.* **2014**, *2014*, 5468–5490; i) A. Breivogel, M. Park, D. Lee, S. Klassen, A. Kühnle, C. Lee, K. Char, K. Heinze, *Eur. J. Inorg. Chem.* **2014**, *2014*, 288–295; j) A. Breivogel, M. Meister, C. Förster, F. Laquai, K. Heinze, *Chem. Eur. J.* **2013**, *19*, 13745–13760; k) S. Otto, J. Moll, C. Förster, D. Geißler, C. Wang, U. Resch-Genger, K. Heinze, *Eur. J. Inorg. Chem.* **2017**, *2017*, 5033–5040.
 [14] S. Otto, N. Scholz, T. Behnke, U. Resch-Genger, K. Heinze, *Chem. Eur. J.* **2017**, *23*, 12131–12135.
 [15] S. Otto, A. M. Nauth, E. Ermilov, N. Scholz, A. Friedrich, U. Resch-Genger, S. Lochbrunner, T. Opatz, K. Heinze, *ChemPhotoChem* **2017**, *1*, 344–349.
 [16] S. Otto, M. Dorn, C. Förster, M. Bauer, M. Seitz, K. Heinze, *Coord. Chem. Rev.* **2018**, *359*, 102–111.
 [17] C. Wang, S. Otto, M. Dorn, E. Kreidt, J. Lebon, L. Sršan, P. Di Martino-Fumo, M. Gerhards, U. Resch-Genger, M. Seitz *et al.*, *Angew. Chem.* **2018**, *130*, 1125–1130; *Angew. Chem. Int. Ed.* **2018**, *57*, 1112–1116.
 [18] K.-Y. Ho, W.-Y. Yu, K.-K. Cheung, C.-M. Che, *J. Chem. Soc., Dalton Trans.* **1999**, 1581–1586.
 [19] a) H.-C. Chang, J.-T. Li, C.-C. Wang, T.-W. Lin, H.-C. Lee, G.-H. Lee, S.-M. Peng, *Eur. J. Inorg. Chem.* **1999**, *1999*, 1243–1251; b) A. Dirvanaukas, R. Galavotti, A. Lunghi, A. Nicolini, F. Roncaglia, F. Totti, A. Cornia, *Dalton Trans* **2018**, *47*, 585–595; c) S.-A. Hua, M.-C. Cheng, C.-h. Chen, S.-M. Peng, *Eur. J. Inorg. Chem.* **2015**, *2015*, 2498.
 [20] A. P. Scott, L. Radom, *J. Phys. Chem.* **1996**, *100*, 16502–16513.
 [21] M.-h. Yang, T.-W. Lin, C.-C. Chou, H.-C. Lee, H.-C. Chang, G.-H. Lee, M.-k. Leung, S.-M. Peng, *Chem. Commun.* **1997**, *27*, 2279–2280.
 [22] M. Maeda, K. Kato, *J. Chem. Eng. Data* **1995**, *40*, 253–256.
 [23] a) C. Würth, J. Pauli, C. Lochmann, M. Spieles, U. Resch-Genger, *Anal. Chem.* **2012**, *84*, 1345–1352; b) C. Würth, M. G. González, R. Niessner, U. Panne, C. Haisch, U. R. Genger, *Talanta* **2012**, *90*, 30–37; c) C. Würth, D. Geissler, T. Behnke, M. Kaiser, U. Resch-Genger, *Anal. Bioanal. Chem.* **2015**, *407*, 59–78.
 [24] N. G. Connelly, W. E. Geiger, *Chem. Rev.* **1996**, *96*, 877–910.
 [25] a) R. H. Blessing, *Acta Crystallogr. A* **1995**, *51*, 33–38; b) SMART Data Collection and SAINT-Plus Data Processing Software for the SMART System (various versions); Bruker Analytical X-ray Instruments, Inc.: Madison: WI, 2000.
 [26] a) G. M. Sheldrick, *SHELXL-2014/7*; University of Göttingen: Göttingen, Germany, 2014; b) G. M. Sheldrick, *Acta Crystallogr. A* **2015**, *71*, 3–8.
 [27] F. Neese, *WIREs Comput. Mol. Sci.* **2012**, *2*, 73–78.
 [28] a) F. Neese, F. Wennmohs, A. Hansen, U. Becker, *Chem. Phys.* **2009**, *356*, 98–109; b) R. Izsak, F. Neese, *J. Chem. Phys.* **2011**, *135*, 144105.
 [29] A. D. Becke, *J. Chem. Phys.* **1993**, *98*, 5648–5652.
 [30] a) A. Schäfer, H. Horn, R. Ahlrichs, *J. Chem. Phys.* **1992**, *97*, 2571–2577; b) A. Schäfer, C. Huber, R. Ahlrichs, *J. Chem. Phys.* **1994**, *100*, 5829–5835.
 [31] a) A. Hönnerscheid, L. van Wüllen, R. Dinnebie, M. Jansen, J. Rahmer, M. Mehring, *Phys. Chem. Chem. Phys.* **2004**, *6*, 2454–2460; b) D. A. Pantazis, X.-Y. Chen, C. R. Landis, F. Neese, *J. Chem. Theory Comput.* **2008**, *4*, 908–919; c) E. van Lenthe, E. J. Baerends, J. G. Snijders, *J. Chem. Phys.* **1993**, *99*, 4597–4610.
 [32] a) S. Grimme, J. Antony, S. Ehrlich, H. Krieg, *J. Chem. Phys.* **2010**, *132*, 154104; b) S. Grimme, S. Ehrlich, L. Goerigk, *J. Comput. Chem.* **2011**, *32*, 1456–1465.
 [33] S. Sinnecker, A. Rajendran, A. Klamt, M. Diedenhofen, F. Neese, *J. Phys. Chem. A* **2006**, *110*, 2235–2245.

3.7 Three-in-One Crystal: The Coordination Diversity of Zinc Polypyridine Complexes

Sven Otto, Johannes Moll, Cristoph Förster, Daniel Geißler, Cui Wang, Ute Resch-Genger and Katja Heinze

Eur. J. Inorg. Chem. **2017**, 43, 5033–5040.



The syntheses, structures, and photophysical properties of two new zinc(II) complexes bearing the tridentate N,N'-dimethyl-N,N'-dipyridin-2-ylpyridine-2,6-diamine (ddpd) ligand are presented. Structural investigations through single-crystal X-ray diffractometry, NMR spectroscopy, and density functional theory calculations revealed a diverse coordination behavior that depends on the counterion. Spectroscopic (UV/Vis and emission spectroscopy) and theoretical techniques (DFT and time-dependent DFT calculations) were employed to explore the photophysical properties of the complexes.

Author Contributions

Sven Otto synthesized and characterized the zinc complexes presented in this manuscript, carried out the electrochemical experiments and performed all DFT calculations as well. Johannes Moll and Sven Otto conducted UV-VIS and emission spectroscopic experiments. Cui Wang, Daniel Geißler and Ute Resch-Genger determined the emission quantum yields and excited state lifetimes at the *Bundesanstalt für Materialforschung und -prüfung* in Berlin, Germany. The crystal structures were solved and refined by Christoph Förster. The manuscript was written by Sven Otto (90%) and Katja Heinze (10%).

Supporting Information

for this article is found at pp. 250.

“Otto, S.; Moll, J.; Förster, C.; Wang, C.; Geißler, D.; Resch-Genger, U.; Heinze, K. *Eur. J. Inorg. Chem.* **2017**, 43, 5033–5040. Copyright Wiley-VCH Verlag GmbH & Co. KGaA. Reproduced with permission.”

Zinc Polypyridine Complexes

Three-in-One Crystal: The Coordination Diversity of Zinc Polypyridine Complexes

Sven Otto,^[a,b] Johannes Moll,^[a] Christoph Förster,^[a] Daniel Geißler,^[c] Cui Wang,^[c,d] Ute Resch-Genger,^{*[c]} and Katja Heinze^{*[a]}

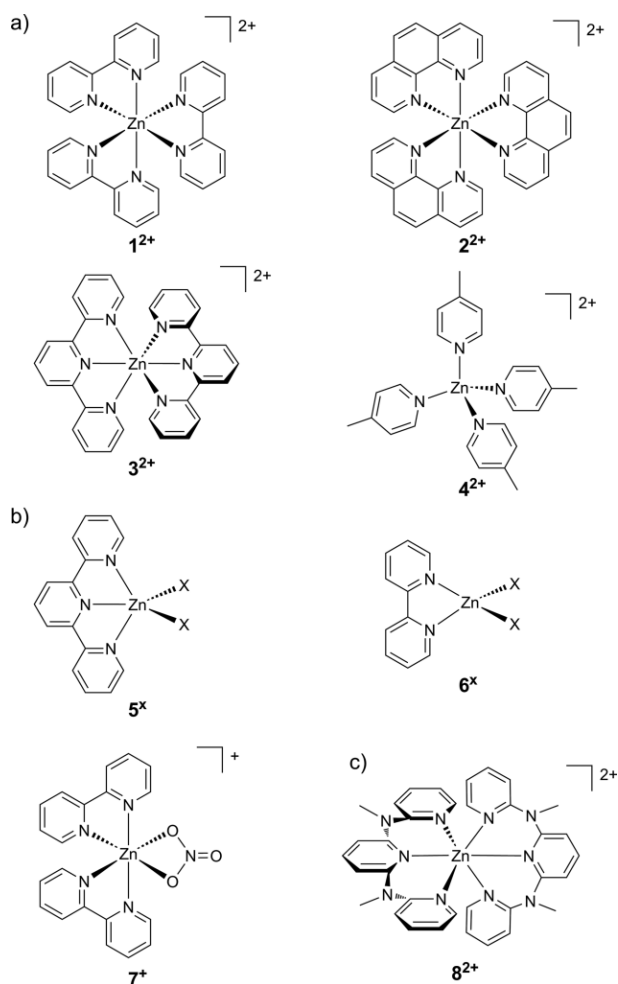
Abstract: The syntheses, structures, and photophysical properties of two new zinc(II) complexes bearing the tridentate *N,N'*-dimethyl-*N,N'*-dipyridin-2-ylpyridine-2,6-diamine (ddpd) ligand are presented. Structural investigations through single-crystal X-ray diffractometry, NMR spectroscopy, and density functional

theory calculations revealed a diverse coordination behavior that depends on the counterion. Spectroscopic (UV/Vis and emission spectroscopy) and theoretical techniques (DFT and time-dependent DFT calculations) were employed to explore the photophysical properties of the complexes.

Introduction

Complexes of transition metals with d^{10} electron configurations (e.g. Zn^{2+} , Cd^{2+} , and Hg^{2+}) exhibit a variety of different coordination numbers and geometries. This is not surprising, as they do not experience any stabilization through variation of the ligand field. Thus, the coordination number and coordination polyhedron are governed by charge compensation and ligand repulsion rather than by the ligand field. Well-studied examples to illustrate this behavior are the 2,2'-bipyridine (bpy), phenanthroline (phen), and 2,2':6',2''-terpyridine (tpy) complexes of zinc(II) (Scheme 1). In the presence of weakly coordinating counterions such as ClO_4^- , SO_4^{2-} , BF_4^- , or PF_6^- , the homoleptic, pseudo-octahedral complexes $[Zn(bpy)_3]^{2+}$ (1^{2+}), $[Zn(phen)_3]^{2+}$ (2^{2+}), and $[Zn(tpy)_2]^{2+}$ (3^{2+}) are formed (Scheme 1a).^[1] If the steric demand of the N-donor ligand is reduced, for example, in 4-methylpyridine (4-Me-py), the geometry changes to tetrahedral in $[Zn(4-Me-py)_4]^{2+}$ (4^{2+}), which has shorter metal–ligand bond lengths, namely, 2.03 versus 2.14 and 2.17 Å in 1^{2+} (both dications as perchlorate salts).^[1d,2]

In the presence of halides, Zn^{2+} cations form heteroleptic complexes with polypyridine ligands. Halides and tpy form five-coordinate complexes $Zn(tpy)X_2$ (5^X) ($X = Cl, Br, I$).^[3] These neu-



Scheme 1. (a) Homoleptic polypyridine zinc(II) complex cations 1^{2+} – 4^{2+} , (b) heteroleptic complexes 5^X , 6^X , and 7^+ , and (c) target complex 8^{2+} .

tral complexes crystallize with either square-pyramidal^[4] or trigonal-bipyramidal geometries.^[5] Neutral tetrahedral complexes

[a] Institute of Inorganic Chemistry and Analytical Chemistry, Johannes Gutenberg University of Mainz, Duesbergweg 10-14, 55128 Mainz, Germany
E-mail: katja.heinze@uni-mainz.de
www.ak-heinze.chemie.uni-mainz.de

[b] Graduate School Materials Science in Mainz, Staudingerweg 9, 55128 Mainz, Germany

[c] Division 1.10 Biophotonics, Federal Institute for Materials Research and Testing (BAM), Richard-Willstätter-Strasse 11, 12489 Berlin, Germany
E-mail: ute.resch@bam.de
www.bam.de/

[d] Freie Universität Berlin, 14195 Berlin, Germany

Supporting information and ORCID(s) from the author(s) for this article are available on the WWW under <https://doi.org/10.1002/ejic.201700948>.

6^X ($X = \text{Cl}, \text{Br}$) form with the bidentate bpy ligand (Scheme 1b).^[1c] Even anions with delocalized charge such as nitrate can coordinate in the first coordination sphere to afford the distorted octahedral monocationic complex 7^+ (Scheme 1b).^[1c]

The bpy and tpy complexes of zinc(II), which are isostructural to $[\text{M}(\text{bpy})_3](\text{X})_2$ and $[\text{M}(\text{tpy})_2](\text{X})_2$ complexes ($\text{M} = \text{Cu}, \text{Fe}, \text{Ru}$), were used previously as diamagnetic and transparent host lattices to study Jahn–Teller distortions in copper(II) complexes,^[1a,1b] spin crossover in iron(II) complexes,^[6] and the character of triplet metal-to-ligand charge-transfer ($^3\text{MLCT}$) transitions in ruthenium(II) complexes.^[7]

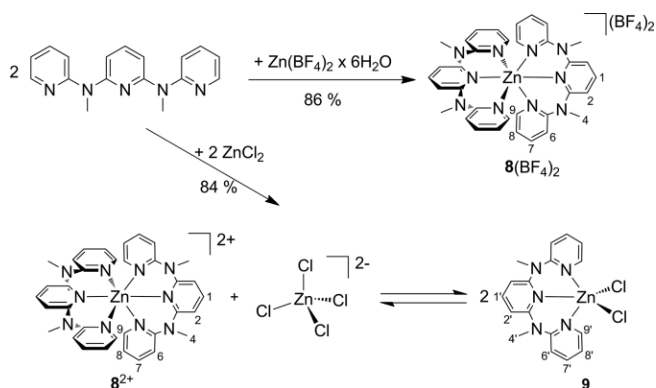
Recently, we explored the tridentate N,N' -dimethyl- N,N' -dipyridin-2-ylpyridin-2,6-diamine (ddpd) ligand in the coordination chemistry of transition-metal complexes.^[8] In contrast to tpy, ddpd is comparably electron-rich and can offer a larger flexible N–M–N bite angle of ca. 90° in several six-coordinate metal complexes.^[8,9] In ruthenium(II), iron(II), and chromium(III) complexes, the large bite angle optimizes metal–ligand orbital overlap and introduces a stronger ligand field, which enables advantageous photophysical properties.^[8,9a,9b,9c,9h,9i,9j,9k] The flexibility of ddpd in the six-coordinate copper(II) complex $[\text{Cu}(\text{ddpd})_2]^{2+}$ induces a dynamic Jahn–Teller distortion with a larger amplitude than that found in $[\text{Cu}(\text{tpy})_2]^{2+}$.^[1b,9g,10] The same flexibility enables an energetically less preferred facial coordination in *fac*- $[\text{Co}(\text{ddpd})_2]^{2+}$ in addition to the thermodynamically favored meridional isomer.^[9d,9e] Furthermore, the electron-donating character of ddpd allows the employment of the $[\text{Co}(\text{ddpd})_2]^{2+/3+}$ redox couple in the electrolyte for dye-sensitized solar cells.^[9d,9f,9m]

Consequently, it is a logical step to synthesize the corresponding zinc(II) complex $[\text{Zn}(\text{ddpd})_2]^{2+}$ ($\mathbf{8}^{2+}$) as a potential host material and to study its intrinsic coordination chemistry and photochemistry (Scheme 1c).

Results and Discussion

Synthesis and Geometric Structure

In this study, we describe the synthesis (Scheme 2) and properties of two new Zn^{2+} complexes with the tridentate ddpd li-



Scheme 2. Synthesis of $\mathbf{8}(\text{BF}_4)_2$ and $[\mathbf{9}][\mathbf{8}](\text{ZnCl}_4)$; atom numbering for NMR spectroscopic assignments.

gand.^[8] The complexes were obtained through the treatment of zinc(II) salts with BF_4^- and Cl^- counterions with ddpd at room temperature in ethanol. Recrystallization from acetonitrile resulted in the pure products.

The reaction of $\text{Zn}(\text{BF}_4)_2 \cdot 6\text{H}_2\text{O}$ with 2.5 equiv. of ddpd led to the expected homoleptic complex $[\text{Zn}(\text{ddpd})_2][\text{BF}_4]_2$ ($\mathbf{8}(\text{BF}_4)_2$) in 86% isolated yield after recrystallization (Scheme 2). Complex formation was confirmed by 1D and 2D NMR spectroscopy (Supporting Information, Figures S1–S5), ESI+ mass spectrometry (Figure S6), and elemental analysis.

The diffusion of diethyl ether into a concentrated solution of $\mathbf{8}(\text{BF}_4)_2$ in acetonitrile yielded colorless single crystals suitable for crystal-structure determination by X-ray diffraction (Figure 1). Complex $\mathbf{8}(\text{BF}_4)_2$ crystallizes with two (disordered) acetonitrile molecules as $[\text{Zn}(\text{ddpd})_2][\text{BF}_4]_2 \cdot 2\text{CH}_3\text{CN}$ in the orthorhombic space group $Fddd$. As anticipated, the zinc(II) complex is isostructural to other homoleptic *mer*- $[\text{M}(\text{ddpd})_2][\text{BF}_4]_2$ complexes ($\text{M} = \text{Fe}, \text{Co}$), and this should allow its application as a host material in solid solutions.^[9d,9h] This should also hold for $[\text{Cu}(\text{ddpd})_2][\text{BF}_4]_2$, which crystallizes in the orthorhombic space group $Fdd2$ with comparable cell metrics.^[9g]

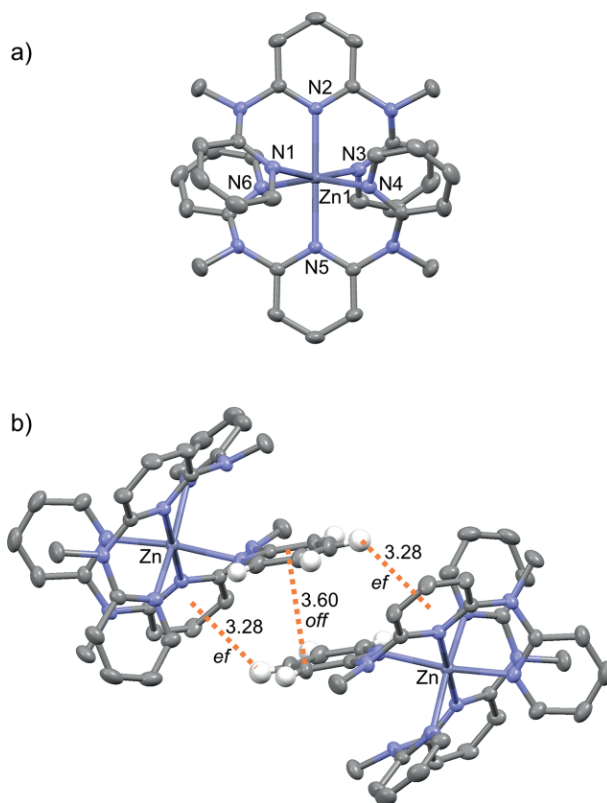


Figure 1. (a) Molecular crystal structure of the cation of $[\text{Zn}(\text{ddpd})_2][\text{BF}_4]_2 \cdot 2\text{CH}_3\text{CN}$ (thermal ellipsoids set at 50% probability, H atoms omitted for clarity) and (b) π interactions between the cations (distances in Å, only relevant H atoms are shown for clarity).

The meridional ZnN_6 coordination geometry of $\mathbf{8}^{2+}$ corresponds to a slightly compressed octahedron with four longer Zn–N bonds to the terminal pyridine rings [Zn1–N1 2.1427(16) Å] and two shorter ones to the central pyridine rings [Zn1–N2 2.127(2) Å] of the ddpd ligand (Figure 1a, Table 1).

The intraligand N1–Zn1–N2 and N1–Zn–N3 angles amount to 82.40(4) and 164.79(8)°, respectively. In contrast to chromium(III), iron(II), and ruthenium(II) complexes of ddpd with large ligand-field stabilization energies from the 90° bite angles, the bite angles in **8**²⁺ are well below 90°. [8,9a,9h]

Table 1. Selected bond lengths [Å] and angles [°] of **8**²⁺ in the different crystalline environments and those obtained from DFT calculations.

	8 (BF ₄) ₂	8 A ²⁺	8 B ²⁺	8 ²⁺ (DFT)
Zn1–N1	2.1427(16)	2.13(3)	2.16(3)	2.156
Zn1–N2	2.127(2)	2.109(5)	2.081(7)	2.168
Zn1–N3	2.1427(16)	2.139(6)	2.113(5)	2.156
Zn1–N4	2.1427(16)	2.285(6)	2.029(5)	2.156
Zn1–N5	2.127(2)	2.166(9)	2.192(6)	2.168
Zn1–N6	2.1427(16)	1.993(15)	2.249(15)	2.156
N1–Zn1–N2	82.40(4)	84.8 (7)	85.5(7)	82.92
N1–Zn1–N3	164.79(8)	165.3(7)	169.8(7)	165.84
N4–Zn1–N5	82.40(4)	77.9(3)	84.3(2)	82.92
N4–Zn1–N6	164.79(8)	164.8(5)	165.2(5)	165.84

The crystal packing in **8**(BF₄)₂ is dominated by intermolecular π interactions, as typically found in meridional pseudo-octahedral complexes. Several offset face-to-face (*off*) and edge-to-face (*ef*) interactions exist between the ligands of neighboring complexes (Figure 1b). Similar to those of isostructural complexes, the **8**²⁺ cations display one *off* interaction between the terminal pyridine rings of neighboring complexes and two *ef* interactions between the central and terminal pyridine rings in every pair of complexes.^[11]

In contrast to the straightforward formation of the homoleptic complex **8**(BF₄)₂, the outcome of the reaction of ddpd with ZnCl₂ was more complicated, as revealed by the ¹H NMR spectrum (Figures 2 and S7). In addition to the signature of dication **8**²⁺, the reaction mixture of ZnCl₂ and ddpd exhibits another set of ¹H NMR resonances. These resonances differ from the signals of uncoordinated ddpd and, hence, have to be assigned to coordinated ddpd; therefore, the spectrum suggests the presence of a second zinc complex (**9**).

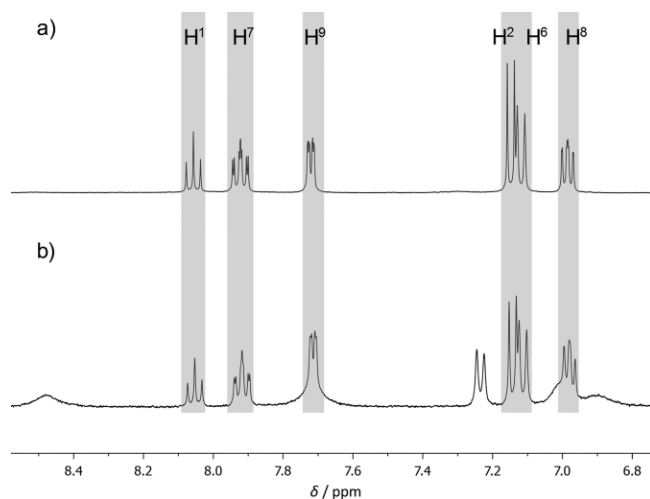


Figure 2. Aromatic region of the ¹H NMR spectra of (a) **8**²⁺ and (b) **8**²⁺ together with **9** in CD₃CN; the resonances of **8**²⁺ are highlighted (see Figures S1 and S7 for the full ¹H NMR spectra).

The integration of the methyl proton resonances (H⁴) at δ = 2.91 (**8**²⁺) and 3.50 ppm (**9**) yields a 1.0:0.9 ratio of the signal

sets (Figure S7). The additional set possesses very broad signals and also overlaps with the resonances of **8**²⁺ in the aromatic region, which prevents a conclusive assignment through 2D NMR spectroscopy methods. The ¹H–¹H COSY spectrum reveals a correlation between the broad resonance superimposed with the signal of H⁹ at δ = 7.73 ppm and the doublet at δ = 7.24 ppm of the second set (Figure S8). On the basis of the chemical shifts and coupling pattern in comparison to the assignments for **8**²⁺, these two resonances could be attributed to either H^{1'} and H^{2'} or to H^{7'} and H^{6'} of **9**, respectively.

The ESI+ mass spectrum of the material provides a hint about the nature of the second species **9** (Figure S9). In addition to the peak at m/z = 323.1, which corresponds to **8**²⁺, a peak with a characteristic chlorine pattern is obtained at m/z = 390.1. This peak perfectly matches a cationic heteroleptic complex species [Zn(ddpd)Cl]⁺ present in the gas phase. In the condensed phase, this could be attributed to the presence of heteroleptic cationic, neutral, or anionic species [Zn(ddpd)Cl_n]²⁻ⁿ (n = 1–3).

Single crystals suitable for crystal-structure determination by X-ray diffraction were obtained through the diffusion of diethyl ether into a concentrated acetonitrile solution (Figure 3). In addition to the dicationic homoleptic complex **8**²⁺ and a solvent

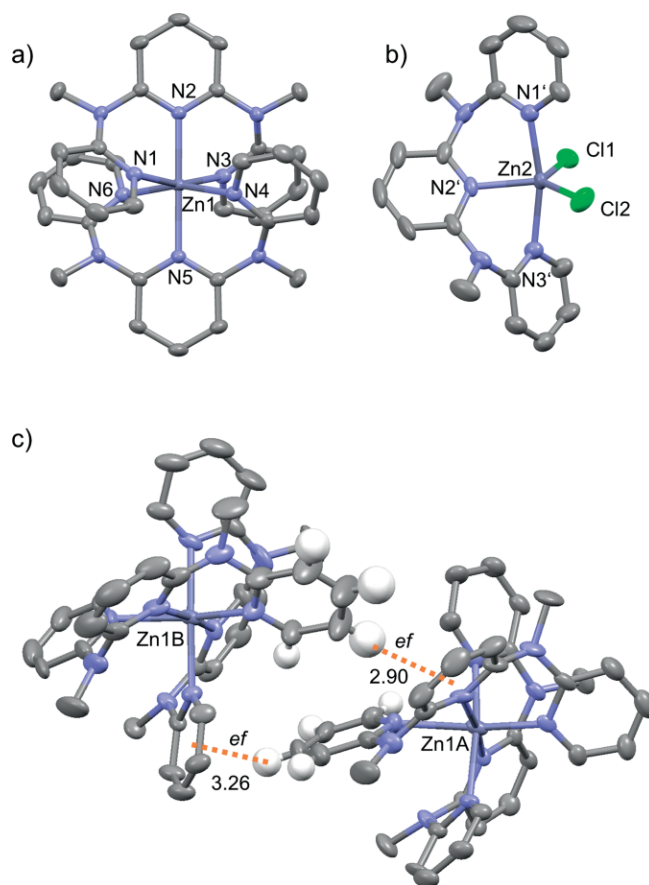


Figure 3. (a) Molecular crystal structures of the **8**A²⁺ cation and (b) the neutral five-coordinate complex **9** of [9][**8**](ZnCl₄)·CH₃CN (thermal ellipsoids set at 50% probability, H atoms omitted for clarity) and (c) π interactions between two **8**A²⁺/**8**B²⁺ cations (distances in Å, only relevant H atoms are shown for clarity).

molecule, the unit cell contains a tetrahedral ZnCl_4^{2-} counterion and a neutral five-coordinate $\text{ZnCl}_2(\text{ddpd})$ complex (**9**). All three zinc(II) complexes are present in a 1:1:1 ratio in the crystal to afford $[\mathbf{9}][\mathbf{8}](\text{ZnCl}_4)$ (triclinic space group, $P\bar{1}$).

The complex cation $\mathbf{8}^{2+}$ in $[\mathbf{9}][\mathbf{8}](\text{ZnCl}_4)$ is disordered over two orientations with 50 % occupancy ($\mathbf{8A}^{2+}$ and $\mathbf{8B}^{2+}$), which results in less accurate metric data (Figure 3a). The Zn–N bond lengths and N–Zn–N bond angles of $\mathbf{8A}^{2+}$ and $\mathbf{8B}^{2+}$ differ slightly and are also slightly distinct from those of $\mathbf{8}^{2+}$ in $\mathbf{8}(\text{BF}_4)_2$ (Table 1). This flexibility of the $[\text{Zn}(\text{ddpd})_2]^{2+}$ cations is certainly attributable to different packing effects and the flexibility of the ddpd ligand.

Similar to the packing interactions in $\mathbf{8}(\text{BF}_4)_2$, interactions between the $\mathbf{8A}^{2+}$ and $\mathbf{8B}^{2+}$ cations exist in $[\mathbf{9}][\mathbf{8}](\text{ZnCl}_4)$. In contrast to the aryl embraces found in $\mathbf{8}(\text{BF}_4)_2$, two *ef* interactions from terminal to terminal and central pyridine rings are established (Figure 3c). Hence, the slightly different bond metrics of $\mathbf{8}^{2+}$, $\mathbf{8A}^{2+}$, and $\mathbf{8B}^{2+}$ can certainly be ascribed to different packing arrangements (Table 1).

The geometry of the five-coordinate complex **9** is distorted trigonal bipyramidal with a geometry index^[12] of $\tau = 0.68$. The idealized trigonal plane is spanned by the two chlorido ligands and the nitrogen atom of the central pyridine ring of ddpd (Figure 3b), and the nitrogen atoms of the terminal pyridine rings are located at apical positions with a $\text{N1}'\text{--Zn2--N3}'$ angle of $166.14(9)^\circ$. All of the $\text{N}_x\text{--Zn--N}_y$ angles in **9** are larger than those in $\text{Zn}(\text{tpy})\text{Cl}_2$ ($\mathbf{5}^{\text{Cl}}$, Table 2). The $\text{N1}'\text{--Zn2--N2}'$ and $\text{N2}'\text{--Zn2--N3}'$ bite angles in **9** amount to $83.90(10)$ and $82.26(10)^\circ$, respectively. The Cl1--Zn2--Cl2 angle of $124.99(4)^\circ$ is slightly larger than the ideal 120° angle of a regular trigonal bipyramid, as expected owing to the Coulombic repulsion of the anionic chlorido ligands. This is in contrast to the structure of $\mathbf{5}^{\text{Cl}}$, in which the chlorido ligands are closer to each other with a Cl--Zn--Cl angle of $116.72(3)^\circ$. However, the Zn–Cl bonds are longer in $\mathbf{5}^{\text{Cl}}$ [Zn--Cl 2.2820(5) Å].^[5] As tpy is a π -accepting ligand, the electron density at the π -donating chlorido ligands and, thus, their mutual repulsion should be reduced.

Table 2. Selected bond lengths [Å] and angles [$^\circ$] of **9** in the crystal structure and from DFT calculations.

	9	$\text{Zn}(\text{tpy})\text{Cl}_2$ ($\mathbf{5}^{\text{Cl}}$) ^[5]	9 (DFT)
Zn2–N1'	2.170(3)	2.1852(19)	2.224
Zn2–N2'	2.104(2)	2.1057(19)	2.155
Zn2–N3'	2.183(3)	2.1852(19)	2.255
Zn2–Cl1	2.2581(8)	2.2820(5)	2.257
Zn2–Cl2	2.2741(9)	2.2820(5)	2.254
N1'–Zn2–N2'	83.90(10)	74.76(4)	75.73
N2'–Zn2–N3'	82.26(10)	74.76(4)	75.73
N1'–Zn2–N3'	166.14(9)	149.53(6)	159.13
Cl1–Zn2–Cl2	124.99(4)	116.72(3)	132.80

Density functional theory [B3LYP, def2-TZVPP, D3(BJ), RIJCOSX, ZORA] calculations of $\mathbf{8}^{2+}$ reproduced the bond angles reasonably well (Table 1). Only the longer calculated distance between the central pyridine rings and the metal ion (Zn1–N2) than that between the zinc ion and the terminal pyridine rings (Zn1–N1) contrast with the experimentally determined data (Table 1). Such a discrepancy has been noted before for analo-

gous cobalt(II) and chromium(III) ddpd complexes^[9a,9d] and might be due to crystal-packing effects.

In the DFT-calculated geometry of **9**, the Zn2–Cl1 and Zn1–Cl2 bond lengths are reproduced fairly well, whereas the distances between the zinc ion and the organic ligand are overestimated, and the discrepancy might again be due to crystal-packing effects. The Cl1--Zn2--Cl2 angle (132.80°) is somewhat overestimated in the DFT-calculated structure (Table 2), probably because no neighboring molecules are taken into account.

As a solution of freshly dissolved single crystals of $[\mathbf{9}][\mathbf{8}](\text{ZnCl}_4)$ in acetonitrile exhibits a ^1H NMR spectrum with a ligand-signal integral ratio of 1:0.9, the ratio of $\mathbf{8}^{2+}$ and **9** must be 0.55:1. As the ratio amounts to 1:1 in the crystal, ligand exchange between $[\mathbf{8}](\text{ZnCl}_4)$ and **9** must occur rapidly (Scheme 2). This equilibration might also account for the rather broad ^1H NMR resonances (Figures 2 and S7).

Optical Properties

The absorption spectrum of $\mathbf{8}(\text{BF}_4)_2$ in CH_2Cl_2 shows maxima at $\lambda = 248, 265$ (sh), and 308 nm (Figure 4). On the basis of time-dependent DFT calculations (TD-DFT), the absorption bands can be assigned to MLCT and $\pi\text{--}\pi^*$ transitions. The TD-DFT-calculated UV/Vis spectrum reproduces the experimental spectrum reasonably well (Figure S10). Although the calculated low-energy excitations at $\lambda = 265$ and 308 nm are of pure $\pi\text{--}\pi^*$ character, mixed $\pi\text{--}\pi^*$ and MLCT transitions appear at higher energies (Figure 5, Table S4).

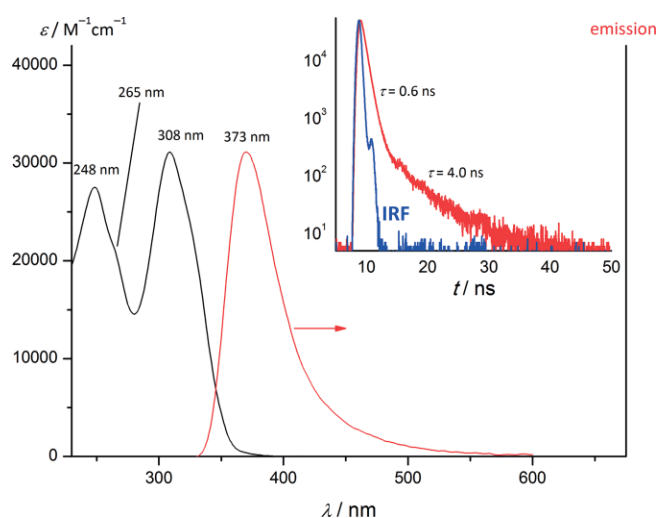


Figure 4. Absorption (black line) and emission (red line, $\lambda_{\text{exc}} = 308$ nm) of $\mathbf{8}(\text{BF}_4)_2$ in CH_2Cl_2 (treated with K_2CO_3) under inert conditions. The inset shows the emission decay curve of $\mathbf{8}(\text{BF}_4)_2$ in CH_2Cl_2 . The instrument response function (IRF) is displayed in blue.

The irradiation of a solution of $\mathbf{8}(\text{BF}_4)_2$ in CH_2Cl_2 at $\lambda = 308$ nm led to an emission band with a maximum at $\lambda = 373$ nm (Figure 4). $[\text{Zn}(\text{tpy})_2][\text{ClO}_4]_2$ (in CH_3CN) shows an emission band at $\lambda = 353$ nm,^[16] whereas $[\text{Zn}(\text{bpy})_3](\text{ClO}_4)_2$ emits at $\lambda = 366$ nm (in the solid state).^[1c] The slightly lower energy of the emission of $\mathbf{8}^{2+}$ is likely due to the presence of electron-donating amine functionalities (Figure 5).

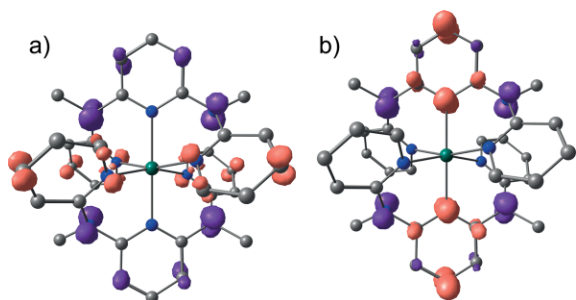


Figure 5. TD-DFT-calculated difference electron densities of the first two transitions of $\mathbf{8}^{2+}$ at $\lambda =$ (a) 310 and (b) 306 nm at a contour value of 0.005 a.u. The purple lobes indicate loss of electron density, and the orange lobes show increased electron density upon excitation; H atoms omitted for clarity.

The Gaussian deconvolution of the absorption and emission spectra of $\mathbf{8}^{2+}$ allows the determination of a Stokes shift of 2715 cm^{-1} (Figures S11 and S12). The emission quantum yield (Φ) amounts to 6.5 % in CH_2Cl_2 with a lifetime (τ) of 0.6 ns. The size of the Stokes shift and the lifetime indicate fluorescence emission. The TD-DFT calculations indicate a negligible contribution of the metal ion, which would have allowed for intersystem crossing and phosphorescence (Figure 5 and Table S4). The emission decay curve can be fitted with a biexponential profile to yield the decay components $\tau_1 = 0.6\text{ ns}$ (96 %) and $\tau_2 = 4.0\text{ ns}$ (4 %). The second decay component is assigned to the presence of traces of free ligand, which is also emissive ($\lambda = 410\text{ nm}$ in CH_2Cl_2 ; Figure S13).^[9a] In the presence of trifluoroacetic acid, ddpd shows emission at $\lambda = 395\text{ nm}$ in CH_2Cl_2 (Figure S14). The observation of the protonated ddpd ligand in the ESI+ mass spectrum also supports this interpretation of facile ligand loss (Experimental Section and Figure S6). Dichloromethane can release HCl, which can result in an equilibrium with $\mathbf{9}$ and $(\text{ZnCl}_4)^{2-}$ (Scheme 2). During this substitution reaction, traces of free ddpd ligand appear in solution and reveal a fluorescence lifetime of $\tau_2 = 4.0\text{ ns}$.^[9a]

The fluorescence of the ddpd ligand shifts to higher energy through protonation in CH_3CN , whereas the protonation of tpy leads to a redshifted emission from $\lambda = 340$ to 412 nm (and to 395 nm upon further protonation) in this solvent.^[13] This opposite behavior can probably be attributed to the different protonation sites. Although tpy can only be protonated at the pyridine rings, which increases their acceptor strengths,^[13c] the NR_3 moieties of ddpd should be more basic than the pyridine rings. For example, the $\text{p}K_a$ value of pyridinium ions [$\text{p}K_a(\text{Hpy}^+) = 5.3$]^[14] is much lower than that of protonated 4-dimethylaminopyridine [HDMAP^+ , $\text{p}K_a(\text{HDMAP}^+) = 9.6$].^[15] Hence, the opposite fluorescence behavior of tpy and ddpd is ascribed to different protonation sites.

On the basis of the TD-DFT calculations, the $(\text{ZnCl}_4)^{2-}$ counterion absorbs only at $\lambda < 200\text{ nm}$ (Figure S15). Hence, a solution of $[\mathbf{9}][\mathbf{8}](\text{ZnCl}_4)$ contains two zinc(II) ddpd complexes that absorb in the UV/Vis region. With the absorption spectrum of $\mathbf{8}^{2+}$ in hand (Figure 4) and the NMR-determined equilibrium concentration, weighted spectral subtraction yields the optical spectrum of $\mathbf{9}$ (Figure 6). The resulting approximate spectrum of $\mathbf{9}$ features two distinct maxima at $\lambda = 340$ and 276 nm . These features can be assigned to ligand-to-ligand charge-transfer

(LL'CT), $\pi-\pi^*$, and MLCT transitions on the basis of the TD-DFT calculations (Figure S16, Table S5). In particular, the low-energy transitions display significant charge transfer between the chlorido and ddpd ligands (Figure 7).

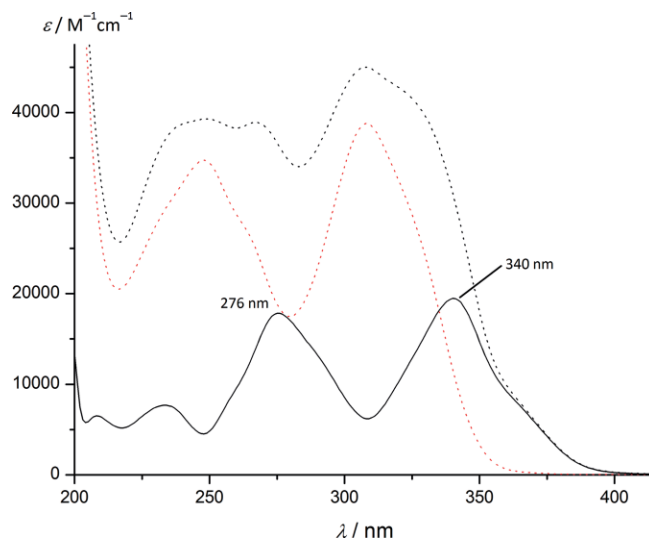


Figure 6. Absorption spectra of $[\mathbf{9}][\mathbf{8}](\text{ZnCl}_4)$ (dotted black line) and $\mathbf{8}(\text{BF}_4)_2$ (dotted red line) in CH_3CN and weighted difference spectrum (black line) representing that of $\mathbf{9}$.

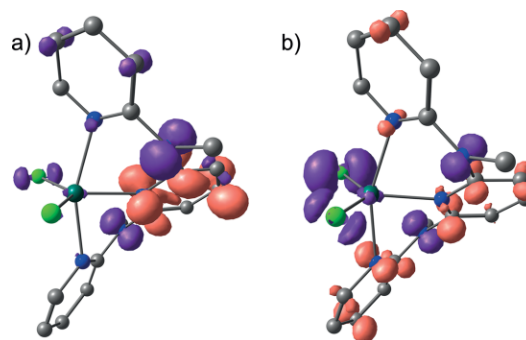


Figure 7. TD-DFT-calculated difference electron densities of the first two intense excitations of $\mathbf{9}$ at $\lambda =$ (a) 320 and (b) 297 nm at a contour value of 0.005 a.u. The purple lobes indicate electron-density loss, and the orange lobes show increased electron density upon excitation; H atoms omitted for clarity.

As the emission spectra of $\mathbf{8}(\text{BF}_4)_2$ and $[\mathbf{9}][\mathbf{8}](\text{ZnCl}_4)$ are essentially superimposable, the five-coordinate complex $\mathbf{9}$ is either nonemissive or only very weakly luminescent. The charge-transfer character and the resulting likely strong distortion of the lowest energy excited states possibly precludes strong emission of $\mathbf{9}$ owing to efficient nonradiative relaxation to the ground state.

To the best of our knowledge, no photophysical data for $\mathbf{5}^{\text{Cl}}$ have been reported, but several complexes of 4'-substituted tpy ligands [$\text{Zn}(4'\text{-Ar-tpy})\text{Cl}_2$, Ar = 4-NMe₂-C₆H₄, 4-NPh₂-C₆H₄, and 4-Me-C₆H₄] have been discussed.^[17] They all show emission bands between $\lambda = 395$ and 629 nm . However, these transitions are of intraligand charge-transfer character between the electron-rich aromatic substituent at the 4'-position and the electron-poor terpyridine. Hence, a comparison with $\mathbf{9}$ is not sensible.

Electrochemical Properties

In contrast to classical noninnocent electron-accepting polypyridine ligands,^[18] ddpd is quite electron-rich. Consequently, no reduction waves are observed in the cyclic voltammogram of ddpd up to -2 V versus ferrocene in CH_3CN (Figures S17 and S18). The irreversible oxidation waves of ddpd at peak potentials of 550 and 1060 mV versus ferrocene are assigned to the oxidation of the two NR_3 groups. Owing to the large positive charge in $\mathbf{8}^{2+}$, these irreversible waves shift to 1170 and 1340 mV, which correspond to the one-electron oxidations of the first and second ligand of $\mathbf{8}(\text{BF}_4)_2$, respectively. At a peak potential of 1670 mV, a second irreversible oxidation of the zinc(II)-coordinated ligands occurs (Figures S19 and S20).

Conclusions

Two new zinc(II) complexes containing the flexible, electron-rich ddpd ligand were prepared. Depending on the coordination ability of the counterion, different structural motifs are realized. The tetrafluoroborate salt $\mathbf{8}(\text{BF}_4)_2$ is isostructural to known homoleptic M^{2+} complexes of ddpd and, hence, can be employed as a host lattice in various magnetic or optical applications. Diamagnetic $\mathbf{8}^{2+}$ is transparent in the optical region above $\lambda = 400$ nm, and fluorescence is only observed upon irradiation at higher energies.

In the presence of chloride anions, three different complexes with different coordination numbers and polyhedra coexist in equilibrium, namely, idealized octahedral, trigonal-bipyramidal,

and tetrahedral coordination complexes. This demonstrates the flexibility of the tridentate ddpd ligand in combination with a d^{10} metal ion that lacks ligand-field stabilization and, furthermore, represents a textbook example of the structural diversity of d^{10} metal ions.

Experimental Section

General Procedures: All reagents were used as received from commercial suppliers (ABCR, Acros, and Sigma–Aldrich). The ligand ddpd was synthesized according to a literature procedure.^[8] The NMR spectra were recorded with a Bruker Avance DRX 400 spectrometer at 400.31 MHz for ^1H and 100.66 MHz for $^{13}\text{C}\{^1\text{H}\}$. All resonances are reported in ppm and were referenced to the solvent signal as an internal standard [CD_3CN (^1H , $\delta = 1.94$ ppm; ^{13}C , $\delta = 1.24$ ppm)]. The UV/Vis/NIR spectra were recorded with a Varian Cary 5000 spectrometer with 1.0 cm cells (Hellma, Suprasil). The emission spectra were recorded with a Varian Cary Eclipse spectrometer. The fluorescence decays were recorded with an Edinburgh Instruments lifetime spectrometer (FLS 920) equipped with a micro-channel plate photomultiplier tube (MCP-PMT; Hamamatsu R3809U-50) with a 330 nm ps laser diode (EPLD, Edinburgh Instruments) for excitation. All measurements were performed under magic-angle conditions (polarization at 0° for the excitation and 54.7° for the emission channel). The luminescence quantum yield was determined with an Ulbricht integrating sphere (Quantaaurus-QY C11347-11, Hamamatsu),^[19] and the relative uncertainty was estimated to be 5%. The ESI MS spectra were recorded with a Micromass Q-TOF-Ultima spectrometer. The IR spectra were recorded with a Yasco FT/IR 4200 spectrometer with samples as KBr disks. The electrochemical measurements were performed with a BioLogic SP-50

Table 3. Results of the crystallographic structure determinations.

	$\mathbf{8}(\text{BF}_4)_2$	$[\mathbf{9}][\mathbf{8}](\text{ZnCl}_4)$
Empirical formula	$\text{C}_{38}\text{H}_{40}\text{B}_2\text{F}_8\text{N}_{12}\text{Zn}$	$\text{C}_{53}\text{H}_{54}\text{Cl}_6\text{N}_{16}\text{Zn}_3$
Formula weight	903.81	1323.93
Crystal color, habit	colorless, block	colorless, block
Crystal dimensions [mm]	$0.46 \times 0.39 \times 0.14$	$0.44 \times 0.20 \times 0.10$
Crystal system	orthorhombic	triclinic
Space group	Fddd	$P\bar{1}$
a [Å]	14.2546(9)	14.9703(7)
b [Å]	21.4548(13)	15.1117(7)
c [Å]	25.9328(16)	15.6079(8)
α [°]	90	67.7140(10)
β [°]	90	86.3840(10)
γ [°]	90	61.8650(10)
V [Å ³]	7931.0(8)	2852.0(2)
Z	8	2
$F(000)$	3712	1352
Density (calcd.) [g cm ⁻³]	1.514	1.542
Absorption coefficient μ [mm ⁻¹]	0.704	1.585
Index ranges	$-18 \leq h \leq 18$ $-28 \leq k \leq 28$ $-34 \leq l \leq 34$	$-20 \leq h \leq 20$ $-20 \leq k \leq 20$ $-21 \leq l \leq 21$
Reflections collected	66057	36676
Independent reflections	2398	14817
Parameters	168	1110
Max./min. transmission	1.10758/0.92733	0.92403/1.06031
Goodness-of-fit on F^2	1.118	1.005
Largest difference peak and hole [e Å ⁻³]	0.38 and -0.32	1.23 and -0.85
R_1 [$I > 2\sigma(I)$]	0.0363	0.0468
R_1 (all data)	0.0394	0.0778
wR_2 [$I > 2\sigma(I)$]	0.0980	0.1066
wR_2 (all data)	0.0994	0.1143

voltammetric analyzer with platinum wires as the counter and working electrode and 0.01 M Ag/AgNO₃ as the reference electrode. The measurements were performed at scan rates of 100 mV s⁻¹ for cyclic voltammetry experiments and 10 mV s⁻¹ for square-wave voltammetry experiments; 0.1 M (nBu₄N)(PF₆) was used as the supporting electrolyte in CH₃CN. Potentials are referenced to the ferrocene/ferrocenium couple [0.40 V vs. the saturated calomel electrode (SCE)],^[20] E_{1/2} = 90 ± 5 mV under the experimental conditions]. The elemental analyses were performed by the microanalytical laboratory of the chemical institutes of the University of Mainz.

Crystal-Structure Determinations

The intensity data were collected with a Bruker AXS Smart 1000 CCD diffractometer with an APEX II detector and an Oxford cooling system with Mo-K_α radiation (λ = 0.71073 Å) at 173(2) K and corrected for absorption and other effects. The diffraction frames were integrated with the SAINT package, and most were corrected for absorption with MULABS.^[21] The structures were solved by direct methods and refined by the full-matrix method based on F² with the SHELX software package.^[22] All non-hydrogen atoms were refined anisotropically, and the positions of all hydrogen atoms were generated with appropriate geometric constraints and allowed to ride on their respective parent carbon atoms with fixed isotropic thermal parameters. See Table 3 for the crystal and structure-refinement data.

CCDC 1555799 [for **8**(BF₄)₂] and 1555798 [for **9**][**8**](ZnCl₄) contain the supplementary crystallographic data for this paper. These data can be obtained free of charge from The Cambridge Crystallographic Data Centre.

DFT Calculations: The DFT calculations of the zinc complexes were performed with the ORCA program package (version 3.0.2).^[23] Tight convergence criteria were chosen for all calculations [keywords TightSCF and TightOpt, convergence criteria for the self-consistent field (SCF) part: energy change 1.0 × 10⁻⁸ E_h, 1-El. energy change 1.0 × 10⁻⁵ E_h, orbital gradient 1.0 × 10⁻⁵, orbital rotation angle 1.0 × 10⁻⁵, direct inversion of the iteration space (DIIS) error 5.0 × 10⁻⁷; for geometry optimizations: energy change: 1.0 × 10⁻⁶ E_h, maximum gradient 1.0 × 10⁻⁴ E_h bohr⁻¹, root mean square (RMS) gradient 3.0 × 10⁻⁵ E_h bohr⁻¹, maximum displacement 21.0 × 10⁻³ bohr, RMS displacement 6.0 × 10⁻⁴ bohr]. All calculations used the resolution of identity (Split-RI-J) approach for the Coulomb term in combination with the chain-of-spheres approximation for the exchange term (COSX).^[24] The geometry optimizations were performed with the B3LYP functional^[25] in combination with the split-valence triple-ζ basis set def2-TZVP of Ahlrichs for all atoms.^[26] The optimized geometries were confirmed to be local minima on the respective potential energy surface by subsequent numerical frequency analysis (N_{imag} = 0). TD-DFT calculations were performed at the same level of theory. The zeroth order regular approximation (ZORA) was used to describe relativistic effects in all calculations.^[27] The empirical dispersion correction D3(BJ) of Grimme was employed.^[28] Explicit counterions and solvent molecules were neglected. Fifty vertical transitions were calculated for the TD-DFT calculations.

[Zn(ddpd)₂](BF₄)₂ [8(BF₄)₂]: Zinc(II) tetrafluoroborate hexahydrate (128 mg, 0.41 mmol) and ddpd (303 mg, 1.04 mmol) were dissolved in ethanol (20 mL). The colorless solution was stirred at room temperature for 24 h. The resulting colorless precipitate was collected by filtration and washed once with diethyl ether (30 mL). The product was dried under reduced pressure. The diffusion of diethyl ether into a concentrated CH₃CN solution yielded diffraction-quality crystals. Yield: 290 mg (0.353 mmol, 86 %). ¹H NMR (CD₃CN, 400 MHz): δ = 8.06 (t, ³J_{H,H} = 8.3 Hz, 2 H, H¹), 7.92 (ddd, ³J_{H,H} = 8.6, ³J_{H,H} =

7.4 Hz, ⁴J_{H,H} = 2.0 Hz, 4 H, H⁷), 7.73 (ddd, ³J_{H,H} = 5.4, ⁴J_{H,H} = 1.9 Hz, ⁵J_{H,H} = 0.6 Hz, 4 H, H⁹), 7.15 (d, ³J_{H,H} = 8.2 Hz, 4 H, H²), 7.12 (d, ³J_{H,H} = 8.6 Hz, 4 H, H⁶), 6.99 (ddd, ³J_{H,H} = 7.3, ³J_{H,H} = 5.5 Hz, ⁴J_{H,H} = 0.7 Hz, 4 H, H⁸), 2.91 (s, 12 H, H⁴) ppm. ¹³C NMR (CD₃CN, 100 MHz): δ = 158.0 (s, C⁵), 157.0 (s, C³), 147.3 (s, C⁹), 143.4 (s, C¹), 142.8 (s, C⁷), 119.7 (s, C⁸), 114.4 (s, C⁶), 113.6 (s, C²), 40.0 (s, C⁴) ppm. MS (ESI+): m/z (%) = 292.1 (100) [ddpd + H]⁺, 323.1 (40) [M - 2BF₄]²⁺, 374.08 (10) [Zn(ddpd)F]⁺. C₃₄H₃₄B₂F₈N₁₀Zn (821.69): calcd. C 49.70, H 4.17, N 17.05; found C 49.24, H 3.92, N 16.92, UV/Vis: λ_{abs} (ε, M⁻¹ cm⁻¹) = 308 (31100), 265 (20900, sh), 248 (27500) nm. IR (KBr): ν̄ = 3444 (br, crystal water), 3110 (w, CH_{ar}), 2972 (w, CH_{al}), 2912 (w, CH_{al}), 2835 (w, CH_{al}), 2600 (w, CH_{al}), 1584 (s), 1492 (s), 1363 (m), 1335 (m), 1232 (m), 1181–977 (br. s, BF), 777 (m) cm⁻¹. CV (CH₃CN): E_p = 1170, 1340, 1670 mV versus Fc/Fc⁺.

[Zn(ddpd)Cl₂][Zn(ddpd)₂][ZnCl₄] {9}[8](ZnCl₄): Anhydrous zinc(II) chloride (73 mg, 0.54 mmol) and ddpd (331 mg, 1.13 mmol) were dissolved in ethanol (20 mL). The colorless solution was stirred at room temperature for 2 h, and the solvent was removed under reduced pressure. The resulting mixture of a colorless solid and a yellow oil was dissolved in acetonitrile (25 mL). After the addition of diethyl ether (25 mL), the colorless solid that precipitated was collected by filtration. The solid was washed with diethyl ether (30 mL) and then dissolved in acetonitrile, and the solvent was removed under reduced pressure. The product was dried under reduced pressure. The diffusion of diethyl ether into a concentrated CH₃CN solution yielded diffraction-quality crystals. Yield: 194 mg (0.151 mmol, 84 %). ¹H NMR (CD₃CN, 400 MHz): δ = 8.48 (br s, 2 H), 8.05 (t, ³J_{H,H} = 8.3 Hz, 2 H, H¹), 7.92 (ddd, ³J_{H,H} = 8.6, ³J_{H,H} = 7.4 Hz, ⁴J_{H,H} = 2.0 Hz, 4 H, H⁷), 7.72 (ddd, ³J_{H,H} = 5.4, ⁴J_{H,H} = 1.9 Hz, ⁵J_{H,H} = 0.6 Hz, 4 H, H⁹, H^x), 7.23 (d, ³J = 8.4 Hz, 2 H), 7.14 (d, ³J_{H,H} = 8.2 Hz, 4 H, H²), 7.11 (d, ³J_{H,H} = 8.6 Hz, 4 H, H⁶), 6.98 (ddd, ³J_{H,H} = 7.3, ³J_{H,H} = 5.5 Hz, ⁴J_{H,H} = 0.7 Hz, 4 H, H⁸), 3.50 (s, 6 H, H⁴) 2.91 (s, 12 H, H⁴) ppm. ¹³C NMR (CD₃CN, 100 MHz): δ = 158.0 (s, C⁵), 157.0 (s, C³), 148.5, 147.3 (s, C⁹), 143.4 (s, C¹), 142.8 (s, C⁷), 119.7 (s, C⁸), 114.5 (s, C⁶), 113.6 (s, C²), 40.0 (s, C⁴) ppm. MS (ESI+): m/z (%) = 292.1 (100) [ddpd + H]⁺, 323.1 (6) [Zn(ddpd)₂]²⁺, 390.0 (27) [ZnCl(ddpd)]⁺. C₃₄H₃₄B₂F₈N₁₀Zn (821.69): calcd. C 47.75, H 4.01, N 16.38; found C 47.31, H 3.83, N 16.04. UV/Vis: λ_{abs} (ε, M⁻¹ cm⁻¹) = 325 (41600, sh), 308 (45000), 267 (38900), 249 (39300) nm.

Acknowledgments

This work was financially supported by the Deutsche Forschungsgemeinschaft (GSC 266, Materials Science in Mainz, scholarship for S. O., HE 2778/10-1 and RE 1203/23-1). Funding from the internal university research funds of the Johannes Gutenberg University, Mainz, is gratefully acknowledged. Parts of this research were conducted using the supercomputer Mogon and advisory services offered by Johannes Gutenberg University Mainz (www.hpc.uni-mainz.de), which is a member of the AHRP and the Gauss Alliance e.V. We thank Regine Jung-Pothmann for the collection of the diffraction data.

Keywords: Luminescence · Photophysics · N ligands · Tridentate ligands · Zinc

- [1] a) J. V. Folgado, W. Henke, R. Allmann, H. Stratemeier, D. Beltran-Porter, T. Rojo, D. Reinen, *Inorg. Chem.* **1990**, *29*, 2035–2042; b) R. Docherty, F. Tuna, C. A. Kilner, E. J. L. McInnes, M. A. Halcrow, *Chem. Commun.* **2012**, *48*, 4055–4057; c) G. H. Eom, H. M. Park, M. Y. Hyun, S. P. Jang, C. Kim, J. H. Lee, S. J. Lee, S.-J. Kim, Y. Kim, *Polyhedron* **2011**, *30*, 1555–1564; d)

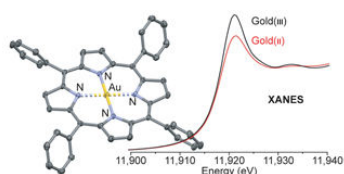
- M. Kurihara, K. Ozutsumi, T. Kawashima, *J. Solution Chem.* **1995**, *24*, 719–734.
- [2] X. M. Chen, R. Q. Wang, X. L. Yu, *Acta Crystallogr., Sect. C* **1995**, *51*, 1545–1547.
- [3] a) J. S. Judge, W. M. Reiff, G. M. Intille, P. Ballway, W. A. Baker, *J. Inorg. Nucl. Chem.* **1967**, *29*, 1711–1716; b) J. E. Douglas, C. J. Wilkins, *Inorg. Chim. Acta* **1969**, *3*, 635–638; c) G. Morgan, F. H. Burstall, *J. Chem. Soc.* **1937**, 1649–1655.
- [4] a) D. E. C. Corbridge, E. G. Cox, *J. Chem. Soc.* **1956**, 594; b) F. W. B. Einstein, B. R. Penfold, *Acta Crystallogr.* **1966**, *20*, 924–926; c) C.-C. Kong, J.-Z. Zhou, J.-H. Yu, S.-L. Li, *Acta Crystallogr., Sect. E* **2014**, *70*, m382–m383.
- [5] a) H. Kooijman, A. L. Spek, A. Mulder, K. van Bommel, W. Verboom, D. N. Reinhoudt, *CCDC 137586: Experimental Crystal Structure Determination*, **2000**; b) M. Vlasse, T. Rojo, D. Beltran-Porter, *Acta Crystallogr., Sect. C* **1983**, *39*, 560–563.
- [6] a) A. Hauser, A. Vef, P. Adler, *J. Chem. Phys.* **1991**, *95*, 8710–8717; b) S. Schenker, A. Hauser, W. Wang, I. Chan, *Chem. Phys. Lett.* **1998**, *297*, 281–286.
- [7] H. Riesen, L. Wallace, E. Krausz, *Inorg. Chem.* **1996**, *35*, 6908–6909.
- [8] A. Breivogel, C. Förster, K. Heinze, *Inorg. Chem.* **2010**, *49*, 7052–7056.
- [9] a) S. Otto, M. Grabolle, C. Förster, C. Kreitner, U. Resch-Genger, K. Heinze, *Angew. Chem. Int. Ed.* **2015**, *54*, 11572–11576; *Angew. Chem.* **2015**, *127*, 11735–11739; b) S. Otto, N. Scholz, T. Behnke, U. Resch-Genger, K. Heinze, *Chem. Eur. J.* **2017**, *23*, 12131–12135; c) S. Otto, A. M. Nauth, E. Ermilov, N. Scholz, A. Friedrich, U. Resch-Genger, S. Lochbrunner, T. Opatz, K. Heinze, *ChemPhotoChem* **2017**, *1*, 344–349; d) C. Förster, K. Mack, L. M. Carrella, V. Ksenofontov, E. Rentschler, K. Heinze, *Polyhedron* **2013**, *52*, 576–581; e) C. Förster, T. E. Gorelik, U. Kolb, V. Ksenofontov, K. Heinze, *Eur. J. Inorg. Chem.* **2015**, 920–924; f) A. K. C. Mengel, W. Cho, A. Breivogel, K. Char, Y. Soo Kang, K. Heinze, *Eur. J. Inorg. Chem.* **2015**, 3299–3306; g) K. Mack, A. Wunsche von Leupoldt, C. Förster, M. Ezhevskaya, D. Hinderberger, K. W. Klinkhammer, K. Heinze, *Inorg. Chem.* **2012**, *51*, 7851–7858; h) A. K. C. Mengel, C. Förster, A. Breivogel, K. Mack, J. R. Ochsmann, F. Laquai, V. Ksenofontov, K. Heinze, *Chem. Eur. J.* **2015**, *21*, 704–714; i) A. K. C. Mengel, C. Bissinger, M. Dorn, O. Back, C. Förster, K. Heinze, *Chem. Eur. J.* **2017**, *23*, 7920–7931; j) A. Breivogel, M. Meister, C. Förster, F. Laquai, K. Heinze, *Chem. Eur. J.* **2013**, *19*, 13745–13760; k) A. Breivogel, C. Kreitner, K. Heinze, *Eur. J. Inorg. Chem.* **2014**, 5468–5490; l) A. Breivogel, M. Park, D. Lee, S. Klassen, A. Kühnle, C. Lee, K. Char, K. Heinze, *Eur. J. Inorg. Chem.* **2014**, 288–295; m) C. Kreitner, A. K. C. Mengel, T. K. Lee, W. Cho, K. Char, Y. S. Kang, K. Heinze, *Chem. Eur. J.* **2016**, *22*, 8915–8928.
- [10] a) R. Allmann, W. Henke, D. Reinen, *Inorg. Chem.* **1978**, *17*, 378–382; b) M. I. Arriortua, T. Rojo, J. M. Amigó, G. Germain, J. P. Declercq, *Acta Crystallogr., Sect. B* **1982**, *38*, 1323–1324; c) W. Henke, D. Reinen, *Z. Anorg. Allg. Chem.* **1977**, *436*, 187–200; d) S. Kremer, W. Henke, D. Reinen, *Inorg. Chem.* **1982**, *21*, 3013–3022; e) J. Valdés-Martínez, R. A. Toscano, D. Salazar-Mendoza, *Acta Crystallogr., Sect. E* **2001**, *57*, m331–m332.
- [11] a) E. C. Constable, K. Harris, C. E. Housecroft, M. Neuburger, J. A. Zampese, *CrystEngComm* **2010**, *12*, 2949; b) C. Janiak, *J. Chem. Soc., Dalton Trans.* **2000**, 3885–3896; c) M. L. Scudder, H. A. Goodwin, I. G. Dance, *New J. Chem.* **1999**, *23*, 695–705.
- [12] A. W. Addison, T. N. Rao, J. Reedijk, J. van Rijn, G. C. Verschoor, *J. Chem. Soc., Dalton Trans.* **1984**, 1349–1356.
- [13] a) N. Yoshikawa, S. Yamabe, N. Kanehisa, H. Takashima, K. Tsukahara, *J. Phys. Org. Chem.* **2009**, *22*, 410–417; b) N. Yoshikawa, S. Yamabe, N. Kanehisa, T. Inoue, H. Takashima, K. Tsukahara, *J. Phys. Org. Chem.* **2010**, *23*, 431–439; c) U. Resch-Genger, Q. Y. Li, J. L. Bricks, V. Kharlanov, W. Rettig, *J. Phys. Chem. A* **2006**, *110*, 10956–10971.
- [14] R. G. Pearson, F. V. Williams, *J. Am. Chem. Soc.* **1953**, *75*, 3073–3075.
- [15] I. Kaljurand, A. Kütt, L. Sooväli, T. Rodima, V. Mäemets, I. Leito, I. A. Koppel, *J. Org. Chem.* **2005**, *70*, 1019–1028.
- [16] G. Albano, V. Balzani, E. C. Constable, M. Maestri, D. R. Smith, *Inorg. Chim. Acta* **1998**, *277*, 225–231.
- [17] a) S. Bhowmik, B. N. Ghosh, V. Marjomäki, K. Rissanen, *J. Am. Chem. Soc.* **2014**, *136*, 5543–5546; b) X. Bi, Y. Pang, *J. Phys. Chem. B* **2016**, *120*, 3311–3317.
- [18] a) C. Scarborough, K. M. Lancaster, S. DeBeer, T. Weyhermüller, S. Sproules, K. Wieghardt, *Inorg. Chem.* **2012**, *51*, 3718–3732; b) M. Wang, J. England, T. Weyhermüller, K. Wieghardt, *Inorg. Chem.* **2014**, *53*, 2276–2287; c) B. de Bruin, E. Bill, E. Bothe, T. Weyhermüller, K. Wieghardt, *Inorg. Chem.* **2000**, *39*, 2936–2947; d) M. K. Kadirov, K. V. Kholin, E. Y. Tselishcheva, V. A. Burirov, A. R. Mustafina, *Russ. Chem. Bull.* **2013**, *62*, 1327–1331.
- [19] a) C. Würth, J. Pauli, C. Lochmann, M. Spieles, U. Resch-Genger, *Anal. Chem.* **2012**, *84*, 1345–1352; b) C. Würth, M. G. González, R. Niessner, U. Panne, C. Haisch, U. R. Genger, *Talanta* **2012**, *90*, 30–37; c) C. Würth, D. Geissler, T. Behnke, M. Kaiser, U. Resch-Genger, *Anal. Bioanal. Chem.* **2015**, *407*, 59–78.
- [20] N. G. Connelly, W. E. Geiger, *Chem. Rev.* **1996**, *96*, 877–910.
- [21] a) R. H. Blessing, *Acta Crystallogr., Sect. A* **1995**, *51*, 33–38; b) *SMART Data Collection and SAINT-Plus Data Processing Software for the SMART System (various versions)*, Bruker Analytical X-ray Instruments, Inc., Madison, WI, **2000**.
- [22] a) G. M. Sheldrick, *SHELXL-2014/7*, University of Göttingen, **2014**; b) G. M. Sheldrick, *Acta Crystallogr., Sect. A* **2015**, *71*, 3–8.
- [23] F. Neese, *WIREs Comput. Mol. Sci.* **2012**, *2*, 73–78.
- [24] a) F. Neese, F. Wennmohs, A. Hansen, U. Becker, *Chem. Phys.* **2009**, *356*, 98–109; b) R. Izsak, F. Neese, *J. Chem. Phys.* **2011**, *135*, 144105.
- [25] A. D. Becke, *J. Chem. Phys.* **1993**, *98*, 5648–5652.
- [26] a) A. Schäfer, H. Horn, R. Ahlrichs, *J. Chem. Phys.* **1992**, *97*, 2571–2577; b) A. Schäfer, C. Huber, R. Ahlrichs, *J. Chem. Phys.* **1994**, *100*, 5829–5835.
- [27] a) A. Hönnerscheid, L. van Wüllen, R. Dinnebier, M. Jansen, J. Rahmer, M. Mehring, *Phys. Chem. Chem. Phys.* **2004**, *6*, 2454–2460; b) D. A. Pantazis, X.-Y. Chen, C. R. Landis, F. Neese, *J. Chem. Theory Comput.* **2008**, *4*, 908–919; c) E. van Lenthe, E. J. Baerends, J. G. Snijders, *J. Chem. Phys.* **1993**, *99*, 4597–4610.
- [28] a) S. Grimme, J. Antony, S. Ehrlich, H. Krieg, *J. Chem. Phys.* **2010**, *132*, 154104; b) S. Grimme, S. Ehrlich, L. Goerigk, *J. Comput. Chem.* **2011**, *32*, 1456–1465.

Received: August 4, 2017

3.8 Structure and reactivity of a mononuclear gold(II) complex

Sebastian Preiß, Christoph Förster, Sven Otto, Matthias Bauer, Patrick Müller, Dariush Hinderberger, Haleh Hashemi Haeri, Luca Carella and Katja Heinze

Nat. Chem. **2017**, *9*, 1249–1255.



Mononuclear gold(II) complexes are very labile (and thus very rare) species. Now, a gold(II) porphyrin complex has been isolated and characterized, and its reactivity towards dioxygen, nitrosobenzene and acids investigated. Owing to a second-order Jahn–Teller distortion, the gold atoms were found to adopt a 2+2 coordination mode in a planar N₄ environment.

Author Contributions

Sebastian Preiß synthesized the gold complexes presented in this manuscript, carried out the X-band EPR, NMR, infrared, UV-vis and mass spectra and studied the reactivity. Sven Otto made the quantum chemical calculations and Christoph Förster solved and refined the crystal structure. Dariush Hinderberger and Haleh Hashemi Haeri measured and interpreted the Q-band EPR spectra at the *Martin-Luther Universität* in Halle, Germany, Patrick Müller and Matthias Bauer measured and interpreted the X-ray absorption spectra at the University of Paderborn, Germany and Luca Carella measured the magnetic susceptibility data. The manuscript was written by Katja Heinze.

Supporting Information

for this article is found at pp. 274.

“Preiß, S.; Förster, C.; Otto, S.; Bauer, M.; Müller, P.; Hinderberger, D.; Haeri, H. H.; Carella, L.; Heinze, K. *Nat. Chem.* **2017**, *9*, 1249–1255. - Published by The Royal Society of Chemistry.”

Structure and reactivity of a mononuclear gold(II) complex

Sebastian Preiß¹, Christoph Förster¹, Sven Otto^{1,2}, Matthias Bauer³, Patrick Müller³,
Dariush Hinderberger⁴, Haleh Hashemi Haeri⁴, Luca Carella¹ and Katja Heinze^{1*}

Mononuclear gold(II) complexes are very rare labile species. Transient gold(II) species have been suggested in homogeneous catalysis and in medical applications, but their geometric and electronic structures have remained essentially unexplored: even fundamental data, such as the ionic radius of gold(II), are unknown. Now, an unprecedentedly stable neutral gold(II) complex of a porphyrin derivative has been isolated, and its structural and spectroscopic features determined. The gold atom adopts a 2+2 coordination mode in between those of gold(III) (four-coordinate square planar) and gold(I) (two-coordinate linear), owing to a second-order Jahn–Teller distortion enabled by the relativistically lowered 6s orbital of gold. The reactivity of this gold(II) complex towards dioxygen, nitrosobenzene and acids is discussed. This study provides insight on the ionic radius of gold(II), and allows it to be placed within the homologous series of nd^9 Cu/Ag/Au divalent ions and the $5d^{8/9/10}$ Pt/Au/Hg ‘relativistic’ triad in the periodic table.

Over the past two decades, gold complexes have attracted a great deal of attention for their role in homogeneous catalysis^{1–3}. Most of the homogeneous gold (pre-)catalysts and intermediates have featured gold in the +I and +III oxidation states^{4–7}, but gold(II) species have also recently been proposed as transient intermediates in photocatalysis, for example by Toste, Glorius and Hashmi and their co-workers^{8–14}. Yet, currently there is a lack of spectroscopic and/or structural evidence for mononuclear gold(II) intermediates in homogeneous catalysis.

In mononuclear species, gold is well known in its favoured oxidation states +I and +III, whereas the +II oxidation state is only very rarely realized¹⁵. Typically, mononuclear Au(II) species dimerize into $[\text{Au(II)}-\text{Au(II)}]^{4+}$ dumbbell complexes or disproportionate into Au(I) and Au(III) (refs 15,16). Only six genuine mononuclear Au(II) complexes have been characterized structurally so far^{17–20}. All of them are ionic compounds and most have been trapped only at low temperature in HF/SbF₅ matrices^{17,19,20}. Apart from a room-temperature X-band electron paramagnetic resonance (EPR) spectrum¹⁸, neither further spectroscopic data nor reactivity or stability studies have been reported so far. The formation of a gold(II) phthalocyanine complex has been reported based on an EPR spectrum²¹, but its preparation could not be reproduced and consequently further characterization is lacking²².

Here we describe the preparation, isolation and characterization of a stable mononuclear gold(II) complex. Gold(III) porphyrin cations have been used as electron acceptors in artificial photosynthetic charge-separation systems^{23–25}. It has also been shown that, after a photoinduced one-electron transfer to a gold(III) porphyrin cation, a gold(II) oxidation state prevails over the gold(III) porphyrin radical anion valence isomer. Indeed, this gold(II) oxidation state had been assigned unambiguously by EPR evidence on species generated *in situ* by the chemical reduction of gold(III) porphyrins^{26–28}. Isolation or further characterization of this material has, however, not yet been reported. Gold(III) porphyrins are used as potent drugs for cancer treatment^{29–32}, but their

biological mode-of-action has not yet been identified fully, and redox reactions, such as those discussed below, might play a role.

For the starting point of this synthesis, we chose a gold(III) porphyrin that was chemically reduced to gold(II) by stoichiometric amounts of cobaltocene or KC₈ and by excess 1-benzyl-1,4-dihydro-nicotinamide. Isolation and purification was then achieved by sublimation or recrystallization. The gold(II) complex was characterized by EPR, NMR, X-ray, ultraviolet–visible (UV–vis) and infrared absorption spectroscopy, as well as by magnetic susceptibility and X-ray diffraction (XRD) analyses. Its reactivity towards oxygen, nitrosobenzene, water and acids is disclosed.

Results and discussion

Synthesis and spectroscopy. $[\text{Au(III)}(\text{TPP})][\text{PF}_6]$ was prepared according to a literature method (in which H₂TPP is meso-tetraphenylporphyrin)²⁸. Reduction of this Au(III) porphyrin at room temperature ($E_{1/2} = -0.97, -1.65, -2.34$ V versus (vs) ferrocene) with 1 equiv. cobaltocene $\text{Co}(\eta^5\text{-C}_5\text{H}_5)_2$, which features a matching redox potential for the first reduction ($E_{1/2} = -1.3$ V vs ferrocene) and hence avoids overreduction, yields a solution of Au(TPP) (Fig. 1)²⁸.

The X-band EPR spectrum of this solution frozen to 77 K has been reported, and displays a rhombic EPR pattern ($g_{zz} = 2.182$, $g_{yy} = 2.056$ and $g_{xx} = 1.982$) with ¹⁹⁷Au and ¹⁴N hyperfine couplings²⁸. The *g* factor deviating from the free-electron value (2.0023) and the hyperfine coupling to gold are only consistent with a metal-centred radical and exclude the formulation of a porphyrin π radical anion²⁸. This electronic description is also consistent with the spin-density plot obtained by density functional theory (DFT) calculations (Fig. 2a). The EPR pattern of the isoelectronic $3d^9$ and $4d^9$ complexes Cu(TPP) and Ag(TPP) are axial, as expected (Cu(TPP), $g_{zz} = 2.187$ and $g_{yy} = g_{xx} = 2.032$; Ag(TPP), $g_{zz} = 2.109$ and $g_{yy} = g_{xx} = 2.038$) (ref. 33). The rhombicity of the X-band EPR spectrum of Au(TPP) was thus unexpected and remained unexplained. Yet, the Q-band EPR spectrum at 50 K of Au(TPP)

¹Institute of Inorganic Chemistry and Analytical Chemistry, Johannes Gutenberg-University, Duesbergweg 10–14, D-55128 Mainz, Germany. ²Graduate School Materials Science in Mainz, Staudingerweg 9, D-55128 Mainz, Germany. ³Department Chemie, University of Paderborn, Warburger Straße 100, D-33098 Paderborn, Germany. ⁴Institute of Chemistry, Martin-Luther-Universität Halle-Wittenberg, von-Danckelmann-Platz 4, D-06120 Halle (Saale), Germany. *e-mail: katja.heinze@uni-mainz.de

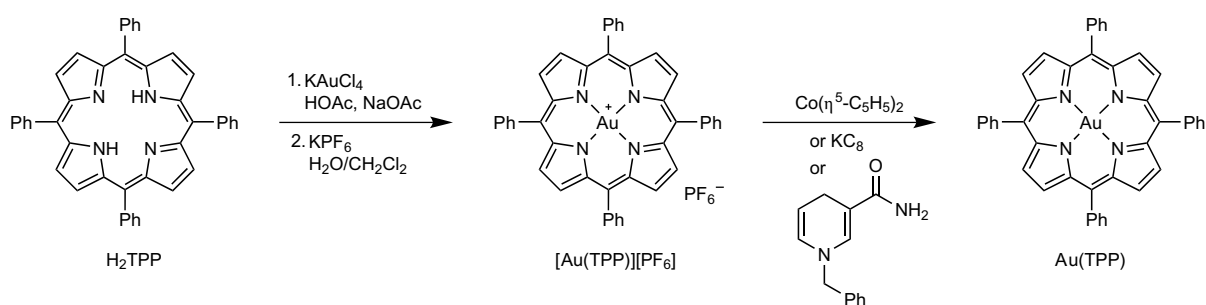


Figure 1 | Preparation of [Au(TPP)][PF₆] and chemical reduction to the Au(I) complex Au(TPP) by cobaltocene, KC₈ or 1-benzyl-1,4-dihydronicotinamide.

prepared *in situ* in CH₂Cl₂ fully confirms the rhombicity of the X-band EPR spectra (Fig. 2b; $g_{zz} = 2.123$, $g_{yy} = 2.057$ and $g_{xx} = 1.968$). Both Cu(TPP) and Ag(TPP) display EPR resonances at room temperature³³, whereas Au(TPP) is EPR silent at room temperature. Hence, the observed EPR spectra at low temperatures are not ascribable to traces of copper(II) or silver(II) species.

Encouraged by the stability of Au(TPP) even at room temperature, we attempted to isolate Au(TPP) from the [Au(TPP)][PF₆]/Co(η⁵-C₅H₅)₂ reaction mixture by sublimation. At approximately 573 K and 5×10^{-3} mbar, a dark purple-red material sublimed (Supplementary Fig. 1). This material showed the same X-band EPR spectra in frozen CH₂Cl₂ solution as the *in situ* prepared species. Reduction using stoichiometric amounts of KC₈ was also successful (Fig. 1). A liquid-injection field-desorption ionization (LIFDI) mass spectrum in THF under an inert atmosphere confirmed the composition of Au(TPP) (C₄₄H₂₈N₄Au), and displayed the expected peak at a mass-to-charge ratio of 809.4 (Supplementary Fig. 2). The UV-vis spectrum of Au(TPP) shows—apart from the expected Soret and Q bands of the porphyrin at 409 and 520 nm—conspicuous bands between 550 and 1,100 nm with extinction coefficients up to 6,500 M⁻¹ cm⁻¹ (Fig. 3 inset (in CH₂Cl₂:THF 4:1 at 77 K)). Such absorption bands in the visible spectral region are absent in the spectra of Cu(TPP) and Ag(TPP) (Supplementary Fig. 3).

Au(TPP) features an infrared absorption band at 595 cm⁻¹ that has no counterpart in the infrared spectra of either Cu(TPP) or [Au(TPP)][PF₆] (Supplementary Figs 4 and 5), which is discussed below. The magnetic susceptibility of Au(TPP) in the solid state at room temperature, $\chi_{\text{M}}T = 0.40$ cm³ K mol⁻¹, is consistent with a $S = \frac{1}{2}$ ground state of the bulk material with an isotropic g factor of $g_{\text{iso}} = 2.073$ (excellently matching the EPR spectral data), which rules out a disproportionation to diamagnetic 'Au(I)(TPP)Au(III)(TPP)' or a dimerization of the radicals to diamagnetic '(TPP)Au–Au(TPP)' in the solid state. At low temperatures, only a very weak intermolecular antiferromagnetic interaction between the radicals is present in the solid state, which precludes a strong metal–metal interaction (Supplementary Fig. 6). The room-temperature ¹H and ¹³C{¹H} NMR spectra of Au(TPP) in solution show paramagnetically shifted, yet reasonably sharp, NMR resonances. The chemical shifts depend slightly on the solvent (Supplementary Figs 7–14). All the observed ¹H resonances are successfully assigned based on ¹H NMR integrals and cross-peaks in the ¹H¹H correlation spectra. Clearly, the pyrrole β-hydrogen nuclei are strongly shifted, whereas the phenyl nuclei (*ortho*, *meta* and *para*) are less affected. This is consistent with a gold-centred radical with (5d_{x²-y²)¹ electron configuration, which supports the EPR and susceptibility data.}

To corroborate further the +II oxidation state of gold, we employed X-ray absorption near-edge structure (XANES) spectroscopy at the gold L₃ edge. Indeed, the first resonance of Au(TPP) after the edge step with a medium intensity caused by the 2p → 5d⁹ transition is perfectly in between that of the gold(I) reference Au₂Cl₂(xantphos) (5d¹⁰ electron configuration, zero

intensity for the 2p → 5d¹⁰ transition) (xantphos, 4,5-bis(diphenylphosphano)-9,9-dimethylxanthene) and the gold(III) porphyrin [Au(TPP)][PF₆] (5d⁸ electron configuration, high intensity for the 2p → 5d⁸ transition) according to deconvolution and difference spectra (Fig. 4 and Supplementary Fig. 15). All the accumulated data are consistent with a mononuclear gold(II) species with essentially negligible intermolecular magnetic interactions in the solid state. Yet, the rhombicity of the EPR resonance and the extra

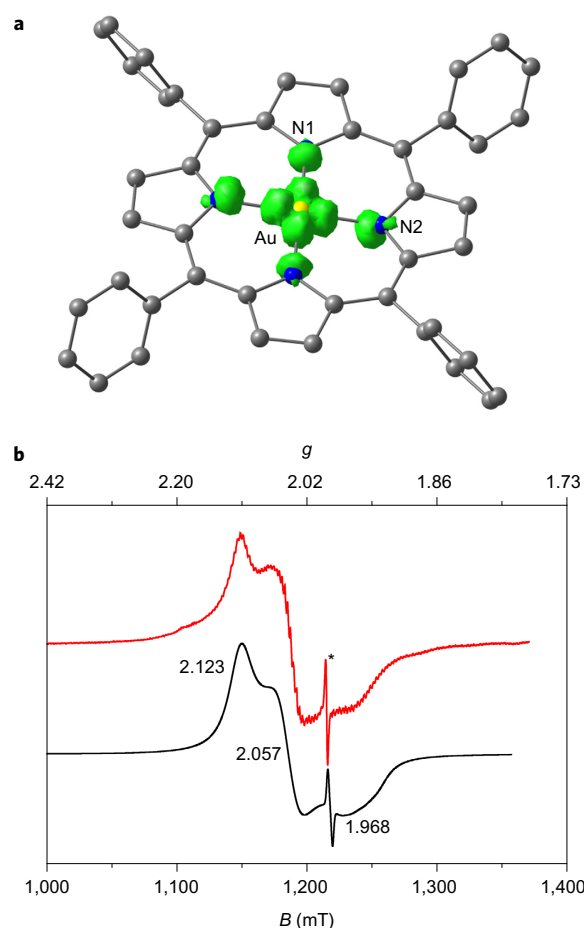


Figure 2 | Electronic structure of Au(TPP). **a**, The spin-density plot of Au(TPP) calculated by DFT (B3LYP, def2-TZVPP, ZORA, D3(BJ), COSMO CH₂Cl₂; isosurface value in green at 0.01 atomic units; H atoms omitted) illustrates the Au-centred radical. **b**, The Q-band EPR spectrum (red) of Au(TPP) in CH₂Cl₂ at 50 K (34 GHz) and the simulated spectrum (black) confirms the Au-centred spin density (the asterisk denotes the presence of a porphyrin radical, <30%).

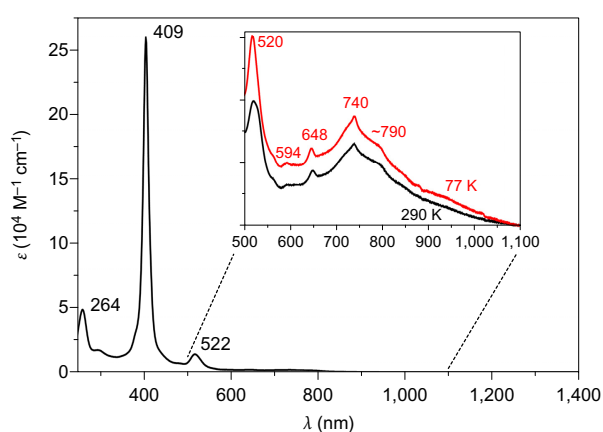


Figure 3 | Absorption spectrum of sublimed Au(TPP) in CH₂Cl₂ at 295 K. The inset shows the zoomed absorption spectrum in CH₂Cl₂:THF (4:1) at 290 K (black) and at 77 K (red), and demonstrates the low-energy charge-transfer bands of Au(TPP) in addition to the expected Soret and Q bands.

bands in the visible and infrared regions remain to be explained (*vide infra*).

Solid-state structure. Extended X-ray absorption fine structure (EXAFS) spectroscopy confirms that gold is coordinated by four nitrogen atoms both in [Au(TPP)][PF₆] and in Au(TPP), as expected, with Au–N distances of 2.010(20) Å and 2.031(20) Å, respectively. Distinct metrical differences of the different oxidation states could not be extracted from the EXAFS data (Supplementary Fig. 16 and Supplementary Table 1).

In the reported solid-state structure of [Au(III)(TPP)][ClO₄] (ref. 29), the coordination geometry of gold is square planar, as expected for a *d*⁸-M(TPP) complex³⁴. Gold–nitrogen distances amount to 2.032(5)–2.033(5) Å and N–Au–N angles to 89.8–90.1(2)°. The porphyrin core is slightly ruffled with the nitrogen atoms alternately 0.047 Å above and below the N₄ plane. The pyrrole rings are bent with Au–N–X angles $\tau = 170.6$ – 172.0° (X, centre of the β carbon atoms of the respective pyrrole).

Single-crystals of Au(TPP), suitable for single-crystal XRD analysis, were obtained by recrystallization from THF at room temperature (Fig. 5a,b). Au(TPP) crystallizes in the triclinic space group *P* $\bar{1}$, isomorphous with the triclinic modifications of H₂TPP (ref. 35) and Ag(TPP) (ref. 36). The molecules of Au(TPP) are isolated with Au...Au distances of 6.17 Å, which substantiates the very weak intermolecular magnetic interactions. No further solvent co-crystallized, as deduced already from the NMR data. The AuN₄ geometry is planar, similar to isoelectronic M(II)(TPP) complexes (M = Cu, Ag)^{36,37}. However, the Au–N bond lengths are significantly distinct, with Au1–N1 = 2.0586(24) and Au1–N2 = 2.0970(23) Å ($\Delta d = 0.038$ Å), whereas Cu(TPP) and Ag(TPP) exhibit essentially equal M–N distances ($\Delta d = 0.000$ and 0.019 Å, respectively)^{36,37}. This bond-length alternation of the AuN₄ core is achieved by bending two of the *trans*-positioned pyrrole rings (N2) with $\tau_2 = 165.2^\circ$, whereas the two other pyrrole rings (N1) are essentially coplanar ($\tau_1 = 178.1^\circ$). A similar bending is observed in H₂TPP, with $\tau_1 = 178.3^\circ$ and $\tau_2 = 169.1^\circ$ with the two NH groups pointing above and below the plane³⁵. The average M–N bond distance in Au(TPP) (2.078(2) Å) is smaller than that in Ag(TPP) (2.092(3) Å) (ref. 36), which suggests that gold(II) is slightly smaller than silver(II), similar to observations made by Schmidbauer and co-workers for the Ag(I)/Au(I) pair³⁸.

Electronic structure and quantum-chemical calculations. The *nd*⁹ electron configuration (in *D*_{4h} symmetry) can invoke a second-order

Jahn–Teller distortion³⁹ by including an excited state with an *nd*⁸ (*n*+1)*s*¹ electron configuration. In the *D*_{4h} point group, the *nd*⁹ ground state possesses *B*_{1g} symmetry, whereas the excited state with the electron configuration *nd*⁸ (*n*+1)*s*¹ belongs to the *A*_{1g} irreducible representation. The direct product *B*_{1g} × *A*_{1g} gives *B*_{1g}, which corresponds to a symmetry-lowering mode *D*_{4h} → *D*_{2h}, that is, the elongation/contraction of two *trans*-positioned Au–N distances. Within the constrained macrocyclic porphyrin ring, this bond-length differentiation is achieved by bending two *trans*-positioned pyrrole rings. In the series Cu–Ag–Au, the second-order Jahn–Teller distortion should increase because of the amplified relativistic lowering of the (*n*+1)*s* orbitals in that series^{40,41}. Indeed, the bond-length differences ($\Delta d = 0.000$ and 0.019–0.039 Å) and the increased bending ($\tau = 175.6^\circ$ and 169.7–165.2°) reflect this trend in the homologous Cu–Ag–Au series. Consequently, the symmetry lowering in Au(TPP) is ascribed to a second-order Jahn–Teller effect promoted by the relativistically lowered 6*s* orbital of gold. The observed distortion in the crystalline state also accounts for the rhombic EPR pattern observed for Au(TPP) in frozen solution (Fig. 2b). Vice versa, the EPR spectrum in frozen solution confirms that this distortion is an intrinsic property of four-coordinate gold(II) and should not be ascribed to packing effects in the crystal. Second-order Jahn–Teller distortions using the 6*s* orbital of gold have been invoked previously for the electronically excited triplet states of Au(I) (GeCl₃)(PR₃)₃, but experimental evidence had been lacking⁴².

In the series of gold oxidation states, *d*⁸-Au(III) prefers a square-planar geometry and *d*¹⁰-Au(I) a linear coordination mode. Gold in the intermediate oxidation state *d*⁹-Au(II) appears to prefer a 2+2 coordination geometry in between four and two coordination (Fig. 5a,b). As the solid-state structure of a [Au(TPP)][−] anion is not available (and probably would not correspond to Au(I) but to a Au(II) porphyrin radical anion species), a comparison with *5d*¹⁰ Hg(TPP) is more appropriate. The solid-state structure of meso-tetra-(*p*-cyanophenyl)porphyrin mercury(II) has been reported in which the mercury(II) ion sits 0.56 Å above the N₄ mean plane and features alternating short and long Hg–N distances (2.177(6), 2.255(6), 2.169(6) and 2.212(6) Å), and alternating τ angles (176.6°, 154.6°, 177.7° and 163.9°)⁴³. Hence, the increasing ionic radius of M(II) in the relativistic triad⁴⁰ with average M–N distances of 2.005, 2.078 and 2.204 Å (M = Pt, Au and Hg, respectively), might also add to the appreciable M(TPP) distortion. However,

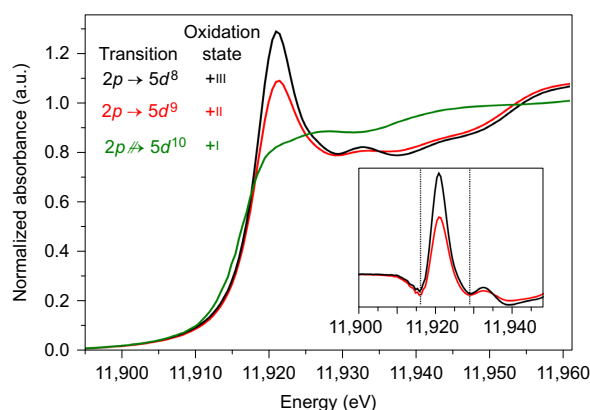


Figure 4 | Experimental normalized XANES spectra of [Au(TPP)][PF₆] (black), Au(TPP) (red) and Au₂Cl₂(xantphos) (green). The inset shows the difference spectra of Au(TPP) (red) and [Au(TPP)][PF₆] (black) with respect to the Au(I) reference Au₂Cl₂(xantphos); the grey dotted lines indicate the region in which analysis was carried out. These confirm the intermediate +II oxidation state of Au(TPP) (see Supplementary Information for the details). a.u., arbitrary units.

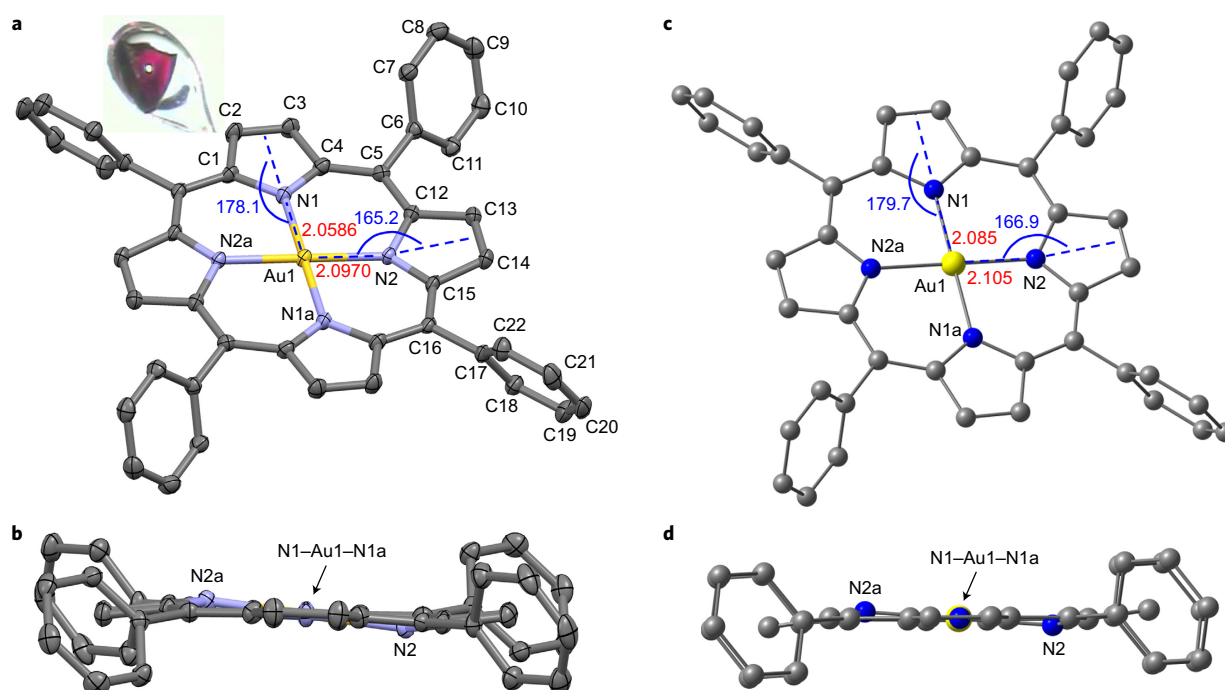


Figure 5 | Molecular structure of the neutral Au(II) complex Au(TPP). **a,b**, Top (**a**) and side (**b**) views along the N1–Au1–N1a axis of the structure obtained by XRD analysis (thermal ellipsoids at 50% probability, hydrogen atoms omitted). Inset: photograph of the examined crystal. **c,d**, Top (**c**) and side (**d**) views along the N1–Au1–N1a axis of the structure obtained by DFT calculation (B3LYP, def2-TZVPP, ZORA, D3(BJ), COSMO (CH₂Cl₂)). The side views illustrate the distorted geometry because of the second-order Jahn–Teller effect. Relevant distances are given in ångströms, and relevant angles are given in degrees.

the average M–N distances are smaller for gold(II) than for silver(II) because of the lanthanide contraction and the relativistic contraction, which suggests that the major part of the distortion arises from the second-order Jahn–Teller distortion and not from the ionic radius.

DFT calculations locate the spin density at the Au centre ($5d_{x^2-y^2}$) and reproduce the second-order Jahn–Teller distortion of Au(TPP) with $\Delta d = 0.020$ Å and $\tau = 166.9^\circ$ (Fig. 5c,d and Supplementary Figs 17 and 18). The distortion is also reflected in the calculated g factor ($g_{zz} = 2.3461$, $g_{yy} = 2.1102$ and $g_{xx} = 1.9625$), which reasonably fits to the experimental data. It is tempting to identify the extra infrared band at 595 cm^{-1} (Supplementary Figs 4 and 5) as the Jahn–Teller modes of Au(TPP) that involve the bending of two *trans* pyrroles. Bending modes of two *trans*-positioned pyrroles are calculated at 574 and 577 cm^{-1} (unscaled), which we tentatively assign to the experimentally observed extra infrared band of Au(TPP). DFT calculations find a transition state between two degenerate Jahn–Teller isomers at 15 kJ mol^{-1} (Supplementary Fig. 19). This low barrier is consistent with the observed averaged ^1H NMR signal set, which suggests an averaged fourfold symmetry of Au(TPP) at room temperature in solution. On cooling to -25°C , only the paramagnetic temperature-dependent Curie shift (*vide supra*, $\delta(\text{H}^b) \approx T^{-1}$) (Supplementary Figs 20 and 21) is detected and the ^1H NMR resonances neither broaden nor split. This demonstrates a rapid interconversion between the Jahn–Teller isomers on the ^1H NMR timescale.

The extra absorption bands of Au(TPP) observed in the visible/near-infrared (NIR) spectral region are assigned to metal-to-ligand charge transfer (MLCT) bands from the gold $5d_{x^2-y^2}$ orbital to porphyrin π^* orbitals and to ligand-to-metal charge transfer bands from the porphyrin's π orbitals to the half-filled $5d_{x^2-y^2}$ orbital according to time-dependent DFT calculations (Supplementary Fig. 22). This interpretation is in accordance with the gold(II) oxidation state that features a singly occupied $5d_{x^2-y^2}$ orbital. In contrast to Cu(TPP) and similar to Ag(TPP) (ref. 44), Au(TPP) is non-emissive

both at room temperature and at 77 K in a CH₂Cl₂:THF (4:1) glass. The non-emissive behaviour of Ag(TPP) has been ascribed to the presence of the low-energy, symmetry-forbidden MLCT state⁴⁴ and the same argument applies to Au(TPP), which also features such low-energy MLCT states.

Stability and reactivity. The inertness of Au(TPP) towards disproportionation (Fig. 6a), an otherwise common reactivity pattern of Au(II) complexes, is reflected in the electrochemical data with $\Delta E = 680\text{ mV}$ (THF, [*n*Bu₄N][PF₆]) for the oxidation and reduction of Au(TPP) to [Au(TPP)]⁺ and [Au(TPP)][−], respectively²⁸. The equilibrium constant for disproportionation is estimated as $K_D = \exp(-\Delta E/25.69) = 3 \times 10^{-12}$ at 298 K . Though the Au(III) porphyrin [Au(TPP)]⁺ is stable and easily accessible, the anion [Au(TPP)][−] appears not particularly favourable, either as a Au(I) valence isomer or, more likely, as a Au(II) porphyrin radical anion.

Thanks to the favourable NMR properties of both [Au(TPP)]⁺ and Au(TPP), the self-exchange reaction (Fig. 6b) between [Au(TPP)]⁺ and Au(TPP) is easily probed by ^1H NMR spectroscopy. The addition of Au(TPP) to a [Au(TPP)]⁺ solution in CD₂Cl₂ shifts the ^1H NMR resonances according to the amount of paramagnetic Au(TPP) added. No distinct resonances for Au(TPP) appear (Supplementary Fig. 23). Hence, electron transfer between [Au(TPP)]⁺ and Au(TPP) is rapid on the ^1H NMR timescale, which suggests small inner- and outer-sphere reorganizations.

The porphyrin macrocycle prohibits the typical dimerization^{15,16} of Au(II) complexes to dumbbell shaped [Au–Au]⁴⁺ dimers by blocking in-plane binding sites (Fig. 6c). According to DFT calculations, the spin density of the 17-valence-electron complex Au(TPP) is distributed in the σ system within the porphyrin AuN₄ plane (xy plane (Supplementary Fig. 18)) and not perpendicular to the ligand plane (z axis), which would be required for dimerization along the z axis. Hence, the formation of Au₂(TPP)₂ dimers is unfavourable for steric reasons.

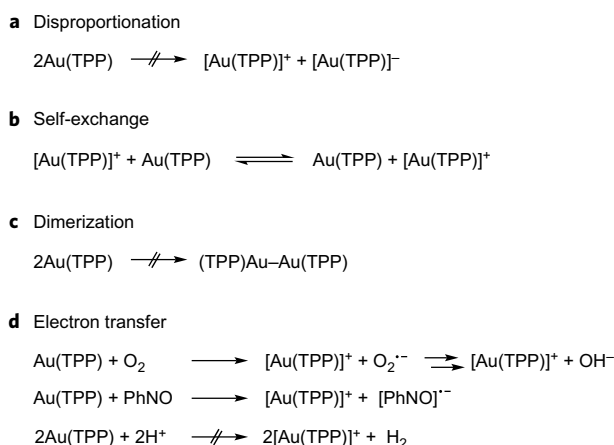


Figure 6 | Studies of the reactivity of Au(TPP). **a**, Towards disproportionation into $[\text{Au(TPP)}]^+$ and $[\text{Au(TPP)}]^-$. **b**, Towards electron self-exchange between $[\text{Au(TPP)}]^+$ and Au(TPP) . **c**, Towards dimerization to a metal-metal bonded dimer $\text{Au}_2(\text{TPP})_2$. **d**, Towards electron transfer to substrates O_2 , PhNO or H^+ .

The porphyrin macrocycle stabilizes the gold(II) oxidation state with respect to disproportionation and dimerization. This also accounts for the exceptional thermal stability of Au(TPP) (vide supra). Yet, redox reactions are feasible. Au(TPP) ($E_{1/2} = -0.96$ V vs ferrocene²⁸) is thermodynamically competent to reduce dioxygen to superoxide ($E_{1/2}(\text{O}_2(\text{dissolved})/\text{O}_2^{\cdot-}) = -0.18$ V vs the normal hydrogen electrode; -0.81 V vs ferrocene⁴⁵). ^1H NMR spectroscopy shows the appearance of $[\text{Au(TPP)}]^+$ after allowing Au(TPP) to stand under a non-inert atmosphere (air, humidity) in d_8 -THF, which confirms the electron transfer (Fig. 6d (Supplementary Fig. 24)). The infrared spectrum of the product shows an absorption band at $3,487\text{ cm}^{-1}$, characteristic for an OH stretching vibration. This infrared spectrum is fully congruent with the infrared spectrum of $[\text{Au(TPP)}][\text{OH}]$ obtained from the anion exchange of $[\text{Au(TPP)}][\text{PF}_6]$ with KOH (Supplementary Fig. 25). Peaks at m/z 825 are observed in the positive electrospray ionization mass spectra of both products and correspond to $[\text{Au(TPP)}(\text{OH})-\text{H}]^+$ (Supplementary Fig. 26). Hence, the final product of Au(TPP) and O_2 is $[\text{Au(TPP)}][\text{OH}]$, which confirms the further reduction of superoxide into hydroxide. Gold(III) hydroxido species are of fundamental importance for the water-splitting reaction and oxygen-reduction reaction (ORR), as has been elegantly demonstrated by Bochmann and co-workers using gold complexes of tridentate C–N–C pincer ligands⁴⁶. Yet, with tridentate ligands, mononuclear Au(II) complexes are not accessible because the dumbbell dimer (C–N–C)Au–Au(C–N–C) forms⁴⁷. In contrast to mononuclear Au(TPP) , this (C–N–C)Au(II)–Au(II)(C–N–C) dimer is kinetically incompetent in the ORR because of its strong Au–Au bond^{46,47}.

To demonstrate further the redox reactivity of Au(TPP) , the spin-trapping agent nitrosobenzene^{48,49} was added to Au(TPP) as an O_2 surrogate (Fig. 6d). The EPR resonance changes from the broad gold(II) resonance (Fig. 2b and Preiß *et al.*²⁸) to a narrow resonance around $g = 2.0$ (Supplementary Fig. 27). This is consistent with a nitroxyl radical anion without the participation of the metal centre^{49,50}. Obviously, electron transfer from Au(TPP) to PhNO without a strong coordination of the resulting $[\text{PhNO}]^{\cdot-}$ radical anion to gold(III)⁵⁰ has occurred. The reduction of PhNO to $[\text{PhNO}]^{\cdot-}$ resembles the initial step of the ORR by Au(TPP) , that is, the formation of reactive oxygen species (ROS) (Fig. 6d). The formation of ROS by $[\text{Au(TPP)}]^+$ drugs has been suggested as one of the pathways that leads to apoptosis^{29,30} and we present direct evidence for ROS formation from Au(TPP) and O_2 . Several natural redox mediators, such as glutathione, thioredoxins or NADH feature redox potentials close

to the Au(III)/Au(II) redox couple and hence the $[\text{Au(TPP)}]^{+/0}$ pair might play a role in, the biological mode of action of Au(III) porphyrin-based anticancer drugs, namely the reduction of $[\text{Au(TPP)}]^+$ to Au(TPP) followed by ROS formation with O_2 and $[\text{Au(TPP)}]^+$ regeneration (Fig. 6d). Indeed, excess 1-benzyl-1,4-dihydropyridine (as the NADH model⁵⁰) reduces $[\text{Au(TPP)}]^+$ to Au(TPP) in the presence of a base (Supplementary Fig. 28).

In the absence of O_2 , Au(TPP) is stable in the presence of water (Supplementary Fig. 29). The coordination of water, protodemetalation to give H_2TPP and the formation of H_2 and $[\text{Au(TPP)}]^+$ do not occur. Even with excess trifluoroacetic acid, Au(TPP) does not reduce protons (Fig. 6d and Supplementary Fig. 30). Hence, Au(TPP) catalyses the ORR, but not the proton reduction reaction. Neither oxygen donor ligands (water and THF) nor nitrogen donor ligands (pyridine) coordinate to Au(TPP) , as shown by ^1H NMR spectroscopy, because of the first-order Jahn–Teller effect that operates in the d^9 electron configuration³⁹.

Conclusion

In the mononuclear Au(II) complex Au(TPP) , the porphyrin macrocycle confers exceptional stability towards Au(II) by blocking the typical reactivity patterns (dimerization and disproportionation) of Au(II). In the planar N_4 coordination environment of Au(TPP) , Au(II) prefers a 2+2 coordination mode, in between that of Au(III) (four-coordinate square planar) and that of Au(I) (two-coordinate linear), because of a second-order Jahn–Teller distortion enabled by the relativistically lowered 6s orbital of Au. The degenerate Jahn–Teller distortion in the xy plane of the macrocycle is dynamic on the ^1H NMR timescale but is frozen in solid matrices.

Electron transfer between Au(TPP) and $[\text{Au(TPP)}]^+$ is fast on the ^1H NMR timescale. Electronic coupling is sufficiently large, although the electron formally transfers between the σ systems of Au ($5d_{x^2-y^2}$ orbitals) and not the π systems of the porphyrins. Electron transfer from Au(TPP) to O_2 gives $[\text{Au(TPP)}]^+$ and superoxide (ROS), and finally hydroxide. Similarly, Au(TPP) reduces PhNO to $[\text{PhNO}]^{\cdot-}$. In oxygen-free water and in the presence of acids, Au(TPP) is stable. The reduction of $[\text{Au(TPP)}]^+$ by an NADH model even produces Au(TPP) . The combined data suggest a decisive role of the $[\text{Au(TPP)}]^{+/0}$ redox couple capable of ROS generation in the presence of reductant and O_2 in Au-based anticancer drugs.

We anticipate that the ease of synthesis and exceptional stability of Au(TPP) will allow future studies of the reactivity of this first isolable Au(II) complex, for example, towards main-group elements, radicals and Lewis acids and bases. Furthermore, clever coordination-geometry design will allow the preparation and isolation of further mononuclear Au(II) complexes and will allow the exploration of this novel class of mononuclear Au(II) coordination compounds in the areas of catalysis, electron transfer and medicinal chemistry.

Methods

Full details of the employed methods are given in Supplementary Information.

Preparation of Au(TPP) by reduction with cobaltocene. Under an inert atmosphere, $[\text{Au(TPP)}][\text{PF}_6]$ (239 mg, 0.250 mmol) was dissolved in CH_2Cl_2 (20 ml). Cobaltocene ($\text{Co}(\eta^5\text{-C}_5\text{H}_5)_2$) (47 mg, 0.250 mmol) was added as a solid. After stirring for 1 h at room temperature, the solvent was removed under reduced pressure. The dark residue was sublimed at approximately 573 K and 5×10^{-3} mbar to give a dark purple material, yield 87 mg (0.107 mmol, 43%). Under these conditions, variable amounts of cobaltocene sublime concomitantly. The presence of some cobaltocene is only seen by NMR spectroscopy after re-oxidation to $[\text{Au(TPP)}]^+$ and cobaltocenium ions. Single crystals of Au(TPP) were obtained by recrystallization from THF at room temperature.

Preparation of Au(TPP) by reduction with KC_8 . Under an inert atmosphere, $[\text{Au(TPP)}][\text{PF}_6]$ (10.0 mg, 0.010 mmol) was dissolved in THF (10 ml). KC_8 (1.5 mg, 0.011 mmol) was added as a solid. After stirring for 12 h at room temperature, solid materials were removed by filtration and the solvent was removed under reduced

pressure. The dark residue was dissolved in CH_2Cl_2 (5 ml) and the brown solution was filtered to remove KPF_6 (the ^{31}P NMR spectrum of the material confirms the successful removal of KPF_6). The solvent was removed under reduced pressure to give the dark purple product in essentially quantitative yield, 7.9 mg (0.0098 mmol, 98%). ^1H NMR (CD_2Cl_2) δ (ppm) = 4.15 (H^{O}), 5.78 (H^{P}), 9.05 (H^{M}), 25.38 (H^{B}). ^1H NMR (d_8 -toluene) δ (ppm) = 2.45 (H^{O}), 4.65 (H^{P}), 9.22 (H^{M}), n.o. (H^{B}). ^1H NMR (d_8 -THF) δ (ppm) = 4.34 (H^{O}), 5.89 (H^{P}), 8.95 (H^{M}), 27.5 (H^{B}). $^{13}\text{C}\{^1\text{H}\}$ NMR (d_8 -THF) δ (ppm) = 133.8 (C^{M}), 137.4 (C^{O}), 230.4 (C^{P}), n.o. (C^{B}). FD^+ (LIFDI, THF) m/z (%) = 809.4 (100, M^+). Infrared (KBr) (cm^{-1}) 1,072(m), 1,015(s), 595(m). UV–vis–NIR (THF): λ (nm) (ϵ ($\text{M}^{-1}\text{cm}^{-1}$)) = 410 (158,480), 523 (10,685), 596 (2,380), 654 (3,865), 741 (5,150). Magnetism (298 K) $\chi_{\text{M}}T = 0.40\text{ cm}^3\text{ K mol}^{-1}$. Elemental analysis calculated (found) for $\text{C}_{44}\text{H}_{28}\text{AuN}_4$: C, 65.27 (65.06); H 3.49 (5.80); N 6.92 (5.13). The consistently low N values might point to nitride formation during combustion analysis.

Data availability. Atomic coordinates and structure factors for the crystal structure of **Au(TPP)** are deposited at the Cambridge Crystallographic Data Centre (CCDC) under the accession code CCDC 1520924; copies of the data can be obtained free of charge from www.ccdc.cam.ac.uk/data_request/cif. All the other data that support the findings of this study are available within Supplementary Information files, and are also available from the corresponding author on reasonable request.

Received 24 January 2017; accepted 27 June 2017;
published online 7 August 2017

References

- Fürstner, A. Gold and platinum catalysis—a convenient tool for generating molecular complexity. *Chem. Soc. Rev.* **38**, 3208–3221 (2009).
- Hashmi, A. S. K. Dual gold catalysis. *Acc. Chem. Res.* **47**, 864–876 (2014).
- Dorel, R. & Echavarren, A. M. Gold(I)-catalyzed activation of alkynes for the construction of molecular complexity. *Chem. Rev.* **115**, 9028–9072 (2015).
- Hashmi, A. K. S. Homogeneous gold catalysis beyond assumptions and proposals—characterized intermediates. *Angew. Chem. Int. Ed.* **49**, 5232–5241 (2010).
- Liu, L. P. & Hammond, G. B. Recent advances in the isolation and reactivity of organogold complexes. *Chem. Soc. Rev.* **41**, 3129–3139 (2012).
- Echavarren, A. M. & Obradors, C. Intriguing mechanistic labyrinths in gold(I) catalysis. *Chem. Commun.* **50**, 16–28 (2014).
- Joost, M., Amgoune, A. & Bourissou, D. Reactivity of gold complexes towards elementary organometallic reactions. *Angew. Chem. Int. Ed.* **54**, 15022–15045 (2015).
- Sahoo, B., Hopkinson, M. N. & Glorius, F. Combining gold and photoredox catalysis: visible light-mediated oxy- and aminoarylation of alkenes. *J. Am. Chem. Soc.* **135**, 5505–5508 (2013).
- Winston, M. S., Wolf, W. J. & Toste, F. D. Photoinitiated oxidative addition of CF_3I to gold(I) and facile aryl– CF_3 reductive elimination. *J. Am. Chem. Soc.* **136**, 7777–7782 (2014).
- Shu, X., Zhang, M., He, Y., Frei, H. & Toste, F. D. Dual visible light photoredox and gold-catalyzed arylative ring expansion. *J. Am. Chem. Soc.* **136**, 5844–5847 (2014).
- Tlahuext-Aca, A., Hopkinson, M. N., Sahoob, B. & Glorius, F. Dual gold/photoredox-catalyzed $\text{C}(\text{sp})\text{–H}$ arylation of terminal alkynes with diazonium salts. *Chem. Sci.* **7**, 89–93 (2016).
- Hopkinson, M. N., Tlahuext-Aca, A. & Glorius, F. Merging visible light photoredox and gold catalysis. *Acc. Chem. Res.* **49**, 2261–2272 (2016).
- Huang, L., Rudolph, M., Rominger, F. & Hashmi, A. S. K. Photosensitizer-free visible-light-mediated gold-catalyzed 1,2-difunctionalization of alkynes. *Angew. Chem. Int. Ed.* **55**, 4808–4813 (2016).
- Kim, S., Rojas-Martin, J. & Toste, D. F. Visible light-mediated gold-catalyzed carbon(sp^2)–carbon(sp) cross-coupling. *Chem. Sci.* **7**, 85–88 (2016).
- Gimeno, M. C. & Laguna, A. in *Comprehensive Coordination Chemistry II* Vol. 6 (eds McCleverty, J. A. & Meyer, T. J.) 999–1145 (Elsevier, 2005).
- Mohamed, A. A., Abdou, H. E. & Fackler, J. P. Jr. Coordination chemistry of gold(II) with amidinate, thiolate and ylido ligands. *Coord. Chem. Rev.* **254**, 1253–1259 (2010).
- Elder, S. H., Lucier, G. M., Hollander, F. J. & Bartlett, N. Synthesis of Au(II) fluoro complexes and their structural and magnetic properties. *J. Am. Chem. Soc.* **119**, 1020–1026 (1997).
- Blake, A. J. *et al.* Bis(1,4,7-trithiacyclononane)gold dication: a paramagnetic, mononuclear Au^{III} complex. *Angew. Chem. Int. Ed.* **29**, 197–198 (1990).
- Seidel, S. & Seppelt, K. Xenon as a complex ligand: the tetra xenono gold(II) cation in $\text{AuXe}_4^{2+}(\text{Sb}_2\text{F}_{11}^-)_2$. *Science* **290**, 117–118 (2000).
- Drews, T., Seidel, S. & Seppelt, K. Gold–xenon complexes. *Angew. Chem. Int. Ed.* **41**, 454–456 (2002).
- MacCragh, A. & Koski, W. S. The phthalocyanine of gold. *J. Am. Chem. Soc.* **87**, 2496–2497 (1965).
- Wong, E. W. Y. *et al.* Gold(II) phthalocyanine revisited: synthesis and spectroscopic properties of gold(III) phthalocyanine and an unprecedented ring-contracted phthalocyanine analogue. *Chem. Eur. J.* **18**, 12404–12410 (2012).
- Brun, A. M., Harriman, A., Heitz, V. & Sauvage, J. P. Charge transfer across oblique bisporphyrins: two-center photoactive molecules. *J. Am. Chem. Soc.* **113**, 8657–8663 (1991).
- Fukuzumi, S. *et al.* Metal-centered photoinduced electron transfer reduction of a gold(III) porphyrin cation linked with a zinc porphyrin to produce a long-lived charge-separated state in nonpolar solvents. *J. Am. Chem. Soc.* **125**, 14984–14985 (2003).
- Fortage, J. *et al.* Single-step electron transfer on the nanometer scale: ultra-fast charge shift in strongly coupled zinc porphyrin–gold porphyrin dyads. *Chem. Eur. J.* **14**, 3467–3480 (2008).
- Kadish, K. M. *et al.* Evidence that gold(III) porphyrins are not electrochemically inert: facile generation of gold(II) 5,10,15,20-tetrakis(3,5-di-*tert*-butylphenyl)porphyrin. *Chem. Commun.* 356–357 (2002).
- Ou, Z. *et al.* Substituent effects on the site of electron transfer during the first reduction for gold(III) porphyrins. *Inorg. Chem.* **43**, 2078–2086 (2004).
- Preiß, S., Melomedov, J., Wünsche von Leupoldt, A. & Heinze, K. Gold(III) tetraarylporphyrin amino acid derivatives: ligand or metal centred redox chemistry? *Chem. Sci.* **7**, 596–610 (2016).
- Che, C.-M. *et al.* Gold(III) porphyrins as a new class of anticancer drugs: cytotoxicity, DNA binding and induction of apoptosis in human cervix epithelioid cancer cells. *Chem. Commun.* 1718–1719 (2003).
- Wang, Y., He, Q. Y., Sun, R. W., Che, C. M. & Chiu, J. F. Gold(III) porphyrin 1a induced apoptosis by mitochondrial death pathways related to reactive oxygen species. *Cancer Res.* **65**, 11553–11564 (2005).
- Lum, C. T., Sun, R. W.-Y., Zou, T. & Che, C.-M. Gold(III) complexes inhibit growth of cisplatin-resistant ovarian cancer in association with upregulation of proapoptotic *PMS2* gene. *Chem. Sci.* **5**, 1579–1584 (2014).
- Hu, D. R. *et al.* Anticancer gold(III) porphyrins target mitochondrial chaperone Hsp60. *Angew. Chem. Int. Ed.* **55**, 1387–1391 (2016).
- Manoharan, P. T. & Rogers, M. T. in *Electron Spin Resonance of Metal Complexes* (ed. Yen, T. F.) 143–173 (Plenum, 1969).
- Hazell, A. Structure of (5,10,15,20-tetraphenyl-21H,23H-porphinato)platinum(II), $\text{C}_{44}\text{H}_{28}\text{N}_4\text{Pt}$. *Acta Cryst. C* **40**, 751–753 (1984).
- Silvers, S. J. & Tulinsky, A. The crystal and molecular structure of tris(4-tetraphenylporphyrin). *J. Am. Chem. Soc.* **89**, 3331–3337 (1967).
- Scheidt, W. R. *et al.* Crystal and molecular structure of the silver(II) and zinc(II) derivatives of meso-tetraphenylporphyrin. An exploration of crystal-packing effects on bond distance. *Inorg. Chem.* **25**, 795–799 (1986).
- Plaza, L. A. & Chojnacki, J. Influence of chloroform on crystalline products yielded in reactions of 5,10,15,20-tetraphenylporphyrin with HCl and copper(II) salts. *Acta Cryst. C* **86**, m24–m28 (2012).
- Bayler, A., Schier, A., Bowmaker, G. A. & Schmidbaur, H. Gold is smaller than silver. Crystal structures of [bis(trimesitylphosphine)gold(II)] and [bis(trimesitylphosphine)silver(II)] tetrafluoroborate. *J. Am. Chem. Soc.* **118**, 7006–7007 (1996).
- Pearson, R. G. Concerning Jahn–Teller effects. *Proc. Natl Acad. Sci. USA* **72**, 2104–2106 (1975).
- Leyva-Pérez, A. & Corma, A. Similarities and differences between the ‘relativistic’ triad gold, platinum, and mercury in catalysis. *Angew. Chem. Int. Ed.* **51**, 614–635 (2012).
- Pyykkö, P. Theoretical chemistry of gold. III. *Chem. Soc. Rev.* **37**, 1967–1997 (2008).
- Bojan, R. V. *et al.* Double Jahn–Teller distortion in AuGe complexes leading to a dual blue–orange emission. *ChemPlusChem* **81**, 176–186 (2016).
- Wang, M. C. *et al.* Mercury complexes of meso-tetra-(*p*-cyanophenyl)porphyrin and *N*-methylporphyrin: meso-tetra-(*p*-cyanophenyl)porphyrinatomercury(II) and chloro(*N*-methyl-meso-tetraphenylporphyrinato)mercury(II). *Inorg. Chem.* **40**, 6064–6068 (2001).
- Antipas, A., Dolphin, D., Gouterman, M. & Johnson, E. C. Porphyrins. 38. Redox potentials, charge transfer transitions, and emission of copper, silver, and gold complexes. *J. Am. Chem. Soc.* **100**, 7705–7709 (1978).
- Koppenol, W. H., Stanbury, D. M. & Bounds, P. L. Electrode potentials of partially reduced oxygen species, from dioxygen to water. *Free Radic. Biol. Med.* **49**, 317–322 (2010).
- Rosca, D.-A., Wright, J. A., Hughes, D. L. & Bochmann, M. Gold peroxide complexes and the conversion of hydroperoxides into gold hydrides by successive oxygen-transfer reactions. *Nat. Commun.* **4**, 2167 (2013).
- Dann, T. *et al.* Electrochemistry of Au^{II} and Au^{III} pincer complexes: determination of the Au^{II}–Au^{III} bond energy. *Chem. Commun.* **49**, 10169–10171 (2013).
- Neidlinger, A., Kienz, T. & Heinze, K. Spin trapping of carbon-centered ferrocenyl radicals with nitrosobenzene. *Organometallics* **34**, 5310–5320 (2015).
- Núñez-Vergara, L. J. *et al.* Nitrosobenzene: electrochemical, UV–visible and EPR spectroscopic studies on the nitrosobenzene free radical generation and its interaction with glutathione. *Electrochim. Acta* **45**, 3555–3561 (2000).
- Zhu, X.-Q. *et al.* Hydride, hydrogen atom, proton, and electron transfer driving forces of various five-membered heterocyclic organic hydrides and their reaction intermediates in acetonitrile. *J. Am. Chem. Soc.* **130**, 2501–2516 (2008).

Acknowledgements

Parts of this research were conducted using the supercomputer Mogon and advisory services offered by Johannes Gutenberg University Mainz (www.hpc.uni-mainz.de), which is a member of the AHRP and the Gauss Alliance. We thank P. Auerbach and M. Mondeshki for collecting the LIFDI mass spectra and assistance with the paramagnetic NMR spectra and R. Jung-Pothmann for collection of the diffraction data. This work was financially supported by the Deutsche Forschungsgemeinschaft (GSC 266, Materials Science in Mainz, scholarship for S.O.). PETRA III is acknowledged for the provision of beamtime at beamline P64. This article is dedicated to G. Huttner on the occasion of his 80th birthday.

Author contributions

S.P. synthesized $[\text{Au}(\text{TPP})][\text{PF}_6]$ and $\text{Au}(\text{TPP})$, measured the X-band EPR, NMR, infrared, UV-Vis and mass spectra and studied the reactivity, S.O. made the quantum chemical calculations, C.F. performed the single-crystal XRD analysis, D.H. and H.H.H. measured

and interpreted the Q-band EPR spectra, P.M. and M.B. measured and interpreted the X-ray absorption spectra and L.C. measured the magnetic susceptibility data. K.H. conceived and designed the experiments and wrote the paper. All of the authors discussed the results and commented on the manuscript.

Additional information

Supplementary information and chemical compound information are available in the [online version of the paper](#). Reprints and permissions information is available online at www.nature.com/reprints. Publisher's note: Springer Nature remains neutral with regard to jurisdictional claims in published maps and institutional affiliations. Correspondence and requests for materials should be addressed to K.H.

Competing financial interests

The authors declare no competing financial interests.

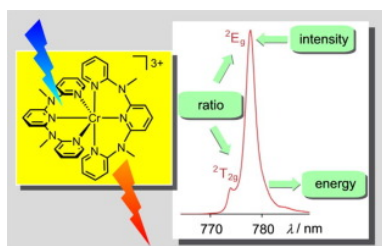
Summary and Outlook

The extraordinary properties of the molecular ruby $[\text{Cr}(\text{ddpd})_2]^{3+}$ have been summarized in the review article “*Understanding and exploiting long-lived near-infrared emission of a molecular ruby*”, which is presented in section 4.1.

4.1 Understanding and exploiting long-lived near-infrared emission of a molecular ruby

Sven Otto, Matthias Dorn, Cristoph Förster, Matthias Bauer, Michael Seitz and Katja Heinze

Coord. Chem. Rev. **2018**, *359*, 102–111.



Enabling strong and long-lived NIR emission from complexes with earth-abundant metal ions is exemplified by embedding chromium(III) in a very strong ligand field yielding the molecular ruby [Cr(ddpd)₂]³⁺. This review aims at illustrating the main non-radiative decay pathways for electronically excited chromium(III) complexes, namely back-intersystem crossing, excited state distortion and multiphonon relaxation and at controlling these pathways by molecular design. The case study of [Cr(ddpd)₂]³⁺ highlights recent successful design strategies and discusses first applications of the highly emissive 3d metal complex as optical sensor molecule and as photosensitizer.

Author Contributions

Sven Otto prepared [Cr₂(bpy)₄(μ-OH)₂](PF₆)₄ and Cristoph Förster solved and refined the crystal structure of [Cr₂(bpy)₄(μ-OH)₂](PF₆)₄ × CH₃CN × 0.5 H₂O. Matthias Dorn synthesized [Cr(ddpd)₂](BF₄)₃ and Matthias Bauer from the University of Paderborn, Germany performed the XANES spectroscopy on it. Michael Seitz conducted the chiral HPLC measurements at the University of Tübingen, Germany. The manuscript was written by Katja Heinze.

“Otto, S.; Dorn, M.; Förster, C.; Bauer, M.; Seitz, M.; Heinze, K. *Chem. Coord. Rev.* **2018**, *359*, 102–111. - Published by The Royal Society of Chemistry.”



Contents lists available at ScienceDirect

Coordination Chemistry Reviews

journal homepage: www.elsevier.com/locate/ccr

Review

Understanding and exploiting long-lived near-infrared emission of a molecular ruby

Sven Otto^{a,b}, Matthias Dorn^a, Christoph Förster^a, Matthias Bauer^c, Michael Seitz^d, Katja Heinze^{a,*}^a Institute of Inorganic Chemistry and Analytical Chemistry, Johannes Gutenberg University of Mainz, Duesbergweg 10-14, 55128 Mainz, Germany^b Graduate School Materials Science in Mainz, Staudingerweg 9, 55128 Mainz, Germany^c Department Chemie, University Paderborn, Warburger Straße 100, 33098 Paderborn, Germany^d Institute of Inorganic Chemistry, University of Tübingen, Auf der Morgenstelle 18, 72076 Tübingen, Germany

ARTICLE INFO

Article history:

Received 26 November 2017

Received in revised form 29 December 2017

Accepted 3 January 2018

Keywords:

Chromium

Spin-flip

Ligand field theory

Luminescence

Excited state dynamics

Ligand bite angle

ABSTRACT

Enabling strong and long-lived NIR emission from complexes with earth-abundant metal ions is exemplified by embedding chromium(III) in a very strong ligand field yielding the molecular ruby $[\text{Cr}(\text{ddpd})_2]^{3+}$. This review aims at illustrating the main non-radiative decay pathways for electronically excited chromium(III) complexes, namely back-intersystem crossing, excited state distortion and multiphonon relaxation and at controlling these pathways by molecular design. The case study of $[\text{Cr}(\text{ddpd})_2]^{3+}$ highlights recent successful design strategies and discusses first applications of the highly emissive 3d metal complex as optical sensor molecule and as photosensitizer.

© 2018 Elsevier B.V. All rights reserved.

Contents

1. Introduction	102
2. Tuning of the chelate ligand for photoluminescence	103
3. Stability and reactivity issues	108
4. Applications	108
5. Future perspectives	109
6. Experimental section	109
6.1. X-ray diffraction of $[\text{Cr}_2(\text{bpy})_4(\mu\text{-OH})_2](\text{PF}_6)_4 \times \text{CH}_3\text{CN} \times \frac{1}{2}\text{H}_2\text{O}$	109
6.2. Crystallographic Data of $[\text{Cr}_2(\text{bpy})_4(\mu\text{-OH})_2](\text{PF}_6)_4 \times \text{CH}_3\text{CN} \times \frac{1}{2}\text{H}_2\text{O}$	110
Acknowledgements	110
Funding	110
Conflicts of interest	110
References	110

1. Introduction

Near-infrared (NIR) luminescence is a strongly growing research field due to its increasing importance in cutting-edge technological applications such as photovoltaic spectral conversion

* Corresponding author. Fax: +49 6131 39 27277.

E-mail address: katja.heinze@uni-mainz.de (K. Heinze).<https://doi.org/10.1016/j.ccr.2018.01.004>

0010-8545/© 2018 Elsevier B.V. All rights reserved.

[1], optical telecommunication [2], light upconverting materials [3], chemical sensors, or bioimaging [4]. Triplet metal-to-ligand charge transfer (³MLCT) emitters based on d⁶, d⁸ or d¹⁰ metal ions such as ruthenium(II), gold(III) or copper(I) can suffer from strong excited state distortions [5]. This can lead to efficient non-radiative relaxation via direct surface crossing of the ³MLCT and the ground state and hence to low photoluminescence quantum yields [5]. In the excited states of emissive lanthanoid complexes, such as

europium(III) or neodymium(III) complexes, excited state distortions are typically absent, leading to long-lived emission with sharp emission bands [6].

Transition metal ions with d^3 electron configuration, e.g., chromium(III) [8] or manganese(IV) [9], experience a comparable electronic situation enabling sharp emission bands as exemplified by the famous 694 nm emission of ruby (Cr^{III} in Al_2O_3) [10]. After excitation in the ligand field bands of chromium(III) in an octahedral field (${}^4\text{A}_{2g} \rightarrow {}^4\text{T}_{1g}$; ${}^4\text{A}_{2g} \rightarrow {}^4\text{T}_{2g}$), intersystem crossing (ISC) leads to population of the emissive doublet states (${}^2\text{E}_g$, ${}^2\text{T}_{1g}$; Fig. 1). For typical molecular chromium(III) complexes, such as $[\text{Cr}(\text{tpy})_2]^{3+}$ or $[\text{Cr}(\text{urea})_6]^{3+}$ however, the ligand field splitting is not as strong as in ruby (Scheme 1) [4,11]. This enables back-ISC processes (k_{BISC}) from the doublet states to the ${}^4\text{T}_{2g}$ state followed by fluorescence, dissociation/substitution (k_{chem}) or non-radiative relaxation via the Jahn–Teller distorted ${}^4\text{T}_{2g}$ state (Fig. 1b) [8]. Consequently, the photoluminescence quantum yields of chromium(III) complexes are not particularly high [4]. Prior to our work, the highest quantum yield has been reported for $[\text{Cr}(\text{phen})_3]^{3+}$ with $\Phi = 0.15\%$ [4]. Other deactivation pathways of tris(bidentate) complexes such as $[\text{Cr}(\text{bpy})_3]^{3+}$, $[\text{Cr}(\text{phen})_3]^{3+}$ or $[\text{Cr}(\text{en})_3]^{3+}$ could be enabled by the trigonal distortion of these complexes as has also been suggested for some trigonally distorted cage complexes of chromium(III) (Fig. 1b; k_{trig}) [12]. In these trigonally distorted complexes, the ${}^4\text{A}_{2g}(\text{O}_h)$ ground state and the ${}^4\text{T}_{2g}(\text{O}_h)$ ligand field excited state mix to give a higher energy ${}^4\text{E}'(\text{D}_{3h})$ ground state and a ${}^4\text{E}''(\text{D}_{3h})$ excited state with a reduced energy difference according to angular overlap calculations (Fig. 1b; k_{trig}) [12]. A further relevant excited

state decay of the low-energy doublet states of chromium(III) complexes is a multiphonon relaxation pathway provided by high-energy oscillators such as CH, NH or OH of the ligand or solvents similar to the situation encountered for NIR-emissive lanthanoid complexes (Fig. 1b, k_{nr}) [13,14].

This review summarizes the efforts on the design of the strongly NIR-emissive chromium(III) complex $[\text{Cr}(\text{ddpd})_2]^{3+}$ (molecular ruby) (Scheme 1), on the understanding of its electronic structure and its excited state dynamics and on initial applications of this NIR luminophor.

2. Tuning of the chelate ligand for photoluminescence

With the back-ISC process to the ${}^4\text{T}_{2g}$ state being one of the most important deactivating pathways of excited chromium(III) complexes, ligand design should increase the energy gap between the ${}^4\text{T}_{2g}$ and the ${}^2\text{E}_g$ states prohibiting the back-ISC (Fig. 1b). As the energy of the ${}^4\text{T}_{2g}$ state increases with increasing ligand field strength Δ_o while the energy of the ${}^2\text{E}_g$ and ${}^2\text{T}_{1g}$ doublet states is essentially independent from Δ_o , a strong ligand field is required delivering a system far to the right side of the ${}^2\text{E}_g/{}^4\text{T}_{2g}$ crossing point in the Tanabe–Sugano diagram (Fig. 1a; $\Delta_o/B > 20$).

To optimize the poor metal–ligand orbital overlap in $[\text{Cr}(\text{tpy})_2]^{3+}$ with the small 79° N–Cr–N bite angle, a ligand forming six-membered chelate rings and $\sim 90^\circ$ bite angles is employed, namely ddpd with a “N–CH₃” unit formally inserted between the pyridine rings of tpy (Scheme 1) [15]. Treatment of CrCl_2 with

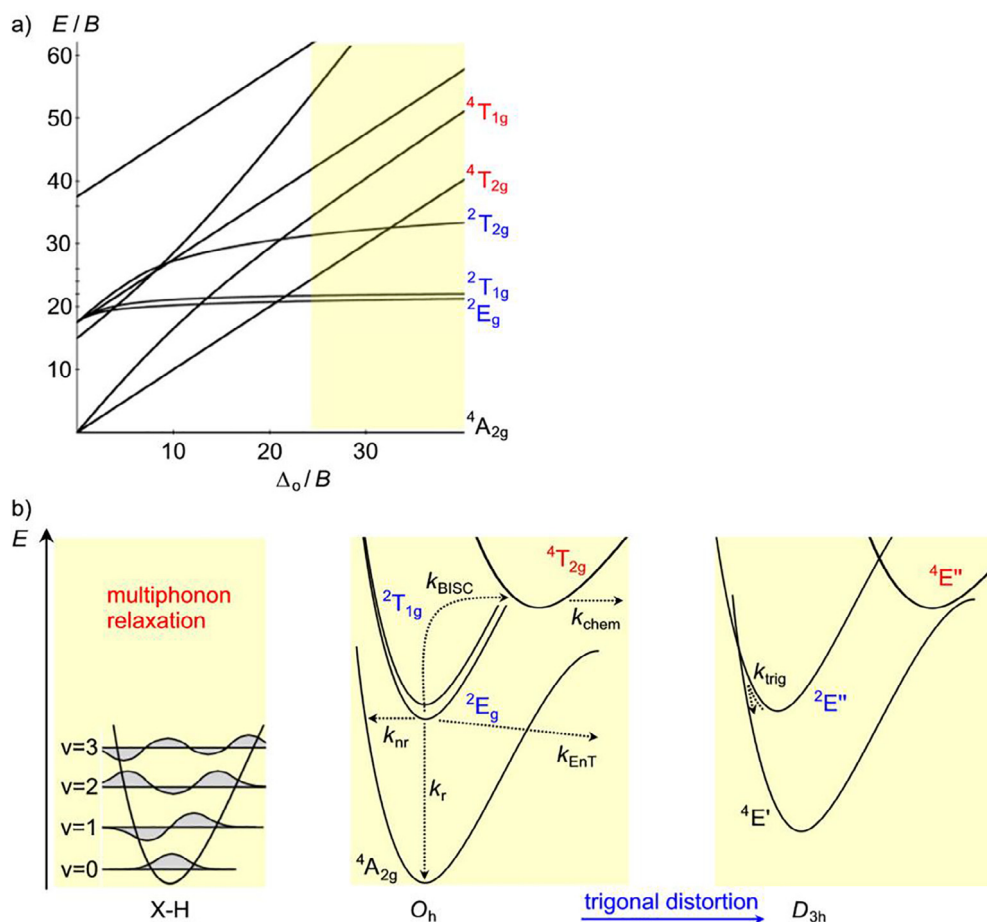
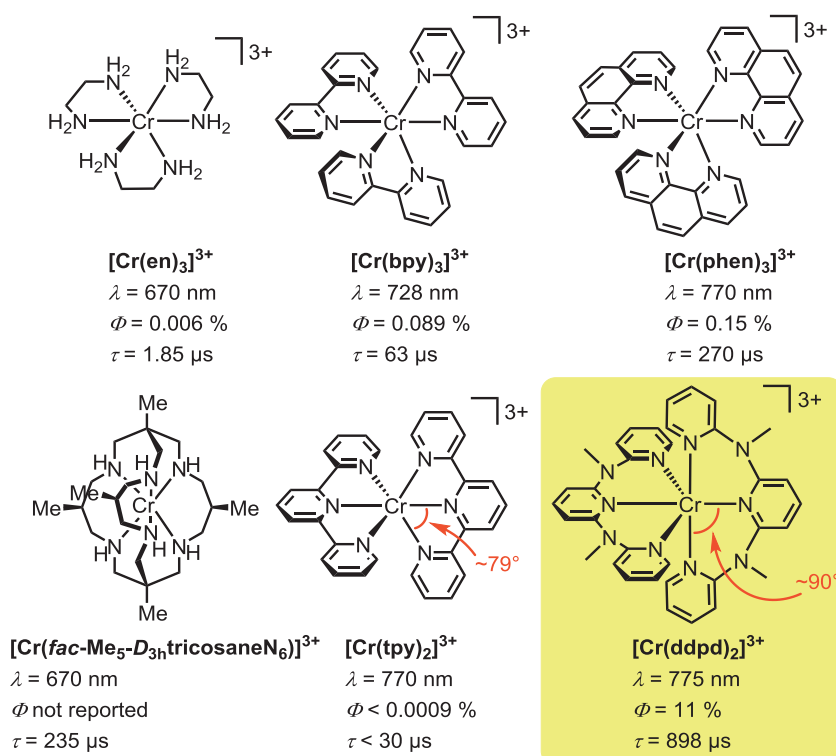


Fig. 1. (a) Tanabe–Sugano diagram [7] of the d^3 electron configuration ($C/B = 4$) with the important doublet and quartet states indicated and with the high-field region ($\Delta_o/B > 20$) highlighted and (b) schematic illustration of decay pathways of electronically excited chromium(III) complexes (radiative decay k_r ; back-ISC k_{BISC} ; chemical reaction k_{chem} ; electronic energy transfer k_{EnT}) (center); non-radiative decay via electronic-to-vibrational energy transfer to high-energy XH oscillators (k_{nr}) (left) and surface crossing in trigonally distorted complexes (k_{trig}) (right).



Scheme 1. Typical chromium(III) complexes and their photoluminescence properties (${}^2\text{E}_g \rightarrow {}^4\text{A}_{2g}$ emission wavelength, quantum yield and lifetime in aqueous solution at room temperature; en = 1,2-ethylene diamine, bpy = 2,2'-bipyridine, phen = 1,10-phenanthroline, tpy = 2,2':6',2''-terpyridine, fac-Me₅-D_{3h}-tricosaneN₆ = facial-1,5,9,13,20-pentamethyl-3,7,11,15,18,22-hexaazabicyclo[7.7.7]tricosane, ddpd = N,N'-dimethyl-N,N'-dipyridine-2-ylpyridine-2,6-diamine [15]) [4,16,17]. Although most complexes more or less strongly deviate from octahedral symmetry, we employ the Mulliken symbols pertinent to the O_h point group throughout.

the ddpd ligand yields the $[\text{Cr}(\text{ddpd})_2]^{3+}$ complex with nearly 90° bite angles and very similar Cr–N distances (2.0383(18)–2.0485(18) Å) according to X-ray crystallographic studies of the BF_4^- and PF_6^- salts (Fig. 2) and quantum chemical studies on the trication [17].

Similar to structurally comparable $[\text{M}(\text{ddpd})_2]^{2+}$ complexes [15], the ddpd ligands are wrapped around the chromium(III) center (Fig. 2b) and the counter ions fill the pockets between the ligands with Cr···B distances between 5.3 and 7.0 Å in the BF_4^- salt (Fig. 2c) [17]. The hexafluoridophosphate salt *rac*- $[\text{Cr}(\text{ddpd})_2](\text{PF}_6)_3 \times 2\text{CH}_3\text{CN}$ represents a fully analogous situation [17]. In contrast to the distorted $[\text{Cr}(\text{tpy})_2]^{3+}$ complex with N–Cr–N angles significantly below 90/180° [18], the $[\text{CrN}_6]$ coordination sphere in $[\text{Cr}(\text{ddpd})_2]^{3+}$ is nearly octahedral providing a strong chromium-nitrogen orbital overlap [17]. This optimized orbital overlap together with the electron donating character of ddpd [15] should deliver a strong ligand field splitting Δ_o .

The Cr K-edge XANES spectrum of $[\text{Cr}(\text{ddpd})_2](\text{BF}_4)_3 \times 3\text{CH}_3\text{CN}$ shows pre-edge features at 5990.4 and 5993.9 eV (Fig. 3) characteristic for the quadrupole $1s \rightarrow 3d$ (E_g , T_{2g}) transitions in chromium(III) ions, similar to those of $[\text{Cr}(\text{CN})_6]^{3-}$ (5990.2, 5990.9 eV), $[\text{Cr}(\text{tpy})_3]^{3+}$ (5990.3, 5992.9 eV) and $[\text{Cr}(\text{bpy})_3]^{3+}$ (5990.4, 5993.1; ^tbpy = 4,4'-di-*tert*-butyl-2,2'-bipyridine) [19]. The intensity of both pre-edge features is significantly decreased compared to those of $[\text{Cr}(\text{tpy})_3]^{3+}$ or $[\text{Cr}(\text{bpy})_3]^{3+}$, respectively [19]. This observation is in-line with an increased octahedrity of $[\text{Cr}(\text{ddpd})_2]^{3+}$ [20]. The EXAFS fit delivers six nitrogen absorbers in the first coordination sphere with essentially identical Cr–N distances of 2.041(20) Å, excellently matching those of the single crystal X-ray diffraction data (Experimental Section) [17].

In the UV/Vis spectral region, $[\text{Cr}(\text{ddpd})_2]^{3+}$ absorbs at 220, 302, 315, 350 and 435 nm essentially independent of the solvent (H_2O or CH_3CN) (Fig. 4a). Time-dependent Density Functional Theory

(TD-DFT) calculations on an optimized geometry of $[\text{Cr}(\text{ddpd})_2]^{3+}$ allowed assigning these bands as $\pi\pi^*$, ligand-to-metal charge transfer (LMCT) and mixed metal-centered MC/LMCT excitations. No metal-to-ligand charge transfer (MLCT) transitions were identified in this energy region because of the weak electron-accepting properties of ddpd and the inaccessible $\text{Cr}^{\text{III/IV}}$ oxidation in this ligand environment. The low-energy absorption maximum is assigned to the ${}^4\text{A}_{2g} \rightarrow {}^4\text{T}_{2g}$ transition (TD-DFT: 428, 437, and 439 nm) and LMCT transitions (TD-DFT: 442, 432, 428, 422 nm) with N–CH₃ nitrogen to t_{2g} character [17]. A thin and clear single crystal of *rac*- $[\text{Cr}(\text{ddpd})_2](\text{BF}_4)_3 \times 3\text{CH}_3\text{CN}$ enabled detecting three Laporte- and spin-forbidden transitions at 697, 736, and 776 nm (Fig. 4b) [17]. These are assigned to ${}^4\text{A}_{2g} \rightarrow {}^2\text{T}_{2g}$ (tentative), ${}^4\text{A}_{2g} \rightarrow {}^2\text{T}_{1g}$, and ${}^4\text{A}_{2g} \rightarrow {}^2\text{E}_g$ excitations, respectively (Fig. 1a; Fig. 4b). If the assignment of the 697 nm band as the ${}^4\text{A}_{2g} \rightarrow {}^2\text{T}_{2g}$ transition is correct, the Δ_o/B ratio of $[\text{Cr}(\text{ddpd})_2]^{3+}$ is not only larger than 20 (i.e., right to the ${}^2\text{E}_g/{}^4\text{T}_{2g}$ crossing point) but $> \approx 32$ (i.e. right to the ${}^2\text{T}_{2g}/{}^4\text{T}_{2g}$ crossing point) in the Tanabe–Sugano diagram (Fig. 1a). Consequently, the state ordering of $[\text{Cr}(\text{ddpd})_2]^{3+}$ would be ${}^4\text{A}_{2g} < {}^2\text{E}_g < {}^2\text{T}_{1g} < {}^2\text{T}_{2g} < {}^4\text{T}_{2g}$.

Excitation of a solution of $[\text{Cr}(\text{ddpd})_2]^{3+}$ at 435 nm leads to a strong, sharp emission band at 775 nm (full width at half maximum height FWHM = 420 cm^{-1}) assigned to the ${}^2\text{E}_g$ emission and a weaker band at 738 nm ascribed to the ${}^2\text{T}_{1g}$ emission (Fig. 4a). Although only a complete ligand-field treatment is capable of reliably extracting Racah parameters *B* and *C* for Cr^{III} complexes [21], *B* and *C* can be estimated from the following equations [8f] and the experimental absorption and emission data [17]:

$$E({}^4\text{T}_{2g}) = \Delta_o$$

$$E({}^2\text{T}_{1g}) = 9B + 3C - 24(B^2/\Delta_o)$$

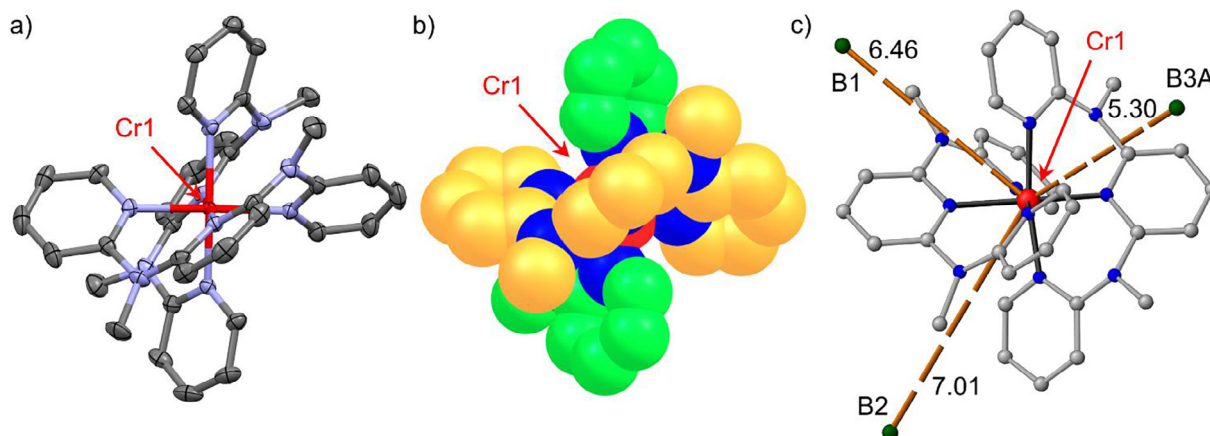


Fig. 2. (a) Molecular structure of the (*P*)-cation of *rac*-[Cr(ddpd)₂](BF₄)₃·3CH₃CN in the solid state (*Pn*; thermal ellipsoids at 50% probability); (b) space-filling representation of (*P*)-[Cr(ddpd)₂]³⁺ with the two ddpd ligands shown in yellow and green, respectively and (c) short anion...cation contacts in crystals of *rac*-[Cr(ddpd)₂](BF₄)₃·3CH₃CN (hydrogen atoms omitted for clarity; distances in Å) [17].

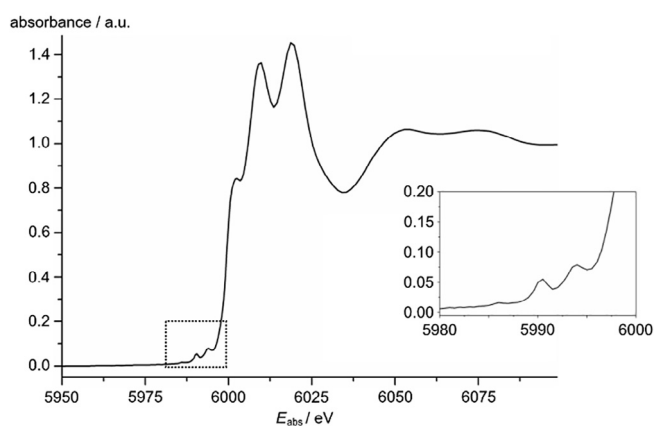


Fig. 3. XANES spectrum of [Cr(ddpd)₂](BF₄)₃·3CH₃CN in the solid state at 293 K; the inset shows details of the pre-edge.

$$E(^2E_g) = 9B + 3C - 50(B^2/\Delta_0).$$

This gives $\Delta_0 = 22,989 \text{ cm}^{-1}$, $B = 756 \text{ cm}^{-1}$ and $\Delta_0/B = 30.4$ demonstrating the envisioned large ligand field splitting in [Cr(ddpd)₂]³⁺ and placing this complex far to right of the ²E_g/⁴T_{2g} crossing point in the Tanabe–Sugano diagram (Fig. 1a). In contrast to the commonly used assumption of $C/B = 4$ for the standard Tanabe–Sugano diagrams, the C/B ratio is estimated as $C/B = 3.2$ for [Cr(ddpd)₂]³⁺ using the above equations. Hence, the standard Tanabe–Sugano diagrams are only rough guides for the estimation and prediction of excited state energies for [Cr(ddpd)₂]³⁺ and other chromium(III) complexes [8f]. A complete ligand field treatment of [Cr(ddpd)₂]³⁺ will be reported in the future.

The luminescence quantum yields of [Cr(ddpd)₂]³⁺ amount to $\Phi = 12.1\%$ and 11.0% in deaerated CH₃CN and H₂O, respectively. These values are dramatically higher than reported for any other Cr^{III} complex in solution at room temperature (Scheme 1). The excitation spectra in the region of the MC/LMCT band at 435 nm closely match the absorption spectra (Fig. 4a). This indicates, that transitions with LMCT and with MC(⁴T_{2g}) character are competent to populate the emissive doublet states.

Concomitantly with the enhanced quantum yields, the luminescence lifetimes strongly increase to $\tau = 899$ and $898 \mu\text{s}$ in deaerated CH₃CN and H₂O, respectively, outperforming almost all known molecular Cr^{III} emitters (Scheme 1). Comparable lifetimes have only been reported for Sargeson's [Cr(*fac*-Me₅-D_{3h}tricosaneN₆)]³⁺

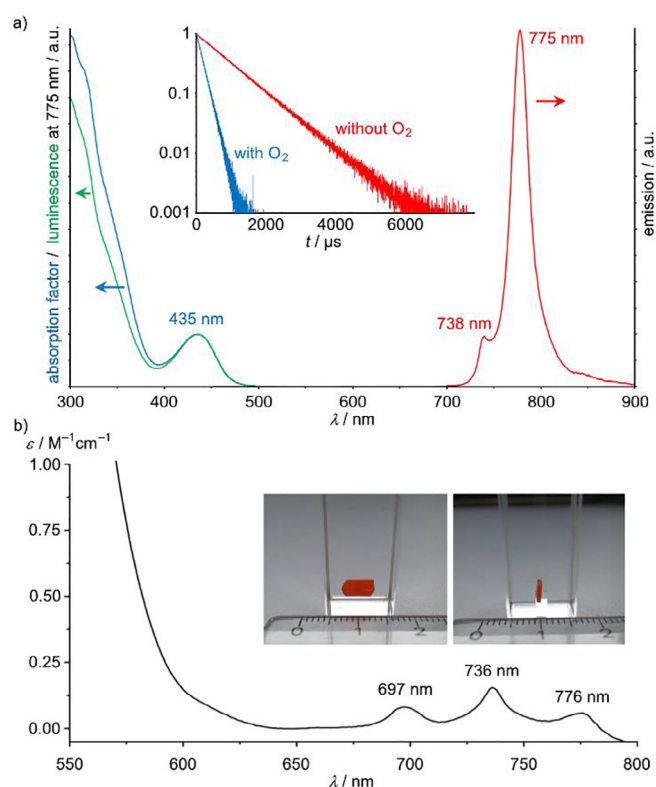


Fig. 4. (a) Absorption factor (blue), excitation ($\lambda_{\text{obs}} = 775 \text{ nm}$, green) and emission spectrum ($\lambda_{\text{exc}} = 435 \text{ nm}$, red) of *rac*-[Cr(ddpd)₂](BF₄)₃ in deaerated H₂O at room temperature; the inset shows the emission decay curves in H₂O in the presence and absence of O₂ and (b) absorption spectrum of a single crystal of *rac*-[Cr(ddpd)₂](BF₄)₃·3CH₃CN (photograph) in the VIS/NIR region [17].

complex with $\tau = 235 \mu\text{s}$ in H₂O [16], [Cr(phen)₃]³⁺ with $\tau = 270 \mu\text{s}$ [4,38b] (Scheme 1) and cyclam chromium(III) complexes with cyano- or alkynyl axial ligands ($\tau = 240\text{--}327 \mu\text{s}$; cyclam = 1,4,8,11-tetraazacyclotetradecane) [8g,h]. Hexacyanido chromate(III) [Cr(CN)₆]³⁻ shows an exceptionally long lifetime of $\tau = 6.0 \text{ ms}$ in DMF [8i,j]. It is interesting to note, that both [Cr(ddpd)₂]³⁺ and [Cr(*fac*-Me₅-D_{3h}tricosaneN₆)]³⁺ display six-membered chelate rings enabling large N–Cr–N bite angles of around 90°. Similarly, the geometry of [Cr(CN)₆]³⁻ is perfectly octahedral. However, in trigonally distorted [CrN₆] complexes such as [Cr(sen)]³⁺ (sen = 4,

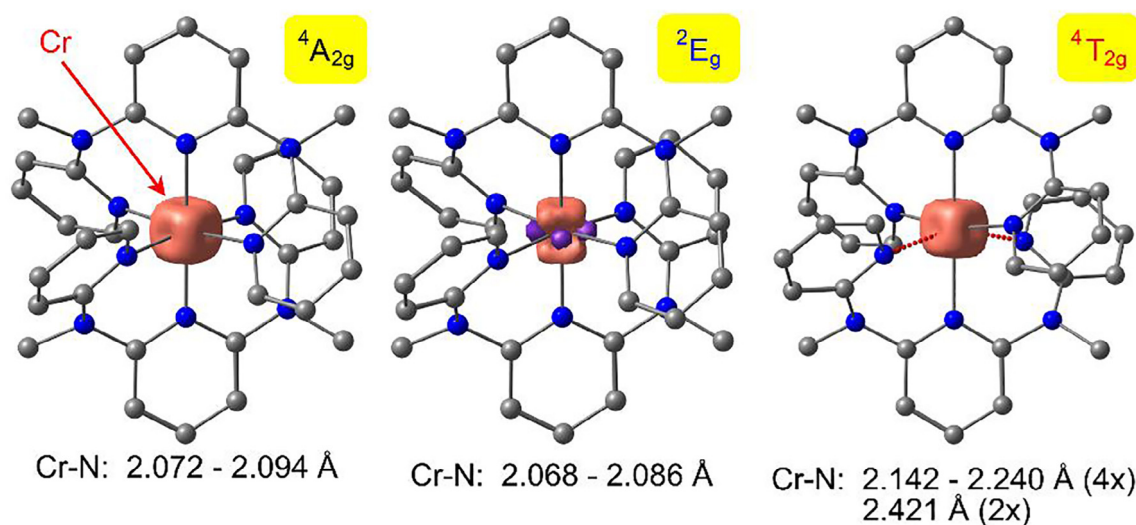


Fig. 5. Metrics of the ${}^4A_{2g}$, 2E_g and ${}^4T_{2g}$ states of $[\text{Cr}(\text{ddpd})_2]^{3+}$ according to DFT calculations (spin density surfaces in orange/purple at a contour value of 0.05 a.u.; hydrogen atoms omitted for clarity) [17].

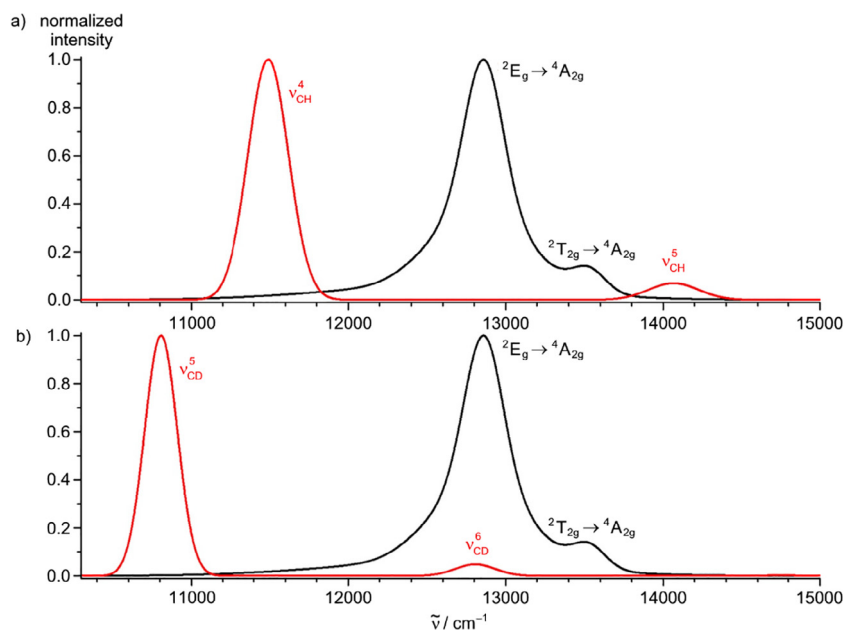


Fig. 6. (a) Normalized 2E_g emission spectrum of $[\text{Cr}(\text{ddpd})_2]^{3+}$ (black) and the relevant vibrational aromatic CH overtone absorption bands (red) showing the lack of substantial spectral overlap which is responsible for the only limited vibrational energy transfer to the CH oscillators (k_{nr}) in $[\text{Cr}(\text{ddpd})_2]^{3+}$ and (b) normalized 2E_g emission spectrum of $[\text{Cr}(\text{ddpd})_2]^{3+}$ (black) and the relevant vibrational aromatic CD overtone absorption bands (red) [26].

4',4''-ethylidynetris(3-azabutane-1-amine)) and others, the trigonal distortion mixes the d orbitals, reduces the excited quartet–doublet energy gap and leads to different relaxed geometries for the doublet excited state and the quartet ground state (Fig. 1b; k_{trig}) [12]. This finally enables an efficient thermally activated excited state relaxation pathway leading to poor quantum yields (k_{trig}). A trigonal distortion is absent in $[\text{Cr}(\text{ddpd})_2]^{3+}$. However, a racemization pathway via a potential intermediate with planarized ddpd ligands is conceivable, which might be relevant for excited state decay of $[\text{Cr}(\text{ddpd})_2]^{3+}$ (see Fig. 2b). This pathway is not likely for $[\text{Cr}(\text{ddpd})_2]^{3+}$ (see Fig. 2b) because in preliminary chiral HPLC (Chiralpak IE, eluents: $\text{CH}_3\text{CN}/\text{MeOH}$) [22] measurements, the complex could be partially resolved into the corresponding enantiomers and the latter seem to be configurationally stable on the HPLC timescale. This finding suggests that configuration inver-

sion via intermediates with planarized ligands is hindered in the ground state. It is conceivable that racemization should also be absent in the excited doublet states and hence such dynamics should not strongly contribute to the non-radiative decay of $[\text{Cr}(\text{ddpd})_2]^{3+}$. Details of the chiral resolution of *rac*- $[\text{Cr}(\text{ddpd})_2]^{3+}$ into (*P*)- and (*M*)- $[\text{Cr}(\text{ddpd})_2]^{3+}$ and their thermal and photochemical configurational stability will be reported elsewhere [22].

The solid material ruby exhibits $\tau = 4270 \mu\text{s}$ [10] while a single crystal of *rac*- $[\text{Cr}(\text{ddpd})_2](\text{BF}_4)_3 \cdot 3\text{CH}_3\text{CN}$ reveals $\tau = 443 \mu\text{s}$ [17] suggesting interactions of the excited complexes with the counterions, nearby ground state Cr^{III} complexes, co-crystallized solvents or high-energy CH oscillators in the solid state.

High energy oscillators indeed affect the quantum yields and lifetime of $[\text{Cr}(\text{ddpd})_2]^{3+}$ also in solution. The ${}^4A_{2g}$ ground state and the luminescent 2E_g excited state of $[\text{Cr}(\text{ddpd})_2]^{3+}$ are weakly

coupled and characterized by very small geometric distortions during/after intraconfigurational transitions between these states. This is confirmed by DFT calculations on the ground state and the lowest energy doublet state of $[\text{Cr}(\text{ddpd})_2]^{3+}$ delivering essentially undisturbed Cr–N bond lengths and N–Cr–N angles for the 2E_g state (Fig. 5) [17].

When back-ISC (k_{BISC}) to the severely Jahn–Teller distorted ${}^4T_{2g}$ state (Fig. 5) and (trigonal) distortions (k_{trig}) are disabled, non-radiative deactivation (k_{nr}) predominantly occurs by multiphonon relaxation involving energy transfer from the emissive metal-centered state to overtones of nearby high-energy oscillators (Fig. 1b; XH = CH, NH or OH stretching vibrations) which are close in energy to the 2E_g – ${}^4A_{2g}$ energy gap. In this situation, one expects a very strong deuteration effect on the photophysical properties because of the drastic alterations of the vibrational signatures after deuteration [13d]. Usually, the deuterated oscillators, having lower vibrational frequencies and reduced anharmonicities, have strongly diminished overtone oscillator strengths compared to the protiated overtone of similar energy, resulting in reduced vibrational quenching and improved luminescence upon isotopic labeling.

A model called the “inductive-resonant mechanism of non-radiative transitions” describing this multiphonon relaxation has been proposed by Ermolaev and Sveshnikova [23] and has been successfully applied to lanthanoid complexes [24]. Within this approach, energy transfer from the excited state to anharmonic oscillators is considered to primarily occur via electric dipole–dipole interactions under inductive-resonant conditions. This model is analogous to the well-known Förster resonance energy transfer [25]. The electronic state at the metal ion is the donor for the resonance energy transfer and a matching vibrational state is the energy acceptor. Within the inductive-resonant theory, the rate for non-radiative deactivation k_{nr} due to Förster energy transfer from the electronic excited state to the oscillator is proportional to a Förster-type spectral overlap integral SOI of the form: $SOI = \int I_{\text{norm}}(\tilde{\nu}) \cdot \varepsilon_{\text{vib}}(\tilde{\nu}) \cdot \tilde{\nu}^{-4} d\tilde{\nu}$.

Conveniently, for isotopologic CH(D) oscillators under identical conditions, the ratio of the non-radiative rate constants k_{nr} equals the ratio of the respective SOI s: $\frac{k_{\text{nr}}^{\text{H}}}{k_{\text{nr}}^{\text{D}}} = \frac{SOI^{\text{H}}}{SOI^{\text{D}}}$.

Experimentally accessible vibrational overtone signatures of aromatic CH(D) oscillator overtones of pyridines, as reported by Seitz [24], yield an interesting result for $[\text{Cr}(\text{ddpd})_2]^{3+}$ [26]. Qualitative analysis of the relative positions of its 2E_g emission (775 nm; $12,903 \text{ cm}^{-1}$) and the energetically close vibrational overtones of aromatic CH oscillators using a simplified model system reveals a very fortunate spectral overlap mismatch between the emission and CH absorption bands (Fig. 6a) [26]. This leads to only limited non-radiative energy transfer (k_{nr}) in the non-deuterated complex

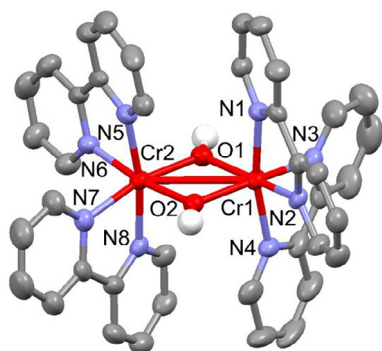


Fig. 7. Molecular structure of the cationic part of the photoanion product of $[\text{Cr}(\text{bpy})_3]^{3+} [\text{Cr}_2(\text{bpy})_4(\mu\text{-OH})_2]^{4+}$ (thermal ellipsoids at 50% probability).

$[\text{Cr}(\text{ddpd})_2]^{3+}$ contributing to its high quantum yield and lifetime. In contrast, the 2E_g emission of $[\text{Cr}(\text{bpy})_3]^{3+}$ (728 nm; $13,737 \text{ cm}^{-1}$; Scheme 1) overlaps considerably with the fourth CH overtone ($\nu = 5$; Fig. 6a) accounting for efficient quantum yield and lifetime reduction.

Ligand deuteration at specific pyridine positions boosts the luminescence lifetimes by factors of 1.4 and 2.0 in H_2O and CH_3CN , respectively, at room temperature [26]. Although, this represents record quantum yields and lifetimes for chromium(III) complexes, the effect is not as pronounced as in lanthanoid complexes, where enhancements of more than 10 have been achieved [13]. This is caused by the corresponding CD oscillators (the fifth CD vibrational overtones; $\nu = 6$) which have considerable spectral overlap with the 2E_g emission spectrum of $[\text{Cr}(\text{ddpd})_2]^{3+}$ and contribute more than usual to the deactivation of the doublet states (Fig. 6b). The selective ligand deuteration study further revealed, that the CH_3 groups of ddpd do not contribute to the multiphonon relaxation of $[\text{Cr}(\text{ddpd})_2]^{3+}$. On the other hand, the α -CH(D) groups are the most active oscillators with high energy transfer efficiency due to their short Cr···H distance of 3 Å and the r^{-6} dependence of the resonance energy transfer efficiency [23,25,26].

In the second coordination sphere, OH and CH oscillators of the solvents H_2O or CH_3CN provide a further multiphonon relaxation pathway (Fig. 1b) [14]. In the solid state of $[\text{Cr}(\text{ddpd})_2](\text{BF}_4)_3 \times 3\text{CH}_3\text{CN}$ and $[\text{Cr}(\text{ddpd})_2](\text{PF}_6)_3 \times 2\text{CH}_3\text{CN}$ Cr···H distances to the co-crystallized CH_3CN molecules are around 5.9–7.7 Å [17,26]. Experimentally, the 2E_g lifetimes are enhanced up to a factor of 1.7 by replacing the solvents with the respective deuterated analogs [26]. In the particular case of $[\text{Cr}(\text{ddpd})_2]^{3+}$, OH oscillators appear slightly more effective as energy acceptors than CH oscillators. This is a combined effect of the higher vibrational energy ($\tilde{\nu}_{\text{OH}} \approx 3400 \text{ cm}^{-1}$ vs. $\tilde{\nu}_{\text{CH}} \approx 2900 \text{ cm}^{-1}$) and the higher anharmonicity ($x_{\text{OH}} \approx 90 \text{ cm}^{-1}$ vs. $x_{\text{CH}} \approx 60 \text{ cm}^{-1}$) [24,27] of the OH oscillators. Combining the best deuterated chromium(III) complex (with $[\text{D}_9]$ -ddpd ligands featuring nearly quantitatively deuterated α -CH(D) groups of the terminal pyridines) and the best solvent (CD_3CN) delivered a record luminescence quantum yield of $\phi = 30\%$ and a record luminescence lifetime of $\tau = 2300 \mu\text{s}$ at room temperature [26].

Replacing the decisive CH oscillator in the α -position of the ligand by e.g., methylation or fluorination might by a further useful strategy to reduce the excited state decay (i) via the ligand CH oscillators and (ii) by blocking the solvent from the metal core (Fig. 2b, c) [26]. However, other factors such as electronics affecting

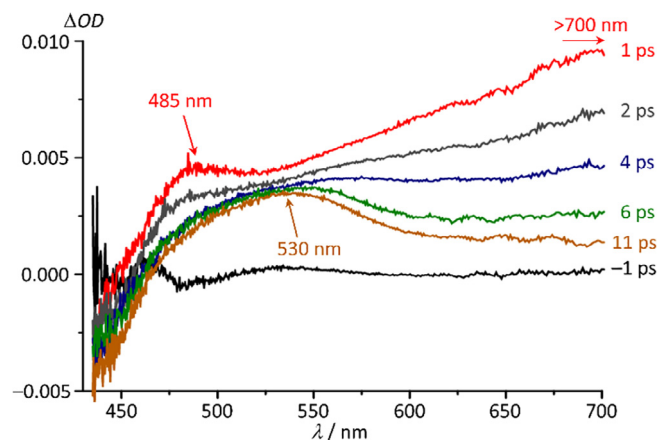


Fig. 8. Transient absorption spectra of $[\text{Cr}(\text{ddpd})_2](\text{BF}_4)_3$ in CH_3CN excited with 440 nm laser pulses showing the population of the 2E_g state characterized by the 530 nm ESA within $\tau = 3.5 \text{ ps}$ via an intermediate state characterized by an ESA at 485 nm and an ESA $>700 \text{ nm}$.

the ligand field splitting and sterics affecting the complex symmetry could also be operative in such modified complexes. The outcome of these combined effects is difficult to predict at this stage and will be explored in the future.

3. Stability and reactivity issues

The π -accepting nature of bpy or tpy accounts for the special redox properties of their chromium complexes, as multielectron reduction of $[\text{Cr}^{\text{III}}(\text{bpy})_3]^{3+}$ or $[\text{Cr}^{\text{III}}(\text{tpy})_2]^{3+}$ does not yield Cr^{II} , Cr^{I} , Cr^0 , Cr^{-1} oxidation states but is ligand centered in all cases [19]. $[\text{Cr}^{\text{III}}(\text{ddpd})_2]^{3+}$ is also reversibly reduced at -1.11 V versus ferrocene [17], yet at much more negative potential than reported for $[\text{Cr}^{\text{III}}(\text{bpy})_3]^{3+}$ or $[\text{Cr}^{\text{III}}(\text{tpy})_2]^{3+}$ (-0.63 V and -0.53 V, respectively) [19]. The electron-rich ddpd ligand is difficult to reduce as no reduction wave is observed up to -2 V vs. ferrocene [15]. Consequently, the reduction of $[\text{Cr}^{\text{III}}(\text{ddpd})_2]^{3+}$ is metal-centered in contrast to the ligand centered reductions of $[\text{Cr}^{\text{III}}(\text{bpy})_3]^{3+}$ or $[\text{Cr}^{\text{III}}(\text{tpy})_2]^{3+}$. This is further confirmed by DFT calculations on $[\text{Cr}^{\text{II}}(\text{ddpd})_2]^{2+}$ [17]. The Jahn-Teller distorted high-spin chromium(II) complex is very sensitive and prone to decomposition.

Thanks to the difficult $\text{Cr}^{\text{III}}/\text{Cr}^{\text{II}}$ reduction and the low 2E_g energy, the oxidative power of the 2E_g state of $[\text{Cr}(\text{ddpd})_2]^{3+}$ is small [$E(\text{Cr}^{\text{III/II}})^* = E(\text{Cr}^{\text{III/II}}) + E_{00}({}^2E_g) = -1.11$ V + 1.60 V = 0.49 V versus ferrocene ($+1.12$ V vs. normal hydrogen electrode (NHE))]. Hence, no severe photooxidative damage to organic material is expected by photoexcited $[\text{Cr}(\text{ddpd})_2]^{3+}$. In contrast, $[\text{Cr}(\text{bpy})_3]^{3+}$ or $[\text{Cr}(\text{tpy})_2]^{3+}$ photooxidize dGMP and hence, cleave DNA in their excited states (ttpy = *p*-tolylterpyridine, dGMP = deoxyguanosine monophosphate) [28,29]. Indeed, dGMP ($E = 1.29$ V vs. NHE) quenches the emission of $[\text{Cr}(\text{bpy})_3]^{3+}$ but not that of $[\text{Cr}(\text{ddpd})_2]^{3+}$ [17]. This allows the use of $[\text{Cr}(\text{bpy})_3]^{3+}$ or $[\text{Cr}(\text{phen})_3]^{3+}$ derivatives as photooxidants [30], while no strong photooxidative power is observed for $[\text{Cr}(\text{ddpd})_2]^{3+}$ (see Section 4).

$[\text{Cr}(\text{bpy})_3]^{3+}$ and $[\text{Cr}(\text{tpy})_2]^{3+}$ are substitutionally labile under alkaline conditions giving the hydroxido complexes $[\text{Cr}(\text{bpy})_2(\text{OH})_2]^+$ and $[\text{Cr}(\text{tpy})(\text{OH})_x]_n^{(3-x)n}$ [31]. Possibly, the π -accepting ligands bpy and tpy reduce the electron density between the ligand axes by π -back-donation from t_{2g} orbitals, facilitating a nucleophilic attack of hydroxide. In contrast, $[\text{Cr}(\text{ddpd})_2]^{3+}$ is essentially substitutionally inert over months in aqueous solution both at low and high pH [17].

This discrepancy in stability is even more pronounced under photolysis conditions. $[\text{Cr}(\text{ddpd})_2]^{3+}$ is perfectly stable in 0.1 M $[n\text{Bu}_4\text{N}]\text{Cl}$ and in $[n\text{Bu}_4\text{N}](\text{OH})$ (pH = 11.4) $\text{H}_2\text{O}/\text{CH}_3\text{CN}$ (1:1)

solution under illumination with LEDs at 430 nm in air according to absorption and emission spectra, while an isoabsorptive solution of $[\text{Cr}(\text{bpy})_3]^{3+}$ undergoes complete photosubstitution within a few hours [17,31a,b]. From the latter solution, single crystals of $[\text{Cr}_2(\text{bpy})_4(\mu\text{-OH})_2](\text{PF}_6)_4$ as the photoanation product of $[\text{Cr}(\text{bpy})_3]^{3+}$ could be isolated and characterized by single crystal X-ray diffraction (Fig. 7; Exp. Section). In spite of the tridentate nature of the ligands, $[\text{Cr}(\text{tpy})_2]^{3+}$ is even less stable toward photodissociation and photosubstitution than $[\text{Cr}(\text{bpy})_3]^{3+}$. This suggests that the chelate effect cannot compensate the lower ligand field splitting of $[\text{Cr}(\text{tpy})_2]^{3+}$. Obviously, the potentially reactive Jahn-Teller distorted ${}^4T_{2g}$ state of $[\text{Cr}(\text{ddpd})_2]^{3+}$ is not repopulated by back-ISC processes, while back-ISC is possible in $[\text{Cr}(\text{bpy})_3]^{3+}$ and $[\text{Cr}(\text{tpy})_2]^{3+}$ after excitation.

To investigate the initial fast processes after excitation and to address the lifetime of the potentially reactive initially populated ${}^4T_{2g}$ ligand field state of $[\text{Cr}(\text{ddpd})_2]^{3+}$, pump-probe transient absorption spectra were determined during 1–11 ps in CH_3CN at room temperature (Fig. 8) [32]. The 2E_g state with a characteristic excited state absorption (ESA) around 530 nm is reached within $\tau = 3.5$ ps. The 530 nm ESA band of the 2E_g state is assigned to several spin-allowed transitions within the t_{2g} set and LMCT transitions involving the bridging nitrogen atoms according to TD-DFT calculations and by comparison with that of $\text{Cr}(\text{acac})_3$ (520 nm; $\text{acac}^- = \text{acetylacetonato}$) [33]. The number of dd bands and the LMCT character of some transitions in this spectral region might account for the rather large full-width-at-half-maximum of the observed ESA.

The rate of $[\text{Cr}(\text{ddpd})_2]^{3+}$ for reaching the 2E_g state is slightly lower compared to $\text{Cr}(\text{acac})_3$ ($\tau = 1.1$ ps). For $\text{Cr}(\text{acac})_3$, it has been suggested that ISC occurs on the sub-ps timescale, which is followed by vibrational relaxation within the doublet state [33]. The initially formed transient of excited $[\text{Cr}(\text{ddpd})_2]^{3+}$ exhibits a broad ESA at $\lambda > 700$ nm (Fig. 8) [32]. $\text{Cr}(\text{acac})_3$ on the other hand, shows only narrowing and a slight red-shift but no low-energy ESA band. This indicates that not only vibrational relaxation and cooling is observed for $[\text{Cr}(\text{ddpd})_2]^{3+}$ but also another process. This could either be ISC from the ${}^4T_{2g}$ state to the doublet states (${}^2T_{2g}$, ${}^2T_{1g}$, 2E_g ; Fig. 1) or internal conversion within the doublet manifold. Indeed, the excited ${}^2T_{2g}$ state might be involved in the excited state dynamics of $[\text{Cr}(\text{ddpd})_2]^{3+}$ according to the approximate Tanabe-Sugano diagram in very strong ligand fields (Fig. 1a) and the suggested energy of the ${}^2T_{2g}$ state (697 nm; $14,347$ cm^{-1} ; Fig. 4b) [17] being lower than the energy of the ${}^4T_{2g}$ state. Such an excited state ordering is reminiscent of molybdenum(III) ions doped into chloride and bromide elpasolite host lattices $2.5\% \text{Mo}^{3+}:\text{Cs}_2\text{NaYX}_6$ ($X = \text{Cl}, \text{Br}$) as the 4d ion molybdenum(III) enables a very strong ligand field splitting [34]. In any case, departure from the ${}^4T_{2g}$ state in $[\text{Cr}(\text{ddpd})_2]^{3+}$ occurs on the lower ps timescale (or even faster) and re-population of this state by back-ISC is not possible. Consequently, bimolecular reactivity of the ${}^4T_{2g}$ state such as substitution or redox reactions (k_{chem} ; Fig. 1b) is not expected. This nicely explains the high photostability of $[\text{Cr}(\text{ddpd})_2]^{3+}$.

4. Applications

The high luminescence quantum yield and lifetime of $[\text{Cr}(\text{ddpd})_2]^{3+}$, its stability and the sharp emission bands enable a plethora of potential applications. An interesting feature of the excited state landscape of d^3 metal complexes in strong ligand fields is based on the close-lying 2E_g and ${}^2T_{1g}$ states (Fig. 1a) with emission at 775 nm and 738 nm for $[\text{Cr}(\text{ddpd})_2]^{3+}$ [17,35]. The energy difference between these doublet states of $\Delta E = 7.7$ kJ mol^{-1} (650 cm^{-1}) is in the range of the thermal energy. As these two doublet states originate from the same $(t_{2g})^3$ electron

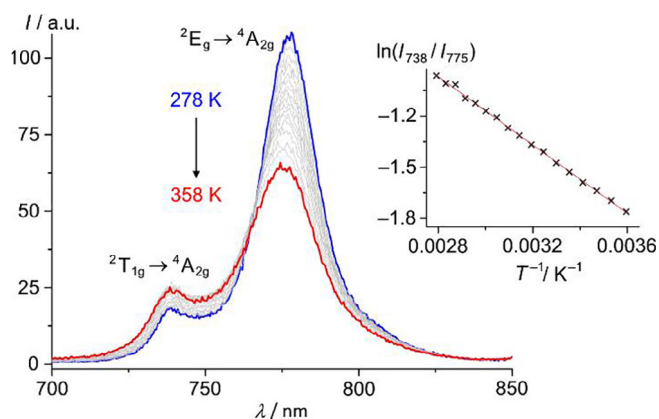


Fig. 9. Variable-temperature (VT) emission spectra of $[\text{Cr}(\text{ddpd})_2](\text{BF}_4)_3$ in air saturated H_2O from 278 to 358 K; the inset shows the respective Boltzmann plot $\ln(I_{738}/I_{775})$ vs. T^{-1} . The temperature-induced changes in emission are fully reversible [35].

configuration as the $^4A_{2g}$ ground state, both are essentially undistorted (Fig. 5) yielding sharp, clearly discernible emission bands with FWHM around 400 cm^{-1} (Fig. 4a) [35].

Heating a solution of $[\text{Cr}(\text{ddpd})_2]^{3+}$ in H_2O from 278 to 358 K diminished the 2E_g emission, while the $^2T_{1g}$ emission increased, enabling ratiometric temperature sensing in the NIR (Fig. 9) [35]. The combined Φ remained constant, and thermal deactivation through high-energy states or thermal decomposition is negligible (see Section 3). The Boltzmann plot $\ln(I_{738}/I_{775})$ versus T^{-1} is linear, and the slope corresponds to ΔE between the 2E_g and $^2T_{1g}$ states (Fig. 9, inset). Hence, $[\text{Cr}(\text{ddpd})_2]^{3+}$ operates as a molecular optical thermometer in the physiological temperature range in water. The applicable temperature range for operation has been expanded using other solvents and solvent mixtures [35]. The molecular ruby $[\text{Cr}(\text{ddpd})_2]^{3+}$ has also been encapsulated in different biocompatible nanocarriers, namely polymer nanoparticles and micelles [35]. These functionalized nanoobjects also operate as optical temperature sensors [35–37].

As expected, the phosphorescence quantum yield of $[\text{Cr}(\text{ddpd})_2]^{3+}$ is sensitive to the presence of O_2 [17,32,38]. In air, Φ is reduced by factors of 5.2 (H_2O) and 17 (CH_3CN) and the lifetimes are correspondingly shortened from 898 μs to 177 μs (H_2O) and 51 μs (CH_3CN) [17]. The bimolecular O_2 quenching constant has been estimated from a Stern–Volmer plot of $[\text{Cr}(\text{ddpd})_2]$ (BF_4) $_3$ in H_2O as $k_q = 1.77 \times 10^7\text{ M}^{-1}\text{ s}^{-1}$ and the Stern–Volmer constant as $K_{SV} = k_d \times \tau = 1.59 \times 10^4\text{ M}^{-1}$ [17]. These quenching efficiencies suggest possible applications of $[\text{Cr}(\text{ddpd})_2]^{3+}$ in optical oxygen sensors [37] and as sensitizer for singlet oxygen formation [39]. The $^1\text{O}_2$ quantum yield of $[\text{Cr}(\text{ddpd})_2]^{3+}$ in DMF and CH_3CN has been experimentally determined as $\Phi(^1\text{O}_2) = 61\%$ [32]. A first application of $[\text{Cr}(\text{ddpd})_2]^{3+}$ in organic photosynthesis via sensitized selective $^1\text{O}_2$ formation has been demonstrated on the selective CH activation of amines by $^1\text{O}_2$ and subsequent trapping with trimethylsilyl cyanide giving synthetically useful α -aminonitriles [32,40]. In contrast to the more common chromium sensitizers based on $[\text{Cr}(\text{bpy})_3]^{3+}$ and $[\text{Cr}(\text{phen})_3]^{3+}$, which can act both as strong photooxidants and as $^1\text{O}_2$ sensitizer [30], $[\text{Cr}(\text{ddpd})_2]^{3+}$ selectively gives $^1\text{O}_2$ without photoinduced electron transfer and accompanying side products (see chapter 3) [32].

Similar to ruby, chromium(III) complexes have been investigated under hydrostatic pressure [11,41,42]. Upon increasing hydrostatic pressure, the ruby emission line shifts to lower energy by $0.8\text{ cm}^{-1}\text{ kbar}^{-1}$ (in the linear low pressure range) [41]. Hence, ruby crystals find application as optical pressure sensors in high pressure settings such as diamond anvil cells [41]. In most pressure studies of molecular chromium(III) complexes, the $^4T_{2g} \rightarrow ^4A_{2g}$ fluorescence is observed, but not the 2E_g phosphorescence due to the too weak ligand field of most complexes [42]. The weak 2E_g emission band of $[\text{Cr}(\text{urea})_6][\text{ClO}_4]_3$ crystals shifts by $5.5\text{ cm}^{-1}\text{ kbar}^{-1}$ to lower energy at 120 K (in the range from 0.001 kbar to 23 kbar) [11]. Crystals of the strongly emissive molecular ruby $[\text{Cr}(\text{ddpd})_2](\text{BF}_4)_3$ have been investigated from 0.001 kbar to 45.469 kbar under hydrostatic pressure [43]. Its strong 2E_g emission band exhibits a linear shift to lower energy with a $13\text{ cm}^{-1}\text{ kbar}^{-1}$ slope [43]. The details of this pressure dependence will be reported in due course [43].

5. Future perspectives

Several further applications of the molecular ruby $[\text{Cr}(\text{ddpd})_2]^{3+}$ are envisioned as well as further developments of the design concept, the underlying theory (including ligand field theory and complete active space self-consistent field combined with N-electron valence perturbation theory to second order calculation studies) and the understanding of the initial ultrafast dynamics of excited states of the d^3 electron configuration.

As pointed out above, the molecular ruby $[\text{Cr}(\text{ddpd})_2]^{3+}$ could find further applications in sensing, including pressure sensing by luminescence energy shifts and oxygen sensing by luminescence quenching. The selective formation of singlet oxygen sensitized by $[\text{Cr}(\text{ddpd})_2]^{3+}$ might be useful in future medical applications such as photodynamic therapy. Studies in this direction are currently underway. The unique optical properties of $[\text{Cr}(\text{ddpd})_2]^{3+}$ might enable further applications in bio-imaging, especially lifetime imaging due to the very long lifetime and in single molecule spectroscopy. The configurational stability of the enantiomers (P) - $[\text{Cr}(\text{ddpd})_2]^{3+}$ and (M) - $[\text{Cr}(\text{ddpd})_2]^{3+}$ could be exploited for circularly polarized NIR emission and corresponding emerging applications. As both the ground state and the excited states of chromium(III) complexes are paramagnetic, the optical properties of the molecular ruby $[\text{Cr}(\text{ddpd})_2]^{3+}$ in magnetic fields will be of fundamental interest and potentially be useful in magneto-optical applications. Studies in this direction are underway.

Further preparative developments will include ligand design and optimization as well as introduction of antennas and groups for functionalization and potential conjugation. Future efforts are also directed toward a deeper understanding of the underlying electronic effects of the pressure dependence of the luminescence energy, the excited state ordering and the excited state dynamics in complexes with a d^3 electron configuration in a strong octahedral ligand field.

6. Experimental section

Experimental details for chiral HPLC measurements can be found in Ref. [22a]. Experimental details for the XANES spectroscopy at beamline P65 (PETRA III, Hamburg) can be found in Ref. [44]. The fitted EXAFS data are collected in the following Table

Abs-Bs ^a	N ^b	$r(\text{Abs-Bs})/\text{\AA}^c$	$\sigma/\text{\AA}^{-1d}$	$R/\%^e; E_i/\text{eV}^f; A_{\text{fac}}^g$
Cr–N	6	2.041 ± 0.020	0.059 ± 0.006	24.66
Cr–C	14.9 ± 3	2.975 ± 0.030	0.077 ± 0.008	1.750
Cr–N	8.9 ± 1.6	3.191 ± 0.032	0.112 ± 0.011	0.800

^a Abs = X-ray absorbing atom, Bs = backscattering atom.

^b Number of backscattering atoms.

^c Distance of absorbing atom to backscattering atom.

^d Debye–Waller factor.

^e Fit index.

^f Fermi energy, that accounts for the shift between theory and experiment.

^g Amplitude reducing factor.

6.1. X-ray diffraction of $[\text{Cr}_2(\text{bpy})_4(\mu\text{-OH})_2](\text{PF}_6)_4 \times \text{CH}_3\text{CN} \times \frac{1}{2}\text{H}_2\text{O}$

Intensity data were collected with a Bruker AXS Smart1000 CCD diffractometer with an APEX II detector and an Oxford cooling system using Mo- K_α radiation ($\lambda = 0.71073\text{ \AA}$). The diffraction frames were integrated using the Bruker SMART software package [45] and most were corrected for absorption with MULABS [46] of the PLATON software package [47]. The structures were solved by direct methods and refined by the full-matrix method based on F^2 using the SHELXL software package [48,49]. All non-hydrogen atoms were refined anisotropically while the positions of all hydrogen atoms were generated with appropriate geometric constraints and allowed to ride on their respective parent atoms with fixed isotropic thermal parameters.

Crystallographic data for the structure reported in this paper have been deposited with the Cambridge Crystallographic Data Centre as supplementary publication no CCDC-1587133. Copies

of the data can be obtained free of charge upon application to CCDC, 12 Union Road, Cambridge CB2 1EZ, U.K. [fax (0.44) 1223-336-033; e-mail deposit@ccdc.cam.ac.uk].

6.2. Crystallographic Data of $[\text{Cr}_2(\text{bpy})_4(\mu\text{-OH})_2](\text{PF}_6)_4 \times \text{CH}_3\text{CN} \times \frac{1}{2}\text{H}_2\text{O}$

$\text{C}_{42}\text{H}_{37}\text{Cr}_2\text{F}_{24}\text{N}_9\text{O}_{2.5}\text{P}_4$ (1391.68); monoclinic; $P2_1/n$; $a = 13.3845$ (9) Å, $b = 21.5090$ (14) Å, $c = 19.0577$ (12) Å, $\beta = 105.183$ (2)°, $V = 5295.0$ (6) Å³; $Z = 4$; density, calcd. = 1.746 g cm^{-3} , $\mu = 0.665 \text{ mm}^{-1}$; $F(0\ 0\ 0) = 2784$; crystal size $0.320 \times 0.190 \times 0.040 \text{ mm}$; $\theta = 1.457\text{--}27.890$ °; $-10 \leq h \leq 17$, $-27 \leq k \leq 28$, $-24 \leq l \leq 24$; rfln collected = 42,946; rfln unique = 12,596 [$R(\text{int}) = 0.0978$]; completeness to $\theta = 25.242$ ° = 100.0%; semi empirical absorption correction from equivalents; max. and min. transmission 0.974 and 0.859; data 12,596; restraints 726, parameters 877; goodness-of-fit on $F^2 = 0.877$; final indices [$I > 2\sigma(I)$] $R_1 = 0.0666$, $wR_2 = 0.1510$; R indices (all data) $R_1 = 0.1928$, $wR_2 = 0.1924$; largest diff. peak and hole 0.632 and -0.764 e Å^{-3} .

Acknowledgements

We gratefully thank all collaboration partners who have contributed to this interdisciplinary research area. Their names can be found in the respective references.

Funding

This work was supported by the Deutsche Forschungsgemeinschaft (GSC 266, Materials Science in Mainz, HE 2778/10-1 and SE 1448/6-1), the Internal University Research Funds of the Johannes Gutenberg University, Mainz (Germany) and the Center for INnovative and Emerging MAterials (CINEMA).

Conflicts of interest

None.

References

- [1] (a) B.M. van der Ende, L. Aarts, A. Meijerink, *PCCP* 11 (2009) 11081–11095; (b) X. Huang, S. Han, W. Huang, X. Liu, *Chem. Soc. Rev.* 42 (2013) 173–201.
- [2] K. Kuriki, Y. Koike, *Chem. Rev.* 102 (2002) 2347–2356.
- [3] (a) F. Auzel, *Chem. Rev.* 104 (2004) 139–174; (b) F. Wang, X. Liu, *Chem. Soc. Rev.* 38 (2009) 976–989; (c) M. Haase, H. Schäfer, *Angew. Chem.* 123 (2011) 5928–5950, *Angew. Chem. Int. Ed.* 50 (2011) 5808–5829; (d) J. Zhou, Z. Liu, F. Li, *Chem. Soc. Rev.* 41 (2012) 1323–1349; (e) H.H. Gorris, O.S. Wolfbeis, *Angew. Chem.* 125 (2013) 3668–3686, *Angew. Chem. Int. Ed.* 52 (2013) 3584–3600.
- [4] H. Xiang, J. Cheng, X. Ma, X. Zhou, J.J. Chruma, *Chem. Soc. Rev.* 42 (2013) 6128–6185.
- [5] (a) C. Kreitner, E. Erdmann, W.W. Seidel, K. Heinze, *Inorg. Chem.* 54 (2015) 11088–11104; (b) C. Kreitner, K. Heinze, *Dalton Trans.* 45 (2016) 5640–5658; (c) C. Kreitner, K. Heinze, *Dalton Trans.* 45 (2016) 13631–13647; (d) W.H. Lam, E.S.-H. Lam, V.W.-W. Yam, *J. Am. Chem. Soc.* 135 (2013) 15135–15143; (e) E.S.-H. Lam, W.H. Lam, V.W.-W. Yam, *Inorg. Chem.* 54 (2015) 3624–3630; (f) M. Iwamura, S. Takeuchi, T. Tahara, *Acc. Chem. Res.* 48 (2015) 782–791.
- [6] (a) J.-C.G. Bünzli, *Coord. Chem. Rev.* 293 (2015) 19–47; (b) J.-C.G. Bünzli, S.V. Eliseeva, *J. Rare Earths* 28 (2010) 824–842; (c) S. Comby, J.-C.G. Bünzli, in: K.A. Gschneidner Jr., J.-C.G. Bünzli, V.K. Pecharsky (Eds.), *Handbook on the Physics and Chemistry of Rare Earths*, Vol. 37, Elsevier, Amsterdam, 2007, p. 217; (d) M.H.V. Werts, in: P. Hänninen, H. Härmä (Eds.), *Lanthanide Luminescence* (Springer Series on Fluorescence 7), Springer, Berlin, 2011, p. 133; (e) J.-C.G. Bünzli, S.V. Eliseeva, in: J. Reedijk, K. Poepelmeier (Eds.), *Comprehensive Inorganic Chemistry II*, Vol. 8, Elsevier, Oxford, 2013, p. 339.
- [7] (a) Y. Tanabe, S. Sugano, *J. Phys. Soc. Jpn.* 9 (1954) 753–766; (b) Y. Tanabe, S. Sugano, *J. Phys. Soc. Jpn.* 9 (1954) 766–779.
- [8] (a) L.S. Forster, *Coord. Chem. Rev.* 227 (2002) 59–92; (b) P.S. Wagenknecht, P.C. Ford, *Coord. Chem. Rev.* 255 (2011) 591–616; (c) A. Hauser, C. Reber, *Struct. Bond.* 172 (2016) 291–312; (d) P.C. Ford, *Chem. Sci.* 7 (2016) 2964–2986; (e) L.A. Büldt, O.S. Wenger, *Chem. Sci.* 8 (2017) 7359–7367; (f) D. Zare, B. Doistau, H. Nozary, C. Besnard, L. Guénée, Y. Suffren, A.-L. Pelé, A. Hauser, C. Piguet, *Dalton Trans.* 46 (2017) 8992–9009; (g) N.A.P. Kane-Maguire, W.S. Crippen, P.K. Miller, *Inorg. Chem.* 22 (1983) 696–698; (h) C. Sun, C.R. Turlington, W.W. Thomas, J.H. Wade, W.M. Stout, D.L. Grisenti, W.P. Forrest, D.G. VanDerveer, P.S. Wagenknecht, *Inorg. Chem.* 50 (2011) 9354–9364; (i) R. Dannöhl-Fickler, H. Kelm, F. Wasgestian, *J. Lumin.* 10 (1975) 103–112; (j) H.-W. Buckels, F. Wasgestian, *Ber. Bunsenges. Phys. Chem.* 87 (1983) 154–158.
- [9] V. Baslon, J.P. Harris, C. Reber, H.E. Colmer, T.A. Jackson, A.P. Forshaw, J.M. Smith, R.A. Kinney, J. Telser, *Can. J. Chem.* 95 (2017) 547–552.
- [10] (a) T.H. Maiman, *Nature* 187 (1960) 493–494; (b) C. Degli Esposti, L. Bizzocchi, *J. Chem. Educ.* 84 (2007) 1316–1318.
- [11] H. Yersin, P. Huber, G. Gietl, D. Trümbach, *Chem. Phys. Lett.* 199 (1992) 1–9.
- [12] (a) M.W. Perkovic, M. Jane Heeg, J.F. Endicott, *Inorg. Chem.* 30 (1991) 3140–3147; (b) A.M. McDaniel, H.-W. Tseng, E.A. Hill, N.H. Damrauer, A.K. Rappé, M.P. Shores, *Inorg. Chem.* 52 (2013) 1368–1378.
- [13] Selected examples: (a) W.DeW. Horrocks Jr., D.R. Sudnick *J. Am. Chem. Soc.* 101 (1979) 334–340; (b) N.A.P. Kane-Maguire, G.-M. Clonts, R.C. Kerr, *Inorg. Chim. Acta* 44 (1980) L157–L160; (c) T.C. Schwendemann, P.S. May, M.T. Berry, *J. Phys. Chem. A* 102 (1998) 8690–8694; (d) W.R. Browne, J.G. Vos, *Coord. Chem. Rev.* 219–221 (2001) 761–787; (e) F. Quochi, R. Orrù, F. Cordella, A. Mura, G. Bongiovanni, F. Artizzu, P. Deplano, M.L. Mercuri, L. Pilia, A. Serpe, *J. Appl. Phys.* 99 (2006) 053520; (f) T. Monguzzi, A. Milani, L. Lodi, M.I. Trioni, R. Tubino, C. Castiglioni, *New J. Chem.* 33 (2009) 1542–1548; (g) C. Bischof, J. Wahsner, J. Scholten, S. Trosien, M. Seitz, *J. Am. Chem. Soc.* 132 (2010) 14334–14335; (h) C. Doffek, N. Alzakhem, M. Molon, M. Seitz, *Inorg. Chem.* 51 (2012) 4539–4545; (i) J. Scholten, G.A. Rosser, J. Wahsner, N. Alzakhem, C. Bischof, F. Stog, A. Beeby, M. Seitz, *J. Am. Chem. Soc.* 134 (2012) 13915–13917; (j) J. Wahsner, M. Seitz, *Inorg. Chem.* 52 (2013) 13301–13303; (k) T. Guden-Silber, C. Doffek, C. Platas-Iglesias, M. Seitz, *Dalton Trans.* 43 (2014) 4238–4241; (l) C. Doffek, J. Wahsner, E. Kreidt, M. Seitz, *Inorg. Chem.* 53 (2014) 3263–3265.
- [14] (a) A. Beeby, I.M. Clarkson, R.S. Dickens, S. Faulkner, D. Parker, L. Royle, A.S. de Sousa, J.A.G. Williams, M. Woods, *J. Chem. Soc., Perkin Trans. 2* (1999) 493–503; (b) R.M. Supkowski, W.D. Horrocks Jr., *Inorg. Chim. Acta* 340 (2002) 44–48.
- [15] (a) A. Breivogel, C. Förster, K. Heinze, *Inorg. Chem.* 49 (2010) 7052–7056; (b) K. Mack, A. Wünsche von Leupoldt, C. Förster, M. Ezhevskaya, D. Hinderberger, K.W. Klinkhammer, K. Heinze, *Inorg. Chem.* 51 (2012) 7851–7858; (c) C. Förster, K. Mack, L.M. Carrella, V. Ksenofontov, E. Rentschler, K. Heinze, *Polyhedron* 52 (2013) 576–581; (d) A. Breivogel, M. Meister, C. Förster, F. Laquai, K. Heinze, *Chem. Eur. J.* 19 (2013) 13745–13760; (e) A. Breivogel, M. Park, D. Lee, S. Klassen, A. Kühnle, C. Lee, K. Char, K. Heinze, *Eur. J. Inorg. Chem.* (2014) 288–295; (f) A. Breivogel, S. Wooh, J. Dietrich, T.Y. Kim, A.S. Kang, K. Char, K. Heinze, *Eur. J. Inorg. Chem.* (2014) 2720–2734; (g) A.K.C. Mengel, W. Cho, A. Breivogel, K. Char, Y.S. Kang, K. Heinze, *Eur. J. Inorg. Chem.* (2015) 3299–3306; (h) C. Förster, T.E. Gorelik, U. Kolb, V. Ksenofontov, K. Heinze, *Eur. J. Inorg. Chem.* (2015) 920–924; (i) A.K.C. Mengel, C. Förster, A. Breivogel, K. Mack, J.R. Ochsmann, F. Laquai, V. Ksenofontov, K. Heinze, *Chem. Eur. J.* 21 (2015) 704–714; (j) C. Kreitner, A.K.C. Mengel, T.K. Lee, W. Cho, K. Char, Y.S. Kang, K. Heinze, *Chem. Eur. J.* 22 (2016) 8915–8928; (k) A.K.C. Mengel, C. Bissinger, M. Dorn, O. Back, C. Förster, K. Heinze, *Chem. Eur. J.* 23 (2017) 7920–7931; (l) S. Otto, J. Moll, C. Förster, D. Geißler, C. Wang, U. Resch-Genger, K. Heinze, *Eur. J. Inorg. Chem.* (2017) 5033–5040.
- [16] K.N. Brown, R.J. Geue, G. Moran, S.F. Ralph, H. Riesen, A.M. Sargeson, *Chem. Commun.* (1998) 2291–2292.
- [17] S. Otto, M. Grabolle, C. Förster, C. Kreitner, U. Resch-Genger, K. Heinze, *Angew. Chem.* 127 (2015) 11735–11739, *Angew. Chem. Int. Ed.* 54 (2015) 11572–11576.
- [18] W.A. Wickramasinghe, P.H. Bird, N. Serpone, *Inorg. Chem.* 21 (1982) 2694–2698.
- [19] (a) C.C. Scarborough, K.M. Lancaster, S. DeBeer, T. Weyhermüller, S. Sproules, K. Wieghardt, *Inorg. Chem.* 51 (2012) 3718–3732; (b) C.C. Scarborough, S. Sproules, T. Weyhermüller, S. DeBeer, K. Wieghardt, *Inorg. Chem.* 50 (2011) 12446–12462.
- [20] T. Yamamoto, *X-Ray Spectrom.* 37 (2008) 572–584.
- [21] A. Hauser, M. Maeder, W.T. Robinson, R. Murugesan, J. Ferguson, *Inorg. Chem.* 26 (1987) 1331–1338.
- [22] (a) E. Kreidt, C. Dee, M. Seitz, *Inorg. Chem.* 56 (2017) 8752–8754; (b) E. Kreidt, C. Dee, K. Heinze, M. Seitz, unpublished results.

- [23] (a) E.B. Sveshnikova, V.L. Ermolaev, *Opt. Spectrosc.* 111 (2011) 34–50;
(b) V.L. Ermolaev, E.B. Sveshnikova, *Russ. Chem. Rev.* 63 (1994) 905–922.
- [24] C. Doffek, N. Alzakhem, C. Bischof, J. Wahsner, T. Guden-Silber, J. Lügger, C. Platas-Iglesias, M. Seitz, *J. Am. Chem. Soc.* 134 (2012) 16413–16423.
- [25] T. Förster, *Ann. Phys.* 437 (1948) 55–75.
- [26] C. Wang, S. Otto, M. Dorn, E. Kreidt, J. Lebon, L. Sršan, P. Di Martino-Fumo, M. Gerhards, U. Resch-Genger, M. Seitz, K. Heinze, *Angew. Chem. Int. Ed.*, doi: <http://doi.org/10.1002/anie.201711350>; *Angew. Chem.* <http://doi.org/10.1002/ange.201711350>.
- [27] R.L. Swofford, M.E. Long, M.S. Burberry, A.C. Albrecht, *J. Chem. Phys.* 66 (1977) 664–668.
- [28] R.T. Watson, N. Desai, J. Wildsmith, J.F. Wheeler, N.A.P. Kane-Maguire, *Inorg. Chem.* 38 (1999) 2683–2687.
- [29] V.G. Vaidyanathan, B.U. Nair, *Eur. J. Inorg. Chem.* (2004) 1840–1846.
- [30] S.M. Stevenson, M.P. Shores, E.M. Ferreira, *Angew. Chem.* 127 (2015) 6606–6610, *Angew. Chem. Int. Ed.* 54 (2015) 6506–6510;
(b) R.F. Higgins, S.M. Fatur, S.G. Shepard, S.M. Stevenson, D.J. Boston, E.M. Ferreira, N.H. Damrauer, A.K. Rappé, M.P. Shores, *J. Am. Chem. Soc.* 138 (2016) 5451–5464;
(c) S.M. Stevenson, R.F. Higgins, M.P. Shores, E.M. Ferreira, *Chem. Sci.* 8 (2017) 654–660.
- [31] (a) M. Maestri, F. Bolletta, N. Serpone, L. Moggi, V. Balzani, *Inorg. Chem.* 15 (1976) 2048–2051;
(b) M.A. Jamieson, N. Serpone, M.S. Henry, M.Z. Hoffman, *Inorg. Chem.* 18 (1979) 214–216;
(c) E.C. Constable, C.E. Housecroft, M. Neuburger, J. Schönle, J.A. Zampese, *Dalton Trans.* 43 (2014) 7227–7235.
- [32] S. Otto, A.M. Nauth, E. Ermilov, N. Scholz, A. Friedrich, U. Resch-Genger, S. Lochbrunner, T. Opatz, K. Heinze, *ChemPhotoChem* 1 (2017) 344–349.
- [33] (a) E.A. Juban, J.K. McCusker, *J. Am. Chem. Soc.* 127 (2005) 6857–6865;
(b) J.N. Schrauben, K.L. Dillmann, W.F. Beck, J.K. McCusker, *Chem. Sci.* 1 (2010) 405–410;
(c) H. Ando, S. Iuchi, H. Sato, *Chem. Phys. Lett.* 535 (2012) 177–181.
- [34] D.R. Gamelin, H.U. Güdel, *J. Phys. Chem. B* 104 (2000) 10222–10234.
- [35] S. Otto, N. Scholz, T. Behnke, U. Resch-Genger, K. Heinze, *Chem. Eur. J.* 23 (2017) 12131–12135.
- [36] X.D. Wang, O.S. Wolfbeis, R.J. Meier, *Chem. Soc. Rev.* 42 (2013) 7834–7869.
- [37] M. Schäferling, *Angew. Chem.* 124 (2012) 3590–3614, *Angew. Chem. Int. Ed.* 51 (2012) 3532–3554.
- [38] (a) B. Brunschwig, N. Sutin, *J. Am. Chem. Soc.* 100 (1978) 7568–7577;
(b) N. Serpone, M.A. Jamieson, M.S. Henry, M.Z. Hoffman, F. Bolletta, M. Maestri, *J. Am. Chem. Soc.* 101 (1979) 2907–2916;
(c) M.Z. Hoffman, F. Bolletta, L. Moggi, G.L. Hug, *J. Phys. Chem. Ref. Data* 18 (1989) 219–543;
(d) K.D. Barker, K.A. Barnett, S.M. Connell, J.W. Glaeser, A.J. Wallace, J. Wildsmith, B.J. Herbert, J.F. Wheeler, N.A.P. Kane-Maguire, *Inorg. Chim. Acta* 316 (2001) 41–49;
(e) M. Isaacs, A.G. Sykes, S. Ronco, *Inorg. Chim. Acta* 359 (2006) 3847–3854.
- [39] (a) M.C. DeRosa, R.J. Crutchley, *Coord. Chem. Rev.* 233–234 (2002) 351–371;
(b) C. Schweitzer, R. Schmidt, *Chem. Rev.* 103 (2003) 1685–1757;
(c) P.R. Ogilby, *Chem. Soc. Rev.* 39 (2010) 3181–3209;
(d) A.O. Terent'ev, D.A. Borisov, V.A. Vil', V.M. Dembitsky, *Beilstein J. Org. Chem.* 10 (2014) 34–114;
(e) K. Gilmore, D. Kopetzki, J.W. Lee, Z. Horváth, D.T. McQuade, A. Seidel-Morgenstern, P.H. Seeberger, *Chem. Commun.* 50 (2014) 12652–12655;
(f) W. Fan, P. Li, *Angew. Chem. Int. Ed.* 53 (2014) 12201–12204, *Angew. Chem.* 126 (2014) 12397–12400;
(g) S. Vukelić, D.B. Ushakov, K. Gilmore, B. Koksich, P.H. Seeberger, *Eur. J. Org. Chem.* (2015) 3036–3039;
(h) A.A. Ghogare, A. Greer, *Chem. Rev.* 116 (2016) 9994–10034;
(i) P. Irmiler, R.F. Winter, *Dalton Trans.* 45 (2016) 10420–10434.
- [40] (a) C. Ferroud, P. Rool, J. Santamaria, *Tetrahedron Lett.* 39 (1998) 9423–9426;
(b) G. Jiang, J. Chen, J.-S. Huang, C.-M. Che, *Org. Lett.* 11 (2009) 4568–4571;
(c) J.C.O. Pacheco, A. Lipp, A.M. Nauth, F. Acke, J.-P. Dietz, T. Opatz, *Chem. Eur. J.* 22 (2016) 5409–5415.
- [41] (a) R.A. Forman, G.J. Piermarini, J.D. Barnett, S. Block, *Science* 176 (1972) 284–285;
(b) K.L. Bray, *Top. Curr. Chem.* 213 (2001) 1–94;
(c) A.D. Chijioke, W.J. Nellis, A. Soldatov, I.F. Silvera, *J. Appl. Phys.* 98 (2005), 114905-1–114905-9.
- [42] (a) S.H. Lee, W.L. Waltz, D.R. Demmer, R.T. Walters, *Inorg. Chem.* 24 (1985) 1531–1538;
(b) D.A. Friesen, S.H. Lee, J. Lilie, W.L. Waltz, L. Vincze, *Inorg. Chem.* 30 (1991) 1975–1980;
(c) J.W. Kenney, J.W. Clymire, *J. Am. Chem. Soc.* 117 (1995) 1645–1646.
- [43] S. Otto, J.P. Harris, P.O. Roy, K. Heinze, C. Reber, manuscript in preparation.
- [44] S. Preiß, C. Förster, S. Otto, M. Bauer, P. Müller, D. Hinderberger, H.H. Haeri, L. Carella, K. Heinze, *Nat. Chem.* 9 (2017) 1249–1255.
- [45] SMART Data Collection and SAINT-Plus Data Processing Software for the SMART System (various versions), Bruker Analytical X-ray Instruments Inc: Madison, WI 2000.
- [46] R.H. Blessing, *Acta Crystallogr., Sect. A* 51 (1995) 33–38.
- [47] A.L. Spek, *Acta Crystallogr., Sect. D* 65 (2009) 148–155.
- [48] G.M. Sheldrick, *Acta Crystallogr., Sect. C* 71 (2015) 3–8.
- [49] G.M. Sheldrick, *SHELXL-2014/7*, University of Göttingen, Göttingen, Germany, 2014.

4.2 Outlook

While the “Molecular Rubies” have now been established as very promising candidates for a plethora of possible applications and been investigated extensively, this work can only be considered the first steps in developing and exploring this new type of highly emissive spin flip NIR emitter. As such, there are studies underway to further investigate $[\text{Cr}(\text{ddpd})_2]^{3+}$ and $[\text{Cr}(\text{H}_2\text{tpda})_2]^{3+}$ as well.

The interaction of $[\text{Cr}(\text{ddpd})_2]^{3+}$ with strong magnetic fields is currently studied by the group of Prof. Dr. Van Slageren in Stuttgart to explore its possible applications as magnetically triggered optical switch or qubits for quantum computing. The influence of strong magnetic fields on the photophysical properties of $[\text{Cr}(\text{ddpd})_2]^{3+}$ is currently further explored by XMCD measurements, conducted by Prof. Dr. Hans-Joachim Elmers from the Institute of Physics at the Johannes Gutenberg-University, Mainz. The group of Prof. Dr. Gerhards from the *Technische Universität Kaiserslautern* is currently investigating the excited state infrared spectra of both complexes and their deuterated isotopologues, just to name three ongoing studies conducted by our collaboration partners.

A more “low-tech” approach to influence the emission intensity of $[\text{Cr}(\text{ddpd})_2]^{3+}$ is the investigation of different counter ions. Comparing the conductivity of the four salts $[\text{Cr}(\text{ddpd})_2](\text{X})_3$ ($\text{X} = \text{Cl}^-$, BF_4^- , PF_6^- , BPh_4^-) with the respective tetrabutylammonium salts and literature values for 2:1 and 3:1 electrolytes in acetonitrile show, that all four complex salts roughly behave as 2:1 electrolytes (section 6.9, figure 6.1–6.4, table 6.1 and 6.2).^[146] This means that the complex forms on average a contact ion pair with one anion in solution.

Comparing the quantum yields Φ of the BF_4^- and BPh_4^- salts in acetonitrile solution (Φ of the Cl^- and PF_6^- salts are not yet measured) reveal a significantly lower relative reduction by quenching with O_2 (quenching factor 17.3 vs. 10.0, section 6.9, table 6.3) for the BPh_4^- . DFT calculations (section 6.9, figure 6.5) on $[\text{Cr}(\text{ddpd})_2]^{3+} \times \text{BPh}_4^-$ show, that the BPh_4^- counter ion in contact covers a large portion of the complex, suggesting that the larger counter ion shields the complex more efficiently against collision with molecular oxygen.

This shows, that even small factors like the choice of counter ion can have large effects on the luminescence property of a transition metal complex.

Beyond the already existing complexes, there is a lot of potential in varying the ligand. Enhancement of the ligands’ σ -donor strength might increase the induced the ligand field splitting further. This could be achieved for example by changing the bridging atom between the pyridines, introducing substituents like methoxy or alkylamine groups to the pyridines or even completely change the first coordination sphere by utilizing *N*-heterocyclic carbenes as strong σ -donors.

It should also be possible to introduce substituents in the ligand backbone without significantly changing the electronic structure of the ligand and thus the resulting complexes. These could then be used as anchor groups, to covalently bind the complex to polymers or biological targets, to antenna molecules increasing the absorbance and ultimately the brightness of the emission, or to assemble systems for sensing multiple analytes simultaneously.

Chromium(III) is not the only transition metal ion exhibiting the favorable d^3 electron configuration, other earth abundant metal ions are vanadium(II), manganese(IV) or molybdenum(III). So far, there exist only a handful of emissive complexes of these metal ions, leaving a wide field for exploring.^[147–149]

Inspection of the d^2 electron configurations' Tanabe-Sugano diagram reveals a quite similar ordering of excited states in comparison to d^3 , making vanadium(III) complexes also suitable candidates for spin flip emitters, but so far emission from vanadium(III) compounds has only been observed in the solid state at low temperatures.^[150]

Expanding this new type of spin flip emitters to other elements would give access to a greater variety of emission wavelengths, as known examples show emission up to 1130 nm.^[149]

References

- [1] F. Blau, *Ber. D. Chem. Ges.* **1888**, *21*, 1077–1078.
- [2] F. Blau, *Monatshefte für Chemie* **1889**, *10*, 375–388.
- [3] G. T. Morgan, F. H. Burstall, *J. Chem. Soc.* **1932**, 20.
- [4] G. Morgan, F. H. Burstall, *J. Chem. Soc.* **1937**, *0*, 1649–1655.
- [5] *Modern Terpyridine Chemistry*, (Eds.: U. S. Schubert, H. Hofmeier, G. R. Newkome), Wiley-VCH Verlag GmbH & Co. KGaA, Weinheim, FRG, **2006**.
- [6] B. O'Regan, M. Grätzel, *Nature* **1991**, *353*, 737–740.
- [7] H. Xu, R. Chen, Q. Sun, W. Lai, Q. Su, W. Huang, X. Liu, *Chem. Soc. Rev.* **2014**, *43*, 3259–3302.
- [8] B. Nemati Bideh, H. Shahroosvand, *Sci. Rep.* **2017**, *7*, 15739.
- [9] A. C. Benniston, G. M. Chapman, A. Harriman, S. A. Rostron, *Inorg. Chem.* **2005**, *44*, 4029–4036.
- [10] S. Zhang, Y. Ding, H. Wei, *Molecules* **2014**, *19*, 11933–11987.
- [11] H. D. Abruna, A. Y. Teng, G. J. Samuels, T. J. Meyer, *J. Am. Chem. Soc.* **1979**, *101*, 6745–6746.
- [12] C. Kreitner, K. Heinze, *Dalton Trans.* **2016**, *45*, 13631–13647.
- [13] B. M. Rosen, K. W. Quasdorf, D. A. Wilson, N. Zhang, A.-M. Resmerita, N. K. Garg, V. Percec, *Chem. Rev.* **2011**, *111*, 1346–1416.
- [14] T. J. Anderson, G. D. Jones, D. A. Vicic, *J. Am. Chem. Soc.* **2004**, *126*, 11113.
- [15] G. D. Jones, C. McFarland, T. J. Anderson, D. A. Vicic, *Chem. Commun.* **2005**, 4211–4213.
- [16] C. C. Scarborough, S. Sproules, T. Weyhermüller, S. DeBeer, K. Wieghardt, *Inorg. Chem.* **2011**, *50*, 12446–12462.
- [17] C. C. Scarborough, K. M. Lancaster, S. DeBeer, T. Weyhermüller, S. Sproules, K. Wieghardt, *Inorg. Chem.* **2012**, *51*, 3718–3732.
- [18] M. Wang, J. England, T. Weyhermüller, K. Wieghardt, *Inorg. Chem.* **2014**, *53*, 2276–2287.
- [19] P. S. Wagenknecht, P. C. Ford, *Coord. Chem. Rev.* **2011**, *255*, 591–616.
- [20] M. Iwamura, S. Takeuchi, T. Tahara, *Acc. Chem. Res.* **2015**, *48*, 782–791.

- [21] B. Hupp, C. Schiller, C. Lenczyk, M. Stanoppi, K. Edkins, A. Lorbach, A. Steffen, *Inorg. Chem.* **2017**, *56*, 8996–9008.
- [22] Y. Zhang, J. L. Petersen, C. Milsmann, *J. Am. Chem. Soc.* **2016**, *138*, 13115–13118.
- [23] P. Chábera, Y. Liu, O. Prakash, E. Thyrhaug, A. E. Nahhas, A. Honarfar, S. Essén, L. A. Fredin, T. C. B. Harlang, K. S. Kjær, K. Handrup, F. Ericson, H. Tatsuno, K. Morgan, J. Schnadt, L. Häggström, T. Ericsson, A. Sobkowiak, S. Lidin, P. Huang, et al., *Nature* **2017**, *543*, 695–699.
- [24] A. K. Pal, C. Li, G. S. Hanan, E. Zysman-Colman, *Angew. Chem. Int. Ed.* **2018**, DOI 10.1002/anie.201802532.
- [25] M. Schulze, A. Steffen, F. Würthner, *Angew. Chem.* **2015**, *127*, 1590–1593.
- [26] S. V. Eliseeva, J.-C. G. Bünzli, *Chem. Soc. Rev.* **2010**, *39*, 189–227.
- [27] E. J. New, D. Parker, D. G. Smith, J. W. Walton, *Curr. Opin. Chem. Biol.* **2010**, *14*, 238–246.
- [28] E. Pershagen, K. E. Borbas, *Coord. Chem. Rev.* **2014**, *273-274*, 30–46.
- [29] C. Doffek, J. Wahsner, E. Kreidt, M. Seitz, *Inorg. Chem.* **2014**, *53*, 3263–3265.
- [30] A. J. Amoroso, S. J. A. Pope, *Chem. Soc. Rev.* **2015**, *44*, 4723–4742.
- [31] C. Doffek, M. Seitz, *Angew. Chem. Int. Ed.* **2015**, *54*, 9719–9721.
- [32] S. Wiktorowski, C. Rosazza, M. J. Winterhalder, E. Daltrozzo, A. Zumbusch, *Chem. Commun.* **2014**, *50*, 4755–4758.
- [33] S. J. Strickler, R. A. Berg, *J. Chem. Phys.* **1962**, *37*, 814–822.
- [34] G. S. Ming Tong, K. T. Chan, X. Chang, C.-M. Che, *Chem. Sci.* **2015**, *6*, 3026–3037.
- [35] R. Englman, J. Jortner, *Mol. Phys.* **1970**, *18*, 145–164.
- [36] B. S. Brunshwig, N. Sutin, *Comments Inorg. Chem.* **1987**, *6*, 209–235.
- [37] V. L. Ermolaev, E. B. Sveshnikova, **1994**, *63*, 905–922.
- [38] T. E. Keyes, F. Weldon, E. Müller, P. Pechy, M. Grätzel, J. G. Vos, *Dalton Trans.* **1995**, *92*, 2705–2706.
- [39] A. Beeby, I. M. Clarkson, R. S. Dickins, S. Faulkner, D. Parker, L. Royle, A. S. de Sousa, J. A. G. Williams, M. Woods, *J. Chem. Soc. Perkin Trans. 2* **1999**, 493–504.
- [40] M. Schulz, J. Hirschmann, A. Draksharapu, G. Singh Bindra, S. Soman, A. Paul, R. Groarke, M. T. Pryce, S. Rau, W. R. Browne, J. G. Vos, *Dalton Trans.* **2011**, *40*, 10545–10552.
- [41] R. Englman, J. Jortner, *J. Lumin.* **1970**, *1-2*, 134–142.

- [42] J. V. Caspar, E. M. Kober, B. P. Sullivan, T. J. Meyer, *J. Am. Chem. Soc.* **1982**, *104*, 630–632.
- [43] T. Förster, *Ann. Phys.* **1948**, *437*, 55–75.
- [44] D. L. Dexter, *J. Chem. Phys.* **1953**, *21*, 836–850.
- [45] *Photochemistry and Photophysics of Coordination Compounds I*, (Eds.: V. Balzani, S. Campagna), Springer Berlin Heidelberg, Berlin, Heidelberg, **2007**.
- [46] D. Rehm, A. Weller, *Ber. Bunsenges. Phys. Chem.* **1969**, *73*, 834–839.
- [47] O. Stern, M. Volmer, *Phys. Z.* **1919**, *20*, 183–188.
- [48] R. J. Mears, L. Reekie, I. M. Jauncey, D. N. Payne, *Electron. Lett.* **1987**, *23*, 1026.
- [49] H. Xiang, J. Cheng, X. Ma, X. Zhou, J. J. Chruma, *Chem. Soc. Rev.* **2013**, *42*, 6128–6185.
- [50] A. de Bettencourt-Dias, *Dalton Trans.* **2007**, 2229–2241.
- [51] A. C. Grimsdale, K. L. Chan, R. E. Martin, P. G. Jokisz, A. B. Holmes, *Chem. Rev.* **2009**, *109*, 897–1091.
- [52] J. O. Escobedo, O. Rusin, S. Lim, R. M. Strongin, *Curr. Opin. Chem. Biol.* **2010**, *14*, 64–70.
- [53] G. Marriott, R. M. Clegg, D. J. Arndt-Jovin, T. M. Jovin, *Biophys. J.* **1991**, *60*, 1374–1387.
- [54] C. CULLANDER, *Journal of Microscopy* **1994**, *176*, 281–286.
- [55] J. W. Lichtman, J.-A. Conchello, *Nat. Methods* **2005**, *2*, 910–919.
- [56] M. Schäferling, *Angew. Chem. Int. Ed.* **2012**, *51*, 3532–3554.
- [57] D. V. Patel, C. N. J. McGhee, *Clin. Experiment. Ophthalmol.* **2007**, *35*, 71–88.
- [58] N. J. Agard, J. M. Baskin, J. A. Prescher, A. Lo, C. R. Bertozzi, *ACS Chem. Biol.* **2006**, *1*, 644–648.
- [59] M. D. Best, *Biochemistry* **2009**, *48*, 6571–6584.
- [60] I. Johnson, *The molecular probes handbook: A guide to fluorescent probes and labeling technologies*, 11. ed., Life Technologies, Carlsbad, Calif., **2010**.
- [61] S. G. Schulman, S. Chen, F. Bai, M. J. Leiner, L. Weis, O. S. Wolfbeis, *Anal. Chim. Acta* **1995**, *304*, 165–170.
- [62] M. J. Leiner, *Anal. Chim. Acta* **1991**, *255*, 209–222.
- [63] A. M. Paradiso, R. Y. Tsien, T. E. Machen, *Proceedings of the National Academy of Sciences* **1984**, *81*, 7436–7440.
- [64] K. Waich, T. Mayr, I. Klimant, *Talanta* **2008**, *77*, 66–72.
- [65] C. von Bültzingslöwen, A. K. McEvoy, C. McDonagh, B. D. MacCraith, I. Klimant, C. Krause, O. S. Wolfbeis, *Analyst* **2002**, *127*, 1478–1483.

- [66] S. M. Grist, L. Chrostowski, K. C. Cheung, *Sensors (Basel)* **2010**, *10*, 9286–9316.
- [67] J. E. Rogers, K. A. Nguyen, D. C. Hufnagle, D. G. McLean, W. Su, K. M. Gossett, A. R. Burke, S. A. Vinogradov, R. Pachter, P. A. Fleitz, *J. Phys. Chem. A* **2003**, *107*, 11331–11339.
- [68] C. Borek, K. Hanson, P. I. Djurovich, M. E. Thompson, K. Aznavour, R. Bau, Y. Sun, S. R. Forrest, J. Brooks, L. Michalski, J. Brown, *Angew. Chem. Int. Ed.* **2007**, *46*, 1109–1112.
- [69] R. R. de Haas, R. P. van Gijlswijk, E. B. van der Tol, J. Veuskens, H. E. van Gijssel, R. B. Tijdens, J. Bonnet, N. P. Verwoerd, H. J. Tanke, *J Histochem Cytochem* **1999**, *47*, 183–196.
- [70] A. Fercher, G. V. Ponomarev, D. Yashunski, D. Papkovsky, *Anal. Bioanal. Chem.* **2010**, *396*, 1793–1803.
- [71] N. Tian, D. Lenkeit, S. Pelz, L. H. Fischer, D. Escudero, R. Schiewek, D. Klink, O. J. Schmitz, L. González, M. Schäferling, E. Holder, *Eur. J. Inorg. Chem.* **2010**, *2010*, 4875–4885.
- [72] I. Klimant, M. Köhl, R. N. Glud, G. Holst, **1997**, *38*, 29–37.
- [73] G. Di Marco, M. Lanza, M. Pieruccini, S. Campagna, **1996**, *8*, 576–580.
- [74] Y. Amao, Y. Ishikawa, I. Okura, *Anal. Chim. Acta* **2001**, *445*, 177–182.
- [75] M. E. Köse, R. J. Crutchley, M. C. Derosa, N. Ananthakrishnan, J. R. Reynolds, K. S. Schanze, *Langmuir* **2005**, *21*, 8255–8262.
- [76] S. Nagl, C. Baleizão, S. M. Borisov, M. Schäferling, M. N. Berberan-Santos, O. S. Wolfbeis, *Angew. Chem. Int. Ed.* **2007**, *46*, 2317–2319.
- [77] S. W. Allison, G. T. Gillies, **1997**, *68*, 2615–2650.
- [78] B. Zelelow, G. E. Khalil, G. Phelan, B. Carlson, M. Gouterman, J. B. Callis, L. R. Dalton, **2003**, *96*, 304–314.
- [79] S. M. Borisov, O. S. Wolfbeis, *Anal. Chem.* **2006**, *78*, 5094–5101.
- [80] G. Liebsch, I. Klimant, O. S. Wolfbeis, **1999**, *11*, 1296–1299.
- [81] J. Feng, K. Tian, D. Hu, S. Wang, S. Li, Y. Zeng, Y. Li, G. Yang, *Angew. Chem. Int. Ed.* **2011**, *50*, 8072–8076.
- [82] G. A. Baker, S. N. Baker, T. M. McCleskey, *Chem. Commun.* **2003**, 2932.
- [83] C. Nellåker, U. Wållgren, H. Karlsson, *Clin Chem* **2007**, *53*, 98–103.
- [84] G. Ke, C. Wang, Y. Ge, N. Zheng, Z. Zhu, C. J. Yang, *J. Am. Chem. Soc.* **2012**, *134*, 18908–18911.
- [85] S. Ebrahimi, Y. Akhlaghi, M. Kompany-Zareh, A. Rinnan, *ACS Nano* **2014**, *8*, 10372–10382.

- [86] Z. Fidan, A. Wende, U. Resch-Genger, *Anal. Bioanal. Chem.* **2017**, *409*, 1519–1529.
- [87] *Handbook of Nanostructured Materials and Nanotechnology*, Elsevier, **2000**.
- [88] Y.-E. L. Koo, Y. Cao, R. Kopelman, S. M. Koo, M. Brasuel, M. A. Philbert, *Anal. Chem.* **2004**, *76*, 2498–2505.
- [89] Y. Cao, Y.-E. Lee Koo, R. Kopelman, *Analyst* **2004**, *129*, 745–750.
- [90] Y.-E. K. Lee, E. E. Ulbrich, G. Kim, H. Hah, C. Stollo, W. Fan, R. Gurjar, S. Koo, R. Kopelman, *Anal. Chem.* **2010**, *82*, 8446–8455.
- [91] J. Napp, T. Behnke, L. Fischer, C. Würth, M. Wottawa, D. M. Katschinski, F. Alves, U. Resch-Genger, M. Schäferling, *Anal. Chem.* **2011**, *83*, 9039–9046.
- [92] X.-d. Wang, H. H. Gorris, J. A. Stolwijk, R. J. Meier, D. B. M. Groegel, J. Wegener, O. S. Wolfbeis, *Chem. Sci.* **2011**, *2*, 901.
- [93] M. I. J. Stich, L. H. Fischer, O. S. Wolfbeis, *Chem. Soc. Rev.* **2010**, *39*, 3102–3114.
- [94] *Pressure and Temperature Sensitive Paints*, Springer-Verlag, Berlin/Heidelberg, **2005**.
- [95] G. Boulon, **2012**, *34*, 499–512.
- [96] Laser Congress 2017 (ASSL, LAC), OSA, Washington, D.C., **2017**.
- [97] Z. Fang, D. Sun, J. Luo, **2017**, *56*, 1.
- [98] P. Pichon, F. P. Druon, J.-P. Blanchot, A. Barbet, F. balembois, P. Georges in Laser Congress 2017 (ASSL, LAC), OSA, Washington, D.C., **2017**, ATu1A.6.
- [99] T. H. MAIMAN, *Nature* **1960**, *187*, 493–494.
- [100] C. Degli Esposti, L. Bizzocchi, **2007**, *84*, 1316.
- [101] G. J. Piermarini, S. Block, J. D. Barnett, R. A. Forman, **1975**, *46*, 2774–2780.
- [102] H. K. Mao, P. M. Bell, J. W. Shaner, D. J. Steinberg, **1978**, *49*, 3276–3283.
- [103] R. G. Munro, G. J. Piermarini, S. Block, W. B. Holzapfel, **1985**, *57*, 165–169.
- [104] M. A. Jamieson, N. Serpone, M. Z. Hoffman, *Coord. Chem. Rev.* **1981**, *39*, 121–179.
- [105] L. S. Forster, *Chem. Rev.* **1990**, *90*, 331–353.
- [106] Alexander D. Kirk, **1999**, *99*, 1607–1640.
- [107] *Photochemistry and Photophysics of Coordination Compounds I*, (Eds.: V. Balzani, S. Campagna), Springer Berlin Heidelberg, Berlin, Heidelberg, **2007**.
- [108] N. A. P. Kane-Maguire, J. Conway, C. H. Langford, **1974**, 801.
- [109] M. Maestri, F. Bolletta, L. Moggi, V. Balzani, M. S. Henry, M. Z. Hoffman, *J. Am. Chem. Soc.* **1978**, *100*, 2694–2701.

- [110] N. Serpone, M. A. Jamieson, M. S. Henry, M. Z. Hoffman, F. Bolletta, M. Maestri, *J. Am. Chem. Soc.* **1979**, *101*, 2907–2916.
- [111] A. D. Kirk, G. B. Porter, *J. Phys. Chem.* **1980**, *84*, 887–891.
- [112] Y. Tanabe, S. Sugano, *J. Phys. Soc. Jpn.* **1954**, *9*, 753–766.
- [113] Y. Tanabe, S. Sugano, *J. Phys. Soc. Jpn.* **1954**, *9*, 766–779.
- [114] J. C. Slater, W. F. Meggers, *Physics Today* **1961**, *14*, 48–50.
- [115] G. Racah, *Phys. Rev.* **1942**, *62*, 438–462.
- [116] M. Kasha, *Discuss. Faraday Soc.* **1950**, *9*, 14.
- [117] E. A. Juban, J. K. McCusker, *J. Am. Chem. Soc.* **2005**, *127*, 6857–6865.
- [118] J. N. Schrauben, K. L. Dillman, W. F. Beck, J. K. McCusker, *Chem. Sci.* **2010**, *1*, 405.
- [119] K. N. Brown, R. J. Geue, A. M. Sargeson, G. Moran, S. F. Ralph, H. Riesen, *Chem. Commun.* **1998**, 2291–2292.
- [120] C. Wang, S. Otto, M. Dorn, E. Kreidt, J. Lebon, L. Sršan, P. Di Martino-Fumo, M. Gerhards, U. Resch-Genger, M. Seitz, K. Heinze, *Angew. Chem. Int. Ed.* **2018**, *57*, 1112–1116.
- [121] J. M. García-Lastra, M. T. Barriuso, J. A. Aramburu, M. Moreno, *Phys. Rev. B* **2005**, *72*, 127.
- [122] S. M. Stevenson, M. P. Shores, E. M. Ferreira, *Angew. Chem. Int. Ed.* **2015**, *54*, 6506–6510.
- [123] R. F. Higgins, S. M. Fatur, S. G. Shepard, S. M. Stevenson, D. J. Boston, E. M. Ferreira, N. H. Damrauer, A. K. Rappé, M. P. Shores, *J. Am. Chem. Soc.* **2016**, *138*, 5451–5464.
- [124] R. T. Watson, N. Desai, J. Wildsmith, J. F. Wheeler, N. A. P. Kane-Maguire, *Inorg. Chem.* **1999**, *38*, 2683–2687.
- [125] S. Otto, M. Grabolle, C. Förster, C. Kreitner, U. Resch-Genger, K. Heinze, *Angew. Chem. Int. Ed.* **2015**, *54*, 11572–11576.
- [126] K. D. Barker, B. R. Benoit, J. A. Bordelon, R. J. Davis, A. S. Delmas, O. V. Mytykh, J. T. Petty, J. F. Wheeler, N. A. Kane-Maguire, *Inorg. Chim. Acta* **2001**, *322*, 74–78.
- [127] S. Torelli, D. Imbert, M. Cantuel, G. Bernardinelli, S. Delahaye, A. Hauser, J.-C. G. Bünzli, C. Piguet, *Chem. Eur. J.* **2005**, *11*, 3228–3242.
- [128] M. Cantuel, F. Gumy, J.-C. G. Bünzli, C. Piguet, *Dalton Trans.* **2006**, 2647–2660.
- [129] L. Aboshyan-Sorgho, H. Nozary, A. Aebischer, J.-C. G. Bünzli, P.-Y. Morgantini, K. R. Kittilstved, A. Hauser, S. V. Eliseeva, S. Petoud, C. Piguet, *J. Am. Chem. Soc.* **2012**, *134*, 12675–12684.

- [130] K. H. Theopold, *Eur. J. Inorg. Chem.* **1998**, 1998, 15–24.
- [131] J. Drzeżdżon, A. Sikorski, L. Chmurzyński, D. Jacewicz, *Sci. Rep.* **2018**, *8*, 2315.
- [132] A. Breivogel, C. Förster, K. Heinze, *Inorg. Chem.* **2010**, *49*, 7052–7056.
- [133] K.-Y. Ho, W.-Y. Yu, K.-K. Cheung, C.-M. Che, *Dalton Trans.* **1999**, 1581–1586.
- [134] C. R. Goldsmith, T. D. P. Stack, *Inorg. Chem.* **2006**, *45*, 6048–6055.
- [135] G. Dyker, O. Muth, *Eur. J. Org. Chem.* **2004**, *21*, 4319–4322.
- [136] K. Mack, A. Wunsche von Leupoldt, C. Förster, M. Ezhevskaya, D. Hinderberger, K. W. Klinkhammer, K. Heinze, *Inorg. Chem.* **2012**, *51*, 7851–7858.
- [137] C. Förster, K. Mack, L. M. Carrella, V. Ksenofontov, E. Rentschler, K. Heinze, *Polyhedron* **2013**, *52*, 576–581.
- [138] C. Förster, T. E. Gorelik, U. Kolb, V. Ksenofontov, K. Heinze, *Eur. J. Inorg. Chem.* **2015**, 2015, 920–924.
- [139] A. K. C. Mengel, W. Cho, A. Breivogel, K. Char, Y. Soo Kang, K. Heinze, *Eur. J. Inorg. Chem.* **2015**, 2015, 3299–3306.
- [140] A. K. C. Mengel, C. Förster, A. Breivogel, K. Mack, J. R. Ochsmann, F. Laquai, V. Ksenofontov, K. Heinze, *Chem. Eur. J.* **2015**, *21*, 704–714.
- [141] A. K. C. Mengel, C. Bissinger, M. Dorn, O. Back, C. Förster, K. Heinze, *Chem. Eur. J.* **2017**, *23*, 7920–7931.
- [142] A. Breivogel, M. Meister, C. Förster, F. Laquai, K. Heinze, *Chem. Eur. J.* **2013**, *19*, 13745–13760.
- [143] A. Breivogel, C. Kreitner, K. Heinze, *Eur. J. Inorg. Chem.* **2014**, 2014, 5468–5490.
- [144] A. Breivogel, M. Park, D. Lee, S. Klassen, A. Kühnle, C. Lee, K. Char, K. Heinze, *Eur. J. Inorg. Chem.* **2014**, 2014, 288–295.
- [145] M. Dorn, K. Mack, L. M. Carrella, E. Rentschler, C. Förster, K. Heinze, *Z. Anorg. Allg. Chem.* **2018**, DOI 10.1002/zaac.201800101.
- [146] W. J. Geary, *Coord. Chem. Rev.* **1971**, *7*, 81–122.
- [147] V. Baslon, J. P. Harris, C. Reber, H. E. Colmer, T. A. Jackson, A. P. Forshaw, J. M. Smith, R. A. Kinney, J. Telsler, *Can. J. Chem.* **2017**, *95*, 547–552.
- [148] R. A. Isovitsch, A. S. Beadle, F. R. Fronczek, A. W. Maverick, *Inorg. Chem.* **1998**, *37*, 4258–4264.
- [149] A. K. Mohammed, R. A. Isovitsch, A. W. Maverick, *Inorg. Chem.* **1998**, *37*, 2779–2785.
- [150] C. D. Flint, P. Greenough, *Chem. Phys. Lett.* **1972**, *16*, 369–370.

- [151] F. Neese, *WIREs Comput. Mol. Sci.* **2012**, *2*, 73–78.
- [152] A. D. Becke, *J. Chem. Phys.* **1993**, *98*, 5648–5652.
- [153] W. J. Hehre, R. F. Stewart, J. A. Pople, *J. Chem. Phys.* **1969**, *51*, 2657–2664.

Appendix

6

6.1 Supporting Information: $[\text{Cr}(\text{ddpd})_2]^{3+}$: a Molecular, Water-Soluble, Highly NIR-Emissive Ruby Analogue

CrCl_2 (95%, ABCR), deoxyguanosine monophosphate (dGMP) and $(\text{HOCH}_2)_3\text{CNH}_3\text{Cl}$ (Tris-HCl) (Sigma-Aldrich) and 2,2'-bipyridine (bpy) (Alpha Aesar) were purchased from commercial suppliers. The ligand ddpd was synthesized according to a literature procedure.¹ $[\text{Cr}(\text{bpy})_3](\text{PF}_6)_2$ was prepared similar to a literature procedure.² Air- or moisture-sensitive reactions were performed in dried glassware under inert gas atmosphere (argon, quality 4.6). Acetonitrile was refluxed over CaH_2 and distilled under argon prior to use in these reactions. UV/Vis spectra were recorded on a Varian Cary 5000 spectrometer in 1 cm cuvettes. Emission spectra were recorded on a Varian Cary Eclipse spectrometer (single crystal $\mathbf{1}(\text{BF}_4)_3 \times 3\text{CH}_3\text{CN}$ and $\mathbf{1}(\text{PF}_6)_3$ in solution) or on an Edinburgh Instruments spectrometer (FSP 920). Luminescence decay curves in the μs -range were measured with an Edinburgh Instruments spectrometer (FSP 920) using a μs Xe-flashlamp and multi-channel scaling mode. Fluorescence decays in the ns-range were recorded using an Edinburgh Instruments lifetime spectrometer (FLS 920) equipped with a MCP-PMT (R3809U-50, Hamamatsu), and a TCSPC module (TCC 900). A supercontinuum laser (SC400-PP, Fianium) was used for excitation wavelengths > 400 nm, for excitation at 330 nm a ps-laserdiode (ELED, Edinburgh Instruments) was used. All luminescence measurements were performed using magic angle condition (polarization 0° in the excitation and 54.7° in the emission channel). Luminescence quantum yields were determined using an Ulbricht integrating sphere (Quantaaurus-QY C11347-11, Hamamatsu).³ Relative uncertainty is estimated to be $\pm 5\%$. Oxygen was removed from the solvents by purging with argon and the oxygen concentration in the sample solutions was measured using an Neofox-GT (sensor Phosphor-R) optical detection system (OceanOptics). For the single crystal absorption and emission spectra a single crystal of $\mathbf{1}(\text{BF}_4)_3 \times 3\text{CH}_3\text{CN}$ of approximate $0.5 \times 0.3 \times 0.1 \text{ cm}^3$ dimension was placed a microcuvette, covered with heptane and analyzed by absorption and emission spectroscopy. ESI⁺ mass spectra were recorded on a Micromass QToF Ultima API mass spectrometer with analyte solutions in acetonitrile. Elemental analyses were performed by the microanalytical laboratory of the chemical institutes of the University of Mainz. Electrochemical experiments were performed with a BioLogic SP-50 voltammetric analyser using platinum wire working and counter electrodes and a 0.01 M Ag/AgNO_3 reference electrode. Measurements were carried out at a scan rate of 100 mV s^{-1} for cyclic voltammetry experiments using 0.1 M $[\text{nBu}_4\text{N}][\text{PF}_6]$ as supporting electrolyte in acetonitrile. Potentials are given relative to the ferrocene/ferrocenium couple (0.40 V vs. SCE^4 , $E_{1/2} = 0.90 \pm 5 \text{ mV}$ under the given conditions). EPR spectra were recorded on a Miniscope MS 300 X-band CW spectrometer (Magnettech GmbH, Germany). Values of g are referenced to Mn^{2+} in ZnS as external standard ($g = 2.118, 2.066, 2.027, 1.906, 1.986, 1.946$). Simulations were performed with the EasySpin program package.⁵ Magnetic susceptibility measurements were carried out with a Quantum Design MPMS-XL7 SQUID magnetometer under an applied magnetic field of 1 T. Experimental susceptibility data were corrected by the underlying diamagnetism using Pascal's constants. The magnetic contribution of the holder was experimentally determined and subtracted from the measured susceptibility data.

Density functional theoretical calculations were carried out using the ORCA program package (version 3.0.2).⁶ Tight convergence criteria were chosen for all calculations (Keywords TightSCF and TightOpt, convergence criteria for the SCF part: energy change $1.0 \cdot 10^{-8} E_h$, 1-El. energy change $1.0 \cdot 10^{-5} E_h$, orbital gradient $1.0 \cdot 10^{-5}$, orbital rotation angle $1.0 \cdot 10^{-5}$, DIIS Error $5.0 \cdot 10^{-7}$; for geometry optimizations: energy change: $1.0 \cdot 10^{-6} E_h$, max. gradient $1.0 \cdot 10^{-4} E_h \text{ bohr}^{-1}$, RMS gradient $3.0 \cdot 10^{-5} E_h \text{ bohr}^{-1}$, max. displacement

$1.0 \cdot 10^{-3}$ bohr, RMS displacement $6.0 \cdot 10^{-4}$ bohr). All calculations make use of the resolution of identity (Split-RI-J) approach for the coulomb term in combination with the chain-of-spheres approximation for the exchange term (COSX).⁷ Geometry optimizations were performed using the B3LYP functional⁸ in combination with Ahlrichs' split-valence double- ξ basis set def2-SV(P) for all atoms which comprises polarization functions for all non-hydrogen atoms.⁹ The optimized geometries were confirmed to be local minima on the respective potential energy surface by subsequent numerical frequency analysis ($N_{imag} = 0$). TD-DFT calculations were performed based on the B3LYP/def2-SV(P) optimized geometry. The ZORA relativistic approximation¹⁰ was used to describe relativistic effects in all calculations. Fifty vertical transitions were calculated in TD-DFT calculations. Explicit counterions and/or solvent molecules were neglected.

Crystal Structure Determinations. Intensity data were collected with a Bruker AXS Smart 1000 CCD diffractometer with an APEX II detector and an Oxford cooling system and corrected for absorption and other effects using Mo K_{α} radiation ($\lambda = 0.71073$ Å) at 173(2) K. The diffraction frames were integrated using the SAINT package, and most were corrected for absorption with MULABS.^{11,12} The structures were solved by direct methods and refined by the full-matrix method based on F^2 using the SHELXTL software package.^{13,14} All non-hydrogen atoms were refined anisotropically, while the positions of all hydrogen atoms were generated with appropriate geometric constraints and allowed to ride on their respective parent carbon atoms with fixed isotropic thermal parameters. See Table S2 for crystal and structure refinement data. **1(PF₆)₃×2CH₃CN** crystallized as small plates resulting in weakly diffracting crystals and a low observed/unique data ratio. Furthermore, **1(PF₆)₃×2CH₃CN** features two independent cations in the unit cell together with the corresponding (partially disordered) counter anions and solvent molecules. The disordered anions have been refined with split-models with the following occupancies for the disordered atoms: **1(PF₆)₃×2CH₃CN** (anion P2, P4, P6: 0.5:0.5), **1(BF₄)₃×3CH₃CN** (anion B2, B3: 0.896(4):0.104(4)). SAME and SADI geometric restraints have been used and the SIMU and DELU instructions in some cases to enable anisotropic refinement of the disordered anions. Crystallographic data (excluding structure factors) for the structure reported in this paper have been deposited with the Cambridge Crystallographic Data Centre as supplementary publication no CCDC-1059802 [**1(BF₄)₃×3CH₃CN**] and CCDC-1059801 [**1(PF₆)₃×2CH₃CN**]. Copies of the data can be obtained free of charge upon application to CCDC, 12 Union Road, Cambridge CB2 1EZ, U.K. [fax (0.44) 1223-336-033; e-mail deposit@ccdc.cam.ac.uk].

Synthesis of $[\text{Cr}(\text{ddpd})_2](\text{BF}_4)_3$ [$\mathbf{1}(\text{BF}_4)_3$]: Anhydrous chromium(II) chloride (220 mg, 1.95 mmol) and ddpd ¹ (810 mg, 2.78 mmol) were dissolved in deaerated $\text{CH}_3\text{CN}/\text{H}_2\text{O}$ (1:1, 45 ml). The deep green solution was stirred under argon for 12 h. Addition of a solution of ammonium tetrafluoroborate (5 ml, 1.06 M in H_2O) yielded a green precipitate. The solid was removed by filtration and extracted once with diethyl ether. The solvents of the orange solution were removed under reduced pressure. The orange residue was dissolved in CH_3CN . Addition of diethyl ether yielded orange crystals, which were dried under reduced pressure. Diffusion of diethyl ether into a concentrated CH_3CN solution yielded large diffraction quality crystals. Yield: 970 mg (1.08 mmol, 78 %).

Synthesis of $[\text{Cr}(\text{ddpd})_2](\text{PF}_6)_3$ [$\mathbf{1}(\text{PF}_6)_3$] (route I): Anhydrous chromium(II) chloride (90 mg, 0.732 mmol) and ddpd ¹ (304 mg, 1.04 mmol) were dissolved in deaerated water (50 ml). The deep green solution was stirred under argon for 15 h. Addition of a solution of potassium hexafluorophosphate (10 ml, 0.17 M in H_2O) yielded a green and orange colored precipitate. The solids were collected by filtration and washed once by diethyl ether. The orange residue was dissolved in CH_3CN . Addition of diethyl ether yielded orange crystals, which were dried under reduced pressure. Diffusion of diethyl ether into a concentrated CH_3CN solution yielded diffraction quality crystals. Yield: 200 mg (0.187 mmol, 36 %).

Synthesis of $[\text{Cr}(\text{ddpd})_2](\text{PF}_6)_3$ [$\mathbf{1}(\text{PF}_6)_3$] (route II): Potassium hexafluorophosphate (97 mg, 0.527 mmol) was added to a concentrated aqueous solution of $[\text{Cr}(\text{ddpd})_2](\text{BF}_4)_3$ (98.6 mg, 0.110 mmol). The resulting orange precipitate was collected by filtration and dissolved in acetonitrile. Slowly adding diethyl ether resulted in precipitation of yellow crystals. Yield: 90.7 mg (0.085 mmol, 77 %).

Synthesis of $[\text{Cr}(\text{bpy})_3](\text{ClO}_4)_3$ ²: 2,2'-Bipyridine (750 mg, 4.80 mmol) was added to a solution of anhydrous chromium(II) chloride (99 mg, 0.806 mmol) in deaerated 0.1 M perchloric acid (40 ml). After stirring the resulting black-purple suspension for 15 minutes at room temperature air was bubbled through the reaction mixture for 5 hours. Yellow crystals precipitated from the yellow solution overnight. The crystals were collected by filtration, washed with ethanol and dried under reduced pressure. Yield: 560 mg (0.684 mmol, 84 %).

Synthesis of $[\text{Cr}(\text{bpy})_3](\text{PF}_6)_3$: Potassium hexafluorophosphate (480 mg, 2.61 mmol) was added to a concentrated aqueous solution of $[\text{Cr}(\text{bpy})_3](\text{ClO}_4)_3$ (410 mg, 0.500 mmol). The resulting yellow precipitate was collected by filtration and dissolved in acetonitrile. Slowly adding diethyl ether resulted in precipitation of yellow crystals. Yield: 348 mg (0.364 mmol, 73 %).

Stability tests: Isoabsorptive solutions (at 430 nm) of $\mathbf{1}(\text{PF}_6)_3$ and $[\text{Cr}(\text{bpy})_3](\text{PF}_6)_3$ in 0.1 M $[\text{nBu}_4\text{N}]\text{Cl}$ $\text{H}_2\text{O}/\text{MeCN}$ (1:1) solution were irradiated with an LED torch at 430 nm under aerobic conditions. Isoabsorptive solutions (at 430 nm) of $\mathbf{1}(\text{PF}_6)_3$ and $[\text{Cr}(\text{bpy})_3](\text{PF}_6)_3$ in 0.1 M $[\text{nBu}_4\text{N}]\text{Cl}$ $\text{H}_2\text{O}/\text{MeCN}$ (1:1) solution with pH = 11.4 adjusted with $[\text{nBu}_4\text{N}](\text{OH})$ were irradiated under the same conditions. The reaction progress was monitored at the respective emission maximum (777 and 727 nm) over a time of 5 hours.

Quenching with dGMP: 3.3×10^{-5} M solutions of $\mathbf{1}(\text{PF}_6)_3$ and $[\text{Cr}(\text{bpy})_3](\text{PF}_6)_3$ in 50 mM aqueous Tris-HCl buffer were titrated with a 6.45 mM solution of deoxyguanosine monophosphate (dGMP) dissolved in the same buffer. Emission quenching was monitored at the respective emission maximum (777 and 727 nm) up to a dGMP concentration of 3.14×10^{-4} M.

- (1) A. Breivogel, C. Förster, K. Heinze, *Inorg. Chem.* **2010**, *49*, 7052-7056.
- (2) B. R. Baker, B. D. Metha, *Inorg. Chem.* **1962**, *4*, 848-854.
- (3) a) C. Würth, D. Geißler, T. Behnke, M. Kaiser, U. Resch-Genger, *Anal. Bioanal. Chem.* **2015**, *407*, 59–78; b) C. Würth, M. G. González, R. Niessner, U. Panne, C. Haisch, U. Resch-Genger, *Talanta* **2012**, *90*, 30–37; c) C. Würth, J. Pauli, C. Lochmann, M. Spieles, U. Resch-Genger, *Anal. Chem.* **2012**, *84*, 1345–1352.
- (4) N. G. Connelly, W. E. Geiger, *Chem. Rev.* **1996**, *96*, 877–910.
- (5) S. Stoll, A. Schweiger, *J. Magn. Reson.* **2006**, *178*, 42–55.
- (6) F. Neese, *WIREs Comput Mol Sci* **2012**, *2*, 73–78.
- (7) a) F. Neese, F. Wennmohs, A. Hansen, U. Becker, *Chem. Phys.* **2009**, *356*, 98–109; b) R. Izsák, F. Neese, *J. Chem. Phys.* **2011**, *135*, 144105.
- (8) A. D. Becke, *J. Chem. Phys.* **1993**, *98*, 5648-5642.
- (9) a) A. Schäfer, H. Horn, R. Ahlrichs, *J. Chem. Phys.* **1992**, *97*, 2571; b) A. Schäfer, C. Huber, R. Ahlrichs, *J. Chem. Phys.* **1994**, *100*, 5829.
- (10) a) E. van Lenthe, E. J. Baerends, J. G. Snijders, *J. Chem. Phys.* **1993**, *99*, 4597; b) C. van Wüllen, *J. Chem. Phys.* **1998**, *109*, 392; c) D. A. Pantazis, X.-Y. Chen, C. R. Landis, F. Neese, *J. Chem. Theory Comput.* **2008**, *4*, 908–919.
- (11) *SMART Data Collection and SAINT-Plus Data Processing Software for the SMART System*, various versions; Bruker Analytical X-ray Instruments, Inc.: Madison, WI, **2000**.
- (12) R. H. Blessing, *Acta Crystallogr.* **1995**, *A51*, 33–38.
- (13) G. M. Sheldrick, *SHELXTL*, version 5.1; Bruker AXS: Madison, WI, **1998**.
- (14) G. M. Sheldrick, *SHELXL-97*; University of Göttingen: Göttingen, Germany, **1997**.

Table S1. Analytical data of **1**(BF₄)₃ and **1**(PF₆)₃.

	1 (BF ₄) ₃	1 (PF ₆) ₃
molecular formula	C ₃₄ H ₃₄ B ₃ CrF ₁₂ N ₁₀	C ₃₄ H ₃₄ CrF ₁₈ N ₁₀ P ₃
molecular mass	895.11 g mol ⁻¹	1069.59 g mol ⁻¹
solubility in CH ₃ CN	122 g l ⁻¹ (0.136 mol l ⁻¹)	222 g l ⁻¹ (0.208 mol l ⁻¹)
solubility in H ₂ O	42.9 g l ⁻¹ (0.048 mol l ⁻¹)	1.73 g l ⁻¹ (0.0016 mol l ⁻¹)
MS (ESI): <i>m/z</i> =	171.5 (13) [M-3BF ₄] ³⁺ , 292.1 (47) [ddpd+H] ⁺ , 362.1 (23) [M-2BF ₄] ²⁺ , 808.2 (100) [M-BF ₄] ⁺ , 1703.4 (15) [2M-BF ₄] ⁺	171.5 (7) [M-3PF ₆] ³⁺ , 291.1 (12) [ddpd] ⁺ , 389.6 (4) [M-2PF ₆] ²⁺ , 924.1 (100) [M-PF ₆] ⁺ , 1994.2 (22) [2M-PF ₆] ⁺
IR (KBr): $\tilde{\nu}$ =	1606 (vs), 1585 (s), 1568 (m), 1497 (vs), 1455 (s), 1435 (vs), 1365 (w), 1343 (s), 1237 (m), 1141 (s), 1095-1035 (vs br, BF) cm ⁻¹	1609 (vs), 1585 (s), 1570 (m), 1499 (vs), 1455 (s), 1437 (vs), 1369 (w), 1346 (s), 1240 (m), 1178 (w), 1141 (s), 838 (vs, PF) cm ⁻¹
Magnetism (300 K): χT =	-	1.833 cm ³ K mol ⁻¹
EPR (77 K) in CH ₃ CN g_{av} =	-	1.990 (broad)
UV/Vis (CH ₃ CN): λ_{max} ($\epsilon/M^{-1} \text{ cm}^{-1}$) =	436 (3770, LMCT+MC), 315 (sh, 25500, LMCT+MC), 302 (28100, LMCT), 220 (sh, 53600, $\pi\pi^*$) nm	436 (4095, LMCT+MC), 315 (sh, 25700, LMCT+MC), 301 (28700, LMCT), 218 (56000, $\pi\pi^*$) nm
UV/Vis (H ₂ O): λ_{max} ($\epsilon/M^{-1} \text{ cm}^{-1}$) =	435 (3980, LMCT+MC), 315 (sh, 24700, LMCT+MC), 301 (27600, LMCT), 217 (sh, 53400, $\pi\pi^*$) nm	436 (3530, LMCT+MC), 315 (sh, 21840, LMCT+MC), 301 (24500, LMCT), 219 (48000, $\pi\pi^*$) nm
UV/Vis (single crystal): λ_{max} ($\epsilon/M^{-1} \text{ cm}^{-1}$) =	776 (<1), 736 (<1), 697(<1) nm	-
Emission (CH ₃ CN, $\lambda_{exc} = 435$): λ_{max} (rel. intensity) =	776 (1.0), 739 (0.20), 500 (very weak) nm	776 (1.0), 738 (0.2), 500 (very weak) nm
Emission (H ₂ O, $\lambda_{exc} = 435$): λ_{max} (rel. intensity) =	777 (1.0), 739 (0.20), 500 (very weak) nm	-
Emission (single crystal, $\lambda_{exc} = 435$): λ_{max} (rel. intensity) =	778 (1.0), 740 (0.2), 594 (0.2) nm	-
Emission (single crystal, $\lambda_{exc} = 435$): τ =	443 μ s	-
CV ([<i>n</i> Bu ₄ N][PF ₆]/CH ₃ CN, vs. Fc): $E_{1/2}$ =	-	-1.11 V (Cr ^{III} /Cr ^{II})
Elemental analysis found / calcd.	C 44.98 (45.22) H 4.17 (3.83) N 15.04 (15.65)	C 37.90 (38.18) H 2.95 (3.20) N 12.98 (13.10)
Photographs of crystals		

Table S2. Summary of X-ray data of **1(BF₄)₃·3CH₃CN** and **1(PF₄)₃·2CH₃CN**.

	1(BF₄)₂·3CH₃CN	1(PF₄)₃·2CH₃CN
Empirical formula	C ₄₀ H ₄₃ B ₃ CrF ₁₂ N ₁₃	C ₃₈ H ₄₀ CrF ₁₈ N ₁₁ P ₃
Formula weight	1018.30	1151.73
Crystal color, habit	red block	orange plate
Crystal dimensions / mm	0.74 x 0.50 x 0.34	0.32 x 0.09 x 0.07
Crystal system	monoclinic	monoclinic
Space group	<i>Pn</i>	<i>P2₁/c</i>
<i>a</i> / Å	11.5125(8)	28.2212(12)
<i>b</i> / Å	16.5554(11)	11.7062(5)
<i>c</i> / Å	12.9721(9)	34.0629(13)
α / °	90	90
β / °	111.890(2)	124.479(3)
γ / °	90	90
<i>V</i> / Å ³	2294.2(3)	9312.7(7)
<i>Z</i>	2	8
<i>F</i> (000)	1042	4664
Density (calcd) / g cm ⁻³	1.474	1.643
Absorption coefficient μ / mm ⁻¹	0.345 (MULABS)	0.467 (MULABS)
Theta range / °	2.02 – 27.90	1.20 – 28.04
Index ranges	-14 ≤ <i>h</i> ≤ 15 -21 ≤ <i>k</i> ≤ 21 -17 ≤ <i>l</i> ≤ 17	-37 ≤ <i>h</i> ≤ 36 -13 ≤ <i>k</i> ≤ 15 -44 ≤ <i>l</i> ≤ 44
Reflections collected	27213	90048
Independent reflections	9828 (<i>R</i> _{int} = 0.0504)	22407 (<i>R</i> _{int} = 0.1510)
Observed reflections	9828	22407
Parameters, restraints	666, 22	1439, 688
Max. / min. transmission	0.784 / 0.892	0.9681 / 0.8650
Goodness-of-fit on <i>F</i> ²	1.041	1.042
Largest difference peak and hole / e Å ⁻³	0.315 / -0.347	1.647 / -1.018
<i>R</i> ₁ (<i>I</i> > 2σ(<i>I</i>))	0.0409	0.1087
<i>R</i> ₁ (all data)	0.0439	0.2304
<i>wR</i> ₂ (<i>I</i> > 2σ(<i>I</i>))	0.1105	0.3165
<i>wR</i> ₂ (all data)	0.1127	0.3529
absolute structure parameter	-0.005(12)	-

Table S3. Selected distances [Å] and angles [deg] of **1(BF₄)₂·3CH₃CN** and **1(PF₄)₃·2CH₃CN**.

	1(BF₄)₂·3CH₃CN	1(PF₄)₃·2CH₃CN (molecule A)	1(PF₄)₃·2CH₃CN (molecule B)
Cr1-N1	2.0485 (0.0018)	2.0410 (0.0058)	2.0395 (0.0069)
Cr1-N3	2.0393 (0.0018)	2.0535 (0.0065)	2.0296 (0.0068)
Cr1-N5	2.0394 (0.0019)	2.0280 (0.0062)	2.0327 (0.0068)
Cr1-N6	2.0446 (0.0017)	2.0398 (0.0067)	2.0400 (0.0061)
Cr1-N8	2.0444 (0.0018)	2.0538 (0.0071)	2.0465 (0.0066)
Cr1-N10	2.0485 (0.0018)	2.0476 (0.0068)	2.0302 (0.0059)
N1-Cr1-N3	85.13 (0.08)	85.74 (0.25)	86.78 (0.28)
N1-Cr1-N5	170.86 (0.08)	172.27 (0.25)	172.57 (0.27)
N1-Cr1-N6	91.06 (0.07)	89.98 (0.25)	90.45 (0.27)
N1-Cr1-N8	95.23 (0.08)	95.47 (0.25)	93.71 (0.27)
N1-Cr1-N10	89.49 (0.07)	90.37 (0.26)	89.23 (0.27)
N3-Cr1-N5	85.74 (0.07)	86.71 (0.26)	86.03 (0.27)
N3-Cr1-N6	95.10 (0.07)	93.89 (0.27)	95.33 (0.26)
N3-Cr1-N8	178.94 (0.08)	178.61 (0.28)	179.01 (0.29)
N3-Cr1-N10	94.02 (0.07)	95.13 (0.27)	91.60 (0.26)
N5-Cr1-N6	89.68 (0.07)	92.20 (0.27)	88.38 (0.27)
N5-Cr1-N8	89.68 (0.07)	92.10 (0.26)	93.51 (0.27)
N5-Cr1-N10	91.22 (0.07)	88.64 (0.27)	92.82 (0.27)
N6-Cr1-N8	85.89 (0.07)	85.42 (0.27)	85.54 (0.25)
N6-Cr1-N10	170.88 (0.07)	170.97 (0.27)	173.03 (0.27)
N8-Cr1-N10	84.99 (0.07)	85.56 (0.27)	87.54 (0.26)

Figure S1. Short anion...cation contacts (Å) in crystals of a) $1(\text{BF}_4)_2 \times 3\text{CH}_3\text{CN}$ and b) $1(\text{PF}_4)_3 \times 2\text{CH}_3\text{CN}$ (F and H atoms omitted) and structure of c) $1(\text{BF}_4)_2 \times 3\text{CH}_3\text{CN}$ and d) $1(\text{PF}_4)_3 \times 2\text{CH}_3\text{CN}$ with thermal ellipsoids at 30 % probability.

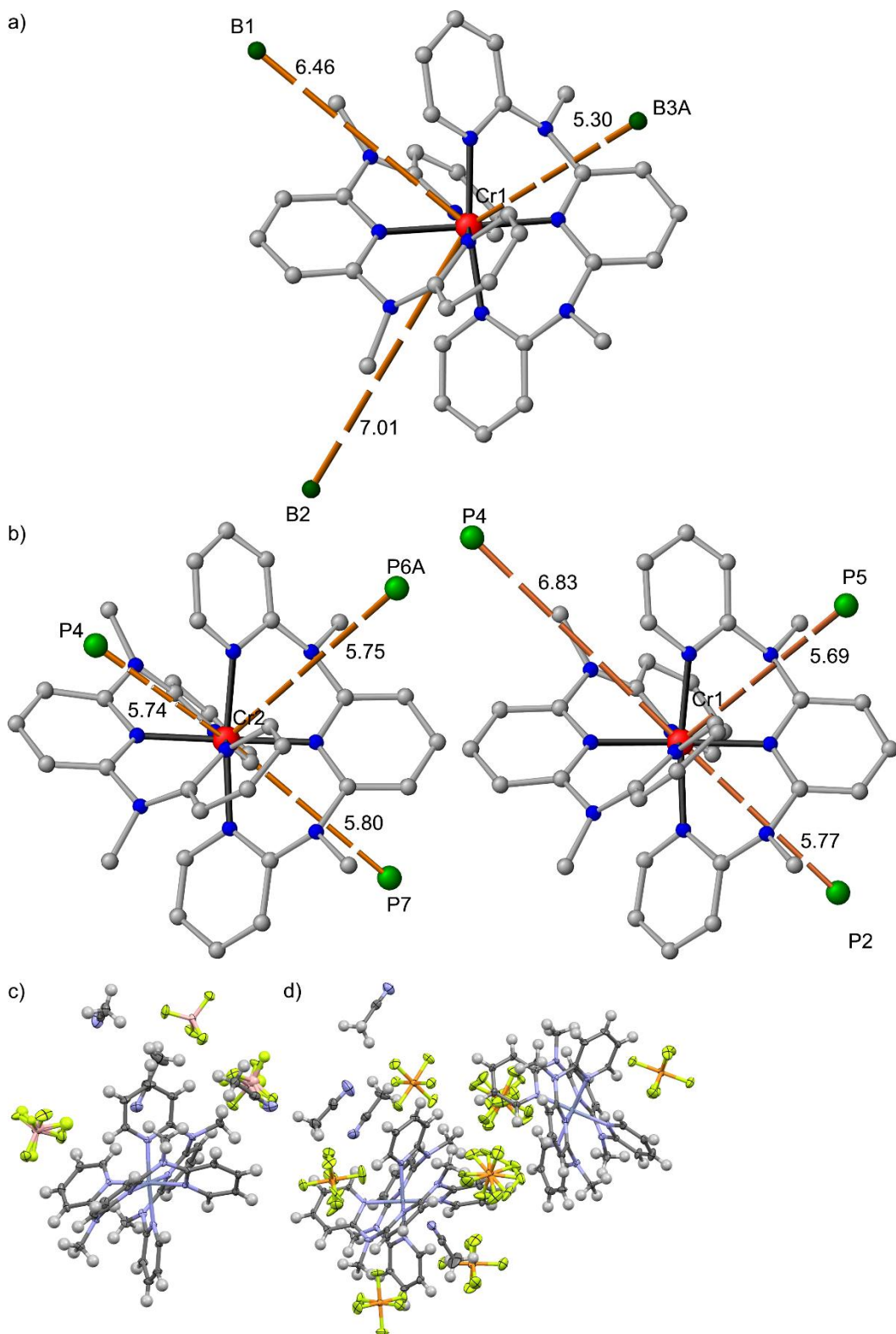
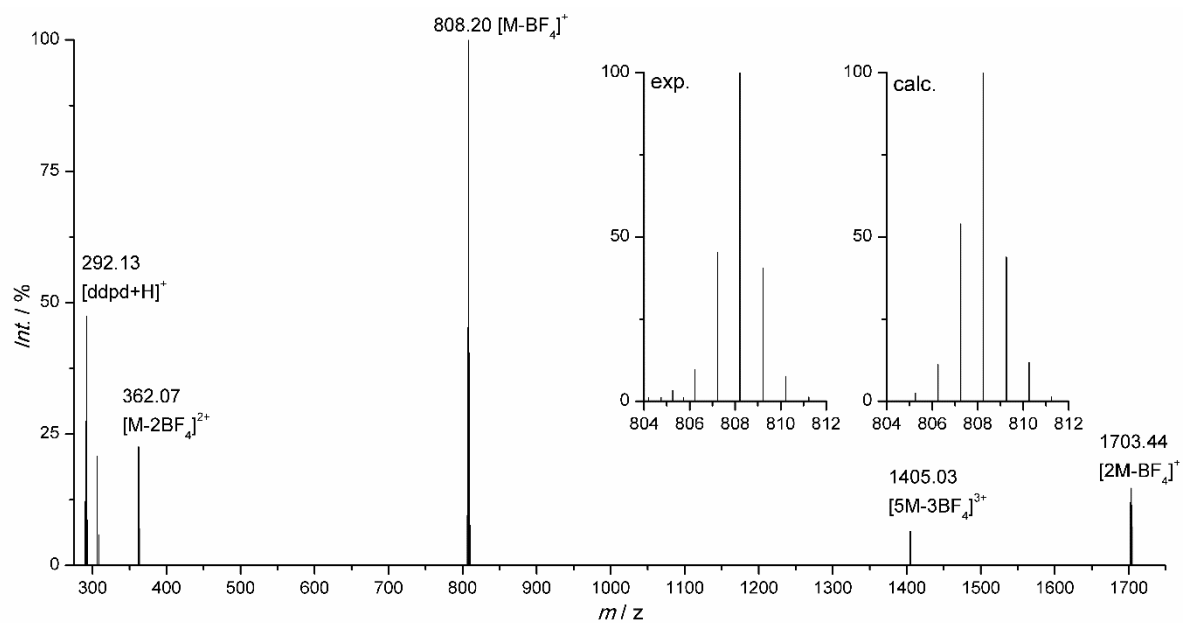


Figure S2. a) ESI mass spectrum of **1**(BF₄)₃ including experimental and calculated isotopic pattern of [M-BF₄]⁺ and b) ESI mass spectrum of **1**(PF₆)₃ including experimental and calculated isotopic pattern of [M-PF₆]⁺.

a)



b)

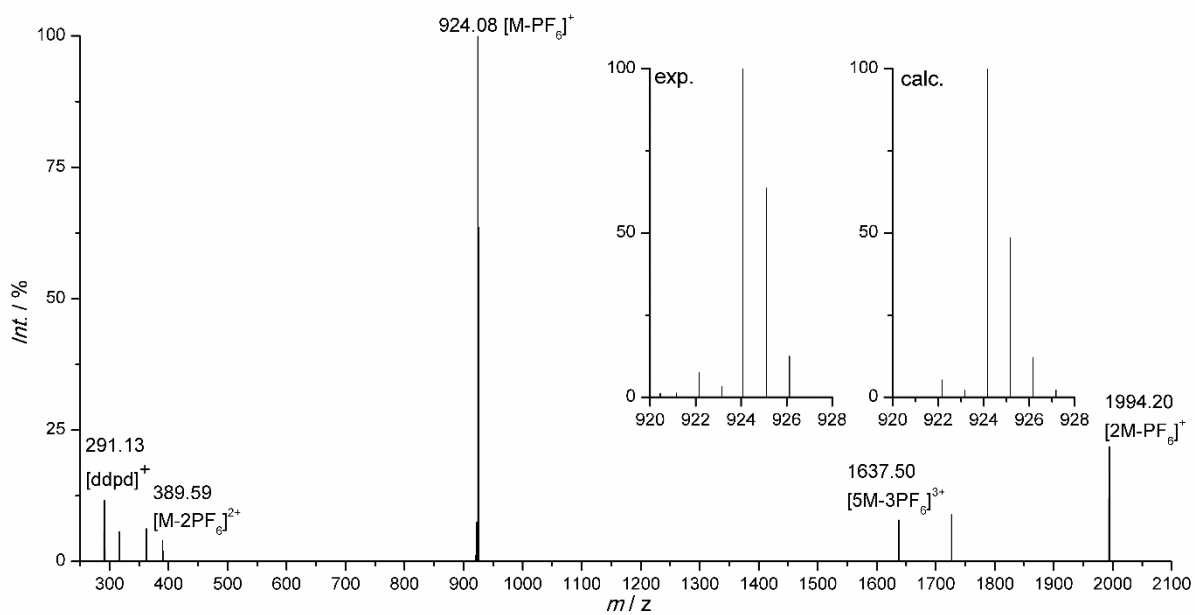


Figure S3. IR spectrum of **1**(BF₄)₃ as KBr disk.

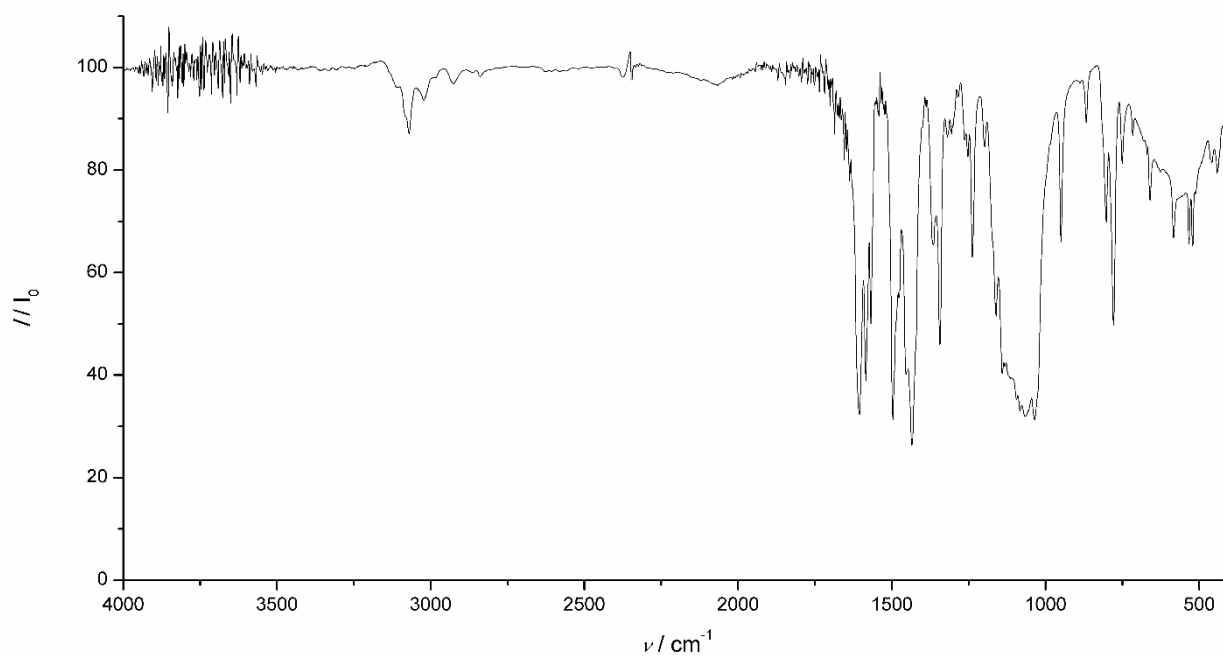


Figure S4. IR spectrum of **1**(PF₆)₃ as KBr disk.

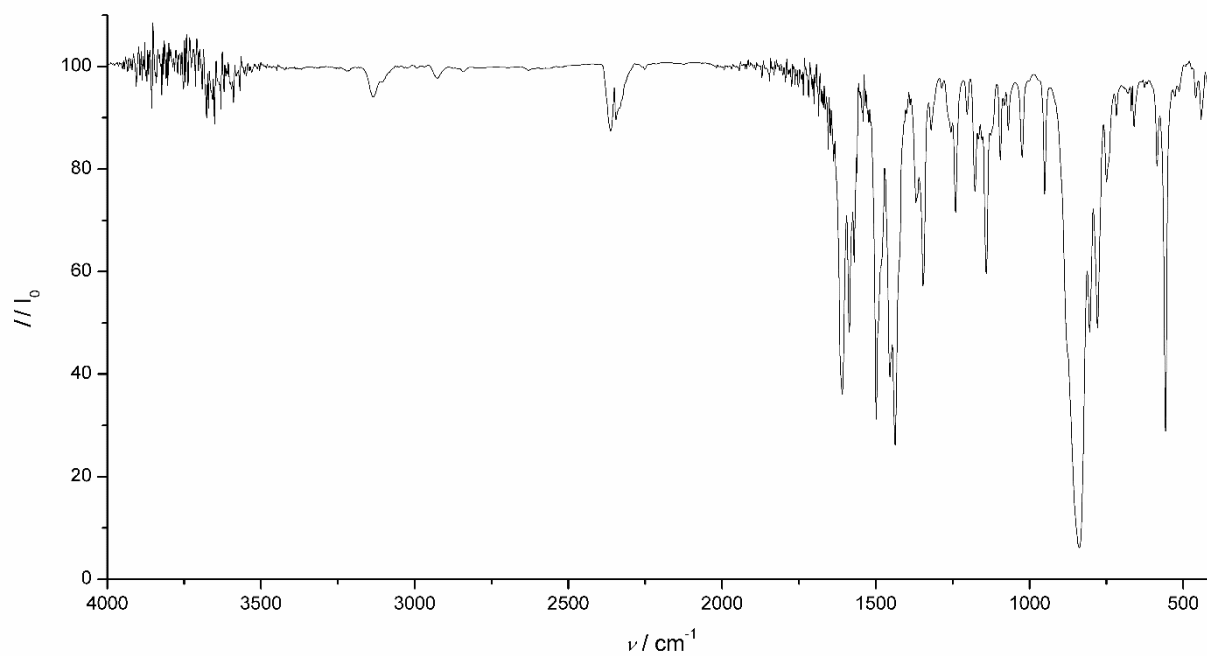


Figure S5. UV/Vis spectra of **1(BF₄)₃** a) in CH₃CN and b) in H₂O.

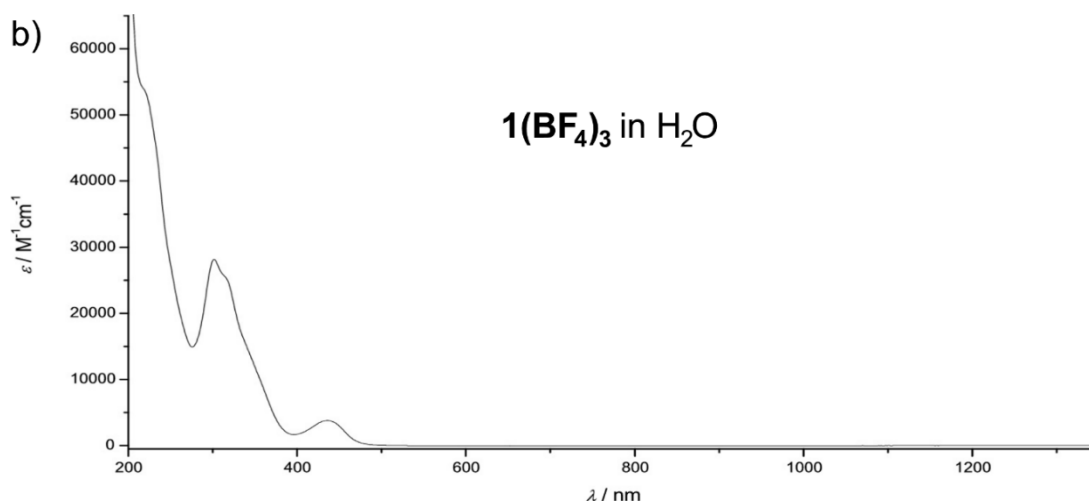
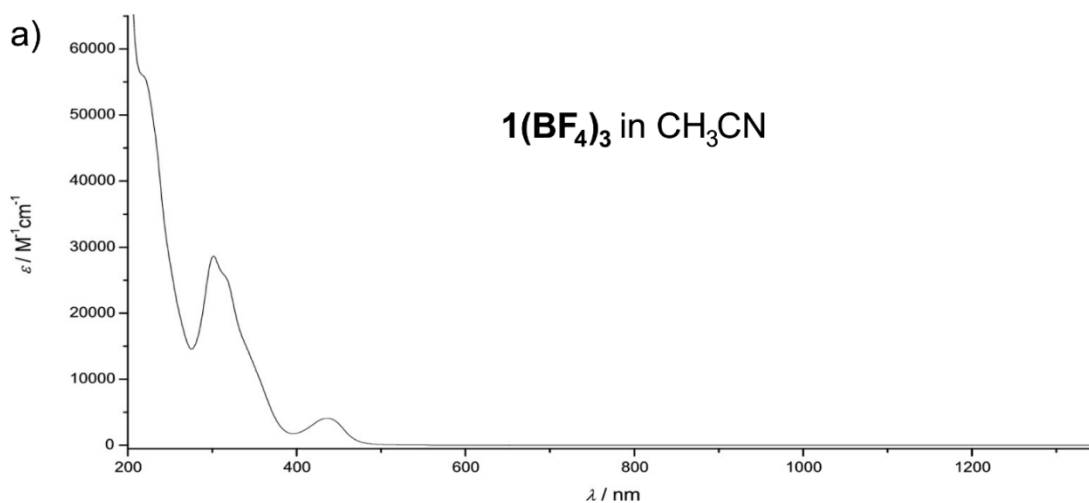


Figure S6. UV/Vis spectrum of **1(PF₆)₃** in CH₃CN.

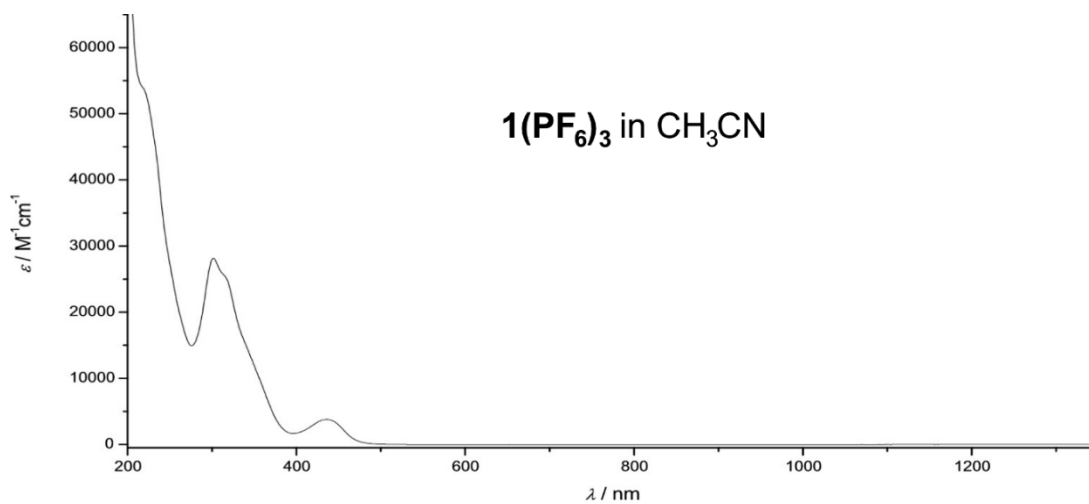


Figure S7. a) Emission spectrum of **1(BF₄)₃** in air-saturated CH₃CN in the region 400 – 600 nm ($\lambda_{\text{exc}} = 430$ nm) and b) decay curves of the broad band luminescence at 500 nm in air-saturated and oxygen-free acetonitrile ($\lambda_{\text{exc}} = 450$ nm, $\lambda_{\text{obs}} = 500$ nm). The fast initial decay resembling the pulse profile of the excitation light pulse (IRF) is caused by Raman and Rayleigh scattered excitation light.

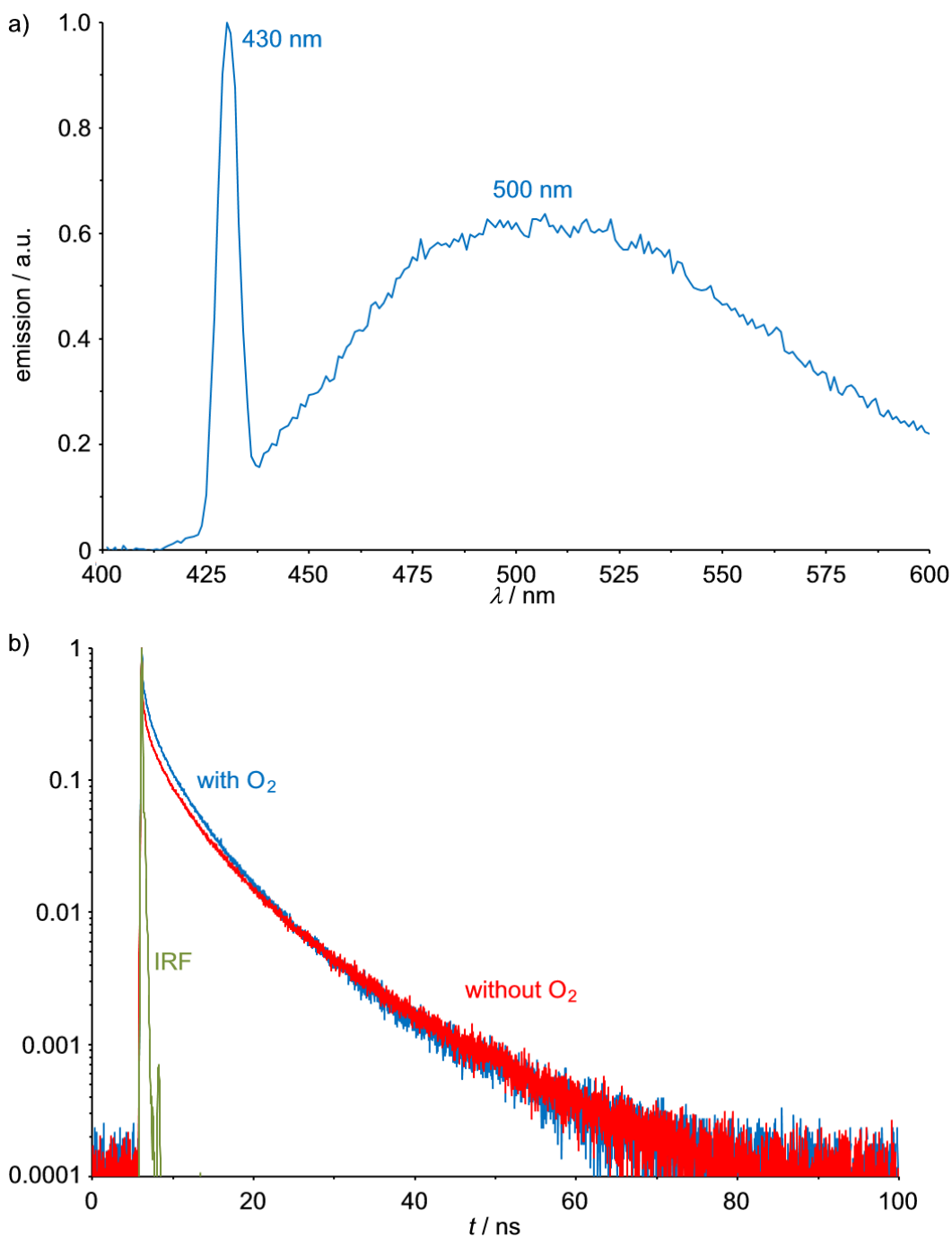


Figure S8. Absorption factor, excitation ($\lambda_{\text{obs}} = 775 \text{ nm}$) and emission spectrum ($\lambda_{\text{exc}} = 435 \text{ nm}$) of **1**(BF₄)₃ in CH₃CN (inset shows decay curve in the presence and absence of O₂, $\lambda_{\text{exc}} = 435 \text{ nm}$, $\lambda_{\text{obs}} = 775 \text{ nm}$).

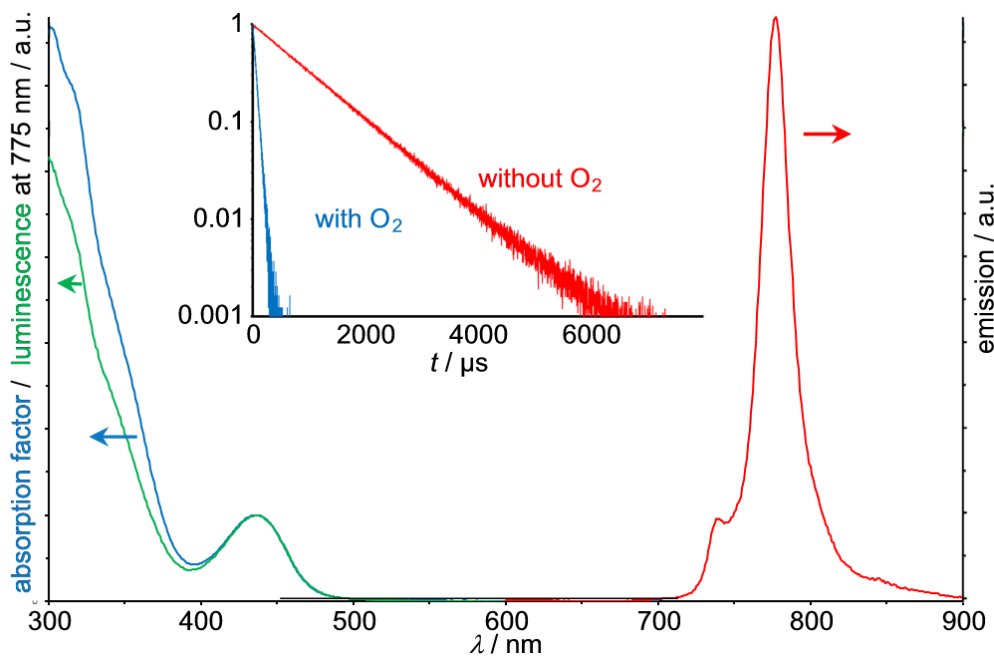


Figure S9. Temperature dependent emission spectra of $1(\text{BF}_4)_3$ in butyronitrile (100 K – 300 K).

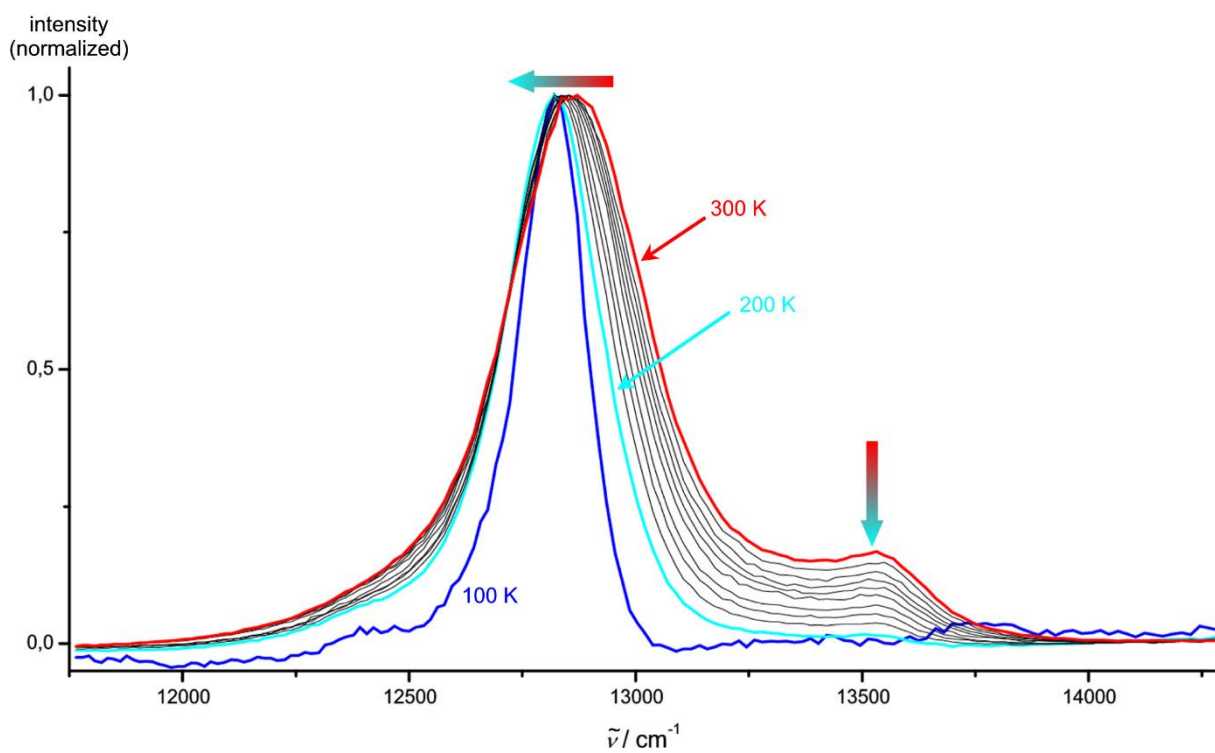


Figure S10. Absorption spectrum of a single crystal of $1(\text{BF}_4)_3 \times 3\text{CH}_3\text{CN}$ and photographs of the measured single crystal of $1(\text{BF}_4)_3 \times 3\text{CH}_3\text{CN}$.

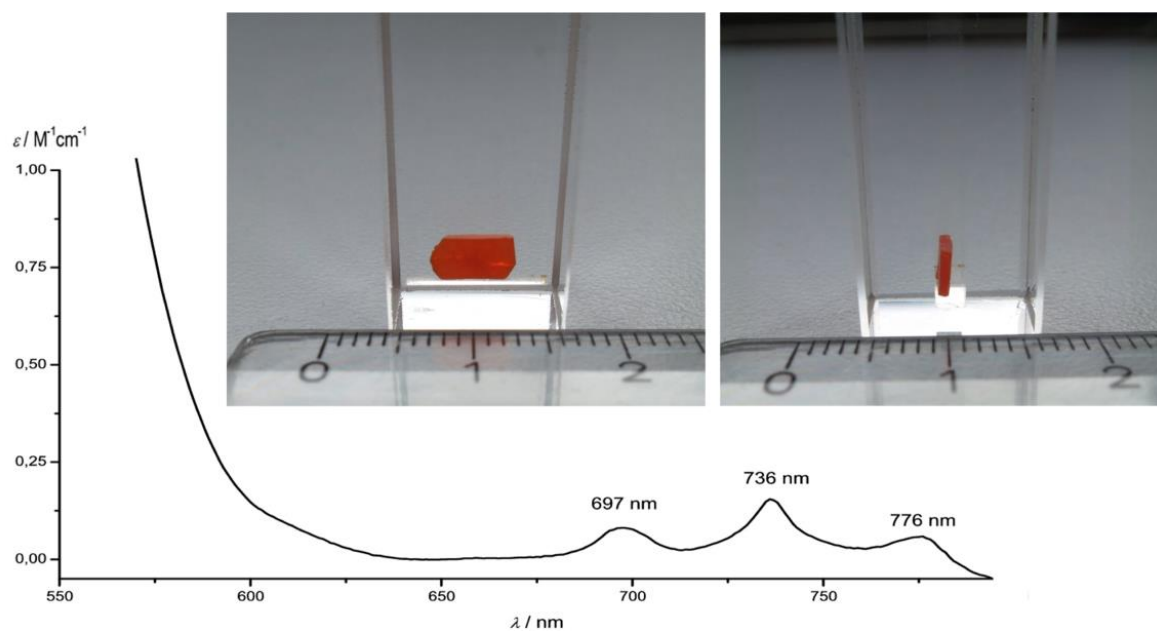


Figure S11. Emission spectrum of a single crystal of $1(\text{BF}_4)_3 \times 3\text{CH}_3\text{CN}$.

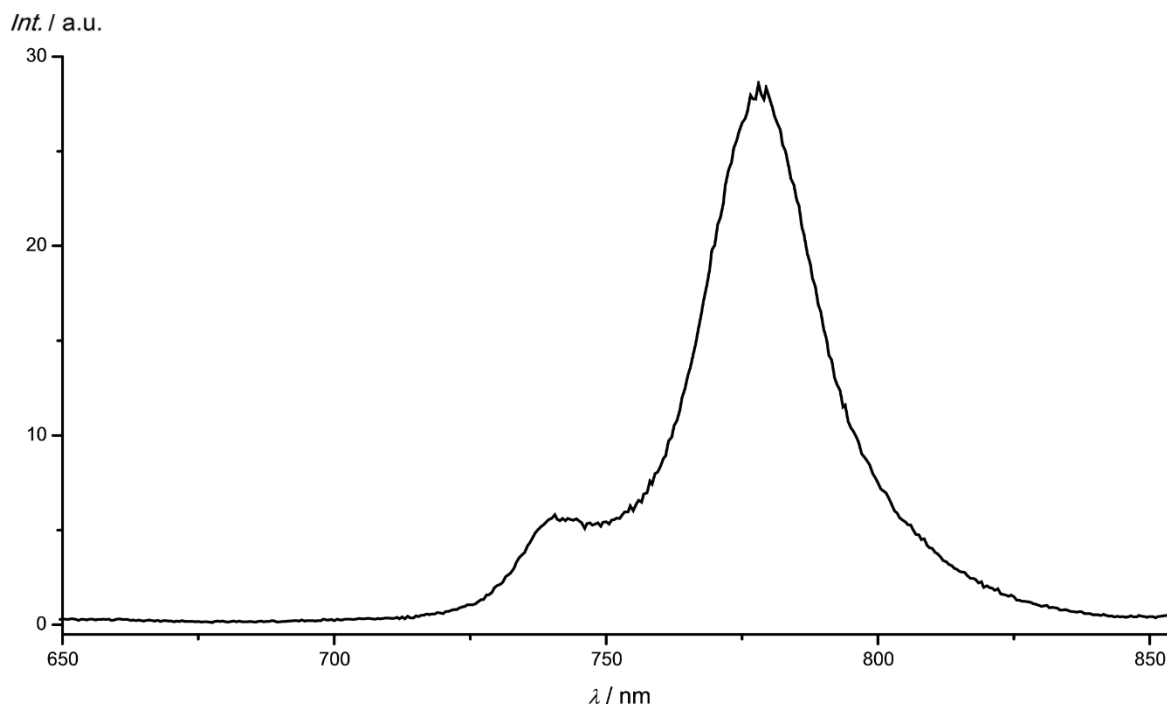


Figure S12. a) Absorption and emission spectra ($\lambda_{\text{exc}} = 330 \text{ nm}$) of ddpd in CH_3CN and b) fluorescence decay curve ($\lambda_{\text{exc}} = 330 \text{ nm}$, $\lambda_{\text{obs}} = 398 \text{ nm}$).

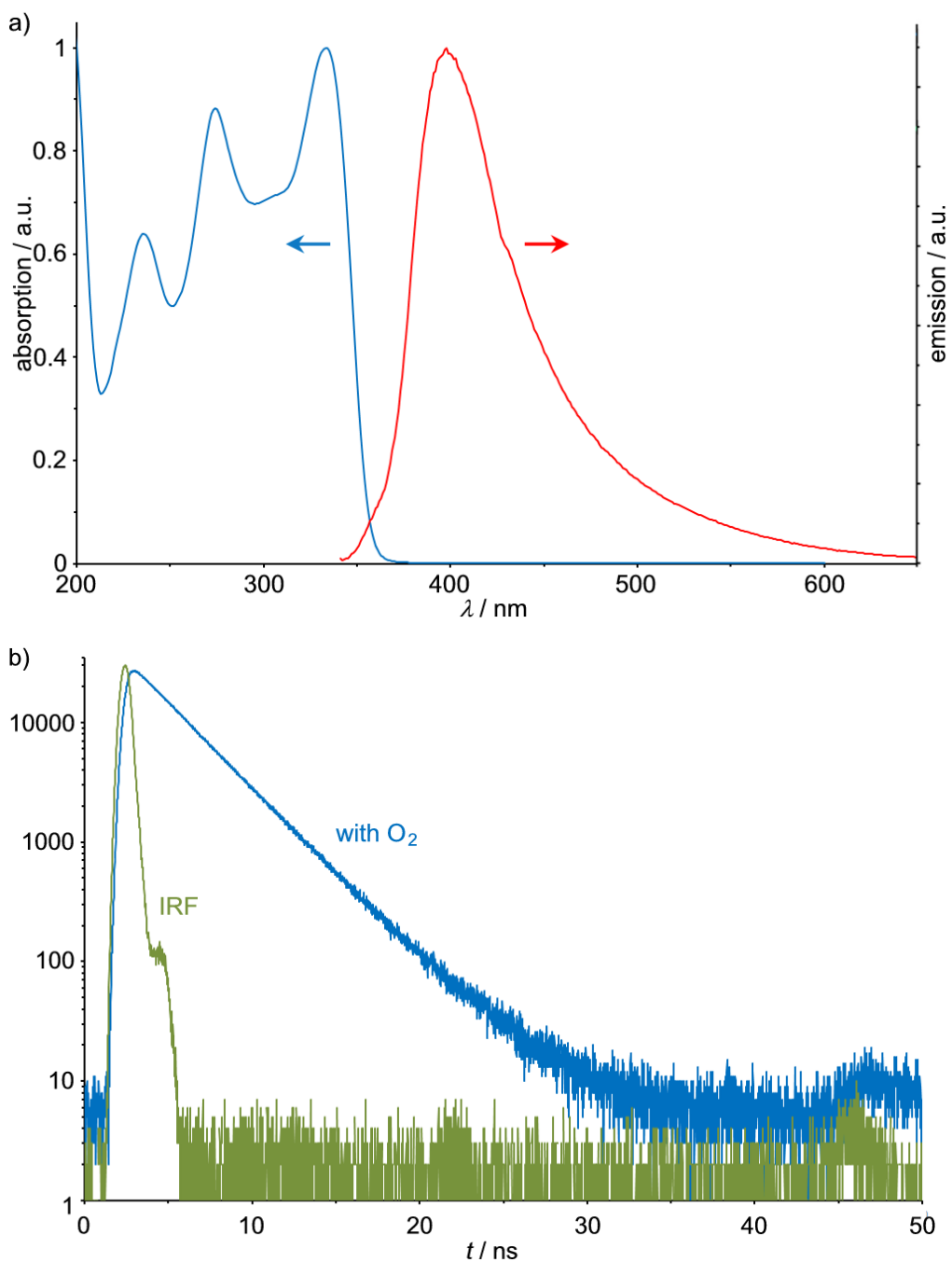


Figure S13. Cyclic voltammogram of **1**(PF₆)₃ in 0.1 M [nBu₄N][PF₆]/CH₃CN, Pt electrodes, referenced against ferrocene.

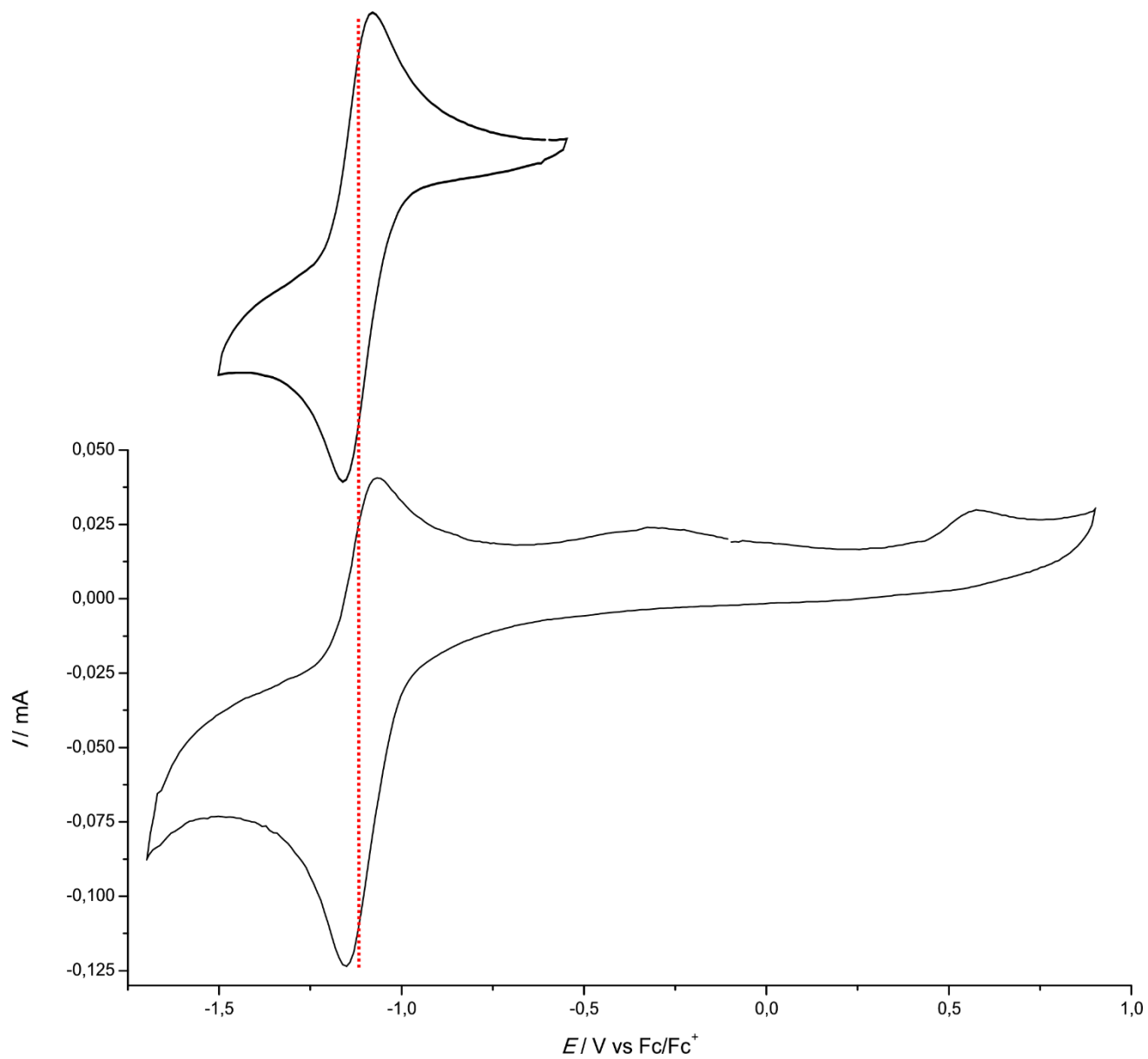


Figure S14. EPR spectrum of **1**(PF₆)₃ at 77 K in CH₃CN, frequency 9.410 GHz.

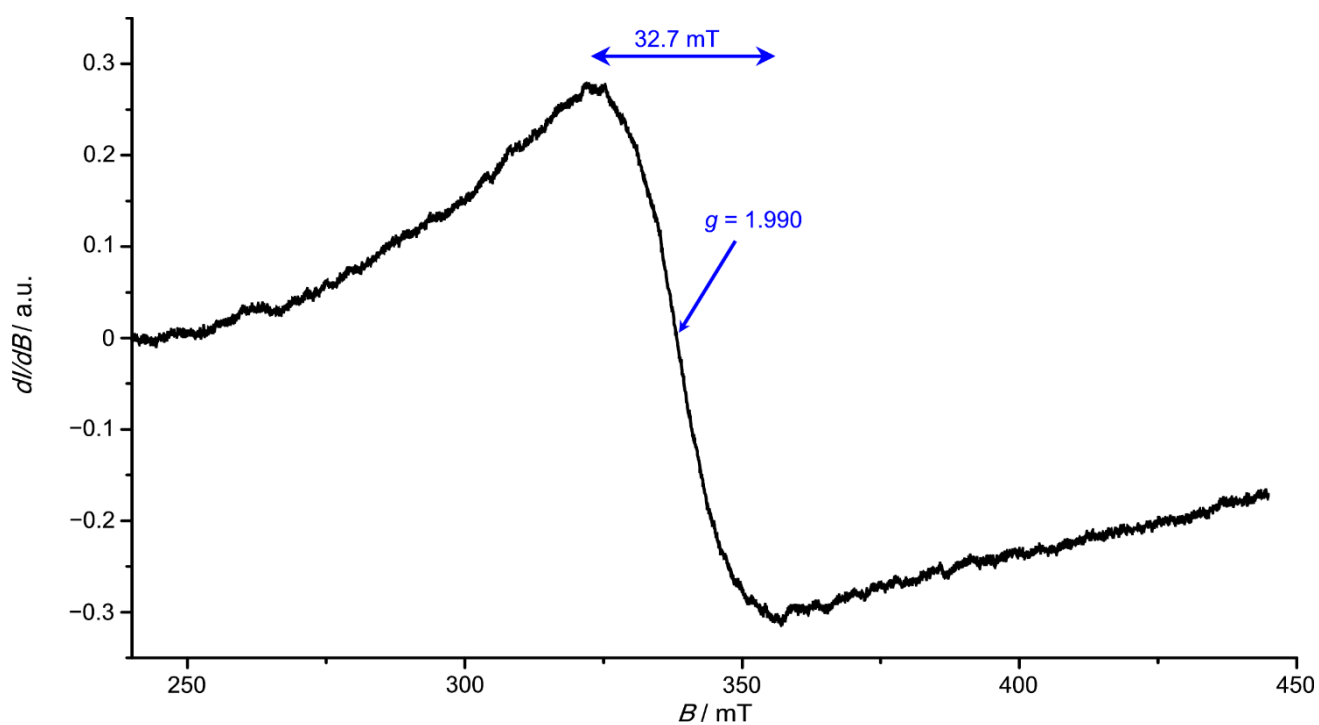


Figure S15. Stern-Volmer plot of **1**(BF₄)₃ in H₂O by quenching with O₂ ($\lambda_{\text{exc}} = 435$ nm, $\lambda_{\text{obs}} = 775$ nm). Dotted line is a linear regression of the data.

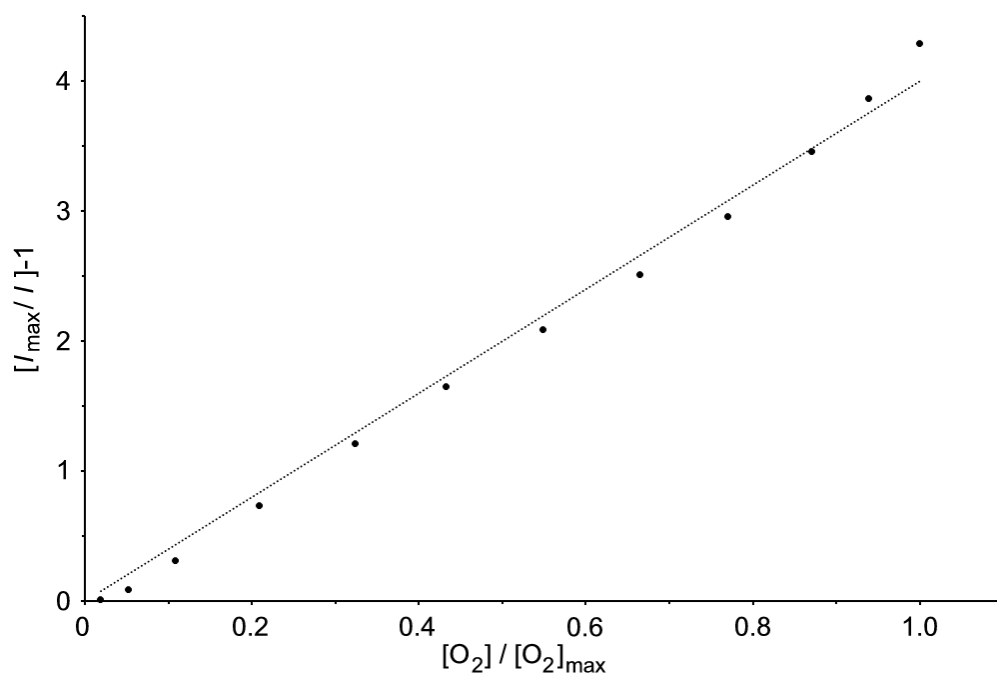


Figure S16. UV/Vis absorption spectra of $1(\text{BF}_4)_3$ under air in H_2O at different pH over time.

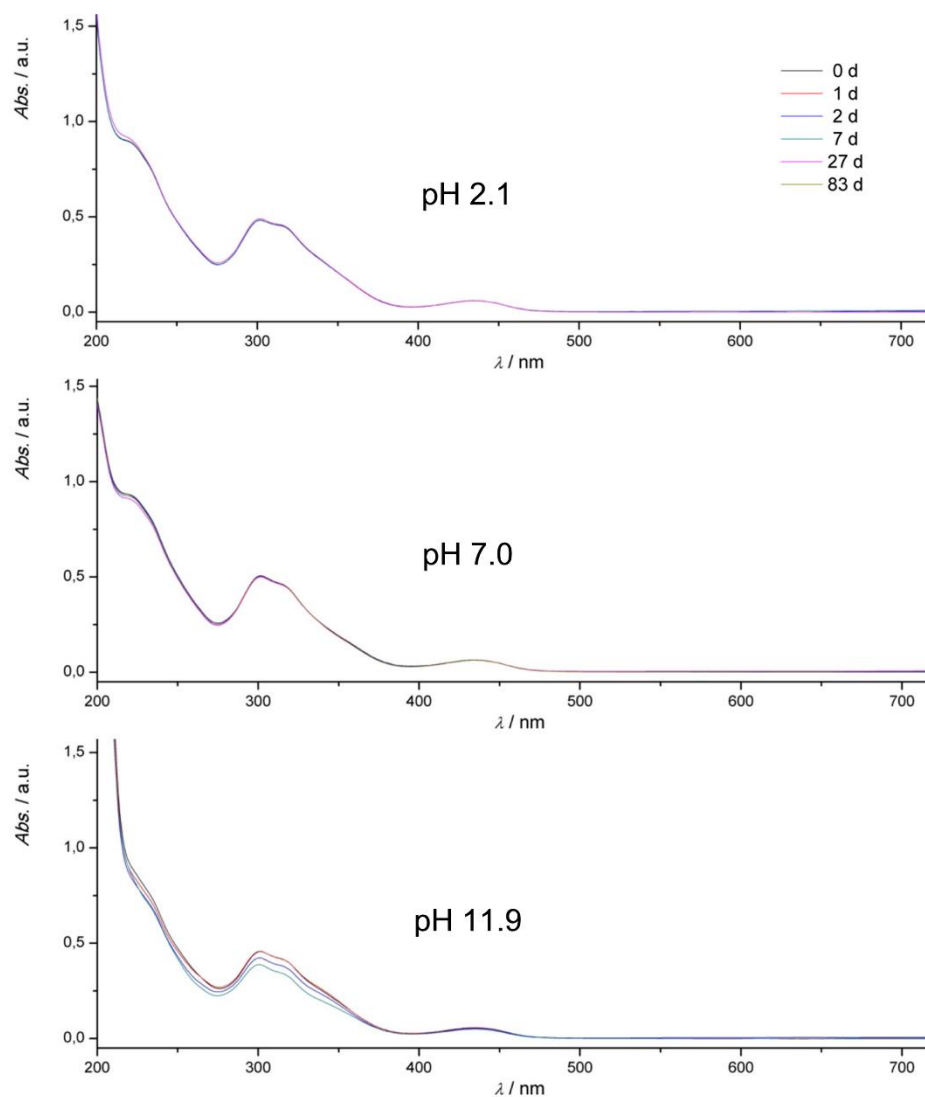


Figure S17. Traces of the intensity of the absorption band at 435 nm of $1(\text{BF}_4)_3$ under air in H_2O at different pH over time.

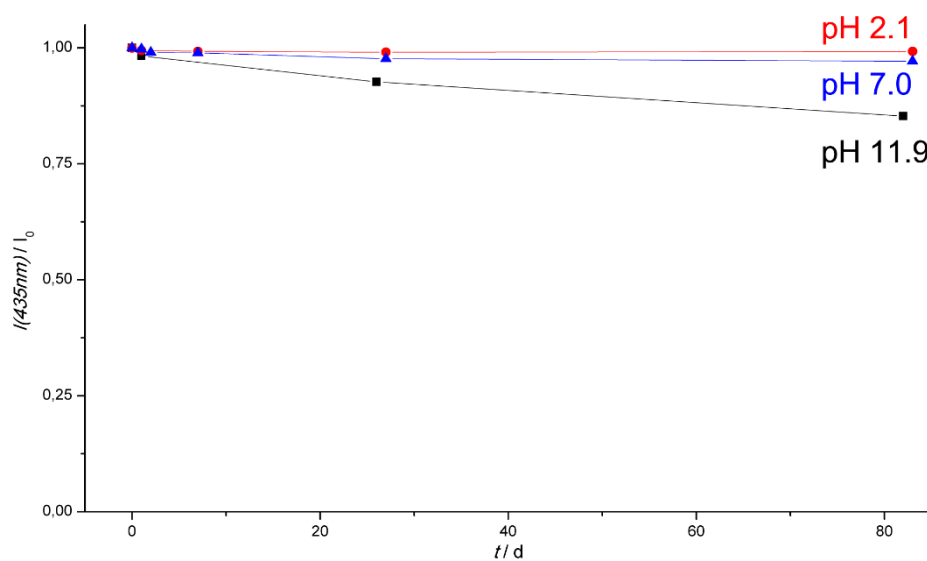


Figure S18. a) Emission spectra of isoabsorptive solutions of $\mathbf{1}(\text{BF}_4)_3$ and $[\text{Cr}(\text{bpy})_3](\text{PF}_6)_2$ in 0.1 mM $[\text{nBu}_4\text{N}]\text{Cl}$ $\text{H}_2\text{O}/\text{MeCN}$ (1:1) solution under aerobic conditions with 430 nm irradiation over time, b) emission spectra of isoabsorptive solutions of $\mathbf{1}(\text{BF}_4)_3$ and $[\text{Cr}(\text{bpy})_3](\text{PF}_6)_2$ in $\text{H}_2\text{O}/\text{MeCN}$ (1:1) solution with pH = 11.4 adjusted with $[\text{nBu}_4\text{N}](\text{OH})$ under aerobic conditions with 430 nm irradiation over time and c) traces of the emission intensity over time.

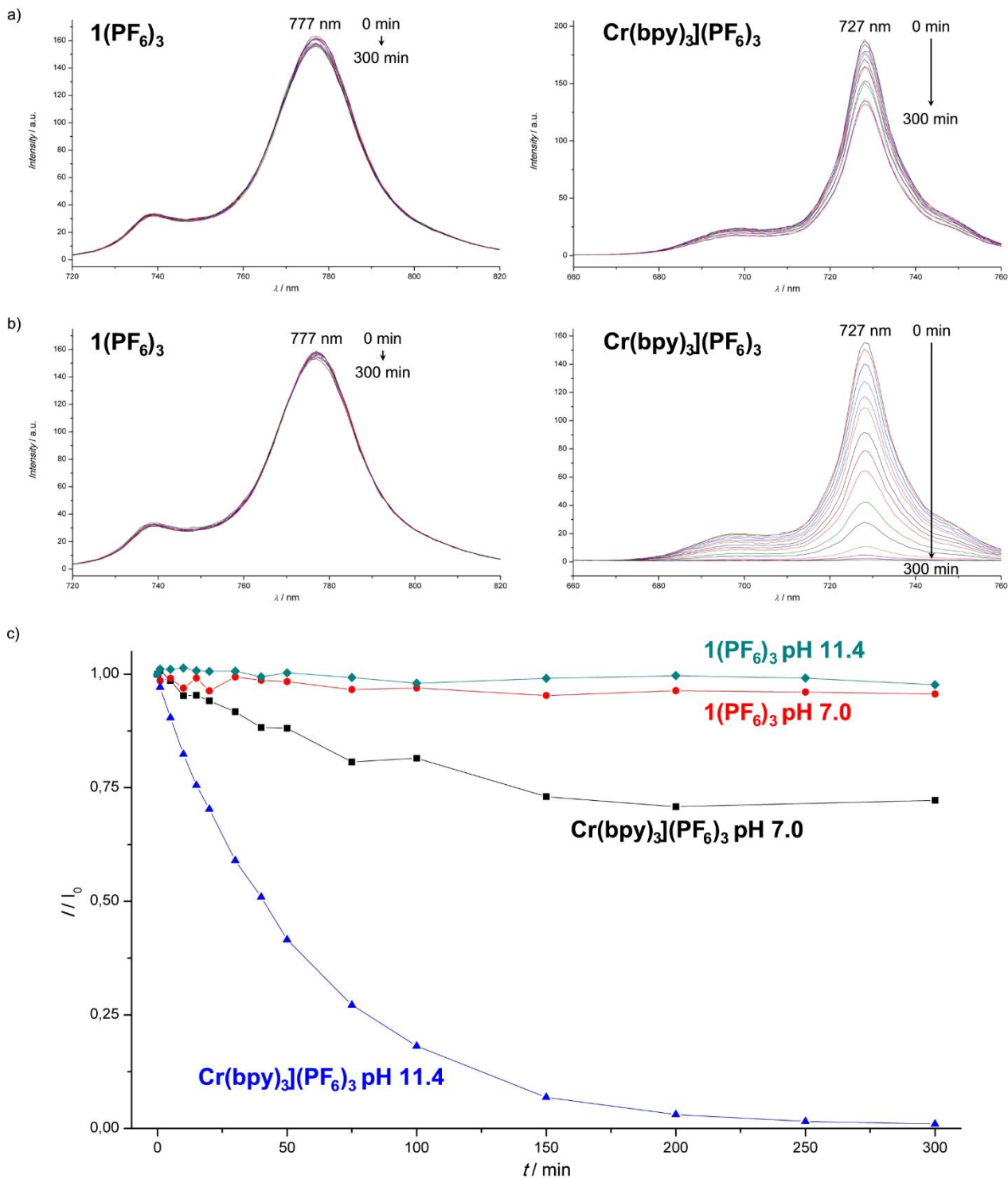


Figure S19. Stern-Volmer plots of **1**(PF₄)₃ ($\lambda_{\text{obs}} = 777$ nm, red) and [Cr(bpy)₃](PF₆)₃ ($\lambda_{\text{obs}} = 727$ nm, blue) by quenching with dGMP in H₂O ($\lambda_{\text{exc}} = 435$ nm). Dotted line is a linear regression of the data.

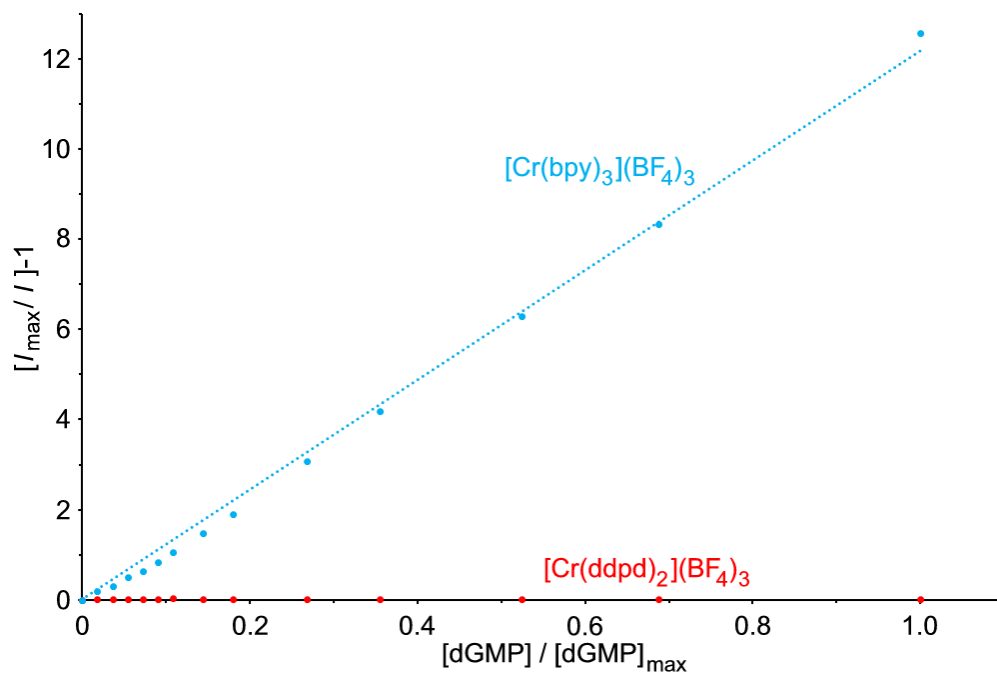
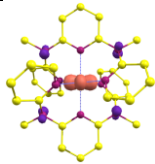
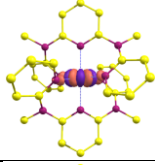
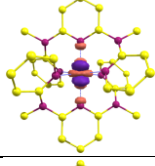
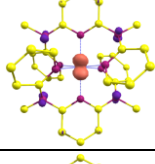
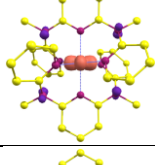
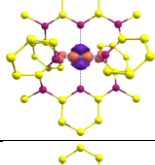
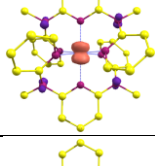
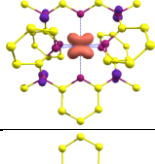
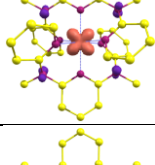
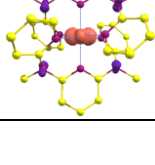
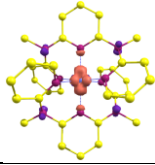
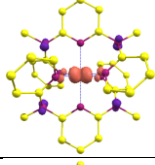
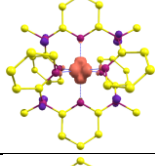
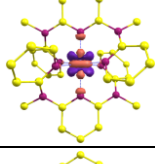
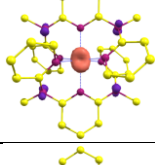
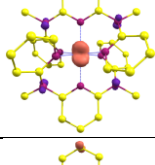
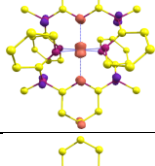
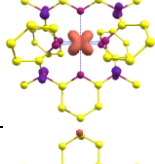
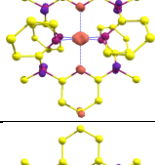
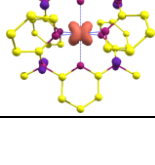


Figure S20. TD-DFT calculated transitions of 1^{3+} (B3LYP, RIJCOSX, Def2-SVP/J, Def2-SVP, ZORA), assignments and corresponding difference electron densities $\psi_{ES} - \psi_{GS}$ at a contour value of 0.005 (purple lobes indicate loss, orange lobes show increase of electron density upon excitation, hydrogen atoms omitted for clarity).

#	λ / nm	character	from	to	difference electron density
1	441.7	LMCT	p (amine-N)	$t_{2g} (d_{xy})$	
2	439.0	MC	$t_{2g} (d_{xy})$	$e_g (d_{x^2-y^2})$	
3	436.9	MC	$t_{2g} (d_{xz})$	$e_g (d_{z^2})$	
4	431.8	LMCT	p (amine-N)	$t_{2g} (d_{xz})$	
5	428.3	LMCT	p (amine-N)	$t_{2g} (d_{xy})$	
6	427.7	MC	$t_{2g} (d_{xz})$	$e_g (d_{x^2-y^2})$	
7	422.2	LMCT	p (amine-N)	$t_{2g} (d_{xz})$	
8	409.8	LMCT	p (amine-N)	$t_{2g} (d_{yz})$	
9	399.5	LMCT	p (amine-N)	$t_{2g} (d_{yz})$	
10	375.7	LMCT	p (amine-N)	$t_{2g} (d_{xy})$	

11	373.4	LMCT	p (amine-N)	$t_{2g} (d_{xy})$	
12	369.5	LMCT	p (amine-N)	$e_g (d_{z^2})$	
13	367.6	LMCT	p (amine-N)	$e_g (d_{x^2-y^2})$	
14	363.6	LMCT	p (amine-N)	$e_g (d_{x^2-y^2} + d_{z^2})$	
15	358.4	MC	$t_{2g} (d_{yz})$	$e_g (d_{z^2})$	
16	357.3	LMCT	p (amine-N)	$t_{2g} (d_{xz})$	
17	356.0	LMCT	p (amine-N)	$t_{2g} (d_{xz})$	
18	352.3	LMCT	p (amine-N)	$t_{2g} (d_{xz})$	
19	350.8	LMCT	p (amine-N)	$t_{2g} (d_{yz})$	
20	348.9	LMCT + $\pi\pi^*$	p (amine-N)	$e_g (d_{x^2-y^2})$	
21	348.0	LMCT	p (amine-N)	$t_{2g} (d_{yz})$	

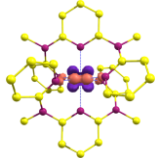
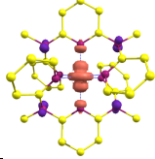
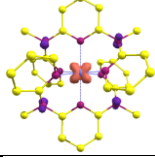
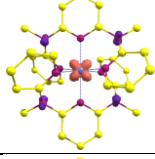
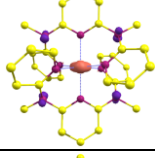
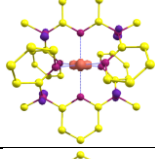
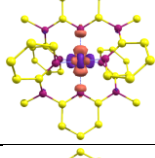
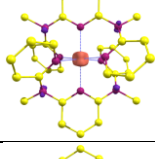
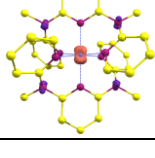
22	347.7	MC	$t_{2g} (d_{xy})$	$e_g (d_{x^2-y^2})$	
23	339.2	LMCT	p (amine-N)	$e_g (d_{z^2})$	
24	338.8	LMCT	p (amine-N)	$t_{2g} (d_{yz})$	
25	336.4	LMCT	p (amine-N)	$t_{2g} (d_{yz})$	
26	333.0	LMCT	p (amine-N)	$t_{2g} (d_{xy})$	
27	329.2	LMCT	p (amine-N)	$t_{2g} (d_{xy})$	
28	327.1	MC	$t_{2g} (d_{xy})$	$e_g (d_{z^2})$	
29	323.5	LMCT	p (amine-N)	$t_{2g} (d_{xy} + d_{xz} + d_{yz})$	
30	322.7	LMCT	p (amine-N)	$t_{2g} (d_{xz})$	

Figure S21. DFT calculated spin density of 1^{3+} (4A_2 ground state) (B3LYP, RIJCOSX, Def2-SVP/J, Def2-SVP, ZORA); isosurface value 0.01 a.u.; hydrogen atoms omitted for clarity; distances in Å.

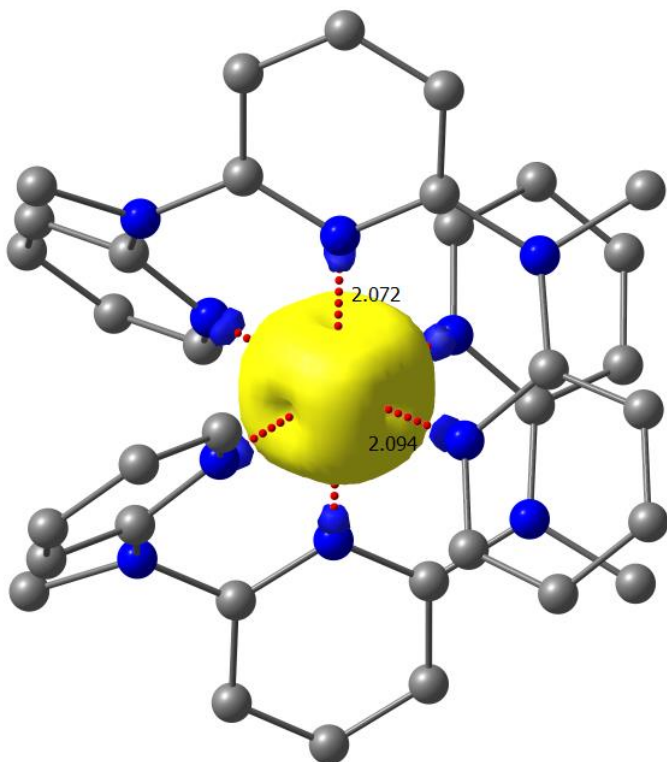


Figure S22. DFT calculated spin density of 1^{3+} (2E state) (B3LYP, RIJCOSX, Def2-SVP/J, Def2-SVP, ZORA); isosurface value 0.01 a.u.; hydrogen atoms omitted for clarity; distances in Å.

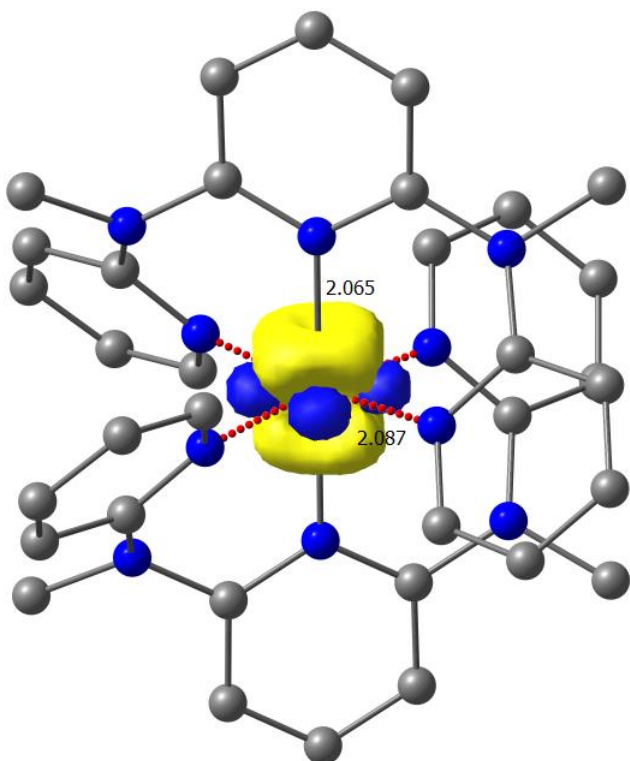


Figure S23. DFT calculated spin density of 1^{3+} (2T_2 state) (B3LYP, RIJCOSX, Def2-SVP/J, Def2-SVP, ZORA); isosurface value 0.01 a.u. (hydrogen atoms omitted for clarity).

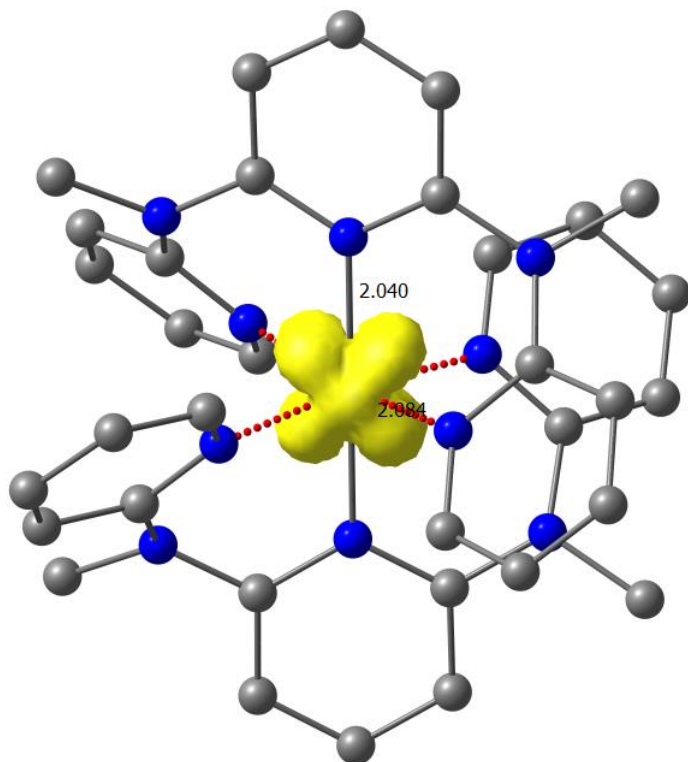


Figure S24. DFT calculated spin density of 1^{3+} (4T_2 state) (B3LYP, RIJCOSX, Def2-SVP/J, Def2-SVP, ZORA); isosurface value 0.01 a.u. (hydrogen atoms omitted for clarity).

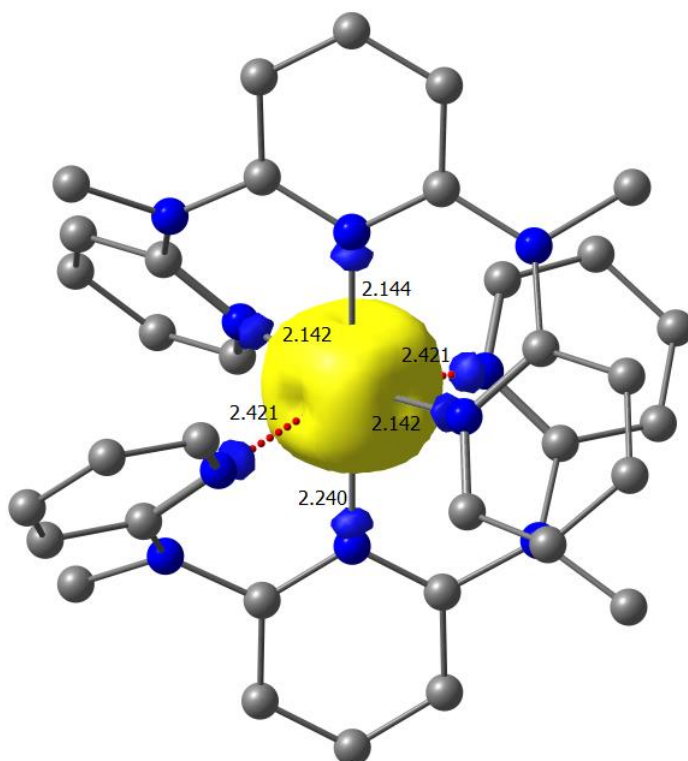


Figure S25. DFT calculated spin density of 1^{2+} (5E state) (B3LYP, RIJCOSX, Def2-SVP/J, Def2-SVP, ZORA); isosurface value 0.01 a.u. (hydrogen atoms omitted for clarity).

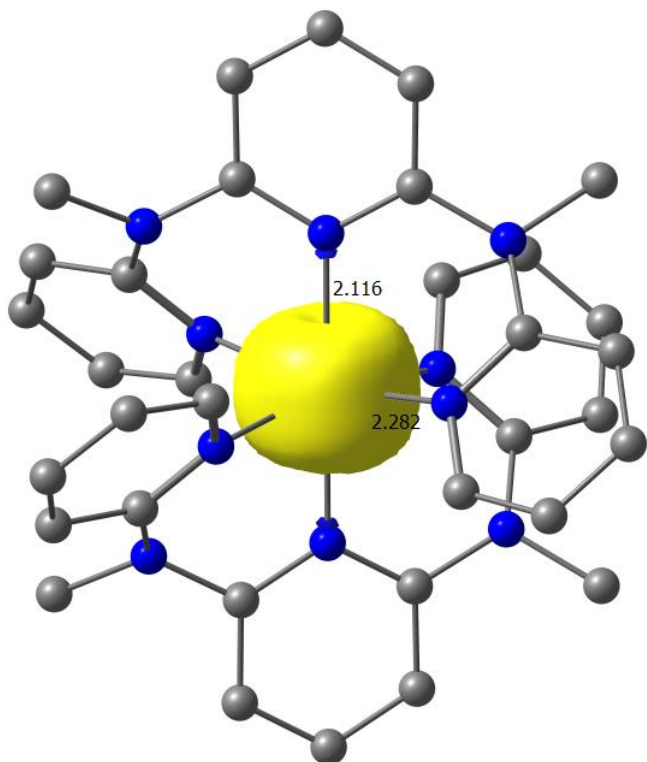


Figure S26. DFT calculated spin density of 1^{2+} (3T_1 state) (B3LYP, RIJCOSX, Def2-SVP/J, Def2-SVP, ZORA); isosurface value 0.01 a.u. (hydrogen atoms omitted for clarity).

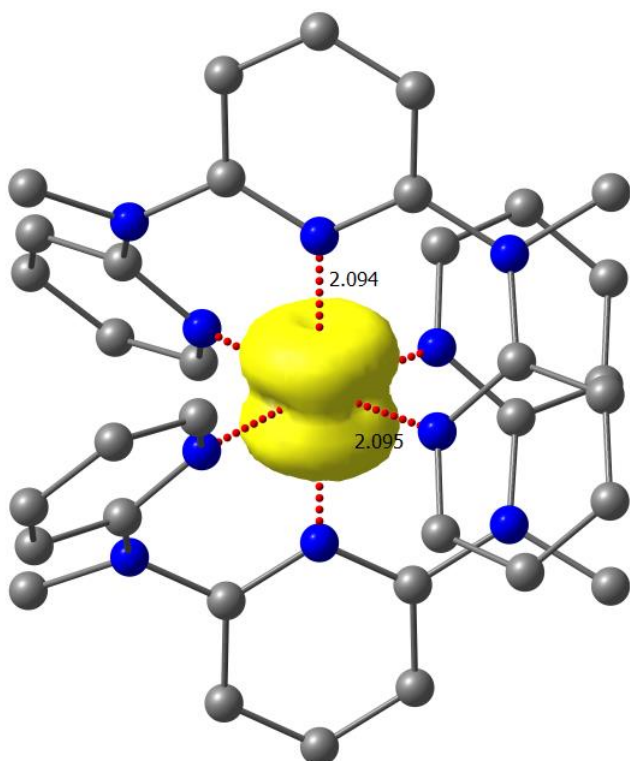


Table S4. Selected distances [Å] and angles [deg] of DFT optimized geometries (B3LYP, RIJCOSX, Def2-SVP/J, Def2-SVP, ZORA).

	1³⁺				1²⁺	
	⁴ A ₂	² E	² T ₂	⁴ T ₂	⁵ E	³ T ₁
Cr1-N1 / Å	2.094	2.087	2.084	2.421	2.282	2.095
Cr1-N3 / Å	2.072	2.065	2.040	2.240	2.116	2.094
Cr1-N5 / Å	2.094	2.087	2.084	2.421	2.282	2.095
Cr1-N6 / Å	2.094	2.087	2.084	2.142	2.282	2.095
Cr1-N8 / Å	2.072	2.065	2.040	2.144	2.116	2.094
Cr1-N10 / Å	2.094	2.087	2.084	2.142	2.282	2.095
N1-Cr1-N3 / °	86.61	86.71	85.89	78.43	83.32	86.41
N1-Cr1-N5 / °	173.23	173.41	171.77	156.86	166.64	172.81
N1-Cr1-N6 / °	92.29	92.60	91.43	92.48	95.88	92.21
N1-Cr1-N8 / °	93.39	93.30	94.11	101.58	96.69	93.59
N1-Cr1-N10 / °	88.11	87.78	89.16	90.00	85.68	88.24
N3-Cr1-N5 / °	86.61	86.70	85.89	78.43	83.32	86.41
N3-Cr1-N6 / °	93.39	93.30	94.11	96.23	96.68	93.59
N3-Cr1-N8 / °	180.00	180.00	180.00	179.99	179.99	180.00
N3-Cr1-N10 / °	93.39	93.30	94.12	96.22	96.67	93.60
N5-Cr1-N6 / °	88.11	87.78	89.16	90.00	85.67	88.24
N5-Cr1-N8 / °	93.39	93.30	94.12	101.56	96.68	93.60
N5-Cr1-N10 / °	92.29	92.60	91.43	95.51	95.89	92.21
N6-Cr1-N8 / °	86.61	86.71	85.89	83.78	83.32	86.41
N6-Cr1-N10 / °	173.23	173.41	171.77	167.55	166.65	172.81
N8-Cr1-N10 / °	86.61	86.70	85.89	83.78	83.32	86.41

Table S5. Cartesian Coordinates of 1^{3+} (4A_2 ground state) (B3LYP, RIJCOSX, Def2-SVP/J, Def2-SVP, ZORA).

6	1.158901880	2.760767451	0.224706652
6	1.182839742	4.161189002	0.216594894
6	0.000088373	4.860583521	-0.000834513
6	-1.182697393	4.161171539	-0.218017322
6	-1.158833616	2.760745225	-0.225638533
7	0.000014817	2.072081362	-0.000340790
1	2.101872453	4.700205243	0.419952948
1	-2.101698883	4.700162380	-0.421574347
6	1.479507091	-0.800775885	2.501102291
6	2.504613912	-0.888335140	3.425803021
6	3.561919051	0.029593708	3.327874008
6	3.526944668	1.002671293	2.336237119
6	2.437747604	1.047984211	1.438261429
7	1.450549983	0.123961358	1.504836689
1	4.389482946	0.003898449	4.036778372
1	0.641895707	-1.491393470	2.541361567
1	2.476624139	-1.647351531	4.205203319
1	4.312859139	1.750175962	2.288737111
6	-2.437730670	1.047587329	-1.438620740
6	-3.526894396	1.002030459	-2.336623948
6	-3.561918522	0.028576101	-3.327890413
6	-2.504680059	-0.889470754	-3.425443709
6	-1.479593876	-0.801635268	-2.500746684
7	-1.450598667	0.123471340	-1.504827693
1	-4.389463896	0.002673403	-4.036808535
1	-4.312752774	1.749614505	-2.289436683
1	-2.476730504	-1.648788247	-4.204551902
1	-0.642033823	-1.492333289	-2.540717029
6	1.158885475	-2.760727762	-0.224635213
6	1.182810108	-4.161148784	-0.216582194
6	0.000041276	-4.860541716	0.000753548
6	-1.182743961	-4.161122325	0.217906195
6	-1.158860604	-2.760695483	0.225600962
7	0.000003175	-2.072027915	0.000394237
1	2.101844407	-4.700167672	-0.419924902
1	-2.101761855	-4.700114754	0.421383314
6	1.479585409	0.800814514	-2.501002806
6	2.504662067	0.888292276	-3.425746928
6	3.561916934	-0.029696369	-3.327843316
6	3.526927205	-1.002741673	-2.336175206
6	2.437765066	-1.047965690	-1.438154006
7	1.450610309	-0.123894682	-1.504713920
1	4.389445375	-0.004079957	-4.036792131
1	0.642010539	1.491477609	-2.541253086
1	2.476679174	1.647285913	-4.205168394
1	4.312794579	-1.750296614	-2.288686839
6	-2.437795759	-1.047569336	1.438579464
6	-3.526980652	-1.002052155	2.336559918
6	-3.562041291	-0.028626902	3.327852841
6	-2.504821878	0.889436887	3.425451647
6	-1.479710824	0.801642677	2.500778435
7	-1.450675927	-0.123440119	1.504838277
1	-4.389600424	-0.002760189	4.036755618
1	-4.312823684	-1.749651018	2.289336669
1	-2.476903545	1.648734800	4.204578890
1	-0.642159238	1.492349164	2.540789527
7	2.355100701	-2.053744841	-0.464103264
6	3.613924474	-2.716830922	-0.069822292
1	3.962675565	-3.458274924	-0.800324496
1	4.390084621	-1.957498612	0.059246156
1	3.469226777	-3.214365488	0.892386521
7	-2.355093821	-2.053683986	0.464880097
6	-3.613902249	-2.716915590	0.070791216
1	-3.962637994	-3.458143688	0.801520437
1	-4.390075096	-1.957636727	-0.058513245
1	-3.469190263	-3.214740146	-0.891265723
7	2.355101759	2.053778179	0.464229738
7	-2.355060483	2.053726320	-0.464939894
6	3.613946700	2.716803934	0.069911194
1	3.962749650	3.458234178	0.800401756
1	4.390067687	1.957434582	-0.059174188
1	3.469248473	3.214338500	-0.892297619
6	-3.613883728	2.716964804	-0.070913985
1	-3.962605185	3.458157976	-0.801685011

1	-4.390053399	1.957683295	0.058398943
1	-3.469202964	3.214829577	0.891126550
1	0.000118007	5.950082217	-0.001036658
1	0.000055564	-5.950040412	0.000898014
24	-0.000024342	0.000048684	0.000057680

Table S6. Cartesian Coordinates of 1^{3+} (2E state) (B3LYP, RIJCOSX, Def2-SVP/J, Def2-SVP, ZORA).

24	0.000040747	-0.000001058	-0.000001058
6	1.158592840	2.755152351	0.225043209
6	1.182742373	4.155480767	0.216659983
6	0.000029105	4.854964717	-0.000784770
6	-1.182685751	4.155415149	-0.218005151
6	-1.158543097	2.755084087	-0.225953923
7	0.000025930	2.065457121	-0.000355078
1	2.101774556	4.694513942	0.419947127
1	-2.101716346	4.694386939	-0.421456341
6	1.468767439	-0.803998574	2.501811389
6	2.494264263	-0.895981222	3.425264847
6	3.555968453	0.016899805	3.326034588
6	3.524249569	0.989619136	2.334155336
6	2.433917419	1.040213773	1.437661871
7	1.442192686	0.120249180	1.504266765
1	4.384057292	-0.012292787	4.034184874
1	0.628292148	-1.490834659	2.543510556
1	2.463334911	-1.654659469	4.204878934
1	4.313333811	1.733666690	2.285826636
6	-2.433892018	1.039749155	-1.437993136
6	-3.524262798	0.988837012	-2.334424158
6	-3.556035658	0.015753078	-3.325943570
6	-2.494328823	-0.897155466	-3.424901832
6	-1.468781197	-0.804827266	-2.501539392
7	-1.442161465	0.119770803	-1.504320741
1	-4.384166832	-0.013707807	-4.034031942
1	-4.313347570	1.732900971	-2.286333588
1	-2.463446038	-1.656122644	-4.204237042
1	-0.628304319	-1.491674463	-2.543035355
6	1.158571673	-2.755166639	-0.225029979
6	1.182709564	-4.155495055	-0.216653633
6	-0.000014288	-4.854969480	0.000763603
6	-1.182726498	-4.155412503	0.217965992
6	-1.158573260	-2.755081441	0.225925876
7	0.000005821	-2.065463471	0.000348728
1	2.101740159	-4.694535109	-0.419925960
1	-2.101763972	-4.694379002	0.421398660
6	1.468833057	0.803987990	-2.501778580
6	2.494362690	0.895976459	-3.425194996
6	3.556061059	-0.016907742	-3.325934574
6	3.524306191	-0.989636070	-2.334064847
6	2.433943877	-1.040233352	-1.437608424
7	1.442224437	-0.120265055	-1.504241365
1	4.384174240	0.012289083	-4.034055755
1	0.628359882	1.490825663	-2.543502089
1	2.463461914	1.654659998	-4.204805378
1	4.313386200	-1.733686799	-2.285717626
6	-2.433929061	-1.039734338	1.437943922
6	-3.524318891	-0.988803674	2.334352190
6	-3.556103393	-0.015709156	3.325860489
6	-2.494392324	0.897193567	3.424830922
6	-1.468826177	0.804845258	2.501492295
7	-1.442192157	-0.119764453	1.504284228
1	-4.384249383	0.013766017	4.033931399
1	-4.313410012	-1.732859695	2.286254741
1	-2.463520123	1.656167624	4.204159782
1	-0.628344536	1.491685576	2.543000429
7	2.354202687	-2.048056186	-0.466032115
6	3.613962575	-2.710903079	-0.074559487
1	3.962276566	-3.450449451	-0.807198509
1	4.389688796	-1.951297713	0.055397979
1	3.470647618	-3.210560704	0.886731203
7	-2.354197395	-2.047892670	0.466718458
6	-3.613968396	-2.710851219	0.075467555
1	-3.962287149	-3.450150466	0.808354761
1	-4.389682975	-1.951276017	-0.054737036
1	-3.470668785	-3.210827409	-0.885660149

7	2.354211683	2.048031843	0.466076566
7	-2.354168820	2.047898491	-0.466756559
6	3.613989034	2.710861274	0.074634630
1	3.962291912	3.450407646	0.807278944
1	4.389709963	1.951245854	-0.055298493
1	3.470706885	3.210515195	-0.886663469
6	-3.613941408	2.710859686	-0.075515710
1	-3.962249578	3.450165812	-0.808400270
1	-4.389661279	1.951286071	0.054673535
1	-3.470650793	3.210826880	0.885617814
1	0.000030163	5.944456534	-0.000964161
1	-0.000023284	-5.944461296	0.000936644

Table S7. Cartesian Coordinates of 1^3+ (2T_2 state) (B3LYP, RIJCOSX, Def2-SVP/J, Def2-SVP, ZORA).

6	1.170854935	2.736475040	0.183882215
6	1.191433051	4.135750922	0.162991884
6	0.000059797	4.834641665	-0.000787416
6	-1.191342562	4.135753039	-0.164358220
6	-1.170824772	2.736469219	-0.184836850
7	0.000000529	2.039822717	-0.000378362
1	2.116994223	4.676666910	0.327115150
1	-2.116880449	4.676658443	-0.328638122
6	1.470923307	-0.741277311	2.512018689
6	2.508793883	-0.832623888	3.423287312
6	3.590736457	0.050325286	3.285387425
6	3.567461124	0.996635497	2.267325012
6	2.464975361	1.042440021	1.386844450
7	1.455323691	0.149758220	1.484683503
1	4.426987325	0.021123168	3.983708773
1	0.615346885	-1.406291714	2.585701329
1	2.469946452	-1.567997698	4.224578615
1	4.370783939	1.722588364	2.188985083
6	-2.465001290	1.042094998	-1.387270438
6	-3.567448953	0.996082507	-2.267786984
6	-3.590748098	0.049433093	-3.285535066
6	-2.508856855	-0.833631442	-3.423105804
6	-1.471016442	-0.742050439	-2.511827127
7	-1.455411534	0.149314769	-1.484782459
1	-4.426966688	0.020062168	-3.983887106
1	-4.370720438	1.722123747	-2.189730165
1	-2.470025299	-1.569273015	-4.224153157
1	-0.615469654	-1.407132577	-2.585261583
6	1.170845410	-2.736497265	-0.183855227
6	1.191424055	-4.135772089	-0.162925208
6	0.000045509	-4.834656482	0.000844038
6	-1.191360554	-4.135763093	0.164370920
6	-1.170841177	-2.736479273	0.184820975
7	-0.000014288	-2.039842296	0.000355607
1	2.116989460	-4.676692311	-0.327005081
1	-2.116900029	-4.676665852	0.328650822
6	1.470982045	0.741229156	-2.512024510
6	2.508877493	0.832565679	-3.423266674
6	3.590814775	-0.050384553	-3.285331332
6	3.567509280	-0.996687356	-2.267262569
6	2.465005524	-1.042473889	-1.386803175
7	1.455364966	-0.149786795	-1.484674507
1	4.427077815	-0.021197782	-3.983638922
1	0.615402977	1.406236151	-2.585744721
1	2.470049641	1.567929434	-4.224568561
1	4.370816219	-1.722655570	-2.188904119
6	-2.465025103	-1.042079123	1.387215404
6	-3.567498167	-0.996022710	2.267700199
6	-3.590824829	-0.049328316	3.285404359
6	-2.508936760	0.833742569	3.422965572
6	-1.471065126	0.742112353	2.511729758
7	-1.455426880	-0.149305773	1.484727424
1	-4.427069348	-0.019914527	3.983724120
1	-4.370775472	-1.722058129	2.189646555
1	-2.470135368	1.569427006	4.223974824
1	-0.615524159	1.407201370	2.585157864
7	2.370580723	-2.038816751	-0.402763684
6	3.621549919	-2.703345898	0.011373607
1	3.977633289	-3.447678679	-0.712707561
1	4.397042243	-1.944711044	0.146917596

1	3.462889879	-3.196225821	0.973641687
7	-2.370593952	-2.038770183	0.403531520
6	-3.621556798	-2.703489305	-0.010317369
1	-3.977572963	-3.447581310	0.714044792
1	-4.397078227	-1.944925361	-0.146089434
1	-3.462923746	-3.196701023	-0.972419817
7	2.370582310	2.038796642	0.402819776
7	-2.370577019	2.038762246	-0.403555333
6	3.621565265	2.703337431	-0.011258775
1	3.977627468	3.447641637	0.712861551
1	4.397059706	1.944705752	-0.146810173
1	3.462932213	3.196254397	-0.973512039
6	-3.621540393	2.703472901	0.010303610
1	-3.977555500	3.447579194	-0.714044263
1	-4.397062881	1.944906310	0.146057154
1	-3.462910517	3.196665568	0.972416642
1	0.000084668	5.924220267	-0.000952519
1	0.000069851	-5.924235084	0.001043538
24	-0.000053447	-0.000004233	-0.000006350

Table S8. Cartesian Coordinates of 1^{3+} (4T_2 state) (B3LYP, RIJCOSX, Def2-SVP/J, Def2-SVP, ZORA).

6	1.148132064	2.843598507	0.208908065
6	1.174651782	4.250573918	0.214528457
6	-0.000741907	4.958628424	-0.000259826
6	-1.175824439	4.250136818	-0.215201570
6	-1.148761785	2.843148177	-0.209796025
7	-0.000176216	2.143238239	-0.000447155
1	2.098280927	4.782252588	0.417620335
1	-2.099654142	4.781473110	-0.418273869
6	1.760317115	-0.457688578	2.780750242
6	2.916700640	-0.521259170	3.555195854
6	3.964335065	0.347156680	3.227969577
6	3.807582180	1.242150457	2.171584148
6	2.589916226	1.250451131	1.453697529
7	1.603102258	0.388950041	1.747760797
1	4.889060666	0.346692062	3.803755700
1	0.918813103	-1.118759023	2.992327477
1	2.991971870	-1.218218945	4.387294798
1	4.602244480	1.946447274	1.948095132
6	-2.589636291	1.249398598	-1.454820972
6	-3.806941347	1.240929116	-2.173280690
6	-3.963149708	0.345737956	-3.229580922
6	-2.915313666	-0.522683715	-3.556172186
6	-1.759301624	-0.458904627	-2.781224385
7	-1.602636582	0.387921849	-1.748284683
1	-4.887609133	0.345115114	-3.805796207
1	-4.601741762	1.945224346	-1.950270580
1	-2.990167376	-1.219797481	-4.388180112
1	-0.917649443	-1.119943850	-2.992303135
6	1.160654515	-2.931317045	-0.119661264
6	1.195118241	-4.347016472	-0.068743300
6	-0.000808054	-5.050271869	0.000291047
6	-1.196447535	-4.346572492	0.069464568
6	-1.161445105	-2.930874652	0.120619604
7	-0.000259826	-2.241177306	0.000497956
1	2.133434701	-4.884226632	-0.156207303
1	-2.134969845	-4.883431278	0.156871420
6	1.642927609	0.571555351	-2.471165147
6	2.735785522	0.634464471	-3.332902780
6	3.776955518	-0.278521861	-3.141697281
6	3.670500931	-1.226403729	-2.125253092
6	2.516415623	-1.242402345	-1.315823043
7	1.536883134	-0.329746748	-1.473515217
1	4.654515550	-0.271435120	-3.787518425
1	0.813607904	1.268783948	-2.569413253
1	2.767459426	1.377730960	-4.127274561
1	4.453915568	-1.967230182	-2.000653017
6	-2.516303966	-1.241403259	1.316960245
6	-3.669998212	-1.225186093	2.126920000
6	-3.775899280	-0.277123775	3.143255708
6	-2.734555185	0.635805406	3.333833602
6	-1.642098917	0.572642810	2.471628177
7	-1.536606904	-0.328838680	1.474067678
1	-4.653164561	-0.269842825	3.789476910

1	-4.453534560	-1.965965977	2.002778193
1	-2.765809452	1.379221652	4.128082086
1	-0.812665439	1.269804202	2.569375152
7	2.365229683	-2.258024193	-0.342272903
6	3.598503720	-2.891307011	0.171822265
1	4.019389079	-3.634832797	-0.517551225
1	4.344743656	-2.112542254	0.348487561
1	3.384243556	-3.369344571	1.129663778
7	-2.365701179	-2.257133588	0.343397934
6	-3.599333470	-2.889904162	-0.170447992
1	-4.020325193	-3.633363801	0.518930790
1	-4.345331572	-2.110835658	-0.346811127
1	-3.385505644	-3.367887746	-1.128416507
7	2.380047175	2.175056079	0.409103756
7	-2.380345101	2.174123140	-0.410165815
6	3.573996993	2.835975709	-0.149408434
1	4.005759060	3.595060893	0.517411522
1	4.339262438	2.081009640	-0.351979601
1	3.312315668	3.311892855	-1.096816159
6	-3.574685981	2.834579210	0.148036806
1	-4.006540655	3.593575492	-0.518823367
1	-4.339742931	2.079315744	0.350305284
1	-3.313463453	3.310492652	1.095577355
1	-0.000959398	6.047881052	-0.000178333
1	-0.001016020	-6.139728760	0.000203733
24	-0.000044451	-0.097065395	0.000069322

Table S9. Cartesian Coordinates of 1^{2+} (5E state) (B3LYP, RIJCOSX, Def2-SVP/J, Def2-SVP, ZORA).

6	1.150245598	2.804388061	0.241551951
6	1.173900879	4.207262348	0.247756025
6	0.000363545	4.909463095	-0.000060326
6	-1.173310318	4.207452323	-0.247781955
6	-1.149920154	2.804576448	-0.241386848
7	0.000094723	2.116036412	0.000134940
1	2.090561290	4.740882040	0.475421837
1	-2.089872301	4.741209072	-0.475522380
6	1.632838845	-0.643941507	2.662211892
6	2.744665116	-0.748689497	3.488351772
6	3.796647791	0.152846498	3.280154391
6	3.687520859	1.116090382	2.281010594
6	2.519363140	1.152341669	1.486838313
7	1.528348034	0.265252213	1.673118759
1	4.687893405	0.119658618	3.905582103
1	0.782348345	-1.314130734	2.783572873
1	2.784487821	-1.501660038	4.272640610
1	4.479760056	1.846115268	2.148960762
6	-2.519362611	1.152706801	-1.486547794
6	-3.687591239	1.116555529	-2.280624295
6	-3.796900738	0.153298945	-3.279734225
6	-2.745033424	-0.748358232	-3.487997223
6	-1.633130421	-0.643706552	-2.661948891
7	-1.528460220	0.265504630	-1.672888566
1	-4.688200328	0.120194674	-3.905088910
1	-4.479742593	1.846668787	-2.148536891
1	-2.785001123	-1.501340944	-4.272267011
1	-0.782711890	-1.313977802	-2.783367023
6	1.150130767	-2.804260000	-0.241589523
6	1.173718843	-4.207134816	-0.247987805
6	0.000165103	-4.909321275	-0.000222254
6	-1.173457958	-4.207279811	0.247622673
6	-1.150010114	-2.804398644	0.241403253
7	0.000028046	-2.115858079	-0.000043922
1	2.090348031	-4.740762446	-0.475762097
1	-2.090034758	-4.741027564	0.475320764
6	1.632996540	0.643902347	-2.662359533
6	2.744847153	0.748547678	-3.488487770
6	3.796776910	-0.153031710	-3.280215776
6	3.687580126	-1.116207859	-2.281012711
6	2.519397007	-1.152345373	-1.486871122
7	1.528430057	-0.265226283	-1.673222477
1	4.688034167	-0.119936436	-3.905631845
1	0.782538320	1.314123325	-2.783792482
1	2.784723834	1.501462655	-4.272826351
1	4.479779635	-1.846267142	-2.148911548

6	-2.519504959	-1.152652296	1.486717131
6	-3.687747876	-1.116646018	2.280777756
6	-3.797137280	-0.153470927	3.279958596
6	-2.745330292	0.748237051	3.488302558
6	-1.633401889	0.643709727	2.662268514
7	-1.528655486	-0.265417316	1.673144688
1	-4.688446925	-0.120475138	3.905304285
1	-4.479844195	-1.846806903	2.148624734
1	-2.785361493	1.501158907	4.272626851
1	-0.783029925	1.314032307	2.783754910
7	2.365461462	-2.113790583	-0.467855131
6	3.588047178	-2.760154663	0.031102393
1	3.996765164	-3.519490148	-0.650956809
1	4.353194087	-1.995838033	0.197388935
1	3.375749732	-3.235018218	0.992315823
7	-2.365413836	-2.114076868	0.467703786
6	-3.587917000	-2.760525088	-0.031357456
1	-3.996585243	-3.519957412	0.650622898
1	-4.353131115	-1.996271429	-0.197613835
1	-3.375530653	-3.235288628	-0.992600521
7	2.365519142	2.113846676	0.467872594
7	-2.365322289	2.114228213	-0.467630231
6	3.588166243	2.760062057	-0.031130968
1	3.996953022	3.519403363	0.650877962
1	4.353237480	1.995661288	-0.197374647
1	3.375907427	3.234875869	-0.992377208
6	-3.587843444	2.760684370	0.031367511
1	-3.996543438	3.520020384	-0.650700688
1	-4.353026338	1.996418011	0.197718083
1	-3.375467681	3.235565387	0.992554482
1	0.000474143	5.998525748	-0.000136528
1	0.000218021	-5.998383929	-0.000294223
24	-0.000042863	0.000154520	0.000106365

Table S10. Cartesian Coordinates of 1^{2+} (3T_1 state) (B3LYP, RIJCOSX, Def2-SVP/J, Def2-SVP, ZORA).

6	-1.153366686	-2.777927611	0.229576141
6	-1.181281315	-4.180979702	0.222985768
6	-0.000121711	-4.879732329	-0.000807524
6	1.181086577	-4.180993989	-0.224391262
6	1.153269317	-2.777937136	-0.230557236
7	-0.000023813	-2.093652214	-0.000384183
1	-2.100110822	-4.717306135	0.433275515
1	2.099877984	-4.717320423	-0.434842408
6	-1.494937900	0.789693325	2.499220537
6	-2.533108519	0.886819576	3.413511292
6	-3.579442756	-0.040233875	3.326782845
6	-3.520293969	-1.029820732	2.349293510
6	-2.432822022	-1.061036897	1.452390990
7	-1.452393107	-0.131574102	1.503981010
1	-4.412365100	-0.013006648	4.028086107
1	-0.657536599	1.481179820	2.542662814
1	-2.515051404	1.658539925	4.180417715
1	-4.293981799	-1.790187054	2.305581881
6	2.432834722	-1.060705103	-1.452804278
6	3.520289735	-1.029267741	-2.349720027
6	3.579532187	-0.039306757	-3.326823591
6	2.533298494	0.887895393	-3.413186906
6	1.495124699	0.790518313	-2.498927373
7	1.452500001	-0.131126418	-1.504043452
1	4.412446593	-0.011898550	-4.028128970
1	4.293895014	-1.789737782	-2.306323259
1	2.515323930	1.659915257	-4.179792757
1	0.657787958	1.482101647	-2.542090244
6	-1.153352927	2.777882630	-0.229516873
6	-1.181265439	4.180935780	-0.222886811
6	-0.000094194	4.879682057	0.000858855
6	1.181120445	4.180930488	0.224356337
6	1.153294188	2.777872576	0.230499555
7	-0.000007938	2.093587654	0.000373070
1	-2.100103943	4.717271739	-0.433111999
1	2.099924023	4.717251630	0.434768324
6	-1.495069135	-0.789716080	-2.499198312
6	-2.533236580	-0.886757662	-3.413501766
6	-3.579514724	0.040358232	-3.326763794

6	-3.520319898	1.029910163	-2.349244296
6	-2.432859064	1.061035310	-1.452324843
7	-1.452477246	0.131521713	-1.503933913
1	-4.412423838	0.013209852	-4.028086107
1	-0.657705936	-1.481248084	-2.542654876
1	-2.515213861	-1.658454199	-4.180432003
1	-4.293957457	1.790328344	-2.305524730
6	2.432887640	1.060659594	1.452717493
6	3.520329424	1.029292083	2.349653350
6	3.579590925	0.039368671	3.326792899
6	2.533390041	-0.887869993	3.413162564
6	1.495225243	-0.790559059	2.498886097
7	1.452577261	0.131054450	1.503973601
1	4.412490515	0.012018674	4.028118916
1	4.293904010	1.789792817	2.306244940
1	2.515430295	-1.659867102	4.179791170
1	0.657911257	-1.482168852	2.542063785
7	-2.346639686	2.068825863	-0.471389506
6	-3.599891752	2.718066022	-0.062840327
1	-3.963542358	3.467316447	-0.780017319
1	-4.371412072	1.952977851	0.063235094
1	-3.452345493	3.205828272	0.904473987
7	2.346618519	2.068797817	0.472141996
6	3.599840951	2.718253351	0.063844706
1	3.963431230	3.467270408	0.781296341
1	4.371405193	1.953251436	-0.062486308
1	3.452284638	3.206351628	-0.903298685
7	-2.346637040	-2.068852322	0.471479995
7	2.346584651	-2.068863964	-0.472250477
6	-3.599911332	-2.718050146	0.062935050
1	-3.963605330	-3.467258237	0.780133209
1	-4.371395139	-1.952929696	-0.063176884
1	-3.452374069	-3.205850497	-0.904360214
6	3.599821901	-2.718291451	-0.063953187
1	3.963434935	-3.467291575	-0.781409585
1	4.371364976	-1.953268898	0.062387881
1	3.452274054	-3.206399254	0.903186499
1	-0.000162987	-5.968862718	-0.000978978
1	-0.000131236	5.968812446	0.001057825
24	0.000055034	-0.000066147	-0.000006350

6.2 Supporting Information: Thermo-Chromium: A Contactless Optical Molecular Thermometer

The ligand ddpd and the complexes $[\text{Cr}(\text{ddpd})_2][\text{BF}_4]_3$ **[1][BF₄]₃** and $[\text{Cr}(\text{ddpd})_2][\text{PF}_6]_3$ **[1][PF₆]₃** were synthesized according to literature procedures.^[1,2] UV/Vis spectra were recorded on a Varian Cary 5000 spectrometer in 1 cm cuvettes. Emission spectra of solutions were recorded on a Varian Cary Eclipse spectrometer ($\lambda_{\text{exc}} = 435$ nm; spectral bandwidths of 10 nm for excitation and 5 nm for emission, respectively). Temperature was measured by either a Peltier element (Varian Type SPVF 1x0 Single Cell Peltier Accessory; high T) or an Oxford cryostat (Oxford Instruments Optistat^{DN}; low T). Photoluminescence spectra of micelles and particles were measured on an Edinburgh Instruments fluorometer (FSP 920) equipped with a Xe lamp, Czerny–Turner double monochromators, a reference channel, and Glan-Thompson polarizer's placed in the excitation and emission channels set to 0° and 54.7°, respectively (magic angle conditions) to render detected emission intensities independent of possible emission anisotropies. All spectra shown here were not corrected for the wavelength-dependent spectral response of the fluorometers detection channel. The spectra were measured with an excitation wavelength of 433 nm, spectral bandwidths of 12 nm for excitation and 4 nm for emission, respectively, an integration time of 0.5 s, a step width of 1 nm, and a scan range of 650 nm to 830 nm. All measurements were performed with solutions, which were flushed with Ar for 20 minutes prior measuring, using 10 mm x 10 mm quartz cuvettes from Hellma GmbH. For temperature-dependent luminescence measurements from 20°C to 70°C, a thermostat (temperature regime from -10°C to 95°C) was used. Prior to its use, the thermostat was calibrated with an external temperature sensing device or probe which was calibrated with an accuracy of $\pm 0.1^\circ\text{C}$. Preparation of dye loaded polystyrene nanoparticles (PSP) was performed following a previously described staining procedure.^[3] In short, 100 nm-sized carboxy-functionalized PSP (PSP-COOH) were stained with the hydrophobic dye **[1][PF₆]₃**. For this purpose, 400 μL of a dye solution in DMF (dye concentration of 2 mmol L^{-1}) were added to 2400 μL of an aqueous suspension of 12 mg PSP-COOH (5 mg mL^{-1}). After 30 minutes of shaking, the suspension was centrifuged. The separated NPs were washed twice with Milli-Q-water followed by resuspension in Milli-Q-water in an ultrasonic bath. For photoluminescence measurements, the particles were diluted with Milli-Q-water to 0.25 mg mL^{-1} .

For the preparation of **[1][PF₆]₃** loaded solutol (Kolliphor[®]HS 15) micelles a mixture of 3.0 mL aqueous solution of solutol (1 mg mL^{-1}) and 30 μL DMF solution of **[1][PF₆]₃** (2 mmol L^{-1}) were sonicated for 45 minutes. Then the mixture was purified via centrifugation to remove excess precipitated **[1][PF₆]₃**. For photoluminescence measurements, the solutions were diluted to 1 mg mL^{-1} .

Figure S1. Total integrated areas (from 11750 – 14600 cm^{-1}) versus temperature for a) $[\mathbf{1}][\text{BF}_4]_3$ in MeCN/PrCN (1:6) from 210 to 300 K (Ar saturated), b) $[\mathbf{1}][\text{BF}_4]_3$ in H_2O from 278 to 358 K (air saturated), c) $[\mathbf{1}][\text{BF}_4]_3$ in water/diethylene glycol (1:2) from 223 to 293 K (air saturated), d) $[\mathbf{1}][\text{BF}_4]_3$ in water/diethylene glycol (1:2) from 273 to 373 K (air saturated), e) $[\mathbf{1}][\text{PF}_6]_3$ in PSP-COOH in H_2O from 293 – 343 K (Ar saturated), f) $[\mathbf{1}][\text{PF}_6]_3$ in PSP-COOH in H_2O from 293 – 343 K (air saturated) and g) $[\mathbf{1}][\text{PF}_6]_3$ in solutol micelles in H_2O from 293 – 343 K (Ar saturated).

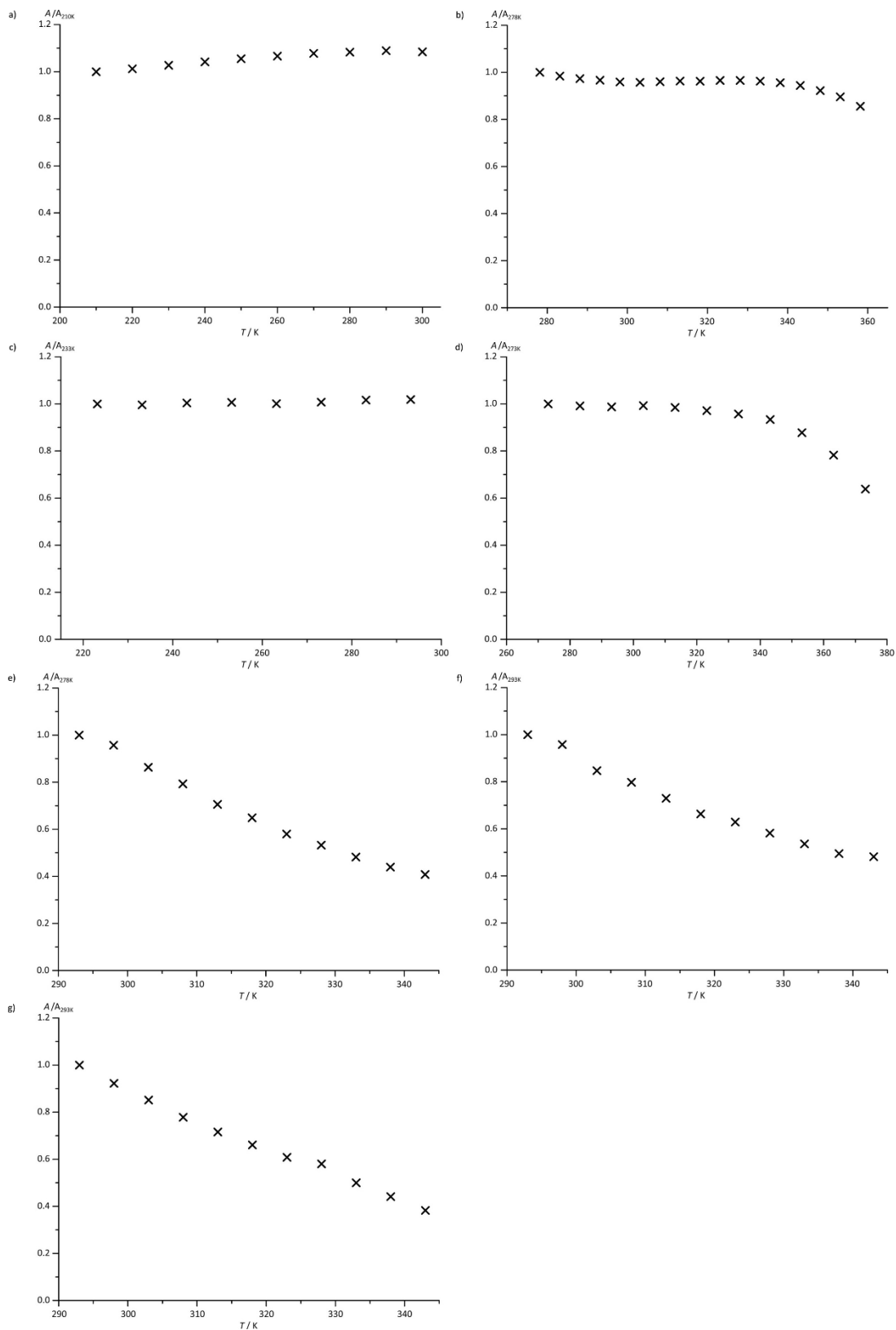


Figure S2. Boltzmann plots $\ln(a_{738}/a_{775})$ vs. T^{-1} of a) $[1][BF_4]_3$ in MeCN/PrCN (1:6) from 210 to 300 K, b) $[1][PF_6]_3$ in PSP-COOH in H_2O from 293 – 343 K (Ar saturated), c) $[1][BF_4]_3$ in H_2O from 278 to 358 K, d) $[1][PF_6]_3$ in solutol in H_2O from 293 – 343 K (Ar saturated), e) $[1][BF_4]_3$ in water/diethylene glycol (1:2) from 273 to 373 K and f) $[1][BF_4]_3$ in water/diethylene glycol (1:2) from 223 to 293 K.

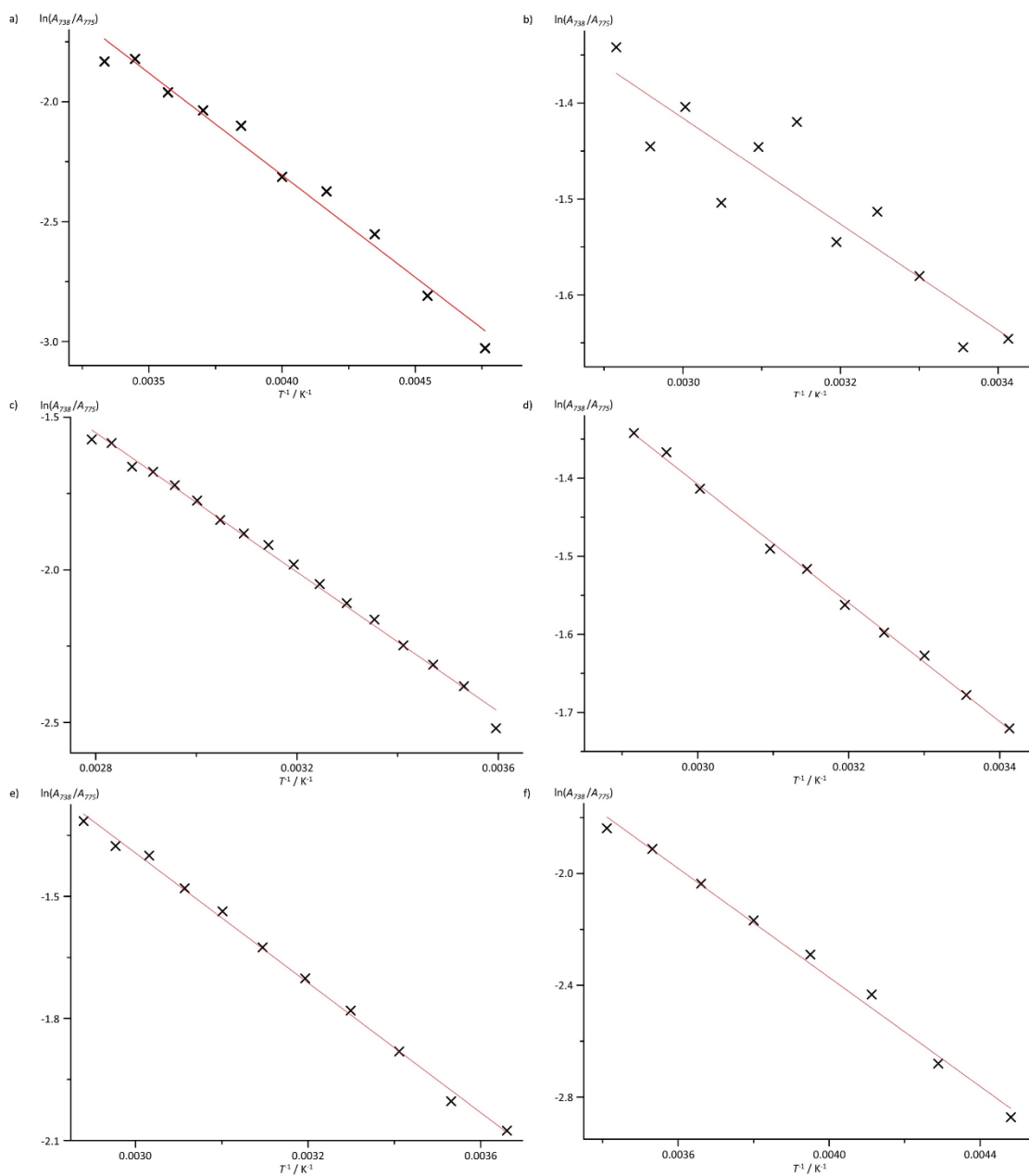


Figure S3. VT emission spectra of $[1][BF_4]_3$ in water/diethylene glycol (1:2) a) from 223 to 293 K (T measurement by Peltier element) and b) from 273 to 373 K (T measurement by Oxford Instruments Optistat^{DN}) (insets show the respective Boltzmann plots $\ln(I_{738}/I_{775})$ vs. T^{-1}).

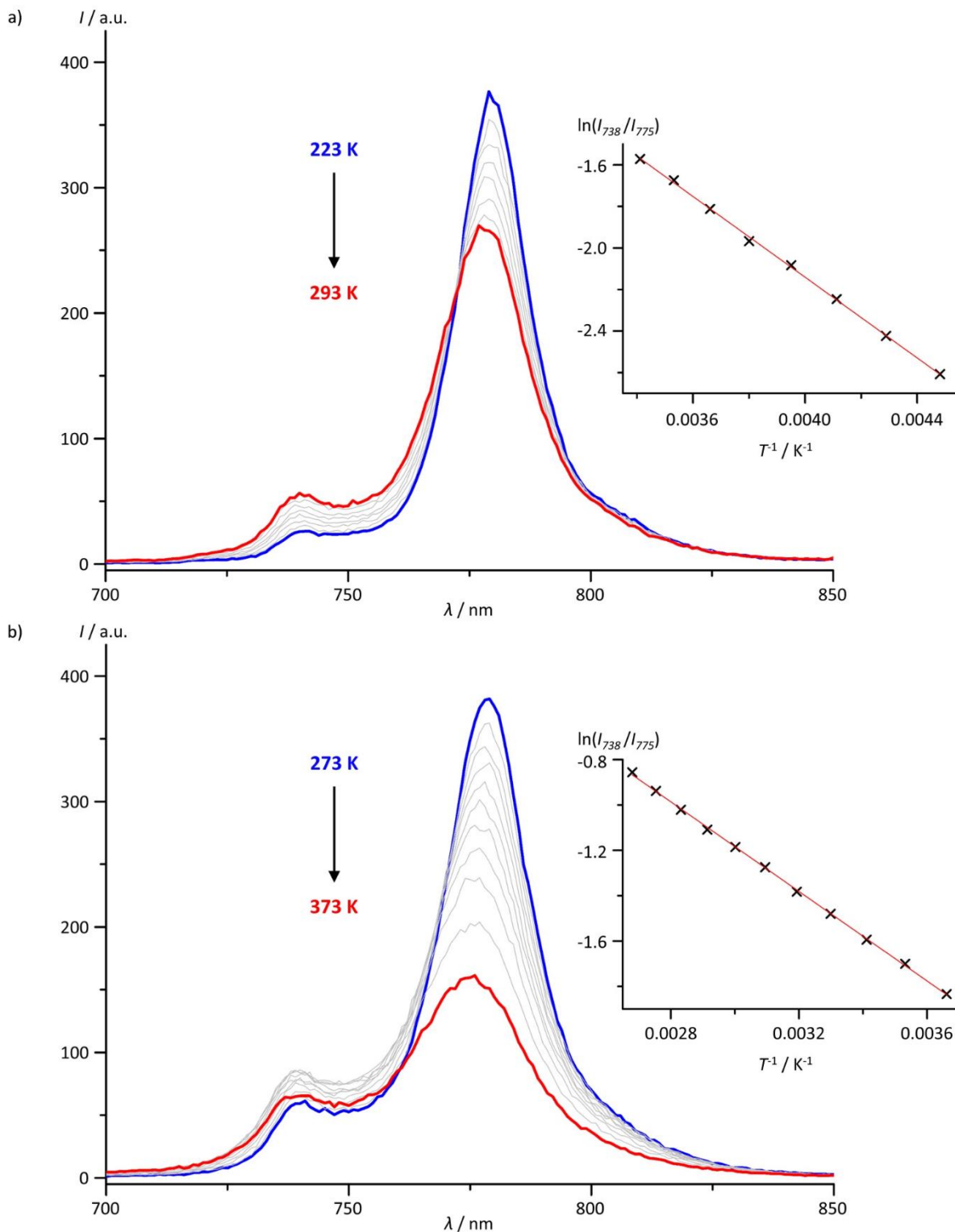


Figure S4. VT emission spectra of $[1][PF_6]_3$ in PSP-COOH in H_2O from 293 – 343 K (air saturated).

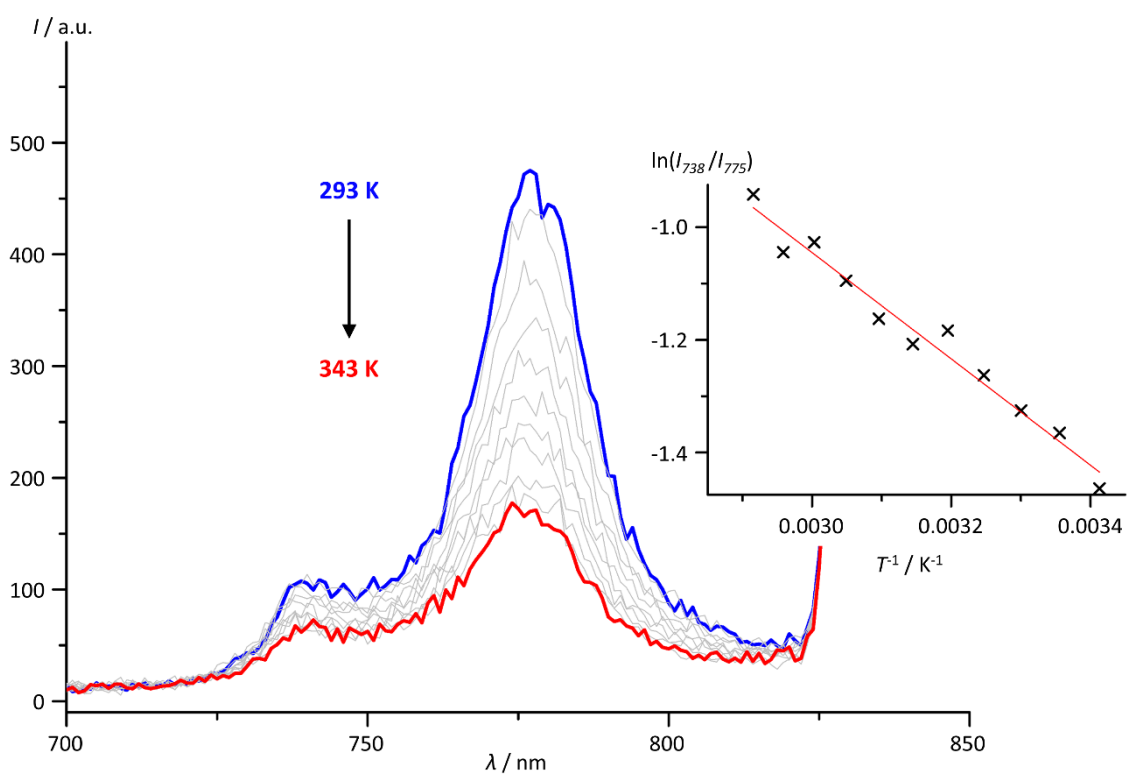
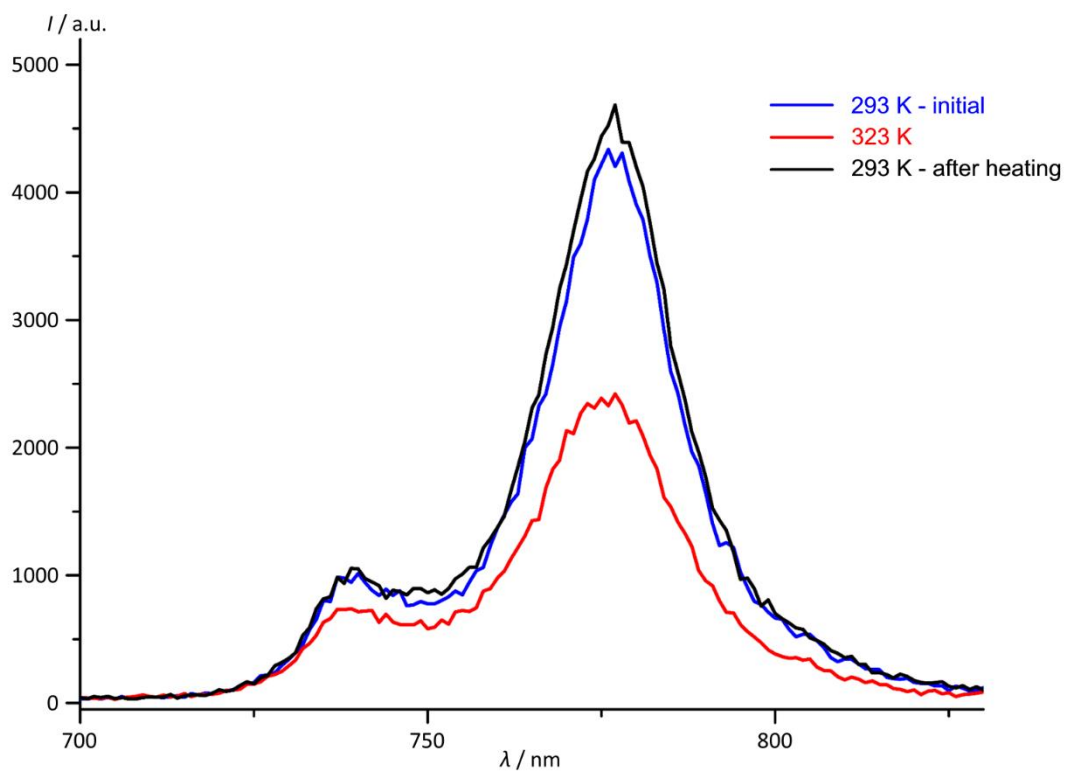


Figure S5. VT emission spectra of $[1][PF_6]_3$ in solutol micelles in H_2O at 293 K, at 323 K, and again at 293 K (Ar saturated).



References

- [1] A. Breivogel, C. Förster, K. Heinze, *Inorg. Chem.* **2010**, *49*, 7052.
- [2] S. Otto, M. Grabolle, C. Förster, U. Resch-Genger, K. Heinze, *Angew. Chem. Int. Ed.* **2015**, *54*, 11572.
- [3] T. Behnke, C. Würth, E. M. Laux, K. Hoffmann, U. Resch-Genger, *Dyes Pigm.* **2012**, *94*, 247.

6.3 Supporting Information: Photo-Chromium: Sensitizer for Visible-Light-Induced Oxidative C–H Bond Functionalization – Electron or Energy Transfer?

The ligand **ddpd** and the photosensitizer **[Cr(ddpd)₂](BF₄)₃** were synthesized according to literature procedures.^{1,2} NEt₃ and NⁿBu₃ were purified by distillation prior to spectroscopic measurements. *N*-phenyl-1,2,3,4-tetrahydroisoquinoline was prepared according to ref. 3. Trimethylsilylcyanide, atropine and rose bengal (4,5,6,7-tetrachloro-2',4',5',7'-tetraiodofluorescein) were used as received.

A 300 MHz **NMR spectrometer** from Bruker was used to record the corresponding NMR spectra with deuterated solvents (CDCl₃: δ_H = 7.26 ppm) as internal reference.⁴ NMR yield determination was achieved by using pyridine or 1,4-bis(trimethylsilyl)benzene as internal standard. **UV/Vis spectra** were recorded on a Varian Cary 5000 spectrometer in 1 cm cuvettes. **Emission spectra** were recorded on a Varian Cary Eclipse spectrometer or on an Edinburgh Instruments spectrometer (FSP 920). Oxygen was removed from the solvents by purging with argon and the oxygen concentration in the sample solutions was measured using a fiber-optic oxygen meter FireStingO2 with solvent-resistant probe from Pyro Science GmbH (Germany). The **singlet oxygen quantum yield** (Φ_{Δ}) of **[Cr(ddpd)₂](BF₄)₃** in DMF was determined relatively by steady-state measurements of the singlet oxygen luminescence peaking at around 1270 nm generated by photosensitization in comparison to that of a reference compound with known Φ_{Δ} using identical instrument settings of the calibrated spectrofluorometer FSP 920 (Edinburgh Instruments). All measurements were performed in quartz cells (1 cm thickness). In order to eliminate unwanted fluorescence/phosphorescence from the emitters, a long-pass filter (cut off wavelength of 1035 nm) was inserted in the detection channel of the spectrofluorometer. As reference, a solution of cycloketotetraphenylporphyrin in DMF was employed ($\Phi_{\Delta}(\text{ref}) = 0.85$).⁵ Φ_{Δ} of **[Cr(ddpd)₂](BF₄)₃** was calculated according to the following equation:

$$\Phi_{\Delta} = \Phi_{\Delta}^{\text{ref}} \frac{I}{I_{\text{ref}}} \frac{OD_{\text{ref}}(\lambda_{\text{exc}})}{OD(\lambda_{\text{exc}})}$$

Here, I , and I_{ref} are the integral intensities of the singlet oxygen luminescence of the sample and the reference and $OD(\lambda_{\text{exc}})$, and $OD_{\text{ref}}(\lambda_{\text{exc}})$ the optical densities (absorbances) of the sample and the reference at the excitation wavelength λ_{exc} of 433 nm, respectively. With this procedure, Φ_{Δ} of **[Cr(ddpd)₂](BF₄)₃** was determined to 0.61 in DMF.

Electrochemical experiments were performed with a BioLogic SP-50 voltammetric analyser using platinum wire working and counter electrodes and a 0.01 M Ag/AgNO₃ reference electrode. Measurements were carried out at a scan rate of 100 mV s⁻¹ for cyclic voltammetry experiments using 0.1 M [ⁿBu₄N][PF₆] as supporting electrolyte in acetonitrile. Potentials are given relative to the ferrocene/ferrocenium couple (0.40 V vs. SCE⁶, $E_{1/2} = 0.90 \pm 5$ mV under the given conditions).

Photoreactions were performed using CFL (Dynasun, 105 W), CFL (Dynasun, 25 W), blue LEDs (462 nm, 100 W), medical blue light PL-S (9 W) or UV-A (440 W, 380 – 315 nm) light sources.

Transient absorption spectra were recorded with a time resolution of 300 fs by a pump-probe spectrometer based on a non-collinear optical parametric amplifier (NOPA) for excitation and a white light continuum for probing. In the setup the f output pulses of a Ti:sapphire laser system operating at repetition rate of 1 kHz and a center wavelength of 800 nm are split up into two beams. One is focused onto a 4 mm thick CaF₂ crystal to generate the supercontinuum and one pumps the NOPA. In the NOPA another white light continuum is generated in a sapphire substrate and a spectral fraction of it around 880 nm is subsequently parametrically amplified by two BBO crystals.⁷ They have a thickness of 1 mm and 2 mm, respectively, are cut at 32° for type 1 phase matching, and are pumped by the second harmonic of the Ti:sapphire laser in a non-collinear geometry. The second crystal is tilted by about 10° to simultaneously amplify and frequency double the 880 nm radiation resulting in pulses at 440 nm which have a pulse duration of about 300 fs and an energy of 0.5 μJ. The output of the NOPA and the white light probe are focused with their polarizations set to magic angle onto the sample to overlapping spots with diameters of approximately 300 μm and 100 μm, respectively. The transmitted probe light is re-collimated and then dispersed by a prism and imaged onto a photodiode array to monitor the pump-induced absorption changes. The time between excitation and probe pulses is adjusted by a retroreflector on a computer controlled linear stage in the excitation beam path. As sample served a degassed acetonitrile solution of the chromium sensitizer with a concentration of 1.3 × 10⁻³ M filled in a fused silica cell with thickness of 1 mm.

General procedure for the photocyanation of tertiary amines

A solution of amine (0.21 mmol, 1.0 equiv), sensitizer (1.0 mol%), and TMSCN (0.63 mmol, 3.0 equiv) in CH₃CN (6 mL) was irradiated under air bubbling with a 105 W fluorescent household bulb (CFL Dynasun) at room temperature. A reaction vial with a septum and two cannulas (1x long, 1xshort) was used. Through a long cannula, the air was bubbled slowly through the solution. The availability of air bubbles is essential for an acceptable reaction kinetics. Upon completion (monitored by TLC), the reaction mixture was poured in concentrated K₂CO₃ solution and extracted with CH₂Cl₂ (3 x 10 mL). The combined organic layers were dried over Na₂SO₄ and the solvent was evaporated under reduced pressure to obtain the crude product. The pure product was isolated by filtration through a plug of

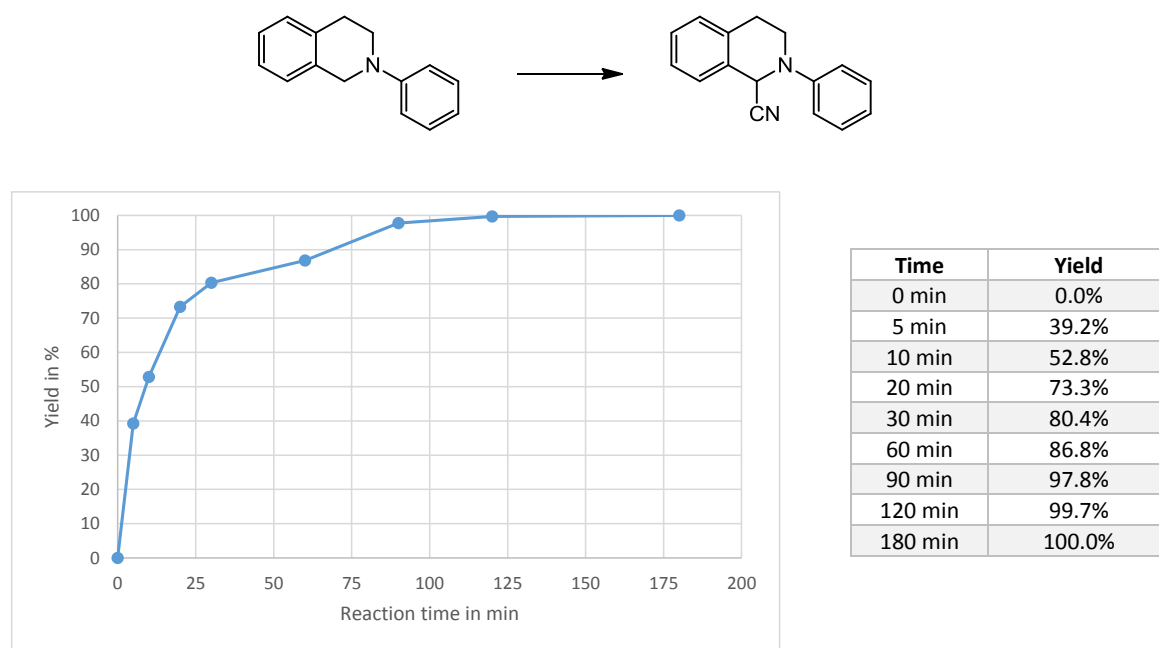
aluminum oxide (basic) using CH_2Cl_2 as the eluent or by column chromatography. The spectral data of the products match those reported in the literature.^{3,8,9}

Catalyst recycling was performed by pouring the reaction mixture onto water (20 mL) and extracting with CH_2Cl_2 (15 mL). The organic phase was extracted with water (2x 10 mL) and the combined aqueous extracts were lyophilized.

Density functional theoretical calculations on the sensitizer were carried out using the ORCA program package (version 3.0.2).¹⁰ Tight convergence criteria were chosen for all calculations (Keywords TightSCF and TightOpt, convergence criteria for the SCF part: energy change 1.0×10^{-8} Eh, 1-El. energy change 1.0×10^{-5} Eh, orbital gradient 1.0×10^{-5} , orbital rotation angle 1.0×10^{-5} , DIIS Error 5.0×10^{-7} ; for geometry optimizations: energy change: 1.0×10^{-6} Eh, max. gradient 1.0×10^{-4} Eh bohr⁻¹, RMS gradient 3.0×10^{-5} Eh bohr⁻¹, max. displacement 21.0×10^{-3} bohr, RMS displacement 6.0×10^{-4} bohr). All calculations make use of the resolution of identity (Split-RI-J) approach for the coulomb term in combination with the chain-of-spheres approximation for the exchange term (COSX).¹¹ Geometry optimizations were performed using the B3LYP functional¹² in combination with Ahlrichs' split-valence triple- ξ basis set def2-TZVPP for all atoms.¹³ The optimized geometries were confirmed to be local minima on the respective potential energy surface by subsequent numerical frequency analysis ($N_{\text{imag}} = 0$). TD-DFT calculations were performed at the same level of theory. The ZORA relativistic approximation¹⁴ was used to describe relativistic effects in all calculations. Grimme's empirical dispersion correction D3(BJ) was employed.¹⁵ Explicit counterions and/or solvent molecules were neglected. Fifty vertical transitions were calculated in TD-DFT calculations.

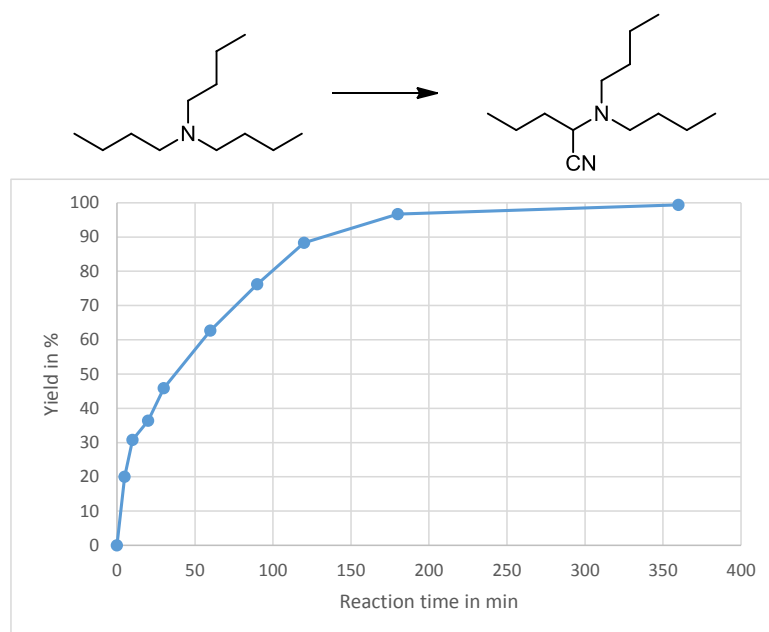
Density functional theory calculations on the amine/O₂ system were carried out with the Gaussian09/DFT series¹⁶ of programs. The B3LYP¹² formulation of density functional theory was used employing the def2TZVP basis set. No symmetry constraints were imposed on the molecules. The presence of energy minima of the ground states was checked by analytical frequency calculations. The calculated transition state exhibits a single imaginary frequency corresponding to the shift of the hydride. Solvent modelling was done employing the integral equation formalism polarizable continuum model (IEFPCM, CH_3CN). The approximate free energies at 298 K were obtained through thermochemical analysis of the frequency calculation, using the thermal correction to the Gibbs free energy as reported by Gaussian09.

Figure S1. Conversion vs. time plot for the photocyanation of Ph-isoq.



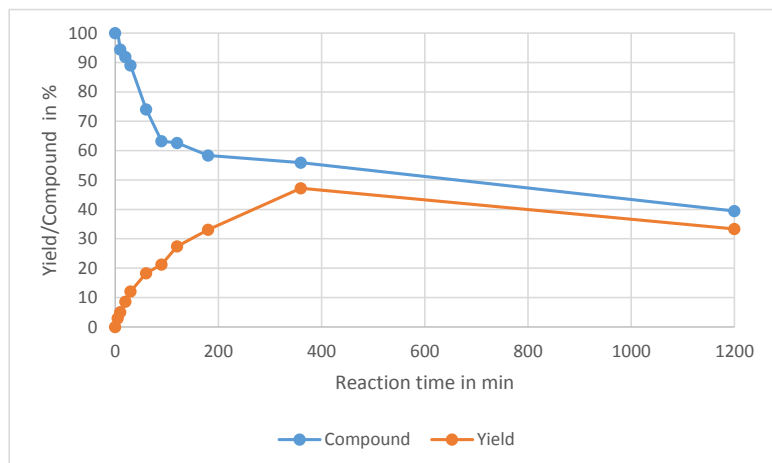
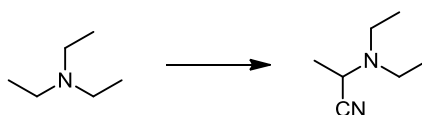
0.21 mmol *N*-Phenyl-1,2,3,4-tetrahydroisoquinoline; 10.0 equiv. TMSCN; 1.0 mol% catalyst; 6.0 mL acetonitrile; 105 W Dynasun; air flow.

Figure S2. Conversion vs. time plot for the photocyanation of *N*^oBu₃.



0.21 mmol Tributylamine; 10.0 equiv. TMSCN; 1.0 mol% catalyst; 6.0 mL acetonitrile; 105 W Dynasun; air flow. The yield has been determined by ¹H NMR spectroscopy with pyridine as internal standard.

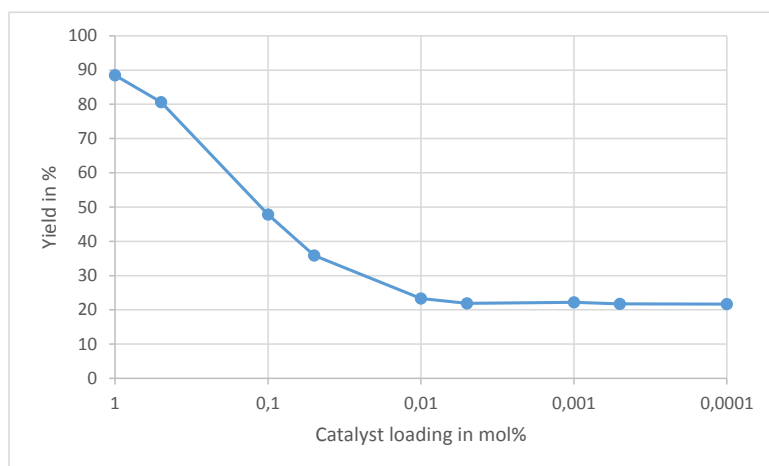
Figure S3. Conversion vs. time plot for the photocyanation of NEt_3 .



Time	Compound	Yield
0	100.0%	0.0%
5	100.1%	3.0%
10	94.4%	5.0%
20	91.9%	8.6%
30	89.1%	12.1%
60	74.0%	18.3%
90	63.3%	21.2%
120	62.6%	27.4%
180	58.4%	33.1%
360	55.9%	47.2%
1200	39.4%	33.3%

0.21 mmol Triethylamine; 10.0 equiv. TMSCN ; 1.0 mol% catalyst; 6.0 mL deuterated acetonitrile; 105 W Dynasun; air flow. The yield has been determined by ^1H NMR spectroscopy with 1,4-Bis(trimethylsilyl)-benzene as internal standard. The notation "Compound" defines the amount of amine and aminonitrile in the reaction mixture ($\text{Compound} = n_{\text{Amine}} + n_{\text{Aminonitrile}}$). The decrease of the amount can be explained by the volatility of the amine and the aminonitrile.

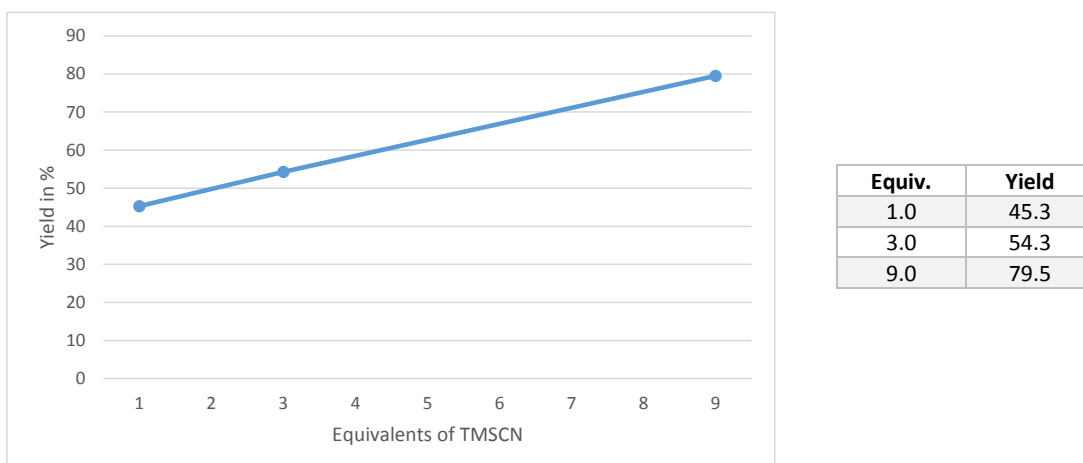
Figure S4. Variation of the catalyst loading.



Mol%	Yield
1.0	88.5%
0.5	80.6%
0.1	47.8%
0.05	35.8%
0.01	23.3%
0.005	21.9%
0.001	22.2%
0.0005	21.8%
0.0001	21.6%

0.21 mmol Ph-isoq; 10.0 equiv. TMSCN ; 6.0 mL acetonitrile; 20 min reaction time, 105 W Dynasun and a continuous air flow.

Figure S5. Variation of the cyanide amount.



0.21 mmol Ph-isoq; 1.0 mol% catalyst; 6.0 mL acetonitrile; 30 min reaction time, 105 W Dynasun and a continuous air flow; yields were determined by ^1H NMR spectroscopy with pyridine as internal standard.

Figure S6. Variation of the light source.

Light source	Yield
105 W CFL (Dynasun)	73%
25 W CFL	43%
PL-S 9W/52/2P (Medical blue light)	41%
Blue LED 100 W	79%
UV-A 440 W	63%

0.21 mmol Ph-isoq; 3.0 equiv. TMSCN; 1.0 mol% catalyst; 6.0 mL acetonitrile; 30 min reaction time, continuous air flow; yields were determined by ^1H NMR spectroscopy with pyridine as internal standard.

Figure S7. TD-DFT calculated absorption spectra (Gaussian line broadening) of the 2E state of $[\text{Cr}(\text{ddpd})_2]^{3+}$ and electron density difference maps of relevant transitions (isosurface value 0.01 a.u. purple = electron density depletion, orange = electron density gain; CH hydrogen atoms omitted).

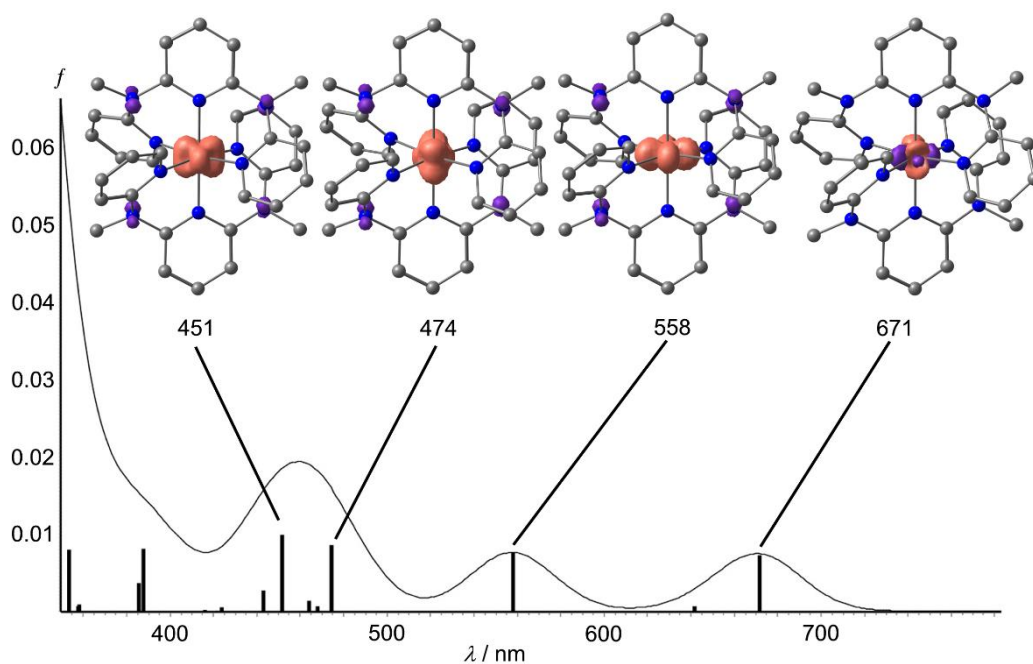


Figure S8. Stern-Volmer plot of $[\text{Cr}(\text{ddpd})_2][\text{BF}_4]_3$ with O_2 in CH_3CN .

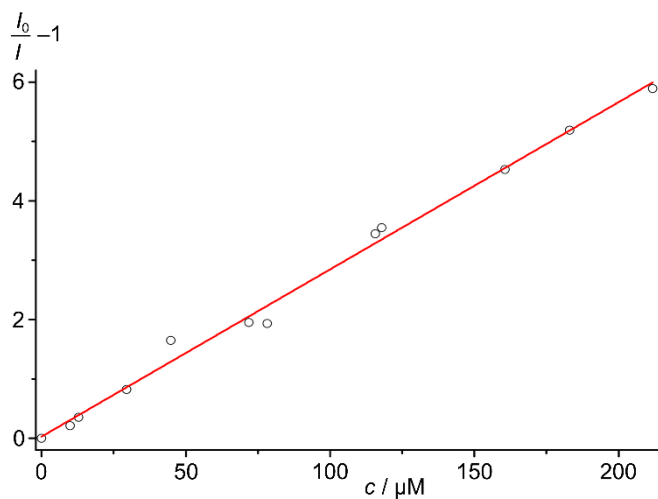


Figure S9. Emission spectra of $[\text{Cr}(\text{ddpd})_2][\text{BF}_4]_3$ in CH_3CN with varying amounts of TMSCN at room temperature.

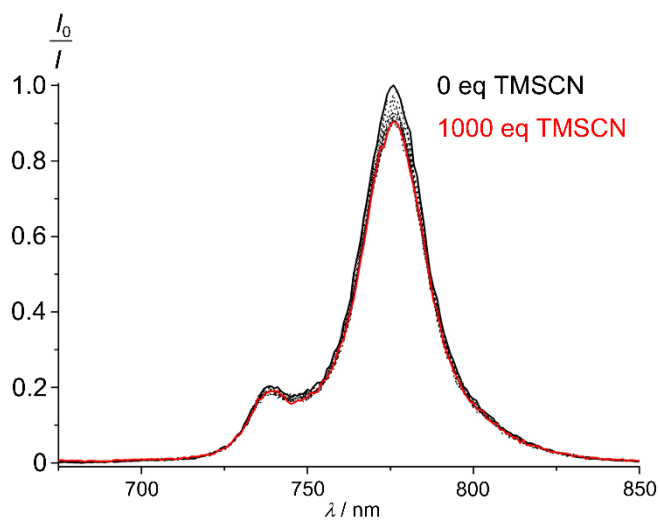
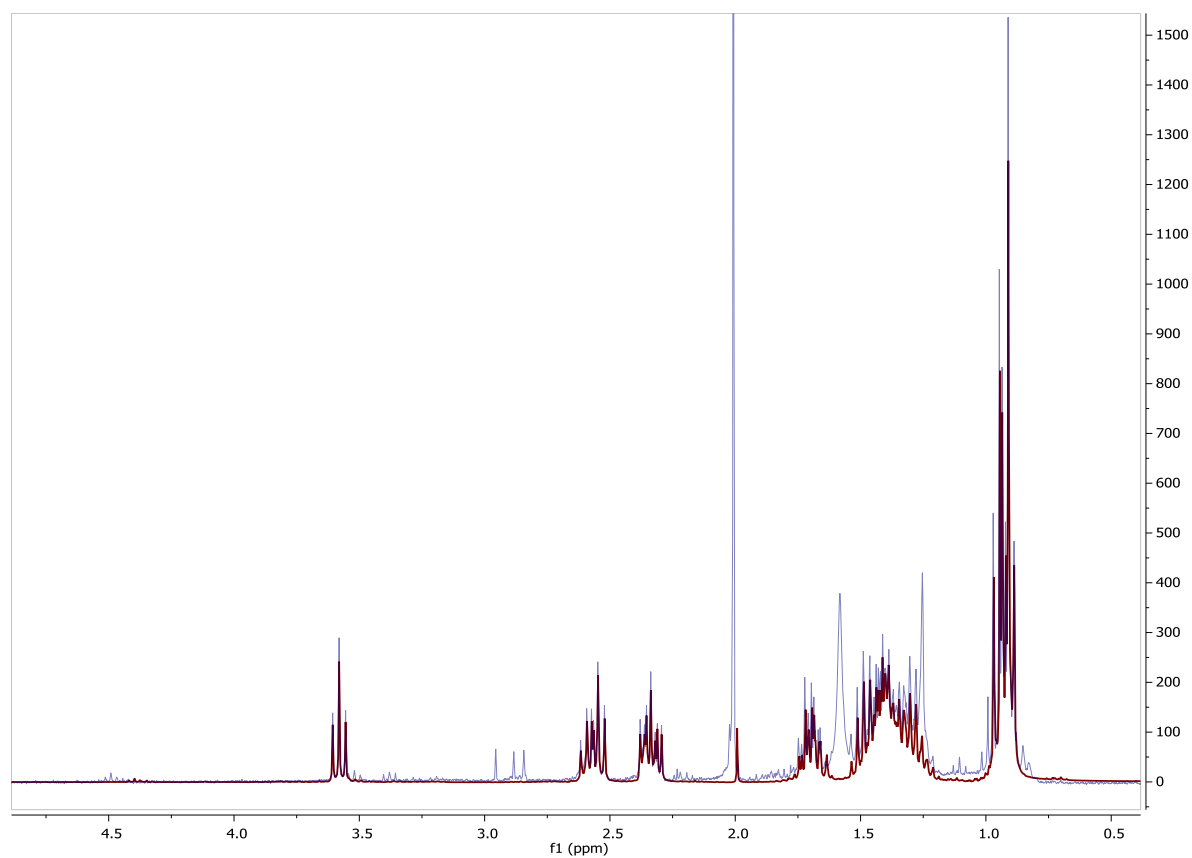


Figure S10. ^1H NMR spectra of the reaction mixtures of the photocyanation of N^nBu_3 using $[\text{Cr}(\text{ddpd})_2][\text{BF}_4]_3$ (red) and rose bengal (blue) in CD_3Cl .



- (1) A. Breivogel, C. Förster, K. Heinze, *Inorg. Chem.* **2010**, *49*, 7052–7056.
- (2) S. Otto, M. Grabolle, C. Förster, C. Kreitner, U. Resch-Genger, K. Heinze, *Angew. Chem.* **2015**, *127*, 11735–11739; *Angew. Chem. Int. Ed.* **2015**, *54*, 11572–11576.
- (3) A. M. Nauth, N. Otto, T. Opatz, *Adv. Synth. Catal.* **2015**, *357*, 3424–3428.
- (4) G. R. Fulmer, A. J. M. Miller, N. H. Sherden, H. E. Gottlieb, A. Nudelman, B. M. Stoltz, J. E. Bercaw, K. I. Goldberg, *Organometallics* **2010**, *29*, 2176–2179.
- (5) S. Jasinski, E.A. Ermilov, N. Jux, B. Röder, *Eur. J. Org. Chem.* **2007**, 1075–1084.
- (6) N. G. Connelly, W. E. Geiger, *Chem. Rev.* **1996**, *96*, 877–910.
- (7) E. Riedle, M. Beutter, S. Lochbrunner, J. Piel, S. Schenkl, S. Spörlein, W. Zinth, *Appl. Phys. B* **2000**, *71*, 457–465.
- (8) J. C. O. Pacheco, A. Lipp, A. M. Nauth, F. Acke, J.-P. Dietz, T. Opatz, *Chem. Eur. J.* **2016**, *22*, 5409–5415.
- (9) A. M. Nauth, A. Lipp, B. Lipp, T. Opatz, *Eur. J. Org. Chem.* **2017**, 2099–2103.
- (10) F. Neese, *WIREs Comput Mol Sci* **2012**, *2*, 73–78.
- (11) a) F. Neese, F. Wennmohs, A. Hansen, U. Becker, *Chem. Phys.* **2009**, *356*, 98–109; b) R. Izsák, F. Neese, *J. Chem. Phys.* **2011**, *135*, 144105.
- (12) A. D. Becke, *J. Chem. Phys.* **1993**, *98*, 5648–5642.
- (13) a) A. Schäfer, H. Horn, R. Ahlrichs, *J. Chem. Phys.* **1992**, *97*, 2571; b) A. Schäfer, C. Huber, R. Ahlrichs, *J. Chem. Phys.* **1994**, *100*, 5829.
- (14) a) E. van Lenthe, E. J. Baerends, J. G. Snijders, *J. Chem. Phys.* **1993**, *99*, 4597; b) C. van Wüllen, *J. Chem. Phys.* **1998**, *109*, 392; c) D. A. Pantazis, X.-Y. Chen, C. R. Landis, F. Neese, *J. Chem. Theory Comput.* **2008**, *4*, 908–919.
- (15) a) S. Grimme, S. Ehrlich, L. Goerigk, *J. Comput. Chem.* **2011**, *32*, 1456–1465; b) S. Grimme, J. Antony, S. Ehrlich, H. Krieg, *J. Chem. Phys.* **2010**, *132*, 154104.
- (16) Gaussian 09, Revision A.02; Gaussian, Inc.: Wallingford CT, **2009**.
- (17) A. D. Becke, *J. Chem. Phys.* **1993**, *98*, 5648–5652.

Cartesian Coordinates of DFT optimized structures

2E state of $[\text{Cr}(\text{ddpd})_2]^{3+}$

24	-0.000029000	0.000004000	0.000014000
6	1.155212000	2.737818000	0.198605000
6	1.180774000	4.126557000	0.193349000
6	0.000238000	4.821225000	-0.000999000
6	-1.180390000	4.126613000	-0.194996000
6	-1.155007000	2.737873000	-0.199542000
7	0.000057000	2.051053000	-0.000297000
1	2.100215000	4.657449000	0.375077000
1	-2.099767000	4.657523000	-0.376990000
6	1.480529000	-0.799504000	2.456691000
6	2.537211000	-0.921061000	3.322666000
6	3.609620000	-0.039955000	3.179602000
6	3.562197000	0.933796000	2.203076000
6	2.442877000	1.018549000	1.365877000
7	1.436381000	0.128246000	1.471190000
1	4.460459000	-0.094109000	3.844902000
1	0.630982000	-1.460148000	2.519224000
1	2.524742000	-1.677530000	4.092872000
1	4.361486000	1.651303000	2.120192000
6	-2.442919000	1.018272000	-1.366046000
6	-3.562328000	0.933249000	-2.203093000
6	-3.609861000	-0.040830000	-3.179279000
6	-2.537498000	-0.922019000	-3.322162000
6	-1.480742000	-0.800210000	-2.456322000
7	-1.436477000	0.127875000	-1.471139000
1	-4.460768000	-0.095186000	-3.844476000
1	-4.361588000	1.650805000	-2.120383000
1	-2.525130000	-1.678742000	-4.092118000
1	-0.631226000	-1.460908000	-2.518690000
6	1.155180000	-2.737818000	-0.198560000
6	1.180736000	-4.126557000	-0.193344000
6	0.000191000	-4.821218000	0.000959000
6	-1.180441000	-4.126604000	0.194929000
6	-1.155049000	-2.737861000	0.199503000
7	0.000027000	-2.051047000	0.000318000
1	2.100183000	-4.657442000	-0.375052000
1	-2.099828000	-4.657514000	0.376875000
6	1.480547000	0.799485000	-2.456651000
6	2.537227000	0.921003000	-3.322628000
6	3.609630000	0.039899000	-3.179524000
6	3.562197000	-0.933824000	-2.202974000
6	2.442871000	-1.018556000	-1.365788000
7	1.436391000	-0.128241000	-1.471128000
1	4.460475000	0.094031000	-3.844818000
1	0.631004000	1.460132000	-2.519203000
1	2.524769000	1.677451000	-4.092854000
1	4.361483000	-1.651332000	-2.120068000
6	-2.442960000	-1.018263000	1.366000000
6	-3.562378000	-0.933247000	2.203031000
6	-3.609932000	0.040838000	3.179211000
6	-2.537576000	0.922029000	3.322113000
6	-1.480806000	0.800222000	2.456291000
7	-1.436522000	-0.127867000	1.471115000
1	-4.460851000	0.095191000	3.844393000
1	-4.361635000	-1.650806000	2.120309000
1	-2.525228000	1.678761000	4.092062000
1	-0.631291000	1.460923000	2.518668000
7	2.345521000	-2.024697000	-0.405466000
6	3.594881000	-2.678440000	0.018064000
1	3.973308000	-3.395156000	-0.711703000
1	4.346163000	-1.911760000	0.184861000
1	3.415190000	-3.189803000	0.958306000
7	-2.345471000	-2.024771000	0.406074000
6	-3.594744000	-2.678830000	-0.017231000
1	-3.973140000	-3.395246000	0.712846000
1	-4.346095000	-1.912304000	-0.184429000
1	-3.414953000	-3.190617000	-0.957222000
7	2.345548000	2.024707000	0.405568000
7	-2.345436000	2.024795000	-0.406137000
6	3.594923000	2.678439000	-0.017940000
1	3.973336000	3.395159000	0.711830000
1	4.346203000	1.911751000	-0.184713000

1	3.415262000	3.189797000	-0.958190000
6	-3.594716000	2.678872000	0.017126000
1	-3.973095000	3.395268000	-0.712980000
1	-4.346070000	1.912351000	0.184330000
1	-3.414943000	3.190683000	0.957107000
1	0.000312000	5.902536000	-0.001269000
1	0.000257000	-5.902529000	0.001210000

Charge transfer complex between $^1\text{O}_2$ and $\text{N}(\text{CH}_2\text{Me})\text{Me}_2$ (A)

7	0.003238000	-0.584804000	-0.070229000
6	-0.891975000	0.285486000	-0.829476000
1	-0.230073000	1.049387000	-1.257783000
1	-1.305690000	-0.288151000	-1.665339000
6	-1.995537000	0.948699000	-0.025544000
1	-1.588997000	1.502494000	0.820629000
1	-2.732383000	0.233564000	0.340444000
1	-2.515184000	1.655605000	-0.673157000
6	-0.532133000	-1.380422000	1.021870000
1	-1.181740000	-2.174821000	0.642532000
1	0.299876000	-1.829378000	1.560887000
1	-1.095782000	-0.747715000	1.700792000
6	0.976374000	-1.256425000	-0.916728000
1	1.572200000	-0.489211000	-1.415574000
1	1.623377000	-1.880416000	-0.305678000
1	0.477252000	-1.870544000	-1.671136000
8	1.094066000	0.645623000	0.844206000
8	1.570198000	1.522975000	0.020076000

$[\text{HO}_2]^*$ and $[\text{N}(\text{CHMe})\text{Me}_2]^*$ (B)

7	0.409694000	0.511743000	-0.037054000
6	1.471435000	-0.194370000	-0.640856000
1	-0.941684000	-0.465905000	-0.255990000
1	1.489004000	-0.115209000	-1.719949000
6	2.073220000	-1.388376000	0.011845000
1	2.564425000	-1.154488000	0.960645000
1	2.823489000	-1.821767000	-0.649107000
1	1.333077000	-2.174625000	0.225643000
6	0.508953000	0.710677000	1.416900000
1	1.357643000	1.355374000	1.672417000
1	-0.408262000	1.176583000	1.772399000
1	0.627632000	-0.245199000	1.921450000
6	0.064227000	1.758479000	-0.736165000
1	-0.066154000	1.554802000	-1.798028000
1	-0.869636000	2.150984000	-0.336586000
1	0.849089000	2.512611000	-0.614582000
8	-2.759792000	-0.414120000	0.239175000
8	-1.781894000	-1.045108000	-0.392834000

$[\text{HO}_2]^-$ and $[\text{N}(\text{CHMe})\text{Me}_2]^+$ (C)

7	0.643970000	0.570780000	0.087881000
6	1.651641000	0.097565000	-0.544276000
1	-1.995971000	-1.906576000	-0.268439000
1	1.826173000	0.521329000	-1.526791000
6	2.570310000	-0.966550000	-0.088712000
1	2.563205000	-1.127657000	0.984742000
1	3.581077000	-0.720580000	-0.415305000
1	2.297280000	-1.902447000	-0.588001000
6	0.168359000	0.115079000	1.398717000
1	0.313342000	0.925344000	2.114058000
1	-0.910159000	-0.082669000	1.272103000
1	0.705812000	-0.767426000	1.722875000
6	-0.200825000	1.625196000	-0.493288000
1	0.119687000	1.833254000	-1.509897000
1	-1.233122000	1.257830000	-0.445890000
1	-0.098439000	2.520759000	0.120246000
8	-2.642927000	-0.164911000	0.259320000

8	-1.958770000	-1.056883000	-0.723009000
---	--------------	--------------	--------------

Transition state between (A) and (C)

7	-0.005175000	0.648136000	-0.083249000
6	0.806383000	-0.296406000	-0.669521000
1	0.068264000	-1.317602000	-0.542352000
1	0.843896000	-0.182177000	-1.751231000
6	2.134332000	-0.659520000	-0.039420000
1	2.023783000	-1.041609000	0.974884000
1	2.811947000	0.197504000	-0.011698000
1	2.602754000	-1.440515000	-0.637556000
6	0.283636000	1.200715000	1.232627000
1	1.025434000	2.002283000	1.153484000
1	-0.633674000	1.606544000	1.652166000
1	0.659988000	0.428768000	1.895353000
6	-0.815931000	1.499331000	-0.946085000
1	-1.111228000	0.943694000	-1.832240000
1	-1.707924000	1.814500000	-0.409871000
1	-0.244390000	2.382949000	-1.247806000
8	-1.563773000	-0.736349000	0.513248000
8	-1.030370000	-1.813152000	-0.028998000

6.4 Supporting Information: Deuterated Molecular Ruby with Record Luminescence Quantum Yield

1. Materials and Methods

NMR spectra were recorded on Bruker AVII+400 spectrometers (^1H : 400 MHz). The chemical shifts (δ) are reported in ppm relative to TMS and the residual solvent signals have been used as internal reference.^[1] Deuterated solvents for NMR spectroscopy and synthesis were purchased with deuteration levels >99.8 %D. Commercially available reagents were used as received: CD_3I (>99.5 %D, stabilized with copper) and 2,6-diaminopyridine from Sigma-Aldrich, PyBroP (98.5 %) from Carl Roth. All reactions were carried out under a dry, dioxygen-free atmosphere of argon using Schlenk techniques. CH_2Cl_2 was dried using CaH_2 , EtN^iPr_2 over solid KOH. Column chromatography was performed with silica gel 60 (Merck, 0.063 – 0.200 mm). Analytical thin layer chromatography (TLC) was done on silica gel 60 F_{254} plates (Merck, coated on aluminium sheets). ESI mass spectrometry was done using Bruker Daltonics Esquire6000 or on a Micromass QToF Ultima API mass spectrometer with analyte solutions in acetonitrile. Deuteration levels of intermediates and products were established by deconvolution of the corresponding ESI mass spectra.

Emission spectra were recorded on a Varian Cary Eclipse spectrofluorometer and on the calibrated spectrofluorometer FSP 920 from Edinburgh Instruments (spectrally corrected emission spectra, traceable to the spectral radiance or spectral photon radiance scale) equipped with different excitation light sources and detectors. For the measurement of the spectrally corrected emission spectra, a continuous xenon lamp was employed. Luminescence decay curves were obtained also with spectrofluorometer FSP 920, yet in this case using a μs xenon flashlamp and multi-channel scaling mode. All luminescence measurements with FSP 920 were performed using magic angle condition (polarization 0° in the excitation and 54.7° in the emission channel). The luminescence decays were analyzed by fitting the obtained decay curves mono-exponentially with the program FAST (Fluorescence Analysis Software Technology, *Edinburgh Instruments Ltd.*). Luminescence quantum yields were determined absolutely with the commercial integrating sphere setup Quantaaurus-QY C11347-11 from Hamamatsu^[2] and special long neck cuvettes from the instrument manufacturer (1x1 cm, quartz; modified for measurements under exclusion of oxygen).

All luminescence measurements were performed with solutions of the chromium(III) complexes in either non-deuterated or in deuterated solvents (D_2O (99.9 %D from Sigma-Aldrich; CD_3CN (99 %D) from abcr; both used as received), under argon atmosphere as well as at different oxygen concentrations using special long neck cuvettes. Due to the long luminescence lifetime of the studied complexes, it was extremely important to make sure that even traces of O_2 were removed for the luminescence studies that could otherwise significantly perturb quantum yield and lifetime measurements. For luminescence studies in the absence of oxygen, O_2 was removed very thoroughly from the solutions by purging the solutions ($V = 3$ mL) with argon for about 30 min and subsequent airtight sealing of the cuvettes. In order to

ensure complete removal of O₂ and control the air tightness of the optical cell during the luminescence measurements, the long neck quartz cuvette was modified and sealed with rubber septum caps. After purging with argon for about 30 min, the luminescence quantum yields of the samples were measured immediately, followed by measuring the lifetimes and emission spectra. When all these measurements were completed, the luminescence quantum yields were determined again and the initial and final values were compared, thereby controlling the absence of O₂ during the complete measurement cycle. The difference in initial and final quantum yield values amounted to a maximum of 2 %. The relative standard deviations of luminescence quantum yield measurements were estimated to be ±5 %.

NIR absorption measurements were performed with a JASCO V-770 spectrophotometer (equipped with a long cuvette holder LSE-701) on solutions of 2,2'-dipyridylamine in CDCl₃ (99.9% D). Depending on the intensity of the CH overtones, rectangular quartz micro cuvettes (Starna, type 28/B/SX, Suprasil 300) with different path lengths were used ($\nu = 2$: 1.0 cm; $\nu > 2$: 5.0 cm)

FTIR investigations were performed with a Bruker VERTEX 80v FTIR spectrometer in combination with a closed cycle helium cryostat (ARS Model DE-202A). The cryo cooler is equipped with CaF₂ windows, a homebuilt pellet holder was used and the temperature was controlled with a Cryo-con Model 32 cryogenic temperature controller. A temperature of approx. 10 K at the cold head results in a temperature of approx. 20 K at the sample, only temperatures of the cold head are denoted. The cryo cooler was hanging from a rack into the sample compartment without touching the spectrometer to prevent vibrations of the cooler to be transferred to the instrument. All spectra are recorded using a liquid nitrogen-cooled MCT (mercury-cadmium-telluride) detector at a resolution of 4 cm⁻¹.

Sample Preparation: The complex (ca. 1 mg) was mixed with dry KBr (ca. 200 mg) (stored in a compartment dryer at 780°C) and grinded to a homogenous mixture. This mixture was filled in an evacuable pellet die with a diameter of 13 mm and sintered at a pressure of 0.75 GPa.

2. Synthetic Procedures

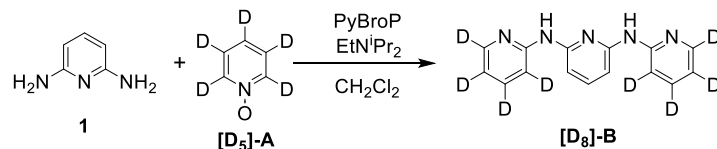
2.1 [D₉]-ddpd via Two-Step Unselective Deuteration of ddpd

The ligand **ddpd**^[3] (310 mg, 1.06 mmol), Pd (10%) on activated charcoal (30 mg) and D₂O (7.5 mL) were irradiated in a microwave vial for 11 h (215°C, 275 W). The resulting mixture was extracted with CH₂Cl₂ (5× 20 mL). The combined organic phases were dried over MgSO₄ and the solvent was removed under reduced pressure. The resulting brown oil (yield: 200 mg, 0.67 mmol, 63 %) was combined with the product of a second similarly scaled reaction and the combined material was used in the next step without further purification. MS (ESI⁺): *m/z* = 287.21 (19 %), 300.20 (100 % [ddpd+H]⁺).

The combined material (301 mg, 1.07 mmol), Pd (10%) on activated charcoal (37 mg) and D₂O (7.5 mL) together were irradiated in a microwave vial (215°C, 275 W). After 6 h, the solution was extracted with CH₂Cl₂. The resulting solution was filtered through celite and dried over MgSO₄. The solvent was removed under reduced pressure. After column chromatography (SiO₂, hexane:EtOAc 1 : 1, *R_f* = 0.21) the product was obtained as a yellow oil. Yield: 119 mg (0.40 mmol, 37 %), ¹H NMR (CD₂Cl₂, 400 MHz): δ/ppm = 8.33 (s, 0.09 H, H⁶), 7.52 (m, 0.66 H, H⁴), 7.44 (s, 0.38 H, H¹), 7.27 (s, 2H, H³), 6.85 (s, 1.15 H, H⁵), 6.71 (t, ³*J*_{HH} = 4.3 Hz, 0.04 H, H²), 3.56 (s, 3.00 H, H⁷) 3.54 (t, ²*J*_{HD} = 1.7 Hz, 1.51 H, H⁷), 352 (m, 0.40 H, H⁷). ESI⁺ MS: *m/z* (int.) = 294.2 (4.56), 295.23 (6.08), 296.22 (43.1), 297.23 (99.8), 298.24 (156), 299.24 (199), 300.25 (252), 301.26 (272), 302.26 (263), 303.27 (220), 304.28 (142), 305.29 (90.3), 306.28 (39.4), 307.29 (10.9), 308.26 (3.34).

2.2 [D₆]-ddpd and [D₁₄]-ddpd via Selective Deuteration

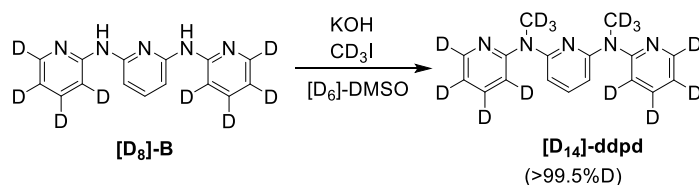
[D₈]-*N,N'*-Bis(2-pyridyl)-2,6-diaminopyridine ([D₈]-B)^[4]



In a 50 mL round-bottom flask, [D₅]-pyridine-N-oxide^[5] ([D₅]-A) (368 mg, 3.68 mmol, 2.4 eq, 99.5 %D) was dissolved in dry CH₂Cl₂ (30 mL) and PyBroP (2.00 g, 4.29 mmol, 2.8 eq) was added. The solution was stirred at room temperature for 30 min, followed by the sequential addition of dry EtN'Pr₂ (1.87 mL, 1.39 g, 10.7 mmol, 7.0 eq) and 2,6-diaminopyridine (167 mg, 1.53 mmol, 1.0 eq). The mixture was stirred at room temperature for 3 h and under reflux for 66 h. Saturated aqueous NaHCO₃ (20 mL) was added, the phases were separated, and the aqueous phase was extracted with additional CH₂Cl₂ (2× 20 mL). The combined organic phases were dried (MgSO₄), concentrated, and the residue was subjected to column chromatography (SiO₂, gradient: n-hexane/EtOAc 1:2 → 1:5, preloading onto SiO₂, detection: UV). The product was obtained as a colorless solid (35 mg, 9 %, >99.5 %D).

¹H NMR (400 MHz, [D₆]-DMSO): δ/ppm = 9.37 (s, 2 H), 7.50 (t, *J* = 8.0 Hz, 1 H), 7.13 (d, *J* = 8.0 Hz, 2 H).

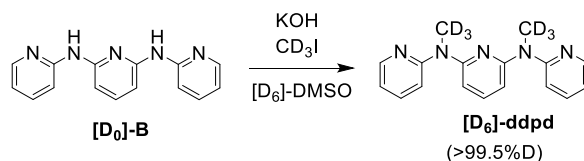
[D₁₄]-ddpd



In a 25 mL round-bottom flask, powdered KOH (21 mg, 0.37 mmol, 4.0 eq) was suspended in [D₆]-DMSO (1.0 mL, NMR grade, 99.8%D), [D₈]-B (25.4 mg, 93.6 μmol, 1.0 eq) was added and the mixture was stirred at ambient temperature for 30 min. CD₃I (13 μL, 30 mg, 0.21 mmol, 2.2 eq) was added to the red-brown suspension and stirring was continued overnight (15 h). Water (10 mL) was added and the yellow aqueous suspension was extracted with a 1:1 (v/v) mixture of Et₂O/THF (3× 10 mL). The combined organic phases were washed with aqueous sat. Na₂CO₃ (10 mL), dried over MgSO₄, and concentrated under reduced pressure. The yellow residue was subjected to column chromatography (SiO₂, n-hexane/EtOAc, gradient 3:1 → 1:1) to yield the product as a pale-yellow oil (20.3 mg, 71 %, >99.5 %D).

¹H NMR (400 MHz, [D₆]-DMSO): δ/ppm = 7.55 (t, *J* = 8.1 Hz, 1 H), 6.74 (d, *J* = 8.1 Hz, 2 H).

[D₆]-ddpd



In a 25 mL round-bottom flask, powdered KOH (410 mg, 7.3 mmol, 4.0 eq) was suspended in [D₆]-DMSO (10 mL, NMR grade, 99.8 %D), [D₀]-B^[6] (481 mg, 1.83 mmol, 1.0 eq) was added and the mixture was stirred at ambient temperature for 30 min. CD₃I (250 μL, 583 mg, 4.02 mmol, 2.2 eq) was added to the red-brown suspension and stirring was continued overnight (15 h). Water (30 mL) was added and the yellow aqueous suspension was extracted with a 1:1 (v/v) mixture of Et₂O/THF (3× 30 mL). The combined organic phases were washed with aqueous sat. Na₂CO₃ (30 mL), dried over MgSO₄, and concentrated under reduced pressure. The yellow residue was subjected to column chromatography (SiO₂, n-hexane/EtOAc, gradient 3:1 → 1:1, preloading onto SiO₂) to yield the product as a pale-yellow oil (414 mg, 76 %, >99.5 %D).

¹H NMR (CD₃CN, 400 MHz): δ/ppm = 8.29 (ddd, *J* = 4.9, 2.1, 0.9 Hz, 2 H), 7.57 (ddd, *J* = 8.5, 7.2, 2.0 Hz, 2 H), 7.53 (t, *J* = 8.1 Hz, 1 H), 7.26 (dt, *J* = 8.4, 0.9 Hz, 2 H), 6.89 (ddd, *J* = 7.2, 4.9, 0.93 Hz, 2 H), 6.71 (d, *J* = 8.0, 2 H).

Complex synthesis [Cr([D_n]-ddpd)₂][BF₄]₃:

The chromium(III) complexes with the deuterated ligands [D₉]-ddpd, [D₆]-ddpd and [D₁₄]-ddpd, respectively, were prepared according to the preparation of the non-deuterated parent complex.^[7]

Complex [4][BF₄]₃ (from the [D₁₄]-ddpd ligand) contained traces of residual chloride ions which could not be removed due to the very small amount of material. In water, these trace amounts of chloride have no effect on the photophysical properties. In acetonitrile, however, chloride ions allow for strong ion pairing which leads to self-quenching.^[8] Such ion-pairing effects have been reported before for [Cr(bpy^R)₃]³⁺ and [Cr(phen^R)₃]³⁺ complexes reducing their ²E lifetime.^[8] Hence, we refrain from reporting and discussing the quantum yield and lifetime data obtained for [4][BF₄]₃ in CH₃CN and CD₃CN.

3. ESI⁺ Mass Spectra of [D₉]-ddpd, [D₆]-ddpd and [D₁₄]-ddpd

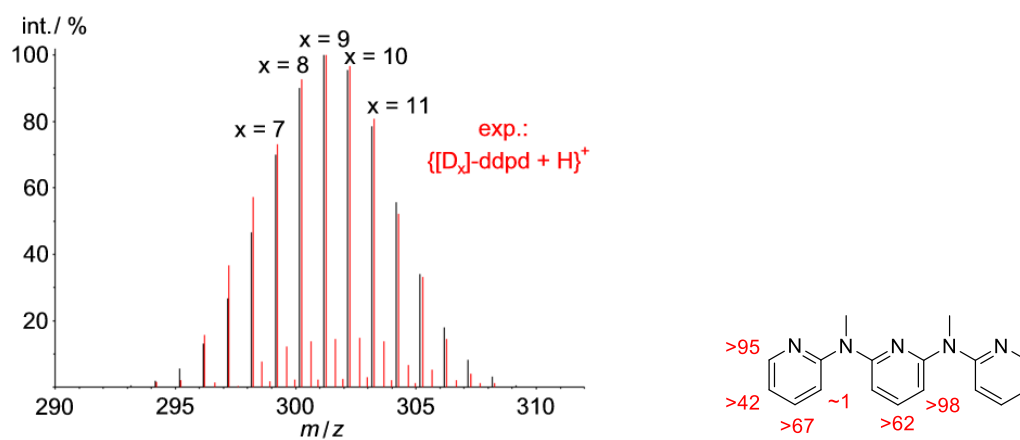


Figure S1. Mass spectrum (ESI⁺ in red) of [D₉]-ddpd and simulation with a Gaussian distribution around the [D₉]-isotopologue (black).

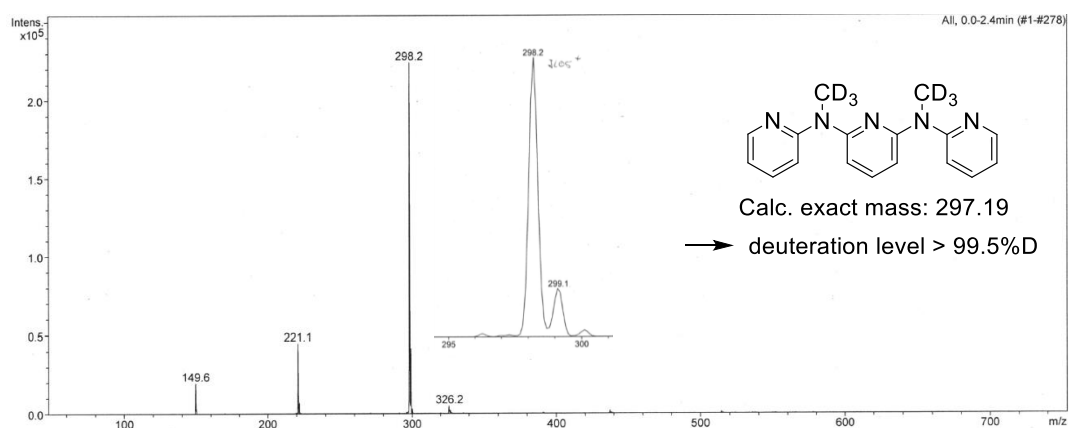


Figure S2. Mass spectrum (ESI⁺) of [D₆]-ddpd.

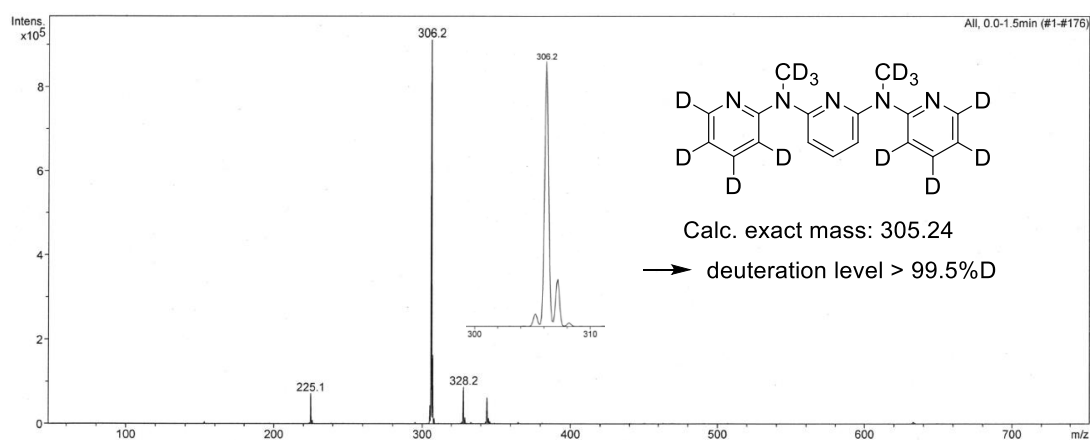


Figure S3. Mass spectrum (ESI⁺) of [D₁₄]-ddpd.

4. ^1H NMR spectra of **ddpd** and **[D₉]-ddpd** in CD_2Cl_2 .

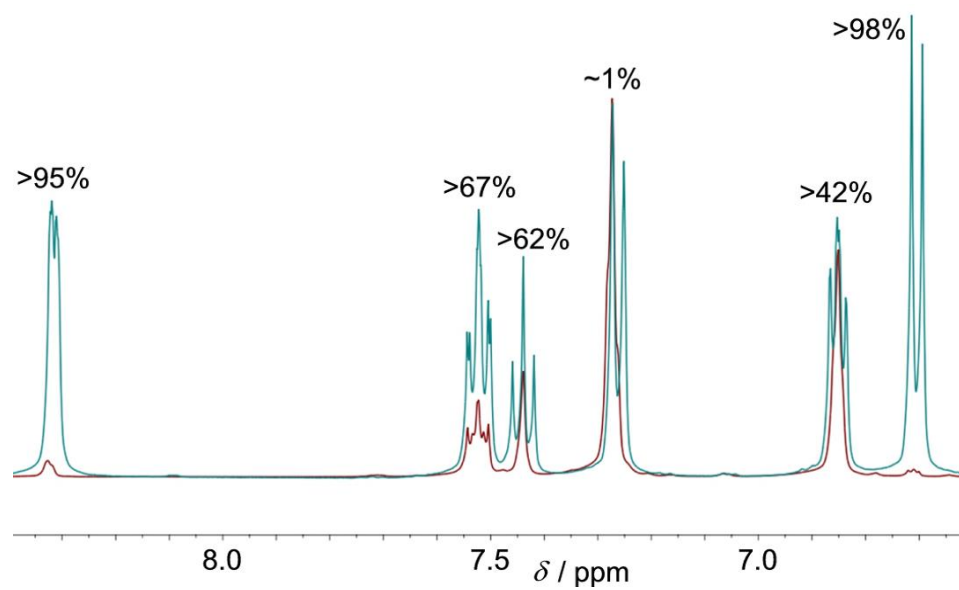


Figure S4. Part of the ^1H NMR spectra of **ddpd** (blue) and **[D₉]-ddpd** (red) in CD_2Cl_2 to obtain the deuteration levels at the pyridine CH positions.

6. Luminescence Spectroscopy

Table S1. Photoluminescence quantum yields Φ / % of [1][BF₄]₃, [2][BF₄]₃, [3][BF₄]₃, and [4][BF₄]₃ in different environments (under Ar). Uncertainty estimated as ca. 5 %.

	[1][BF ₄] ₃	[2][BF ₄] ₃	[3][BF ₄] ₃	[4][BF ₄] ₃
H ₂ O	11.0	12.4	9.0	11.5
D ₂ O	14.2	22.4	14.1	21.6
CH ₃ CN	12.1	22.0	12.4	-
CD ₃ CN	11.7	30.1	14.4	-

Table S2. Photoluminescence quantum yields Φ / % of [1][BF₄]₃, [2][BF₄]₃, [3][BF₄]₃, and [4][BF₄]₃ in different environments (solvents saturated with O₂). Uncertainty estimated as ca. 5 %.

	[1][BF ₄] ₃	[2][BF ₄] ₃	[3][BF ₄] ₃	[4][BF ₄] ₃
H ₂ O	2.1	3.1	2.0	2.4
D ₂ O	2.0	2.5	2.2	2.1
CH ₃ CN	0.6	0.7	0.6	-
CD ₃ CN	0.6	0.6	0.6	-

Table S3. Radiative lifetimes τ_{rad} / ms of [1][BF₄]₃, [2][BF₄]₃, [3][BF₄]₃ and [4][BF₄]₃ in different environments (under Ar). Uncertainty estimated to ca. 10 %.

	[1][BF ₄] ₃	[2][BF ₄] ₃	[3][BF ₄] ₃	[4][BF ₄] ₃
H ₂ O	8.16	10.48	9.67	10.43
D ₂ O	8.20	7.59	8.51	9.72
CH ₃ CN	7.43	8.18	7.34	-
CD ₃ CN	6.92	7.64	6.94	-
ratio CH ₃ CN/H ₂ O	0.91	0.78	0.76	-
ratio D/H (H ₂ O)	1.00	0.72	0.88	0.93
ratio D/H (CH ₃ CN)	0.93	0.93	0.95	-

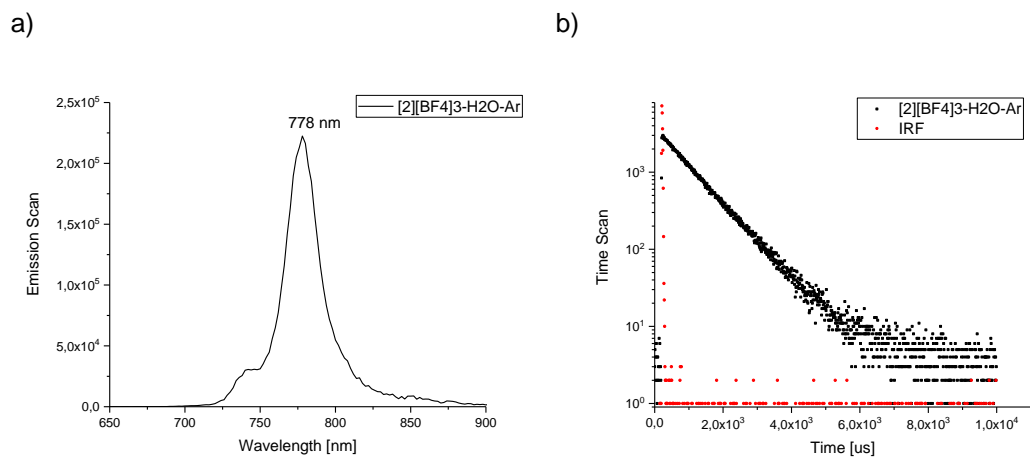


Figure S5. a) Spectrally corrected emission spectrum and b) luminescence decay profile of $[2][\text{BF}_4]_3$ in H_2O under Ar atmosphere ($\text{H}_2\text{O} / \text{Ar}$) [$\lambda_{\text{exc}} = 434 \text{ nm}$; $\lambda_{\text{em}} = 778 \text{ nm}$].

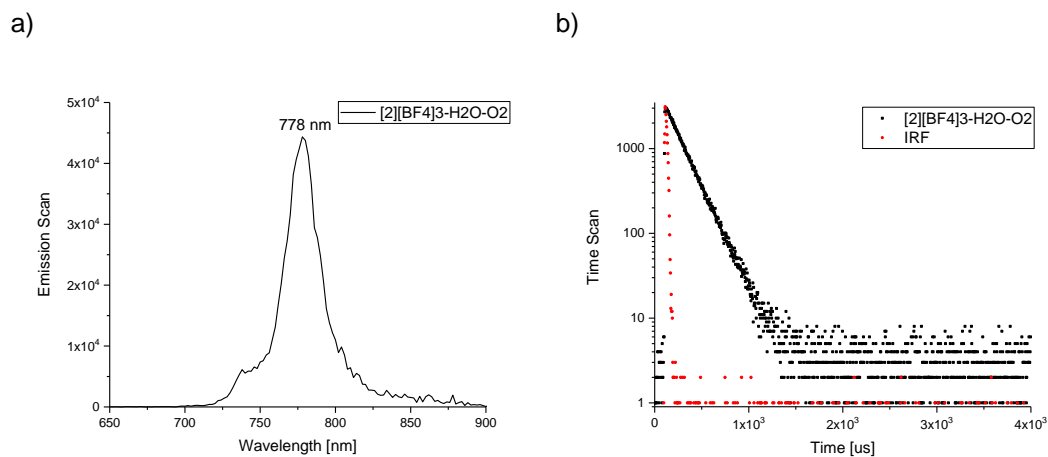


Figure S6. a) Spectrally corrected emission spectrum and b) luminescence decay profile of $[2][\text{BF}_4]_3$ in air-saturated H_2O ($\text{H}_2\text{O} / \text{O}_2$) [$\lambda_{\text{exc}} = 434 \text{ nm}$; $\lambda_{\text{em}} = 778 \text{ nm}$].

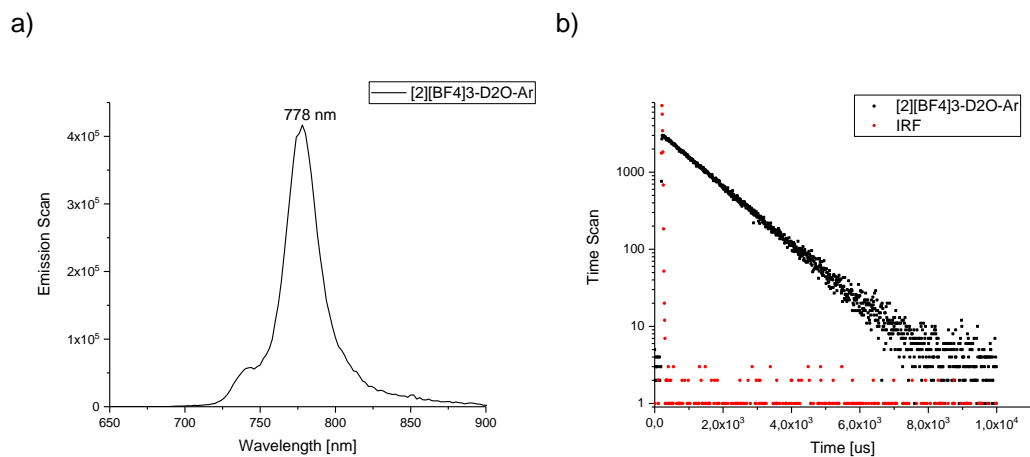


Figure S7. a) Spectrally corrected emission spectrum and b) luminescence decay profile of $[2][\text{BF}_4]_3$ in D_2O under Ar atmosphere ($\text{D}_2\text{O} / \text{Ar}$) [$\lambda_{\text{exc}} = 434 \text{ nm}$; $\lambda_{\text{em}} = 778 \text{ nm}$].

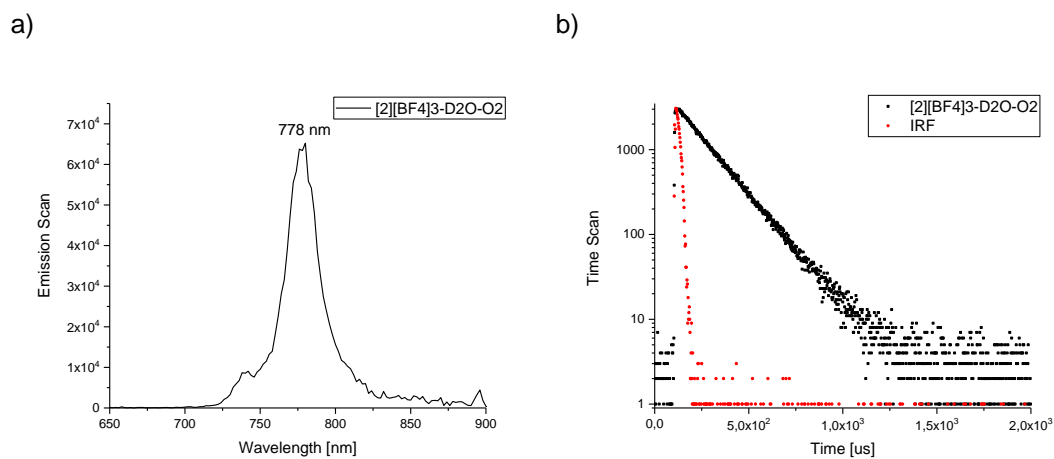


Figure S8. a) Spectrally corrected emission spectrum and b) luminescence decay profile of $[2][\text{BF}_4]_3$ in air-saturated D_2O ($\text{D}_2\text{O} / \text{O}_2$) [$\lambda_{\text{exc}} = 434 \text{ nm}$; $\lambda_{\text{em}} = 778 \text{ nm}$].

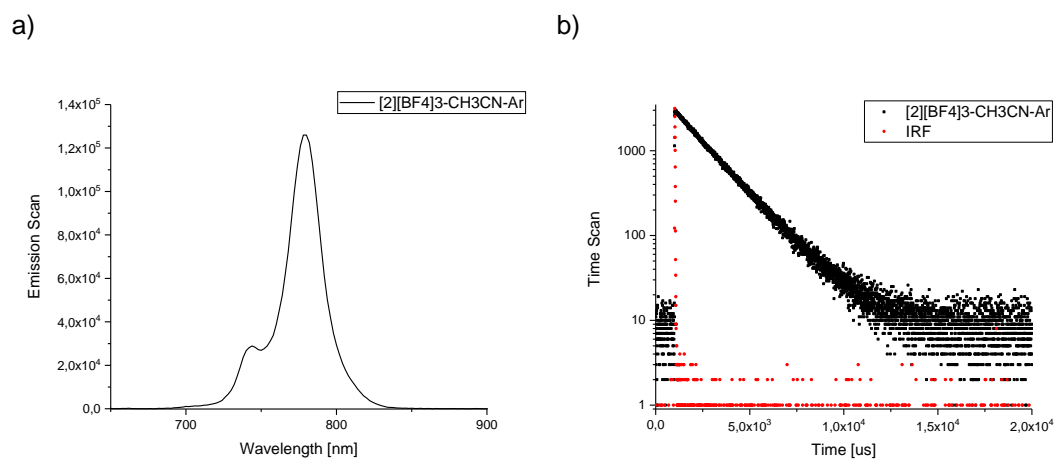


Figure S9. a) Spectrally corrected emission spectrum and b) luminescence decay profile of [2][BF₄]₃ in CH₃CN under Ar atmosphere (CH₃CN / Ar) [$\lambda_{exc} = 435$ nm; $\lambda_{em} = 778$ nm].

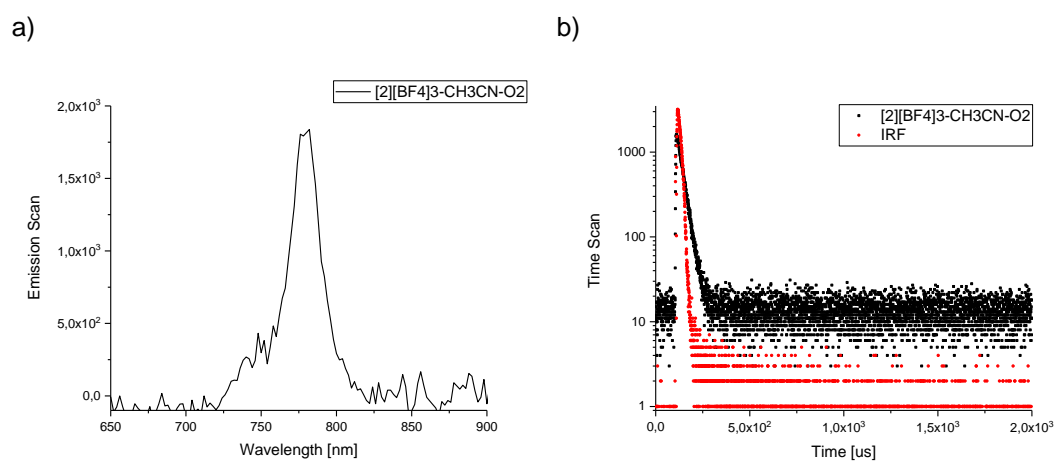


Figure S10. a) Spectrally corrected emission spectrum and b) luminescence decay profile of [2][BF₄]₃ in air-saturated CH₃CN (CH₃CN / O₂) [$\lambda_{exc} = 435$ nm; $\lambda_{em} = 778$ nm].

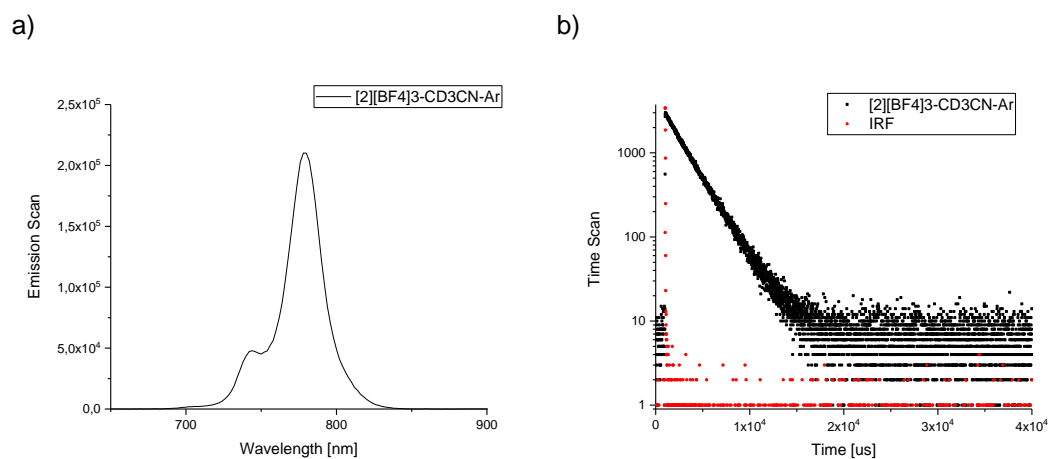


Figure S11. a) Spectrally corrected emission spectrum and b) luminescence decay profile of [2][BF₄]₃ in CD₃CN under Ar atmosphere (CD₃CN / Ar) [$\lambda_{exc} = 435$ nm; $\lambda_{em} = 778$ nm].

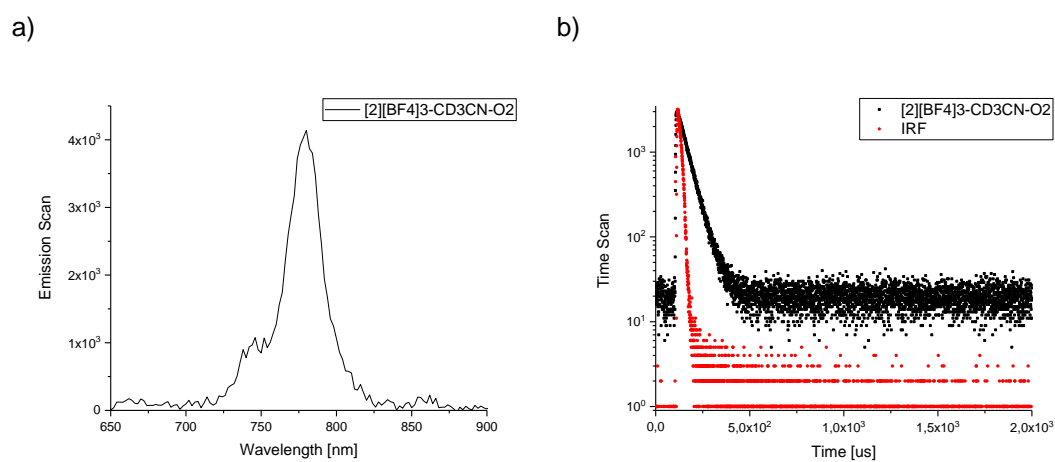


Figure S12. a) Spectrally corrected emission spectrum and b) luminescence decay profile of [2][BF₄]₃ in air-saturated CD₃CN (CD₃CN / O₂) [$\lambda_{exc} = 435$ nm; $\lambda_{em} = 778$ nm].

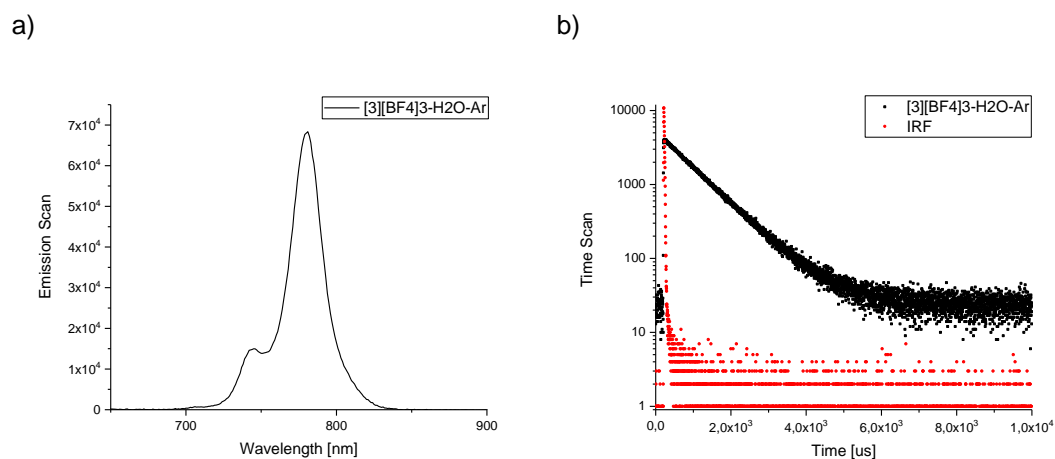


Figure S13. a) Spectrally corrected emission spectrum and b) luminescence decay profile of $[3][BF_4]_3$ in H_2O / Ar [$\lambda_{exc} = 434 \text{ nm}$; $\lambda_{em} = 780 \text{ nm}$].

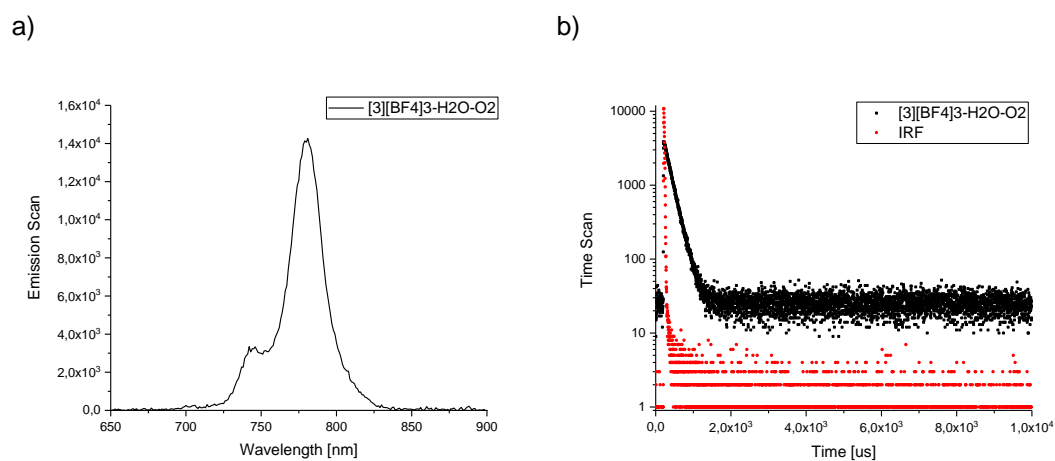


Figure S14. a) Spectrally corrected emission spectrum and b) luminescence decay profile of $[3][BF_4]_3$ in H_2O / O_2 [$\lambda_{exc} = 434 \text{ nm}$; $\lambda_{em} = 780 \text{ nm}$].

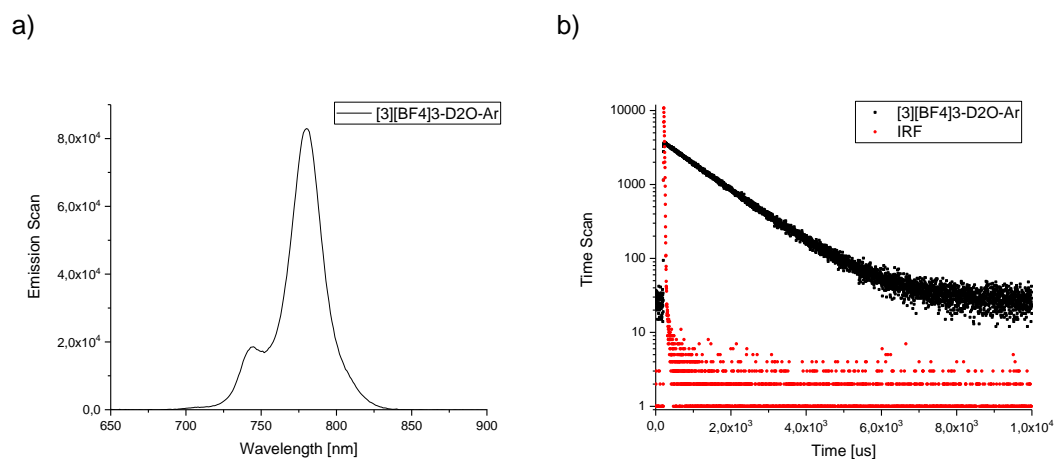


Figure S15. a) Spectrally corrected emission spectrum and b) luminescence decay profile of [3][BF₄]₃ in D₂O / Ar [$\lambda_{exc} = 435$ nm; $\lambda_{em} = 780$ nm].

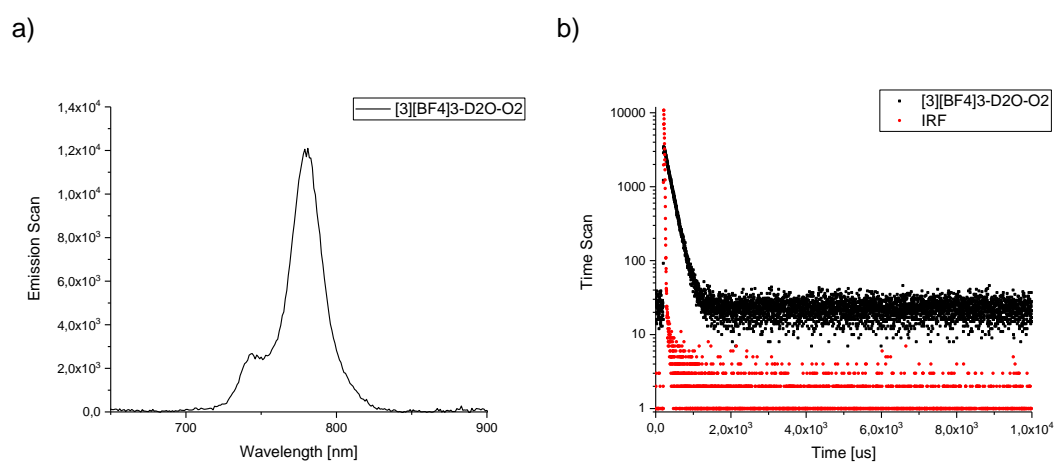


Figure S16. a) Spectrally corrected emission spectrum and b) luminescence decay profile of [3][BF₄]₃ in D₂O / O₂ [$\lambda_{exc} = 435$ nm; $\lambda_{em} = 780$ nm].

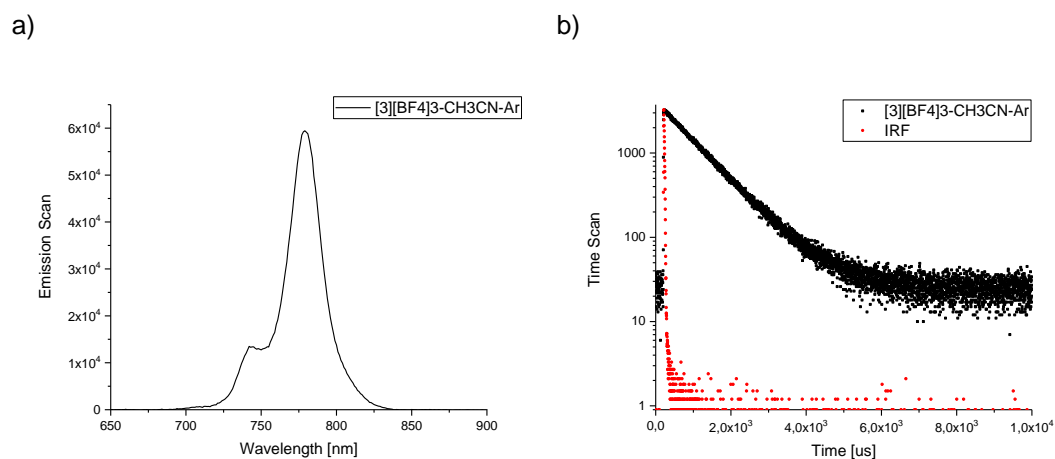


Figure S17. a) Spectrally corrected emission spectrum and b) luminescence decay profile of $[3][BF_4]_3$ in CH_3CN / Ar [$\lambda_{exc} = 435 \text{ nm}$; $\lambda_{em} = 780 \text{ nm}$].

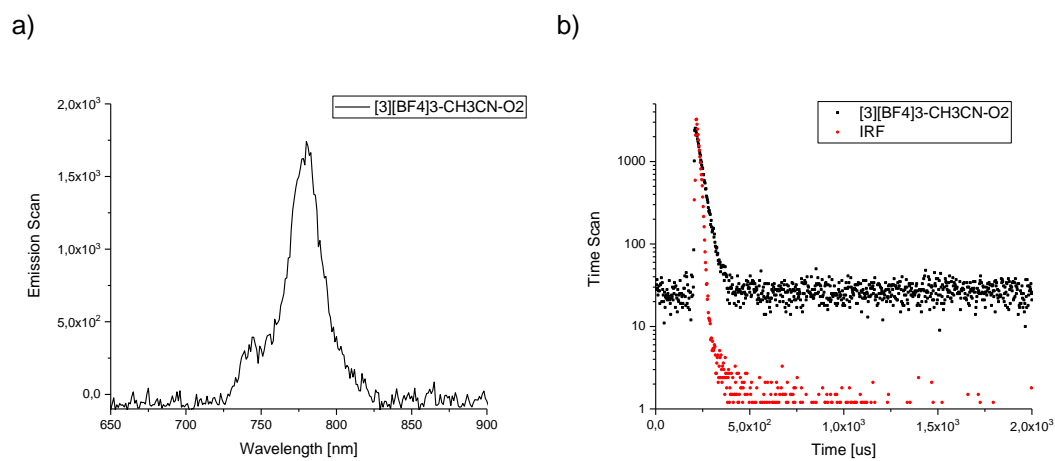


Figure S18. a) Spectrally corrected emission spectrum and b) luminescence decay profile of $[3][BF_4]_3$ in CH_3CN / O_2 [$\lambda_{exc} = 435 \text{ nm}$; $\lambda_{em} = 780 \text{ nm}$].

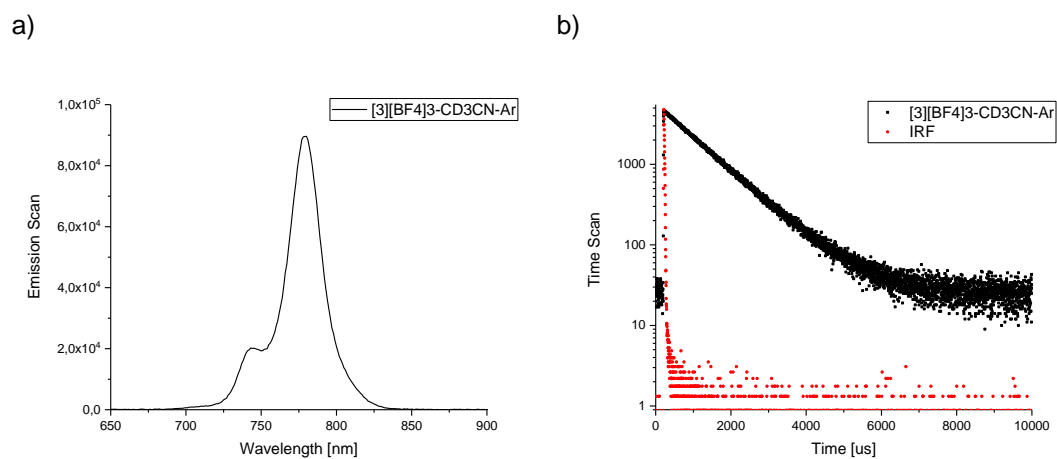


Figure S19. a) Spectrally corrected emission spectrum and b) luminescence decay profile of $[3][\text{BF}_4]_3$ in $\text{CD}_3\text{CN} / \text{Ar}$ [$\lambda_{\text{exc}} = 435 \text{ nm}$; $\lambda_{\text{em}} = 780 \text{ nm}$].

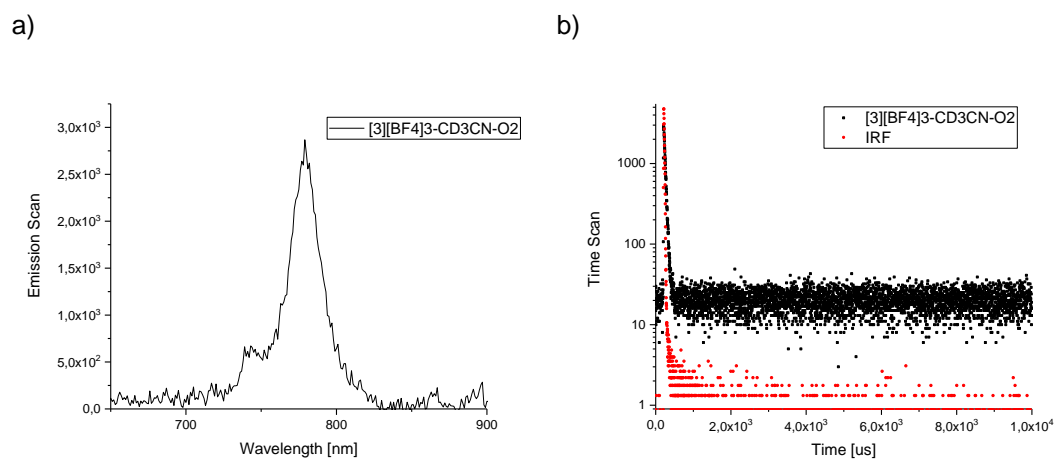


Figure S20. a) Spectrally corrected emission spectrum and b) luminescence decay profile of $[3][\text{BF}_4]_3$ in $\text{CD}_3\text{CN} / \text{O}_2$ [$\lambda_{\text{exc}} = 435 \text{ nm}$; $\lambda_{\text{em}} = 780 \text{ nm}$].

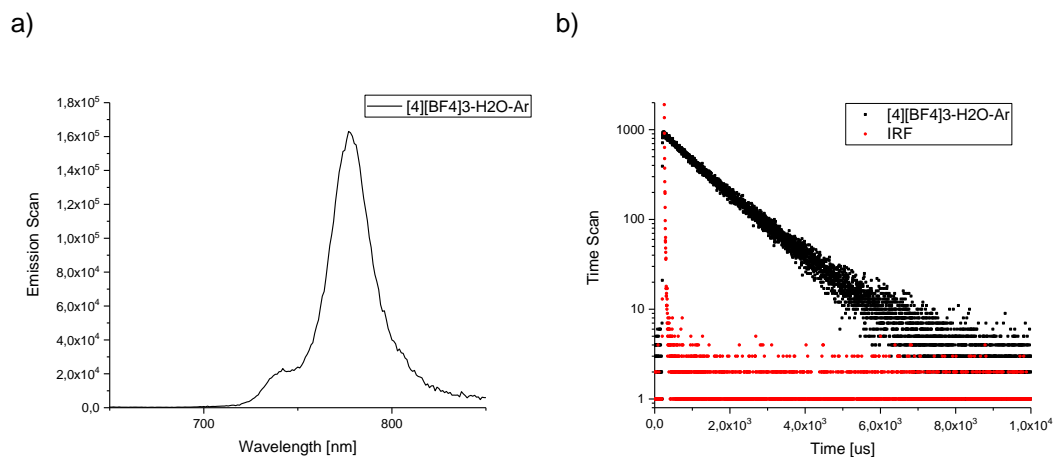


Figure S21. a) Spectrally corrected emission spectrum and b) luminescence decay profile of [4][BF₄]₃ in H₂O / Ar [$\lambda_{exc} = 434$ nm; $\lambda_{em} = 778$ nm].

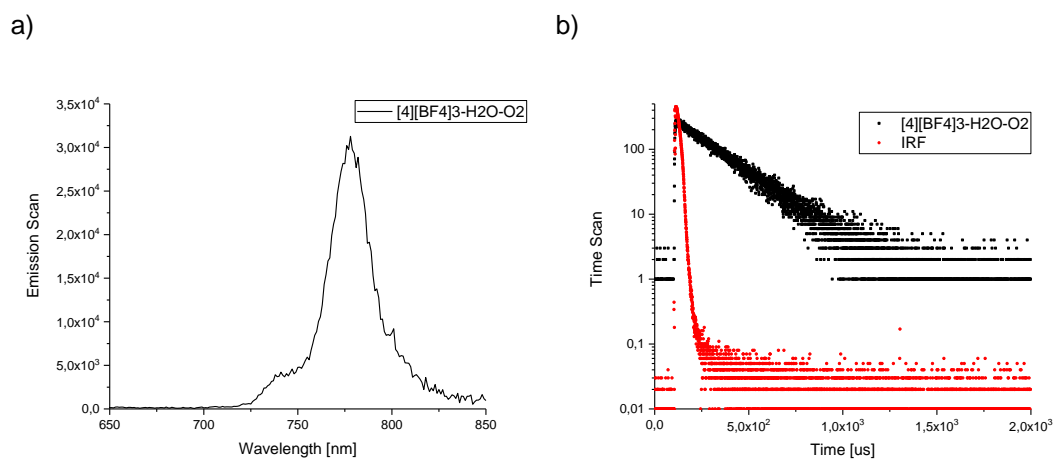


Figure S22. a) Spectrally corrected emission spectrum and b) luminescence decay profile of [4][BF₄]₃ in H₂O / O₂ [$\lambda_{exc} = 434$ nm; $\lambda_{em} = 778$ nm].

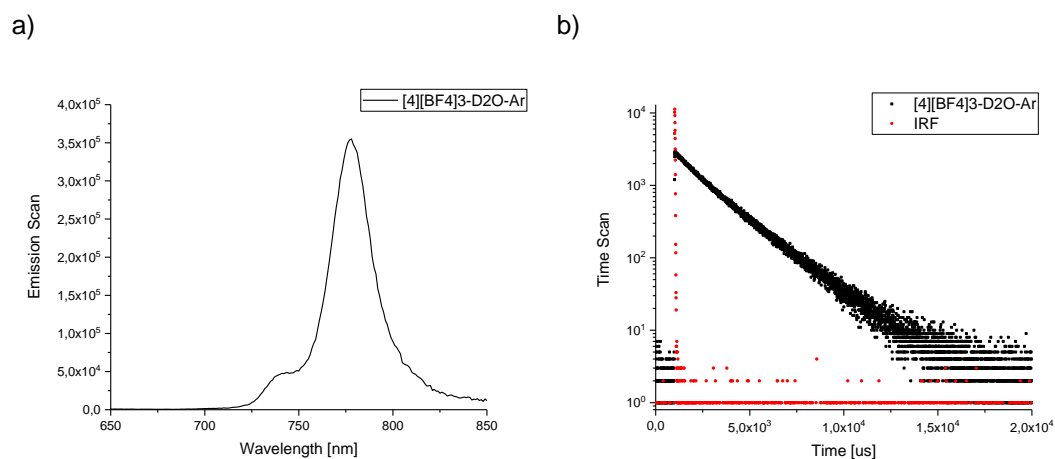


Figure S23. a) Spectrally corrected emission spectrum and b) luminescence decay profile of $[4][BF_4]_3$ in D_2O / Ar [$\lambda_{exc} = 434 \text{ nm}$; $\lambda_{em} = 778 \text{ nm}$].

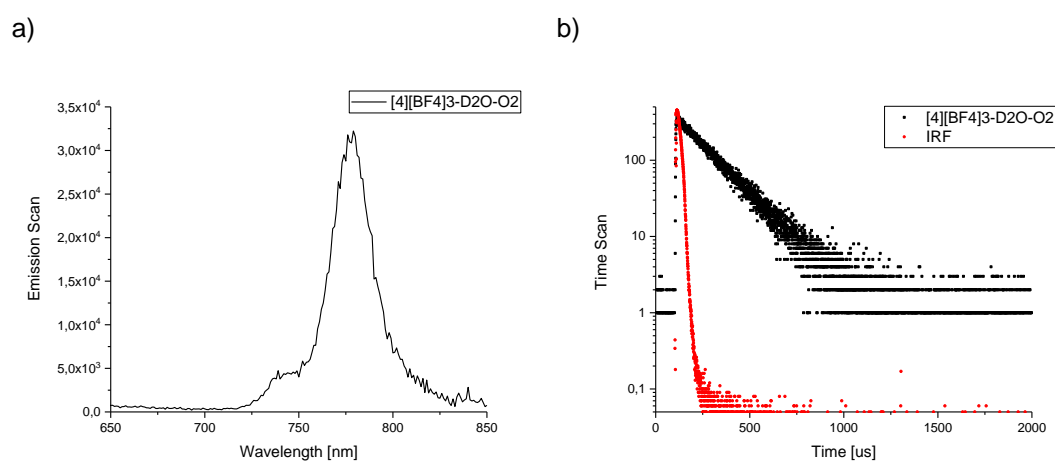


Figure S24. a) Spectrally corrected emission spectrum and b) luminescence decay profile of $[4][BF_4]_3$ in D_2O / O_2 [$\lambda_{exc} = 434 \text{ nm}$; $\lambda_{em} = 778 \text{ nm}$].

7. NIR Absorption Spectroscopy / Vibrational Overtone Analysis

Since the isotopologic chromium(III) complexes were not available in sufficient quantities, the analysis of the position and intensity of the CH and CD vibrational overtones in the chromium complexes was carried out on simpler pyridine-containing model compounds. The vibrational signatures of the protiated and deuterated methyl protons in **ddpd** were not investigated because deuteration did not show any effect on the non-radiative deactivation of the 2E state (see the article). Due to strong absorption by most organic compounds in the NIR region, only a limited number of solvents can be used and protic solvents such as H₂O and D₂O are highly problematic in this respect. With these constraints in mind, we chose 2,2'-dipyridylamine (**DPA**, Figure S25) in CDCl₃ as our model system.

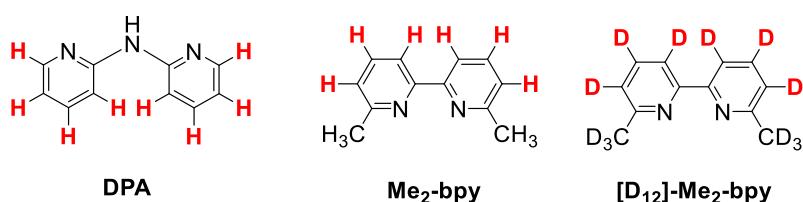


Figure S25. Model compounds used for the analysis of vibrational CH and CD overtones.

The aromatic CH overtone energies of **DPA** (Figure S26) could be measured up to the third overtone ($\nu = 4$) and showed a well-behaved Morse progression and could reasonably well be fitted with Gaussian functions of the form $y(x) = A * \exp(-0.5 * ((x-x_c)/\sigma)^2)$ defined by amplitude A , center wavenumber x_c , and Gaussian width σ . This behavior has been seen before in related pyridine systems.^[9,10] Unfortunately, the perdeuterated analogon of **DPA** was not available which precluded the analysis of the aromatic CD oscillator overtones in this case. Instead, we used previously obtained vibrational overtone data from the isotopologues of 6,6'-dimethyl-2,2'-bipyridine (**Me₂-bpy** and **[D₁₂]-Me₂-bpy**, Figure S25).^[10] Despite the drastic approximations made in this case, the latter two compounds had already proven very appropriate for this type of analysis within the context of a local-mode, anharmonic Morse oscillator model for the non-radiative deactivation of ytterbium(III) NIR-luminescence in very similar tris(bipyridine)-based lanthanide cryptates.^[9]

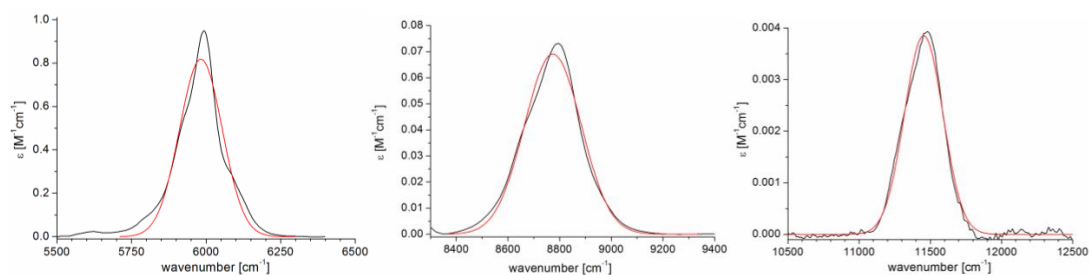


Figure S26. NIR absorption bands of the aromatic CH vibrational overtones in 2,2'-dipyridylamine (solid black) in CDCl_3 ($c = 0.537 \text{ M}$) in the region $\nu = 2$ (left), $\nu = 3$ (middle), and $\nu = 4$ (right) with single Gaussian fit functions (red).

The data for **Me₂-bpy** and **[D₁₂]-Me₂-bpy** (Figures S27 and S28), however, did not fully cover the spectral region of the emission in the chromium complexes (ca. 11000 – 14000 cm^{-1}) but the spectral characteristics of the required higher aromatic C-(H/D) overtones can be extrapolated from the systematic changes seen in the lower, measured overtones. For this purpose, each overtone band was fitted with a single Gaussian which had been shown to be the best model in the case of 2,2'-dipyridylamine (*vide supra*). The properties of these Gaussians are summarized in Table S4 and were used for the prediction of the higher overtone bands.

The validity of using **[D_x]-Me₂-bpy** instead of the chemically more appropriate model **DPA** was confirmed by the very close resemblance of the extracted single Gaussian fits of the measured CH overtones of these two model systems (Figure S29).

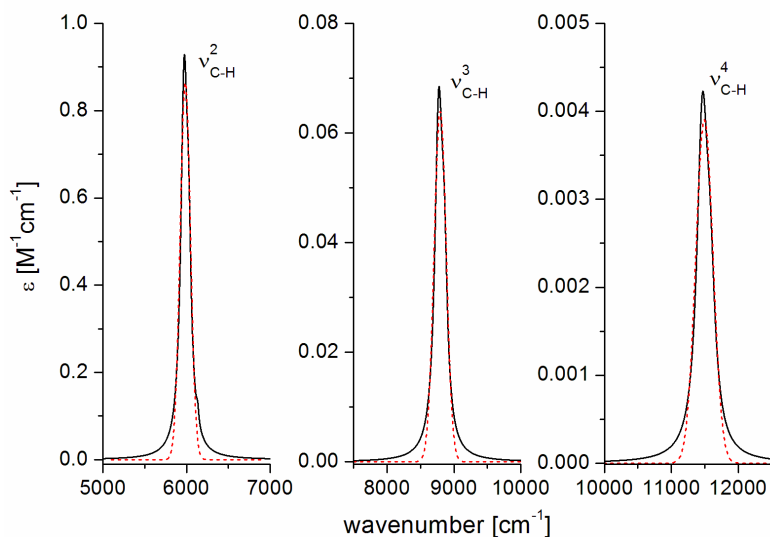


Figure S27. Reconstructed vibrational overtone absorption bands ($\nu = 2, 3$, and 4) for the aromatic CH oscillators of **Me₂-bpy** (black) with single Gaussian fits (dashed red).

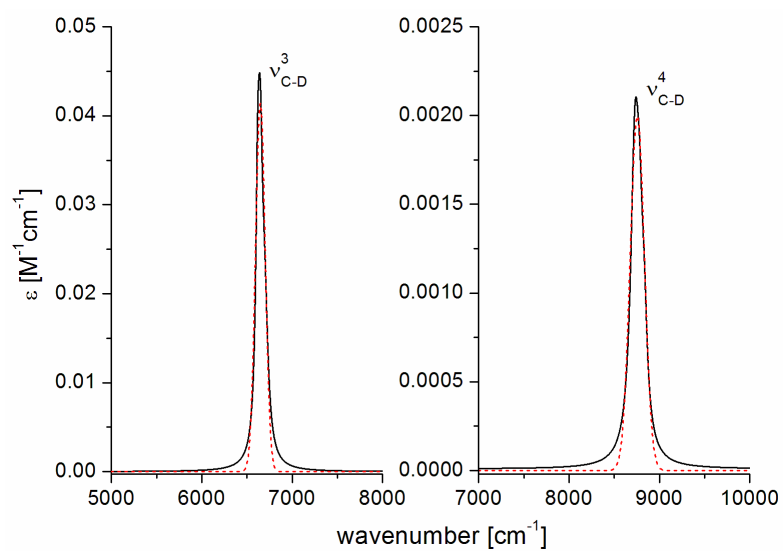


Figure S28. Reconstructed vibrational overtone absorption bands ($\nu = 3$ and 4) for the aromatic CD oscillators of **Me₂-bpy** (black) with single Gaussian fits (dashed red).

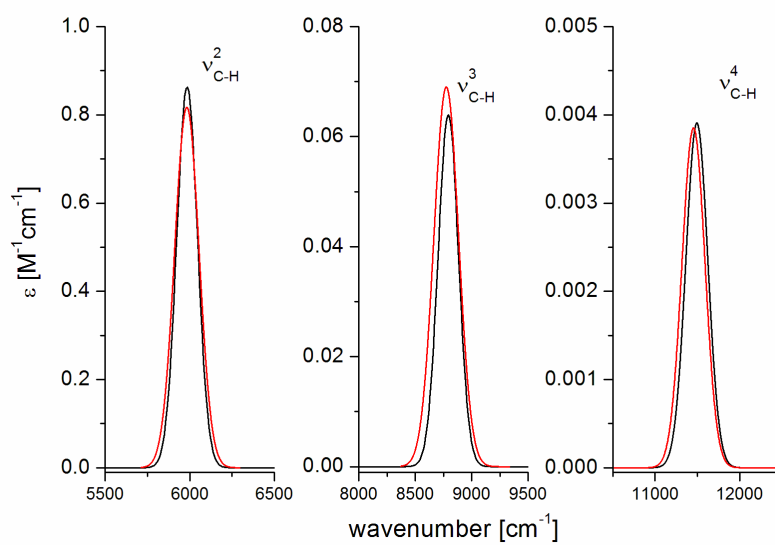


Figure S29. Comparison of the obtained Gaussian fits of the vibrational CH overtone absorption bands of **Me₂-bpy** (black) and **DPA** (red).

Table S4. Parameters of the Gaussians (x_c : center wavenumber; σ : Gaussian width; A : amplitude) describing the aromatic CH and CD overtones in **Me₂-bpy** and **[D₁₂]-Me₂-bpy**.

CH Oscillators			
ν	maximum x_c [cm ⁻¹]	σ [cm ⁻¹]	A [M ⁻¹ cm ⁻¹]
2 ^[a]	5984.4	61.13	8.639E-1
3 ^[a]	8792.0	90.21	6.399E-2
4 ^[a]	11493.4	129.1	3.910E-3
5 ^[b]	14065.3 ^[c]	161.5 ^[d]	2.716E-4 ^[e]
CD Oscillators			
ν	maximum x_c [cm ⁻¹]	σ [cm ⁻¹]	A [M ⁻¹ cm ⁻¹]
3 ^[a]	6647.4	53.15	4.15E-2
4 ^[a]	8754.7	78.45	2.00E-3
5 ^[b]	10807.6 ^[f]	103.75 ^[g]	9.65E-05 ^[h]
6 ^[b]	12806.1 ^[f]	129.05 ^[g]	4.65E-06 ^[h]
7 ^[b]	14750.3 ^[f]	154.35 ^[g]	2.25E-07 ^[h]

^[a] Based on Gaussian fits of measured data.

^[b] Based on extrapolated parameters using the fit relations in [c-h].

^[c] Calculated using $x_c = \nu^*3170 \text{ cm}^{-1} - \nu^*(\nu+1)*59 \text{ cm}^{-1}$ (see Figure S30).

^[d] Calculated using $\sigma = 34.0 \text{ cm}^{-1} * \nu - 8.53 \text{ cm}^{-1}$ (see Figure S32).

^[e] Calculated using $\log(A) = 2.295 - \nu^*1.172$ (see Figure S31).

^[f] Calculated using $x_c = \nu^*2324 \text{ cm}^{-1} - \nu^*(\nu+1)*27 \text{ cm}^{-1}$ (see Figure S30).

^[g] Calculated using $\sigma = 25.0 \text{ cm}^{-1} * \nu - 22.8 \text{ cm}^{-1}$ (see Figure S32).

^[h] Calculated using $\log(A) = 2.567 - \nu^*1.137$ (see Figure S31).

In particular, the overtone positions x_c could be predicted with the appropriate Morse relationship obtained by Birge-Sponer plots (Figure S30), the Gaussian amplitudes A by extrapolation of the semi-logarithmic relationship with the vibrational quantum number ν (Figure S31), and the Gaussians widths σ by extending the proportionality with ν obtained in Figure S32.

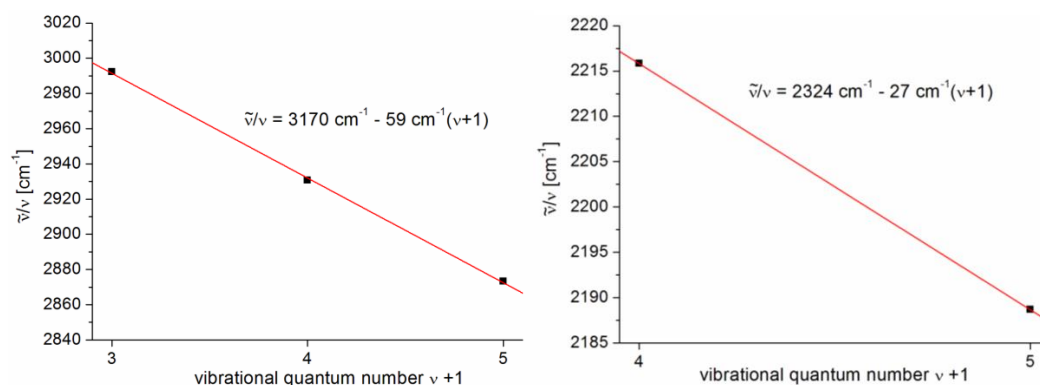


Figure S30. Birge-Sponer plots for the determination of the Gaussian parameter x_c (see Table S4) with linear relationships (red) – Left: CH oscillators; Right: CD oscillators.

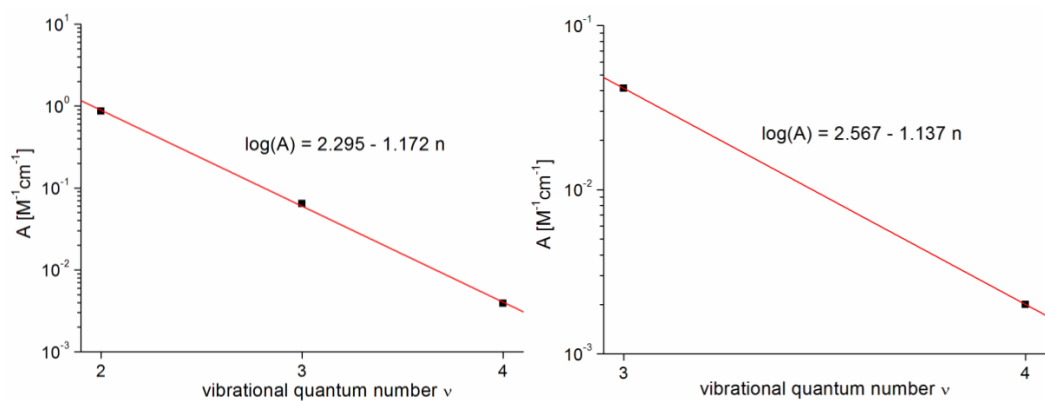


Figure S31. Semi-logarithmic plot of the Gaussian amplitudes A of the oscillator overtones with linear relationships (red) – Left: CH oscillators; Right: CD oscillators.

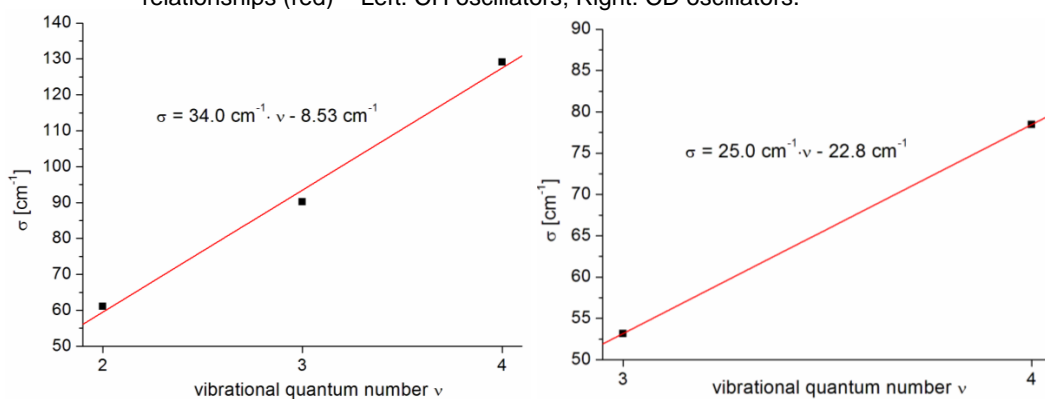


Figure S32. Plot of the Gaussian widths σ of the oscillator overtones with linear relationships (red) – Left: CH oscillators; Right: CD oscillators.

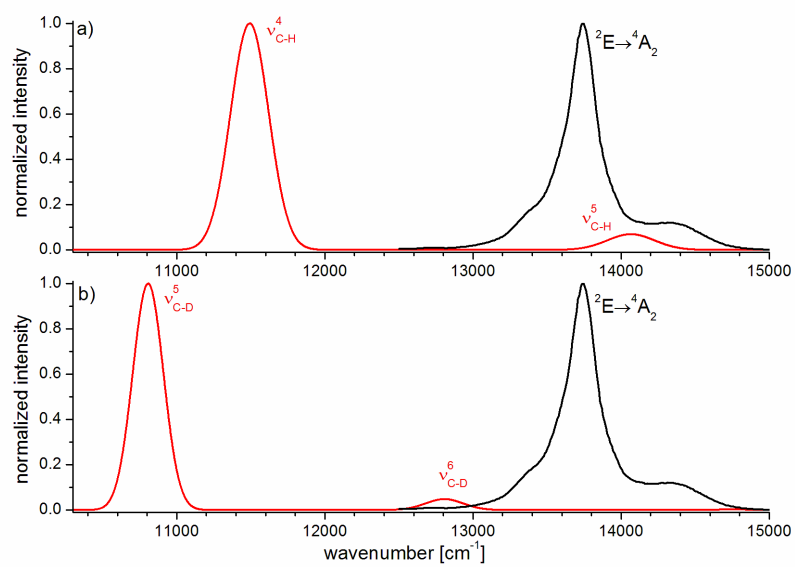


Figure S33. a) Normalized ²E emission spectrum of [Cr(bpy)₃]³⁺ (black) and the relevant vibrational aromatic CH overtone absorption bands (red). b) Normalized ²E emission spectrum of [Cr(bpy)₃]³⁺ (black) and the relevant vibrational aromatic CD overtone absorption bands (red).

7. VT-FTIR Spectroscopy of [1][BF₄]₃ and [3][BF₄]₃

In order to investigate the influence of temperature changes on the vibrational modes of [Cr(ddpd)₂](BF₄)₃, Fourier transform infrared spectroscopy (FTIR) measurements with deuterium labelled **D₆-ddpd** and unlabelled **ddpd** ligands in the chromium(III) complex were performed ([3][BF₄]₃ and [1][BF₄]₃). For the FTIR measurements at various temperatures, the complexes have been embedded in a KBr matrix (KBr pellets); these pellets are mounted in a closed cycle helium cryostat. Temperature dependent spectra for the peak temperatures 290 K and 10 K in comparison to the DFT calculated spectra are shown in Figures S34 – S35 in the range from 2050 to 3150 cm⁻¹.

The observed absorption bands located between 3150 cm⁻¹ and 2850 cm⁻¹ are due to aliphatic and aromatic CH stretching vibrations of the ligands. The corresponding CD stretching oscillations of the deuterium labelled methyl groups are located around 2100 and 2250 cm⁻¹. The spectra calculated at the DFT level of theory (optimized structure, B3LYP functional, def2-TZVP basis set)^[11] reproduce the experimental IR spectra of each complex. Additional bands like the band around 2350 cm⁻¹ in the experimental spectra arise from traces of CO₂. A list of assignments of vibrational bands is given in Tables S5 – S6. Clear changes in the IR spectra are observed by the change in temperature. In general all bands but especially the CH bands show a temperature depending increase of intensity (narrowing) at lower temperatures. This probably arises from a reduction of combination vibrations with low frequency motions, i.e. a higher population of the $\nu = 0$ states can increase the intensity of a fundamental vibrational transition. In comparison to the unlabelled spectra the deuterium labelling leads to a slight red-shift by 1 – 3 cm⁻¹ in the fingerprint region.

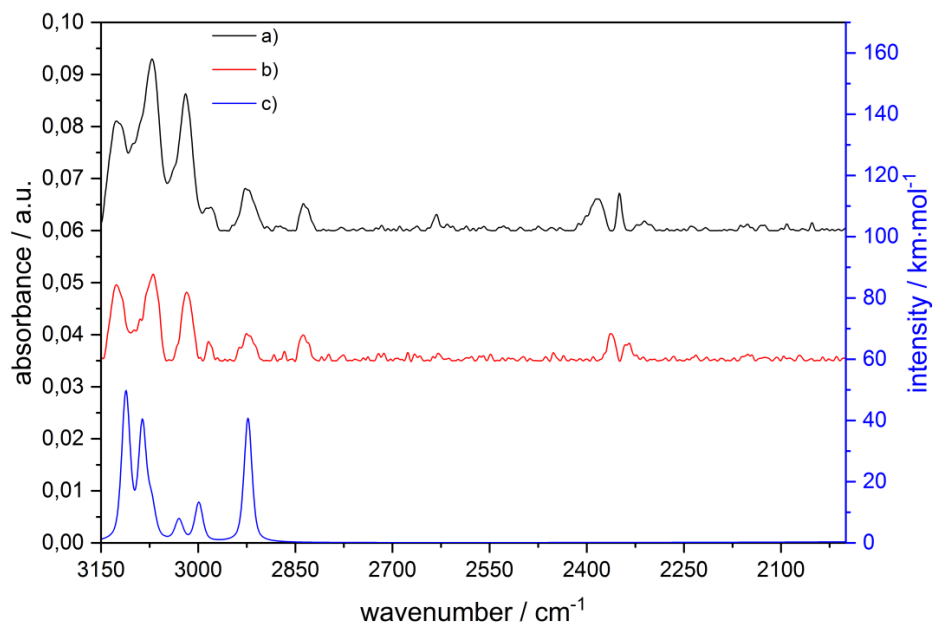


Figure S34. FTIR spectrum (CH/CD region) of **[1][BF₄]₃** at a) 10 K (black) b) 290 K (red) in comparison to c) DFT calculated spectrum of **1³⁺** (blue; def2-TZVP/B3LYP, FWHM 15 cm⁻¹).

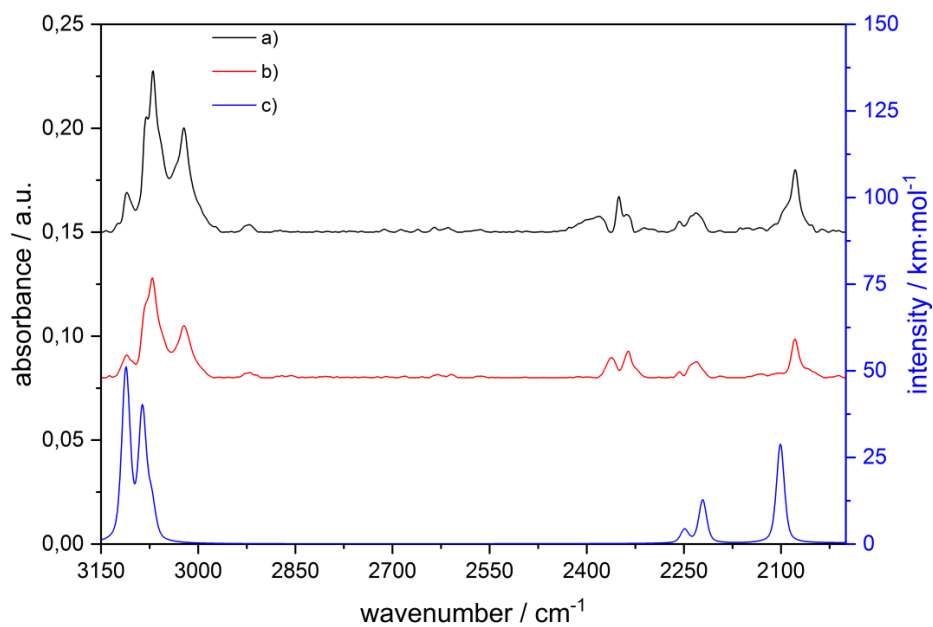


Figure S35. FTIR spectrum (CH/CD region) of **[3][BF₄]₃** at a) 10 K b) 290 K in comparison to c) DFT calculated spectrum of **3³⁺** (def2-TZVP/B3LYP, FWHM 15 cm⁻¹).

Table S5. IR bands of **1³⁺**.

$\tilde{\nu} / \text{cm}^{-1}$	description
3126	Antisymmetric CH stretching of central and terminal pyridine moieties
3070	Antisymmetric CH stretching of terminal pyridine moieties
3019	Antisymmetric CH stretching of terminal pyridine moieties
2981	Antisymmetric CH stretching of methyl moieties
2926	Antisymmetric CH stretching of methyl moieties
2837	Antisymmetric CH stretching of methyl moieties

Table S6. IR bands of **3³⁺**.

$\tilde{\nu} / \text{cm}^{-1}$	description
3110	Antisymmetric CH stretching of central and terminal pyridine moieties
3069	Antisymmetric CH stretching of terminal pyridine moieties
3022	Antisymmetric CH stretching of terminal pyridine moieties
2257	Antisymmetric CD stretching of methyl moieties
2231	Antisymmetric CD stretching of methyl moieties
2078	Antisymmetric CD stretching of methyl moieties

8. References

- [1] G. R. Fulmer, A. J. M. Miller, N. H. Sherden, H. E. Gottlieb, A. Nudelman, B. M. Stoltz, J. E. Bercaw, K. I. Goldberg, *Organometallics* **2010**, *29*, 2176–2179.
- [2] a) C. Würth, D. Geißler, T. Behnke, M. Kaiser, U. Resch-Genger, *Anal. Bioanal. Chem.* **2015**, *407*, 59–78; b) C. Würth, M. G. González, R. Niessner, U. Panne, C. Haisch, U. Resch-Genger, *Talanta* **2012**, *90*, 30–37; c) C. Würth, J. Pauli, C. Lochmann, M. Spieles, U. Resch-Genger, *Anal. Chem.* **2012**, *84*, 1345–1352.
- [3] A. Breivogel, C. Förster, K. Heinze, *Inorg. Chem.* **2010**, *49*, 7052–7056.
- [4] In analogy to: A. T. Londregan, S. Jennings, L. Wei, *Org. Lett.* **2010**, *12*, 5254–5257.
- [5] A. K. Jha, N. Jain, *Chem. Commun.* **2016**, *52*, 1831–1834.
- [6] K.-Y. Ho, W.-Y. Yu, K.-K. Cheung, C.-M. Che, *J. Chem. Soc., Dalton Trans.* **1999**, 1581–1586.
- [7] S. Otto, M. Grabolle, C. Förster, C. Kreitner, U. Resch-Genger, K. Heinze, *Angew. Chem.* **2015**, *127*, 11735–11739; *Angew. Chem. Int. Ed.* **2015**, *54*, 11572–11576.
- [8] N. Serpone, M. A. Jamieson, R. Siriam, M. Z. Hoffman, *Inorg. Chem.* **1981**, *20*, 3983–3988.
- [9] a) R. Bini, R.; P. Foggi, R. G. Della Valle, *J. Phys. Chem.* **1991**, *95*, 3027; b) H. G. Kjaergaard, R. J. Proos, D. M. Turnbull, B. R. Henry, *J. Phys. Chem.* **1996**, *100*, 19273; c) D. L. Snavelly, J. A. Overly, V. A. Walters, *Chem. Phys.* **1995**, *201*, 567; d) R. H. Page, R. Y. Shen, Y. T. Lee, *J. Chem. Phys.* **1988**, *88*, 4621.
- [10] a) C. Doffek, N. Alzakhem, C. Bischof, J. Wahsner, T. Güden-Silber, J. Lügger, C. Platas-Iglesias, M. Seitz, *J. Am. Chem. Soc.* **2012**, *134*, 16413–16423; b) C. Doffek, J. Wahsner, E. Kreidt, M. Seitz, *Inorg. Chem.* **2014**, *53*, 3263–3265.
- [11] Gaussian 09, Revision D, M. J. Frisch, G. W. Trucks, H. B. Schlegel, G. E. Scuseria, M. A. Robb, J. R. Cheeseman, G. Scalmani, V. Barone, G. A. Petersson, H. Nakatsuji, X. Li, M. Caricato, A. Marenich, J. Bloino, B. G. Janesko, R. Gomperts, B. Mennucci, H. P. Hratchian, J. V. Ortiz, A. F. Izmaylov, J. L. Sonnenberg, D. Williams-Young, F. Ding, F. Lipparini, F. Egidi, J. Goings, B. Peng, A. Petrone, T. Henderson, D. Ranasinghe, V. G. Zakrzewski, J. Gao, N. Rega, G. Zheng, W. Liang, M. Hada, M. Ehara, K. Toyota, R. Fukuda, J. Hasegawa, M. Ishida, T. Nakajima, Y. Honda, O. Kitao, H. Nakai, T. Vreven, K. Throssell, J. A. Montgomery, Jr., J. E. Peralta, F. Ogliaro, M. Bearpark, J. J. Heyd, E. Brothers, K. N. Kudin, V. N. Staroverov, T. Keith, R. Kobayashi, J. Normand, K. Raghavachari, A. Rendell, J. C. Burant, S. S. Iyengar, J. Tomasi, M. Cossi, J. M. Millam, M. Klene, C. Adamo, R. Cammi, J. W. Ochterski, R. L. Martin, K. Morokuma, O. Farkas, J. B. Foresman, and D. J. Fox, Gaussian, Inc., Wallingford CT, **2016**.

6.5 Supporting Information: Molecular ruby under pressure

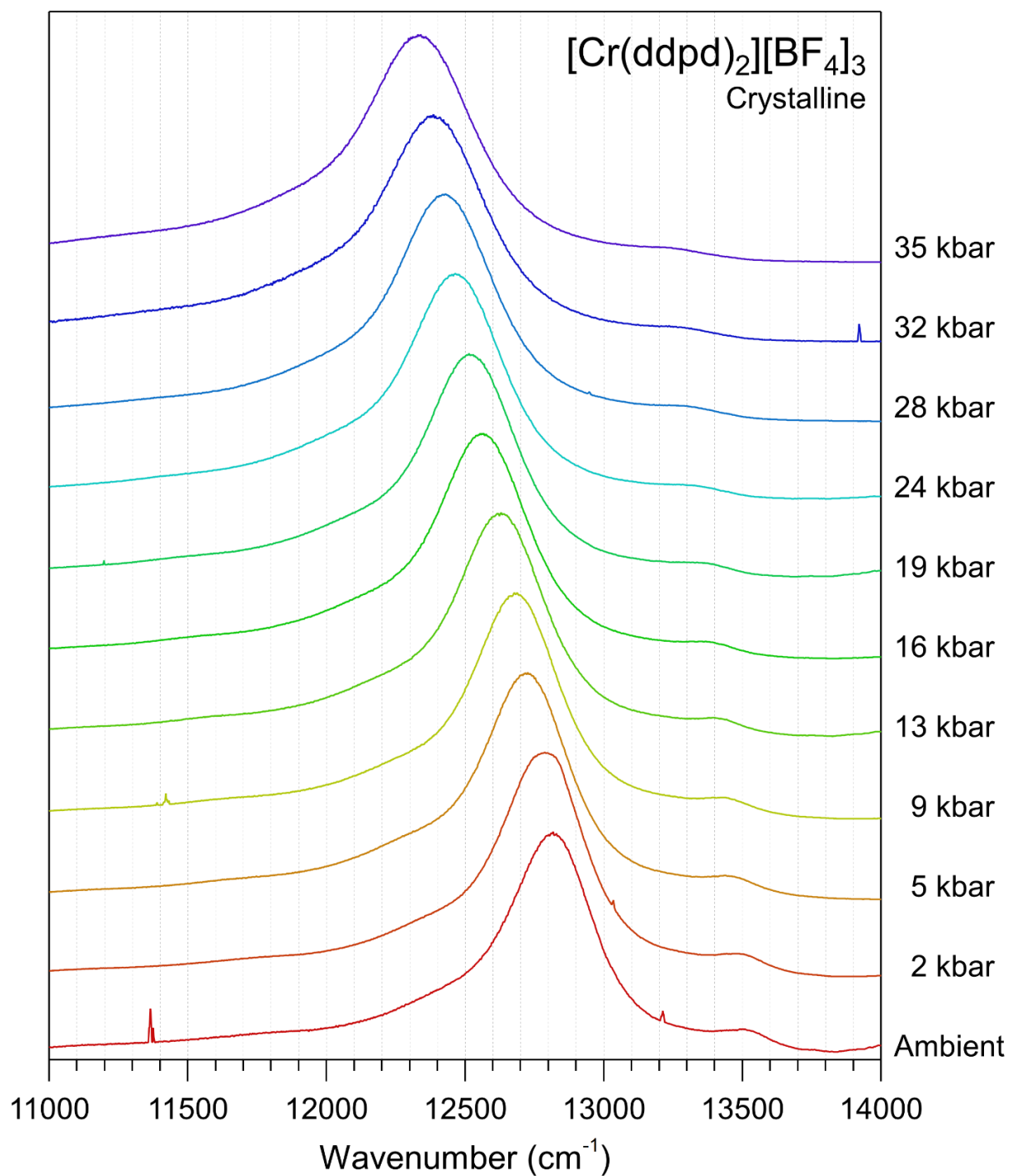


Figure S 1: Pressure-dependent luminescence spectra of $[\text{Cr}(\text{ddpd})_2][\text{BF}_4]_3$ following excitation at 488 nm, in the crystalline phase at ambient temperature.

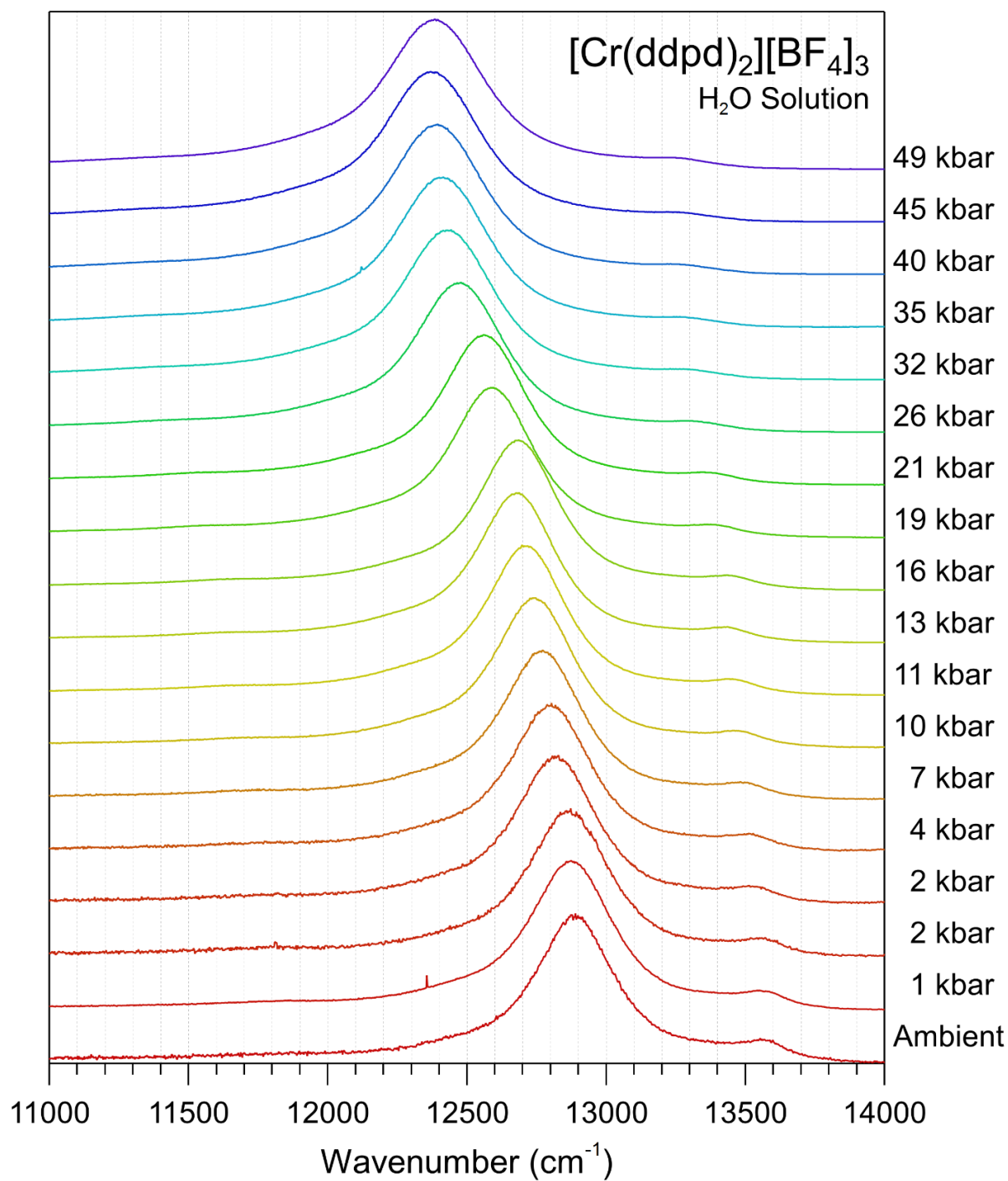


Figure S 2: Pressure-dependent luminescence spectra of $[\text{Cr}(\text{ddpd})_2][\text{BF}_4]_3$ following excitation at 488 nm, in aqueous solution at ambient temperature.

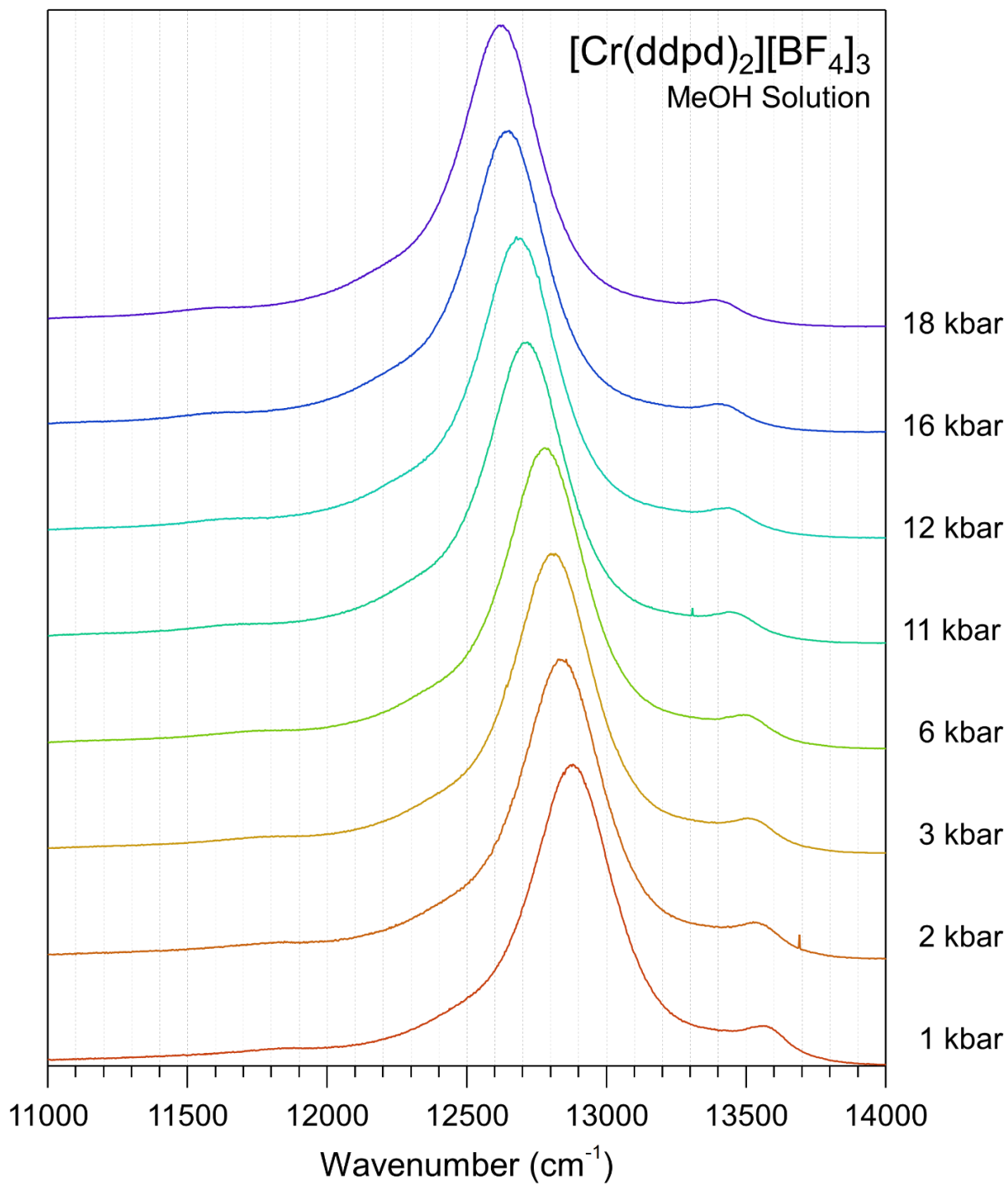


Figure S 3: Pressure-dependent luminescence spectra of $[\text{Cr}(\text{ddpd})_2][\text{BF}_4]_3$ following excitation at 488 nm, in methanol solution at ambient temperature.

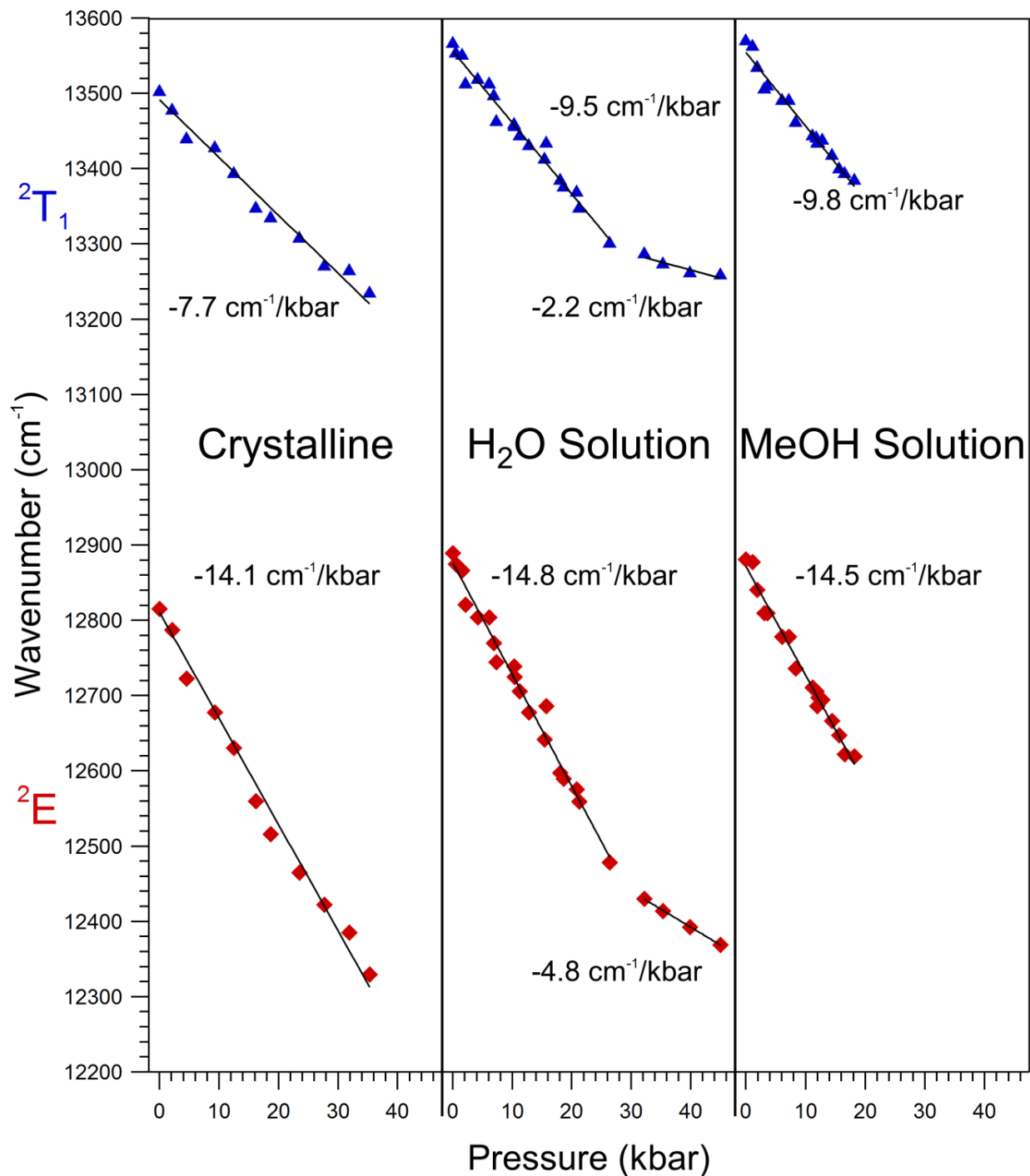
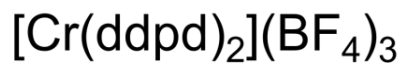


Figure S 4: Pressure-induced shifts of luminescence maxima of [Cr(ddpd)₂](BF₄)₃ following excitation at 488 nm, in crystalline phase, aqueous solution, and methanol solution, at ambient temperature.

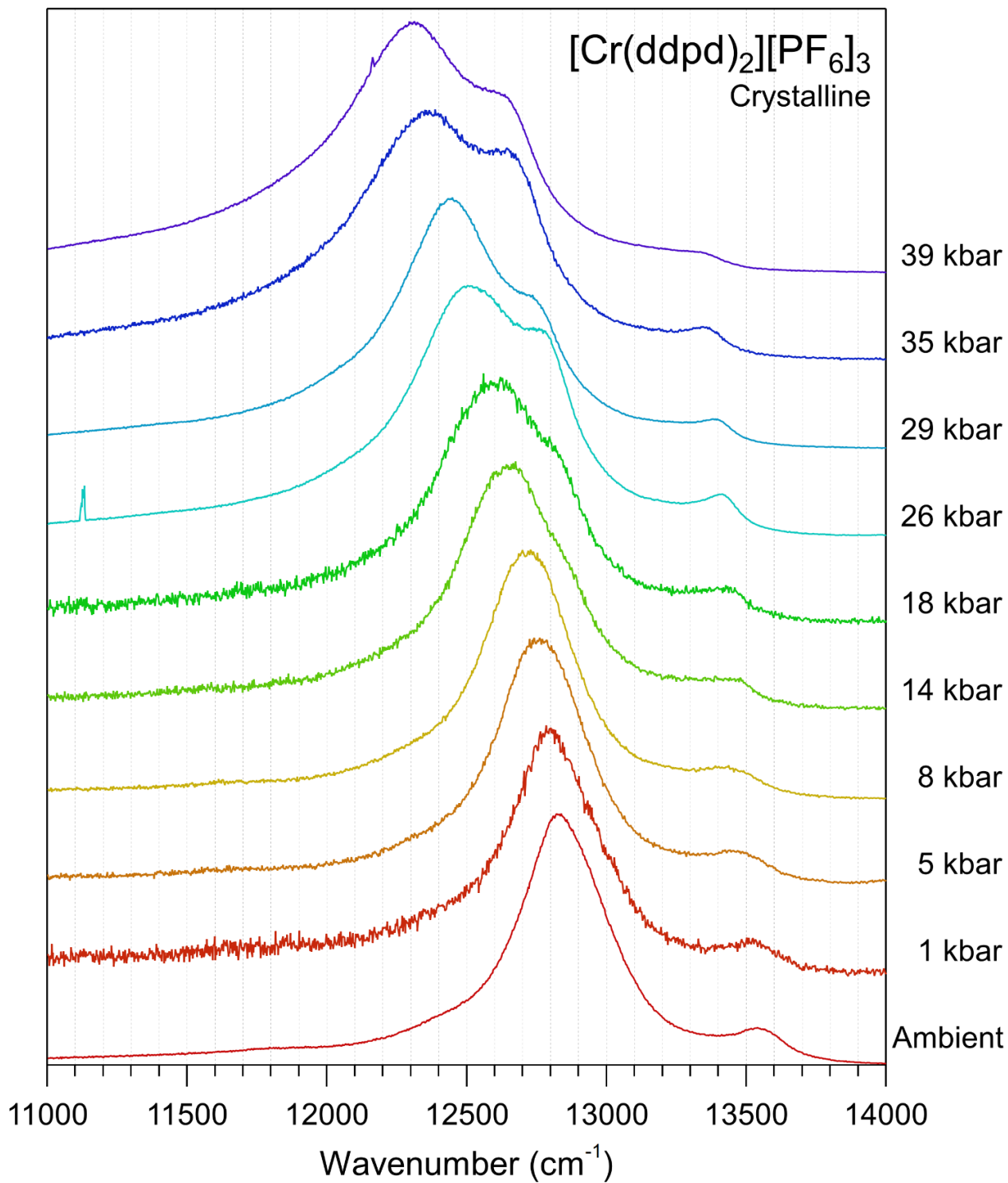


Figure S 5: Pressure-dependent luminescence spectra of $[\text{Cr}(\text{ddpd})_2][\text{PF}_6]_3$ following excitation at 488 nm, in the crystalline phase at ambient temperature.

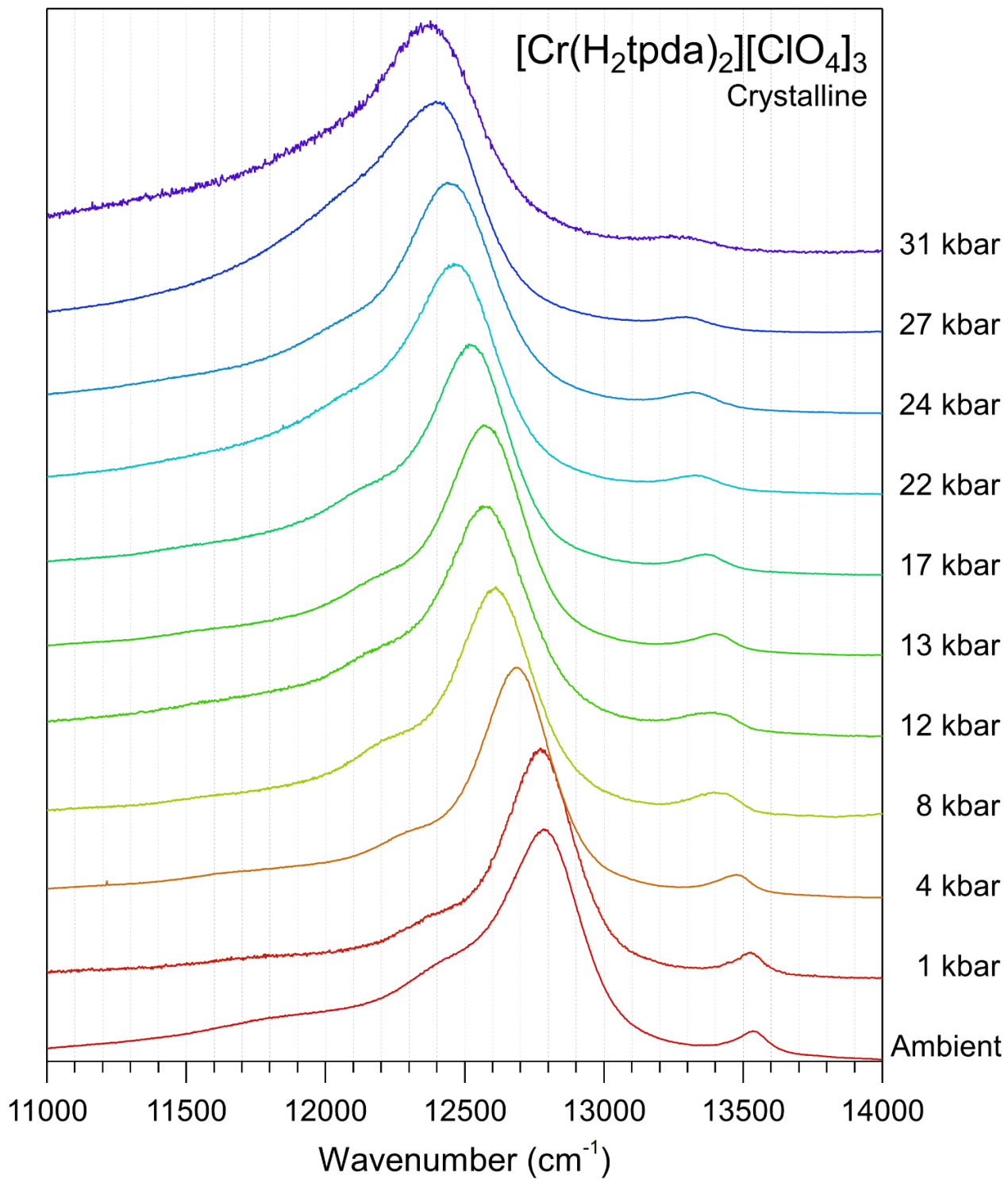


Figure S 6: Pressure-dependent luminescence spectra of $[\text{Cr}(\text{H}_2\text{tpda})_2][\text{ClO}_4]_3$ following excitation at 488 nm, in the crystalline phase at ambient temperature.

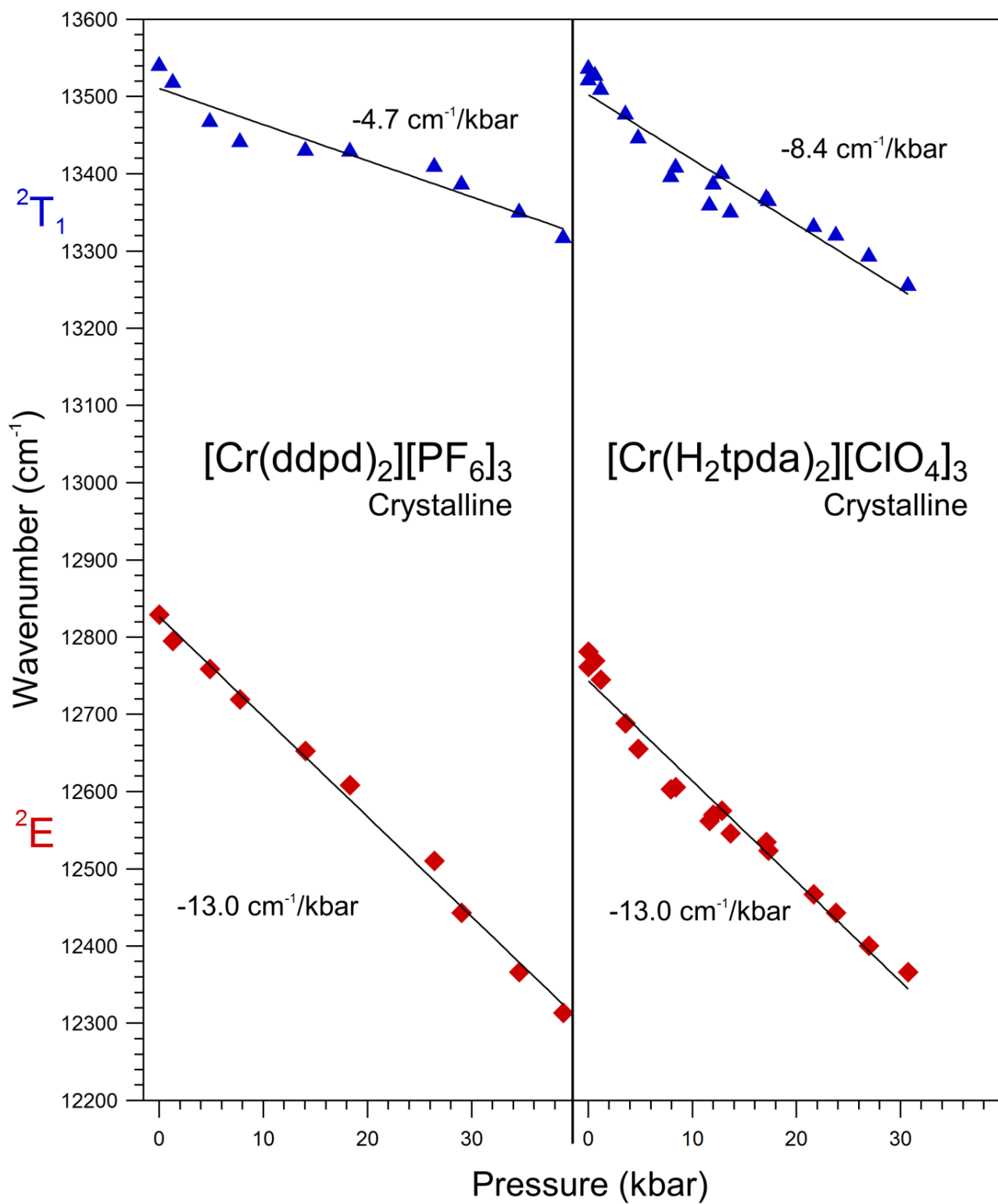


Figure S 7: Pressure-induced shifts of luminescence maxima of [Cr(ddpd)₂][PF₆]₃ and [Cr(H₂tpda)₂][ClO₄]₃ following excitation at 488 nm, in crystalline phase, at ambient temperature.

Table S 1: Collected literature values for pressure-induced shifts of the ${}^2E \rightarrow {}^4A_2$ luminescence maximum in Cr^{3+} -containing species.

Species	${}^2E \rightarrow {}^4A_2 E_{\text{max}}$ (cm^{-1}) (Ambient Pressure)	Shift ($\text{cm}^{-1}/\text{kbar}$)	Reference
$\text{Al}_2\text{O}_3:\text{Cr}^{3+}$ (Ruby)	14 405	-0.74	a
	–	-0.72	b
	14 403	-0.759	c
$\text{MgO}:\text{Cr}^{3+}$	–	0.044 nm/kbar	d
$\text{BeAl}_2\text{O}_4:\text{Cr}^{3+}$	~14 699	-0.53	e
	14 699	-0.62	f
	14 695	-0.75	g
$\text{Cs}_2\text{NaYCl}_6:\text{Cr}^{3+}$	14 415*	-3.7	h
$\text{La}_3\text{Lu}_2\text{Ga}_3\text{O}_{12}:\text{Cr}^{3+}$	14 350 \pm 50†	-0.8 \pm 0.3 [>100 kbar]	i
$\text{YAG}:\text{Cr}^{3+}$	14 514	-0.79	j
	14 515	-0.8	k
$\text{GGG}:\text{Cr}^{3+}$	~14 380†	-0.65 [>30 kbar]	l
$\text{GSGG}:\text{Cr}^{3+}$	~14 380†	-0.64 [>50 kbar]	
$\text{N20S80}:\text{Cr}^{3+}$	14 660	-2.44 [>40 kbar]	m
$\text{CGGG}:\text{Cr}^{3+}$	14 480	-1.73	n
$\text{LiSc}(\text{WO}_4)_2:\text{Cr}^{3+}$	~13 867*	-2.5	o
$\text{LiNbO}_3:\text{Cr}^{3+}$	13 745*	-2.5	p
$\text{LiAlSi}_2\text{O}_6:\text{Cr}^{3+}$	14 481.2	-0.55 \pm 0.02	q
$[\text{Cr}(\text{NH}_3)_6](\text{NO}_3)_3$	15 224 \pm 2	-4 \pm 1	r
{trio}(ClO_4) $_3$ ‡	~14 165	-8.1 \pm 0.5	s
	~14 475	-5.4 \pm 0.3	
	~14 595[14 K]†	-4.1 \pm 0.2*	
{rhodo}Cl $_5$ ·H $_2$ O‡	~14 585	-5.6 \pm 0.6	s
	~14 680	-4.8 \pm 0.4	
	~14 165[14 K]†	-4.2 \pm 0.4*	
$[\text{Cr}(\text{urea})_6](\text{ClO}_4)_3$	14 191 [1.3 K]	-5.4 \pm 0.5	t
$[\text{Cr}(\text{urea})_6]_3$	–	-3.1 \pm 0.5	
$[\text{CrF}_6](\text{NH}_4)_3$	15 583†	-7.8 [>88 kbar]	u

* Position taken from absorption measurements.

† Not observed at ambient conditions; position has been extrapolated from measurements to higher pressure.

‡ Binuclear Cr^{3+} – Cr^{3+} complexes where the centres are exchange-coupled, resulting in multiple electronic origins.

- a) Piermarini, G. J.; Block, S.; Barnett, J. D.; Forman, R. A. *J. Appl. Phys.* **1975**, *46*, 2774–2780.
b) Mao, H. K.; Bell, P. M.; Shaner, J. W.; Steinberg, D. J. *J. Appl. Phys.* **1978**, *49*, 3276–3283.
c) Munro, R. G.; Piermarini, G. J.; Block, S.; Holzapfel, W. B. *J. Appl. Phys.* **1985**, *57*, 165–169.
d) Chopelas, A.; Nicol, M.; *J. Geophys. Res.* **1982**, *87*, 8591–8597.
e) Kottke, T.; Williams, F. *Phys. Rev. B* **1983**, *28*, 1923–1927.
f) Liu, J.; Tang, R.; Wang, Y.; Jia, W.; Shang, Y.; He, S. *J. Lumin.* **1988**, *40&41*, 419–420.
g) Jahren, A. H.; Kruger, M. B.; Jeanloz, R. *J. Appl. Phys.* **1992**, *71*, 1579–1582.
h) Rinzler, A. G.; Dolan, J. F.; Kappers, L. A.; Hamilton, D. S.; Bartram, R. H. *J. Phys. Chem. Solids* **1993**, *54*, 89–100.
i) Galanciak, D.; Perlin, P.; Grinberg, M.; Suchocki, A. *J. Lumin.* **1994**, *60&61*, 223–226.
j) Wamsley, P. R.; Bray, K. L. *J. Lumin.* **1994**, *59*, 11–17.
k) Shen, Y. R.; Bray, K. L. *Phys. Rev. B* **1997**, *56*, 10882–10891.
l) Hömmerich, U.; Bray, K. L. *Phys. Rev. B* **1995**, *51*, 12133–12141.
m) Quérel, G.; Reynard, B. *Chem. Geol.* **1996**, *128*, 65–75.
n) Grinberg, M.; Barzowska, J.; Shen, Y. R.; Bray, K. L.; Padyak, B. V.; Buchynskii, P. P. *Phys. Rev. B* **2002**, *65*, 064203.
o) Grinberg, M.; Barzowska, J.; Shen, Y. R.; Bray, K. L.; Dereñ, P.; Hanuza, J. *J. Lumin.* **2003**, *102–103*, 699–704.
p) Sánchez-Alejo, M. A.; Rodríguez, F.; Barreda-Argüeso, J. A.; Camarillo, I.; Flores J., C.; Murrieta S., H.; Hernández A., J. M.; Jaque, F.; Camarillo, E. *Opt. Mater.* **2016**, *60*, 94–100.
q) O'Bannon III, E.; Williams, Q. *Am. Mineral.* **2016**, *101*, 1406–1413.
r) Lee, S. H.; Waltz, W. L.; Demmer, D. R.; Walters, R. T. *Inorg. Chem.* **1985**, *24*, 1531–1538.
s) Riesen, H.; Güdel, H. U. *J. Chem. Phys.* **1987**, *87*, 3166–3172.
t) Yersin, H.; Huber, P.; Gietl, G.; Trümbach, D. *Chem. Phys. Lett.* **1992**, *199*, 1–9.
u) Kenney III, J. W.; Clymire, J. W.; Agnew, S. F. *J. Am. Chem. Soc.* **1995**, *117*, 1645–1646.

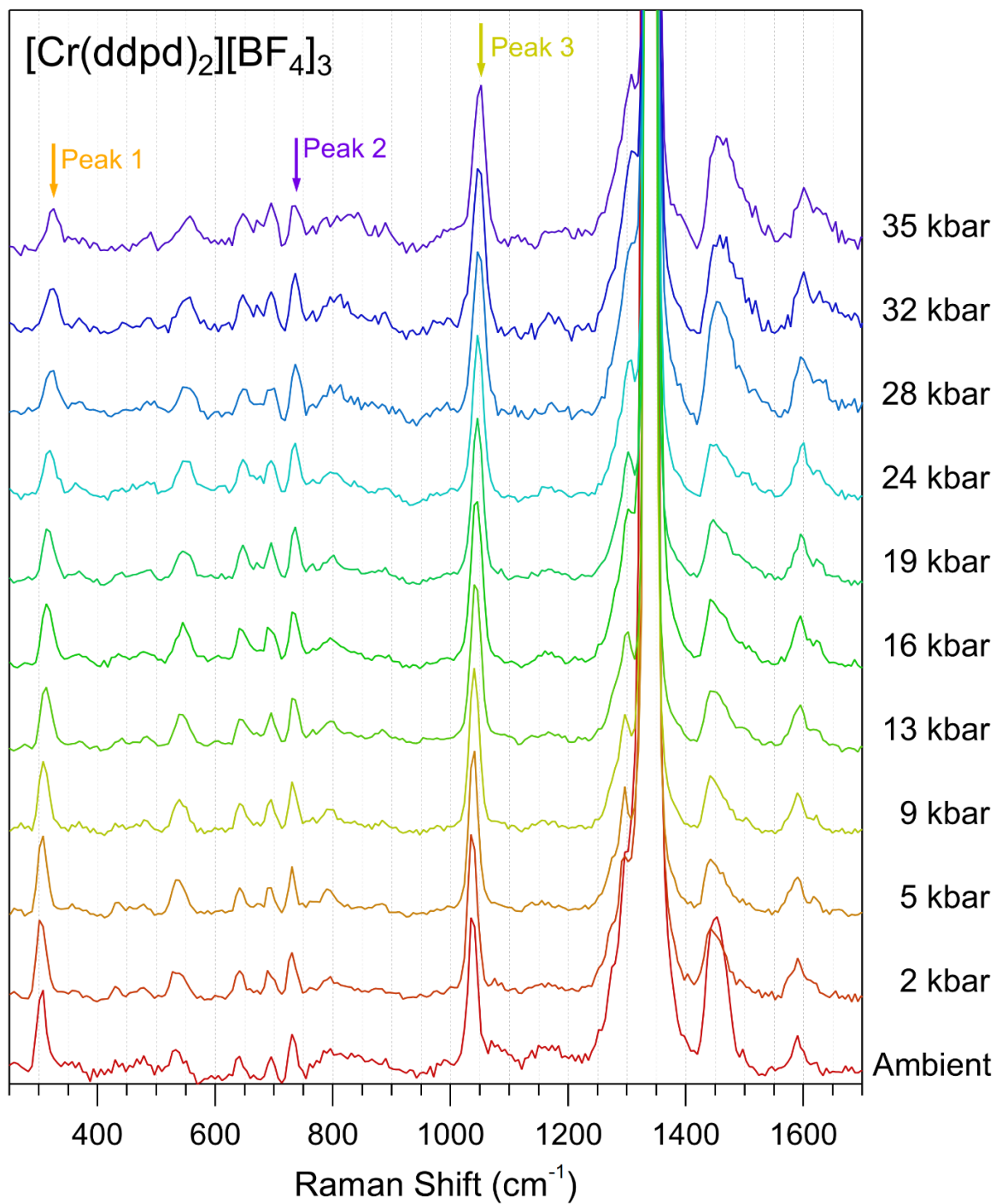


Figure S 8: Pressure-dependent Raman spectra of crystalline $[\text{Cr}(\text{ddpd})_2][\text{BF}_4]_3$ at ambient temperature. Incident light was 514 nm.

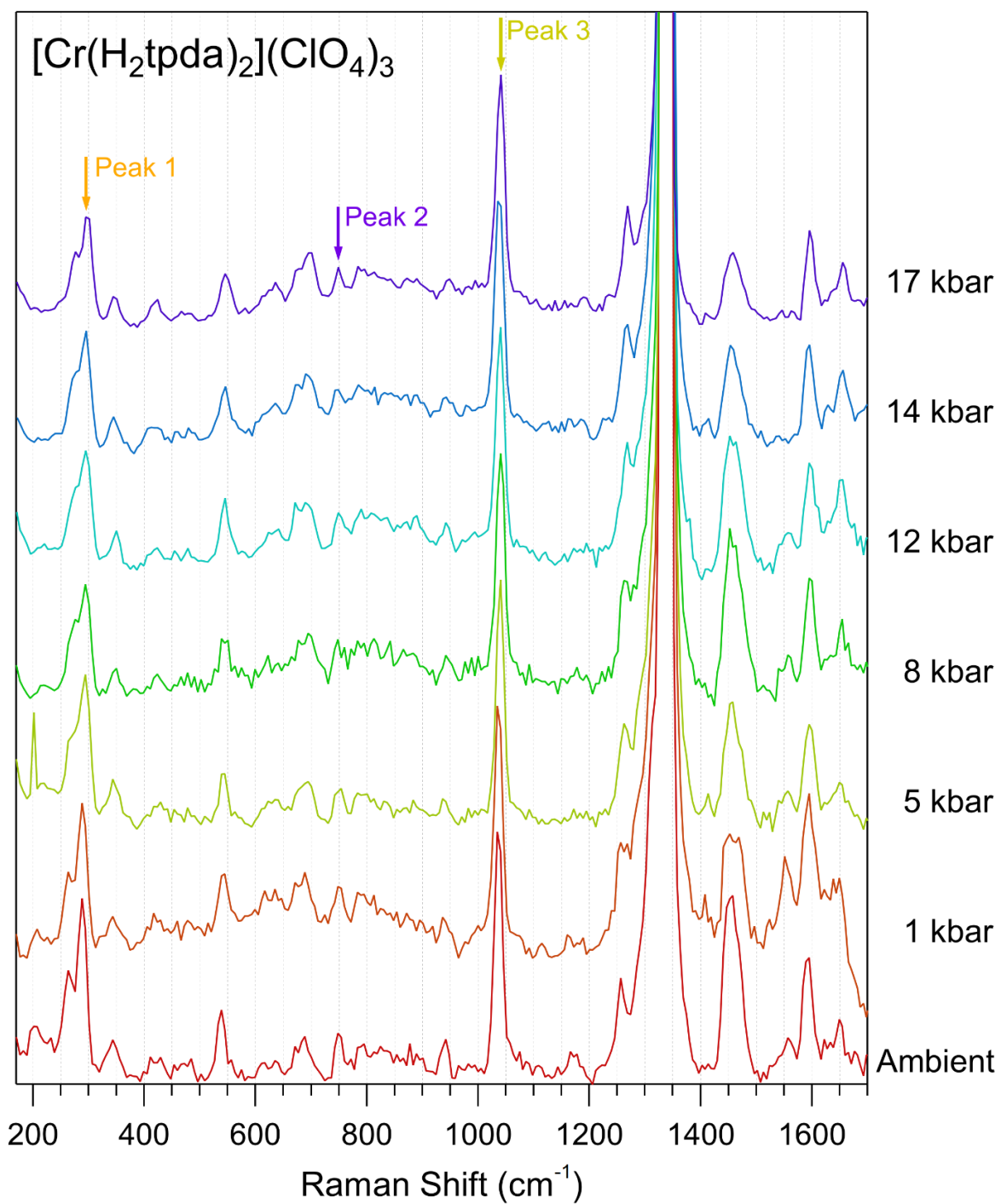


Figure S 9: Pressure-dependent Raman spectra of crystalline $[\text{Cr}(\text{H}_2\text{tpda})_2](\text{ClO}_4)_3$ at ambient temperature. Incident light was 514 nm.

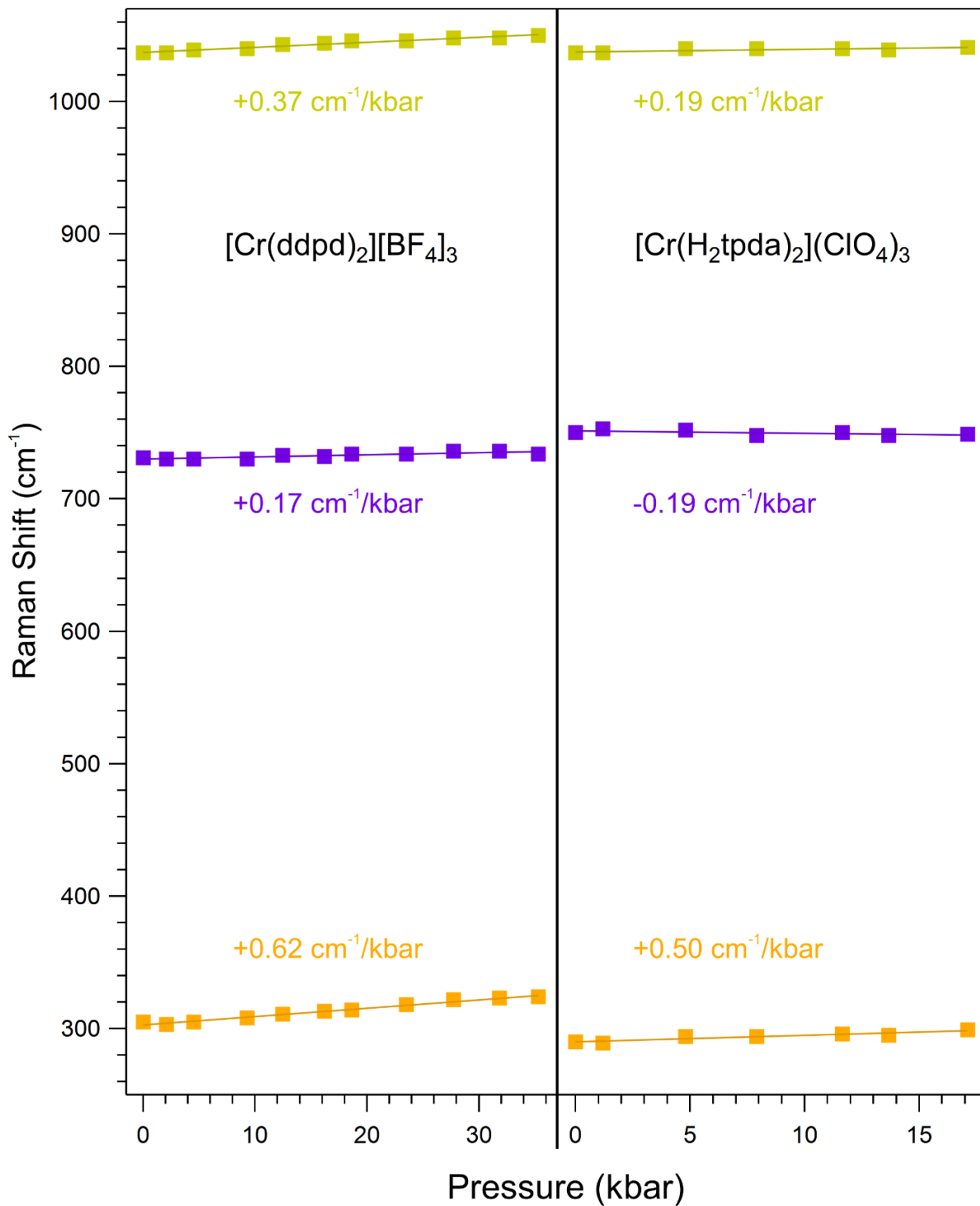


Figure S 10: Pressure dependence of selected Raman peaks for crystalline $[\text{Cr}(\text{ddpd})_2][\text{BF}_4]_3$ and $[\text{Cr}(\text{H}_2\text{tpda})_2][\text{ClO}_4]_3$. Incident light was 514 nm.

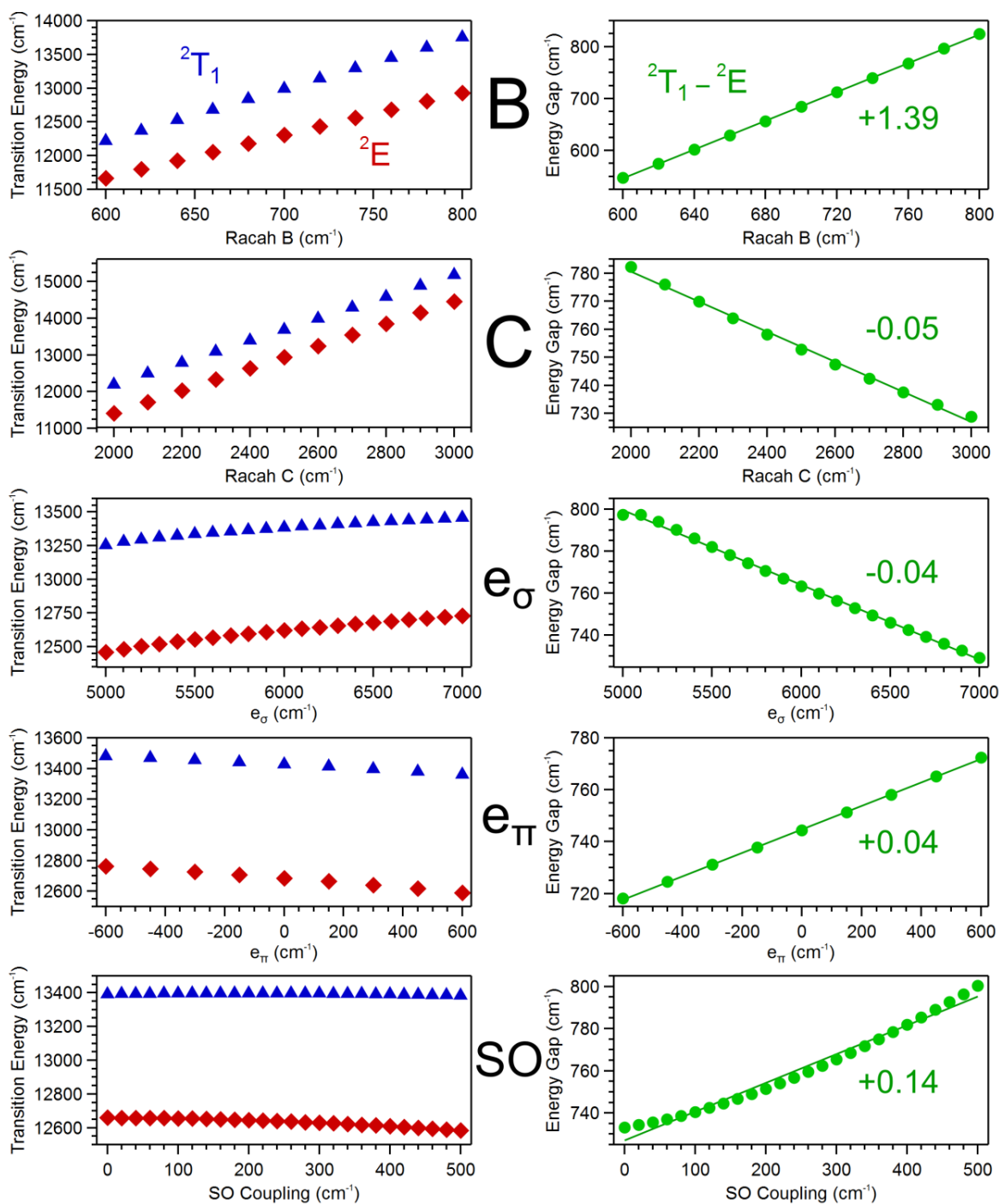


Figure S 11: Model ligand field calculations at perfect octahedral geometry, varying each parameter individually. Results are shown for the two lowest lying doublet states, and the energetic separation between them. Centre parameters are $B = 753 \text{ cm}^{-1}$, $C = 2402 \text{ cm}^{-1}$, $e_{\sigma} = 6150 \text{ cm}^{-1}$, $e_{\pi} = 300 \text{ cm}^{-1}$, spin-orbit coupling constant (SO) = 250 cm^{-1} . Although increasing the Racah B parameter recreates the experimental trend of an increasing energy gap between these doublet states, the unanimous conclusion from the literature is that this parameter should decrease with increasing pressure.

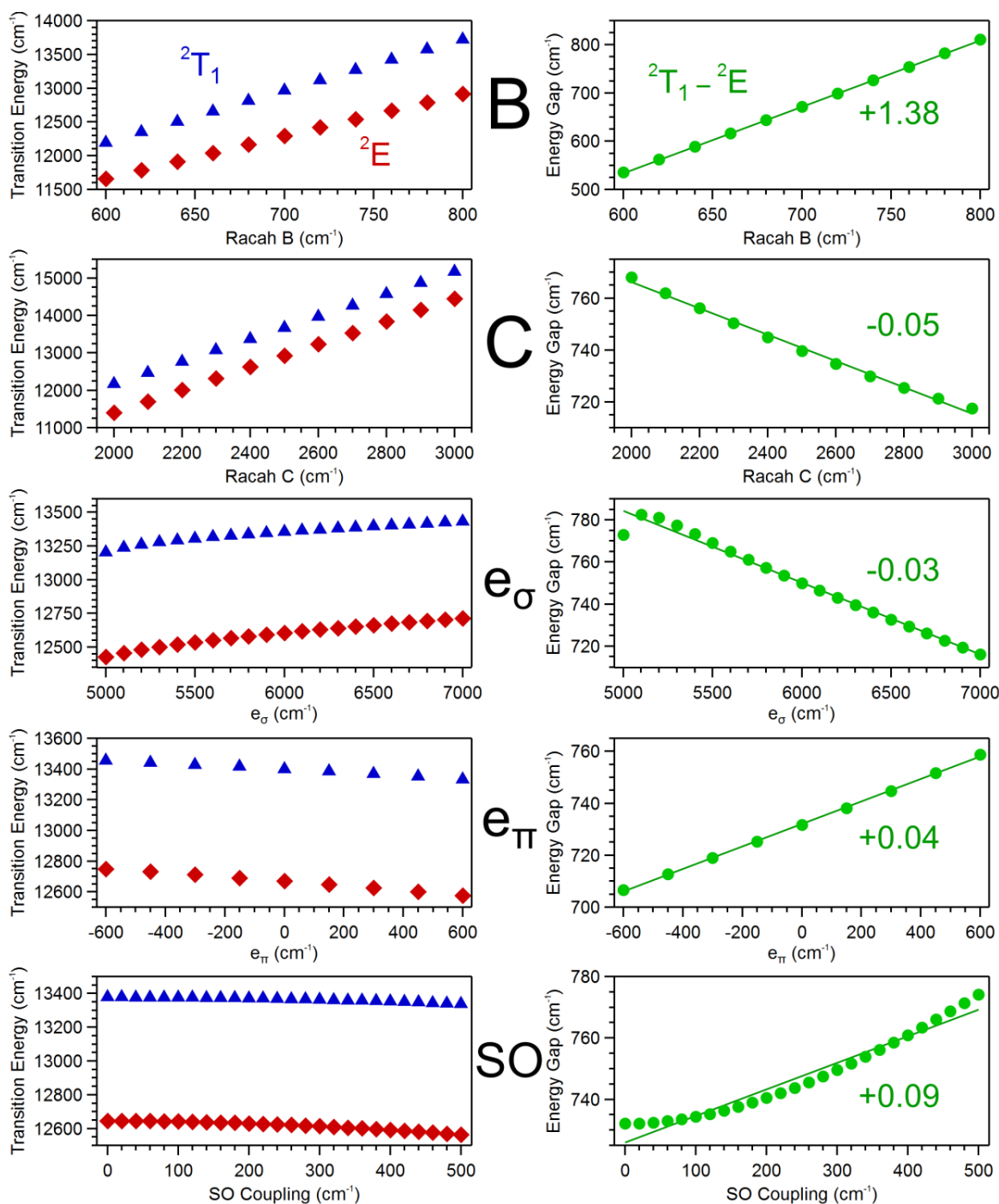


Figure S 12: Model ligand field calculations at the exact coordination geometry, varying each parameter individually. Results are shown for the two lowest lying doublet states, and the energetic separation between them. Centre parameters are $B = 753 \text{ cm}^{-1}$, $C = 2402 \text{ cm}^{-1}$, $e_\sigma = 6150 \text{ cm}^{-1}$, $e_\pi = 300 \text{ cm}^{-1}$, spin-orbit coupling constant (SO) = 250 cm^{-1} . Although increasing the Racah B parameter recreates the experimental trend of an increasing energy gap between these doublet states, the unanimous conclusion from the literature is that this parameter should decrease with increasing pressure.

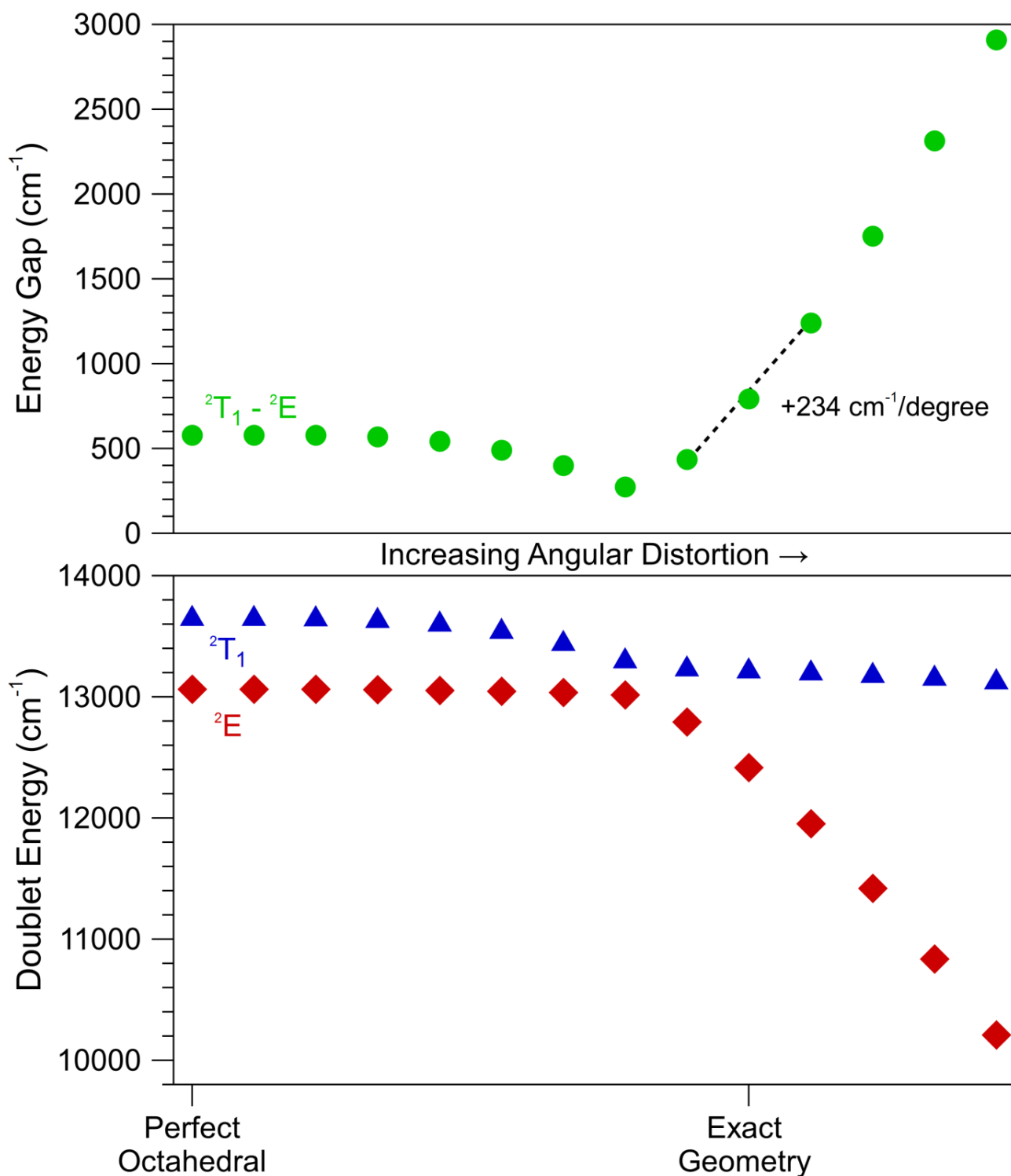


Figure S 13: Model ligand field calculations, holding parameters constant and varying the angular part of the geometry from perfect octahedral angles (90°) to the exact coordination environment and beyond. Cr–N bond lengths are all equal to 0.01 \AA , and so bond length changes are neglected. Results are shown for the two lowest lying doublet states, and the energetic separation between them. Parameters are $B = 753 \text{ cm}^{-1}$, $C = 2402 \text{ cm}^{-1}$, $e_\sigma = 6150 \text{ cm}^{-1}$, $e_\pi = 300 \text{ cm}^{-1}$, spin-orbit coupling constant (SO) = 250 cm^{-1} .

	Perfect Octahedral		Exact Geometry	
	Elevation / °	Azimuth / °	Elevation / °	Azimuth / °
N1	0	90	19.475374	75.789185
N3	90	0	90.084591	0.676251
N5	180	270	160.617787	283.396213
N6	90	270	71.836380	265.333230
N8	90	180	90.590345	179.852073
N10	90	90	107.954140	94.945447

Table S 2: Spherical coordinates of the coordination environment of Cr³⁺ used to calculate the plots in Figure S 13. Structures between the perfect octahedral and exact geometries were obtained by a simple linear interpolation of the structures in spherical coordinates, and the extrapolation to more distorted geometries obtained in the same way. In AOM calculations, the bond lengths are related to the parameters e_{σ} and e_{π} ; here differences between bond lengths were all within 0.01 Å, and so were neglected by holding these parameters constant at $e_{\sigma} = 6150 \text{ cm}^{-1}$, $e_{\pi} = 300 \text{ cm}^{-1}$. Other parameters used were $B = 753 \text{ cm}^{-1}$, $C = 2402 \text{ cm}^{-1}$, $SO = 250 \text{ cm}^{-1}$.

Selected computational details and results

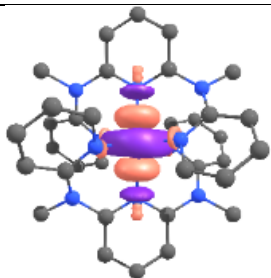
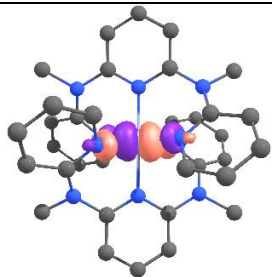
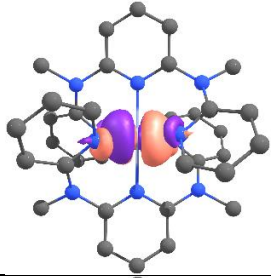
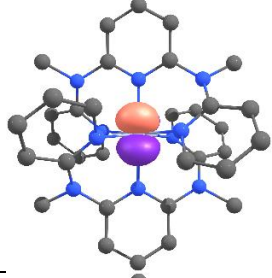
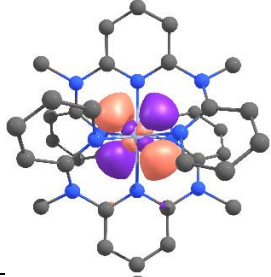
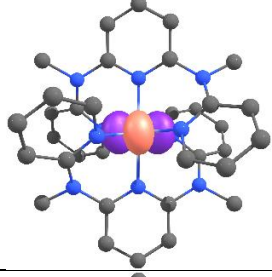
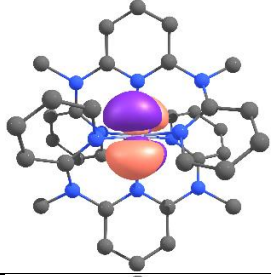
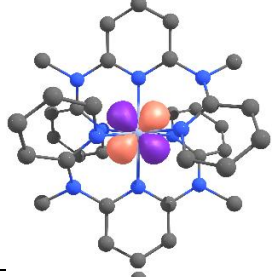
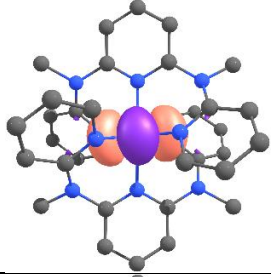
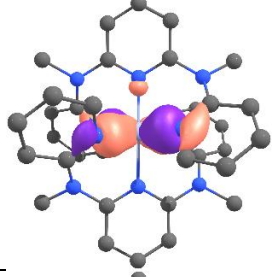
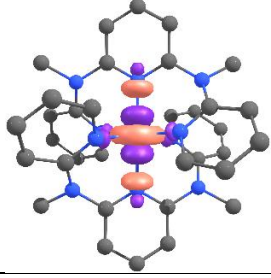
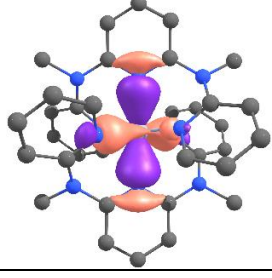
DFT calculations were carried out using the ORCA program package (version 4.0.1).^[1] Tight convergence criteria were chosen for all calculations (Keywords TightSCF and TightOpt, convergence criteria for the SCF part: energy change $1.0 \times 10^{-8} E_h$, 1-El. energy change $1.0 \times 10^{-5} E_h$, orbital gradient 1.0×10^{-5} , orbital rotation angle 1.0×10^{-5} , DIIS Error 5.0×10^{-7} ; for geometry optimizations: energy change: $1.0 \times 10^{-6} E_h$, max. gradient $1.0 \times 10^{-4} E_h a_0^{-1}$, RMS gradient $3.0 \times 10^{-5} E_h a_0^{-1}$, max. displacement $21.0 \times 10^{-3} a_0$, RMS displacement $6.0 \times 10^{-4} a_0$). All calculations make use of the resolution of identity (Split-RI-J) approach for the Coulomb term in combination with the chain-of-spheres approximation for the exchange term (COSX).^[5,6] The ZORA relativistic approximation was used to describe relativistic effects in all calculations.^[7] To account for solvent effects, a conductor-like screening model (CPCM) modeling methanol was used in all calculations.^[8] Geometry optimizations were performed using Ahlrichs' split valence triple- ζ basis set def2-TZVPP which comprises polarization functions for all non-hydrogen atoms.^[9,10] Atom-pairwise dispersion correction was performed with the Becke-Johnson damping scheme (D3BJ).^[11,12] The presence of energy minima was checked by numerical frequency calculations. Explicit counter ions and/or solvent molecules were not taken into account.

In the CASSCF calculations, dynamic electron correlation was taken into account by fully internally contracted N-electron valence state perturbation theory (FIC-NEVPT2)^[13-15]. For CASSCF(7,12) FIC NEVPT2 calculations (def2-TZVPP,^[9,10] def2-JK,^[16] RI-JK,^[17,18] ZORA,^[7] CPCM(methanol)^[8]), the active space consisted of the ligand field orbitals t_{2g} , e_g in idealized O_h symmetry and of the two Cr-N σ bonding counterparts to the e_g orbitals and an additional set of five d orbitals, corresponding to 7 electrons correlated in 12 active orbitals. After obtaining relative energies from a state averaged calculation (SA-CASSCF(7,12)-FIC-NEVPT2), the spin densities were extracted from individual calculations where full weight were given to the respective states.

Table S 3: DFT calculated Cartesian coordinates of $[\text{Cr}(\text{ddpd})_2]^{3+}$ (units of Å).

Cr	-0.00024583427119	0.00106572345006	-0.01358810610339
N	-0.00009858280460	0.00161510848220	2.02896554869729
N	-0.00124463954192	0.00114823497022	-2.04967144418433
N	-2.04384357865739	0.20164372809851	0.10324949644280
N	2.04412323669867	-0.20137855215603	0.10133904960632
N	-0.14144095650755	-2.04309154748316	-0.13655862320329
N	0.13965255210851	2.04526340593157	-0.13659469211440
C	-1.02046893622471	-0.57330685799010	2.71011497275603
C	-1.04465290033261	-0.58104521677517	4.09852412650760
C	0.00270311683714	0.00140863756871	4.78851965066574
C	1.04859252578535	0.58422532959139	4.09658369550822
C	1.02138333802930	0.57659976499127	2.70841853016544
H	-1.87755153823438	-1.01243324356414	4.62678327735150
H	1.88356706524938	1.01424308163650	4.62267604998991
C	-2.70105679311438	0.89052342199833	-0.85670600814303
C	-4.05232239951073	0.77428878442288	-1.05797327500955
C	-4.76831284268511	-0.08450729499475	-0.22398412641316
C	-4.11849709700692	-0.74448816076699	0.79789428586236
C	-2.73948579902062	-0.56558891669583	0.96280390198657
H	-5.83174009055709	-0.22330091646332	-0.35987670795027
H	-2.09568303780977	1.52283339801772	-1.48591408859857
H	-4.52991075533413	1.32839246298616	-1.85084106571967
H	-4.67318792427963	-1.36823649335716	1.47728337044230
C	2.74107071062800	0.56220644608708	0.96307011699061
C	4.12182415591782	0.73216907120392	0.80497281005239
C	4.77169095191699	0.06968367044828	-0.21538603803593
C	4.05360155696960	-0.78325296945372	-1.05346575012340
C	2.70096717587133	-0.89277573046308	-0.85694029659826
H	5.83666311072485	0.20106411779076	-0.34646464247789
H	4.67763474828431	1.35014050407951	1.48898692127584
H	4.53072670827051	-1.33927807582990	-1.84528353137582
C	2.09494276071752	-1.52208977286709	-1.48861366610746
H	-0.7459601876230	-0.90625291449257	-2.72844764095410
C	-0.75892328024997	-0.92657974820954	-4.11650628921386
C	-0.00783652205627	0.00763193870247	-4.80720942068291
C	0.74726320166029	0.93813573731659	-4.11584095949560
C	0.74029784763855	0.91121745827261	-2.72795401063710
H	-1.32438991408438	-1.67663812401337	-4.64324843869130
H	1.31090506231559	1.69032265280538	-4.64170508123708
C	0.43283706130344	-2.80186348668097	0.82306226386275
C	0.06377340501057	-4.10119419724987	1.05602426685033
C	-0.94497928642936	-4.64692410487673	0.26228714283265
C	-1.49214411092165	-3.90341238360014	-0.76274725353255
C	-1.04567749621075	-2.59086026784055	-0.96998826005689
H	-1.28799234286438	-5.65782392874565	0.43103339957240
H	1.18244439259881	-2.31542684286239	1.42589317867591
H	0.53562509639082	-4.66377058116149	1.84620014531755
H	-2.23327411895081	-4.33863544628871	-1.41076479524627
C	1.04758074591079	2.59121791654735	-0.96725458745681
C	1.49963539275562	3.90124252398268	-0.75591738367303
C	0.95126988812166	4.64553904085565	0.26791616356712
C	-0.06332997419949	4.10309184856915	1.05655168938873
C	-0.43556869027200	2.80499888493366	0.82174553431153
H	1.29804370214771	5.65465382289587	0.43974075560036
H	2.24654527278635	4.33369121086676	-1.39929910073219
H	-0.53641688744103	4.66704647277294	1.84499175091267
H	-1.18896921205196	2.32062863053312	1.42166459161548
N	-1.53514791249478	-1.82359207459135	-2.01822530029275
C	-2.78494506267310	-2.26172276181512	-2.66070677793998
H	-2.63749899419550	-3.10694793514265	-3.33305028778971
H	-3.49039295376109	-2.53872075142151	-1.88317581752941
H	-3.19470542715159	-1.42489831544804	-3.21547241128641
N	1.53398852254178	1.82447512521337	-2.01691457993312
C	2.78464822258746	2.25919050307421	-2.65977347284057
H	2.64032514810225	3.10936166996565	-3.32649193707391
H	3.49351965616991	2.52762121878576	-1.88227507532042
H	3.18821680181747	1.42337274249485	-3.22053700849678
N	-2.05823579519516	-1.19194835667198	1.99940203677541
N	2.05812075736750	1.19430009787184	1.99532588648186
C	-2.72359408312656	-2.32214237765989	2.66191883214168
H	-3.50076914400918	-2.00336680247247	3.35681156894926
H	-3.16003425737957	-2.95794913962031	1.89708425542531
H	-1.97153856424990	-2.89275729288162	3.19683836121611
C	2.72140049777739	2.32866168863509	2.65272153468935
H	3.49636999322570	2.01549355028203	3.35230378619177
H	3.16075203091677	2.95951848876060	1.88535049695084
H	1.96727088117249	2.90262336197113	3.18116257738531
H	0.00393306174896	0.00070267905365	5.86933542910265
H	-0.01070836345372	0.01031839168982	-5.88803788884678

Table S 4: Active orbitals used in the CASSCF(7,12)-FIC-NEVPT2 calculation at a contour value of 0.05 a.u. (hydrogen atoms omitted for clarity).

E / Hartree 1.67074		0.08666	
1.56519		-0.12015	
1.02660		-0.12142	
1.02042		-0.13304	
0.99692		-0.59678	
0.09661		-0.59997	

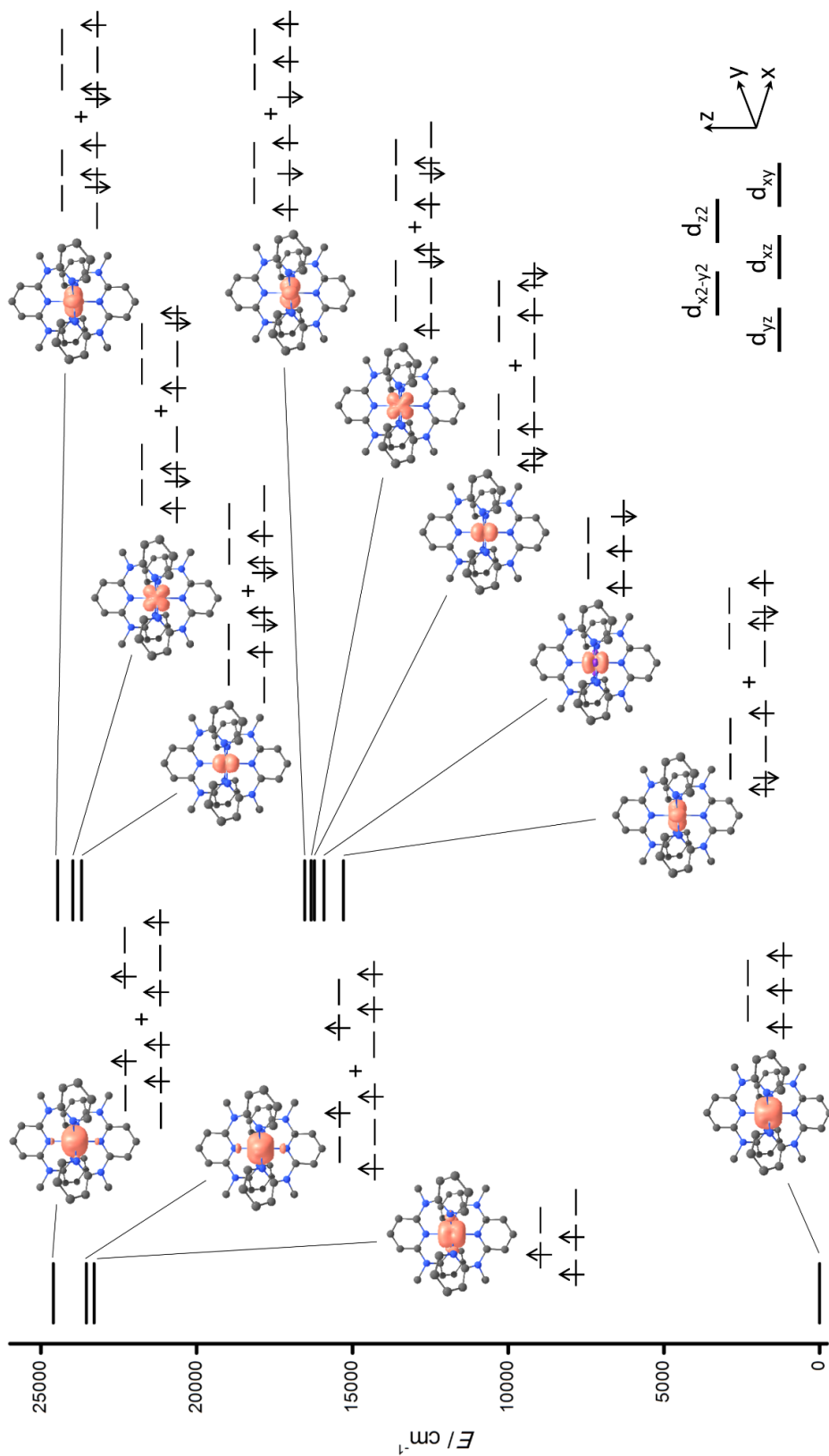


Figure S 14: Energy diagram of $[\text{Cr}(\text{ddpd})_2]^{3+}$ constructed from CAS(7,12)-FIC-NEVPT2 energies and spin densities (0.05 a.u. isosurface value, hydrogen atoms omitted for clarity).

References

- [1] Neese, F., *WIREs Comput. Mol. Sci.* **2012**, *2*, 73–78.
- [2] Becke, A. D., *J. Chem. Phys.* **1993**, *98*, 5648–5652.
- [3] Lee, C.; Yang, W.; Parr, R. G., *Phys. Rev. B* **1988**, *37*, 785–789.
- [4] Miehllich, B.; Savin, A.; Stoll, H.; Preuss, H., *Chem. Phys. Lett.* **1989**, *157*, 200–206.
- [5] Neese, F.; Wennmohs, F.; Hansen, A.; U. Becker, *Chem. Phys.* **2009**, *356*, 98–109.
- [6] Izsák, R.; Neese, F., *J. Chem. Phys.* **2011**, *135*, 144105.
- [7] Pantazis, D. A.; Chen, X.-Y.; Landis, C. R.; Neese, F., *J. Chem. Theory Comput.* **2008**, *4*, 908–919.
- [8] Sinnecker, S.; Rajendran, A.; Klamt, A.; Diedenhofen, M.; Neese, F., *J. Phys. Chem. A* **2006**, *110*, 2235–2245.
- [9] Weigend, F.; Ahlrichs, R., *Phys. Chem. Chem. Phys.* **2005**, *7*, 3297–3305.
- [10] Weigend, F., *Phys. Chem. Chem. Phys.* **2006**, *8*, 1057–1065.
- [11] Grimme, S.; Antony, J.; Ehrlich, S.; Krieg, H., *J. Chem. Phys.* **2010**, *132*, 154104.
- [12] Grimme, S.; Ehrlich, S.; Goerigk, L., *J. Comput. Chem.* **2011**, *32*, 1456–1465.
- [13] Angeli, C.; Cimiraglia, R.; Malrieu, J.-P., *Chem. Phys. Lett.* **2001**, *350*, 297–305.
- [14] Angeli, C.; Cimiraglia, R.; Evangelisti, S.; Leininger, T.; Malrieu, J.-P., *J. Chem. Phys.* **2001**, *114*, 10252–10264.
- [15] Angeli, C.; Cimiraglia, R.; Malrieu, J.-P., *J. Chem. Phys.* **2002**, *117*, 9138–9153.
- [16] Weigend, F., *J. Comput. Chem.* **2008**, *29*, 167–175.
- [17] Weigend, F.; Kattannek, M.; Ahlrichs, R., *J. Chem. Phys.* **2009**, *130*, 164106.
- [18] Kossmann, S.; Neese, F., *Chem. Phys. Lett.* **2009**, *481*, 240–243.

6.6 Supporting Information: A strongly luminescent chromium(III) complex acid

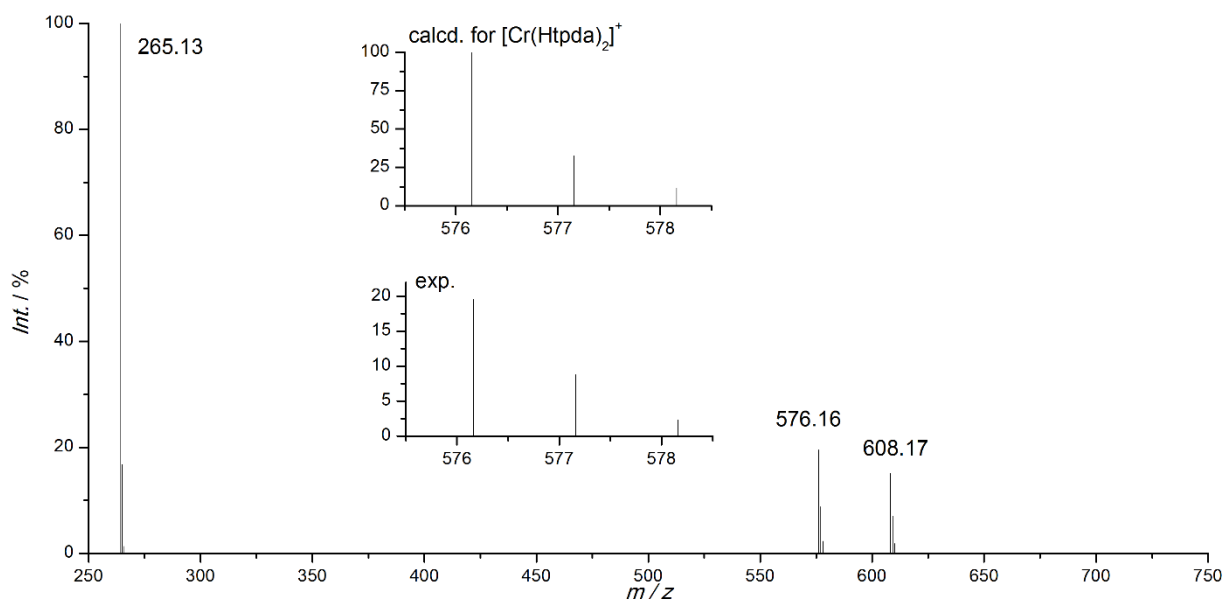


Figure S1. ESI⁺ mass spectrum of $2[\text{Cr}(\text{Htpda})_2]^+$ in CH_3OH .

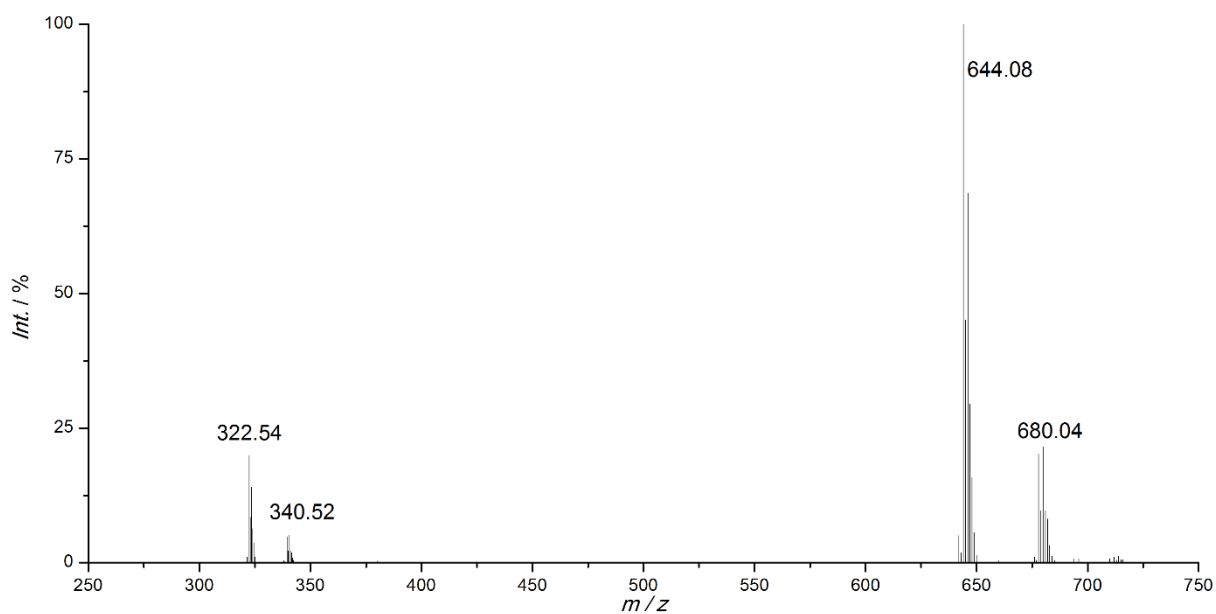


Figure S2. ESI⁺ mass spectrum of $\{[\text{D}_4]-2\}[\text{Cr}(\text{Htpda})_2]^+$ in CH_3OH .

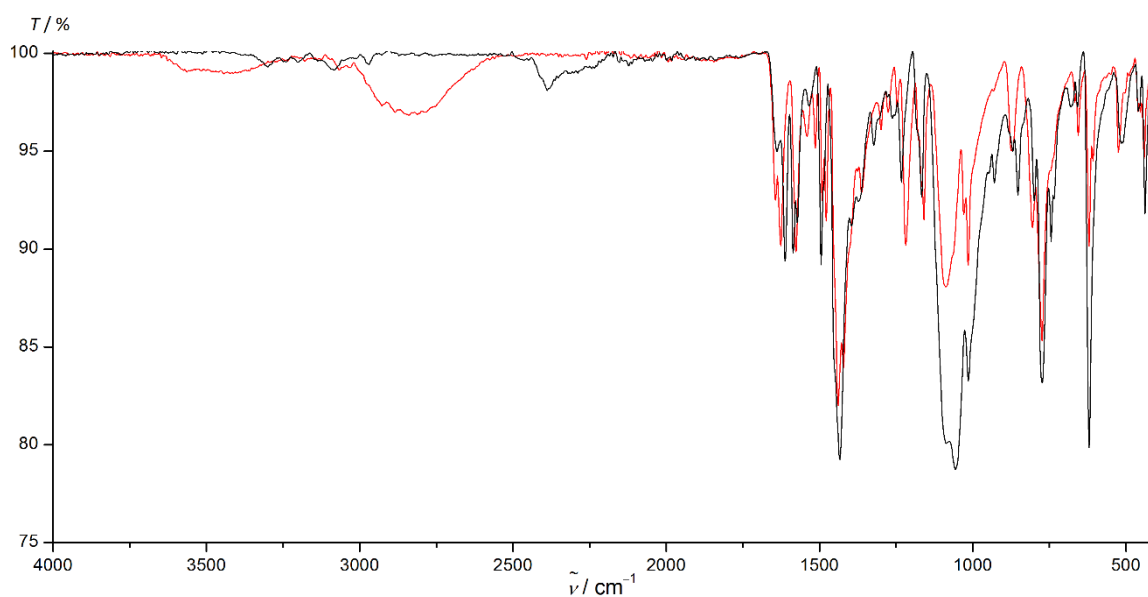


Figure S3. ATR-IR spectra of solid $2[\text{ClO}_4]_3$ (red) and $\{[\text{D}_4]-2\}[\text{ClO}_4]_3$ (black).

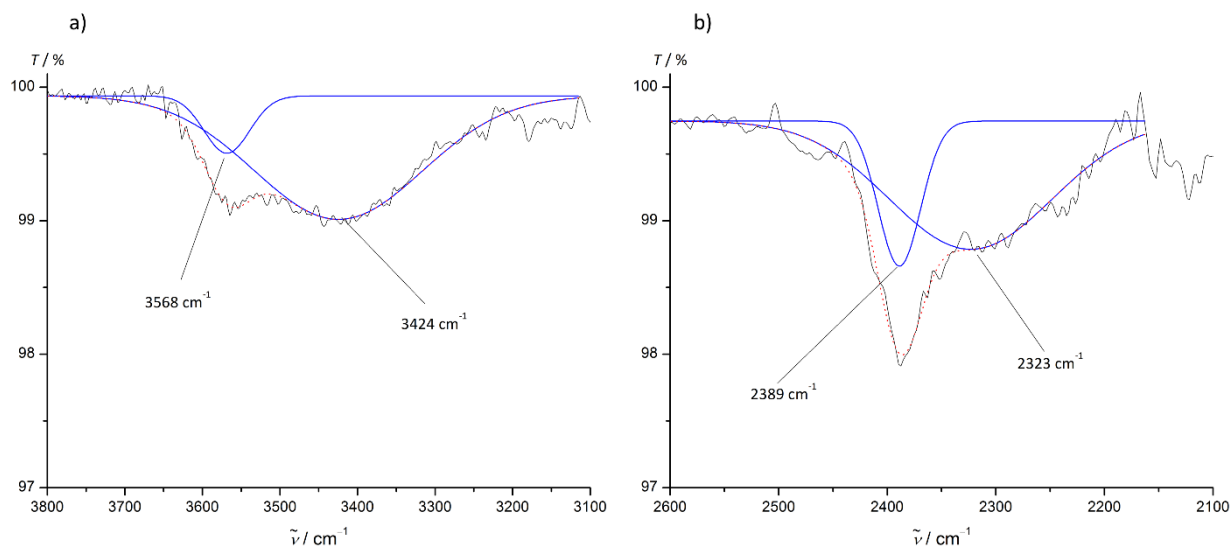


Figure S4. NH/D region of ATR-IR spectra fitted with two Gaussian functions (blue lines) and sum of these (red dotted line) of solid a) $2[\text{ClO}_4]_3$ and b) $\{[\text{D}_4]-2\}[\text{ClO}_4]_3$.

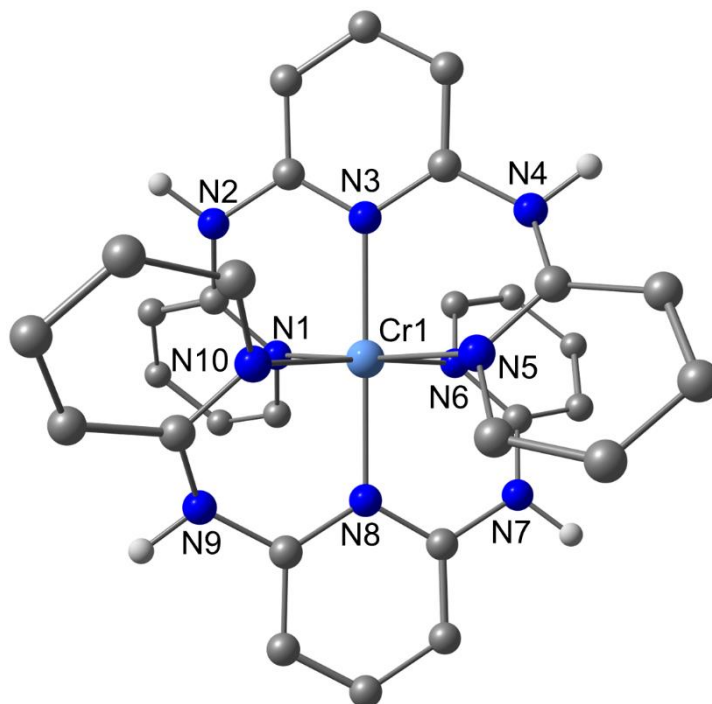


Figure S5. DFT calculated structure of 2^{3+} (all hydrogen atoms except NH protons omitted for clarity).

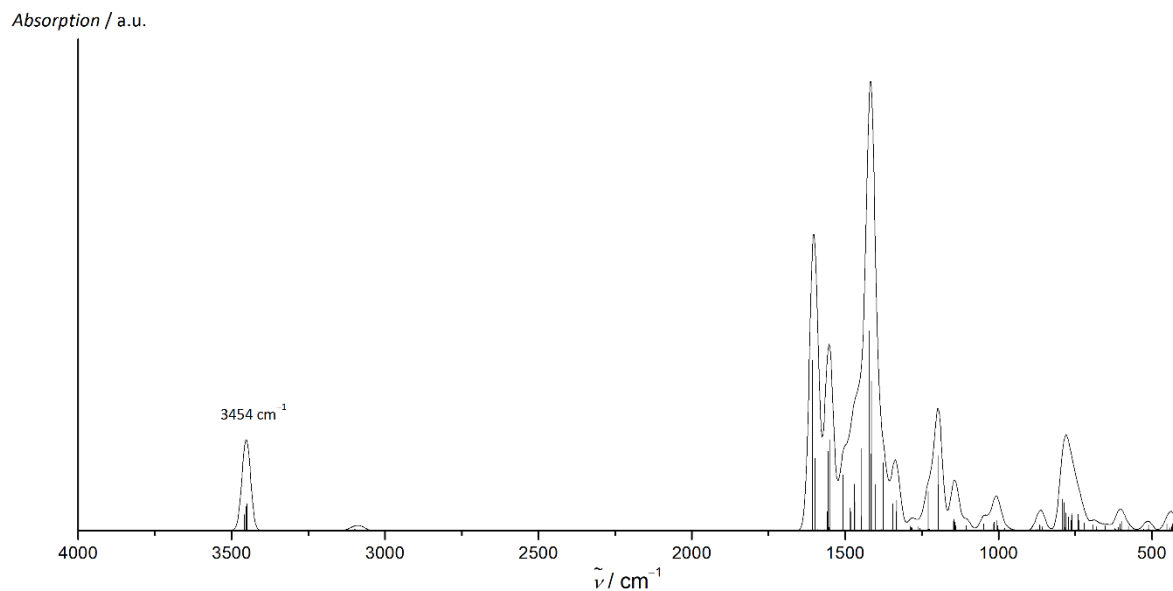


Figure S6. DFT calculated IR spectrum of 2^{3+} (scaled with Scott and Radoms scaling factor of 0.9614 for the B3LYP functional,^[1] FWHM = 35 cm^{-1} , the band at 3454 cm^{-1} corresponds to the NH stretching vibrations, which are found within 5 cm^{-1} of this value).

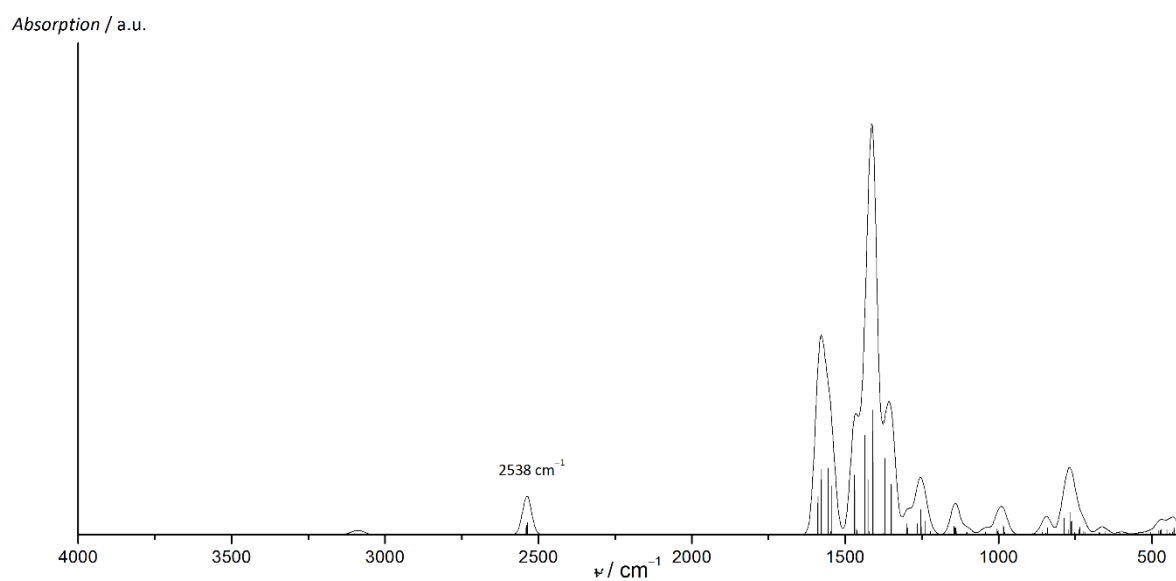


Figure S7. DFT calculated IR spectrum of $[\mathbf{D}_4]-2^{3+}$ (scaled with Scott and Radoms scaling factor of 0.9614 for the B3LYP functional,^[1] FWHM = 35 cm^{-1} , the band at 2638 cm^{-1} corresponds to the ND stretching vibrations which are found within 5 cm^{-1} of this value).

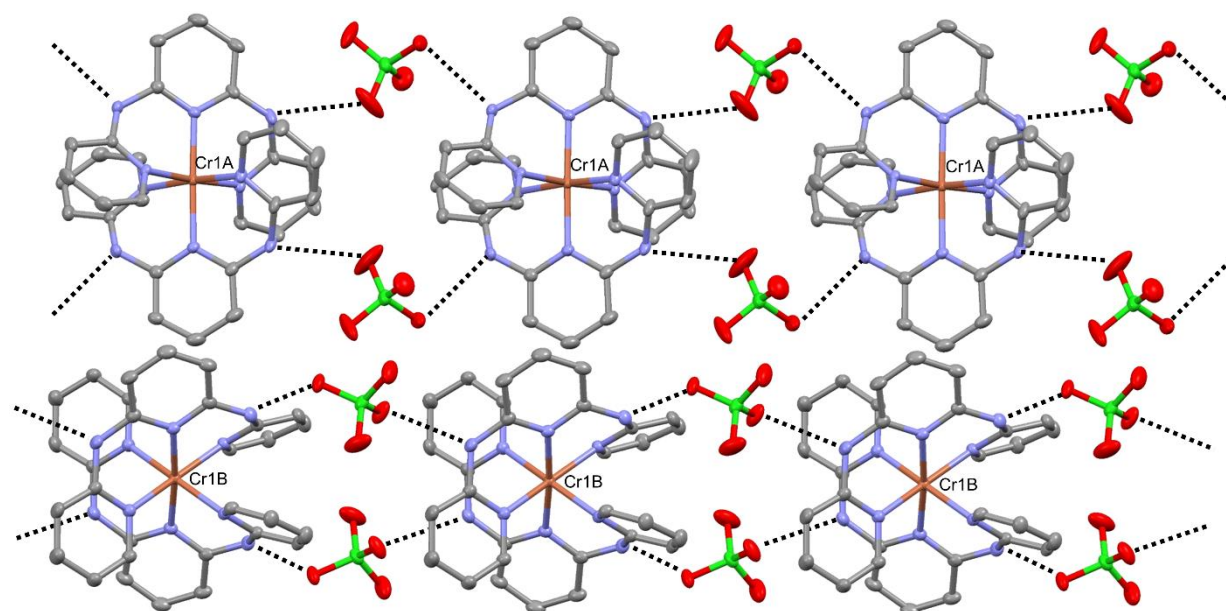


Figure S8. Hydrogen bonding network in crystals of $[\text{Cr}(\text{H}_2\text{tpda})_2][\text{ClO}_4]_3 \times \text{CH}_3\text{CN}$, the third counter ion, which is not involved in the hydrogen bonds is omitted for clarity.

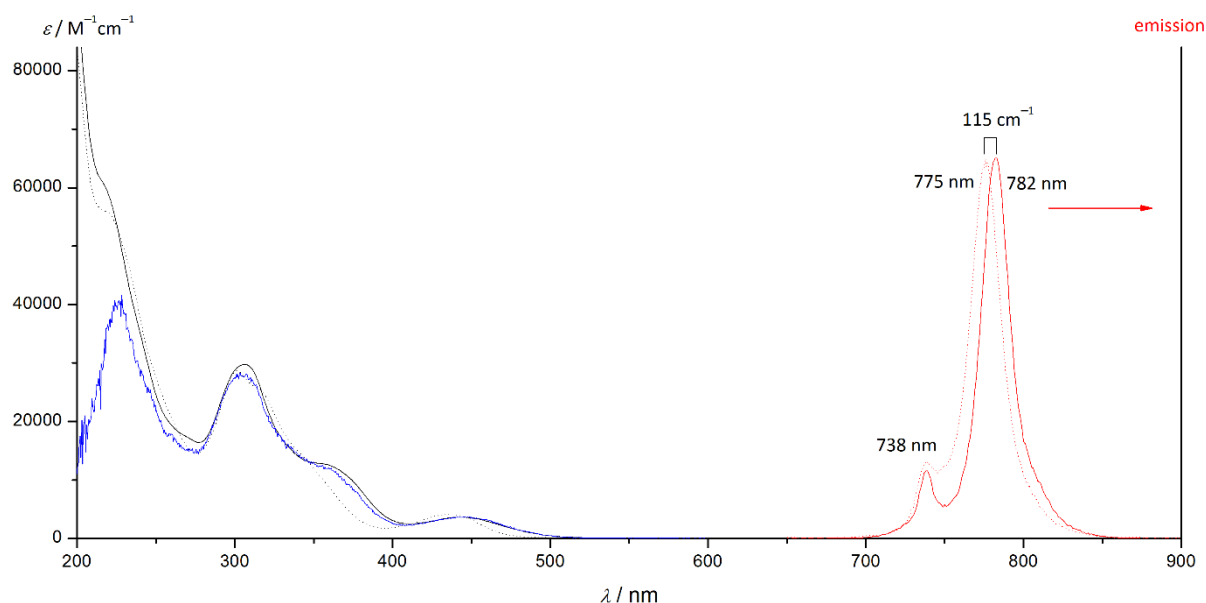


Figure S9. Absorption (black), emission (red, $\lambda_{exc} = 442$ nm) and excitation spectrum (blue, $\lambda_{exc} = 782$ nm) of $2[\text{ClO}_4]_3$ in acetonitrile (0.1 M HClO_4 , 10.9 $\mu\text{l/ml}$ aqueous HClO_4 (60 %)) and absorption (black, dashed) and emission spectrum (red, dashed, $\lambda_{exc} = 442$ nm) of $1[\text{BF}_4]_3$ in acetonitrile under inert conditions.

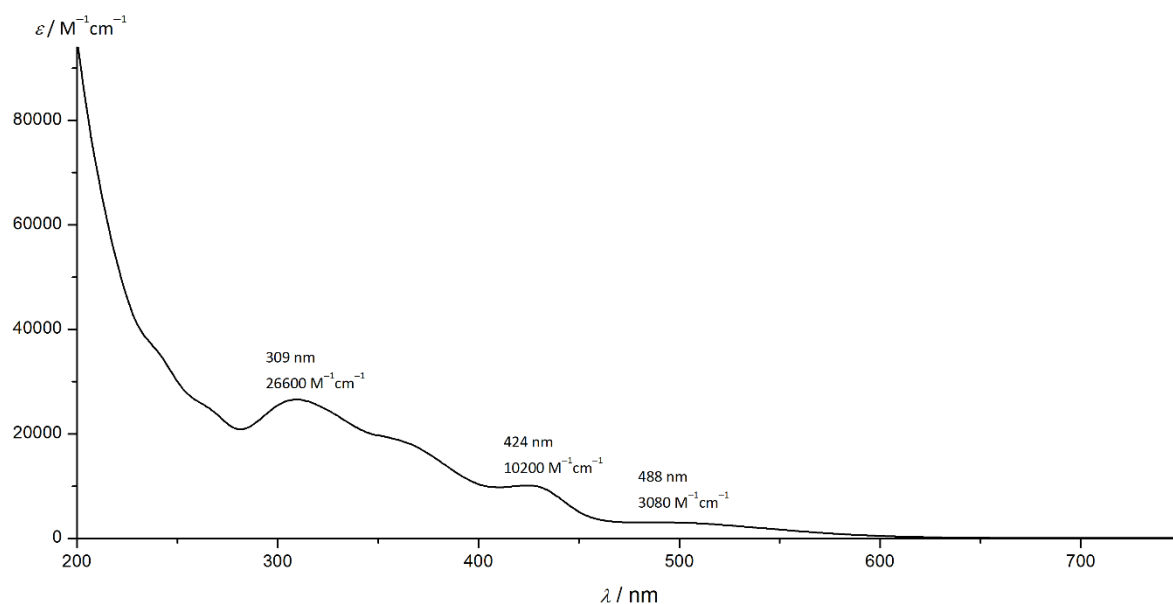


Figure S10. UV-VIS spectrum of $2[\text{ClO}_4]_3$ in aqueous solution after 30 min at $\text{pH} = 9.9$.

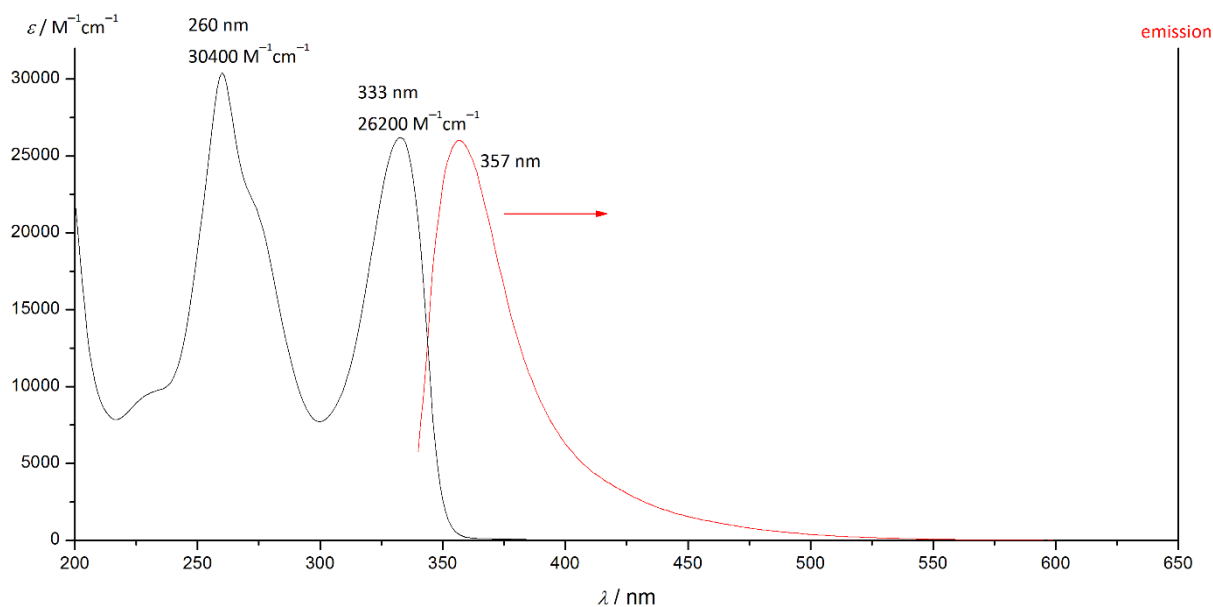


Figure S11. Absorption (black) and emission spectrum (red, $\lambda_{\text{exc}} = 333 \text{ nm}$) of H_2tpda in acetonitrile.

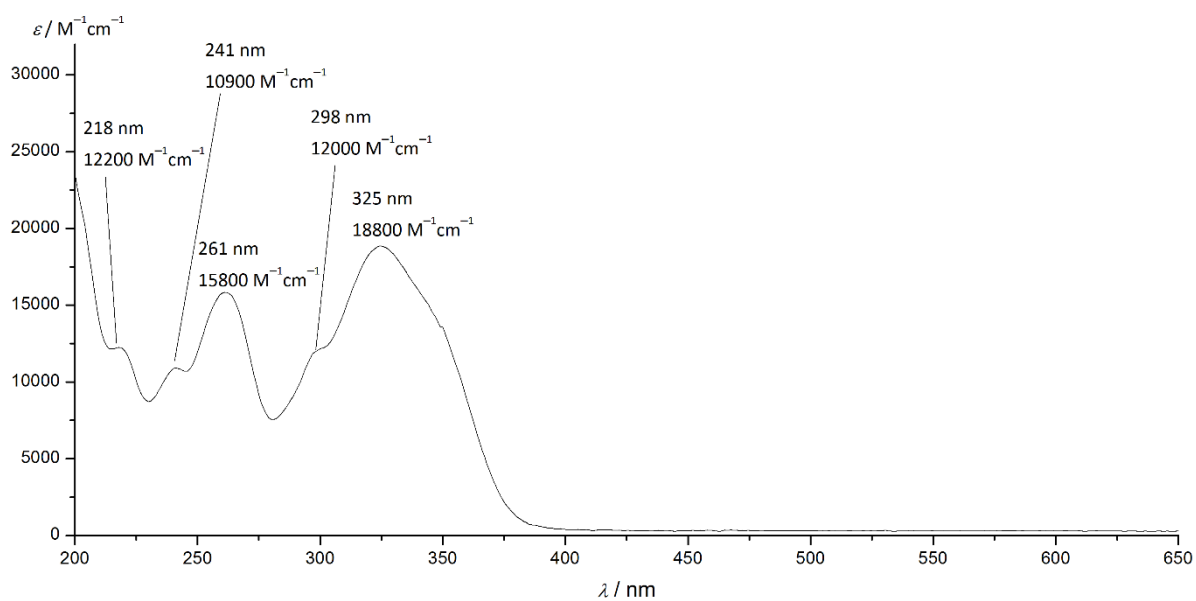


Figure S12. Absorption spectrum of $[\text{H}_3\text{tpda}][\text{ClO}_4]$ in acetonitrile (0.1 M HClO_4 , 10.9 $\mu\text{l/ml}$ aqueous HClO_4 (60 %)).

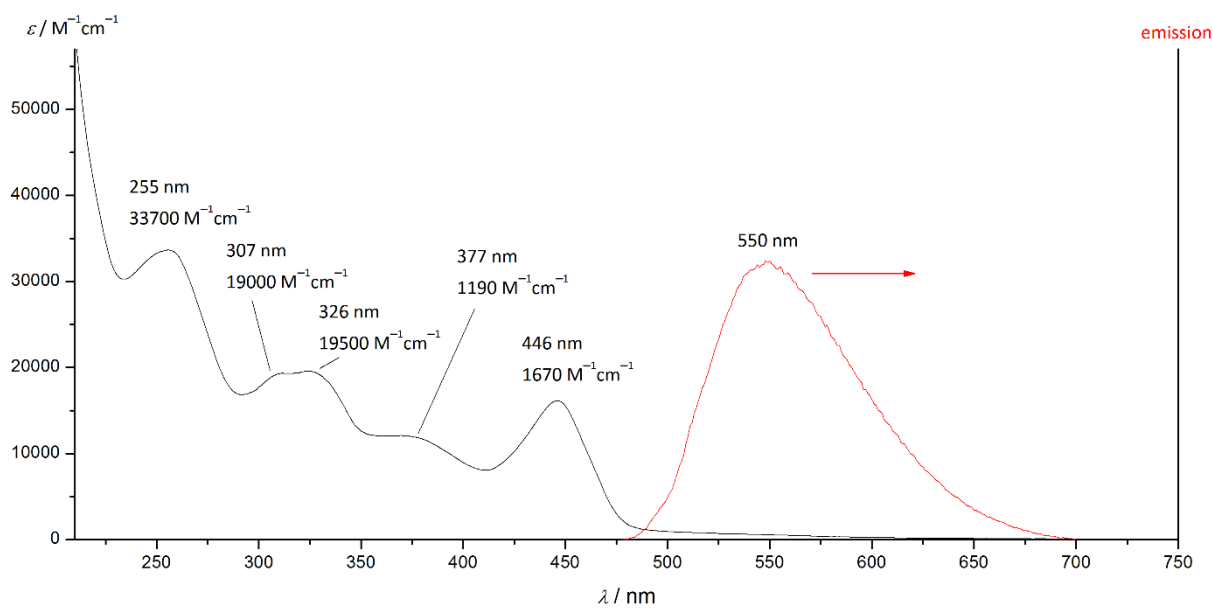


Figure S13. Absorption spectrum (black) and emission spectrum (red, $\lambda_{exc} = 445$ nm) of $[NBu_4][Htpda]$ in acetonitrile.

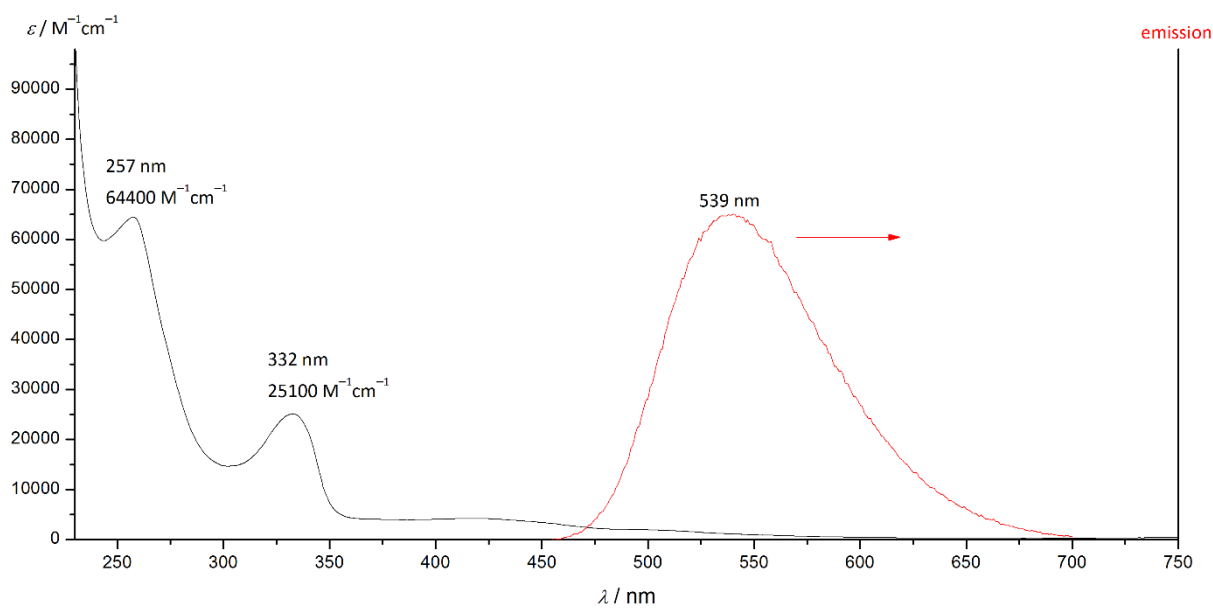


Figure S14. Absorption spectrum (black) and emission spectrum (red, $\lambda_{exc} = 445$ nm) of $[NBu_4]_2[tpda]$ in acetonitrile.

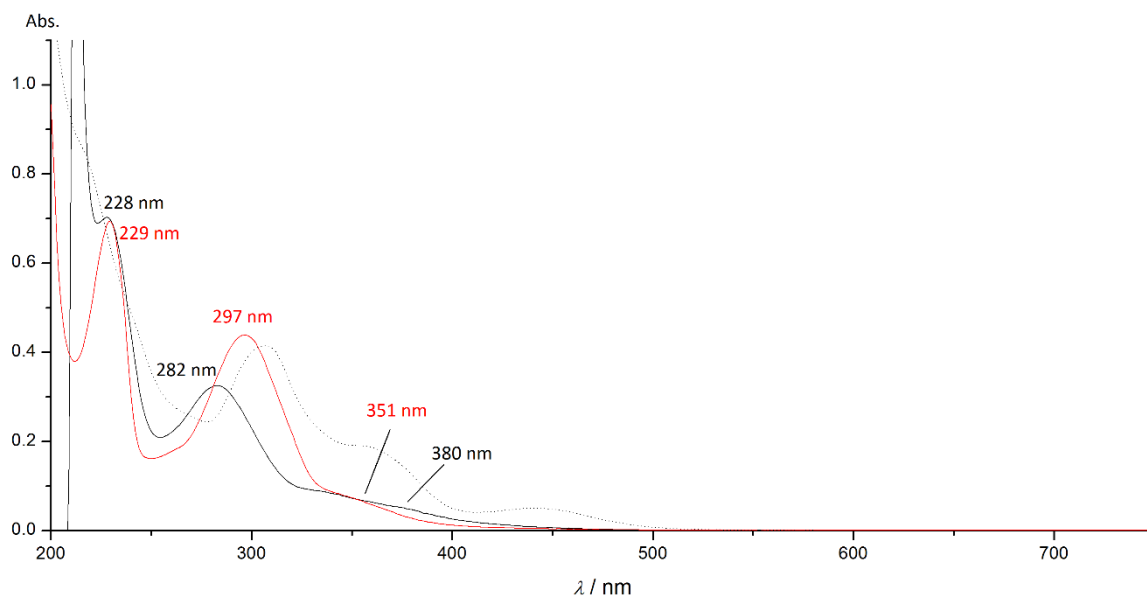


Figure S15. UV-VIS spectrum of $2[\text{ClO}_4]_3$ in aqueous solution at pH = 4.9 (dotted), after 12 h at pH = 9.9 (black) and subsequent acidification with HClO_4 (red).

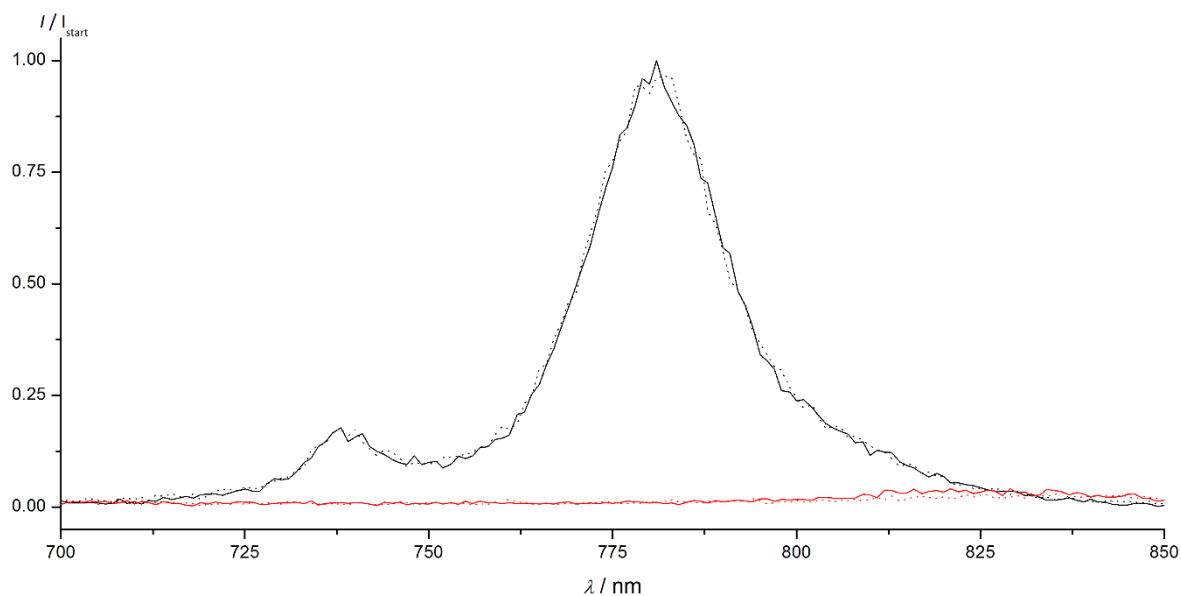


Figure S16. Emission spectrum of $2[\text{ClO}_4]_3$ in CH_3CN (black), after deprotonation with $\text{P}_1\text{-}^t\text{Bu}$ (red), 12 h later (red, dotted) and 12 h later after protonation with an excess of aqueous HClO_4 (black, dotted).

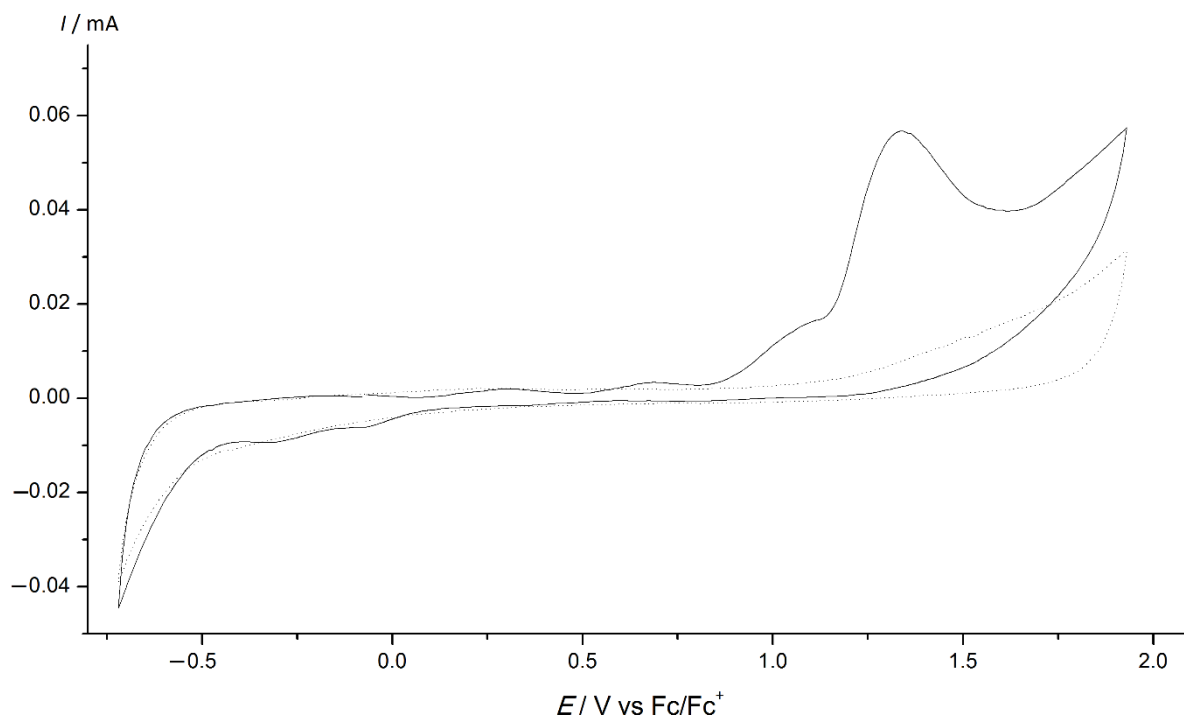


Figure S17. Cyclic voltammogram of $1[\text{ClO}_4]_3$ in 0.1 M HClO_4 (10.9 $\mu\text{l/ml}$ aqueous HClO_4 (60 %) in acetonitrile), glassy carbon electrode as working electrode, referenced against ferrocene; dotted: cyclic voltammogram of the solvent containing perchloric acid (10.9 $\mu\text{l/ml}$ aqueous HClO_4 (60 %)).

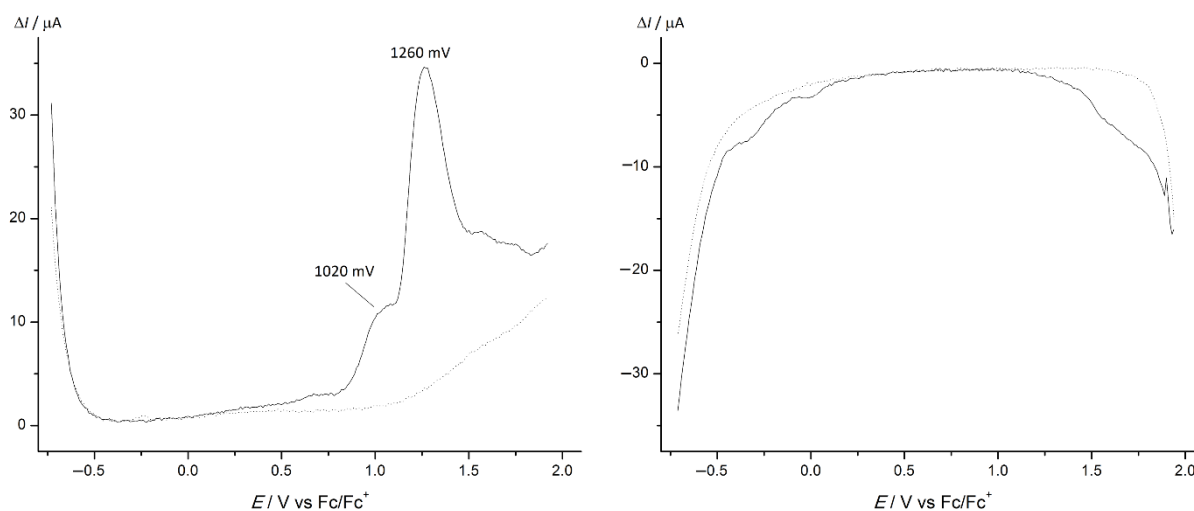


Figure S18. Square wave voltammogram of $1[\text{ClO}_4]_3$ in 0.1 M HClO_4 (10.9 $\mu\text{l/ml}$ aqueous HClO_4 (60 %) in acetonitrile), glassy carbon electrode as working electrode, referenced against ferrocene; dotted: square wave voltammogram of the solvent containing perchloric acid (10.9 $\mu\text{l/ml}$ aqueous HClO_4 (60 %)).

Table S1. Photoluminescence quantum yields Φ / % of **2[ClO₄]₃**, **3[ClO₄]₃** and **1[BF₄]₃**^[2] in different environments (under Ar). Uncertainty estimated as ca. 5 %.

	2[ClO₄]₃	3[ClO₄]₃	1[BF₄]₃
H ₂ O	6.3	6.0	11.0
D ₂ O	15.4	15.0	14.0
CH ₃ CN	8.8	12.0	12.1
CD ₃ CN	8.9	12.5	11.7

Table S2. Photoluminescence quantum yields Φ / % of **2[ClO₄]₃**, **3[ClO₄]₃** and **1[BF₄]₃**^[2] in different environments (in air equilibrated solutions). Uncertainty estimated as ca. 5 %.

	2[ClO₄]₃	3[ClO₄]₃	1[BF₄]₃
H ₂ O	1.5	1.4	2.1
D ₂ O	1.8	1.9	2.0
CH ₃ CN	0.8	0.8	0.6
CD ₃ CN	0.7	0.9	0.6

Table S3. ²E lifetimes τ / μ s of **2[ClO₄]₃**, **3[ClO₄]₃** and **1[BF₄]₃**^[2] in different environments (under Ar). Uncertainty estimated as ca. 10 %.

	2[ClO₄]₃	3[ClO₄]₃	1[BF₄]₃
H ₂ O	670	690	898
D ₂ O	1500	1500	1164
CH ₃ CN	770	1100	898
CD ₃ CN	790	1200	810

Table S4. 2E lifetimes $\tau / \mu\text{s}$ of $2[\text{ClO}_4]_3$, $3[\text{ClO}_4]_3$ and $1[\text{BF}_4]_3$ ^[2] in different environments (in air equilibrated solutions). Uncertainty estimated as ca. 10 %.

	$2[\text{ClO}_4]_3$	$3[\text{ClO}_4]_3$	$1[\text{BF}_4]_3$
H ₂ O	150	160	177
D ₂ O	140	170	150
CH ₃ CN	55	54	44
CD ₃ CN	52	56	24

Table S5. Data of the crystal structure determination of **2[ClO₄]₃·CH₃CN**.

Empirical formula	C ₃₂ H ₂₉ Cl ₃ CrN ₁₁ O ₁₂	
Formula weight	918.01	
Temperature	100(2) K	
Wavelength	0.71073 Å	
Crystal system	monoclinic	
Space group	<i>P2/c</i>	
Unit cell dimensions	<i>a</i> = 20.2076(5) Å	$\alpha = 90^\circ$
	<i>b</i> = 11.2343(4) Å	$\beta = 106.186(2)^\circ$
	<i>c</i> = 17.6130(5) Å	$\gamma = 90^\circ$
Volume	3840.0(2) Å ³	
<i>Z</i>	4	
Density (calculated)	1.588 g cm ⁻³	
Absorption coefficient	0.584 mm ⁻¹	
<i>F</i> (000)	1876	
Crystal size	0.330 x 0.220 x 0.130 mm ³	
Theta range for data collection	2.099 to 28.265°.	
Index ranges	-24 ≤ <i>h</i> ≤ 26, -14 ≤ <i>k</i> ≤ 13, -23 ≤ <i>l</i> ≤ 23	
Reflections collected	24718	
Independent reflections	9441 [<i>R</i> (int) = 0.0574]	
Completeness to theta = 25.242°	99.8 %	
Absorption correction	semi-empirical from equivalents	
Max. and min. transmission	1.143 and 0.873	
Refinement method	full-matrix least-squares on <i>F</i> ²	
Data / restraints / parameters	9441 / 0 / 600	
Goodness-of-fit on <i>F</i> ²	1.050	
Final <i>R</i> indices [<i>I</i> > 2σ(<i>I</i>)]	<i>R</i> ₁ = 0.0532, <i>wR</i> ₂ = 0.1323	
<i>R</i> indices (all data)	<i>R</i> ₁ = 0.0780, <i>wR</i> ₂ = 0.1520	
Largest diff. peak and hole	1.537 and -0.630 eÅ ⁻¹	

Table S6. DFT calculated Cartesian coordinates of 2^{3+} and 3^{3+} .

Cr	0.00047635404446	-0.00273241064236	-0.00457263587405
N	0.00042643380855	-0.00226806932250	2.05008668035908
N	0.00150475482498	-0.00119191051550	-2.05844489033606
N	-2.04753323859913	0.20081317376750	0.06292959135546
N	2.04858156459588	-0.20561242046984	0.06287487463881
N	-0.15905276528197	-2.05391370200604	-0.07342908048818
N	0.15879643543344	2.04868804055190	-0.07220849160818
C	-1.04296979882813	-0.51834169058772	2.74225088690500
C	-1.06054514346312	-0.55415249856191	4.12975787124284
C	-0.00112408818169	0.00275559515237	4.82297828133384
C	1.05903314153351	0.55712213920147	4.12905233620503
C	1.04316827140893	0.51617458737426	2.74149606415827
H	-1.91142026612937	-0.97782884086674	4.64108479465651
H	1.90966677734320	0.98207444947756	4.63955929053520
C	-2.70004823587023	0.84144132901625	-0.93818145563763
C	-4.05302190211817	0.73865121212202	-1.12361380342275
C	-4.78577963618206	-0.06437858875367	-0.24345636484103
C	-4.14460371317486	-0.66860482261323	0.81412166063178
C	-2.76486216819427	-0.48981164571721	0.96101905687202
H	-5.85080053186746	-0.19316994744688	-0.37598248634610
H	-2.08861008886198	1.43035625493276	-1.60182262798276
H	-4.52491706236122	1.25950540948347	-1.94212907386239
H	-4.68329891791745	-1.25591005783597	1.54354049410295
C	2.76525871959439	0.48834546142281	0.95886930901967
C	4.14379241795729	0.67454006696907	0.80774130595169
C	4.78451864786387	0.07259073454334	-0.25140707156523
C	4.05309840574682	-0.73475581388493	-1.12893407400107
C	2.70122044494739	-0.84385640584546	-0.93967713177351
H	5.84842367496317	0.20658363613258	-0.38759818851853
H	4.68202675796841	1.26491691225146	1.53533182636929
H	4.52502378695469	-1.25431953392295	-1.94825141120587
H	2.09031115521874	-1.43525265113531	-1.60152935089795
C	-0.69007363538650	-0.93682837626815	-2.75158777295453
C	-0.72891269004851	-0.94613655415822	-4.13908304424077
C	-0.00033783129036	0.00322580945990	-4.83230511628746
C	0.72975397810068	0.95016931768711	-4.13692102515993
C	0.69300471560503	0.93625785727093	-2.74963093772248
H	-1.29315257053483	-1.70968265224234	-4.65192443248856
H	1.29220852383814	1.71617976873184	-4.64796917144552
C	0.34946753776162	-2.80537969390803	0.93350558156580
C	-0.00663325684757	-4.11312517671206	1.12998806225909
C	-0.93116223892914	-4.68891435259806	0.25252956268406
C	-1.40278282129232	-3.95730232020866	-0.81319857899237
C	-0.97162579623535	-2.63457004495779	-0.96837315742565
H	-1.25753092406333	-5.70941996970657	0.39358671844503
H	1.04182956558771	-2.30833499465207	1.59293248420284
H	0.41512545827214	-4.66726254588328	1.95373282843468
H	-2.07778377255710	-4.38358181332802	-1.54122019656316
C	0.97458042249792	2.63010969749231	-0.96377592652911
C	1.40647734577816	3.95201367341813	-0.80481286496228
C	0.93186045281183	4.68249842869179	0.26031292349331
C	0.00339644977551	4.10640044546827	1.13339524871056
C	-0.35296777728599	2.79924368835567	0.93374610733879
H	1.25882416412644	5.70246616011893	0.40393953140794
H	2.08514520608892	4.37844775766098	-1.52896674021882
H	-0.42056865132492	4.65982241316832	1.95647839397789
H	-1.04867358792111	2.30194816582613	1.58948654238075
N	-1.39513306617096	-1.91479277918277	-2.06663886638165
N	1.39983115270104	1.91129260482545	-2.06189222962690
N	-2.13142592396047	-1.03849869456400	2.05793173675424

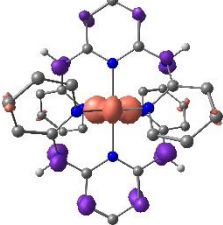
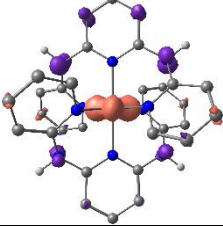
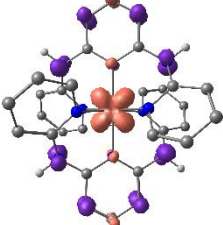
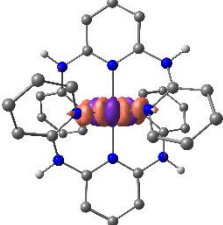
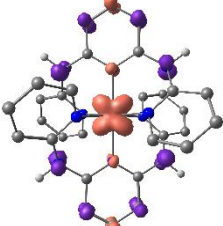
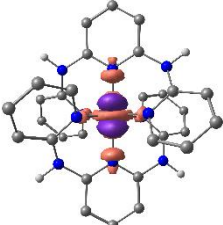
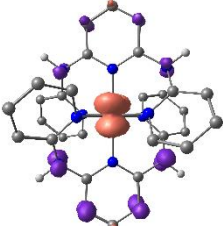
N	2.13244705346152	1.03364586361070	2.05727133185800
H	-0.00177868905507	0.00466455996217	5.90366894557228
H	-0.00151666401181	0.00532594951050	-5.91305629094473
H	2.75914917504644	1.54709486069607	2.65886614605496
H	-2.01211774443455	-2.43992493073777	-2.66827108100378
H	2.02297731914717	2.43324925911573	-2.66024888991657
H	-2.75964206642698	-1.54825237423373	2.66141499174791

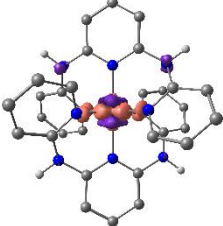
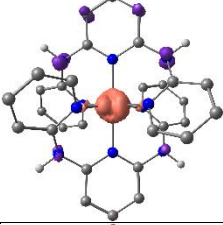
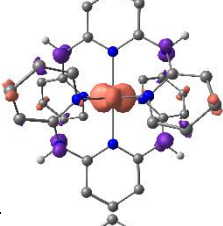
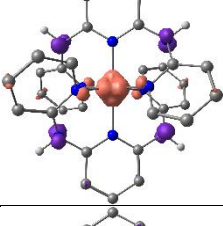
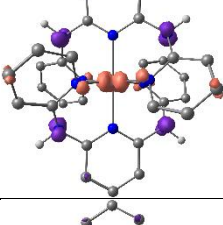
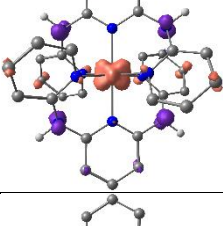
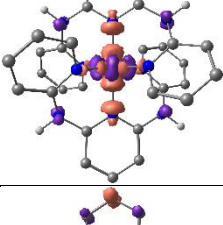
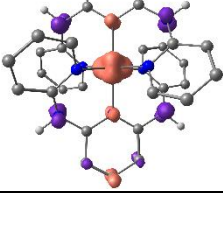
Table S7. DFT calculated Cartesian coordinates of 4^{2+} .

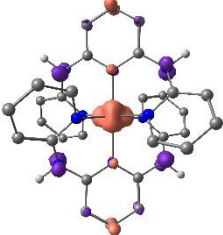
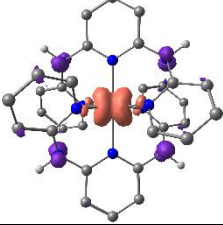
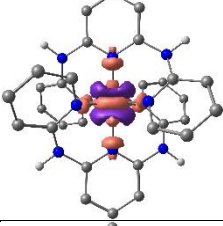
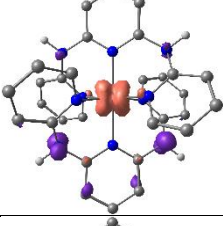
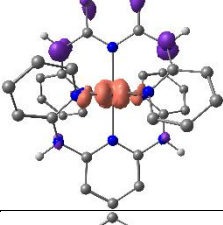
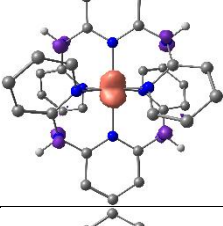
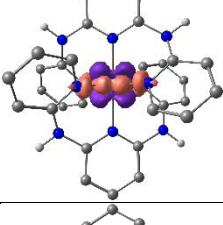
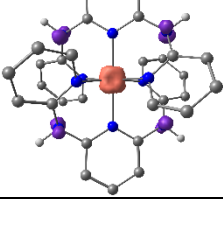
Cr	0.03885926211124	-0.05440151524304	0.03684905224512
N	0.03023827990851	-0.07029152366137	2.06473474520733
N	0.01750820311226	-0.02555474708189	-2.03588250678404
N	-2.02580475179108	0.19812638511508	0.07983503475505
N	2.04752138296378	-0.27949977941767	0.08958871511912
N	-0.16588263524259	-2.10393844803352	-0.06195971474893
N	0.22425875310450	2.00665941194093	-0.01317422150377
C	-1.04629955371876	-0.52508115780203	2.75326670945099
C	-1.11796405508115	-0.50000124013014	4.13034562108127
C	-0.05798731637097	0.06955046508412	4.83695910641422
C	1.02959079979256	0.55586452630301	4.15981152804816
C	1.11010931763309	0.44856808635066	2.75116186554711
H	-2.00013198558768	-0.87074309942018	4.62964488612681
H	1.87218731638855	0.99121206084199	4.67385594916646
C	-2.66332471404051	0.85073932249958	-0.92135605282885
C	-4.01431585387796	0.75728798942371	-1.12763465218583
C	-4.76239159845501	-0.05269858032926	-0.26494977623025
C	-4.13786792010987	-0.67087908034741	0.79317785611318
C	-2.575701696014808	-0.49846366895479	0.96237696309730
H	-5.82628611021527	-0.17543431105532	-0.41313813701267
H	-2.04036731419380	1.44432247527289	-1.57059201326693
H	-4.47365873632309	1.28966583008702	-1.94601303745092
H	-4.68836819100722	-1.26510222828509	1.50827211132652
C	2.75398148699776	0.44241788384180	1.01223758277997
C	4.11669335166255	0.73985112819402	0.73028895679855
C	4.74100177999111	0.19081777243243	-0.35560313391170
C	4.02618666756713	-0.68271063506909	-1.19857417024749
C	2.69874850180193	-0.87429313520345	-0.94388310224103
H	5.78070498066509	0.41198206003455	-0.55630389813642
H	4.64199174171932	1.37381227024767	1.42916265875160
H	4.49312108242637	-1.17433784433650	-2.03804103228802
H	2.09666695516660	-1.49970020749640	-1.58460350717876
C	-0.67978007033607	-0.95019102924541	-2.73514247291454
C	-0.72455913219909	-0.94862180158944	-4.12334953640554
C	0.00275093967745	0.00558592046678	-4.81163505920491
C	0.73811601108181	0.94288233312080	-4.11018120991475
C	0.70810163368012	0.91413692582868	-2.72115240662218
H	-1.29382964860859	-1.70557470589548	-4.64055054100589
H	1.29969681385582	1.71297431809525	-4.61622682537428
C	0.32878342988725	-2.86743889303587	0.94047183575514
C	-0.03711806042088	-4.17598197207211	1.12072267169407
C	-0.95869857112248	-4.73590044123159	0.23076315956310
C	-1.41864312835549	-3.98890948199330	-0.82978885539400
C	-0.97679693323540	-2.66718459460445	-0.96681046886903
H	-1.29295086861486	-5.75578525775000	0.35796143522030
H	1.01600417853006	-2.37640722705571	1.60949819169525
H	0.37428655634751	-4.74161547884371	1.94204524263868
H	-2.09240380461694	-4.40272154077670	-1.56617000544247

C	1.01606499633164	2.59341928301119	-0.92024954035238
C	1.44347150888199	3.91851375725681	-0.77141676747219
C	0.99179132878491	4.64591722686963	0.30589562482330
C	0.09338170613440	4.06107335946132	1.20293448172377
C	-0.25874852342558	2.75053301128273	1.00914411679210
H	1.31462612053341	5.66849831870038	0.44108229379711
H	2.10078338900116	4.35005496399178	-1.51228093332888
H	-0.31050522135407	4.60878993021990	2.03997490354184
H	-0.92968964384011	2.24539511398237	1.68390159256011
N	-1.39108719544858	-1.93195748851627	-2.05980339136608
N	1.42043819883219	1.88399968672949	-2.03329747762438
N	-2.13430824436491	-1.06006641677448	2.05252033945104
N	2.25792190658144	0.84968477034965	2.18460115031356
H	-0.10315199562146	0.13161943315800	5.91576946447365
H	-0.00436051342858	0.01898018919782	-5.89240143848134
H	-2.00511218804371	-2.44979226749221	-2.67020585472831
H	2.02682256889702	2.41658440259458	-2.63871550469567
H	-2.77113771085070	-1.55652081324274	2.65706039914063

Table S8. TD-DFT calculated transitions of 2^{3+} , assignments and corresponding difference electron densities $\Psi_{ES} - \Psi_{GS}$ at a contour value of 0.005 a.u. (purple lobes indicate loss, orange lobes show increase of electron density upon excitation, all hydrogen atoms except NH protons omitted for clarity).

#	λ / nm	character	Difference electron density
1	448.5	LMCT	
2	443.3	LMCT	
3	433.2	LMCT	
4	427.3	MC	
5	427.0	LMCT + $\pi\pi^*$	
6	419.2	MC	
7	410.8	LMCT	

8	405.5	MC	
9	404.5	LMCT	
10	376.5	LMCT + $\pi\pi^*$	
11	373.9	LMCT	
12	369.4	LMCT + $\pi\pi^*$	
13	368.1	LMCT + $\pi\pi^*$	
14	362.3	MC	
15	360.6	LMCT + $\pi\pi^*$	

16	351.3	LMCT + $\pi\pi^*$	
17	347.5	LMCT	
18	344.7	MC	
19	342.2	LMCT	
20	342.1	LMCT	
21	340.3	LMCT	
22	333.5	MC	
23	333.4	LMCT	

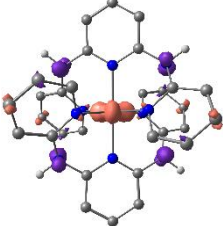
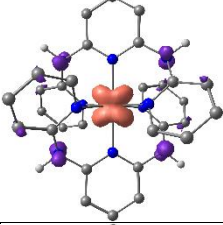
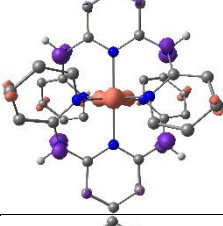
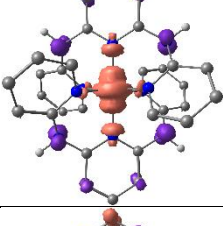
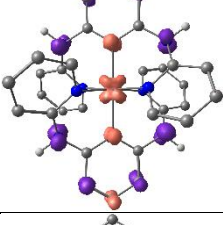
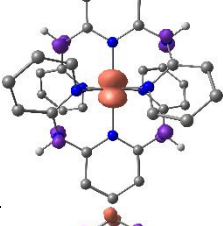
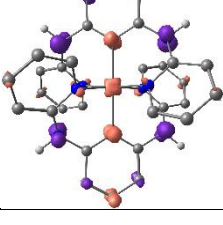
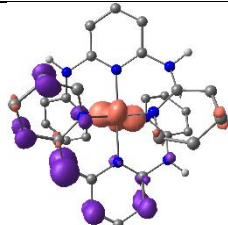
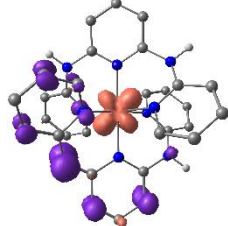
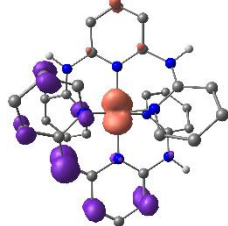
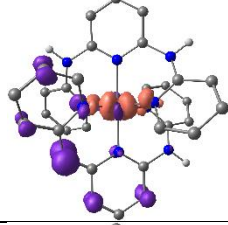
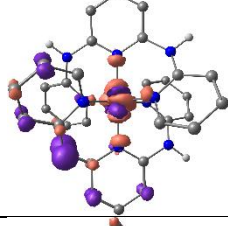
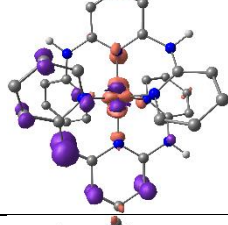
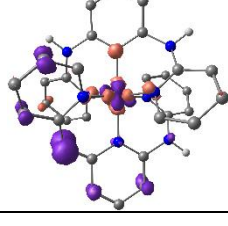
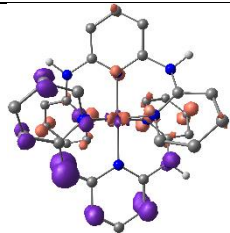
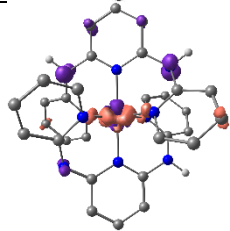
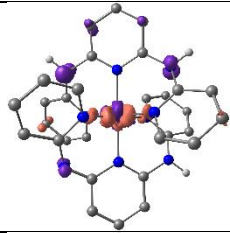
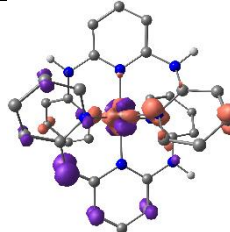
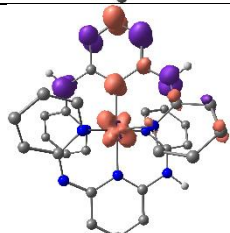
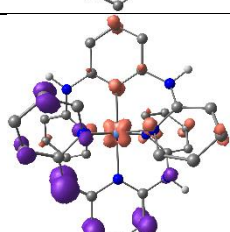
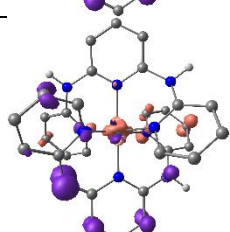
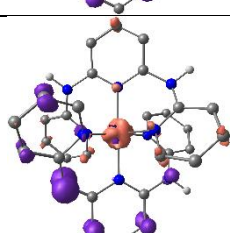
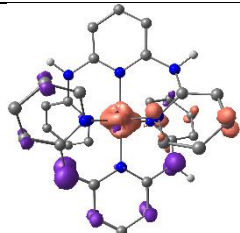
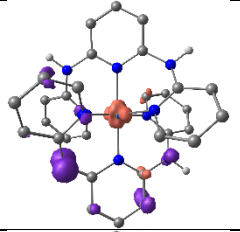
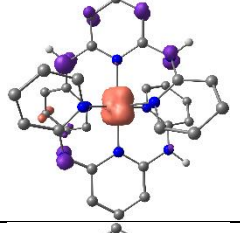
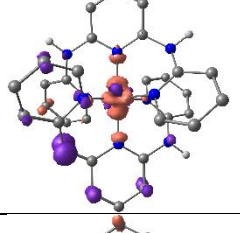
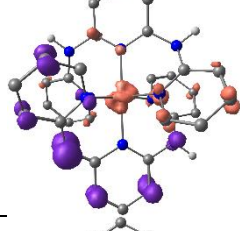
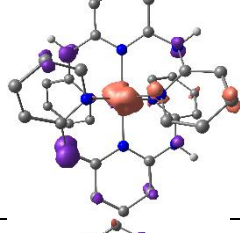
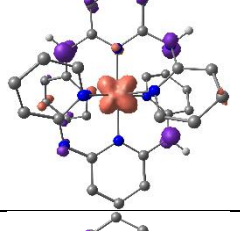
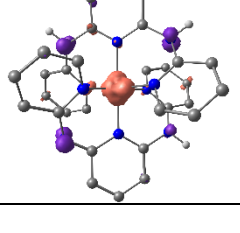
24	330.6	LMCT + $\pi\pi^*$	
25	330.8	LMCT	
26	323.1	LMCT + $\pi\pi^*$	
27	323.0	LMCT	
28	320.3	LMCT + $\pi\pi^*$	
29	319.0	LMCT	
30	315.4	LMCT + $\pi\pi^*$	

Table S9. TD-DFT calculated transitions of 4^{2+} , assignments and corresponding difference electron densities $\Psi_{ES} - \Psi_{GS}$ at a contour value of 0.005 a.u. (purple lobes indicate loss, orange lobes show increase of electron density upon excitation, all hydrogen atoms except NH protons omitted for clarity).

#	λ / nm	character	Difference electron density
1	611.7	LMCT + LL'CT	
2	573.4	LMCT + LL'CT	
3	523.1	LMCT + LL'CT	
4	502.9	MC + LMCT	
5	460.2	MC + LMCT	
6	451.1	MC + LMCT	
7	439.0	MC + LMCT	

8	445.1	MC + LL'CT	
9	415.2	MC + LMCT	
10	412.5	MC + LMCT	
11	418.9	MC + LL'CT	
12	406.0	LMCT + $\pi\pi^*$	
13	422.3	LMCT + LL'CT	
14	406.2	LMCT + LL'CT + MC	
15	390.1	LMCT + LL'CT + MC	

16	385.3	LMCT + LL'CT + MC	
17	383.2	MLCT	
18	378.1	MLCT	
19	379.2	MC + LMCT + LL'CT	
20	383.5	LL'CT + LMCT	
21	363.2	LMCT	
22	359.3	LMCT	
23	357.7	LMCT	

24	354.5	LMCT + $\pi\pi^*$	
25	356.8	LMCT + MC	
26	350.7	MC + LMCT	
27	356.2	LMCT + LL' CT	
28	339.2	LMCT + $\pi\pi^*$	
29	338.0	LMCT + $\pi\pi^*$	
30	340.1	LMCT + $\pi\pi^*$	

Literature

- [1] A. P. Scott, L. Radom, *J. Phys. Chem.* **1996**, *100*, 16502–16513.
[2] S. Otto, M. Grabolle, C. Förster, C. Kreitner, U. Resch-Genger, K. Heinze, *Angew. Chem.* **2015**, *127*, 11735–11739; *Angew. Chem. Int. Ed.* **2015**, *54*, 11572–11576.

6.7 Supporting Information: Three-in-One Crystal: The Coordination Diversity of Zinc Polypyridine Complexes

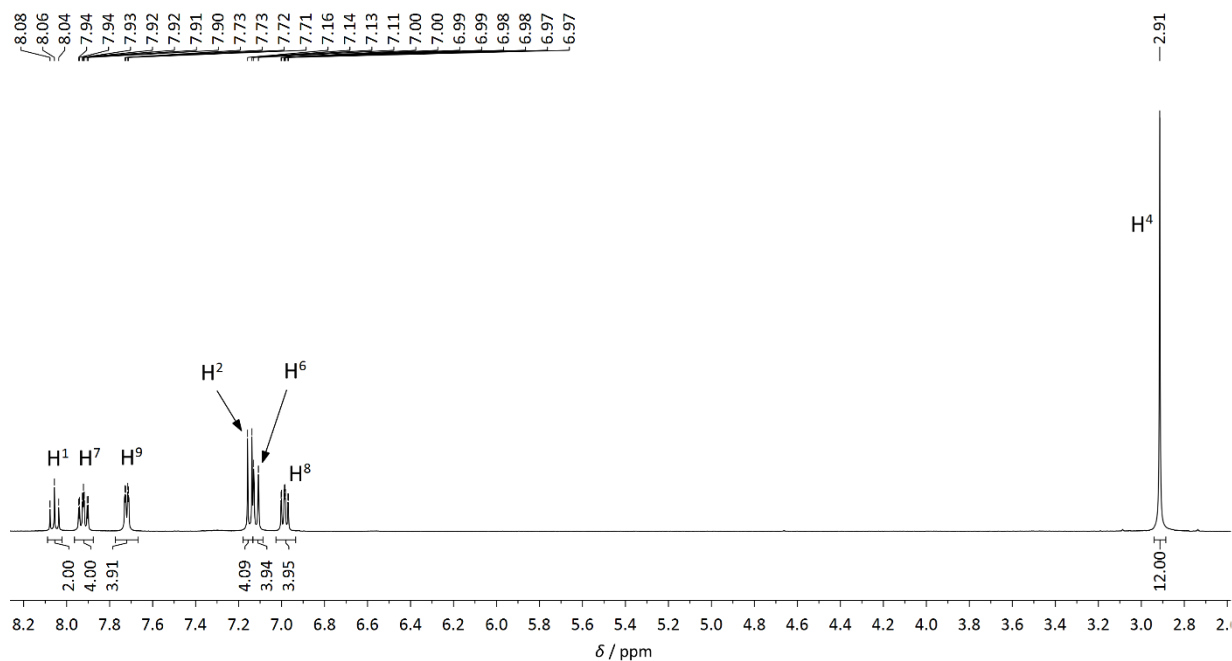


Figure S1. ^1H NMR spectrum of **8**(BF_4) $_2$ in CD_3CN .

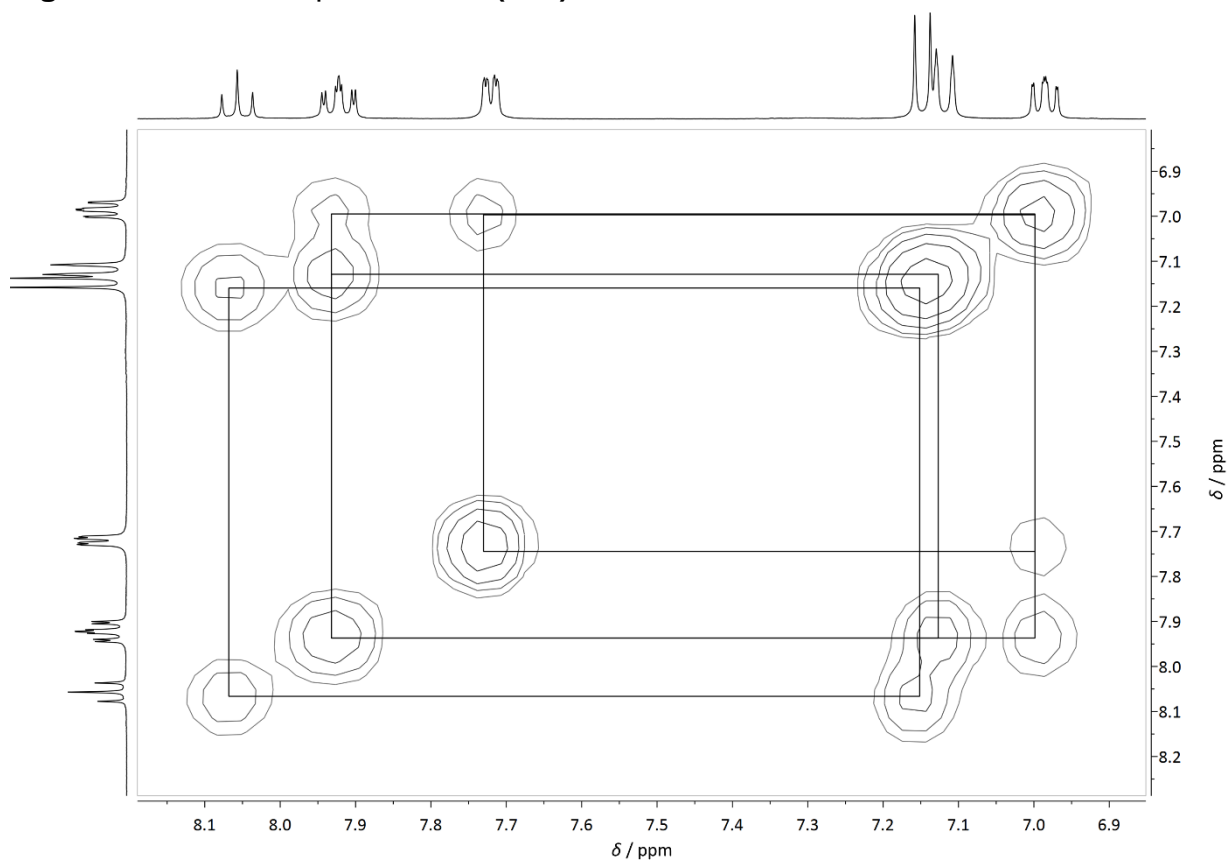


Figure S2. $^1\text{H}^1\text{H}$ COSY NMR spectrum of **8**(BF_4) $_2$ in CD_3CN .

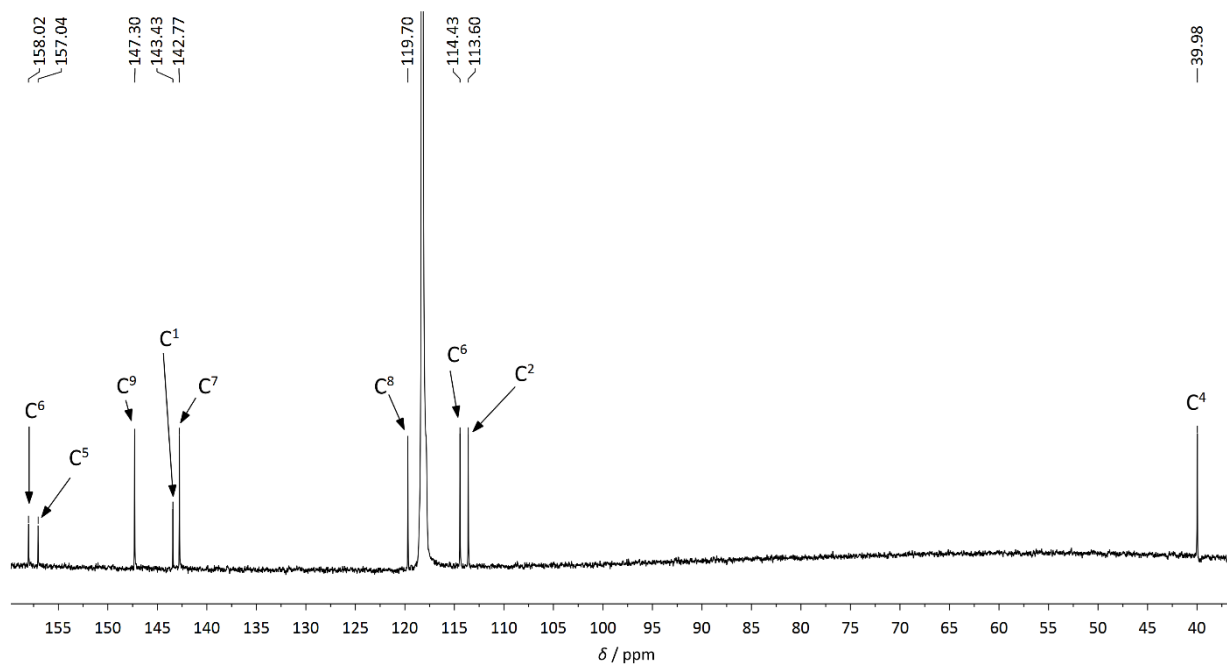


Figure S3. ^{13}C NMR spectrum of $8(\text{BF}_4)_2$ in CD_3CN .

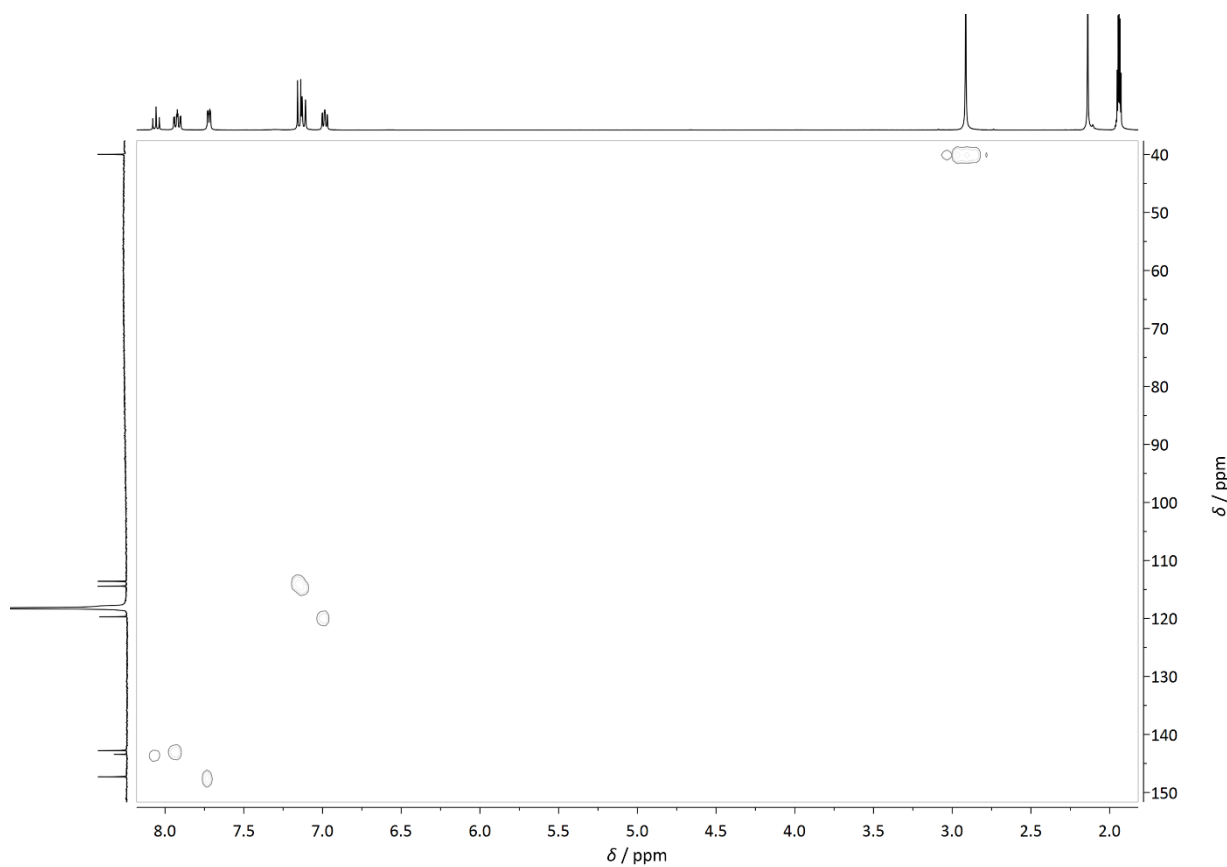


Figure S4. $^1\text{H}^{13}\text{C}$ HSQC NMR spectrum of $8(\text{BF}_4)_2$ in CD_3CN .

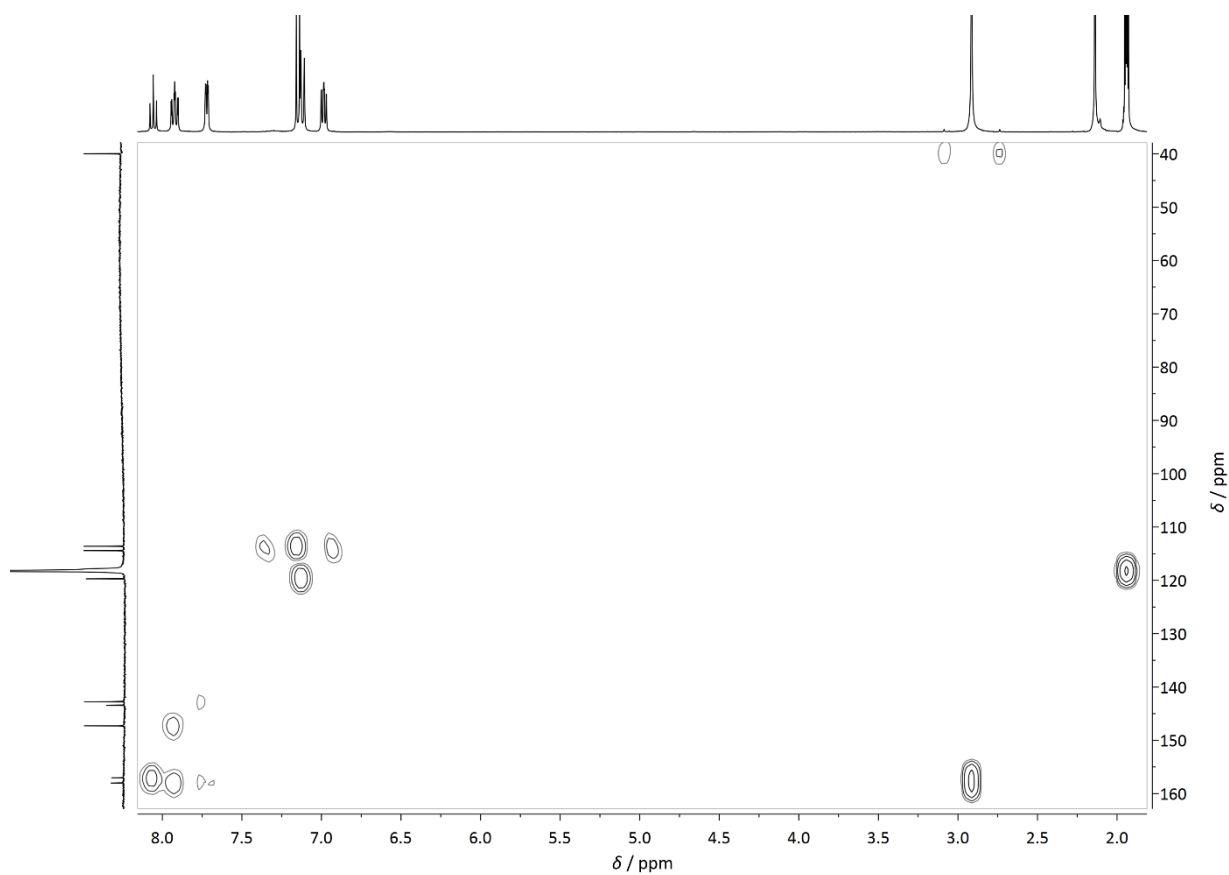


Figure S5. $^1\text{H}^{13}\text{C}$ HMBC NMR spectrum of $8(\text{BF}_4)_2$ in CD_3CN .

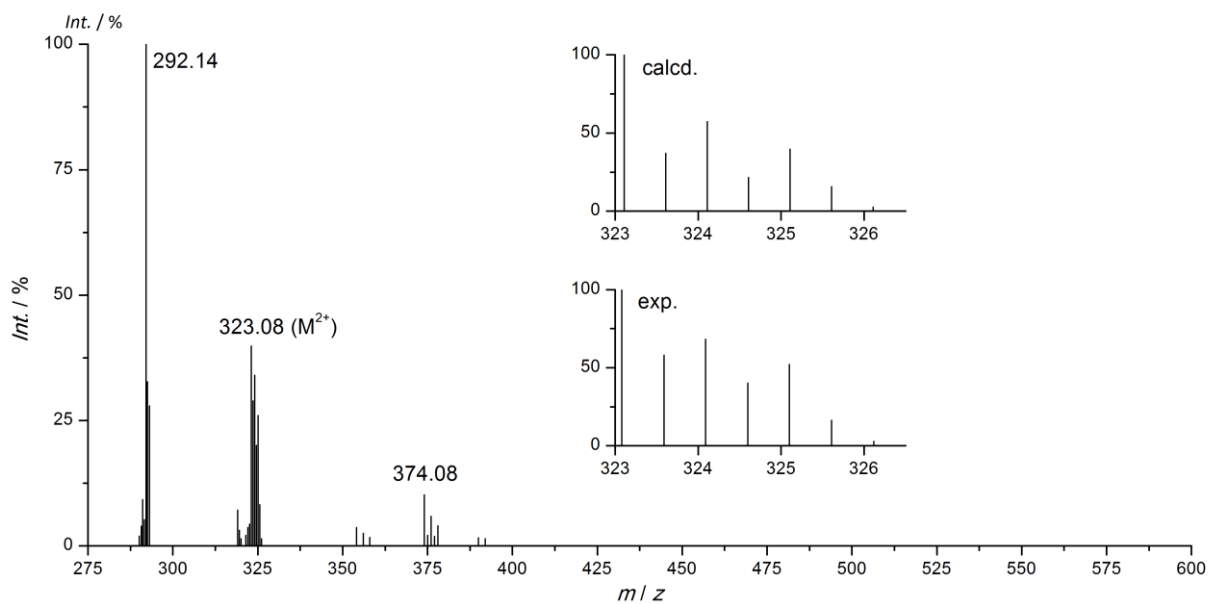


Figure S6. ESI^+ mass spectrum of $8(\text{BF}_4)_2$ in CH_3CN .

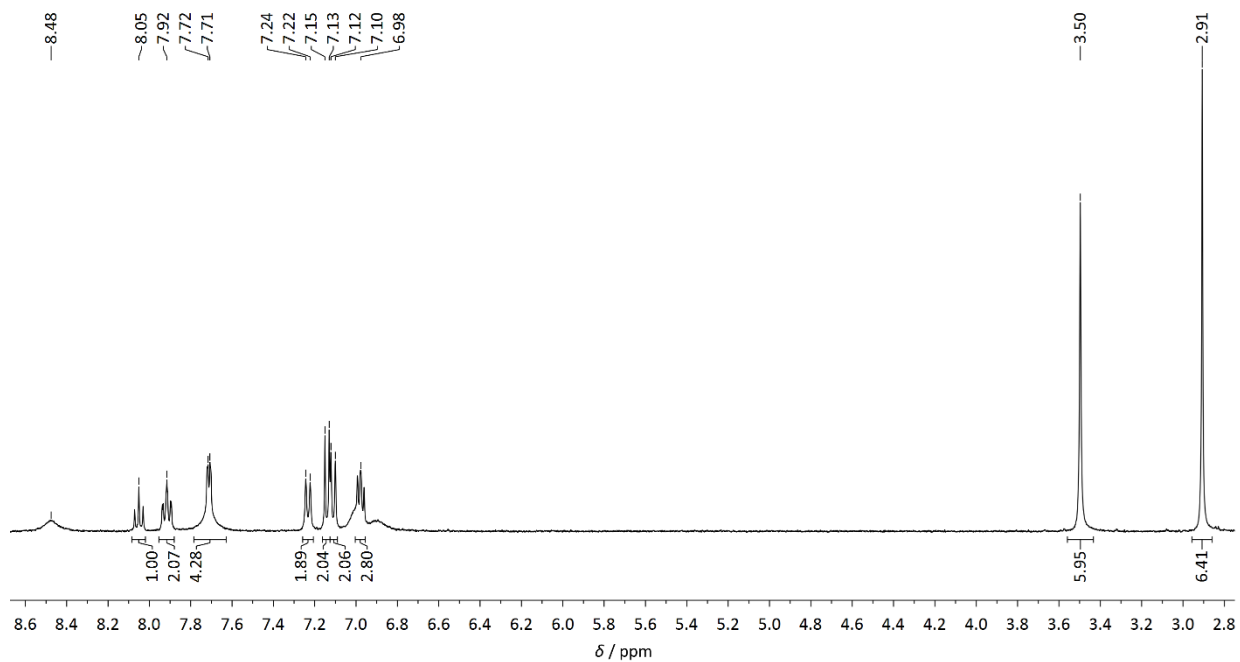


Figure S7. ^1H NMR spectrum of $[\mathbf{9}][\mathbf{8}](\text{ZnCl}_4)$ in CD_3CN .

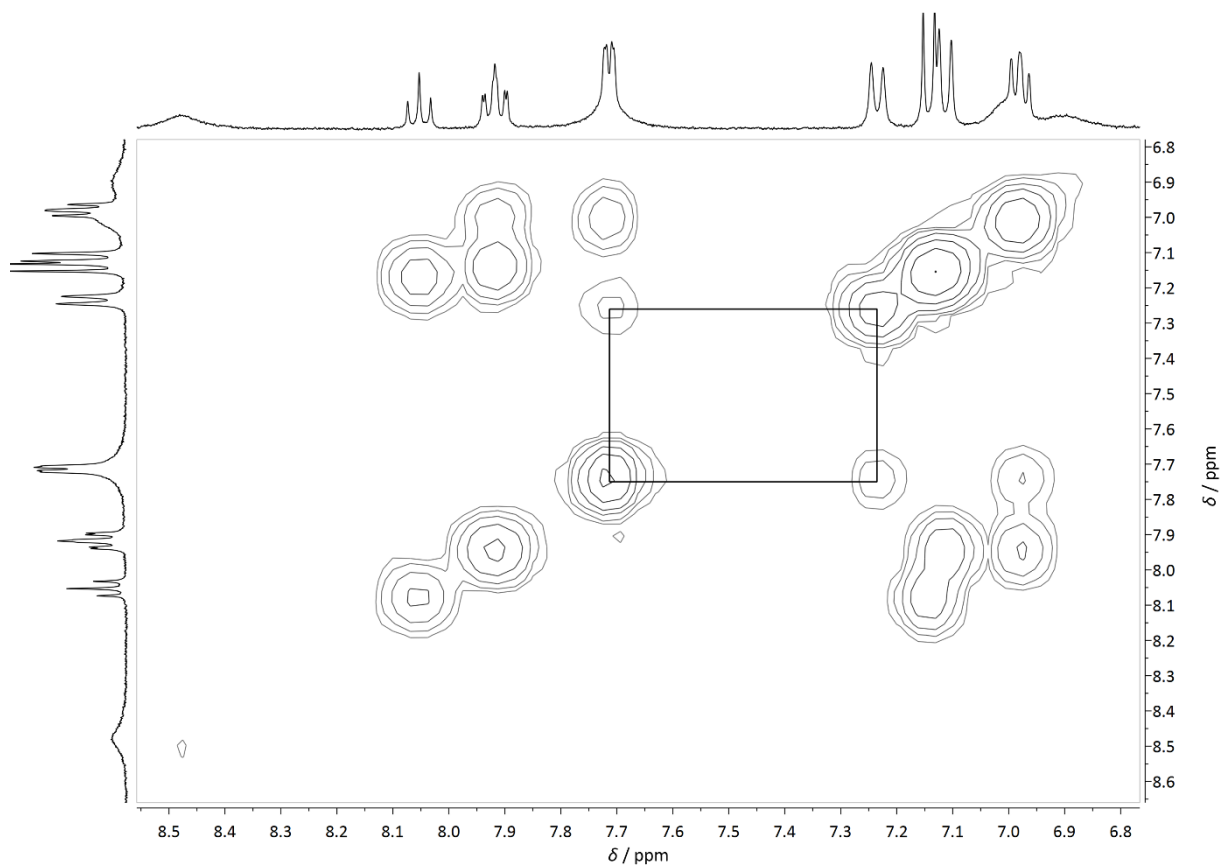


Figure S8. ^1H ^1H COSY NMR spectrum of $[\mathbf{9}][\mathbf{8}](\text{ZnCl}_4)$ in CD_3CN .

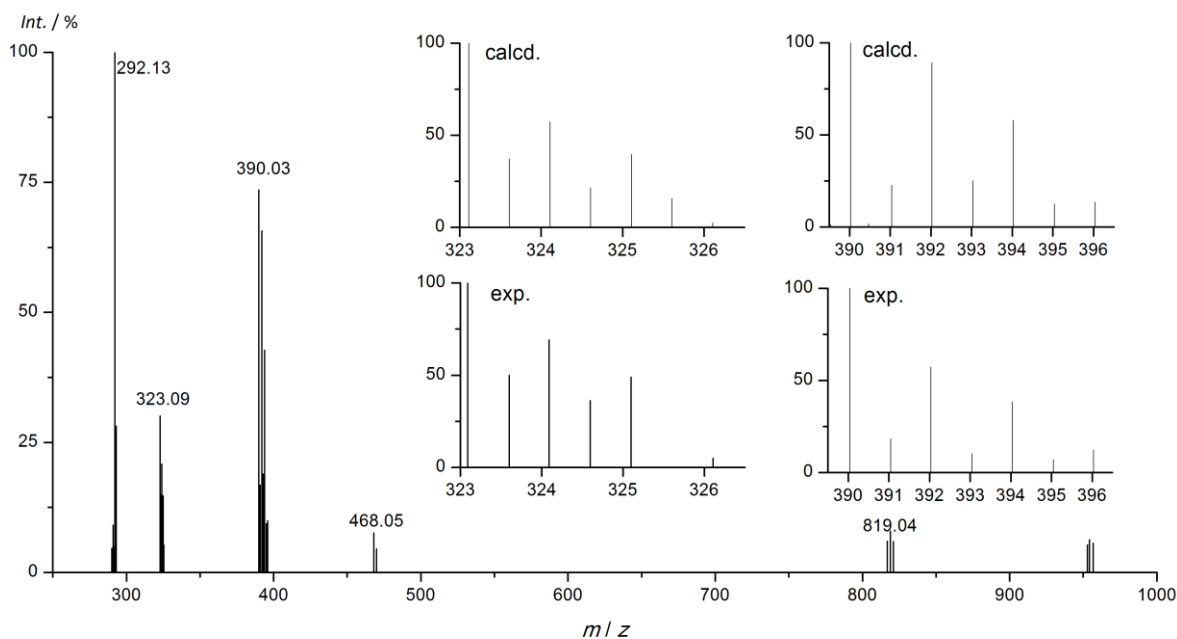


Figure S9. ESI⁺ mass spectrum of [9][8](ZnCl₄) in CH₃CN.

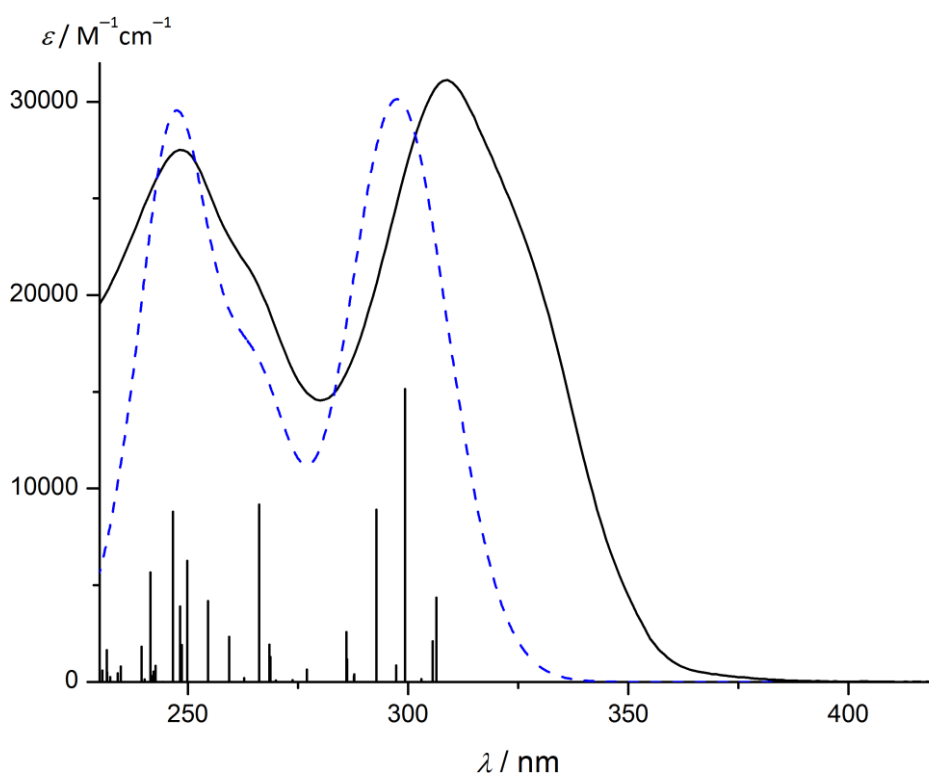


Figure S10. UV-VIS spectrum of 8(BF₄)₂ in CH₂Cl₂ (black line), calculated (TD-DFT, 50 excitations) oscillator strengths and simulated spectrum of 8²⁺ (blue dashed line, FWHM = 2500 cm⁻¹).

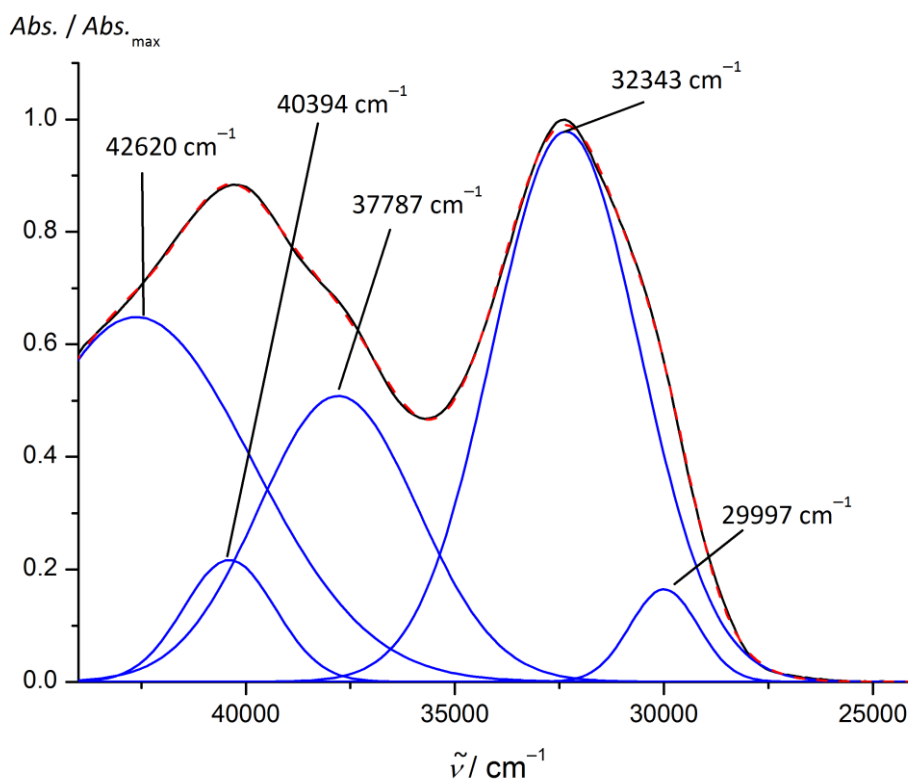


Figure S11. UV-VIS spectrum of **8(BF₄)₂** in CH₂Cl₂ (black line), 5 fitted Gaussian functions (blue lines) and sum of these (red dashed line).

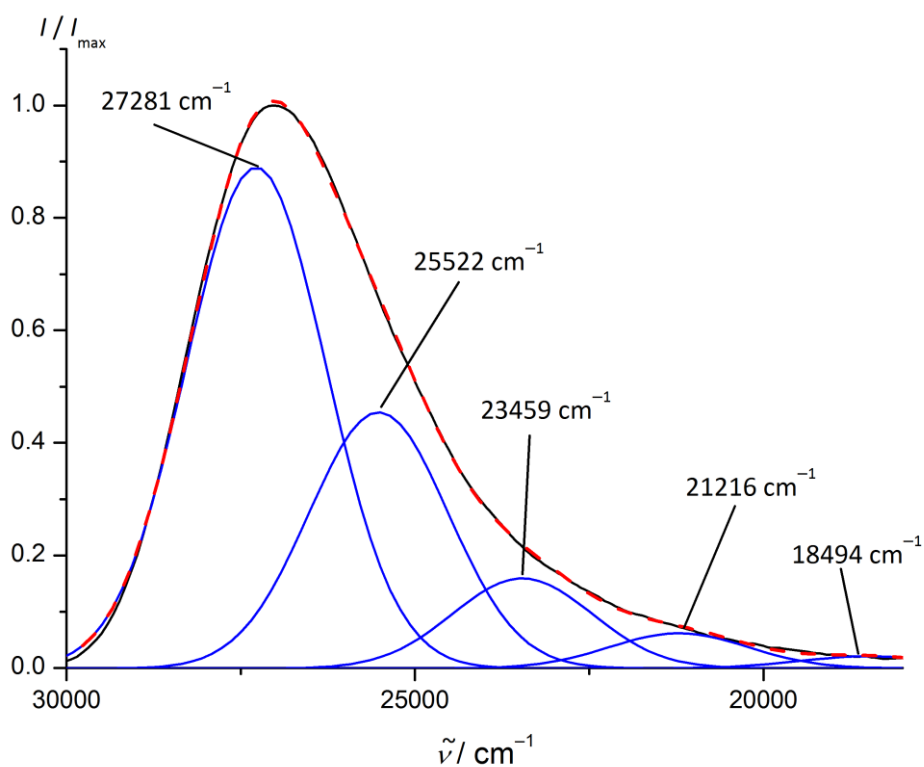


Figure S12. Emission spectrum of **8(BF₄)₂** in CH₂Cl₂ (black line), 5 fitted Gaussian functions (FWHTM = 2355 cm⁻¹, blue lines) and sum of these (red dashed line).

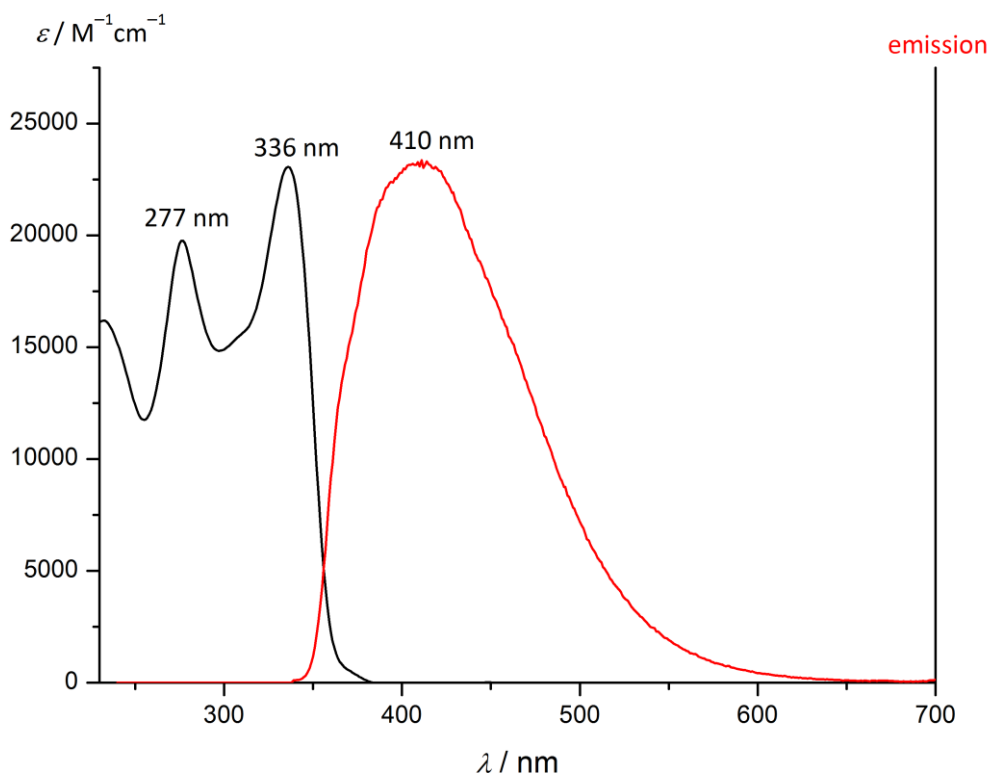


Figure S13. Absorption (black line) and emission spectra (red line, $\lambda_{\text{exc}} = 336 \text{ nm}$) of ddpd in HCl-free CH₂Cl₂.

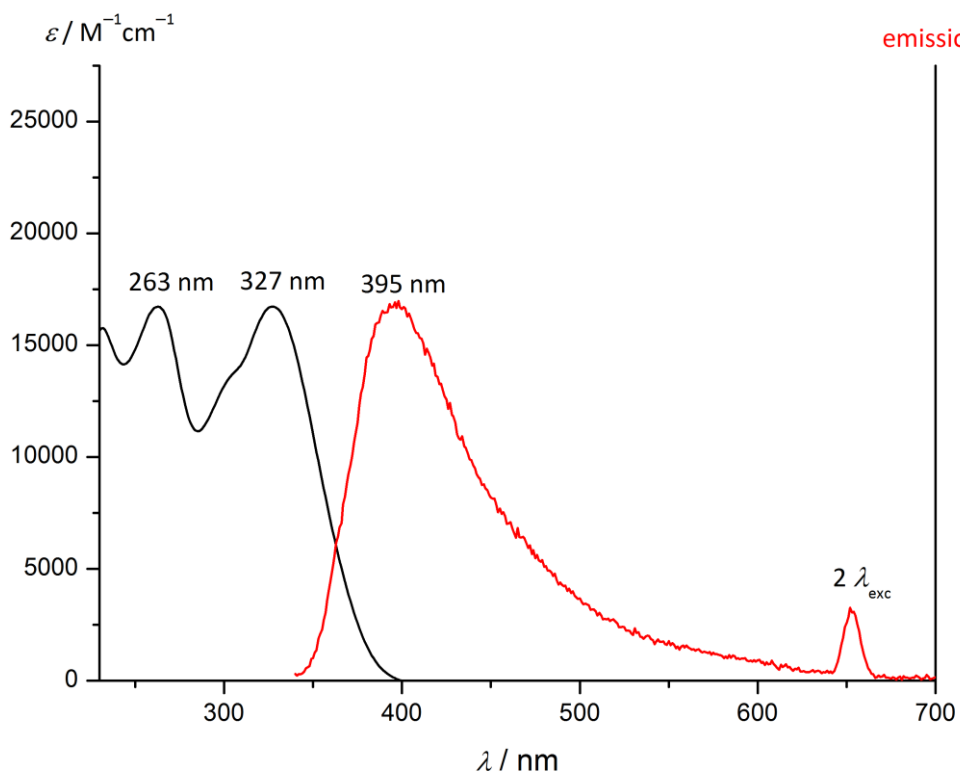


Figure S14. Absorption (black line) and emission spectra (red line, $\lambda_{\text{exc}} = 327 \text{ nm}$) of ddpd in acidic CH₂Cl₂ (200 eq TFA).

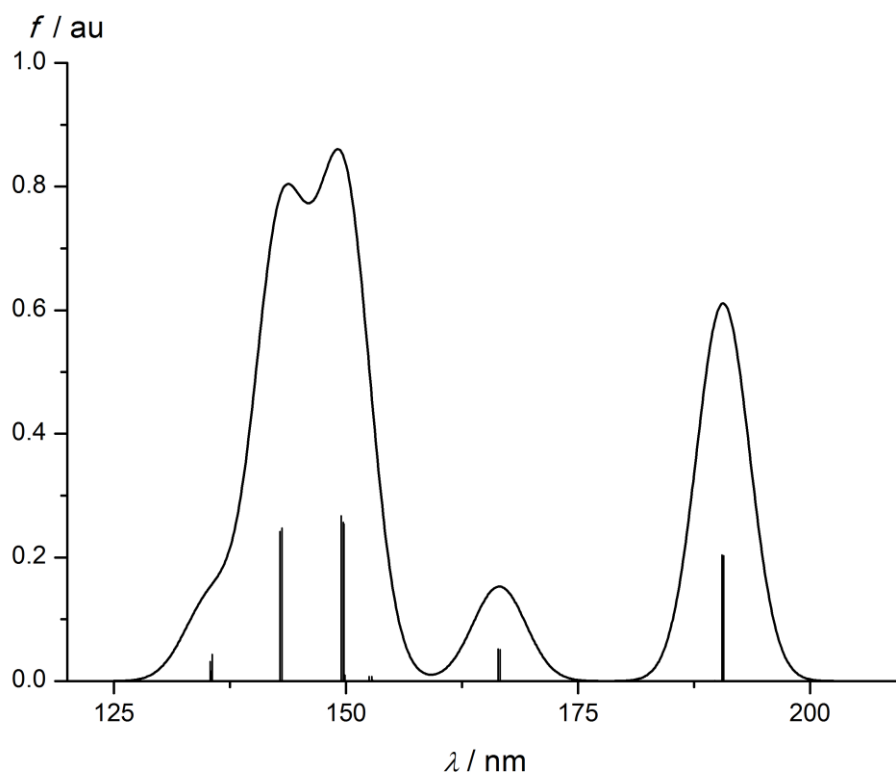


Figure S15. Calculated absorption spectrum of $(\text{ZnCl}_4)^{2-}$ (TD-DFT, oscillator strengths and fitted spectrum, FWHM = 2500 cm^{-1}).

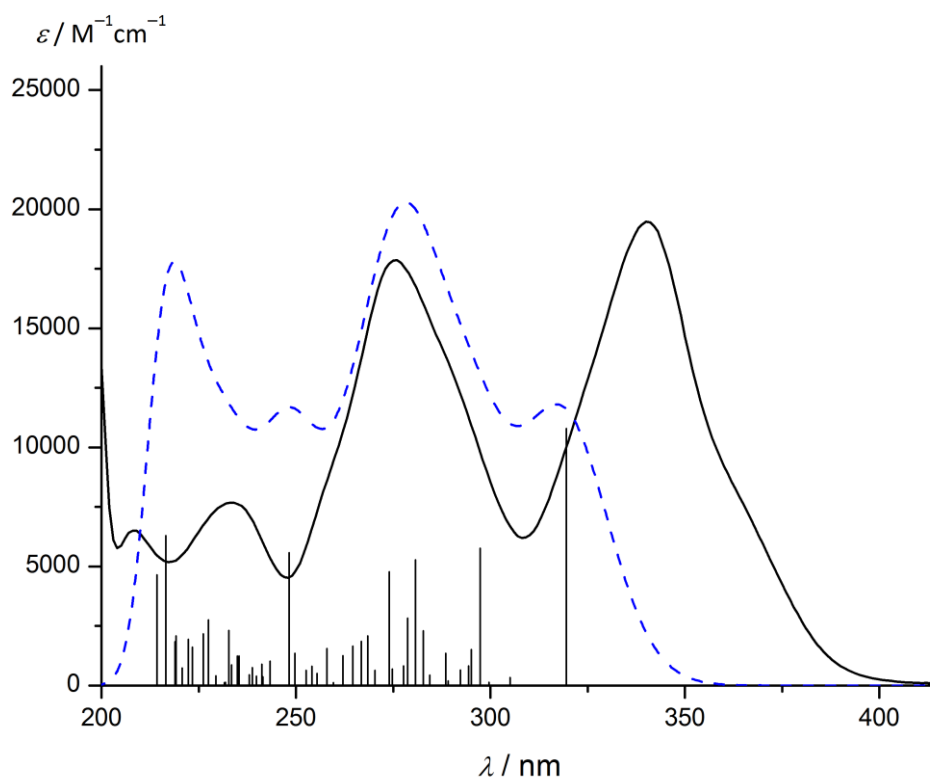


Figure S16. UV-VIS spectrum of **9** in CH_3CN (black line), calculated (TD-DFT, 50 excitations) oscillator strengths and simulated spectrum (blue dashed line, FWHM = 2500 cm^{-1}).

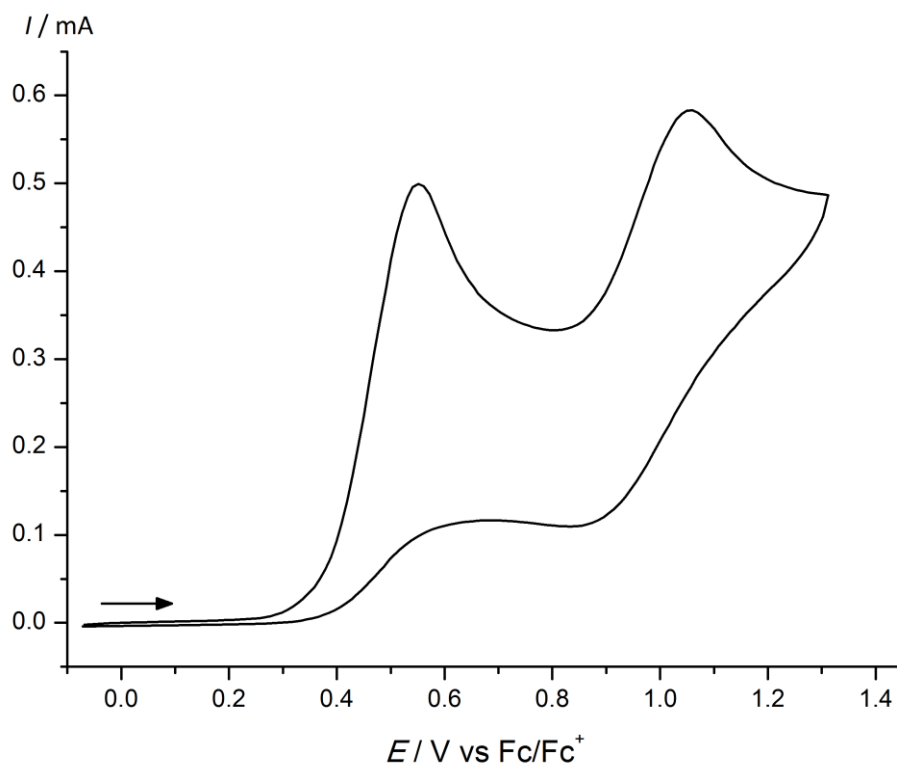


Figure S17. Cyclic voltammogram of ddpd in 0.1 M $(n\text{Bu}_4\text{N})(\text{PF}_6)/\text{CH}_3\text{CN}$, Pt electrodes, referenced against ferrocene.

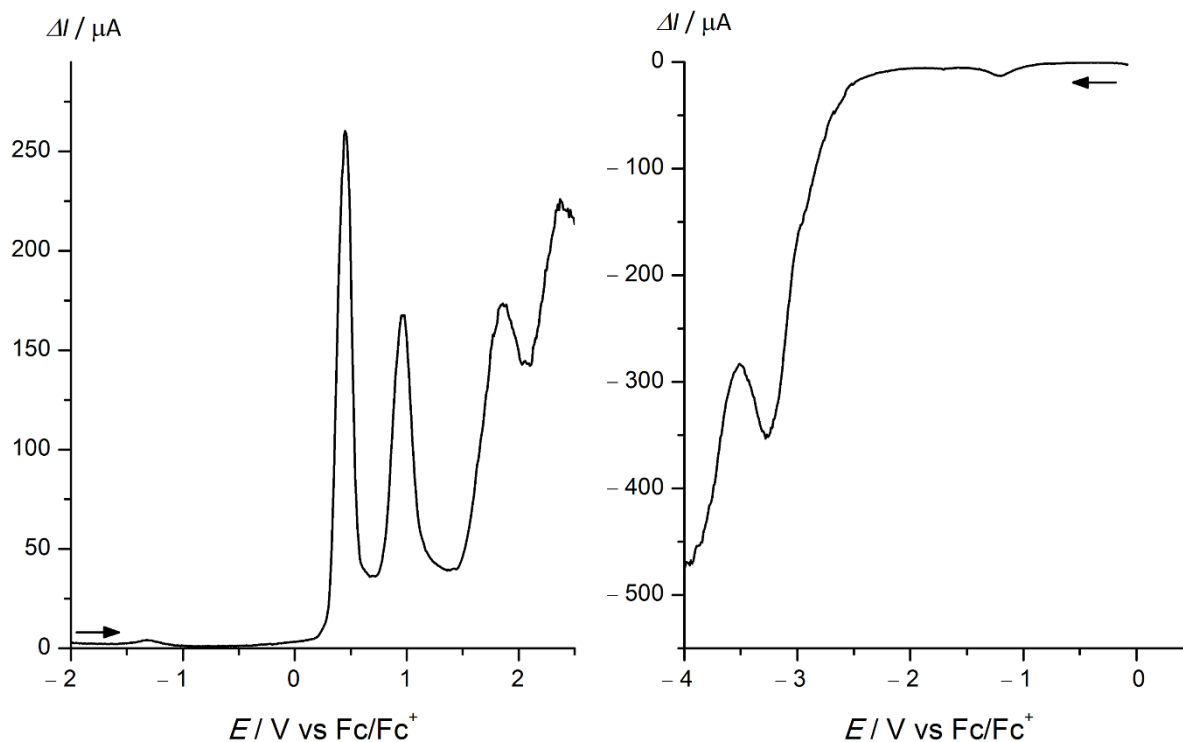


Figure S18. Square wave voltammograms of ddpd in 0.1 M $(n\text{Bu}_4\text{N})(\text{PF}_6)/\text{CH}_3\text{CN}$, Pt electrodes, referenced against ferrocene.

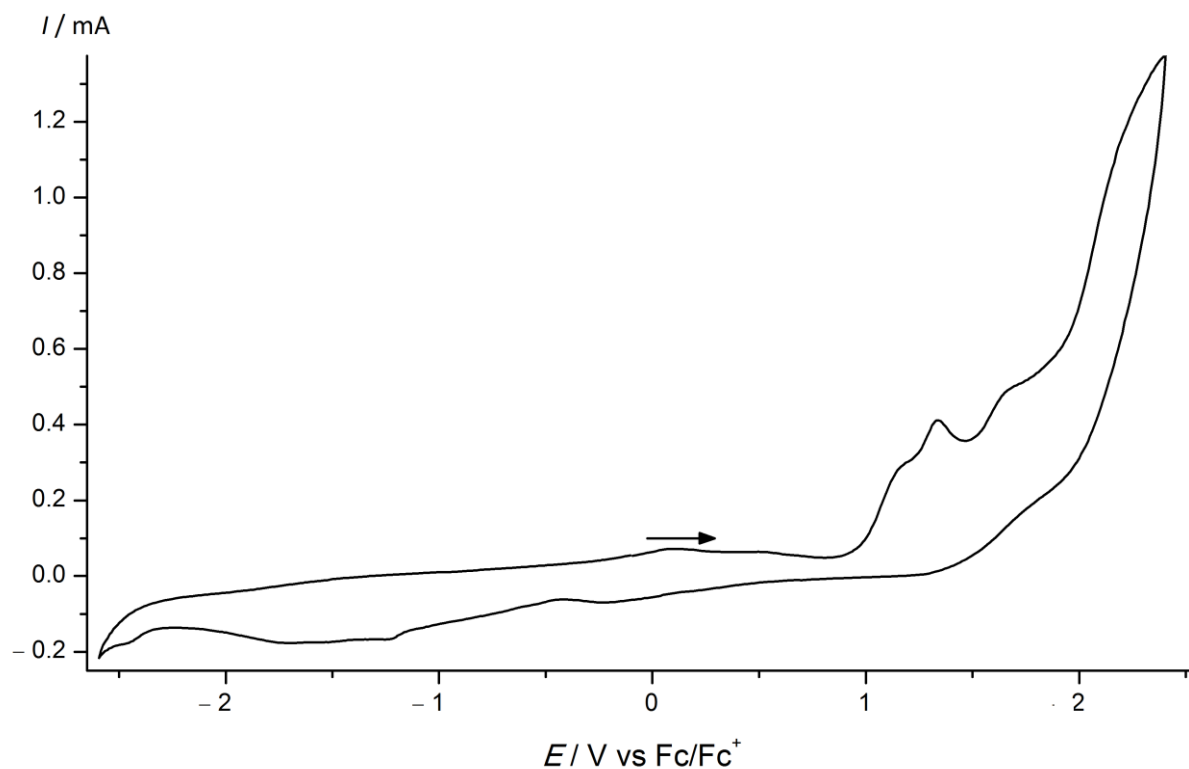


Figure S19. Cyclic voltammogram of **8(BF₄)₂** in 0.1 M (*n*Bu₄N)(PF₆)/CH₃CN, Pt electrodes, referenced against ferrocene.

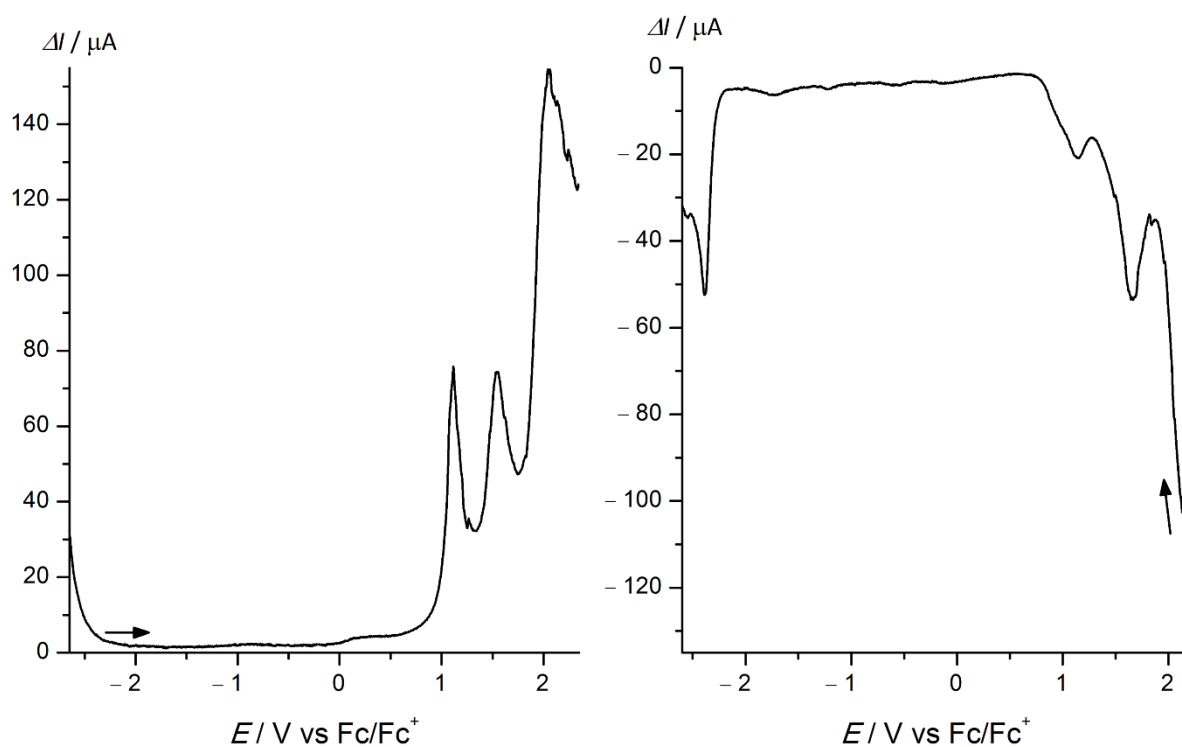


Figure S20. Square wave voltammograms of **8(BF₄)₂** in 0.1 M (*n*Bu₄N)(PF₆)/CH₃CN, Pt electrodes, referenced against ferrocene.

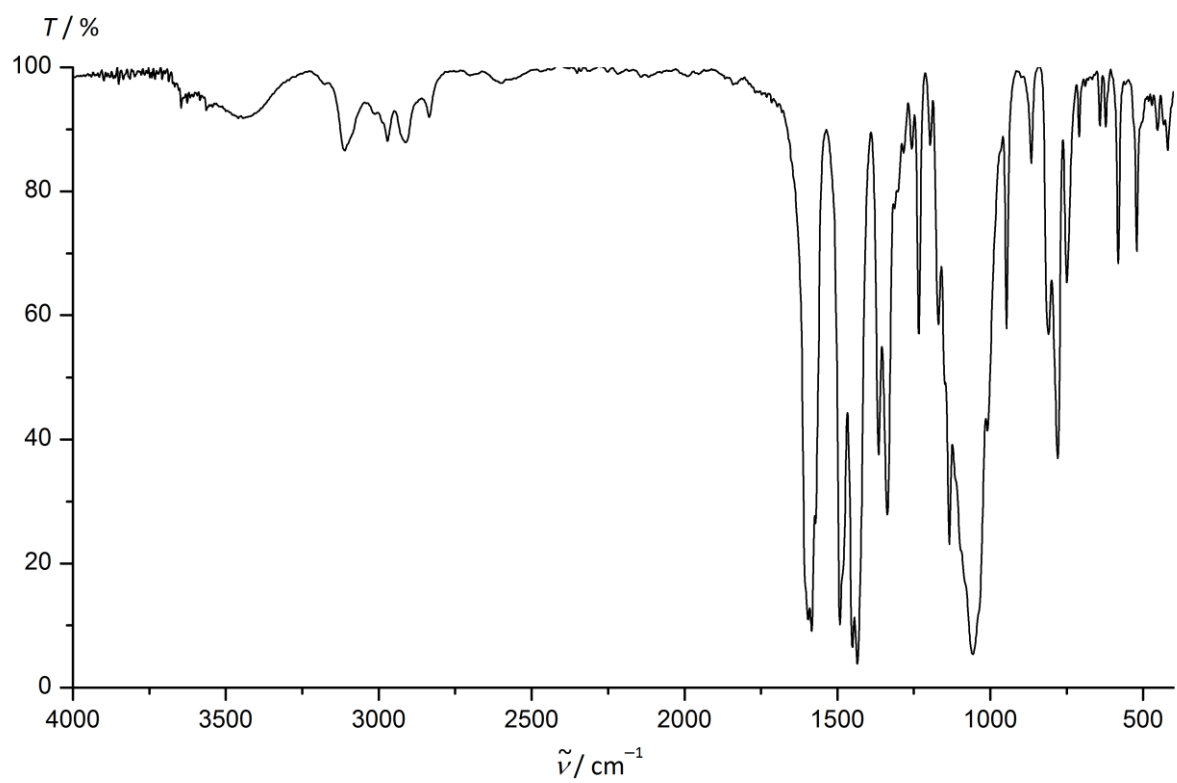


Figure S21. IR spectrum of **8(BF₄)₂** as KBr disk.

Table S1. DFT calculated Cartesian coordinates of **8²⁺**.

C	1.14888586352742	2.84423389071681	0.17786878508352
C	1.18283227175888	4.23666205422362	0.18144323677078
C	-0.00009135542087	4.93039970507246	-0.00077034346710
C	-1.18297957235486	4.23656077353748	-0.18281829466872
C	-1.14896576409907	2.84413180944266	-0.17891504914059
N	-0.00002321448935	2.16766191432941	-0.00044131515217
H	2.10507436291635	4.76651343914209	0.35299649350112
H	-2.10524355719982	4.76633032042069	-0.35450504106824
C	1.61077329860535	-0.65658476414551	2.48826753147402
C	2.72481040815101	-0.78688404174255	3.28739629260820
C	3.78358677283146	0.09138552829487	3.06960637447966
C	3.67759214467842	1.06164533450915	2.09177385692617
C	2.50209085243850	1.13921561278900	1.33053004441602
N	1.50534434537859	0.26600129043972	1.52053747704266
H	4.67807640380560	0.03633452240396	3.67467838785707
H	0.76145850218919	-1.31661777393191	2.59513495257478
H	2.76591082125151	-1.54598320056014	4.05375546836523
H	4.47648905383340	1.77030428999630	1.95048415754620
C	-2.50207089606930	1.13869169166645	-1.33108471596794
C	-3.67749892217649	1.06090898689952	-2.09242400924497
C	-3.78343264330202	0.09030369437643	-3.06991771925648
C	-2.72466605411051	-0.78807976457245	-3.28730134173495
C	-1.61069941480153	-0.65753882619760	-2.48811460933202
N	-1.50533595999953	0.26537938134374	-1.52069370743361
H	-4.67786182549419	0.03507387504090	-3.67506172331862
H	-4.47637808346672	1.76965549390785	-1.95146653472013
H	-2.76572509967918	-1.54744924911304	-4.05339511181307
H	-0.76139050159575	-1.31762857163530	-2.59467977128779
C	1.14885097628337	-2.84424131925075	-0.17790129644833
C	1.18276345570968	-4.23666755149193	-0.18160549817397
C	-0.00018082031321	-4.93039348655303	0.00051215755694
C	-1.18305368820698	-4.23654328606221	0.18260144070160
C	-1.14901217691145	-2.84411519449001	0.17882310205948
N	-0.00004749673283	-2.16765563364405	0.00044044248607
H	2.10499684316707	-4.76652438460790	-0.35318940453953
H	-2.10532975774396	-4.76631294223498	0.35421939279234
C	1.61087129853936	0.65658276176034	-2.48820959347387
C	2.72495879414697	0.78691497299098	-3.28726109220918
C	3.78374213141743	-0.09132916877868	-3.06940095954062
C	3.67770183601995	-1.06160896605754	-2.09159349813421
C	2.50214507003408	-1.13921757572360	-1.33043639418803
N	1.50539655666540	-0.26601719239705	-1.52049791124941
H	4.67827597914255	-0.03624650894495	-3.67440567549517
H	0.76154843836186	1.31659842849190	-2.59512155808720
H	2.76610210547801	1.54602345255242	-4.05360824992325
H	4.47660654578999	-1.77024953618679	-1.95025924249904
C	-2.50208622283447	-1.13869568347595	1.33107502110250
C	-3.67748332988314	-1.06097279850328	2.09246579228993
C	-3.78343004447438	-0.09036485535105	3.06995458100208
C	-2.72469987985221	0.78807635623604	3.28728067870460
C	-1.61075104026013	0.65757621570899	2.48806588644426
N	-1.50537991712435	-0.26534528806348	1.52064993220760
H	-4.67783888356451	-0.03517159474467	3.67513315071964
H	-4.47633372531631	-1.76975949428654	1.95154373867198
H	-2.76577079191820	1.54745679494295	4.05336346510231
H	-0.76146752469703	1.31770303467795	2.59459747857094
N	2.34982795620961	-2.12506964648110	-0.34901223099644
C	3.57068457315495	-2.76494020790874	0.14826898363122
H	3.99848303515963	-3.48892777193161	-0.54873179814527
H	4.30947334042420	-1.99410107504661	0.35170388853944

H	3.34233768029288	-3.26921042491142	1.08207223506209
N	-2.34991375241636	-2.12482979821485	0.34990280917025
C	-3.57087389237159	-2.76470209669752	-0.14712358366197
H	-3.99862471747907	-3.48856530348816	0.55003413791563
H	-4.30964213633066	-1.99384605682280	-0.35056625252199
H	-3.34268505003265	-3.26911933524007	-1.08088592244191
N	2.34983609207133	2.12504282486115	0.34906908800979
N	-2.34987851892894	2.12484839542177	-0.34994196969475
C	3.57073357536397	2.76485990435987	-0.14817995292920
H	3.99850467352507	3.48888525100193	0.54879829753825
H	4.30951906647882	1.99399353292506	-0.35152014853323
H	3.34245291846695	3.26907338918251	-1.08202999302136
C	-3.57081828003720	2.76475243258611	0.14708997195145
H	-3.99859315014318	3.48857382913305	-0.55009686196789
H	-4.30958316673487	1.99391273247536	0.35061103956910
H	-3.34259084492166	3.26922718348570	1.08081221729201
H	-0.00011933794724	6.01151524594186	-0.00089835724428
H	-0.00023577611689	-6.01150885469324	0.00053628061920
Zn	-0.00004125571617	-0.00000712310593	0.00000346437029

Table S2. DFT calculated Cartesian coordinates of **9**.

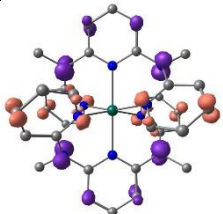
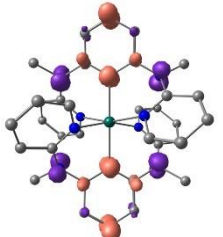
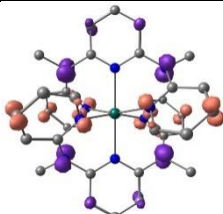
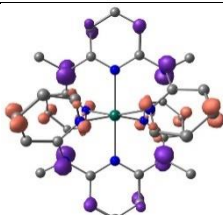
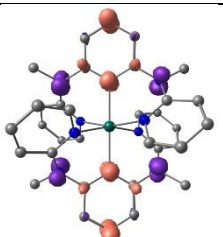
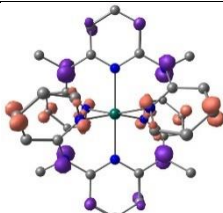
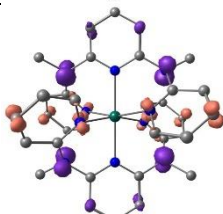
C	2.01453968766747	-1.88080384968230	-1.11461611684207
C	2.55351832936437	-3.09824831791946	-1.53985468481278
C	1.72435613897740	-4.20138364287224	-1.61372673750960
C	0.39073122069289	-4.08487901769171	-1.26050829109040
C	-0.07620349035814	-2.84747584886593	-0.82059537695667
N	0.72719363527215	-1.77651506749197	-0.75452620331344
H	3.58661356436425	-3.16133781530523	-1.84165186753803
H	-0.26781859567689	-4.93846183959343	-1.28720317807415
C	0.84795177109798	2.00038248717340	-2.17964521634433
C	1.74985824841444	2.85752443458704	-2.78243581450521
C	3.09061274280014	2.49068466208806	-2.78663227037288
C	3.47806937521498	1.29070385943383	-2.21771211666256
C	2.49738561503837	0.47784849373463	-1.63492691278444
N	1.21869450679181	0.85142346686408	-1.60910688176993
H	3.83449132332182	3.13122619643244	-3.24144456649682
H	-0.20823576660327	2.22456137358276	-2.10360543393349
H	1.41414890800382	3.78701189546676	-3.21738293073710
H	4.51164166156375	0.98622091209179	-2.24357288245404
C	-1.80138453785974	-2.27762793206564	0.82951268968501
C	-2.98232115112842	-2.73032290498005	1.43200781829924
C	-3.28816322737418	-2.27823078031219	2.70358350289213
C	-2.42378452105282	-1.40902710114924	3.35858186636791
C	-1.28575353552773	-1.00381627955786	2.68518731870159
N	-0.99525341632203	-1.41580033412061	1.44980309885646
H	-4.19751606350327	-2.61422071734960	3.18399000049810
H	-3.63754276526424	-3.42523877911292	0.93330770642157
H	-2.63427612162229	-1.04071081827400	4.35143385483283
H	-0.58052522029056	-0.29952694218302	3.10765656619002
N	2.83979120970871	-0.75154268236234	-1.06271206749634
C	4.22364383997380	-0.94891859425845	-0.65073262329748
H	4.90017773162573	-1.16826229744208	-1.48286158696892
H	4.56228375180468	-0.04934198098612	-0.14181782589119
H	4.26223928945145	-1.76902918388792	0.06022039362954
N	-1.42379239515326	-2.71612018397111	-0.44219042153521
C	-2.40977141139252	-3.42141928606776	-1.24802699514311
H	-2.61444548296897	-4.43745271647072	-0.89417522709495
H	-3.33702644569785	-2.85212528641997	-1.24356853993245
H	-2.05101758547498	-3.47191961320102	-2.27165439720412
H	2.11624362479822	-5.15246084724814	-1.94815915908127

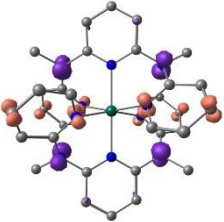
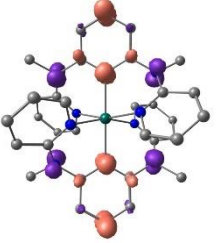
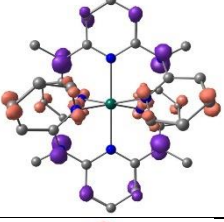
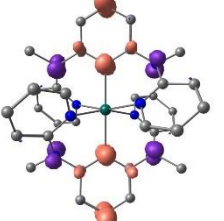
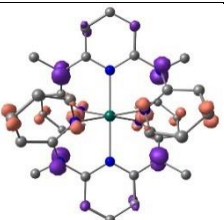
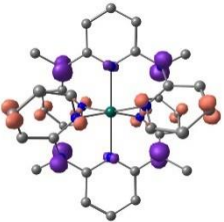
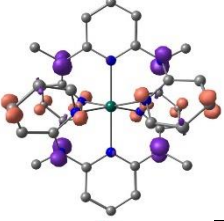
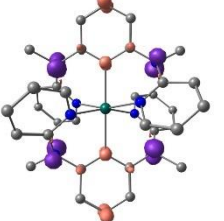
Zn	0.01649757740145	0.07294880072389	0.09199616586468
Cl	-1.97611435914099	0.81380505454696	-0.65579014847967
Cl	1.46882256006247	0.86450997611742	1.62710403808354

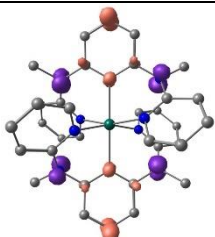
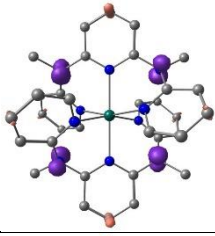
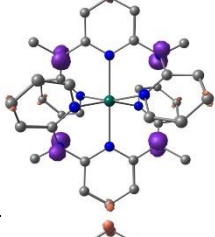
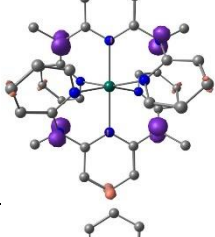
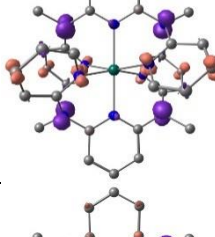
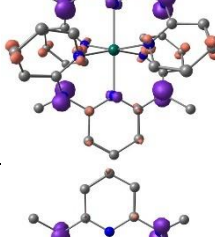
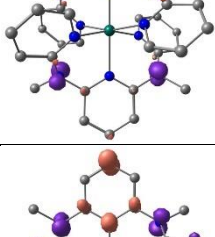
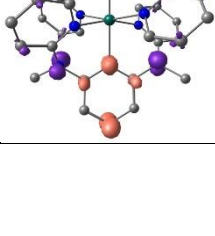
Table S3. DFT calculated Cartesian coordinates of $(\text{ZnCl}_4)^{2-}$.

Zn	-0.84924255993613	-0.05025423622777	-0.40694440196623
Cl	-1.01470323609521	0.24704097833007	1.92350843640124
Cl	-2.75944984292541	-1.17195518496072	-1.20473257466024
Cl	-0.68494449451016	2.05873627633422	-1.43730368174303
Cl	1.05721806046691	-1.32744429347579	-0.91296782003173

Table S4. TD-DFT calculated transitions of $\mathbf{8}^{2+}$, assignments and corresponding difference electron densities $\Psi_{ES} - \Psi_{GS}$ at a contour value of 0.005 a.u. (purple lobes indicate loss, orange lobes show increase of electron density upon excitation, hydrogen atoms omitted for clarity).

#	λ / nm	character	Difference electron density
1	310.0	$\pi\pi^*$	
2	306.4	$\pi\pi^*$	
3	305.6	$\pi\pi^*$	
4	303.0	$\pi\pi^*$	
5	299.3	$\pi\pi^*$	
6	297.3	$\pi\pi^*$	
7	292.8	$\pi\pi^*$	

8	291.4	$\pi\pi^*$	
9	287.8	$\pi\pi^*$	
10	287.7	$\pi\pi^*$	
11	286.2	$\pi\pi^*$	
12	286.0	$\pi\pi^*$	
13	277.8	$\pi\pi^*$	
14	277.0	$\pi\pi^*$	
15	273.9	$\pi\pi^*$	

16	273.8	$\pi\pi^*$	
17	272.4	$\pi\pi^*$	
18	270.0	$\pi\pi^*$	
19	269.5	$\pi\pi^*$	
20	268.7	$\pi\pi^*$	
21	268.5	$\pi\pi^*$	
22	266.2	$\pi\pi^*$	
23	262.8	$\pi\pi^*$	

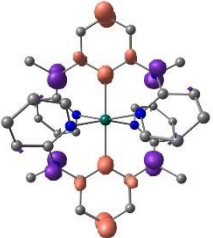
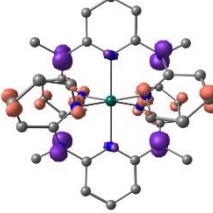
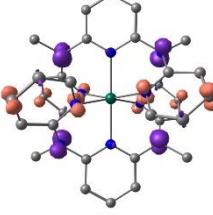
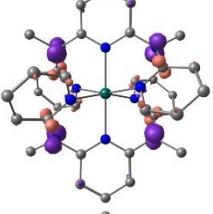
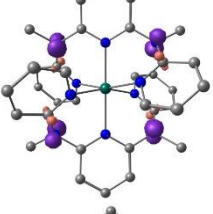
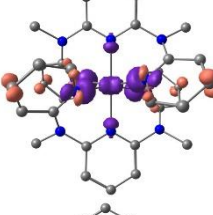
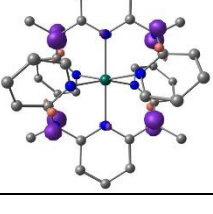
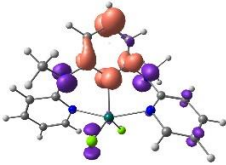
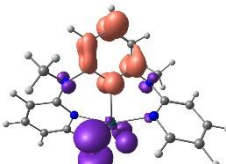
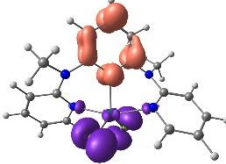
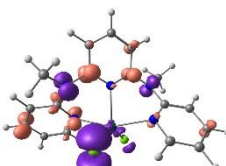
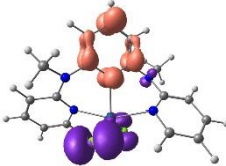
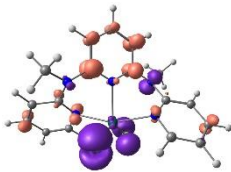
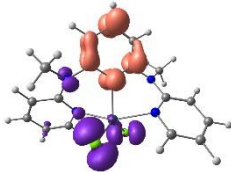
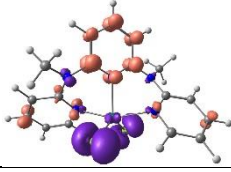
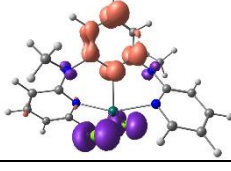
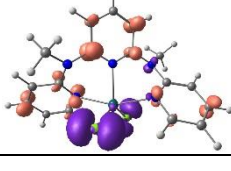
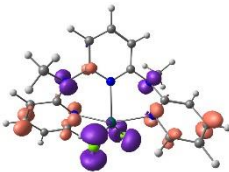
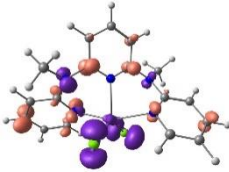
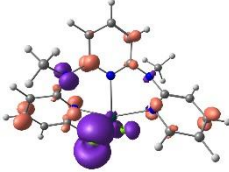
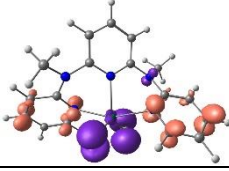
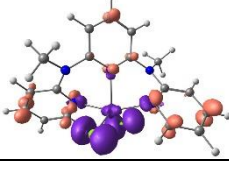
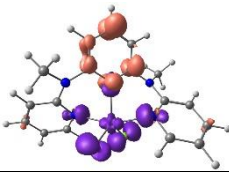
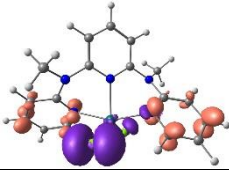
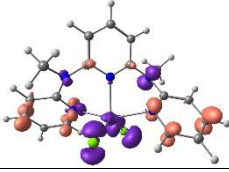
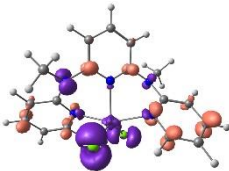
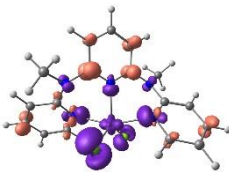
24	262.3	$\pi\pi^*$	
25	259.4	$\pi\pi^*$	
26	259.2	$\pi\pi^*$	
27	254.6	$\pi\pi^*$	
28	249.9	$\pi\pi^*$	
29	248.6	MLCT	
30	248.2	$\pi\pi^*$	

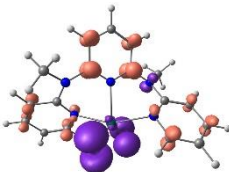
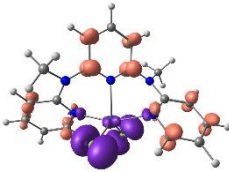
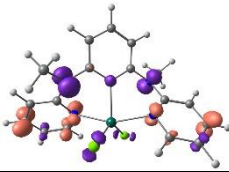
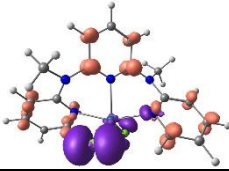
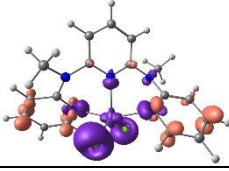
Table S5. TD-DFT calculated transitions of **9**, assignments and corresponding difference electron densities $\psi_{ES}-\psi_{GS}$ at a contour value of 0.005 a.u. (purple lobes indicate loss, orange lobes show increase of electron density upon excitation).

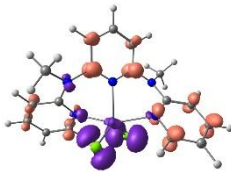
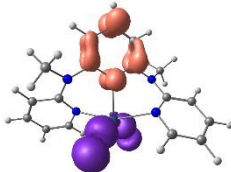
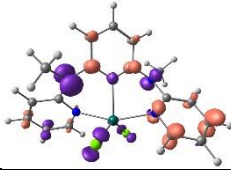
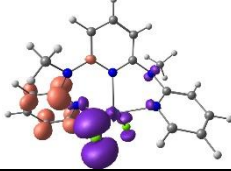
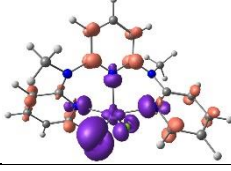
#	λ / nm	character	Difference electron density
1	319.5	LL'CT + $\pi\pi^*$	
2	305.0	LL'CT	
3	299.6	LL'CT	
4	297.4	LL'CT + $\pi\pi^*$	
5	295.1	LL'CT	

6	294.4	LL' CT	
7	292.2	LL' CT	
8	289.1	LL' CT	
9	288.5	LL' CT	
10	284.4	LL' CT	

11	282.7	LL'CT + $\pi\pi^*$	
12	280.7	LL'CT + $\pi\pi^*$	
13	278.7	LL'CT + $\pi\pi^*$	
14	277.6	LL'CT	
15	274.8	LL'CT	

16	274.0	LL' CT	
17	270.3	LL' CT	
18	268.4	LL' CT	
19	266.8	LL' CT + $\pi\pi^*$	
20	264.6	LL' CT + $\pi\pi^*$	

21	262.1	LL' CT	
22	259.6	LL' CT	
23	257.9	$\pi\pi^* + \text{LL}' \text{CT}$	
24	255.4	LL' CT	
25	254.1	LL' CT	

26	252.6	LL' CT	
27	249.7	LL' CT	
28	248.2	$\pi\pi^* + LL' CT$	
29	243.3	LL' CT	
30	241.5	LL' CT	

6.8 Supporting Information: Structure and reactivity of a mononuclear gold(II) complex

General considerations. All reactions were performed under an argon atmosphere unless otherwise noted. Dichloromethane was dried with CaH₂ and distilled prior to use. THF and toluene were distilled from potassium. All reagents were used as received from commercial suppliers (Acros, Sigma-Aldrich, ABCR). **[Au(TPP)][PF₆]** was prepared according to ref. ^[1]. NMR spectra were recorded on a Bruker DRX 400 spectrometer at 400.31 MHz (¹H) and 100.05 MHz (¹³C{¹H}). All resonances are reported in ppm vs the solvent signal as internal standard: CD₂Cl₂ (¹H, δ 5.32 ppm; ¹³C, δ 54.00 ppm); d₈-THF (¹H, δ 1.73, 3.58 ppm; ¹³C, δ 25.37, 67.57 ppm); d₈-toluene (¹H, δ 2.09, 6.98, 7.00, 7.09 ppm; ¹³C, δ 20.40, 125.49, 128.33, 129.24, 137.86 ppm).^[2] IR spectra were recorded with a BioRad Excalibur FTS 3100 spectrometer as KBr disks. UV/vis/near-IR spectra were recorded on a Varian Cary 5000 spectrometer by using 1.0 cm cells (Hellma, Suprasil). Emission spectra were recorded on a Varian Cary Eclipse spectrometer. X-band (9.4 GHz) CW EPR spectra (ca. 5 × 10⁻³ mM) were measured on a Miniscope MS 300 at 77 K cooled by liquid nitrogen in a finger Dewar (Magnettech GmbH, Berlin, Germany). *g* factors are referenced to external Mn²⁺ in ZnS (*g* = 2.118, 2.066, 2.027, 1.986, 1.946, 1.906). Q-band (33.9 GHz) CW EPR measurements were conducted on a Bruker EMX-plus spectrometer, using an ER5106QT resonator. All spectra were recorded at 50 K using a mercury iTC temperature controller (Oxford instruments). A microwave power of 1 mW, 100 KHz modulation frequency, modulation amplitude of 0.5 mT and 7858 points were used during measurements. A concentration of 2.5 mM was found to produce the best spectral shape. Samples were prepared by dissolving **[Au(TPP)][PF₆]** and Co(η^5 -C₅H₅)₂ in anhydrous dichloromethane under inert conditions. Simulations of EPR spectra were performed with EasySpin (v 5.0.0) for MatLab (R2015a).^[3] Variable-temperature magnetic susceptibility measurements were carried out with a Quantum Design MPMS-XL7 SQUID magnetometer in the temperature range 2–300 K under an applied magnetic field of 1 T. Experimental susceptibility data were corrected by the underlying diamagnetism using Pascal's constants. The temperature dependent magnetic contribution of the holder was experimentally determined and subtracted from the measured susceptibility data. FD⁺ mass spectra were recorded on a Thermo Scientific DFS with LIFDI upgrade (Linden CMS). ESI⁺ mass spectra were recorded on a Micromass Q-TOF-Ultima spectrometer. Elemental analyses were performed by the microanalytical laboratory of the chemical institutes of the University of Mainz. XAS spectral measurements were performed at beamline P65 of PETRA III (Hamburg, Germany) under ambient conditions at 293 K. A Si(111) double crystal monochromator was used for measurements at the Au L₃ edge (11.918 keV). The second monochromator crystal was tilt for optimal harmonic rejection. The spectra were recorded in transmission mode with ionization chambers filled with nitrogen. The individual pressures were adjusted to optimize the signal to noise ratio. Energy calibration was performed with a gold metal foil. The solid samples were handled in a glove box and embedded in an oxygen free boron nitride matrix and pressed into self-supporting pellets. The XANES spectra were analyzed by the peak fitting approach.^[4-8] The edge step in this process is modeled by an arctan function. Only the white line was adjusted after the rising edge, using a Gauss function. All parameters (energy, integral intensity and width) were allowed to float in the fit. Difference spectra were obtained without shifting the energy, followed by numerical integration using the program Athena. To determine the smooth part of the EXAFS spectra^[9], corrected for pre-edge absorption, a piecewise polynomial was used. It was adjusted in such a way that the low-*R* components of the resulting Fourier transform were minimal. After division of the background-subtracted spectrum by its smooth part, the photon energy was converted to photoelectron wave numbers *k*. The resulting $\chi(k)$ -function was weighted with *k*³. Single scattering data analysis was performed in *k*-space according to the curved wave formalism of the EXCURV98 program with XALPHA phase and amplitude functions.^[10] The mean free path of the scattered electrons was calculated from the imaginary part of the potential

(VPI set to -4.00). An amplitude reduction factor of 0.8 was used to reproduce the crystallographic coordination numbers in a free floating fit.

Crystal Structure Determination. Intensity data were collected with a Bruker AXS Smart1000 CCD diffractometer with an APEX II detector and an Oxford cooling system and corrected for absorption and other effects using Mo K_{α} radiation ($\lambda = 0.71073 \text{ \AA}$). The diffraction frames were integrated using the SAINT package, and most were corrected for absorption with MULABS^[11,12] The structures were solved by direct methods and refined by the full-matrix method based on F^2 using the SHELXTL software package.^[13,14] All non-hydrogen atoms were refined anisotropically, while the positions of all hydrogen atoms were generated with appropriate geometric constraints and allowed to ride on their respective parent carbon atoms with fixed isotropic thermal parameters.

Crystal data for Au(TPP): $C_{44}H_{28}AuN_4$ (788.51); $T = 173 \text{ K}$; purple plate; $0.20 \times 0.15 \times 0.05 \text{ mm}^3$; triclinic; $P\bar{1}$; $a = 6.1691(2) \text{ \AA}$; $b = 10.6043(4) \text{ \AA}$; $c = 12.4939(5) \text{ \AA}$; $\alpha = 97.4790(10)^\circ$; $\beta = 97.4530(10)^\circ$; $\gamma = 99.9250(10)^\circ$; $V = 788.51(5) \text{ \AA}^3$; $Z = 1$; $F(000) = 399$; $\rho = 1.705 \text{ g cm}^{-3}$; $\mu = 4.705 \text{ mm}^{-1}$; θ range $2.375\text{--}27.939^\circ$; index ranges $-8 \leq h \leq 8$, $-13 \leq k \leq 13$, $-16 \leq l \leq 16$; 9273 reflections collected; 3774 independent reflections; parameters 223; maximum/minimum transmission 1.35416/0.73982; goodness of fit on F^2 1.066; largest difference peak and hole $1.367/-0.006 \text{ e \AA}^{-3}$; $R_1(I > 2\sigma) = 0.0246$; $R_1(\text{all data}) = 0.0249$; $wR_2(I > 2\sigma) = 0.0569$; $wR_2(\text{all data}) = 0.0569$.

DFT calculations. These were carried out with the ORCA 3.0.2/DFT series of programs.^[15] Tight convergence criteria were chosen for all calculations (Keywords TightSCF and TightOpt). For geometry optimizations and energy calculations, the B3LYP formulation^[16] of density functional theory was used employing the def2-TZVPP basis set with the zeroth order regular approximation (ZORA)^[17], or Schwerdtfeger's ECP basis set for gold,^[18] the RIJCOSX approximation^[19,20], at GRID7 for C, H, N and an even higher accuracy for the gold atom (Keyword SpecialGridIntAcc 20). To account for solvent effects, a conductor-like screening model (COSMO CH_2Cl_2) modelling dichloromethane was used in all calculations.^[21] Grimme's empirical dispersion correction D3(BJ) was employed.^[22,23] No symmetry constraints were imposed on the molecules. Transition state searches were performed at the B3LYP/def2-SVP level (ZORA, COSMO CH_2Cl_2).^[24] The presence of energy minima of the ground states and saddle points for transition states was checked by numerical frequency calculations for the def2-SVP optimized geometries (ZORA, COSMO CH_2Cl_2). The approximate free energies at 298 K were obtained through thermochemical analysis of the frequency calculation, using the thermal correction to Gibbs free energy as reported by ORCA 3.0.2. The calculation of the g tensor and the time-dependent DFT calculations were done at the B3LYP, def2-TZVPP, ZORA, D3(BJ), COSMO (CH_2Cl_2) level using the optimized geometry, yet simplified by replacing the Ph groups by hydrogen atoms.

Figure S1. Photograph of **Au(TPP)** sublimed onto the cold finger of the sublimation apparatus.



Figure S2. LIFDI mass spectrum of **Au(TPP)** in THF; inset shows calculated (calcd. for $C_{44}H_{28}N_4Au$) and experimental isotopic pattern.

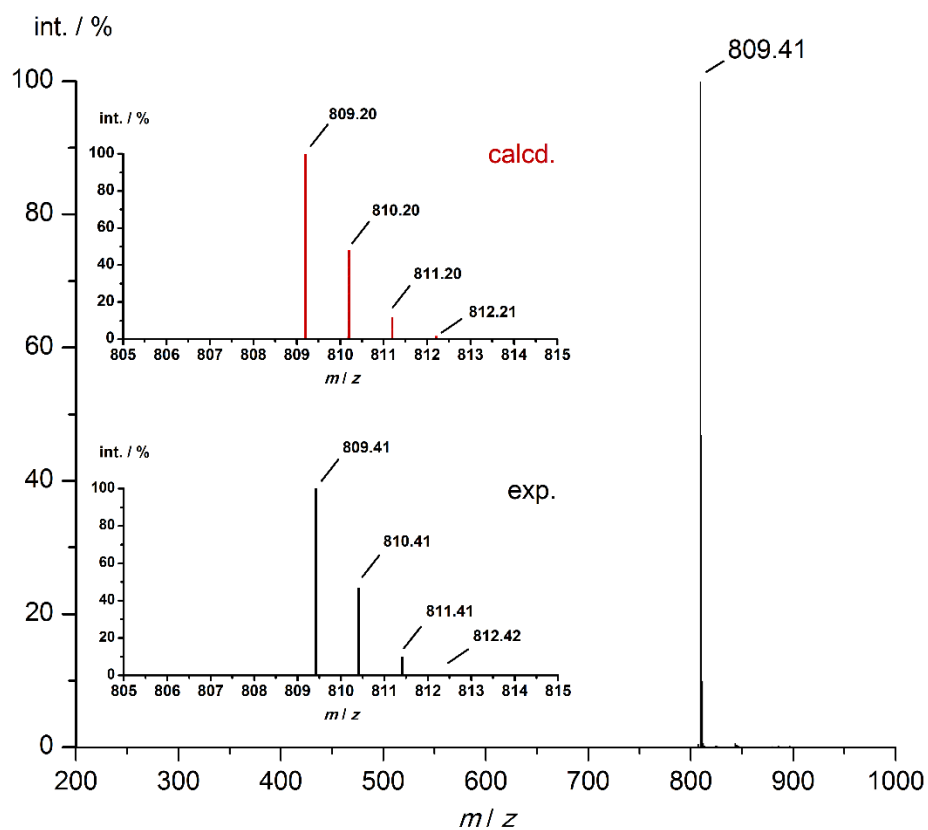


Figure S3. UV/Vis spectra of **Au(TPP)** (red), **[Au(TPP)][PF₆]** (black) and **Cu(TPP)** (blue) in THF. Inset shows expanded low energy region.

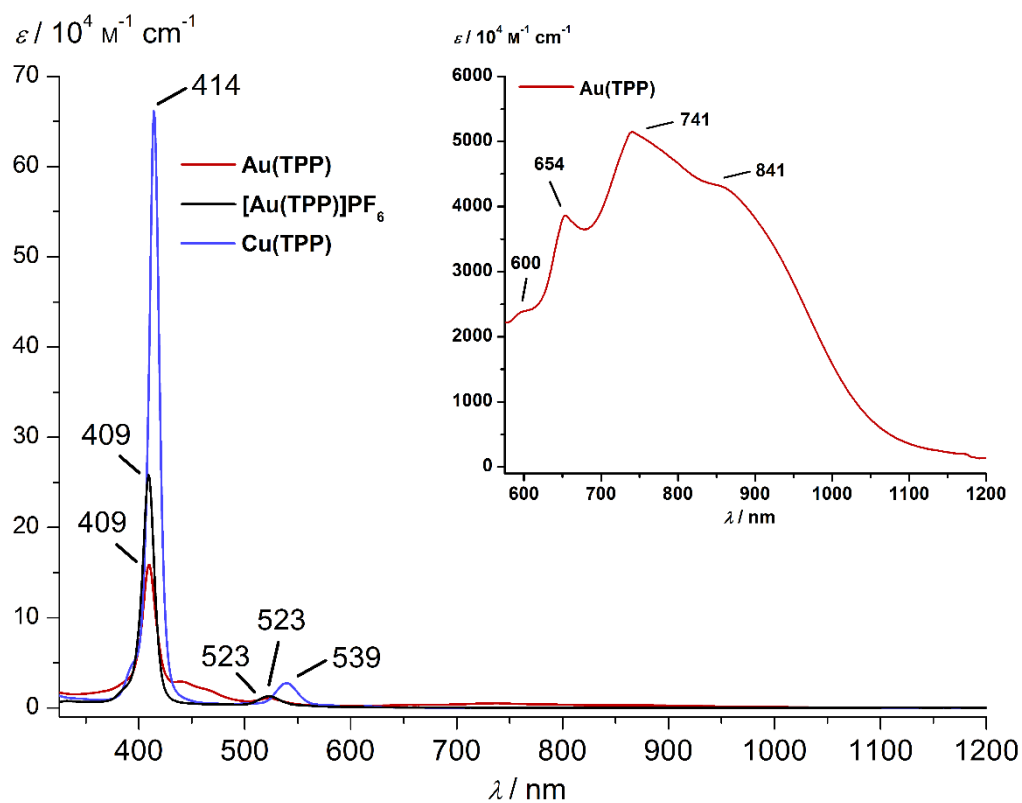


Figure S4. IR spectra of **Au(TPP)** (red) and **[Au(TPP)][PF₆]** (black) as KBr disks.

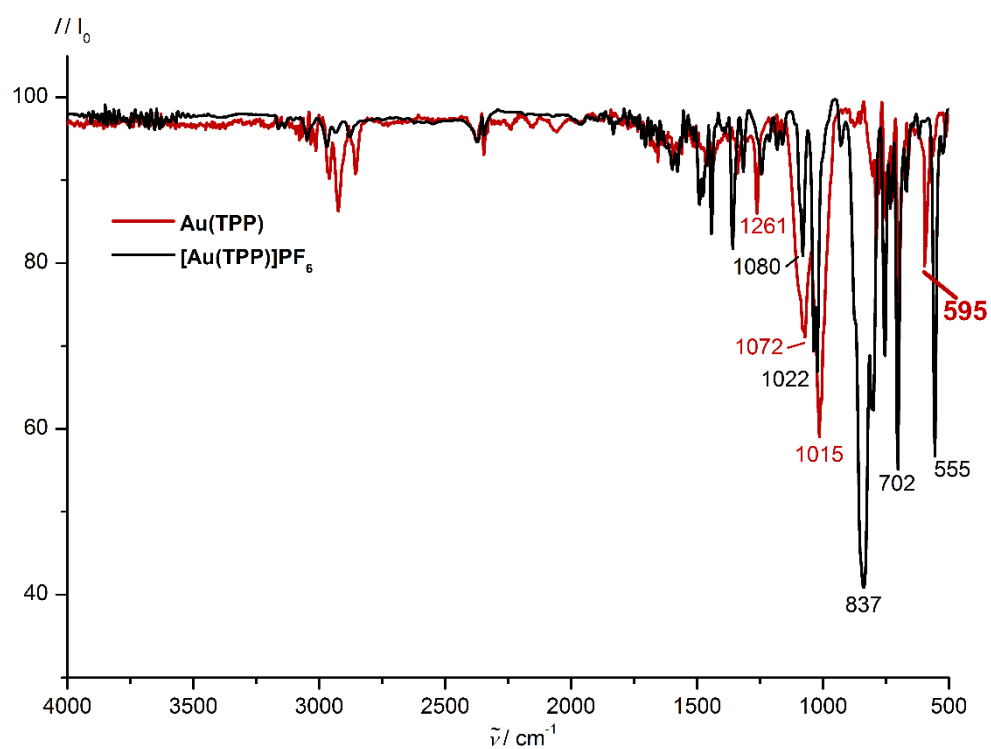


Figure S5. IR spectra of **Au(TPP)** (red) and **Cu(TPP)** (blue) as KBr disks.

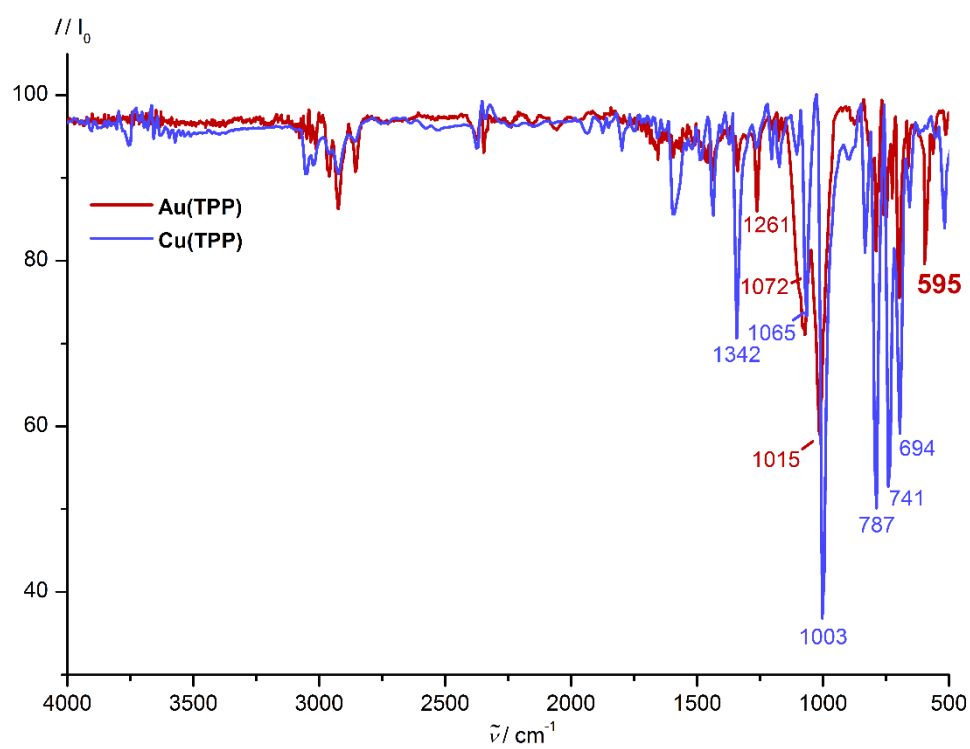


Figure S6. Magnetic susceptibility versus temperature plot of **Au(TPP)**; fit to a Hamiltonian with $g = 2.073$ and $zJ = -1.09 \text{ cm}^{-1}$.

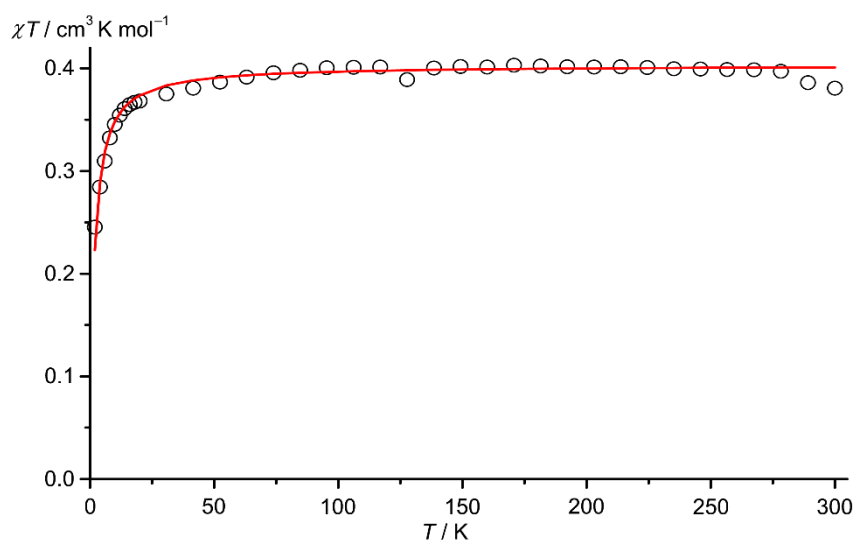


Figure S7. ^1H NMR spectrum of **Au(TPP)** in CD_2Cl_2 at 293 K. Asterisk denotes residual solvent resonance.

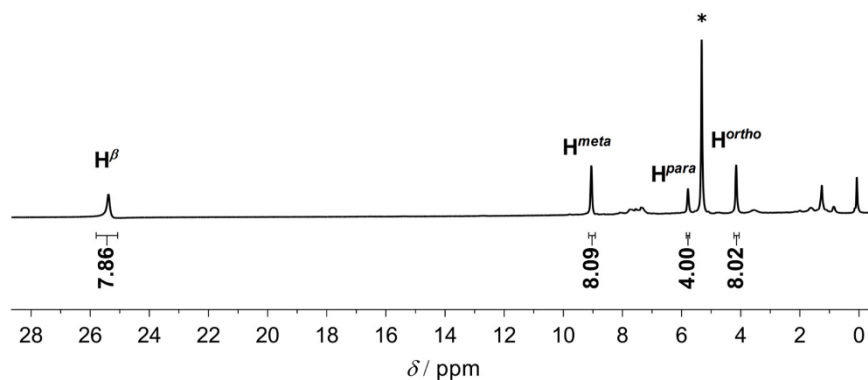


Figure S8. ^1H NMR spectrum of **Au(TPP)** in d_8 -THF at 293 K. Asterisks denote residual solvent resonances.

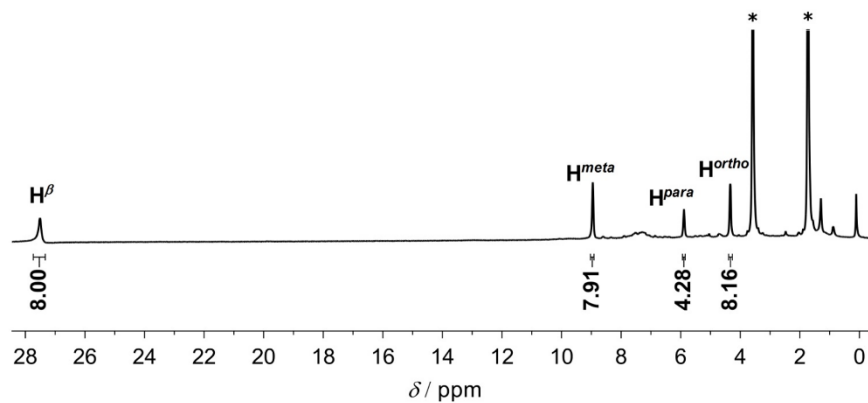


Figure S9. ^1H NMR spectrum of **Au(TPP)** in d_8 -toluene at 293 K. Asterisks denote residual solvent resonances.

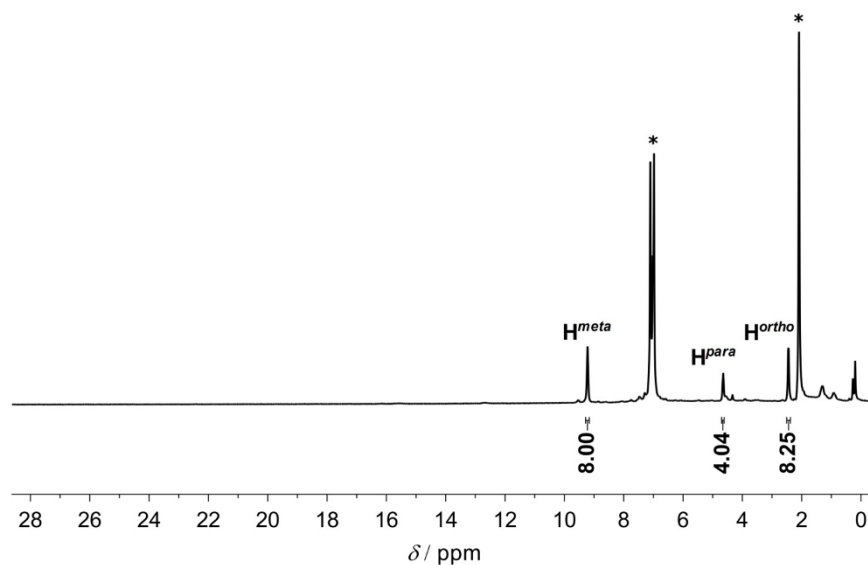


Figure S10. $^1\text{H}^1\text{H}$ COSY of **Au(TPP)** in CD_2Cl_2 at 293 K. Asterisk denotes residual solvent resonance.

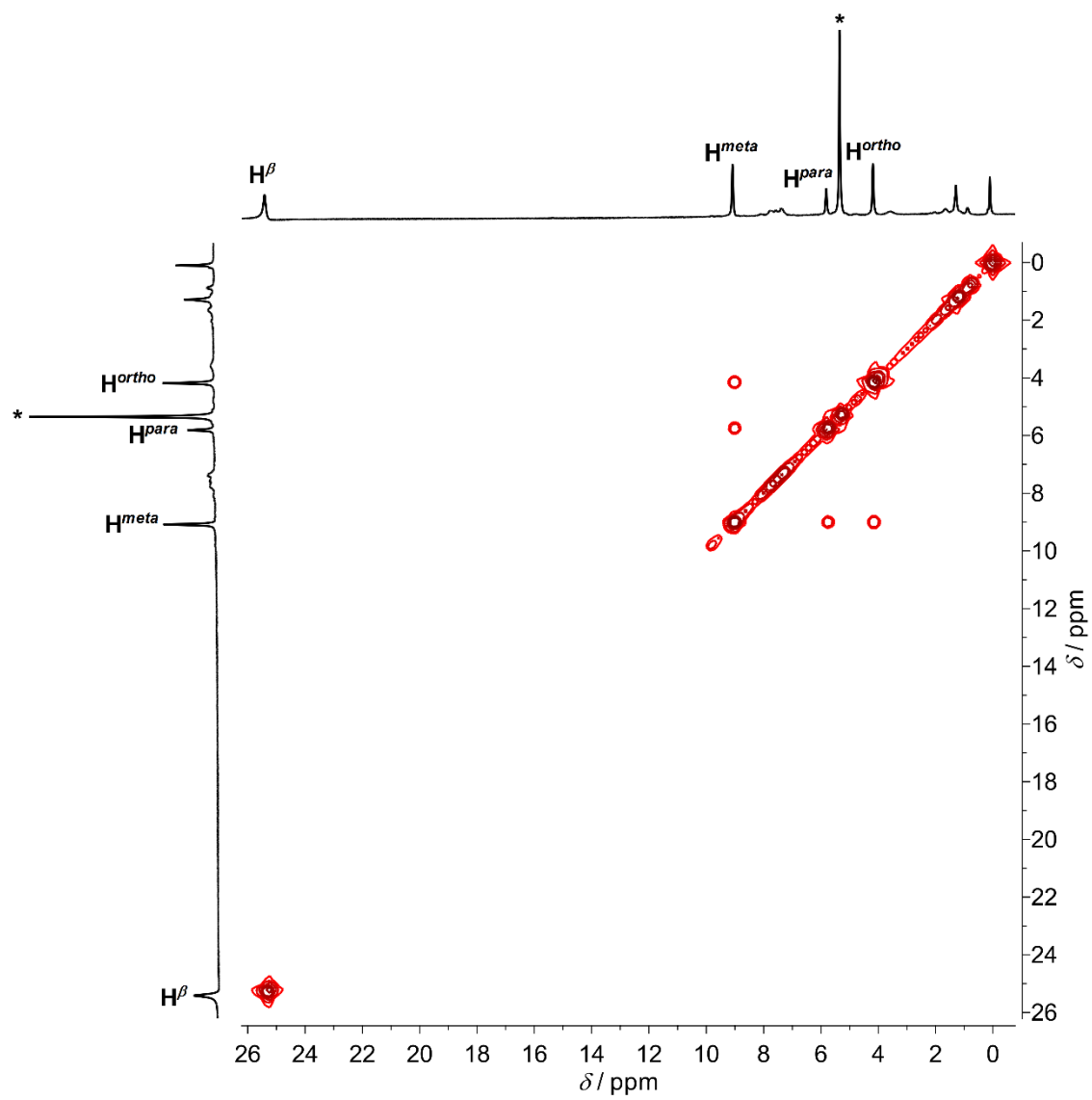


Figure S11. $^1\text{H}^1\text{H}$ COSY of **Au(TPP)** in d_8 -THF at 293 K. Asterisks denote residual solvent resonances.

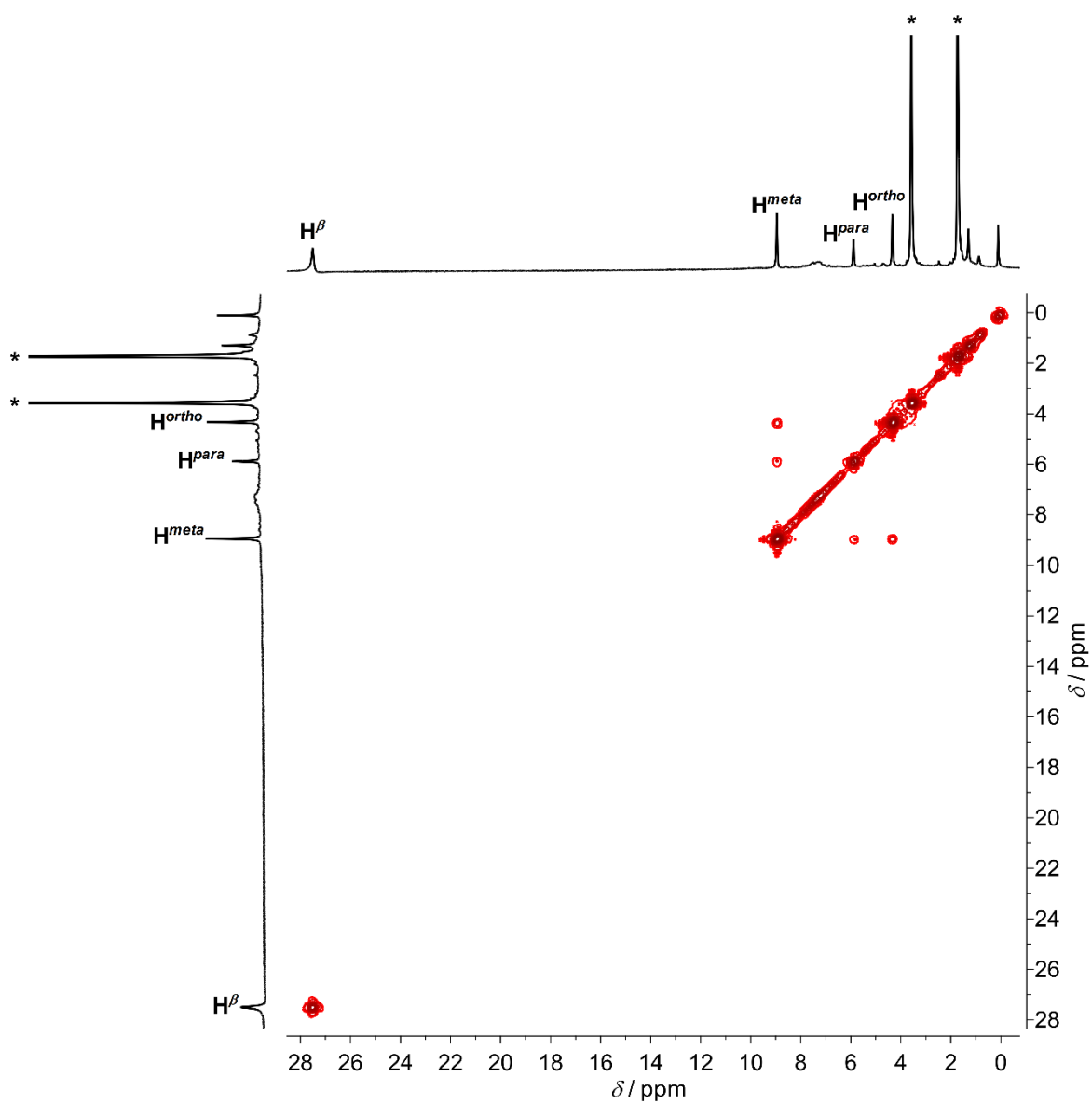


Figure S12. $^1\text{H}^1\text{H}$ COSY of **Au(TPP)** in d_8 -toluene at 293 K. Asterisks denote residual solvent resonances.

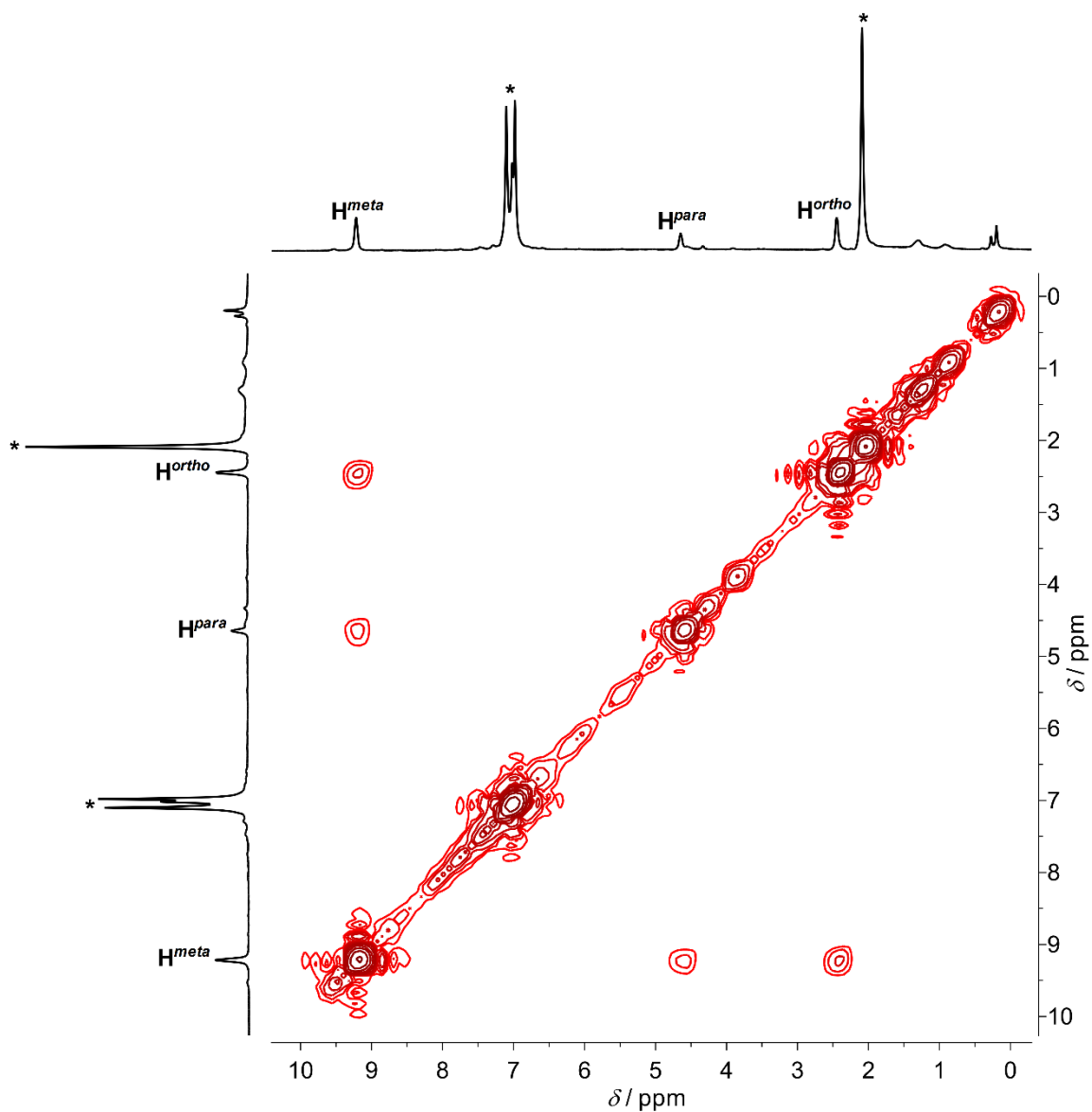


Figure S13. $^{13}\text{C}\{^1\text{H}\}$ NMR spectrum of **Au(TPP)** in d_8 -THF at 293 K. Asterisks denote residual solvent resonances.

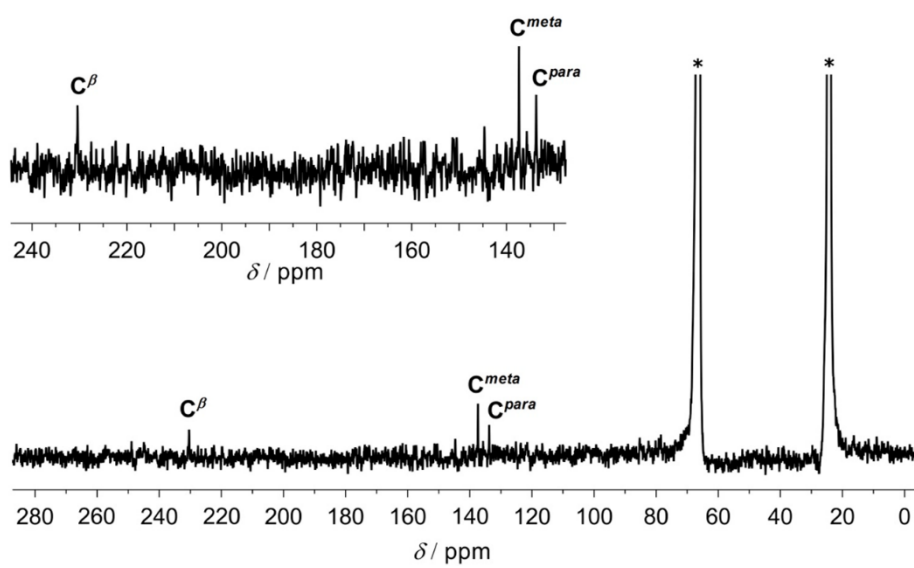


Figure S14. $^1\text{H}^{13}\text{C}$ COSY of **Au(TPP)** in $\text{d}_8\text{-THF}$ at 293 K. Asterisks denote residual solvent resonances.

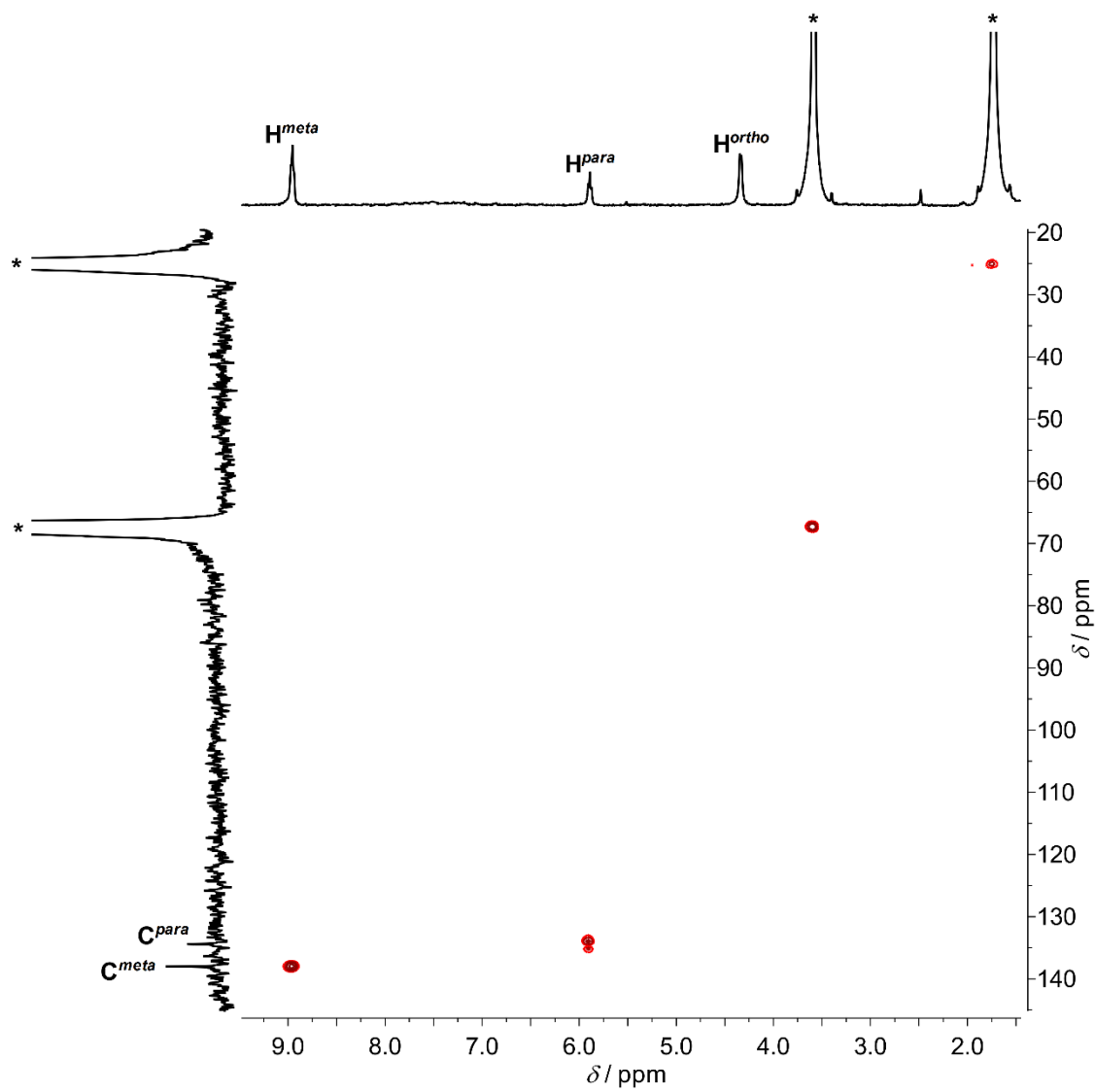


Figure S15: XANES deconvolution of **Au(TPP)** (left, red) and **[Au(TPP)][PF₆]** (right, black).

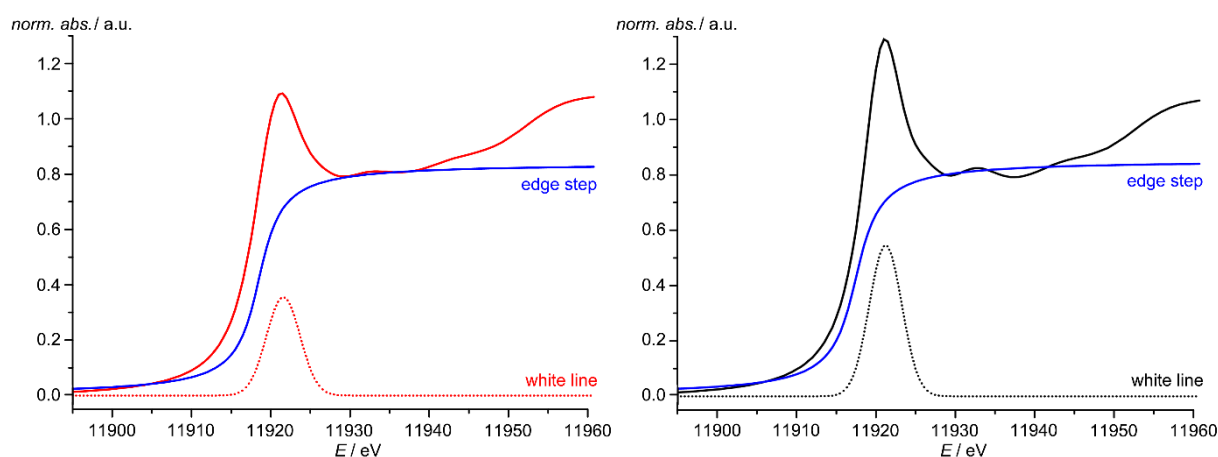


Figure S16. Experimental Fourier transformed EXAFS functions of **[Au(TPP)][PF₆]** (top, black) and **Au(TPP)** (bottom, red) and the calculated functions according to the structural parameters given in Table S1.

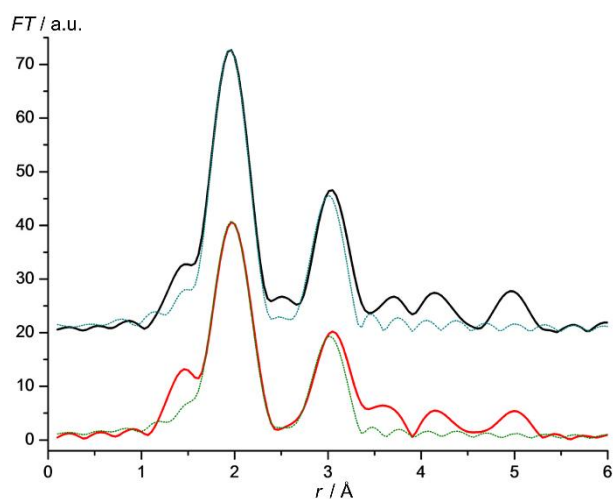


Table S1. Structure parameters extracted from analysis of the experimental EXAFS data.

	Abs-Bs ^a	$N(\text{Bs})^b$	$R(\text{Abs-Bs})^c$ [Å]	σ^d [Å ²]	E_f^e [eV] R [%] ^f
Au(TPP)	Au-N	3.9 ± 0.4	2.031 ± 0.020	0.009 ± 0.001	-0.289
	Au-C	4.5 ± 0.5	3.038 ± 0.031	0.006 ± 0.001	27.88
[Au(TPP)][PF₆]	Au-N	4.3 ± 0.4	2.010 ± 0.020	0.007 ± 0.001	-0.384
	Au-C	4.6 ± 0.5	3.025 ± 0.030	0.003 ± 0.001	25.51

^a Abs = X-ray absorbing atom, Bs = backscattering atom. ^b N = Number of neighbor backscattering atoms. ^c Distance between Abs and Bs. ^d σ = Debye-Waller like factor. ^e E_f = Shift between experimental and theoretical EXAFS function. ^f R = Quality of fit.

Figure S17. Molecular structure **Au(TPP)** by DFT calculation (B3LYP, ECP basis set, COSMO CH₂Cl₂) including side view along the N1-Au1-N1a axis. Relevant distances are given in Å, relevant angles are given in deg (H atoms omitted).

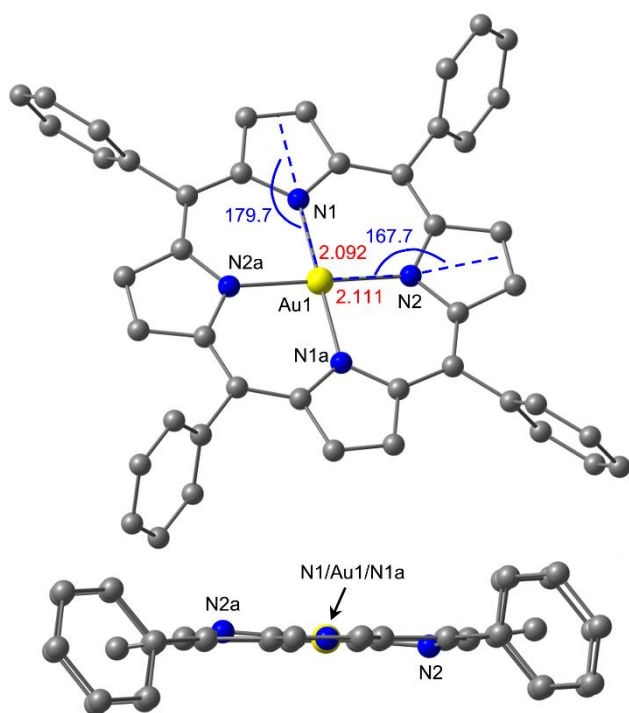


Figure S18. Spin density plots of **Au(TPP)** (in green) calculated by DFT, a) B3LYP, def2-TZVPP, ZORA, D3(BJ), COSMO CH₂Cl₂ and b) B3LYP, ECP, COSMO CH₂Cl₂ (isosurface value in green at 0.01 a.u.; H atoms omitted).

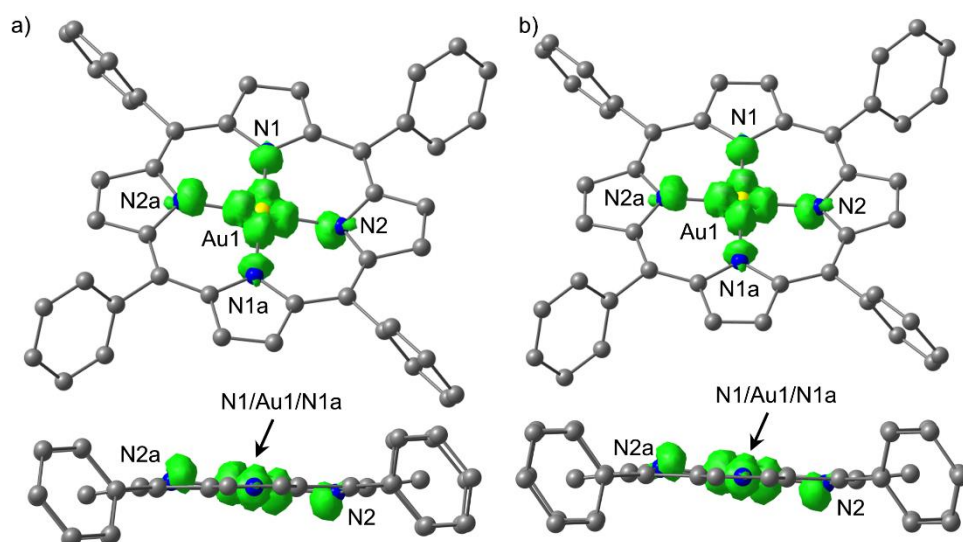


Figure S19. DFT calculated transition state between SOJT isomers of **Au(TPP)** (negative frequency 112 cm^{-1}) (B3LYP, def-SVP, ZORA, COSMO CH_2Cl_2 ; scaled displacement vectors shown; relevant distances are given in Å, relevant angles are given in deg.).

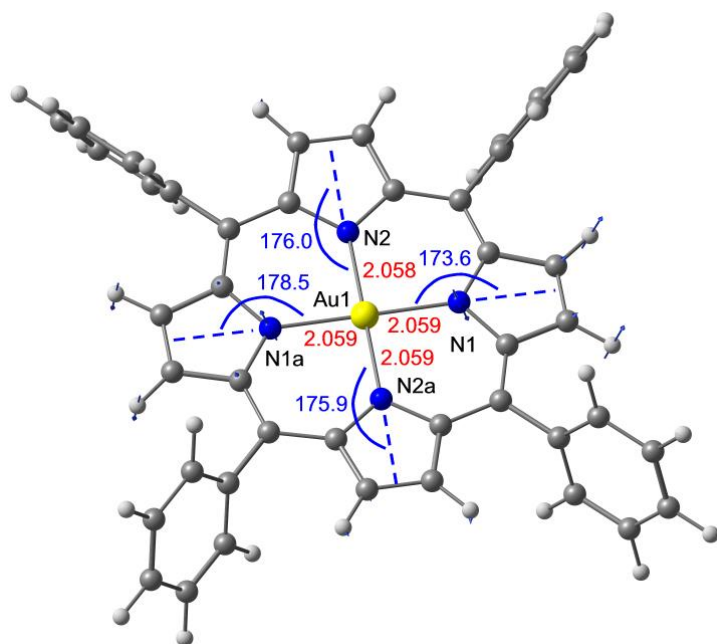


Figure S20. Variable-temperature ^1H NMR spectra of **Au(TPP)** in CD_2Cl_2 (248 – 298 K). Asterisk denotes residual solvent resonance.

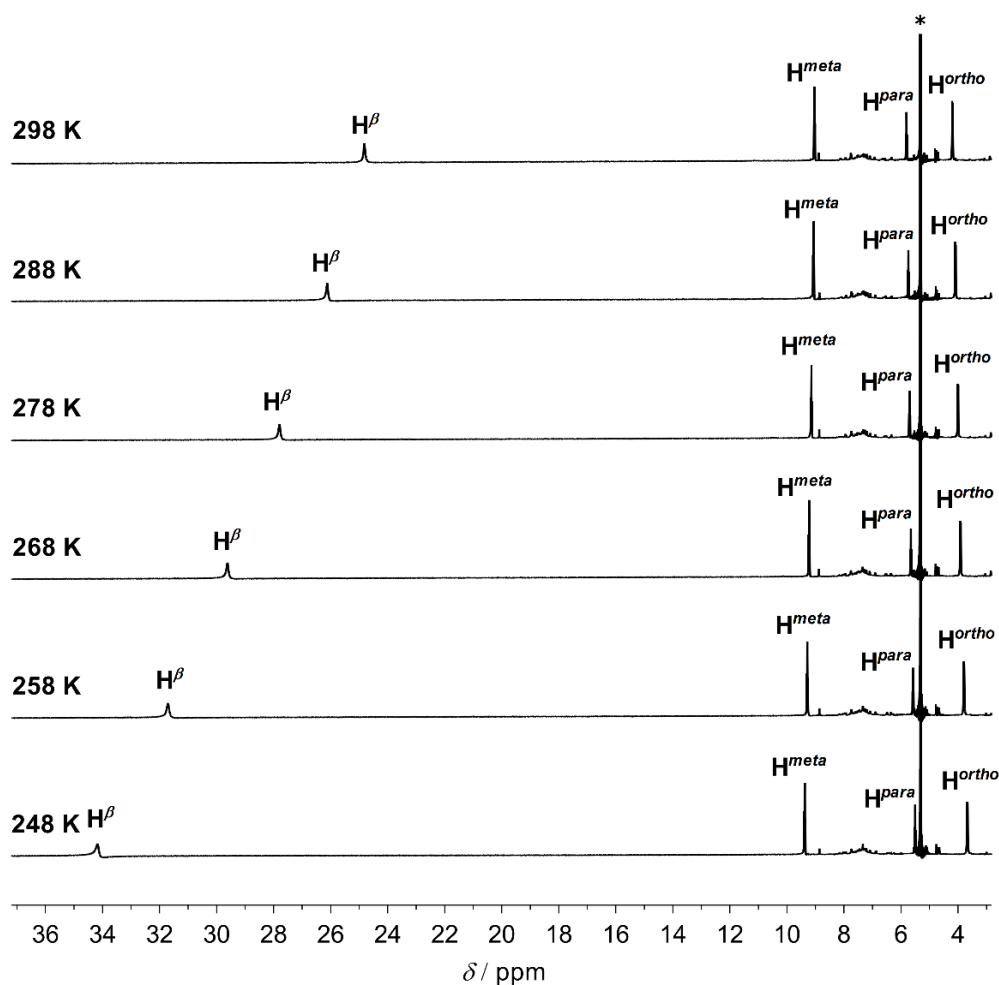


Figure S21. Plot of $\delta(\text{H}^\beta)$ of **Au(TPP)** vs. T^{-1} .

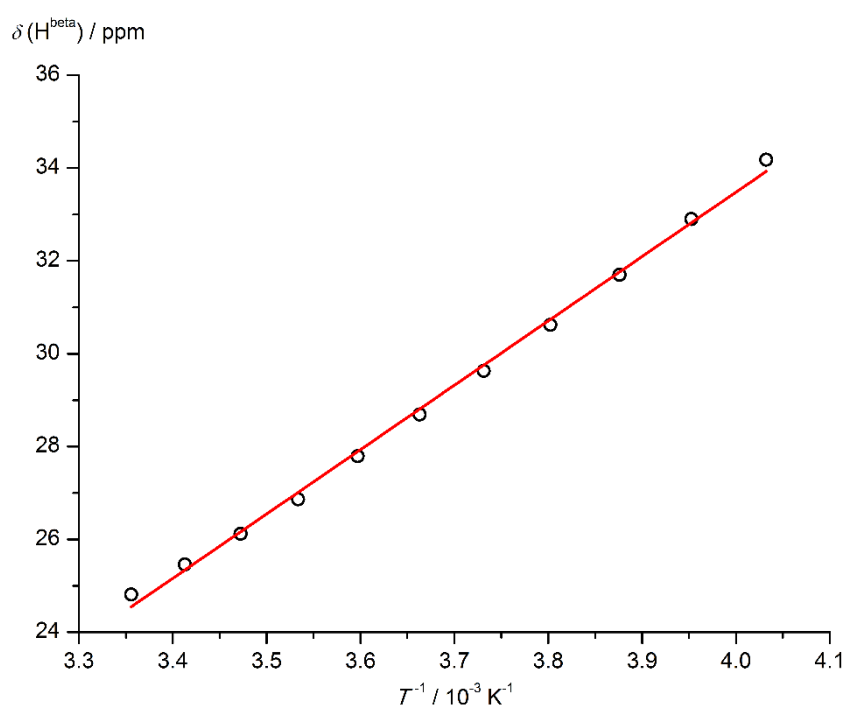


Figure S22. TD-DFT (B3LYP, def2-TZVPP, ZORA, COSMO CH₂Cl₂, D3(BJ)) calculated UV/Vis spectrum of **Au(P)** including electron density difference maps of relevant excited states (isosurface values 0.005 a.u.; purple lobes indicate loss, orange lobes show increase of electron density upon excitation, H atoms omitted). The phenyl rings of optimized **Au(TPP)** have been replaced by hydrogen atoms.

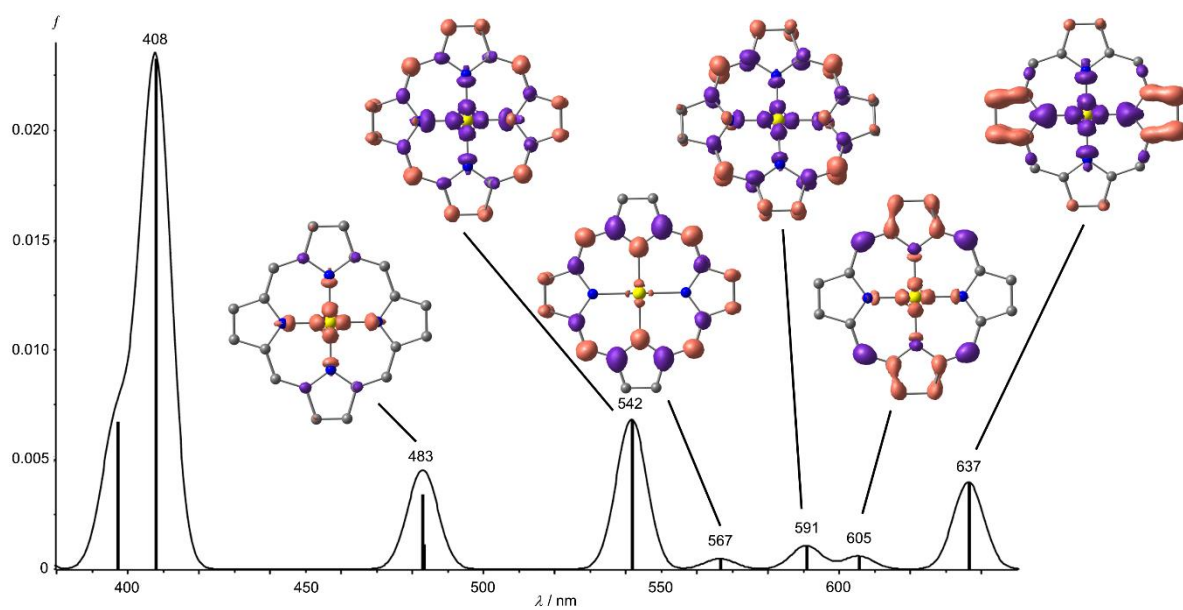


Figure S23. ^1H NMR spectra of $[\text{Au}(\text{TPP})][\text{PF}_6]$ in the presence of increasing amounts of $\text{Au}(\text{TPP})$ in CD_2Cl_2 .

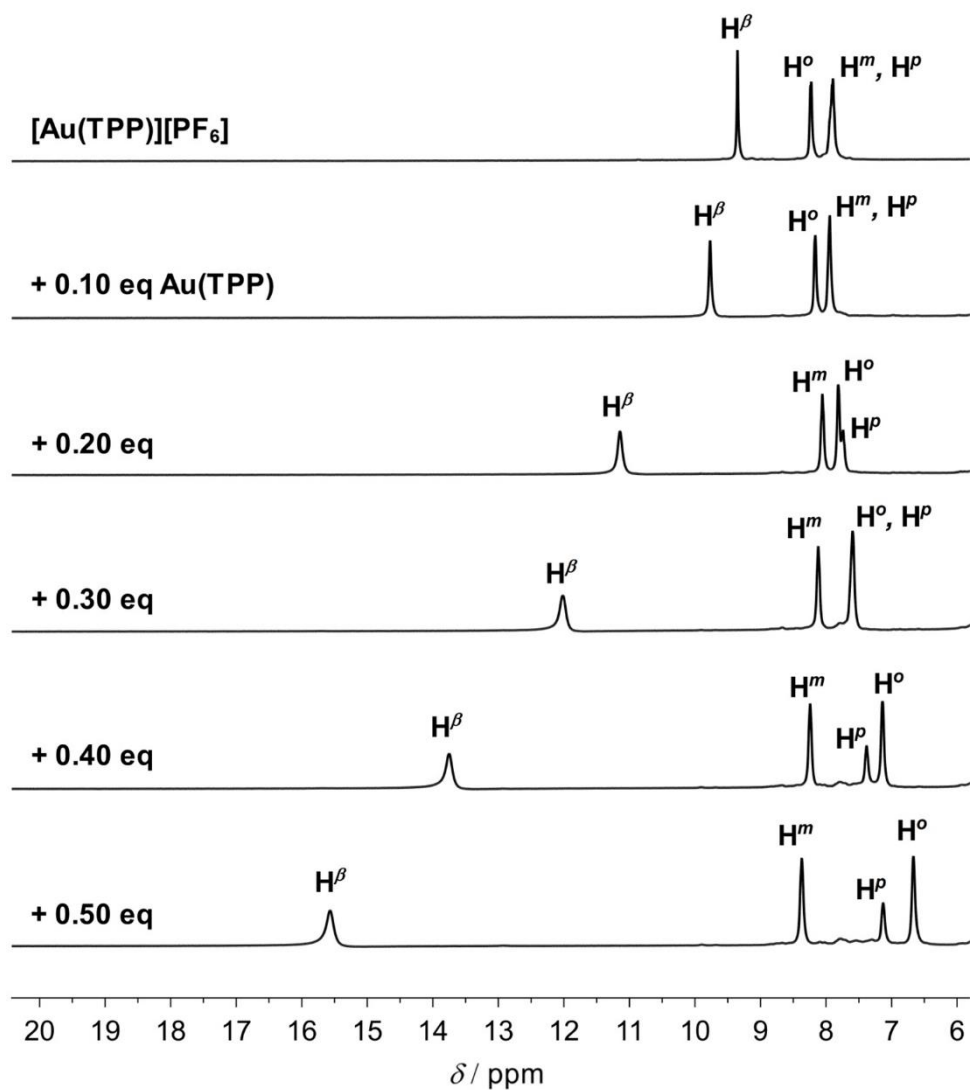


Figure S24. ^1H NMR spectra of **Au(TPP)** in the presence of O_2 / H_2O (open NMR tube) in d_8 -THF.

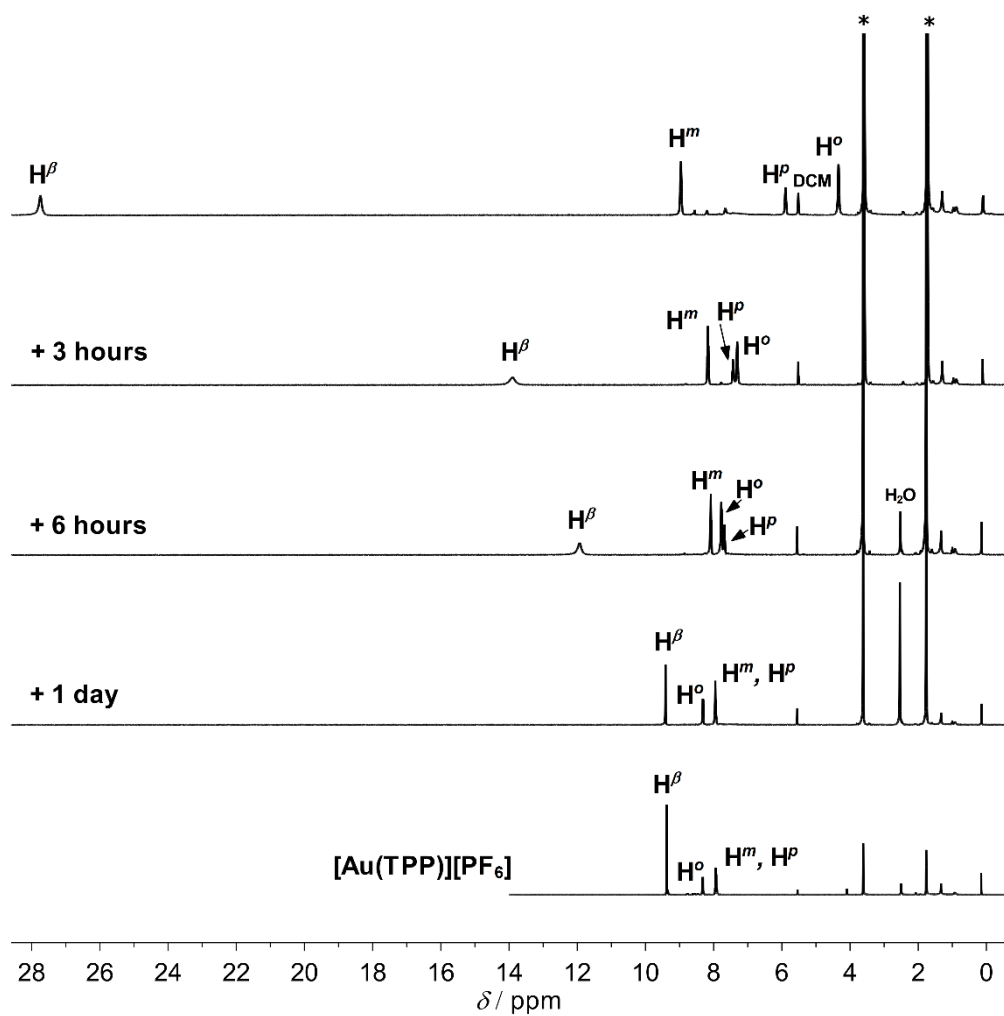


Figure S25. IR spectra (KBr) a) of **Au(TPP)** after reaction with O_2 , b) of **[Au(TPP)](OH)** and c) KBr.

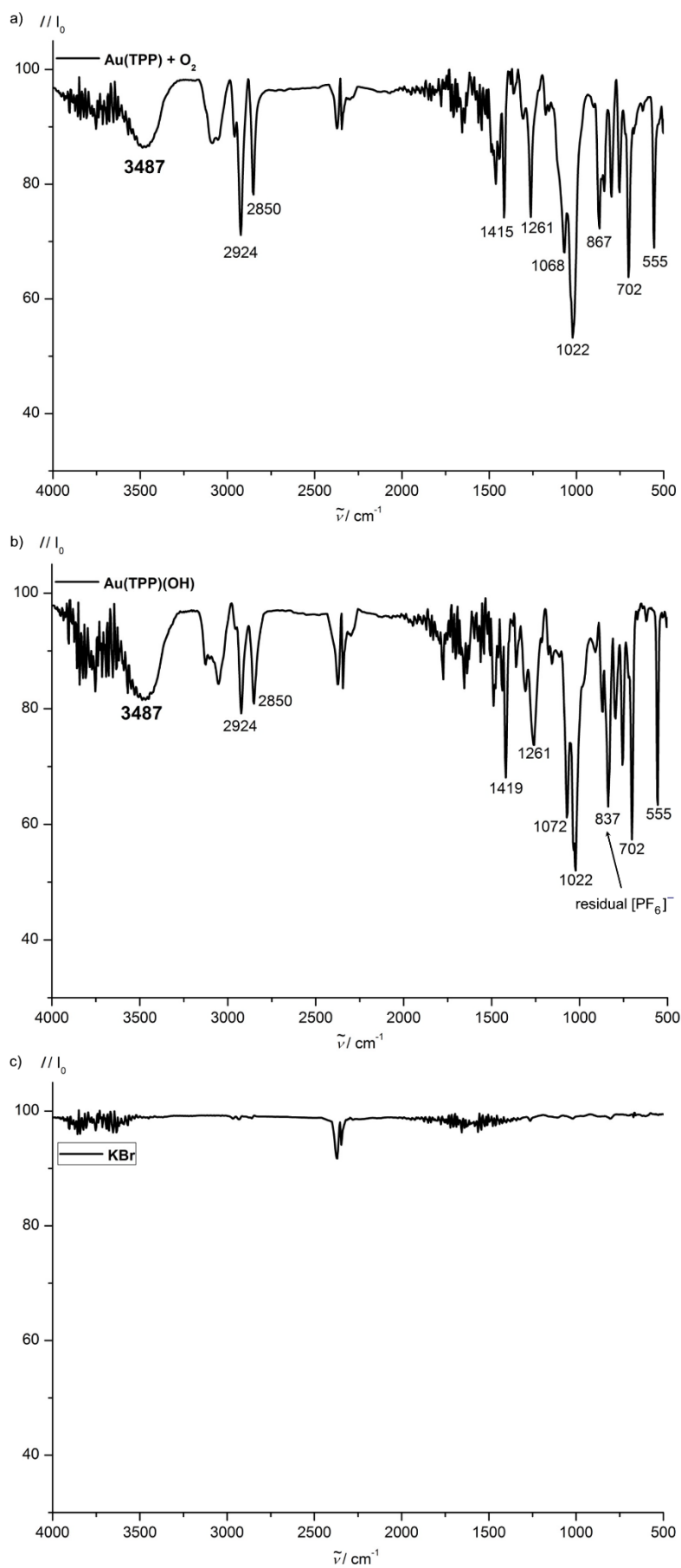
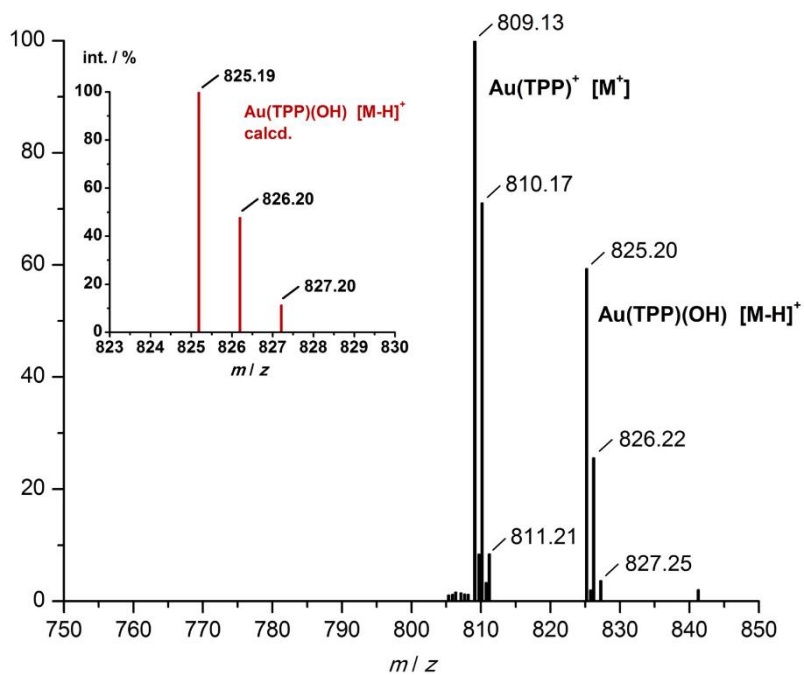


Figure S26. ESI⁺ mass spectrum (THF/MeOH 1:1) a) of **Au(TPP)** after reaction with O₂ and b) of **[Au(TPP)][OH]**.

a) int. / %



b) int. / %

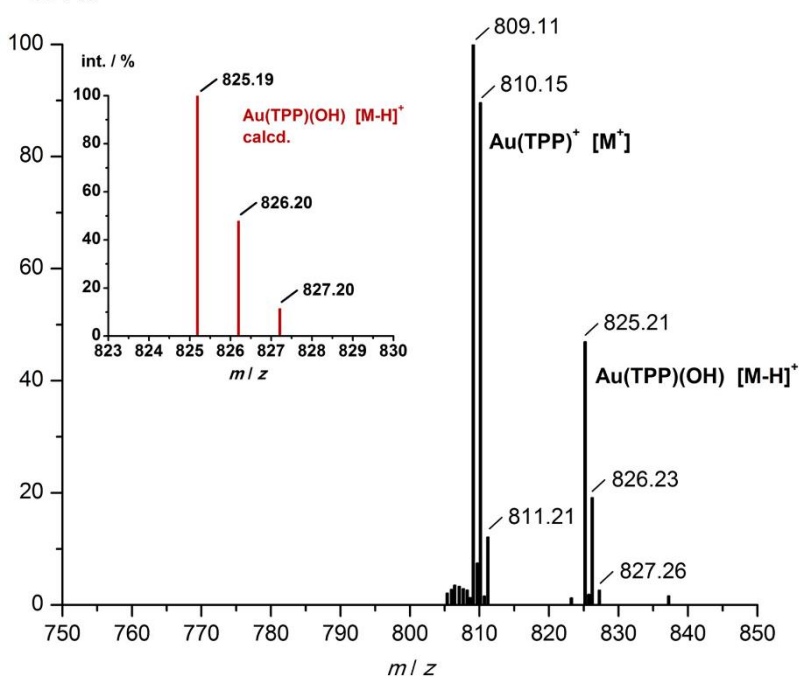


Figure S27. X-band EPR spectrum of **Au(TPP)** and PhNO in CH₂Cl₂ at 77 K (red) including simulation (black) with $g = 2.021, 2.017, 2.003$ and $A(^{14}\text{N}) = 11, 5, 10$ G, linewidth pp Gauss 1.0 MHz; linewidth pp Lorentz 0.1 MHz.

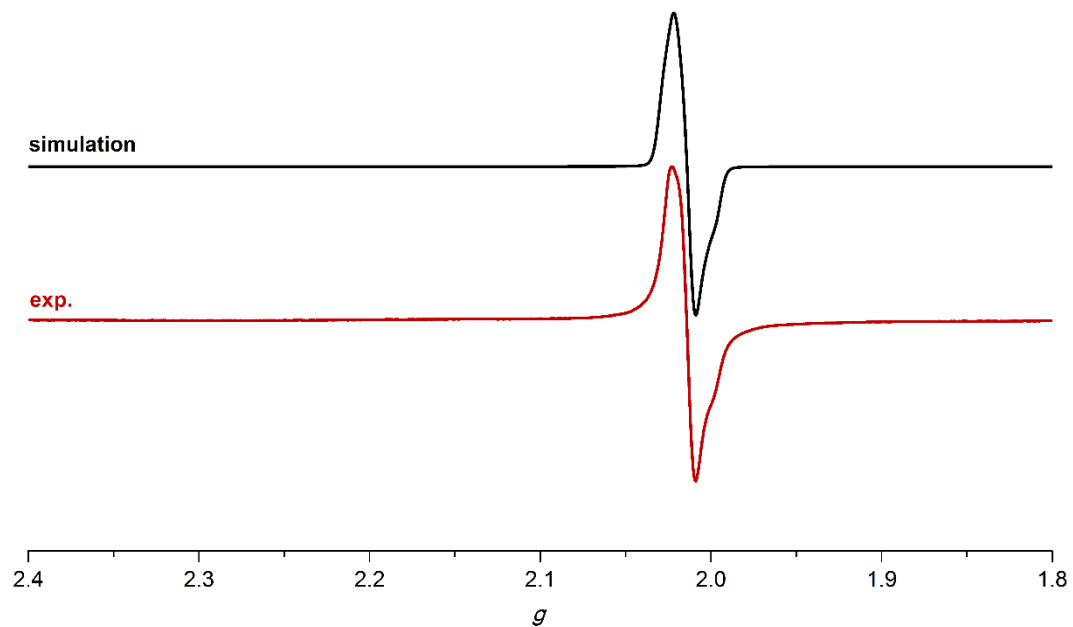


Figure S28. ^1H NMR spectra of a) 1-benzyl-1,4-dihydropyridinamide (BNAH), b) $[\text{Au}(\text{TPP})][\text{OH}] + 2 \text{ eq BNAH}$, c) $[\text{Au}(\text{TPP})][\text{OH}] + 15 \text{ eq BNAH} + 15 \text{ eq KOH}$ and d) $[\text{Au}(\text{TPP})][\text{OH}] + 15 \text{ eq BNAH} + 15 \text{ eq KOH}$ after 6h in $\text{d}_8\text{-THF}$. Asterisks denote residual solvent resonances.

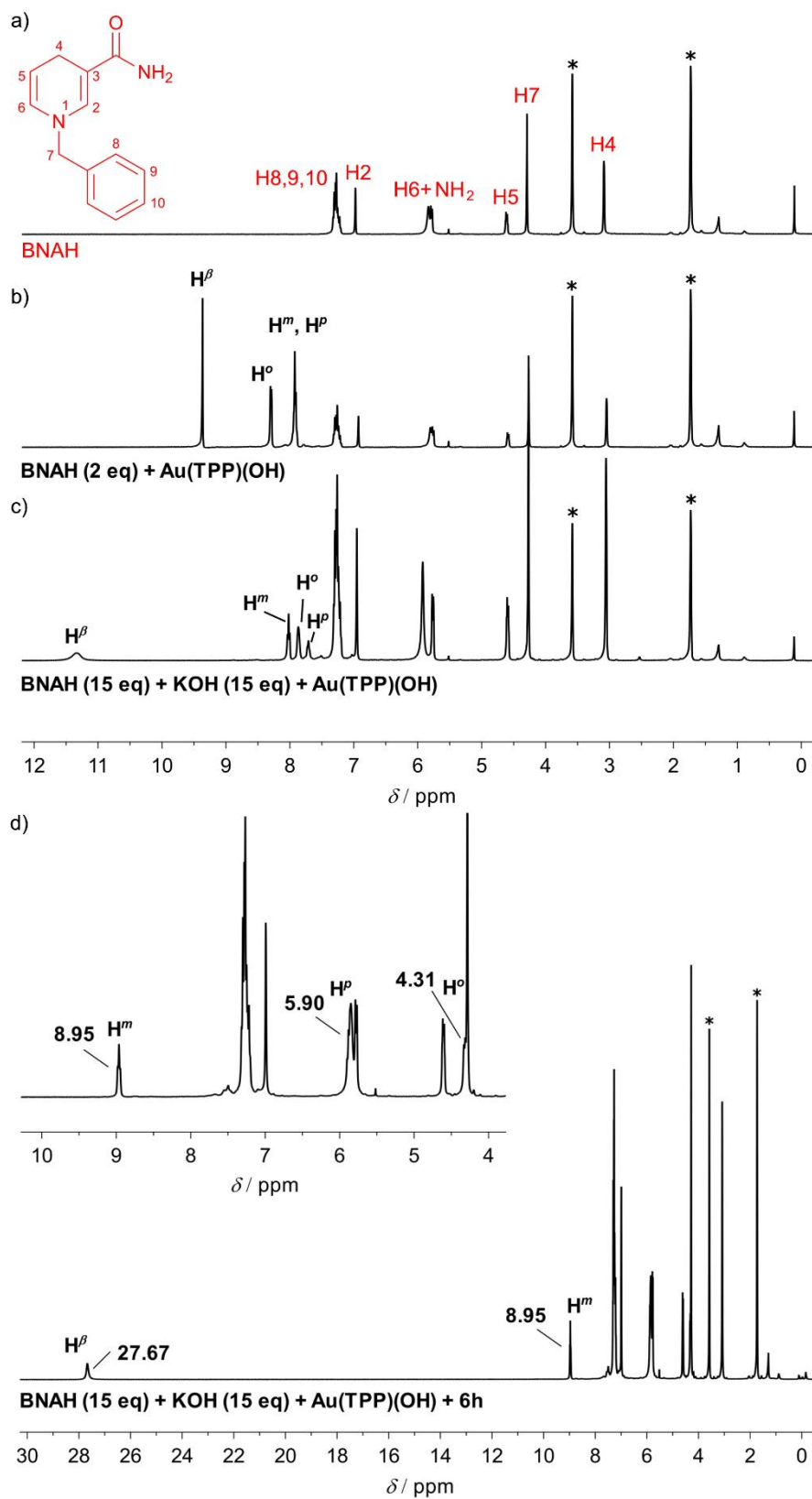


Figure S29. ^1H NMR spectrum of **Au(TPP)** in the presence of excess H_2O in d_8 -THF. Asterisks denote residual solvent resonances.

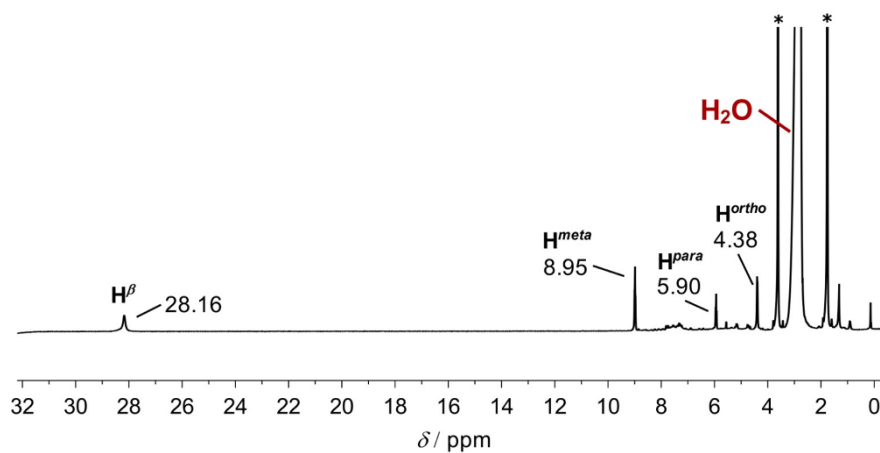
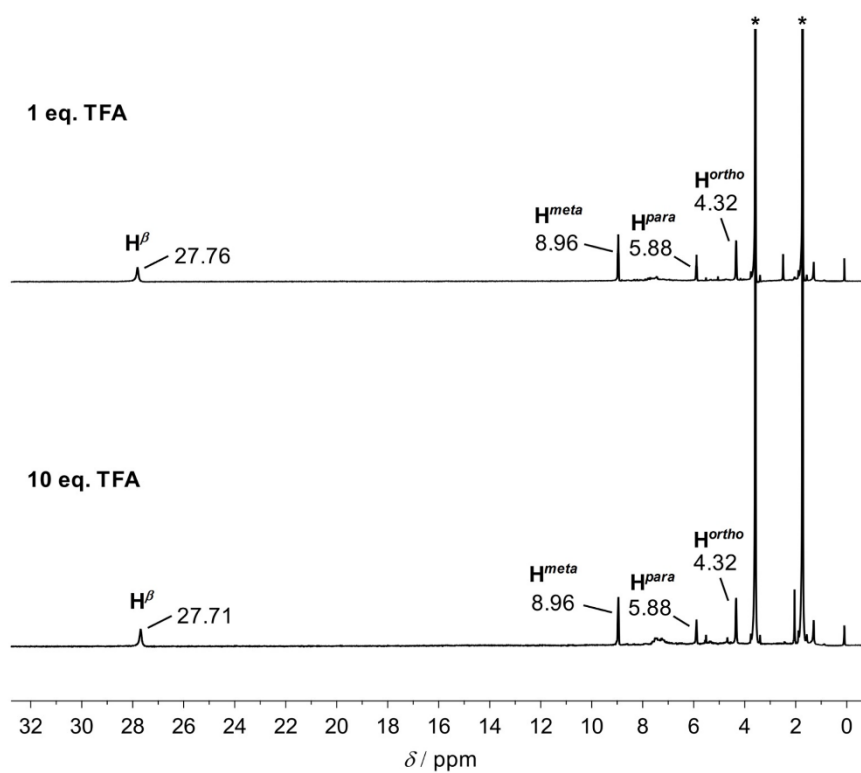


Figure S30. ^1H NMR spectra of **Au(TPP)** in the presence of increasing amounts of TFA in d_8 -THF. Asterisks denote residual solvent resonances.



Cartesian Coordinates of DFT calculated compounds:

Au(TPP) [B3LYP, ECP, COSMO CH₂Cl₂]

79	1.360403000	4.255488000	6.118248000
7	0.109603000	2.843312000	5.214163000
7	0.322107000	4.009871000	7.939408000
6	0.127478000	2.497925000	3.887823000
6	-0.890263000	1.503375000	3.676657000
1	-1.105458000	1.022344000	2.738516000
6	-1.495589000	1.272526000	4.874721000
1	-2.313021000	0.600308000	5.068850000
6	-0.865220000	2.120507000	5.851268000
6	-1.204231000	2.193779000	7.219156000
6	-2.271343000	1.262743000	7.705084000
6	-2.039843000	-0.113162000	7.788694000
1	-1.075195000	-0.509784000	7.500105000
6	-3.031020000	-0.973629000	8.248813000
1	-2.831666000	-2.035410000	8.313269000
6	-4.272536000	-0.471825000	8.627294000
1	-5.044560000	-1.141204000	8.983415000
6	-4.514915000	0.895692000	8.545706000
1	-5.478333000	1.294984000	8.834932000
6	-3.520824000	1.756006000	8.090881000
1	-3.716337000	2.818621000	8.028095000
6	-0.610383000	3.031356000	8.175483000
6	-0.837479000	2.967696000	9.601856000
1	-1.511105000	2.287490000	10.093551000
6	-0.025168000	3.882289000	10.188378000
1	0.078402000	4.078218000	11.241527000
6	0.726214000	4.536002000	9.140615000
6	1.729779000	5.496241000	9.337634000
6	1.928889000	5.989244000	10.737466000
6	0.984853000	6.830044000	11.333312000
1	0.109196000	7.129572000	10.772216000
6	1.163953000	7.290986000	12.633541000
1	0.425089000	7.945915000	13.076705000
6	2.288145000	6.912772000	13.360716000
1	2.426924000	7.268915000	14.373050000
6	3.232799000	6.073030000	12.778539000
1	4.108092000	5.769685000	13.338093000
6	3.055520000	5.617481000	11.476416000
1	3.792242000	4.961560000	11.031237000
7	2.611247000	5.667688000	7.022316000
7	2.398591000	4.501303000	4.297011000
6	2.593364000	6.013074000	8.348657000
6	3.611266000	7.007446000	8.559866000
1	3.826571000	7.488366000	9.498035000
6	4.216615000	7.238277000	7.361817000
1	5.034104000	7.910429000	7.167728000
6	3.586118000	6.390457000	6.385214000
6	3.925074000	6.317268000	5.017297000
6	4.992192000	7.248251000	4.531331000
6	4.761182000	8.624313000	4.448887000
1	3.796930000	9.021113000	4.738537000
6	5.752334000	9.484724000	3.988617000
1	5.553337000	10.546625000	3.925052000
6	6.993332000	8.982694000	3.608726000
1	7.765320000	9.652012000	3.252412000
6	7.235235000	7.615018000	3.689132000
1	8.198256000	7.215546000	3.398839000
6	6.241188000	6.754787000	4.144198000
1	6.436298000	5.692048000	4.206044000
6	3.331103000	5.479795000	4.060934000
6	3.557996000	5.543610000	2.634533000
1	4.231588000	6.223831000	2.142826000
6	2.745616000	4.629081000	2.048006000
1	2.641878000	4.433307000	0.994840000
6	1.994398000	3.975241000	3.095798000

6	0.990927000	3.014908000	2.898814000
6	0.791772000	2.521934000	1.498971000
6	1.735597000	1.680840000	0.903210000
1	2.611118000	1.381017000	1.464368000
6	1.556425000	1.219906000	-0.397014000
1	2.295129000	0.564769000	-0.840137000
6	0.432433000	1.598489000	-1.124296000
1	0.293634000	1.242388000	-2.136643000
6	-0.511995000	2.438542000	-0.542208000
1	-1.387130000	2.742194000	-1.101844000
6	-0.334696000	2.894023000	0.759938000
1	-1.071256000	3.550203000	1.205013000

Au(TPP) [B3LYP, def2-SVP/ZORA, COSMO CH₂Cl₂]

79	1.360625000	4.255308000	6.118274000
7	0.098067000	2.830951000	5.206632000
7	0.349382000	3.971837000	7.961646000
6	0.113660000	2.491206000	3.877720000
6	-0.907046000	1.485342000	3.661881000
1	-1.127406000	1.005714000	2.715377000
6	-1.513331000	1.251455000	4.866564000
1	-2.332549000	0.570052000	5.064397000
6	-0.872393000	2.103918000	5.847859000
6	-1.207380000	2.173711000	7.224887000
6	-2.284912000	1.249015000	7.710951000
6	-2.079232000	-0.142367000	7.750893000
1	-1.122198000	-0.551840000	7.429214000
6	-3.084177000	-1.000810000	8.209702000
1	-2.904278000	-2.075218000	8.239235000
6	-4.313792000	-0.482435000	8.632790000
1	-5.097175000	-1.151016000	8.988452000
6	-4.530610000	0.900001000	8.596963000
1	-5.485643000	1.312636000	8.921260000
6	-3.523608000	1.758302000	8.142185000
1	-3.700025000	2.833152000	8.112432000
6	-0.604295000	3.013060000	8.192398000
6	-0.856800000	2.965695000	9.621702000
1	-1.551407000	2.295539000	10.114899000
6	-0.038412000	3.887287000	10.212310000
1	0.050678000	4.100484000	11.271304000
6	0.734490000	4.520519000	9.158601000
6	1.743021000	5.494543000	9.353810000
6	1.934448000	5.996520000	10.755284000
6	0.954272000	6.799498000	11.366851000
1	0.055291000	7.063500000	10.810654000
6	1.127319000	7.268806000	12.673511000
1	0.359594000	7.894309000	13.128376000
6	2.282123000	6.938746000	13.392440000
1	2.416487000	7.302485000	14.410655000
6	3.263031000	6.137767000	12.795755000
1	4.162863000	5.871222000	13.349607000
6	3.091259000	5.672239000	11.487645000
1	3.855548000	5.043871000	11.031470000
7	2.622917000	5.679946000	7.029831000
7	2.371615000	4.539059000	4.274802000
6	2.607239000	6.019772000	8.358725000
6	3.627915000	7.025666000	8.574546000
1	3.848291000	7.505310000	9.521031000
6	4.234229000	7.259522000	7.369878000
1	5.053379000	7.941003000	7.172061000
6	3.593355000	6.407006000	6.388588000
6	3.928350000	6.337223000	5.011551000
6	5.005774000	7.262002000	4.525434000
6	4.800335000	8.653449000	4.486411000
1	3.843585000	9.062925000	4.808914000
6	5.805156000	9.511978000	4.027500000
1	5.625428000	10.586435000	3.998694000

6	7.034394000	8.993617000	3.603291000
1	7.817669000	9.662248000	3.247485000
6	7.250976000	7.611115000	3.638174000
1	8.205725000	7.198486000	3.313044000
6	6.244124000	6.752749000	4.093152000
1	6.420347000	5.677849000	4.122153000
6	3.325227000	5.497893000	4.044028000
6	3.577569000	5.545380000	2.614694000
1	4.272139000	6.215543000	2.121464000
6	2.759123000	4.623837000	2.024093000
1	2.669846000	4.410781000	0.965083000
6	1.986357000	3.990508000	3.077833000
6	0.977832000	3.016487000	2.882635000
6	0.786283000	2.514607000	1.481136000
6	1.766061000	1.711031000	0.869719000
1	2.664816000	1.446497000	1.426032000
6	1.592834000	1.241707000	-0.436913000
1	2.360219000	0.615717000	-0.891682000
6	0.438311000	1.572423000	-1.155988000
1	0.303845000	1.208695000	-2.174192000
6	-0.542165000	2.374048000	-0.559466000
1	-1.441789000	2.641080000	-1.113421000
6	-0.370267000	2.839520000	0.748650000
1	-1.134246000	3.468360000	1.204704000

Au(TPP) [B3LYP, def2-TZVPP/ZORA, D3(BJ), COSMO CH₂Cl₂]

79	1.360160000	4.255798000	6.118159000
7	0.113477000	2.848413000	5.217549000
7	0.308034000	4.029716000	7.927828000
6	0.136611000	2.496187000	3.892230000
6	-0.882045000	1.504159000	3.679960000
1	-1.090306000	1.020208000	2.742003000
6	-1.495966000	1.281162000	4.877522000
1	-2.317718000	0.615031000	5.073100000
6	-0.867470000	2.130600000	5.852685000
6	-1.212490000	2.209822000	7.214813000
6	-2.274039000	1.281878000	7.700593000
6	-2.064213000	-0.098531000	7.716453000
1	-1.118696000	-0.495717000	7.372300000
6	-3.052548000	-0.959303000	8.179067000
1	-2.872241000	-2.026102000	8.191428000
6	-4.267480000	-0.451215000	8.628448000
1	-5.037636000	-1.121126000	8.987011000
6	-4.486291000	0.922465000	8.615100000
1	-5.429164000	1.325737000	8.960188000
6	-3.494984000	1.782569000	8.156618000
1	-3.667467000	2.850538000	8.145669000
6	-0.623647000	3.049404000	8.165422000
6	-0.848169000	2.983061000	9.592194000
1	-1.518682000	2.298019000	10.080980000
6	-0.035476000	3.898899000	10.178935000
1	0.074312000	4.094344000	11.231361000
6	0.712848000	4.554944000	9.130332000
6	1.716475000	5.507616000	9.329021000
6	1.914621000	5.996829000	10.724044000
6	0.937519000	6.778525000	11.343086000
1	0.038376000	7.033327000	10.798012000
6	1.115075000	7.234588000	12.644316000
1	0.350953000	7.844089000	13.108362000
6	2.271202000	6.909630000	13.346370000
1	2.409277000	7.262187000	14.359841000
6	3.248989000	6.128026000	12.738718000
1	4.148714000	5.866316000	13.279770000
6	3.072300000	5.676936000	11.436006000
1	3.831920000	5.065787000	10.967263000
7	2.606960000	5.663050000	7.018820000
7	2.412434000	4.481683000	4.308567000

6	2.583904000	6.015183000	8.344168000
6	3.602627000	7.007141000	8.556451000
1	3.810999000	7.490985000	9.494431000
6	4.216511000	7.230174000	7.358887000
1	5.038246000	7.896321000	7.163320000
6	3.587973000	6.380792000	6.383702000
6	3.933043000	6.301511000	5.021588000
6	4.994707000	7.229280000	4.535788000
6	4.785308000	8.609760000	4.520404000
1	3.840077000	9.007171000	4.865065000
6	5.773722000	9.470357000	4.057639000
1	5.593730000	10.537212000	4.045620000
6	6.988288000	8.962007000	3.607559000
1	7.758483000	9.631766000	3.248794000
6	7.206690000	7.588256000	3.620454000
1	8.149287000	7.184776000	3.274864000
6	6.215331000	6.728344000	4.079167000
1	6.387494000	5.660323000	4.089734000
6	3.344187000	5.461917000	4.070976000
6	3.568774000	5.528167000	2.644204000
1	4.239377000	6.213107000	2.155411000
6	2.756090000	4.612319000	2.057465000
1	2.646311000	4.416838000	1.005039000
6	2.007682000	3.956388000	3.106068000
6	1.004070000	3.003713000	2.907392000
6	0.806109000	2.514284000	1.512410000
6	1.782948000	1.731798000	0.893965000
1	2.681682000	1.476524000	1.439495000
6	1.605579000	1.275469000	-0.407197000
1	2.369483000	0.665371000	-0.870818000
6	0.449948000	1.601010000	-1.109801000
1	0.312063000	1.248295000	-2.123241000
6	-0.527544000	2.383452000	-0.502760000
1	-1.426873000	2.645626000	-1.044244000
6	-0.351078000	2.834747000	0.799918000
1	-1.110469000	3.446547000	1.268196000

Au(TPP) [B3LYP, def2-SVP/ZORA, COSMO CH₂Cl₂]

79	1.360625000	4.255308000	6.118274000
7	0.098067000	2.830951000	5.206632000
7	0.349382000	3.971837000	7.961646000
6	0.113660000	2.491206000	3.877720000
6	-0.907046000	1.485342000	3.661881000
1	-1.127406000	1.005714000	2.715377000
6	-1.513331000	1.251455000	4.866564000
1	-2.332549000	0.570052000	5.064397000
6	-0.872393000	2.103918000	5.847859000
6	-1.207380000	2.173711000	7.224887000
6	-2.284912000	1.249015000	7.710951000
6	-2.079232000	-0.142367000	7.750893000
1	-1.122198000	-0.551840000	7.429214000
6	-3.084177000	-1.000810000	8.209702000
1	-2.904278000	-2.075218000	8.239235000
6	-4.313792000	-0.482435000	8.632790000
1	-5.097175000	-1.151016000	8.988452000
6	-4.530610000	0.900001000	8.596963000
1	-5.485643000	1.312636000	8.921260000
6	-3.523608000	1.758302000	8.142185000
1	-3.700025000	2.833152000	8.112432000
6	-0.604295000	3.013060000	8.192398000
6	-0.856800000	2.965695000	9.621702000
1	-1.551407000	2.295539000	10.114899000
6	-0.038412000	3.887287000	10.212310000
1	0.050678000	4.100484000	11.271304000
6	0.734490000	4.520519000	9.158601000
6	1.743021000	5.494543000	9.353810000
6	1.934448000	5.996520000	10.755284000

6	0.954272000	6.799498000	11.366851000
1	0.055291000	7.063500000	10.810654000
6	1.127319000	7.268806000	12.673511000
1	0.359594000	7.894309000	13.128376000
6	2.282123000	6.938746000	13.392440000
1	2.416487000	7.302485000	14.410655000
6	3.263031000	6.137767000	12.795755000
1	4.162863000	5.871222000	13.349607000
6	3.091259000	5.672239000	11.487645000
1	3.855548000	5.043871000	11.031470000
7	2.622917000	5.679946000	7.029831000
7	2.371615000	4.539059000	4.274802000
6	2.607239000	6.019772000	8.358725000
6	3.627915000	7.025666000	8.574546000
1	3.848291000	7.505310000	9.521031000
6	4.234229000	7.259522000	7.369878000
1	5.053379000	7.941003000	7.172061000
6	3.593355000	6.407006000	6.388588000
6	3.928350000	6.337223000	5.011551000
6	5.005774000	7.262002000	4.525434000
6	4.800335000	8.653449000	4.486411000
1	3.843585000	9.062925000	4.808914000
6	5.805156000	9.511978000	4.027500000
1	5.625428000	10.586435000	3.998694000
6	7.034394000	8.993617000	3.603291000
1	7.817669000	9.662248000	3.247485000
6	7.250976000	7.611115000	3.638174000
1	8.205725000	7.198486000	3.313044000
6	6.244124000	6.752749000	4.093152000
1	6.420347000	5.677849000	4.122153000
6	3.325227000	5.497893000	4.044028000
6	3.577569000	5.545380000	2.614694000
1	4.272139000	6.215543000	2.121464000
6	2.759123000	4.623837000	2.024093000
1	2.669846000	4.410781000	0.965083000
6	1.986357000	3.990508000	3.077833000
6	0.977832000	3.016487000	2.882635000
6	0.786283000	2.514607000	1.481136000
6	1.766061000	1.711031000	0.869719000
1	2.664816000	1.446497000	1.426032000
6	1.592834000	1.241707000	-0.436913000
1	2.360219000	0.615717000	-0.891682000
6	0.438311000	1.572423000	-1.155988000
1	0.303845000	1.208695000	-2.174192000
6	-0.542165000	2.374048000	-0.559466000
1	-1.441789000	2.641080000	-1.113421000
6	-0.370267000	2.839520000	0.748650000
1	-1.134246000	3.468360000	1.204704000

Transition state **Au(TPP)** [B3LYP, def2-SVP/ZORA, COSMO CH₂Cl₂]

79	1.364397000	4.251975000	6.119462000
7	0.120803000	2.869681000	5.236237000
7	0.438453000	3.927600000	7.929393000
6	0.145582000	2.480060000	3.906558000
6	-0.793471000	1.426623000	3.722457000
1	-0.970408000	0.908513000	2.787774000
6	-1.390910000	1.185416000	4.944540000
1	-2.160320000	0.457242000	5.171650000
6	-0.824449000	2.092724000	5.883099000
6	-1.190292000	2.174363000	7.253296000
6	-2.282501000	1.263009000	7.730476000
6	-1.985859000	0.112857000	8.483098000
1	-0.947541000	-0.118519000	8.719569000
6	-3.007541000	-0.735146000	8.926066000
1	-2.758846000	-1.622540000	9.507700000
6	-4.342598000	-0.446393000	8.621029000
1	-5.138411000	-1.105978000	8.965853000

6	-4.649874000	0.694527000	7.869909000
1	-5.686960000	0.928330000	7.630100000
6	-3.627560000	1.540870000	7.427081000
1	-3.872329000	2.428973000	6.844998000
6	-0.581787000	3.018103000	8.171941000
6	-0.913166000	3.074959000	9.580673000
1	-1.690422000	2.486039000	10.053063000
6	-0.079095000	3.973635000	10.167896000
1	-0.044227000	4.260930000	11.212109000
6	0.792435000	4.505610000	9.141015000
6	1.801136000	5.431468000	9.366651000
6	2.022466000	5.921271000	10.767516000
6	1.597517000	7.205622000	11.152427000
1	1.100384000	7.845604000	10.423876000
6	1.800501000	7.663853000	12.458760000
1	1.459897000	8.659747000	12.741083000
6	2.435640000	6.845417000	13.400661000
1	2.594023000	7.202001000	14.418088000
6	2.866101000	5.566865000	13.028143000
1	3.363507000	4.924021000	13.754029000
6	2.661601000	5.109338000	11.721229000
1	3.002003000	4.114586000	11.434822000
7	2.602327000	5.639495000	7.003566000
7	2.302727000	4.565648000	4.313844000
6	2.661140000	5.935052000	8.354624000
6	3.724541000	6.854153000	8.575993000
1	4.001477000	7.262546000	9.540479000
6	4.297739000	7.127812000	7.349133000
1	5.143660000	7.773081000	7.145303000
6	3.595030000	6.369923000	6.370612000
6	3.885312000	6.368233000	4.980574000
6	4.938010000	7.315346000	4.490590000
6	4.727035000	8.706487000	4.523464000
1	3.784174000	9.095766000	4.906244000
6	5.707814000	9.590079000	4.061191000
1	5.523110000	10.663816000	4.087514000
6	6.920302000	9.098009000	3.562695000
1	7.685076000	9.786309000	3.204085000
6	7.143948000	7.716924000	3.528156000
1	8.085992000	7.324538000	3.145834000
6	6.160607000	6.833625000	3.987856000
1	6.342841000	5.759567000	3.963984000
6	3.242270000	5.556445000	4.054091000
6	3.446148000	5.624882000	2.622753000
1	4.114061000	6.320754000	2.129238000
6	2.640875000	4.695470000	2.042825000
1	2.525186000	4.488336000	0.985605000
6	1.908641000	4.024891000	3.095733000
6	0.961517000	3.030656000	2.883590000
6	0.763012000	2.522646000	1.487677000
6	1.758567000	1.754712000	0.856558000
1	2.676984000	1.523402000	1.395362000
6	1.577917000	1.280263000	-0.447592000
1	2.359284000	0.684066000	-0.918370000
6	0.397899000	1.567471000	-1.143012000
1	0.256927000	1.199544000	-2.158855000
6	-0.600727000	2.330606000	-0.525573000
1	-1.520853000	2.562953000	-1.061281000
6	-0.420504000	2.801501000	0.779138000
1	-1.199660000	3.398215000	1.252302000

- [1] Preiß, S., Melomedov, J., Wünsche von Leupoldt, A. & Heinze, K. Gold(III) tetraarylporphyrin amino acid derivatives: ligand or metal centred redox chemistry?. *Chem. Sci.* **7**, 596–610 (2016).
- [2] Fulmer, G. R., Miller, A. J. M., Sherden, N. H., Gottlieb, H. E., Nudelman, A., Stoltz, B. M., Bercaw, J. E. & Goldberg, K. I. NMR Chemical Shifts of Trace Impurities: Common Laboratory Solvents, Organics, and Gases in Deuterated Solvents Relevant to the Organometallic Chemist. *Organometallics* **29**, 2176–2179 (2010).
- [3] Stoll, S. & Schweiger, A. EasySpin, a comprehensive software package for spectral simulation and analysis in EPR. *J. Magn. Reson.* **178**, 42–55 (2006).
- [4] Bauer, M., Heusel, G., Mangold, S. & Bertagnolli, H. Spectroscopic set-up for simultaneous UV-Vis/(Q)EXAFS in situ and in operando studies of homogeneous reactions under laboratory conditions. *J. Synchr. Rad.* **17**, 273–279 (2010).
- [5] Villa, A., Dimitratos, N., Chan-Thaw, C. E., Hammond, C., Veith, G. M., Wang, D., Manzoli, M., Prati, L. & Hutchings, G. J. Characterisation of gold catalysts. *Chem. Soc. Rev.* **45**, 4953–4994 (2016).
- [6] van Bokhoven, J. A. & Miller, J. T. d Electron Density and Reactivity of the d Band as a Function of Particle Size in Supported Gold Catalysts. *J. Phys. Chem. C* **111**, 9245–9249 (2007).
- [7] Serrano-Becerra, J. M., Maier, A. F. G., González-Gallardo, S., Moos, E., Kaub, C., Gaffga, M., Niedner-Schatteburg, G., Roesky, P. W., Breher, F. & Paradies, J. Mono- vs. Dinuclear Gold-Catalyzed Intermolecular Hydroamidation. *Eur. J. Org. Chem.* 4515–4522 (2014).
- [8] Bus, E., Miller, J. T. & van Bokhoven, J. A. Hydrogen Chemisorption on Al₂O₃-Supported Gold Catalysts. *J. Phys. Chem. B* **109**, 14581–14587 (2005).
- [9] Bauer, M. & Bertagnolli, H. in *Methods in Physical Chemistry*, Wiley-VCH, 231–269 (2012).
- [10] Gurman, S. J., Binsted, N. & Ross, I. A rapid, exact curved-wave theory for EXAFS calculations. *J. Phys. C: Solid State Phys.* **17**, 143–151 (1984).
- [11] SMART Data Collection and SAINT-Plus Data Processing Software for the SMART System (various versions); Bruker Analytical X-Ray Instruments, Inc., Madison, WI (2000).
- [12] Blessing, R. H. An empirical correction for absorption anisotropy. *Acta Crystallogr., Sect. A* **51**, 33–38 (1995).
- [13] Sheldrick, G. M. SHELXTL, version 5.1, Bruker AXS, Madison, WI (1998).
- [14] Sheldrick, G. M. SHELXL-97, University of Göttingen, Germany (1997).
- [15] Neese, F. The ORCA program system. *WIREs Comput Mol Sci* **2**, 73–78 (2012).
- [16] Becke, A. D. Density-functional thermochemistry. III. The role of exact exchange. *J. Chem. Phys.* **98**, 5648–5652 (1993).
- [17] Pantazis, D. A., Chen, X.-Y., Landis, C. R. & Neese, F. All-Electron Scalar Relativistic Basis Sets for Third-Row Transition Metal Atoms. *J. Chem. Theory Comput.* **4**, 908–919 (2008).
- [18] Theilacker, K., Schlegel, H. B., Kaupp, M. & Schwerdtfeger, P. Relativistic and Solvation Effects on the Stability of Gold(III) Halides in Aqueous Solution. *Inorg. Chem.* **54**, 9869–9875 (2015).

- [19] Neese, F., Wennmohs, F., Hansen, A. & Becker, U. Efficient, approximate and parallel Hartree–Fock and hybrid DFT calculations. A ‘chain-of-spheres’ algorithm for the Hartree–Fock exchange. *Chem. Phys.* **356**, 98–109 (2009).
- [20] Izsák, R. & Neese, F. An overlap fitted chain of spheres exchange method. *J. Chem. Phys.* **135**, 144105 (2011).
- [21] Sinnecker, S., Rajendran, A., Klamt, A., Diedenhofen, M. & Neese, F. Calculation of Solvent Shifts on Electronic g -Tensors with the Conductor-Like Screening Model (COSMO) and Its Self-Consistent Generalization to Real Solvents (Direct COSMO-RS). *J. Phys. Chem. A* **110**, 2235–2245 (2006).
- [22] Grimme, S., Ehrlich, S. & Goerigk, L. Effect of the damping function in dispersion corrected density functional theory. *J. Comput. Chem.* **32**, 1456–1465 (2011).
- [23] Grimme, S., Antony, J., Ehrlich, S. & Krieg, H. A consistent and accurate ab initio parametrization of density functional dispersion correction (DFT-D) for the 94 elements H–Pu. *J. Chem. Phys.* **132**, 154104 (2010).
- [24] Petrenko, T., Kossmann, S. & Neese, F. Efficient time-dependent density functional theory approximations for hybrid density functionals: Analytical gradients and parallelization. *J. Chem. Phys.* **134**, 054116 (2011).

6.9 Conductivity measurements of $[\text{Cr}(\text{ddpd})_2](\text{X})_3$

Conductivities were measured with a Greisinger conductivity cell, model 6MH 3431 LFE-210 with platinum electrodes in the concentration range 10^{-6} – 10^{-4} in dry acetonitrile under inert atmosphere. The equivalent conductivity Λ_e was plotted as a function of $c^{0.5}$ and to determine Λ_0 , Λ_e was extrapolated to infinite dilution.

The density functional theoretical calculation on $[\text{Cr}(\text{ddpd})_2]^{3+} \times \text{BPh}_4^-$ was carried out using the ORCA program package (version 4.0.1).^[151] Tight convergence criteria were chosen for all calculations (Keywords TightSCF and TightOpt, convergence criteria for the SCF part: energy change 1.0×10^{-6} Eh, 1-El. energy change 1.0×10^{-5} Eh, orbital gradient 1.0×10^{-5} orbital rotation angle 1.0×10^{-5} , DDIS Error 5.0×10^{-7} ; for geometry optimizations: energy change 1.0×10^{-6} Eh, max. gradient 1.0×10^{-4} bohr⁻¹, RMS gradient 3.0×10^{-5} bohr⁻¹, max. displacement 21.0×10^{-3} bohr, RMS displacement 6.0×10^{-4} bohr). The geometry optimization was performed using the B3LYP functional^[152] in combination with the minimal STO-3G basis set for all atoms.^[153]

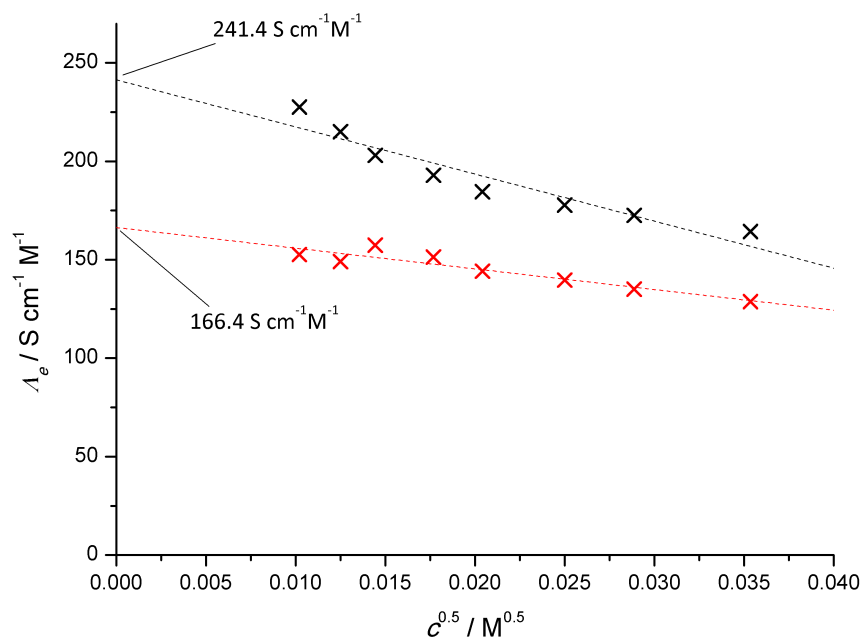


Fig. 6.1: Conductivity measurements of $[\text{Cr}(\text{ddpd})_2]\text{Cl}_3$ (black) and $[\text{N}^i\text{Bu}_4]\text{Cl}$ (red) in acetonitrile.

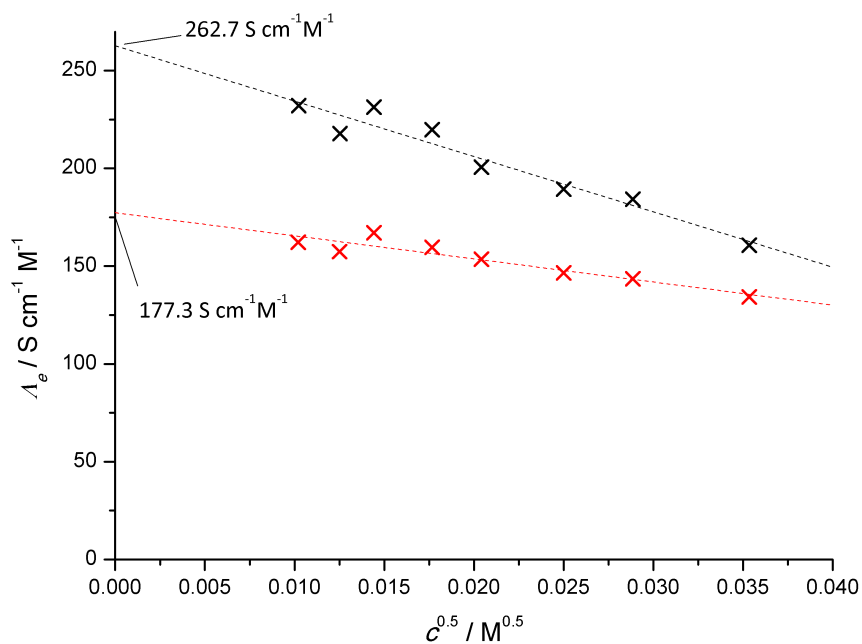


Fig. 6.2: Conductivity measurements of $[\text{Cr}(\text{ddpd})_2](\text{BF}_4)_3$ (black) and $[\text{N}^n\text{Bu}_4]\text{BF}_4$ (red) in acetonitrile.

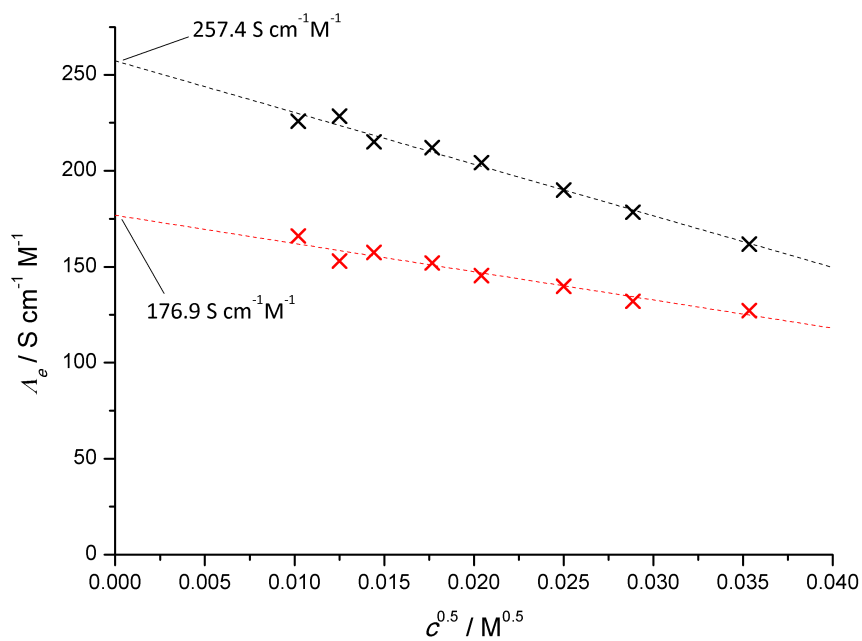


Fig. 6.3: Conductivity measurements of $[\text{Cr}(\text{ddpd})_2](\text{PF}_6)_3$ (black) and $[\text{N}^n\text{Bu}_4]\text{PF}_6$ (red) in acetonitrile.

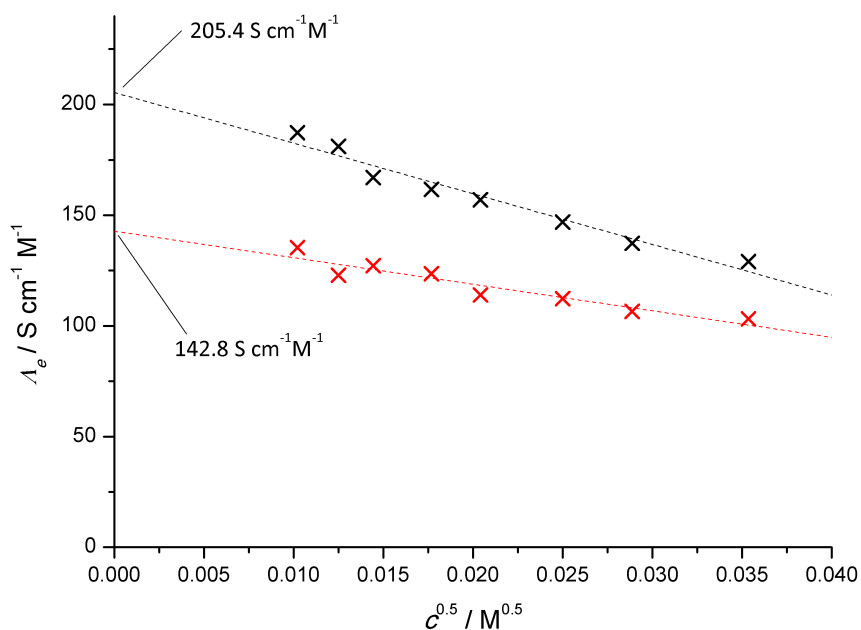


Fig. 6.4: Conductivity measurements of $[\text{Cr}(\text{ddpd})_2](\text{BPh}_4)_3$ (black) and $[\text{N}^n\text{Bu}_4]\text{BPh}_4$ (red) in acetonitrile.

Tab. 6.1: Molar conductivities of $[\text{Cr}(\text{ddpd})_2](\text{X})_3$ and $[\text{N}^n\text{Bu}_4]\text{X}$ ($\text{X} = \text{Cl}^-, \text{BF}_4^-, \text{PF}_6^-, \text{BPh}_4^-$) in acetonitrile.

X	$\Lambda_0 / \text{cm}^{-1}\text{M}^{-1}$	
	$[\text{Cr}(\text{ddpd})_2](\text{X})_3$	$[\text{N}^n\text{Bu}_4]\text{X}$
Cl^-	241.4	166.4
BF_4^-	262.7	177.3
PF_6^-	257.4	176.9
BPh_4^-	205.4	142.8

Tab. 6.2: Literature reported ranges for the molar conductivities 1:1, 2:1 and 3:1 electrolytes in acetonitrile.^[146]

	$\Lambda_0 / \text{cm}^{-1}\text{M}^{-1}$
1:1	120–160
2:1	220–300
3:1	340–420

Tab. 6.3: Luminescence quantum yields of $[\text{Cr}(\text{ddpd})_2](\text{BF}_4)_3$ and $[\text{Cr}(\text{ddpd})_2](\text{BPh}_4)_3$ in acetonitrile under air and inert conditions.

	$\Phi(\text{Ar})$	$\Phi(\text{air})$	$\Phi(\text{Ar})/\Phi(\text{air})$
$[\text{Cr}(\text{ddpd})_2](\text{BF}_4)_3$	12.1 %	0.7 %	17.3
$[\text{Cr}(\text{ddpd})_2](\text{BPh}_4)_3$	9.0 %	0.9 %	10.0

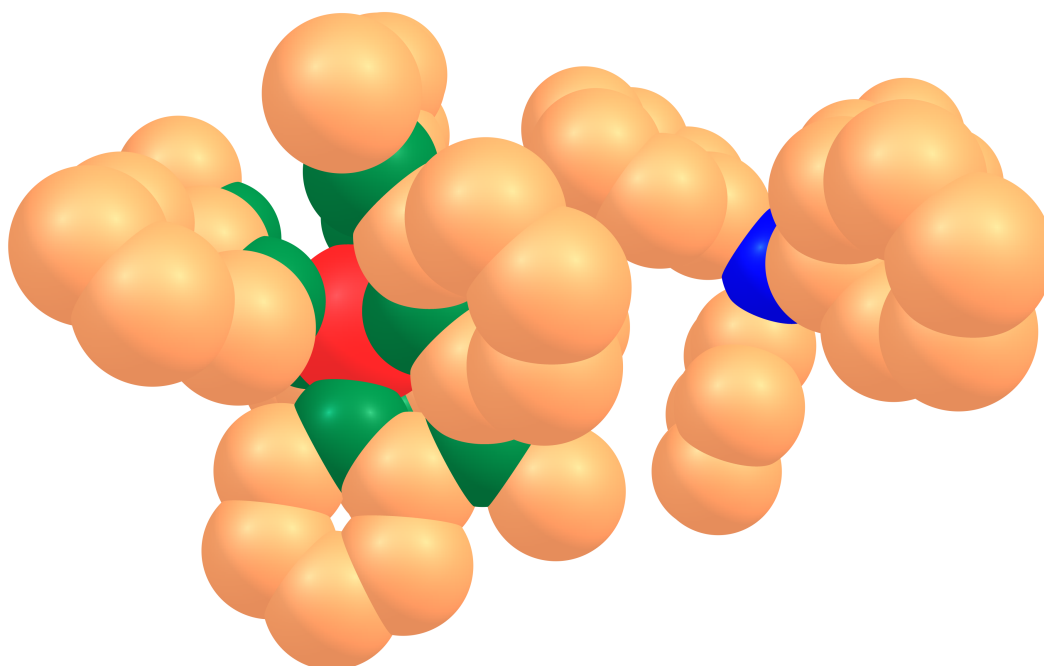


Fig. 6.5: Space-filling representation of the DFT optimized structure of $[\text{Cr}(\text{ddpd})_2]^{3+} \times \text{BPh}_4^-$ (B = blue, C = orange, N = green, Cr = red, hydrogen atoms omitted for clarity, B3LYP-STO-3G).

Tab. 6.4: Cartesian coordinates DFT calculated structure of $[\text{Cr}(\text{ddpd})_2]^{3+} \times \text{BPh}_4^-$ (B3LYP-STO-3G).

```
Cr 0.14239216079050 -0.32068061707277 -0.23567250126273
N 0.21063250969079 -0.26616412667747 1.74071022939497
N 0.07062722466724 -0.36883404086079 -2.21427389216910
N -1.52140642742132 0.80697386222971 -0.15931880373488
N 1.80772855861760 -1.43835399024675 -0.21961480746363
N -0.92481118757853 -2.02168242495919 -0.19805692463029
N 1.19404459675912 1.38668307341107 -0.36764252098685
C -0.96120365296627 -0.28698151371867 2.55053723044369
C -0.92105685950531 -0.28452155110835 3.95990395928752
C 0.31756286611214 -0.24584334852116 4.62785982939001
C 1.50593068800826 -0.21496543960051 3.86547604677810
C 1.43945895250698 -0.22898901696466 2.46035825792065
H -1.85531168318908 -0.27999390115196 4.53183895277689
H 2.48034245466673 -0.20743100937886 4.36609843237307
C -1.79513254194856 1.77373436588260 -1.14036463898954
C -2.99780318932722 2.47062376710557 -1.23778738371671
C -4.02449136798680 2.20414045330762 -0.29257655242771
C -3.78652390060062 1.27634532323886 0.72818501618310
C -2.52911730607719 0.60801934548276 0.80464421909773
```

H -4.98517598587640 2.74023420396812 -0.34110432763953
H -0.98318850112413 1.94414108670939 -1.86219458512582
H -3.13758964463061 3.21106504418640 -2.03724976098762
H -4.54731057935016 1.09207531680863 1.49541507799879
C 2.87972373376276 -1.18257206955633 0.65027654851159
C 4.12916189327256 -1.85072079542490 0.52604670131063
C 4.29922886327008 -2.83090096187303 -0.46381171324205
C 3.21038676422213 -3.15574574760364 -1.30935562366376
C 2.00854395915157 -2.46010397933073 -1.15945089382739
H 5.26388132723663 -3.35141119976514 -0.58457059900459
H 4.94399830961829 -1.61770951954172 1.22086978586043
H 3.29144744757803 -3.92957809640082 -2.09135775265371
H 1.15598582228688 -2.69846216880466 -1.81579152717034
C -1.05771131110558 -0.85907343217734 -2.92470500663435
C -1.11236551139196 -0.92341900381232 -4.33154228001100
C -0.00109977581726 -0.51265660123341 -5.09577147625647
C 1.14238839820267 -0.02357474058414 -4.43375843682293
C 1.15931123460408 0.05092209905933 -3.02557523643345
H -2.00099237121646 -1.32991249346655 -4.82723690196463
H 2.00900229260304 0.32131393676786 -5.00911438108879
C -0.69617441307751 -3.00475530107206 0.77586842095512
C -1.50218590247063 -4.13007469930176 0.95272795373366
C -2.62125341242298 -4.31182790916679 0.09987026709998
C -2.86601671970004 -3.37858730985861 -0.91570667490419
C -1.99772205314046 -2.25896953275029 -1.07466510745045
H -3.27460994025325 -5.19182901382763 0.21146705121112
H 0.17396050670645 -2.82366847298247 1.42368604798776
H -1.26087144150616 -4.85680544677977 1.74077936962950
H -3.69550917895212 -3.52905761374729 -1.61633055400047
C 2.19751320350442 1.58023816118595 -1.33335922633372
C 3.06223704707478 2.71601963662416 -1.30259564293336
C 2.88461806756088 3.70102240608746 -0.32508615365285
C 1.83592528230895 3.55754124319515 0.62120806702810
C 1.03216984561648 2.41918133861761 0.56793418144152
H 3.53437517762918 4.59049774530417 -0.31105344640942
H 3.83548750513592 2.83028485795206 -2.07153497011716
H 1.65044430187109 4.32288503643735 1.38726858159242
H 0.22003707688884 2.26468440971245 1.29332909888689
N -2.20029606889563 -1.28555435689077 -2.12221328511830
C -3.53721417574492 -1.31469785330236 -2.82416980399606
H -3.65176732476395 -2.19086690479267 -3.49206725653810
H -4.33026991638408 -1.33449032327833 -2.05712667923696

H -3.63424505441669 -0.38875238682450 -3.41574957169835
N 2.33676706306366 0.56058807946244 -2.33862925893844
C 3.64110441995872 0.51698015787206 -3.09906101077884
H 3.71443100949183 1.31788816445885 -3.86048366571195
H 4.46505302011736 0.62466192382013 -2.37376460961506
H 3.72945471085806 -0.47017315502300 -3.58703566337181
N -2.24146322517785 -0.33499290295337 1.85658132736909
N 2.65609186578770 -0.16673998338757 1.65989457302592
C -3.41832404382757 -0.85273067955650 2.64787856641997
H -3.81860720055670 -0.10379257523465 3.35915400974124
H -4.21234672144123 -1.14326107802651 1.93899245251439
H -3.09202403680208 -1.74708607805485 3.20502219393750
C 3.88189071627275 0.37890305206828 2.35077162627464
H 4.33487875305774 -0.34333640660162 3.05810318677180
H 4.62412212748606 0.64466382834284 1.57878579610150
H 3.59086320410049 1.29154022155159 2.89795232668708
H 0.35943872572094 -0.23589655163846 5.72671216950686
H -0.02597896365385 -0.57429197676543 -6.19420986810070
B 3.75014988553495 -4.94634489312812 -5.21961191643701
C 3.38868806532516 -4.41480450218488 -6.73030864975968
C 4.37153668625739 -3.77981693863401 -7.55976086302584
C 2.11686523432251 -4.66213847529477 -7.34361156266401
C 4.07835165828967 -3.33588488743191 -8.85952676146391
C 1.81592715769274 -4.22225409919537 -8.64283713477033
C 2.79392709487936 -3.54835937856172 -9.40891474355918
H 5.38394812405273 -3.62542558407732 -7.16294731679885
H 1.34803958191317 -5.20404001620089 -6.77682566449096
H 4.85268022142562 -2.83565514087870 -9.45778033809843
H 0.82305102784633 -4.41428243850415 -9.07281636225305
H 2.56558195028561 -3.21560246734388 -10.43120301300947
C 2.44653033376174 -5.10029186154240 -4.24077880754465
C 2.38270781298861 -6.12128781553985 -3.24752672896447
C 1.33280969513385 -4.21404347665080 -4.27970198976674
C 1.28064197452161 -6.27453469966045 -2.38309188431898
C 0.21954508267124 -4.35986221492914 -3.42709736601935
C 0.18376572719623 -5.39684418218552 -2.47507733871986
H 3.21461861622354 -6.83452952275651 -3.16560026910951
H 1.32538543103308 -3.40114677476924 -5.01912173127552
H 1.27004299041703 -7.09169827087598 -1.64831863733494
H -0.63743190822420 -3.67982631419740 -3.52715073630914
H -0.69031057774223 -5.53125270604476 -1.82527259607813
C 4.34609427011719 -6.39504347856788 -5.70518128233318

C 3.49066460365366 -7.52729237762144 -5.93058503298342
C 5.73551292566199 -6.57791684045418 -6.02046396858448
C 3.99511840183725 -8.77008018940238 -6.34117826620122
C 6.24670012936017 -7.81796841384112 -6.43131711597541
C 5.37955152108665 -8.92559284094366 -6.59177140440008
H 2.41156686598822 -7.42241435717430 -5.75305867685503
H 6.42256868931248 -5.72790362482666 -5.90858010014345
H 3.31712382167180 -9.62420436667494 -6.47727829401198
H 7.32043589565916 -7.93193727965079 -6.63629356901132
H 5.77642130471176 -9.89541018090486 -6.92478745195906
C 4.86498833037506 -4.03846121775824 -4.43643640602480
C 5.71114755926489 -4.61388964391692 -3.44479688461524
C 5.04308321026805 -2.64542486604268 -4.66266240105060
C 6.68638420192868 -3.86806826423672 -2.75323587737892
C 6.02475335261194 -1.88879387046238 -3.98932162894037
C 6.85535771275726 -2.49640079377183 -3.02934022000922
H 5.62110793562475 -5.68714108536329 -3.22548640202361
H 4.42190781279559 -2.14592279348025 -5.41899612170684
H 7.33731837289912 -4.36337669393154 -2.01885923070975
H 6.16480465390109 -0.82679018215155 -4.23413069244171
H 7.63549546516824 -1.91654281743206 -2.51833613929756

Acknowledgments

Firstly, I want to sincerely thank [REDACTED] for the opportunity to work in her research group. I greatly appreciate the freedom I was given to pursue my own ideas and all the discussions that provided valuable feedback. It was great learning from her and together with her about chromium(III).

I thank [REDACTED], for many helpful discussions and the swift resolving of even the most complicated crystal structures.

Special thanks go to [REDACTED], [REDACTED] and [REDACTED], for all the scientific and non-scientific brainstorming, that provided new perspectives on literally everything. I thoroughly enjoyed the time we spent together at, who knows how many conferences.

I would like to thank the *Graduate School of Excellence MAINZ* for their financial and ideological support. My research and my personal development benefited greatly from the participation in the summer school, conferences abroad as well as my three months research stay at the Université de Montréal, which would not have been possible without the generous funding.

Thanks to all my collaboration partners, who helped to tap the full potential of this project. I want to especially thank [REDACTED], [REDACTED] and [REDACTED] for the great time in Montréal and Toronto (seriously, CN towers are all over the place...).

A great thank you goes to the whole [REDACTED] group. You all contribute to the great atmosphere, that made the dark times a little less darker and more often, made research just a lot fun. To all the current and future members of the elder council, I say: don't let the young ones dance on your noses, but remember, they will one day have replace you... ;-)

[REDACTED], [REDACTED] and [REDACTED] did a great and fast job proofreading this work, thanks a lot.

■■■■, it's great to have you in the team, thank you for tolerating and staying in this, sometime somewhat testosterone ruled mob, it wouldn't be the same without you - if you ever need a mean looking "big brother", count me in... ;-)

Many thanks go also to all the students - ■■■■, ■■■■, ■■■■, ■■■■, ■■■■, ■■■■, ■■■■ and ■■■■, who worked with me during lab courses or as part of their bachelor thesis. Not only did your synthetic work help me a lot, your presence also enriched all our time in the group (as it still does in some cases).

I would also like to thank the analytical department of the chemistry institutes for the fast and accurate measurement of all mass spectra and elemental analyses I submitted during the past three and a bit years.

I want to thank all my friends, for just having a good time with all of you climbing, drinking beer or just endless discussions about non-sense. ■■■■ and ■■■■, the decision to move in together was one of the best of my life, we had greatest time together.

I thank my parents ■■■■ and ■■■■, to whom I am deeply grateful for their unquestioning support and love and I'm sorry for sometimes just being a terrible son.

■■■■, thank you for taking me as I am, tolerating my horrible mood of the last weeks and just being who you are. I can't imagine a better climbing partner than you and I'm thoroughly looking forward to the time to come together with you.

